Chimie à la surface des grains dans les régions de formation stellaire

Vianney Taquet

UNIVERSITÉ DE GRENOBLE

THÈSE

Pour obtenir le grade de

DOCTEUR DE L'UNIVERSITÉ DE GRENOBLE

Spécialité : **ASTROPHYSIQUE - PHYSIQUE & MILIEUX DILUES**

Arrêté ministérial : du 7 aout 2006

Présentée par

Vianney Taquet

Thèse dirigée par **Cecilia Ceccarelli**
et codirigée par **Claudine Kahane**

préparée au sein **de l'Institut d'Astrophysique et de Planétologie de Grenoble**
et de **l'Ecole Doctorale de Physique**

Grain surface chemistry in star-forming regions

Thèse soutenue publiquement le **26 septembre 2012**,
devant le jury composé de :

M. Eric Quirico
Professeur, Université de Grenoble (France), Président
M. Eric Herbst
Professeur, University of Virginia (USA), Rapporteur
M. Jean-Hugues Fillion
Professeur, Université Pierre et Marie Curie (Paris, France), Rapporteur
Mme Paola Caselli
Professeur, University of Leeds (UK), Examinateur
Mme Cecilia Ceccarelli
Astronome, Institut de Planétologie et d'Astrophysique de Grenoble (France), Directeur de thèse
Mme Claudine Kahane
Professeur, Université de Grenoble (France), Co-Directeur de thèse

Remerciements

Ca y est, nous y sommes, voici le moment tant redouté : l'écriture des remerciements ! Ce chapitre est peut-etre également le plus difficile à écrire car il s'agit de n'oublier personne tant j'ai de gens à remercier.

Tout d'abord, je souhaiterais commencer par remercier chaleureusement mes deux directrices de thèse Cecilia et Claudine. Ce fut un réel plaisir d'apprendre le metier de chercheur à leurs cotés. Malgrè leur emploi du temps d'enseignant-chercheur (qui vaut facilement un emploi du temps de ministre !), elles ont su trouver du temps pour passer de longues heures a discuter de chimie et de formation stellaire. Leur complementarité a vraiment joué un role primordial dans le bon déroulement de ce travail. Je me rappellerai longtemps de nos réunions où Cecilia, la tete toujours dans les étoiles, proposait des idées qui fusaient dans tous les sens tandis que Claudine essayait de garder les pieds sur Terre afin d'éviter de partir dans le décor.

Je voudrais remercier Jean-Hugues Fillion et Eric Herbst pour avoir accepté d'etre les rapporteurs de cette thèse ainsi que Paola Caselli et Eric Quirico d'avoir participé à mon Jury de thèse en tant qu'examinateurs. Les discussions que nous avons pu avoir me seront, j'en suis sur, très utiles pour la suite de mon travail.

Je tiens également à remercier un grand nombre de collègues qui m'ont beaucoup apporté durant ces trois ans. Merci à Phillip qui m'a appris tant de choses sur le monde (pas si) merveilleux de la chimie quantique, Alex pour son oreille attentive lors de mes nombreux moments de doute et pour m'avoir inculquer sa rigueur scientifique sans faille, ainsi que Roberto et Ana pour leur patience et pour leur aide dans la réduction des données interférométriques. Un grand merci également à tous les membres d'Astromol et notamment à Alex F., Pierre, Aurore, Bertrand, Laurent, et Sébastien pour leurs conseils et pour les nombreuses discussions que nous avons pu avoir. Mon travail s'est inscrit dans le projet ANR FORCOMS. J'ai donc eu la chance de rencontrer des collègues astronomes, chimistes, et spectroscopistes provenant de laboratoires de Grenoble, Toulouse, et Lille. Je tiens donc à tous les remercier et notamment Audrey, Céline, et Denis pour leurs conseils avisés et pour la relecture de certains de mes chapitres de thèse. Enfin, je tiens à remercier Valentine Wakelam, Naoki Watanabe, Guillaume Pineau des Forets, Yasuhiro Oba, Tetsuya Hama, Edith Fayolle, et Xander Tielens pour les discussions que nous avons pu avoir par e-mail ou lors de conférences. Je tiens à finir ce paragraphe par remercier différents membres du labo qui m'ont aidé dans mon travail de tous les jours et pour leur gentillesse : Valérie, Fabienne, Stéphane, et Richard.

Une thèse, c'est long, éprouvant, mais également très enrichissant. J'ai eu la chance de travailler aux cotés de collègues et d'amis extraordinaires (j'en fais peut-etre un peu trop, non ?). Un grand merci donc aux "vieux" qui m'ont supporté tant bien que mal pendant ces trois ans : Jérémy, Rémi, Fabrice, Nico, Astrid, Susana, et Jean-Yves. Et merci également aux plus jeunes qui ont la lourde tache de nous succéder : Illya, Sam, Florian, Jack, ma co-bureau Romane (l'atmosphère n'est plus la meme, sans moi, non ?), ou Julien. Encore désolé si j'oublie certains !

Last, but not least, je tiens à remercier du fond du coeur ma mère, mon père, ainsi que mon frère qui m'ont toujours poussé à faire le métier qui me faisait réver et qui ont continué à me soutenir durant ces très longues années d'études.

Le mot de la fin ira à ma femme Aurélia qui a réussi, tant bien que mal, à me supporter pendant ces trois années. Un grand merci pour son soutien, son amour, et pour avoir accepté de quitter sa vie de Chtit pour partager mon reve américain.

Acknowledgments

Here we are, this is the dreaded moment: the acknowledgments! This chapter is perhaps the most difficult chapter to write because one must not forget no one since I have so many people to thank.

First, I would like to start by deeply thanking my two thesis supervisors, Cecilia and Claudine. It was a real pleasure to learn the work of a researcher at their sides. Despite their busy schedule of teacher and researcher (which is surely as busy as a minister schedule!), they were able to find some time to spend long hours to discuss of chemistry and star formation. Their complementarity has really played a prominent role in the smooth progress of this work. I will remember many times when Cecilia, head still in the stars, proposed so many ideas going in so many directions while Claudine was trying to keep our feet on the ground.

I would like to thank Jean-Hugues Fillion and Eric Herbst for agreeing to be the referee of this thesis manuscript and Paola Caselli and Eric Quirico to be part of the referee of my thesis defence. I'm sure that the discussions we have had will be very useful for the rest of my carreer.

I also want to thank many colleagues who have help me a lot during these three years. Phillip who taught me so much about the (not so) wonderful world of quantum chemistry, Alex for his careful listening during the moments of doubt and for teaching me his famour scientific rigor, and Roberto and Ana for their patience and for their help in the reduction of interferometric data. A big thanks also to all the members of the Astromol team including Alex F. Pierre, Aurore, Bertrand, Laurent, and Sebastien for their help and for the discussions we have had. My work has been part of the ANR FORCOMS. So I had the chance to meet various astronomers, chemists, spectroscopists from laboratories of Grenoble, Toulouse and Lille. I want to thank all of them, and in particular Audrey, Celine, and Denis for their advice and for reviewing some of my thesis chapters. Finally, I would like to thank Valentine Wakelam, Naoki Watanabe, Guillaume Pineau des Forets, Yasuhiro Oba, Tetsuya Hama, Edith Fayolle, and Xander Tielens for the fruitful discussions we have had via e-mail or during conferences. I want to finish this section by thanking several members of the lab who helped me in my everyday work and for their kindness: Valerie, Fabienne Stephane, and Richard.

A thesis is a long, challenging but also very rewarding work. I had the opportunity to work alongside colleagues and wonderful friends. A special thanks to the "old" members who supported me somehow during those three years: Jérémy, Rémi, Fabrice, Nico, Astrid, Susana, JY. Thanks to the younger students who have the tricky task to succeed us: Illya, Sam, Florian, Jack, my office-mate Romane (the atmosphere is not the same without me, right?) or Julien. Again, sorry if I am forgetting someone!

Last, but not least, I want to thank from all my heart my mother, my father and my brother, who always pushed me to do the job that I've wanted to do and who have continued to support me during these long years of studies.

The last words go to my wife, Aurelia who has managed somehow to support me during these three years. I am really grateful for her support, love, and for agreeing to leave her "Chtit" life to share my american dream in the US.

Grain surface chemistry in star-forming regions

Abstract The first stages of star formation are accompanied by an evolution of the chemistry, starting from simple molecules in cold dark clouds to the detection of complex organic molecules around Class 0 protostars. Although mostly composed of gas, these clouds also contain small amounts of microscopic dust. The contribution of this dust is nevertheless important because it acts as a catalyst for the formation of key molecules seen in cold interstellar ices, such as water or methanol. These ices are believed to be the first step towards the rich chemistry seen in the warm envelope of protostars. During my thesis, I focused on this first step and I did so by taking a twofold approach.

i) Modelling. I have developed an astrochemical model coupling the chemistry in the gas phase and on the grain surfaces. This model follows the multilayer formation of interstellar ices and allows us to investigate the influence of key physical, chemical, and surface parameters, such as the grain porosity, on the chemical composition of ices via a multiparameter approach. The model has been applied to predict the chemical differentiation and the deuteration of interstellar ices. To this end, I have built up a chemical network taking into account the most recent experimental and theoretical works. I applied then the model to various cases. For example, I showed that ices are heterogeneous and their composition are sensitive to the physical conditions as well as several grain surface parameters. The high deuteration of formaldehyde, and methanol observed around low-mass protostars has been predicted by a dense ($n_H \sim 5 \times 10^6$ cm^{-3}) and fast ($\sim$ 5000 years) phase while the lower deuteration of water is predicted for typical molecular cloud conditions. The deuterium fractionation is very sensitive and can be used as a tracer of the physical conditions.

ii) Observations. I have been involved in observational projects whose goals are related to the grain surface chemical problems. I obtained the following three results. We showed an evolution of the selective deuteration with the protostar type, the [CH_2DOH]/[CH_3OD] abundance ratio decreasing with the protostar mass. Interferometric mapping of deuterated water towards low-mass protostars has allowed us to constrain a relatively high deuteration level of water in new sources. Finally, we detected several complex organic molecules in a cold prestellar core for the first time, challenging the current scenario of complex organic molecules in warm conditions.

Chimie à la surface des grains dans les régions de formation stellaire

Résumé Les premières étapes de la formation stellaire sont accompagnées d'une évolution de la chimie, à partir de molécules simples dans les nuages froids et sombres vers la détection de molécules organiques complexes autour des étoiles de Classe 0. Bien que principalement composés de gaz, ces nuages contiennent également une petite quantité de poussière microscopique. La contribution de cette poussière est toutefois importante car elle agit comme un catalyseur pour la formation de molécules clés observées dans les glaces froides interstellaires, telles que l'eau ou le méthanol. Ces glaces seraient la première étape d'une chimie riche observée dans les enveloppes tièdes des protoétoiles. Durant cette thèse, je me suis concentré sur la première étape en utilisant une double approche.

i) Modélisation. J'ai développé un modèle astrochimique couplant la chimie en phase gazeuse et à la surface des grains. Ce modèle suit la formation multicouche des glaces interstellaires et, grace à une approche multiparamètre, nous permet également d'étudier l'influence de paramètres physiques, chimiques, et de surface, tels que la porosité des grains, sur la composition chimique des glaces. Le modèle a ensuite été utilisé pour prédire la différenciation chimique et la deutération des glaces interstellaires. Ainsi, j'ai construit un réseau chimique en prenant en compte les travaux expérimentaux et théoriques les plus récents. J'ai ensuite appliqué ce modèle à différents cas. J'ai par exemple montré que les glaces sont très hétérogènes et que leurs compositions sont très sensibles aux conditions physiques ainsi qu'à différents paramètres de surface. La deutération élevée du formaldehyde et du méthanol a été prédite pour une phase dense ($n_H \sim 5 \times 10^6$ cm^{-3}) et rapide ($\sim$ 5000 ans) tandis que la deutération plus faible de l'eau est prédite pour des conditions typiques de nuages moléculaires. La deutération est très sensible et peut donc etre utilisée comme un traceur des conditions physiques.

ii) Observations. J'ai été impliqué dans différents projets observationnels dont les buts étaient reliés aux problèmes de la chimie à la surface des grains. J'ai obtenu les trois résultats suivants. Nous avons montré une évolution de la deutération sélective du méthanol avec le type de la protoétoile, le rapport d'abondance [CH_2DOH]/[CH_3OD] diminuant avec la masse de la protoétoile. Une cartographie interféromètrique de l'eau deutérée vers deux protoétoiles de faible masse nous a permis de contraindre un degré relativement élevé de deutération de l'eau dans de nouvelles sources. Finalement, nous avons détecté pour la première fois plusieurs molécules organiques complexes dans un coeur prestellaire, remettant en question le scénario actuel de formation des molécules organiques complexes dans des conditions tièdes.

Contents

II Ice formation and deuteration: Comparisons with observations

III Millimetric observations

Conclusions and Perspectives

Bibliography

Appendix

List of Figures

List of Tables

Chapter 1

Introduction

Contents

The formation of low-mass stars and planetary systems like our Solar System is accompanied by a chemical evolution, starting from simple molecules in cold molecular clouds to the chemical complexity found on the Earth. Interstellar dust plays a crucial role in the chemical complexity observed around low-mass protostars. In this chapter, I will emphasize the role of this dust on three examples which have motivated this thesis: ice formation, deuteration enhancement, and the formation of complex organic molecules.

1.1 From molecular clouds to planetary systems

1.1.1 Molecular clouds and prestellar cores

Low-mass stars like our Sun form in cold dark clouds whose sizes range from a few to 15 parsecs. They are known to show irregular and filamentary shapes, with hierarchical and fractal structures (see Table 1.1 for a summary of cloud physical properties). Clouds display embedded clumps with densities of $10^3 - 10^4$ cm^{-3} and sizes of 0.3 - 3 parsec. Inside these clouds, smaller cores have been observed, with localized increases of density induced by a slow accumulation of matter toward their center. These cold cores are believed to be the first stages of star formation because of the simultaneous presence of stars in formation and starless cores in the same regions of cold clouds (Beichman et al., 1986). They are, therefore, called prestellar cores. Their density profiles are consistent with the Bonnor-Ebert (BE) model of isothermal spheres, in which gravitation is balanced by internal thermal pressures (see Ebert, 1955; Bonnor, 1956; Bacmann et al., 2000). Figure 1.1 shows spatial structures of density, temperature, and visual extinctions of two typical isolated prestellar cores, computed by Galli et al. (2002). Prestellar cores display large densities (up to $n_H = 10^6$ cm^{-3}) and cold temperatures (down to 8 K) at their center. Studies of molecular line transitions have revealed internal velocities inside prestellar cores attributed to low rotational or inward motions. However, only 10-20% of the cores show a motion attributed to gravitational collapse (di Francesco et al., 2007).

Table 1.1: Properties of dark clouds, clumps, and cores (adapted from Bergin & Tafalla, 2007).

	Clouds	Clumps	Cores
Mass ($M_\odot$)	$10^3 - 10^4$	50 - 500	0.5 - 5
Size (pc)	2 - 15	0.3 - 3	0.03 - 0.2
Mean density (cm^{-3})	50 - 500	$10^3 - 10^4$	$10^4 - 10^5$
Velocity extent (km s^{-1})	2 - 5	0.3 - 3	0.1 - 0.3
Gas temperature (K)	10 - 30	10 - 20	8 - 12
Examples	Taurus, Oph, Musca	B213, L1709	L1544, L1498, B68
References	Cambrésy (1999)	Williams et al. (1994)	Motte et al. (1998)

1.1.2 Gravitational collapse and star formation

After $\sim 10^5$ yr, cold prestellar cores gravitationally collapse once the gravitational forces overcome the internal (thermal, magnetic, and turbulent) pressures, when the mass of the core exceeds the Bonnor-Ebert mass (Shu, 1977). The near "free-fall" collapse allows the formation of an hydrostatic embryo at the center of the core, called a protostar.

The star formation process has been divided into several phases through the study of its Spectral Energy distribution (SED) (Lada & Wilking, 1984; Adams et al., 1987; André, 1994). Figure 1.2 gives a schematic description of the star formation process and shows typical objects representative of each phase, together with their expected SED.

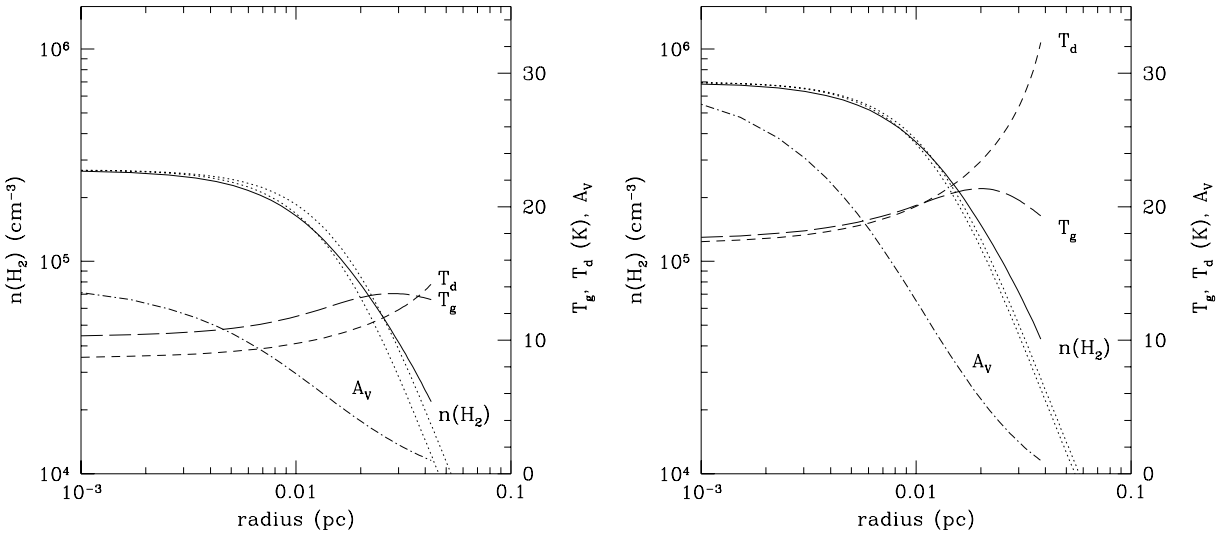

Figure 1.1: Structure of molecular hydrogen density $n(\mathrm{H_2})$, gas T_g and dust T_d temperatures, and visual extinction A_V for two typical isolated and marginally stable prestellar cores calculated by Galli et al. (2002): left) $M = M_\odot$ and exposed to the standard ISRF ($G_0 = 1$), right) $M = 1.6M_\odot$ bound by an external pressure $P_{ext} = 10^6$ K cm^{-3} and exposed to a higher radiation field ($G_0 = 100$).

1.1.2.1 Class 0 phase and hot corinos

Once the gravitational collapse of the prestellar core is onset, a central protostar forms at the center of the envelope and accretes material from its surroundings. The SED is emitted by the circumstellar envelope, following a cold (10 - 30 K) black body emission in the sub-millimetric and millimetric domains. At this stage, most of the mass is still located in the envelope. Some Class 0 protostars are also identified by a bipolar outflow triggered by the interaction of the collimated jet coming from the protostar with the surrounding envelope. The age of Class 0 protostars is about $\sim 10^4 - 10^5$ yr (Andre et al., 2000; Evans et al., 2003, 2009; Maury et al., 2011).

The newborn protostar gradually heats its surrounding envelope, affecting its physical and chemical structure. Figure 1.3 shows the physical (density, and temperature) structure of the envelope of the Class 0 protostar IRAS 16293 derived by Crimier et al. (2010b). The structure is in good agreement with the "inside-out" collapsing envelope model by Shu (1977). Density and temperatures display power-law evolutions in the envelope with high values of 10^9 cm^{-3} and 300 K at the center, respectively.

1.1.2.2 Class I to Class III

The Class I phase ($10^4 - 10^5$ yr) refers to protostars that show an evolved accretion. Most of the spherical envelope has either been accreted by the protostar or is forming a protoplanetary disk. Bipolar outflows are still observed. The SED is shifted to the mid- and far-infrared domains, indicating warmer regions. The SED includes the black body emission from the protostar and an IR excess coming from the disk.

Classical T Tauri stars, during the Class II phase ($10^5 - 3 \times 10^6$ yr), display no (or almost no) spherical envelope remanent and an evolved circumstellar disk. The SED is an addition of a black body emission from the star, starting from the visible and an IR excess coming from the circumstellar disk. The transition between Class I and Class II is characterized by the onset of deuterium fusion reactions.

The Class III phase ($3 \times 10^6 - 5 \times 10^7$ yr) corresponds to the weak-lined T Tauri stars. At this stage, the gas is dissipated in the disk and the dust is likely formed by larger grains than in

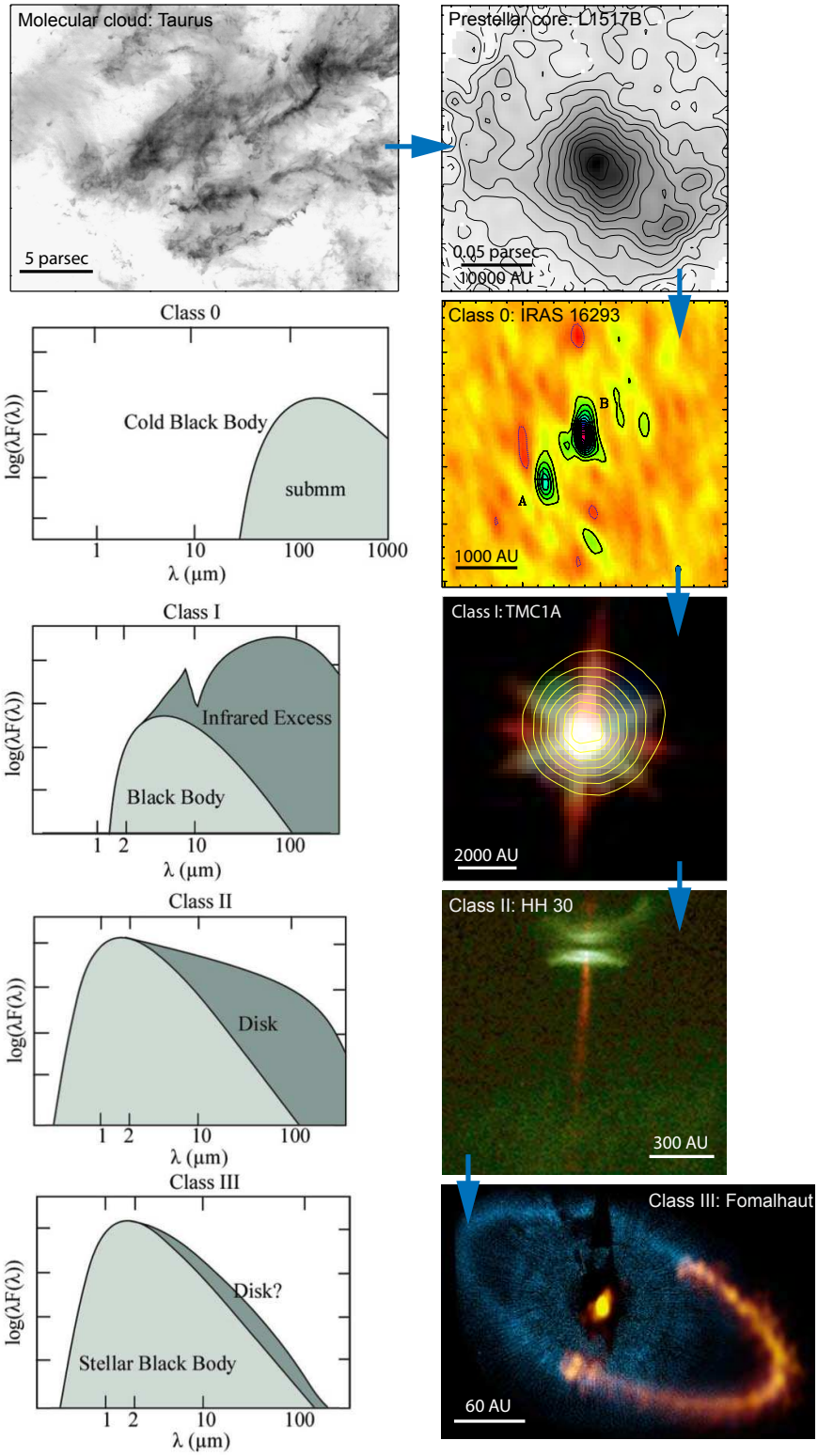

Figure 1.2: Schematic description of the different phases of star formation following the nomenclature of André (1994): i) Molecular cloud (Taurus; Goldsmith et al., 2008), ii) Starless core (L1517B; Tafalla et al., 2004), iii) Class 0 phase (IRAS 16293; Bottinelli et al., 2004b), iv) Class I phase (TMC1A; Di Francesco et al., 2008; Jørgensen et al., 2009), v) Class II phase (HH30, from the Hubble website), vi) Class III (Fomalhaut; Boley et al., 2012).

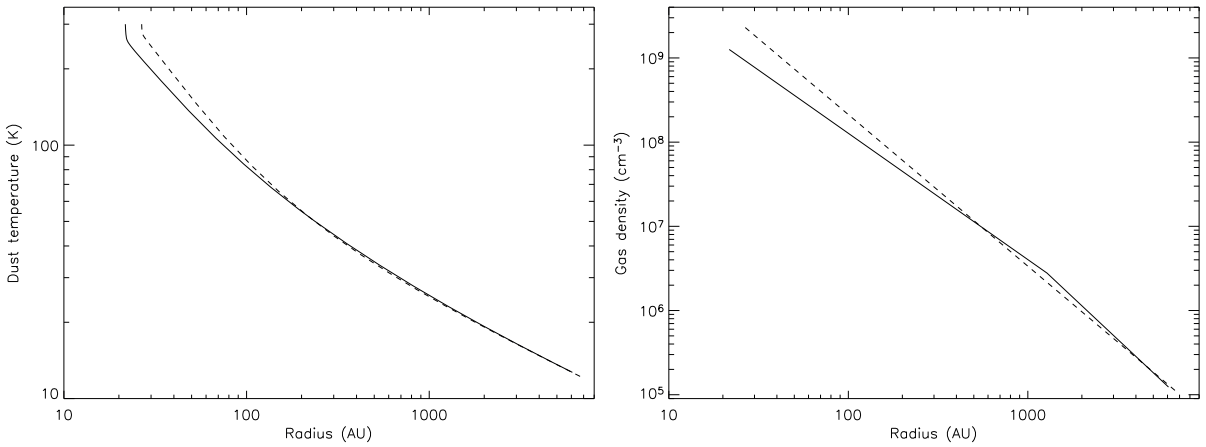

Figure 1.3: Temperature (left) and density (right) structures of the envelope around the low-mass Class 0 protostar IRAS 16293, derived by Crimier et al. (2010b).

the ISM (planetesimals forming subsequently planets and debris disks).

1.2 Star formation and chemical complexity

1.2.1 General Description

The star formation process is accompanied by an active chemistry, starting from simple molecules in dark clouds, "complex" organic molecules[1] around Class 0 protostars and in comets, while amino acids have been found in the meteorites of the Solar System. In spite of their low fraction (1% by mass, $\sim 10^{-12}$ in abundance relative to H nuclei) and their tiny size (smaller than $\sim 0.1\mu$m), interstellar dust particles play a crucial role in the formation of key species important for the chemical evolution and the deuteration process. Figure 1.4 illustrates the role of grains in the chemistry involved during the star formation process.

In dark clouds where the flux of UV photons is limited, atomic gas coming from diffuse clouds becomes gradually molecular (Frerking et al., 1982). The formation of simple molecules, such as CO, OH, or N_2, or more complex unsaturated molecules is triggered by cosmic ray-induced ion-neutral reactions (Herbst & Klemperer, 1973) while interstellar ices, mainly composed of water, start to form (step 0 of Fig. 1.4).

Dark and prestellar cores display a gradual increase of the density and a decrease of the temperature. Most heavy molecules (CO), therefore, freeze-out onto grains and form another component of interstellar ices (step 1 of Fig. 1.4). The depletion of abundant species (CO, N_2) in dense cores triggers the formation of highly-deuterated species (Roberts et al., 2003). Once the core collapses, the central protostar warms-up its surroundings inducing a gradual increase of the temperature. Light species quickly desorb at low temperatures while the bulk of interstellar ices desorb at $T \sim 100$ K (steps 2 and 3) (Ceccarelli et al., 1996). The desorption of ices induces a complex chemistry observed in the so-called hot corinos around low-mass protostars where a variety of deuterated species and complex organic molecules are observed (Cazaux et al., 2003; Parise et al., 2006).

The envelope material progressively falls-in to form a layered circumstellar disk. Species observed in the Class 0 phase can eventually freeze-out onto grains near the midplane, photodissociate or maybe form second-generation complex molecules toward the disk surface (step 4) (e.g.

[1] A complex organic molecule (COM) is defined as a molecule which contains carbon and consists of more than five atoms.

Visser et al., 2009, 2011). Circumstellar disks subsequently form planetary systems, including planets, meteorites, or comets via dust coagulation. In contrast with planets, comets and meteorites have not evolved since the formation of the Solar System and contain pristine material coming from the pre-solar nebula. Comparison of their chemical composition with interstellar material allows us to investigate the eventual molecular reprocessing during the star formation process. Observations of the chemical composition of comets suggest a similar composition as in Class 0 protostars (Bockelée-Morvan et al., 2000). However, their relative abundances tend to vary from one comet to another, implying a formation in different parts of the solar nebula (Mumma & Charnley, 2011). High isotopic fractionation of meteoritic amino acids, and in particular an enrichment of the D/H ratio, could also indicate some memory of their interstellar heritage (Pizzarello, 2011).

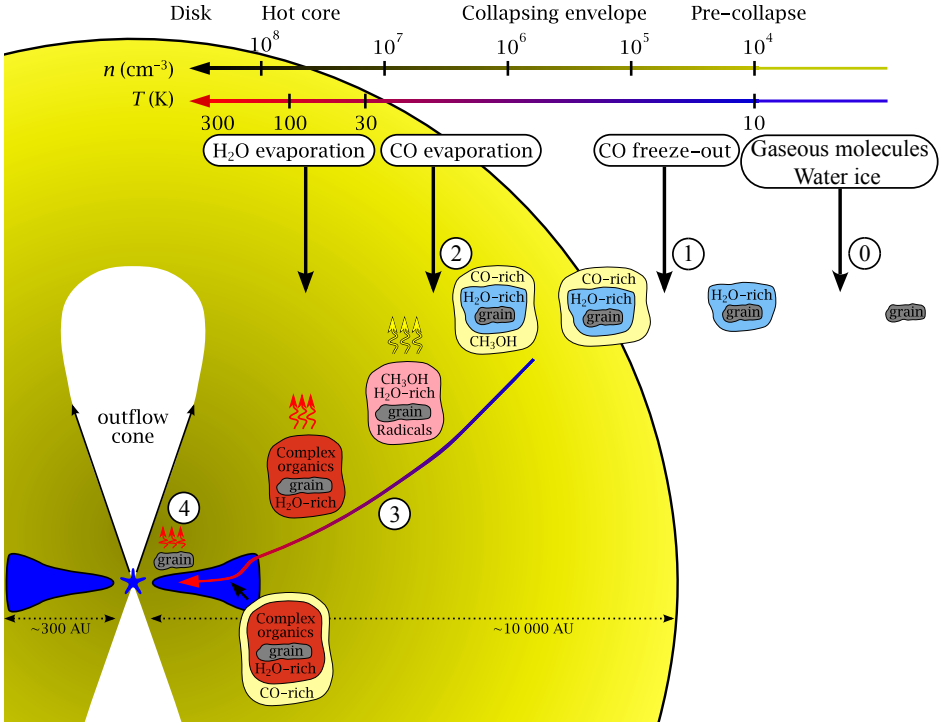

Figure 1.4: Cartoon representation of the chemical evolution involving interstellar grains during the early stages of star formation, adapted from Herbst & van Dishoeck (2009) and Visser (2009).

This section outlines the importance of interstellar dust in the chemical evolution during the early stages of star formation. I will now focus on three main items that are of particular importance for this thesis: the formation and the composition of interstellar ices, the large deuterium fractionation, and the formation of complex organic molecules. For each item, I will present the state-of-the-art observations, our current theoretical understanding, and the main limitations that motivated this work.

1.2.2 Ice formation

1.2.2.1 Observations

The chemical composition of interstellar ices can be probed through the detection of near infrared (IR) absorption bands (3 - 20 μm) in the emission of field stars. Numerous studies have been conducted toward dark clouds, dark cores, and protostellar envelopes, mainly in the Taurus and Ophiuchus clouds. They have revealed that interstellar ices are mainly composed of water (H_2O), but contain other compounds, such as carbon dioxide (CO_2), carbon monoxide (CO), or

methanol (CH_3OH) in significant quantities. IR absorption bands have also been attributed to other solid species, such as methane (CH_4), ammonia (NH_3), or XCN (e.g. Gibb et al., 2004). Table 1.2 presents the typical chemical composition of observed ices in different regions.

Visual extinction-dependent observational studies of ices and comparisons with laboratory spectra have shown that ice composition depends on the physical conditions inside molecular clouds. Interstellar water ice is observed in the Taurus molecular cloud above a visual extinction threshold of 3.2 mag (Whittet et al., 1988). The linear increase of its column density with A_V suggests that water starts to form in translucent regions (Whittet et al., 2001). This is supported by spatial mapping of water ice toward the Serpens core region by Pontoppidan et al. (2004), showing a constant abundance inside the observed region. The column density of solid CO_2 increases linearly with the column density of water ice in dark clouds (Whittet et al., 2007), suggesting that most CO_2 forms in parallel with water at low visual extinctions. Moreover, abundant CO_2:H_2O mixtures are needed to reproduce the CO_2 absorption bands toward protostars (Pontoppidan et al., 2008). The low quartile values shown in Table 1.2 suggest that the CO_2 abundance does not vary significantly with respect to water. Similarly, the small abundance deviations of NH_3, and CH_4 also suggest that these two species also form along with water.

Solid CO is also observed, but at higher visual extinctions above a threshold of $A_V > 8 - 9$ mag (Whittet et al., 2007), and is present in several ice mixtures. Pontoppidan (2006) observed a spatial increase of the pure CO ice toward the center of the Ophiuchus-F MM2 protostar while the CO:H_2O mixture remains constant with low abundances, suggesting that most CO likely depletes after the formation of water in colder and darker regions. Finally, methanol is observed above a threshold of $A_V \sim 15$ mag (Whittet et al., 2011), with abundances from less than 5 to more than 20% relative to water. Most methanol is likely formed after the formation of water and CO_2, when CO is already located in the ices. A low fraction of methanol could also be formed at lower visual extinctions but with low efficiencies, under the detection limit. This claim is supported by strong abundance variations of pure CO, CO:H_2O, and CH_3OH ices, as shown in Table 1.2, implying that CO and CH_3OH do not form with water. Figure 1.5 presents a cartoon picture depicting the ice composition deduced from observations.

Table 1.2: Abundance medians (in %), lower and upper quartile value with respect to water ice, and detection thresholds of ices and individual ice components. Table adapted from Öberg et al. (2011a) and visual extinction thresholds taken from Whittet et al. (1988, 2001, 2007, 2011).

Ice Feature	Abundance relative to H_2O			A_V Threshold
	Low Mass	High Mass	Core	(mag)
H_2O	100	100	100	3.2
CO_2	29^{35}_{22}	13^{22}_{12}	38^{41}_{32}	3.2
Pure CO_2	$2^{4}_{0.3}$	2^{2}_{1}	...	...
CO_2:H_2O	20^{23}_{15}	9^{15}_{6}	24	...
CO_2:CO	5^{7}_{4}	5^{6}_{2}	6	...
CO	38^{61}_{20}	13^{19}_{7}	31	8
Pure CO	21^{36}_{7}	3^{6}_{2}	...	...
CO:H_2O	13^{19}_{7}	10^{12}_{5}	...	...
CO:CO_2	2^{3}_{1}	$1.3^{1.6}_{0.4}$	...	...
CH_3OH	7^{12}_{5}	8^{16}_{8}	8^{10}_{7}	15
NH_3	5^{6}_{4}	16^{17}_{10}	...	...
CH_4	5^{7}_{4}	16^{17}_{10}	...	...

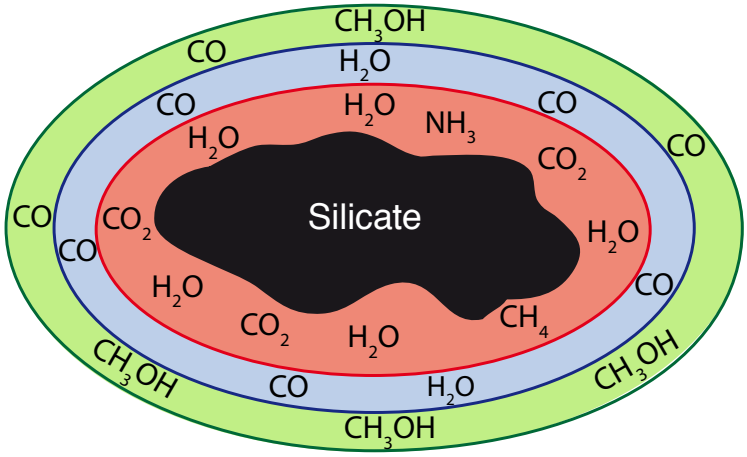

Figure 1.5: Cartoon representation of a typical interstellar ice deduced from infrared observational studies: the red component refers to the polar water-rich mixture formed at low visual extinctions, the blue component shows the CO-rich ice either mixed with CO or pure CO ice, the green ice is the outer part of grain mantles probably composed of CO and methanol.

1.2.2.2 Modelling

The basic processes of grain surface chemistry have been understood for some time (Watson, 1976). Interstellar ices are formed via the accretion of gaseous species which stay stuck to the grain surfaces at low temperatures via physisorption interactions. The mobility of light species, even at low temperatures, triggers a complex surface chemistry forming hydrogenated polar ices (water, methanol, ammonia, methane) while non-polar ices (carbon monoxide, carbon dioxide, molecular oxygen) also exist. The formation of water has been thought to occur via the sequential hydrogenation of O, O_2, and O_3 for some time (Tielens & Hagen, 1982). However, their actual formation has been demonstrated only recently on interstellar ice analogues (Miyauchi et al., 2008; Mokrane et al., 2009; Dulieu et al., 2010). The formation of formaldehyde and methanol in the solid state (i.e, on the grain/ice surfaces), via the sequential hydrogenation of CO proposed by Charnley et al. (1997), has been experimentally demonstrated by Watanabe & Kouchi (2002). Similarly, ammonia and methane are believed to form via the sequential hydrogenation of atomic N and C, respectively (see Allen & Robinson, 1977). The high abundance of solid CO_2 is more challenging because it involves reactions with activation energies between heavier species (CO, O, or OH Ruffle & Herbst, 2001b).

Numerous astrochemical models, using several numerical methods, have been built to understand the formation of ices and predict their chemical composition. The first realistic ice predictions were published by Tielens & Hagen (1982) who followed ice formation with a Monte Carlo method. With a sophisticated chemical network applied on grain surfaces, they showed that interstellar ices are mainly composed of water, whose absolute abundance weakly depends on the total density. Ices display a significant abundance of H_2CO while other compounds, such as N_2, O_2, or CO, are also present but in negligible quantities. However, the Monte-Carlo model does not provide actual time-dependent calculations of gas-grain chemistry, Hasegawa et al. (1992), therefore, adapted the rate equations to couple grain surfaces with gas phase chemistry. These authors followed the gradual formation of ices for one set of physical conditions ($n_H = 2 \times 10^4$ cm^{-3} and $T = 10$ K) with different initial abundances. Water ice is the main ice constituent while CO is progressively destroyed to form carbon dioxide, formaldehyde, and methanol. The model has been subsequently utilized to study different effects on ice chemistry.

Cosmic ray-induced desorption (Hasegawa & Herbst, 1993a), surface photochemistry (Ruffle & Herbst, 2001a), or desorption by exothermic reactions (Garrod et al., 2007) have been taken into account while Ruffle & Herbst (2001) investigated the sensitivity to physical conditions (density and temperature) of the ice composition to explain the high abundance of CO_2 in ices (20-30% relative to water). In spite of their easy and fast computations, the rate equations do not take stochastic effects, induced by the finite grain sizes, into account. Several modified-rate approaches have, therefore, been proposed to tackle this issue (Caselli et al., 1998; Garrod, 2008) while new, but more cumbersome, time-dependent Monte-Carlo methods have been developed (Charnley, 2001b; Chang et al., 2005; Vasyunin et al., 2009).

The abundances of a few main ice components (water, CO) are now quite well predicted. For example, the absolute abundance of water is found to be robust against the variation of physical conditions, and surface parameters with typical abundances of $\sim 10^{-4}$ relative to H nuclei (e.g. Ruffle & Herbst, 2001b; Nguyen et al., 2002; Hollenbach et al., 2009). The formation of CO, CO_2, H_2CO, or CH_3OH are found to vary with the physical conditions (Ruffle & Herbst, 2001b). Their formation efficiency also suffers from a lack of quantitative constraints on the activation barriers of the chemical reactions. In general, formaldehyde is found to be as abundant as methanol while most observations of H_2CO only yield upper limits that are lower than the predictions (see Ruffle & Herbst, 2001b; Öberg et al., 2011a). Astrochemists have struggled to predict the high abundance of carbon dioxide in ices. Ruffle & Herbst (2001b) succeeded to reproduce ice observations by invoking the formation from the CO + OH reaction at temperatures slightly higher than 10 K. However, these authors used activation barriers that have been subsequently adjusted to higher values (Yu et al., 2001; Talbi et al., 2006).

1.2.2.3 Current limitations

Most gas-grain astrochemical models consider fully reactive and homogeneous grain mantles. However, infrared observations have shown that ices are heterogeneous and contain several polar and non-polar components. In reality, for such cold conditions, the bulk of the mantle is mostly inert and chemical reactions mainly occur on the outermost layers, as highlighted by several experimental studies (Watanabe et al., 2003, 2004; Ioppolo et al., 2010). The microscopic Continuous-Time-Random-Walk (CTRW) model developed by Chang et al. (2005) follows the microscopic evolution of ices on a realistic grain surface. This model shows that H atoms hardly penetrate into the bulk and mantles can display a chemical differentiation (Cuppen et al., 2009). A three-phase model, based on the rate equations approach, has been developed by Hasegawa & Herbst (1993b). This method distinguishes the surface and the bulk and considers the progressive trapping of particles within the mantle but does not allow us to follow the chemical differentiation inside ice mantles. Their predicted abundances were found to be similar to the predictions of the "normal" two-phase model for stable species but this model can predict significant differences in abundances for reactive particles.

The CTRW model has also been applied to study the effect of grain surface roughness on H_2 formation (Cuppen & Herbst, 2005). Although it is now clear that grain porosity plays a strong role on surface chemistry, so far "macroscopic" models have only considered perfectly smooth and regular surfaces.

1.2.3 Extreme deuteration

1.2.3.1 Observations

Following the work by Frerking et al. (1982), CO is commonly used to trace the total column density (and, therefore, the continuum emission) in molecular clouds. However, it appears that CO does not trace the dust continuum peak seen in the center of prestellar cores (Caselli et al.,

1999; Bacmann et al., 2002; Bergin et al., 2002). In order to reproduce observations toward L1544, more than 90 % of CO needs to be removed from the gas, and up to 99 % toward the core nucleus. This depletion is likely due to the freeze-out of gaseous CO species on interstellar grain surfaces when the temperature is lower than 20 K (desorption temperature of CO, see Collings et al., 2004).

Prestellar cores are characterized by a strong increase of the deuteration level seen in several molecules, such as N_2H^+, NH_3, H_2CO, H_2S, or CH_3OH (see Ceccarelli et al., 2007). Multiply deuterated molecules have been detected in several cores, with deuterium ratios higher than 1 %, representing a deuteration enhancement by more than three orders of magnitudes relative to the cosmic D/H ratio $\sim 10^{-5}$ (Linsky, 2003). Figure 1.6, showing the deuterium fractionation of several molecules as function of the CO depletion observed in a sample of prestellar cores, clearly emphasizes the increase of the deuteration level with the CO depletion, and suggests that CO depletion is a key parameter for deuteration.

Observations toward Class 0 protostars have revealed an enrichment of deuteration of several molecules compared to the cosmic deuterium reservoir. Several isotopologues of H_2O, H_2CO, CH_3OH and H_2S have been detected in high abundances while a few other molecules also show high abundances of their singly deuterated species (NH, NH_3, $HCOOCH_3$). Figure 1.6 summarizes all the deuteration levels observed around low-mass protostars. Methanol is found to be the most enriched molecule in deuterium with $[CH_2DOH]/[CH_3OH]$ ratios of $\sim 50\%$ while formaldehyde and water, for example, show lower deuterations equal to 15% and 3%, respectively. Doubly and triply deuterated isotopologues of methanol have also been detected in significant abundances. Methanol deuteration seems to occur more efficiently on the methyl group than on the hydroxyl group, because the $[CH_2DOH]/[CH_3OD]$ ratio displays observed values between 10 and 20 around low-mass protostars (Parise et al., 2006). Unlike in pre-stellar cores, no correlation between the CO depletion and deuterium fractionation is observed, so that the deuteration process is thought to occur in the previous pre-collapse phase.

1.2.3.2 Modelling

The deuteration process of gaseous species, resulting from the lower zero-point energy (ZPE) of deuterium bonds relative to bonds with hydrogen, has been known for some time (Millar et al., 1989). However, the strong increase of deuteration levels observed in the center of prestellar cores has been explained only recently (Roberts et al., 2003). The deuterium reservoir is initially located in HD, the deuterated isotopologue of H_2, and the deuterium chemistry is onset by deuterium exchange between HD and H_3^+. Before its freeze-out, CO is the main destroyer of H_3^+ and limits the deuteration increase. The CO freeze-out in prestellar cores decreases the destruction of H_3^+, increasing the reactivity of deuteration reactions. High deuteration levels can thus be reached at high CO depletions increasing with the density. Figure 1.7 shows the evolution of the deuteration of H_3^+ isotopologues and other deuterated molecules with the CO depletion, at high density ($n_H = 2 \times 10^6$ cm^{-3}). High deuterium fractionations of H_3^+ isotopologues (H_2D^+, HD_2^+, D_3^+), N_2D^+, DCO^+ higher than 1 can be reached at $n_H > 10^6$ cm^{-3} while deuteration levels higher than 10 % are also predicted for HDCO and NH_2D (Roberts et al., 2003, 2004).

The high deuteration of species observed around Class 0 protostars likely reflects the formation and deuteration in ices. Indeed, they are thought to be mainly formed in ices and the timescale of the alteration of deuteration in the gas phase after desorption ($\sim 10^5$ yr, Charnley et al., 1997; Osamura et al., 2004) is much higher than the typical age of Class 0 protostars ($\sim 10^4$ yr, Andre et al., 2000). As their main isotopologues, it is believed that deuterated ice species are formed via addition reactions and should strongly depend on the abundance of gaseous atomic deuterium accreting on grain surfaces. Several grain surface chemical models have been developed to predict ice deuteration (Tielens, 1983; Charnley et al., 1997; Caselli et al., 2002;

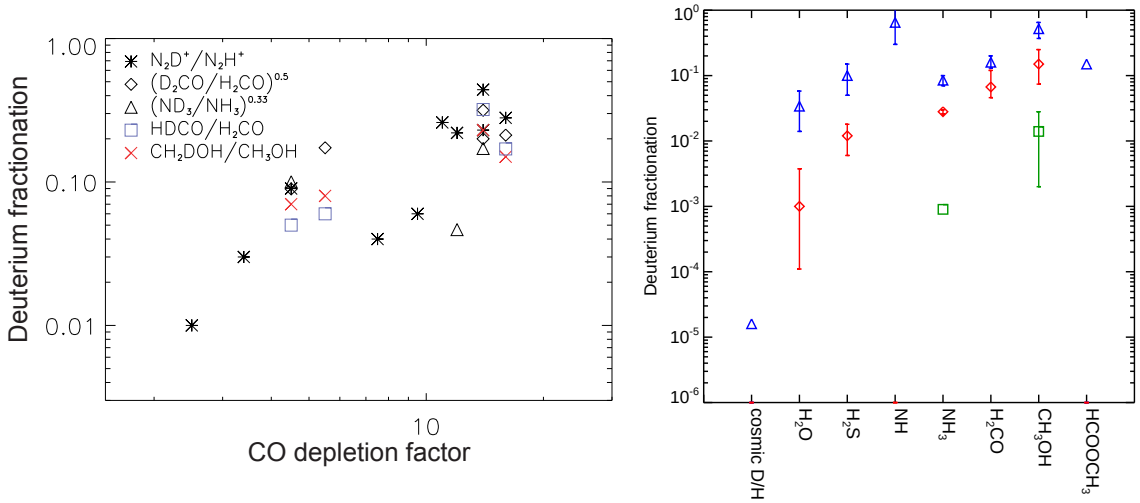

Figure 1.6: left) Deuterium fractionation as function of CO depletion factor in a sample of prestellar cores. Figure taken from Bacmann et al. (2007) and adapted from Ceccarelli et al. (2007). right) Deuterium fractionation of several molecules assumed to be partly (or mainly) formed on interstellar grain surfaces and observed around low-mass Class 0 protostars. Triangles: simple deuteration, diamonds: double deuteration, square: triple deuteration.
References. left) N_2D^+ (Crapsi et al., 2005), HDCO (Bacmann et al., 2007), D_2CO (Bacmann et al., 2003), ND_3 (Roueff et al., 2005), CH_2DOH (Bacmann et al., 2007).
right) Cosmic D/H: Linsky (2003), H_2O: Vastel et al. (2010); Coutens et al. (2012), H_2S: van Dishoeck et al. (1995); Vastel et al. (2004), NH: Bacmann et al. (2010), NH_3: van Dishoeck et al. (1995); Loinard et al. (2001); van der Tak et al. (2002), H_2CO: van Dishoeck et al. (1995); Ceccarelli et al. (1998); Loinard et al. (2001); Ceccarelli et al. (2001); Parise et al. (2006), CH_3OH: Parise et al. (2002, 2004, 2006), $HCOOCH_3$: Demyk et al. (2010)

Stantcheva & Herbst, 2003). More recent works by Caselli et al. (2002) and Stantcheva & Herbst (2003) applied several numerical approaches (modified rate equations, Monte-Carlo, and Master Equation methods) to the deuteration of water, formaldehyde, and methanol following the chemical network proposed by Charnley et al. (1997). They decreased the activation barriers of deuterated reactions between 35 and 300 K depending on the reaction, because of the different ZPE of deuterated species. They used a high atomic D/H ratio of 0.3 in the gas phase following the results by Roberts et al. (2003), allowing them to predict high deuteration levels. Most observed deuteration levels can be reproduced but they require us to assume different D/H ratio values (see Parise et al., 2006).

1.2.3.3 Current limitations

While it is now clear that CO depletion plays a major role in increasing the atomic D/H ratio in the gas phase and, therefore, on the grain surfaces (Roberts et al., 2003), a full model coupling the gas and grain chemistry that *simultaneously* reproduces the observed deuteration of the main ice components was still missing at the beginning of my thesis. As emphasised by Parise et al. (2006), the use of a constant [D]/[H] ratio assumed by Caselli et al. (2002) and Stantcheva & Herbst (2003) is i) unable to predict all of the deuterium fractionations at the same time and ii) is not necessarily correct, as water, formaldehyde and methanol may be formed on the grains at different times, and therefore at different moments of the CO freeze-out.

Moreover, the high $[CH_2DOH]/[CH_3OD]$ ratio observed by Parise et al. (2006) toward low-mass protostars is 20 times higher than the low ratio of ~ 1 found by Jacq et al. (1993) toward the high-mass hot core Orion IRc2. In the two cases, the values are not predicted by the theory since statistical models suggest a $[CH_2DOH]/[CH_3OD]$ ratio of 3 (Charnley et al., 1997). Clearly,

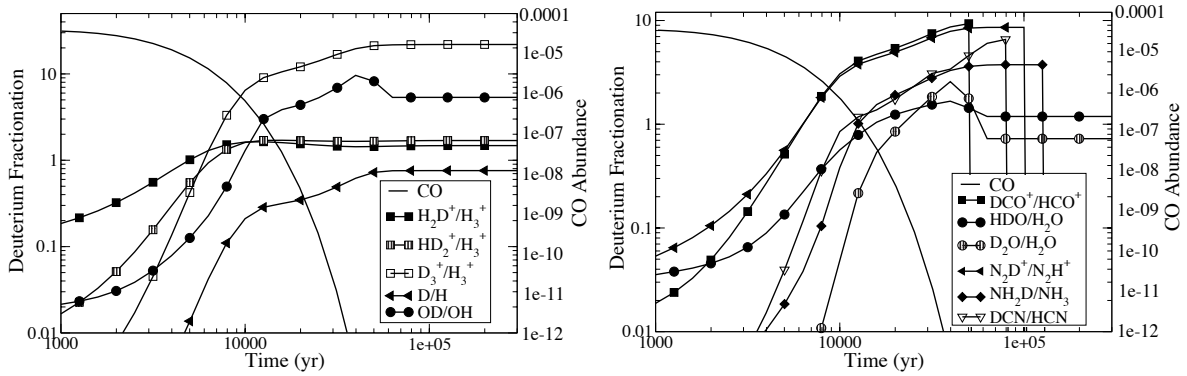

Figure 1.7: Deuterium fractionation of selected species and absolute abundance of CO as function of time, at $n_H = 2 \times 10^6$ cm^{-3}, $T = 10$ K computed by Roberts et al. (2004).

other processes than simple addition reactions of solid CO and formaldehyde contribute to the deuteration of methanol.

1.2.4 Complex Organic Molecules

1.2.4.1 Observations

It has been known for some time that the envelopes of high-mass protostars are enriched in complex organic molecules (COMs) (e.g. Blake et al., 1987; Sutton et al., 1995; Herbst & van Dishoeck, 2009).

Due to their lower luminosities, the search for COMs around low-mass protostars requires more sensitive telescopes. It has been shown more recently that low-mass protostars display a very similar chemistry as their massive counterparts, with the discovery of a hot core around IRAS 16293 (Cazaux et al., 2003). Smaller in size ($\sim$ 100 AU), they have been called *hot corinos* (Bottinelli et al., 2004a). All the typical COMs of high-mass hot cores have been found in hot corinos with similar or even higher abundances. The detected COMs are essentially O- and N-bearing species: formic acid (HCOOH), acetaldehyde (CH_3CHO), methyl formate (CH_3OCHO), dimethyl ether (CH_3OCH_3), acetic acid (CH_3COOH), methyl cyanide (CH_3CN), ethyl cyanide (C_2H_5CN), and propyne (CH_3CCH). Most species have also been detected around several other low-mass protostars by Bottinelli et al. (2004a) and Bottinelli et al. (2007). The abundances of methyl formate, formic acid, and dimethyl ether are found to be very similar as those of methanol and formaldehyde among the four low-mass protostars observed by Bottinelli et al. (2007), as shown in Table 1.3.

Table 1.3: Absolute abundances of formaldehyde and methanol relative to H nuclei and abundances of COMs relative to methanol in low-mass protostars.

Molecule	IRAS 16293	IRAS4A	IRAS4B	IRAS2A	Ref.
$X(H_2CO)$	1×10^{-7}	2×10^{-8}	3×10^{-6}	2×10^{-7}	1, 2, 3
$X(CH_3OH)$	1×10^{-7}	$< 1 \times 10^{-8}$	7×10^{-7}	3×10^{-7}	4
$X_{meth}(HCOOCH_3-A)$	1.7	> 3.4	1.6	< 2.2	5, 2, 6
$X_{meth}(HCOOH)$	0.62	> 0.46	< 1.4	< 0.4	5, 2, 6
$X_{meth}(CH_3OCH_3)$	0.10	/	0.4	0.10	5, 2, 6, 7
$X_{meth}(CH_3CN)$	0.10	> 0.16	0.13	0.029	5, 2, 6
$X_{meth}(C_2H_5CN)$	0.12	/	1.1	< 0.33	5, 2, 6

References. (1) Ceccarelli et al. (2000), (2) Bottinelli et al. (2004a), (3) Maret et al. (2004), (4) Maret et al. (2005), (5) Cazaux et al. (2003), (6) Bottinelli et al. (2007), (7) Jørgensen et al. (2005b).

Interferometric observations of COMs toward low-mass protostars by Bottinelli et al. (2004b); Kuan et al. (2004) and Jørgensen et al. (2005a) show that the emission of COMs is concentrated in compact regions consistent with the region where ices sublimate at $T > 100$ K deduced by Ceccarelli et al. (2000); Maret et al. (2004) and Crimier et al. (2010b). The spatial structure of COMs emission is very similar to that of formaldehyde and methanol, suggesting that COMs are daughter molecules of H_2CO and CH_3OH.

More recently, Requena-Torres et al. (2006) and Requena-Torres et al. (2008) have detected a variety of COMs in large abundances toward molecular clouds of the Galactic center, colder ($T_d \sim 20$ K) than hot corinos. Öberg et al. (2010) detected lines of a few COMs (methyl formate and acetaldehyde) with similar abundances as methanol, toward a cold core located near the protostar B1-b. Subsequently, Öberg et al. (2011b) have detected several lines of COMs toward two low-mass protostars. The low rotational temperature of methanol (10-15 K) and the large beam of the IRAM telescope seem to indicate that the COMs emission is distributed over a large and cold envelope.

1.2.4.2 Modelling

The detection of complex organic molecules in the warm protostar envelopes had previously been attributed to ion-neutral reactions triggered by the desorption of icy species, and in particular of methanol (Millar et al., 1991; Charnley et al., 1992; Caselli et al., 1993; Rodgers & Charnley, 2003). However, more recent experimental/theoretical works have shown that methyl formate production by ion-neutral reactions in the gas phase is not efficient enough (Horn et al., 2004) while the branching ratios of dissociative recombination reactions forming neutral COMs from ions appeared to be lower than expected (Hamberg et al., 2010).

It is now admitted that COMs, detected around low- to high-mass protostars, are formed on the warm surfaces of interstellar ices during the warm-up of protostellar envelopes. Following the chemical network proposed by Allen & Robinson (1977), Garrod & Herbst (2006) and Garrod et al. (2008) predicted an efficient formation of COMs via recombinations of radicals at temperatures between 20 and 40 K. Radicals, formed via the photodissociation of the main ice constituents start indeed to diffuse significantly at temperatures higher than 20 K while H cannot stay bound on the surface, allowing the recombination between radicals. Depending on the timescale of the warm-up phase, the absolute abundances relative to H nuclei of typical COMs show predicted values between 10^{-7} and 10^{-9}, when high initial abundances methanol and formaldehyde are considered. Figure 1.8 gives the predictions by Garrod et al. (2008) for an intermediate warm-up timescale, illustrating the different desorption temperatures of solid species and the abundances of the main ice constituents and COMs. However, if the abundance of the main icy species is lowered to values consistent with ice observations then the absolute abundance of COMs is strongly reduced and becomes lower than 10^{-8}.

The recent observations of COMs in cold regions have been attributed to ice formation and subsequent photodesorption at low temperatures. Formation of COMs via ice irradiation by UV photons and cosmic-rays has been observed in experimental works (see Gerakines et al., 1996; Bennett & Kaiser, 2007; Öberg et al., 2009c). However, no astrochemical models have been able to reproduce these observations, so far.

1.2.4.3 Current limitations

Although the abundances of the simplest COMs, such as formaldehyde (H_2CO) and methanol (CH_3OH), are now quite well predicted, astrochemical models still fail to reproduce the abundance of more complex ones, such as methyl formate ($HCOOCH_3$) believed to be formed via recombination of solid HCO and CH_3O radicals at warm temperatures ($20 < T < 40$ K).

Figure 1.9 shows the observed and the predicted methyl formate to methanol gas phase

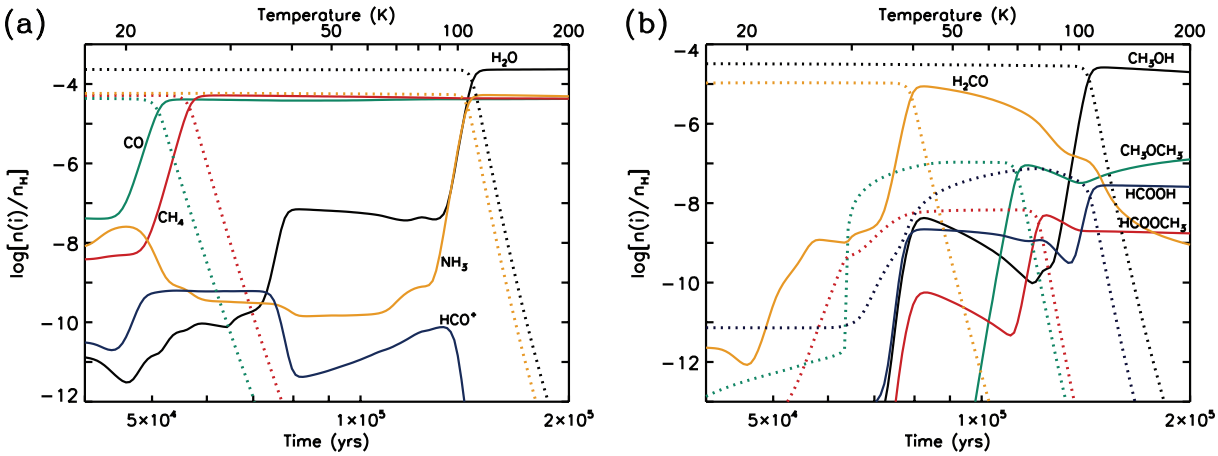

Figure 1.8: Abundances of the main ice components (left panel) and complex organic molecules (right panel) in ice mantles (solid lines) and in the gas phase (dashed lines) computed by Garrod et al. (2008).

abundance ratios as a function of the gas phase methanol abundance. We notice that while the absolute methanol abundances may suffer from the uncertainty on the source size and H_2 column density, the methanol to methyl formate abundance ratios are almost unaffected by these uncertainties. Therefore, unless the observed methanol abundance is always lower than 10^{-7}, which is certainly not the case, no model can reproduce all of the observations. Specifically, the observed ratios are roughly independent of the methanol abundance and are about 0.1 and 1 in hot cores and hot corinos respectively, regardless of the telescope used for the observations. State-of-art astrochemical models consequently underestimate the methyl formate to methanol abundance ratios and always predict a decreasing ratio with increasing methanol abundance (because methyl formate is in competition with methanol formation).

As described previously, the new generation of COMs formation models predicts that COMs are synthesized during the warm-up phase thanks to the increased mobility of radicals, formed on the grain surfaces during the previous cold phase (see Garrod & Herbst, 2006). The abundance of radicals in the mantles during the cold phase is, therefore, a key point. In these works, UV photons from cosmic rays play a major role in synthesising radicals during this phase. However, as for any model, a series of inevitable assumptions are adopted to treat the process.

The first important assumption regards the photodissociation rates on the ices. They are assumed to be the same as those in the gas phase, computed by Sternberg et al. (1987) and Gredel et al. (1989). However, there are various reasons to think that this may be a serious overestimate. First, grain surfaces could absorb part of the UV photon energy, ending up with a lower dissociation rate. Second, once the molecule is broken, if it is broken, being not in the gas phase but on a surface with almost no mobility, the photoproducts may recombine almost instantaneously. In addition, some products can even have enough energy to sublimate (see for example Andersson et al., 2006). Thus, the products of the photodissociation are likely different from those in the gas phase, and the overall formation rate of the assumed products (and radicals) may be severely lower than assumed.

A second point is related to the flux of CR induced UV photons in dense clouds. The exact value is fairly uncertain, because it largely depends on the primary cosmic ray energy spectrum, and on the grain extinction cross section, which are also uncertain (see for example Padovani et al., 2009). For example, Shen et al. (2004) have shown that the typical uncertainty on the low-energy cosmic ray spectrum leads to a variation of the UV flux of more than one order of magnitude.

Another important assumption regards the penetration of the UV photons through the bulk of the mantle. It is possible that UV photons penetrate in deep layers (see Gerakines et al., 2001)

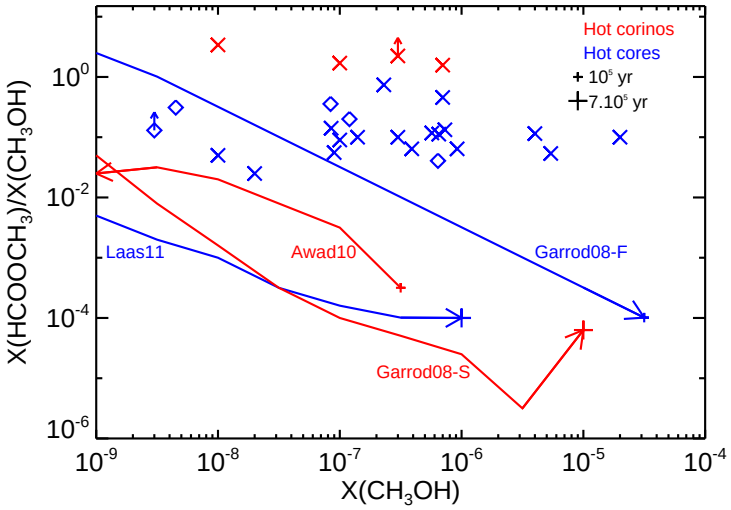

Figure 1.9: Gas phase methyl formate to methanol abundance ratio as function of the gas phase abundance of methanol. Observations of hot corinos with single-dish telescopes are represented by red crosses: NGC1333-4A by Bottinelli et al. (2004a), IRAS16293 by Cazaux et al. (2003), NGC1333-2A and -4B by Bottinelli et al. (2007). Observations of hot cores with single-dish telescopes are represented by blue crosses: G34.3+0.15 by Mehringer & Snyder (1996), SgrB2(N) and SgrB2(M) by Nummelin et al. (2000), G327.3-0.6 by Gibb et al. (2000), OMC1 by Sutton et al. (1995), G34.3+0.2, SgrB2(N), DR23(OH), W51, Orion Hot-Core by Ikeda et al. (2001), AFGL2591, G24.78, G75.78, NGC6334, NGC7538, W3(H2O), W33A by Bisschop et al. (2007). Observations of hot cores with interferometers are represented by blue diamonds: G34.3+0.15 by MacDonald et al. (1996), G19.61-0.23 by Qin et al. (2010), Orion KL, G29.96 by Beuther et al. (2009), and G47.47+0.05 by Remijan et al. (2004). The red curves report the predictions of the methyl formate to methanol abundance ratio appropriate to the hot corinos case by Garrod et al. (2008, their Fig. 6) and Awad et al. (2010, their Fig. 5). The blue curves report the predictions appropriate to the hot cores case by Garrod et al. (2008, their Fig. 4) and Laas et al. (2011, their Fig. 5). The arrows represent the direction of the time in each model and the ticks refer to timescales.

but it is likely that they affect the composition of ices in a limited number of layers(see Muñoz Caro et al., 2010). "Homogeneous" grain mantles, used in most astrochemical models, tend to overpredict the formation of radicals by UV photolysis.

1.3 Objectives of this thesis

The basic processes of grain surface chemistry occurring in the early stages of star formation start now to be quite well understood. However, as described in this introduction, several open questions still remain. In particular, the formation of heterogeneous astrophysical ices, the high deuteration degree of icy species, as well as the high abundance of complex organic molecules (COMs) remain open issues. In this thesis, I have tried to tackle these problems through the development of a new astrochemical model as well as new complementary millimetric observations. Although the initial goal of this thesis was the understanding of COMs formation, I was forced to focus myself on the theoretical formation and the deuteration of interstellar ices in the cold phase (from step 0 to step 2 in Fig. 1.4) before being able to attack the COMs formation problem. During my thesis, the model predictions have been compared with millimetric observations of protostars that are thought to reflect the composition of their precursor ices.

This manuscript is divided in three parts.

In the first part, I describe the astrochemical model that I have developed during this thesis. The modelling of grain surface chemistry was based on a carefull understanding of the physical and chemical processes on cold surfaces, described in chapter 2. In chapter 3, I describe the astro-

chemical model itself by outlining its novelties compared to previous works. This astrochemical model uses the rate equations introduced by Hasegawa et al. (1992) for a coupled gas-grain chemistry in a way that permits us to follow the ice multilayering structure. Therefore, it benefits from the advantages of the rate equation method (computer speed) and of the microscopic CTRW approach. The effect of UV photolysis on surface species is usually taken into account in astrochemical models by considering homogeneous ices and using gas phase photodissociation rates, by analogy. In our model, we incorporated the results of molecular dynamics simulations and experimental works to study the behaviour of the photoproducts after UV photodissociation on the ice surface. Laboratory experiments, numerical simulations of grain coagulation, mantle formation, and astronomical observations all demonstrate that interstellar grains are porous (Jones, 2011). The presence of pores creates traps for molecules and atoms on the grain surfaces, leading to an enhancement of reactivity on the grains. GRAINOBLE includes pores, following the treatment of Perets & Biham (2006). Some key surface chemical reactions may display activation barriers. Their reaction probabilities have usually been computed by assuming rectangular square barriers, with poorly known widths and heights. The Eckart Model was used to compute more accurate reaction probabilities of key reactions.

In the second part, I describe the model predictions and the comparisons between the theoretical results and the infrared and millimetric observations. Many parameters in the microphysics of the problem have highly uncertain values or follow distributions. Additionally, several macroscopic parameters are also either uncertain or vary depending on the astronomical object. The influence of input parameters on grain surface chemistry was investigated by running grids of models where several input parameters were varied and by computing the distributions and the standard deviations of chemical abundances and molecular fractionations. Detailed chemical networks, using new theoretical and experimental works, were first applied to the formation of ices to investigate the survival of radicals, believed to affect the subsequent formation of COMs (chapter 5). The deuteration of ices was then studied and compared to observations toward low-mass protostars to constrain the physical evolution and the formation pathways (chapters 6 and 7).

In the third part, I described several observational projects that have been carried out to answer some of the main questions highlighted previously and which will be compared to our theoretical predictions. Methanol shows a selective deuteration. Around low-mass protostars, the deuteration seems to occur on the methyl group rather than the hydroxyl group, as revealed by Parise et al. (2006) whereas Jacq et al. (1993) shows a ratio of 1 in a high-mass hot core. Further observations were performed toward two intermediate-mass and two high-mass protostars to extend the investigation of the dependence of the selective deuteration on the protostar mass (chapter 8). The water deuteration has been constrained toward only one low-mass protostar by Coutens et al. (2012), so far. We carried out new interferometric observations of HDO toward two low-mass protostars in order to evaluate its emission and to estimate the deuterium fractionation of water in other low-mass protostars (chapter 9). Several COMs have been detected in cold regions by Öberg et al. (2010) and Öberg et al. (2011b). The presence of nearby protostars suggests the formation of COMs by photolytic processes. We performed new observations toward one prestellar core, shielded from any strong UV source, to extend previous observational results which would challenge the current hypothesis of COMs formation in warm grain surfaces (chapter 10).

Part I

Modelling of interstellar grain surface chemistry

Chapter 2

Physical and chemical processes on interstellar grain surfaces

Contents

Processus physiques et chimiques à la surface des grains interstellaires

Dans ce chapitre, je passe en revue les processus physiques et chimiques survenant à la surface des grains interstellaires. Le modèle astrochimique développé durant ma thèse et décrit dans le prochain chapitre, étudie la formation des glaces interstellaires et dépend donc de plusieurs paramètres physiques et chimiques qui nécessitent d'etre correctement compris. La formation des glaces froides est un sujet brulant qui a vu un progrès considérable durant la dernière décennie grace à l'avènement de nouvelles techniques expérimentales et de calculs de chimie quantique de plus en plus puissants.

Je commence ce chapitre en résumant rapidement les conditions physiques au sein des nuages moléculaires et pertinents pour la formation des glaces, et en décrivant la composition, la taille, et la forme des grains interstellaires où les glaces se forment. Je présenterai ensuite les interactions physiques, d'un point de vue théorique, entre une particule adsorbée et une surface.

Dans les parties suivantes, je m'attarde sur les processus importants pour la formation des glaces: accrétion, mobilité, réaction, et desorption. Notre compréhension actuelle de chaque processus repose à la fois sur des travaux expérimentaux et théoriques. Je vais donc décrire chaque processus des deux points de vue en comparant leurs résultats et en accentuant leurs accords et leurs divergences.

Dans la section 2.8, je présente les différentes méthodes numériques disponibles pour étudier la chimie à la surface des grains. Les méthodes simples et rapides ne permettent généralement pas de traiter les effets stochastiques et hétérogènes induits par les petits grains poreux alors que les méthodes stochastiques plus réalistes sont plus lourds et la plupart d'entre eux ont été appliqués à des réseaux chimiques limités.

Abstract

In this chapter, I review the physical and chemical processes occurring on interstellar grain surfaces. The astrochemical model, developed during my thesis and described in the next chapter, studies the formation of interstellar ices and, therefore, depends on several physical and chemical parameters which need to be carefully understood. Over the last decade, significant progress has been made in surface chemistry, particularly in the study of cold ices, thanks to the advent of new experimental techniques and increasing powerful quantum chemistry calculations.

I will start by briefly summarizing the physical conditions within molecular clouds relevant for ice formation, and by describing the composition, size, and shape of interstellar dust particles where ices form. Then, I will present the theoretical physical interactions of adsorbed particles with a surface.

In the following sections, I will focus on the the main processes relevant for ice formation: accretion, mobility, reaction, and desorption. Our current understanding of each process relies either on laboratory or theoretical works. I will, therefore, describe each process from the two sides by comparing their results and outlining the agreements and the discrepancies.

In section 2.8, I will present the different numerical methods available to study grain surface chemistry. Easy and fast methods usually do not treat the stochastic and heterogeneous effects induced by small and porous grains whereas more exact stochastic are more cumbersome and most of them have been applied to limited chemical networks.

2.1 Physical conditions in molecular clouds

2.1.1 Structure of a cloud

As described in the previous chapter, interstellar ices are observed in cold molecular clouds and dense cores with total densities of H nuclei from $\sim 10^3$ to $\sim 10^6$ cm^{-3} and temperatures between ~ 10 and ~ 30 K.

Figure 2.1 shows typical profiles of gas and grain temperatures as well as the flux of UV photons as a function of the visual extinction A_V for a molecular cloud with a density $n_H = 10^4$ cm^{-3} irradiated by a typical interstellar radiation field ($F(\mathrm{UV}) = 2{\times}10^9$ photon cm^{-2}), computed with the Meudon PDR code (see Le Petit et al., 2006). Except at the edges of the cloud, and for most of the nearby molecular clouds, the (gas and grain) temperatures and the flux of UV photons are expected to display low values, allowing the formation of interstellar ices.

2.1.2 Interstellar grains

Our current knowledge of interstellar dust is mainly based on the wavelength-dependent dust absorption curve.

The study of the extinction curve in the infrared, visible, and UV wavelength ranges constrains the size of interstellar dust particles. The extinction saturates when the grain size becomes comparable to the wavelength. Interstellar grains, therefore, span a range of sizes. By fitting absorption spectra observed in diffuse clouds, Mathis et al. (1977) showed that the grain size distribution can be approximated by a power-law distribution: $n(a)da \propto a^{-3.5}da$ where $n(a)$ is the derivative of the density of grains having a diameter a, with a between 5×10^{-3} and 0.3 μm.

Absorption features in the extinction spectra are used to constrain the chemical composition of refractory dust. For example, the strong 9.7 and 18 μm absorption bands are attributed to amorphous silicate grains, while the 2175 Å absorption feature is attributed to graphite. Amorphous carbon is also detected via the 3.4 μm feature.

Observations (Mathis, 1996), numerical simulations (Ossenkopf, 1993; Ormel et al., 2009),

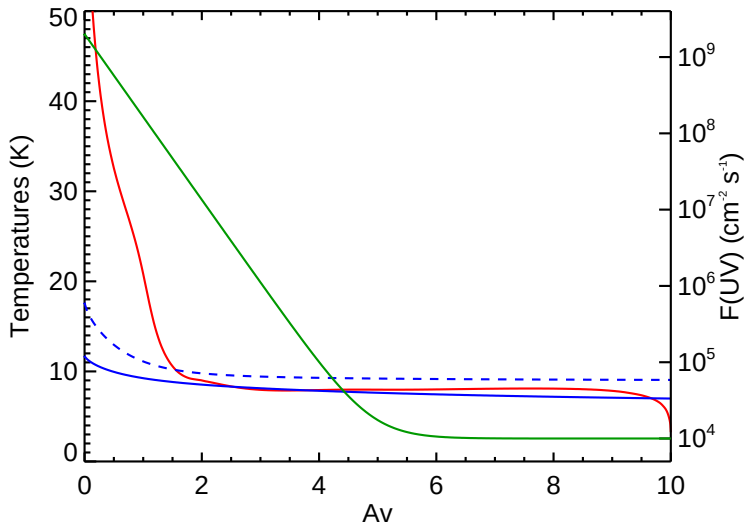

Figure 2.1: Profiles of gas (red) and grain (blue) temperatures and flux of UV photons (green) as function of the visual extinction A_V computed with the Meudon PDR code (Le Petit et al., 2006), for a typical molecular cloud ($n_H = 10^4$ cm^{-3}, $G_0 = 10$). Solid blue line refers to the temperature of big grains ($a_d = 0.1\mu$m) while dashed blue line represents the temperature of small grains ($a_d = 5 \times 10^{-3}\mu$m).

and analyses of Solar System bodies have provided the evidence that interstellar grain particles have highly fluffy and porous structures. Furthermore, it is believed that dust coagulation, increasing with the total density, induces an increase of the grain sizes, especially when they are covered by ices (Ormel et al., 2009). Prestellar cores are, therefore, believed to display more narrow grain size distributions. Astrochemical models generally use constant grain sizes, at around 0.1 μm (see for example Tielens & Hagen, 1982; Hasegawa et al., 1992).

2.2 Physical interactions on grain surfaces

Gas phase particles approaching a surface can be bonded either via a van der Waals interaction (physisorption) at large distances or via an interaction in which a chemical bond is formed (chemisorption) at shorter scales (see Tielens & Allamandola, 1987; Kolasinski, 2002; Cazaux & Tielens, 2004; Tielens, 2005).

At long distances, physisorption is due to weak van der Waals-London or electric field-dipole forces with energies of approximately 0.01 eV. The attractive forces are only due to mutually induced dipole moments between the adsorbed species and the surface particle. Therefore, no charge exchanges are involved for this interaction. Physisorbed species do not experience strong directional interactions. Their interaction with the surface do not show strong variations and they are as strong as the interactions with other physisorbed particles.

Chemisorption leads to the formation of chemical bonds, which have higher energies, of a few eV. Unlike physisorption, chemisorption induces charge exchange between the accreted species and the neighbouring surface particle. Electrons responsible for the bonding move in orbitals between surface particles and accreted species, leading to the formation of a covalent bond or possibly to a ionic bond. Therefore, chemical bonds are highly directional. Adsorbate species undergoing chemisorption stick at specific sites and exhibit binding interactions that depend strongly on their exact position and orientation relative to the substrate.

Figure 2.2 summarizes the two interactions by showing the interaction energy profile between an adsorbate and the surface. A gas phase species approaching the surface falls in a first physisorbed potential well at large distances. To undergo chemisorption, the accreted species must

overcome a energy barrier to fall in the second chemisorbed potential well, deeper in energy. Note that the interaction energy not only depends on the distance to the surface but also on the location on the surface. A perfect regular lattice (such as a perfect crystal) will show a regular variation of the potential energy while a disordered material (such as an interstellar grain surface) may show a variation in the potential well and the width of energy barriers.

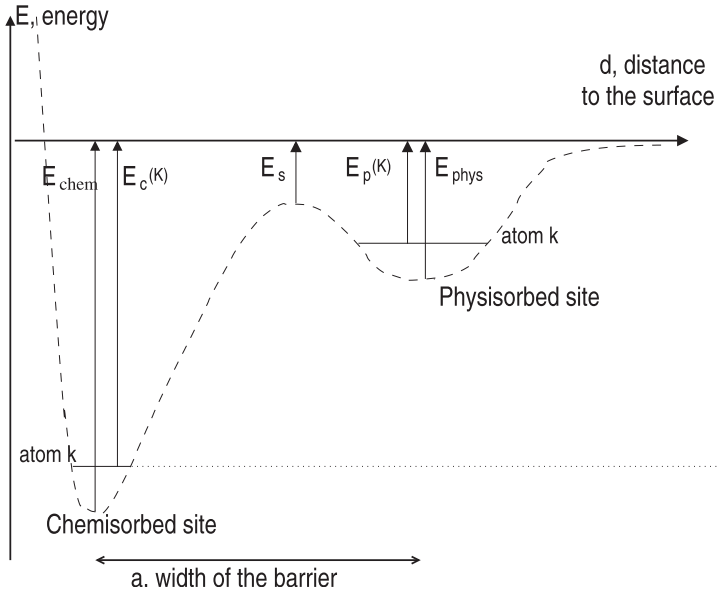

Figure 2.2: The interactions between an adsorbate and a grain surface as a function of the distance to the surface. E_{phys} refers to the binding energy via physisorption while E_{chem} stands for the binding energy via chemisorption. Figure taken from Cazaux & Tielens (2004).

In molecular clouds, chemisorption is relevant only for H_2 formation on refractory bare grain surfaces. As shown by Cazaux & Tielens (2004) or Cuppen et al. (2010b), the high recombination efficiency of H atoms (up to 1 at cold temperatures) is due to the possibility of forming chemical interactions. Chemisorbed sites on bare grain surfaces are then quickly covered by a strongly bonded layer of ice on which species experience only physisorption. Thereafter, ices will form only via physisorption.

2.3 Accretion on interstellar grains

A gas-phase particle i accretes onto an interstellar grain surface with a rate (in s^{-1}), given by

$$K_{acc}(i) = S(T_g, T_d)\sigma_d(a_d)v(i)n_d(a_d) \tag{2.1}$$

where T_g and T_d are the gas and grain temperatures, respectively, $S(T_g, T_d)$ is the sticking coefficient of the particle i, $\sigma_d(a_d)$ is the cross section of the grain which is function of the grain size a_d, $v(i)$ is the thermal velocity of species i, and $n_d(a_d)$ is the density of the grain.

Comparisons between the observed absorption 3 μm band of water and laboratory experiments have shown that grain mantles are mainly composed of amorphous solid water (ASW) (Smith et al., 1989). Moreover, high-density ASW (ρ = 1.1 g cm^{-3}) is found when the ice is formed at temperatures lower than 30 K (Jenniskens et al., 1995). Thus, sticking coefficients and binding energies of adsorbed species need to be applied on ASW ice.

2.3.1 Sticking coefficient

The sticking coefficient of a gas phase species approaching a grain surface depends mainly on the ratio between its translational energy and its binding energy, and the transfer efficiency of its excess kinetic energy to the surface. Therefore, the sticking coefficient tends to increase with the species mass.

Quantitative values for sticking coefficients of gas phase H and H_2 particles on crystalline and ASW ices have been deduced via Molecular Dynamics (MD) simulations (Al-Halabi et al., 2002; Hornekær et al., 2005; Al-Halabi & van Dishoeck, 2007) and experimental works (Manicò et al., 2001; Hornekær et al., 2003, 2005). MD simulations show that the sticking coefficient decreases with both incident energy E_i and surface temperature T_d. Figure 2.3 presents the sticking coefficient P_s of H atoms on ASW and crystalline ices as a function of the incident energy E_i at 10 K (taken from Al-Halabi & van Dishoeck, 2007). It is seen that P_s strongly decreases with E_i from unity to ~ 0 at $E_i > 500$ K while the structure of water ice does not show significant influence on P_s. For an effective collision energy of about 80 K, computed by Al-Halabi & van Dishoeck (2007), the sticking coefficient is about 0.8. The sticking coefficient of H_2 deduced by Hornekær et al. (2005) shows higher values, close to unity at $T_d = 10$ K and 0.8 at $T_d = 90$ K, for a similar incident energy of 110 K.

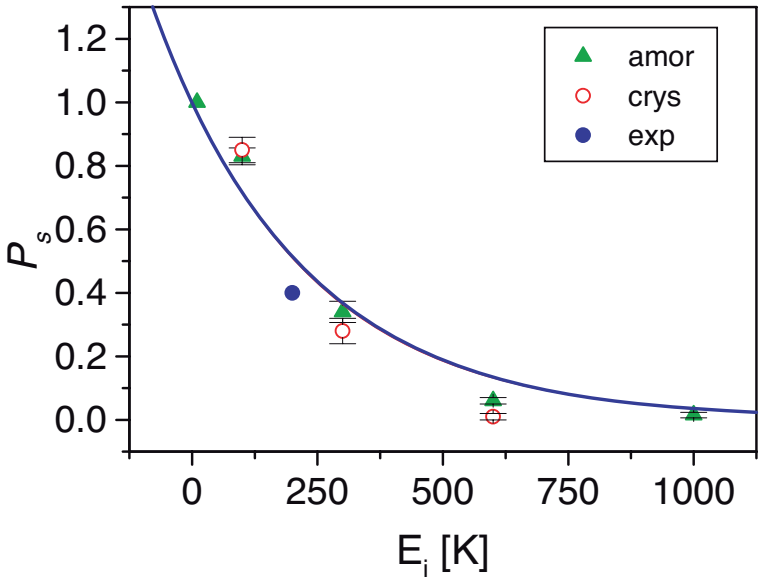

Figure 2.3: Adsorption probability P_s of gas phase H atoms on ASW and crystalline ices as function of the incident energy E_i. Green triangles show MD simulations relative to ASW ice by Al-Halabi & van Dishoeck (2007). Red circles refer to MD simulations relative to crystalline ice by Al-Halabi et al. (2002). The blue circle stands for the experimental value deduced by Manicò et al. (2001). Figure taken from Al-Halabi & van Dishoeck (2007).

Tielens (2005) estimated the sticking coefficient of H atoms on grain surfaces, considering incident energies relevant to cold conditions, as follows:

$$S(T_g, T_d) = \left(1 + 4 \times 10^{-2}(T_g + T_d)^{1/2} + 2 \times 10^{-3} T_g + 8 \times 10^{-6} T^2\right)^{-1} \tag{2.2}$$

The sticking coefficient here decreases with the temperature, from 0.8 at 10 K to 0.5 at 100 K.

To our knowledge, the most comprehensive experimental study of the sticking coefficient has been carried out by Matar et al. (2010). These authors measured the sticking coefficients of H_2, and D_2 on non-porous ASW ices as a function of the beam temperature via a statistic modelling of their experiments. Moreover, they have been able to estimate the thermal sticking coefficient

of H, D, H_2, HD, and D_2 via a simple expression:

$$S(T) = S_0 \frac{1 + \beta T/T_0}{(1 + T/T_0)^\beta} \tag{2.3}$$

where β is equal to 2.5, while S_0 and T_0 are function of the considered species ($S_0 = 1$ for H and D and about 0.8 for H_2, HD, and D_2). With this expression, the sticking coefficient is equal to 0.95 at 10 K and to 0.5 at 100 K.

The behaviour of heavier particles on astrophysically relevant ices have also been studied theoretically (Zhang & Buch, 1990; Buch, 1990, 1992; Takahashi & Williams, 2000; Al-Halabi et al., 2004) and experimentally (Collings et al., 2003b; Bisschop et al., 2006). These works suggest a high sticking coefficient, close to unity, in cold conditions. Indeed, Zhang & Buch (1990) and Al-Halabi et al. (2004) found a sticking coefficient of water and CO particles on ASW ices close to 1 with molecular dynamics simulations. By measuring the gas load reaching their mass spectrometer, Bisschop et al. (2006) deduced a lower limit to the sticking coefficient of CO and N_2 relative to CO and N_2 ices at 14 K. In the three cases ($CO_g \rightarrow CO_{ice}$, $N_2 \rightarrow N_{2,ice}$, $N_2 \rightarrow CO_{ice}$), the sticking coefficient is higher than 0.85. Therefore, it can be reasonably considered that the sticking coefficient of heavier molecules remains close to unity.

2.3.2 Binding energies

2.3.2.1 Light species

It is believed that most solid molecules observed in interstellar ices are formed thanks to the mobility of light particles (H, D, H_2, HD, D_2) on the surface. Therefore, one needs to pay great attention to the behaviour of these volatile species on ices.

Once light particles stick onto the ice, they show a distribution of their binding energies of physisorption depending on the ice properties, the adsorption conditions and the coverage of the accreted particles. MD simulations and experimental TPD works have been performed in order to constrain these effects on the binding energy distribution.

Perets et al. (2005) have experimentally highlighted the influence of the ice density on the HD and D_2 binding energies. Molecules adsorbed on low-density amorphous ices (LDI) desorb following 3 desorption peaks which are at lower temperatures than the only observed desorption peak of molecules evaporating from a high-density amorphous ice (HDI). This suggests lower binding energies on LDI than on HDI ices. By depositing D_2 on ASW, Hornekær et al. (2005) have shown that D_2 is more efficiently bound to porous surfaces. Furthermore, binding energies follow broad distributions between 300 and 500 K and between 400 and 600 K for non-porous and porous ASW ices, respectively. More recently, Fillion et al. (2009) qualitatively confirmed this result. Although the energy distributions are somehow different, these authors showed that D_2 is more efficiently bound with more porous ASW ices than with compact ices. Moreover, they showed that the binding energy distribution tends to increase with the thickness of the porous substrate. Amiaud et al. (2006) studied the link between the binding energy distribution of D_2 with its coverage on a porous ASW ice and with the ice temperature. In particular, their TPD showed a decrease of the D_2 desorption peak with the relative coverage suggesting that the D_2 binding energy decreases with D_2 coverage, from $\sim$ 700 K to $\sim$ 350 K while distributions broaden. They also showed that cold ices (10 K) are able to contain more D_2 species with low binding energies ($\sim$ 400 K) while warmer ices ($>$ 20 K) only contain a low fraction of D_2 which are trapped into the ice pores with high E_b ($\sim$ 900 K).

The experimental results have been confirmed by theoretical MD calculations. For example, Hornekær et al. (2005) and Al-Halabi & van Dishoeck (2007) found that the binding energy distributions are essentially function of the interactions with other surfaces particles surrounding the adsorbed species. As seen in Figure 2.4, the binding energy of H shows a broader and a higher

distribution on porous amorphous water ice than on a more structured crystalline ice, induced by the irregular shape of the surface. Ice density also has a strong importance since adsorbed species will interact more efficiently with a dense ice than with a sparse ice. Finally, H_2 coverage plays a key role in the binding energy of light species with the surface because interactions with an H_2 molecule are much weaker than with water. Pierre et al. (1985) theoretically estimated the binding energy of H, D on perfect quantum crystals of H_2, and D_2 by solving the three-dimensional Schrödinger equation. Depending on the isotopic effect, the structure of the crystal, or the potential used to describe the interaction between the adatom and the atoms of the substrate, the binding energy varies between 25 and 50 K. Therefore, we can argue that the binding energy of light atoms (H, D) on a H_2 substrate is approximately 10 times smaller than with water.

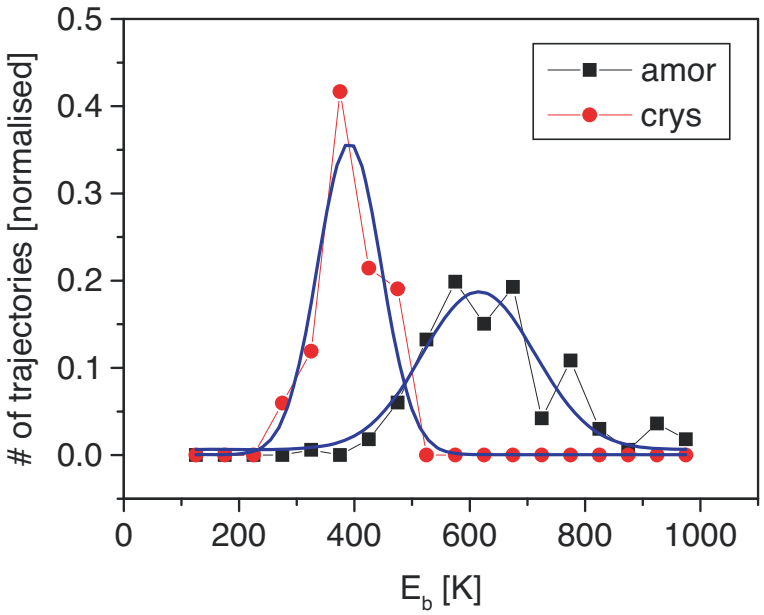

Figure 2.4: Binding energy distribution of H atoms on ASW (black) and crystalline (red) ices computed with MD simulations by Al-Halabi et al. (2004) and Al-Halabi & van Dishoeck (2007).

2.3.2.2 Heavy species

Binding energies relative to water ice of several key species for the formation of interstellar ices have been estimated theoretically and experimentally via molecular beam studies, diffusion experiments in low-temperature matrices, or Temperature Programmed Desorption (TPD). Table 2.1 lists the binding energies of selected species.

Binding energies of C, N, and O atoms relative to water have been estimated to be greater than 800 K by Watson (1976), based on pioneer experimental works. However to our knowledge, more accurate values have not been measured so far, except for atomic O who binding energy with respect to a graphitic surface has been computed by Bergeron et al. (2008) giving a value of $\sim$ 1400 K.

Molecules show higher binding energies than atoms, induced by their higher mass and the formation of new types of interactions. The high abundance of water allows the formation of hydrogen bonds in the ice. The formation of a hydrogen bond requires i) a donor group constituted by an electronegative atom (O, N, F) and a hydrogen atom bound by a covalent bond, ii) an acceptor, namely an electronegative atom which has a pair of free electrons. A H_2O molecule is generally bound with water ice via four hydrogen bonds. By measuring the evaporation rate of amorphous water ice at 150 K, Speedy et al. (1996) and Fraser et al. (2001)

deduced a binding energy of water relative to ASW of ~ 5700 K. By assuming that the binding energy of water is two times the binding energy of OH (which allows the formation of two hydrogen bonds), the binding energy of OH is estimated to be ~ 2850 K.

Using a Temperature Programmed Desorption technique, Collings et al. (2004) performed a systematic study of the thermal desorption characteristics of 16 astrophysically relevant molecules. By fitting their results with a kinetic model, they derived the binding energies whose values, presented in Table 2.1, were published by Garrod & Herbst (2006). We distinguish three types of molecules: i) the volatile CO-like molecules (CO, O_2, N_2, CH_4) starting to desorb at low temperatures but showing several desorption peaks induced by their mixing with water ice, ii) the water-like molecules (NH_3, CH_3OH, HCOOH) which have a desorption behaviour similar to that of water, since they interact with water ice via hydrogen bonds and, therefore, show similar E_b values, iii) intermediate species (H_2S, SO_2, CH_3CN) which display intermediate desorption characteristics between the CO-like and water-like species. The binding energy of CO_2 relative to ASW has been evaluated by Sandford & Allamandola (1990) and can be considered as an intermediate species.

Table 2.1: List of selected species and binding energies relative to amorphous solid water ice.

Species	E_b(water ice) (K)
H	400 - 800 [a]
D	400 - 800 [a]
H_2	400 - 800 [a]
HD	400 - 800 [a]
D_2	400 - 800 [a]
C	800 [b]
N	800 [b]
O	800 [b]
CO	1150 [c]
CO_2	2690 [d]
O_2	1000 [c]
O_3	1800 [e]
N_2	1000 [c]
CH_4	1300 [c]
NH_3	3000 [c]
OH	2820 [g]
H_2O	5640 [g]
H_2O_2	5640 [g]
H_2CO	2050 [f]
CH_3OH	5530 [c]

References. [a] Hornekær et al. (2005); Al-Halabi & van Dishoeck (2007); [b] Tielens & Allamandola (1987); [c] Collings et al. (2004); [d] Sandford & Allamandola (1990); [e]: Cuppen & Herbst (2007); [f] Garrod & Herbst (2006); [g] Speedy et al. (1996)

The binding energies of species which have not been measured so far are typically evaluated by adding the binding energies of their constituent parts (see Cuppen & Herbst, 2007).

2.3.2.3 Deuterated species

It is believed that deuterated species are more attractively bound to ices than their main isotopologues. Indeed, their higher mass produce a lower zero-point energy and, therefore, a higher binding energy (Tielens, 1983). Tielens (1983) estimated a difference in binding energy between

H and D of 30 % (350 K and 450 K respectively). However, the differences of binding energy between H, H_2 and their deuterated counterparts seem to be lower even if they still remain poorly constrained. Experiments by Perets et al. (2005) and Kristensen et al. (2011) have both shown that distribution peaks of the H_2, HD, and D_2 binding energies are very close (less than 5 meV $\sim$ 60 K). These differences remain much smaller than the typical full-width-at-half-maximum (FWHM) of binding energy distributions shown by MD simulations ($\sim$ 195 K for an amorphous ice, Al-Halabi & van Dishoeck, 2007). Jing et al. (2011) succeeded to deduce the binding energy of HDO and D_2O via TPD spectra and showed that the binding energy difference between the two molecules is only 2.5 % which is lower than the uncertainties.

2.4 Diffusion and mobility

2.4.1 Thermal and tunnelling mobilities

Adsorbed species that stick on grain surfaces can move, or diffuse, along the surface mainly via two mechanisms: i) thermal hopping over the energy barrier, ii) quantum mechanical tunnelling through the energy barrier.

All species experience diffusion via thermal hopping. The hopping rate from site to site is essentially function of the energy against diffusion E_d, and the surface temperature T_d

$$K_{hop} = \nu_0 \exp\left(-\frac{E_d}{kT_d}\right) \tag{2.4}$$

where ν_0 is the vibrational frequency of the adsorbed species along the surface. Tielens & Allamandola (1987) estimated the value of ν_0 by considering a symmetric harmonic potential given by Landau & Lifshitz (1960)

$$\nu_0 = \sqrt{\frac{2E_b}{(\pi d_s)^2 m}} \tag{2.5}$$

where E_b is the binding energy between the adsorbate and the substrate, m is the mass of the adsorbate, and d_s is the distance between two sites. A hydrogen atom (E_b = 500 K and $m = m_p$) shows a vibrational frequency of 3.5×10^{12} s^{-1} while ν_0 of a CO molecule (E_b = 1150 K and $m = 28m_p$) is equal to 1.9×10^{11} s^{-1}. d_s (or the number density of surface sites N_s) has been evaluated by Jenniskens et al. (1995) to be 3.1 Å ($N_s = 10^{15}$ cm^{-2}) for a high-density ASW ice, representative of interstellar ices. However, d_s depends on the structure of the surface and its chemical composition, and can vary within a few Å. Biham et al. (2001) deduced a surface density of sites s of $5 \cdot 10^{15}$ cm^{-2} (d_s = 1.4 Å) for an amorphous carbon surface and of $2 \cdot 10^{14}$ cm^{-2} (d_s = 7 Å) for an olivine surface from experiments by Pirronello et al. (1999).

It is believed that light particles can also diffuse via quantum mechanical tunnelling through the diffusion energy barrier. The tunnelling rate mostly depends on the mass of the adsorbed species as well as the width and the height of the barrier. Diffusion rate via quantum tunnelling is generally considered by assuming a probability of tunnelling through a rectangular barrier with height E_d and width a. In this case, the diffusion rate is given by

$$K_{tun} = \nu_0 \exp\left(-\frac{2a}{\hbar}\sqrt{2mE_d}\right) \tag{2.6}$$

However, the width of the barrier against diffusion is poorly constrained. In several grain surface chemical models, a width a = 1 Å is assumed, which represents a much thinner barrier than the actual distance between two sites of 3 Å. Estimating the diffusion rate via quantum tunnelling requires a knowledge of the energy barrier profile on astrophysically relevant surfaces.

Experimental works aiming at studying the formation of H_2 via H recombinations on astrophysically relevant surfaces (olivine, amorphous carbon, and ASW ices) have shown that molecular hydrogen is mostly formed during the heat pulse. This suggests that atomic hydrogen starts to diffuse significantly along the surface at temperatures higher than 9 K (Pirronello et al., 1997b,a, 1999; Katz et al., 1999; Perets et al., 2005). These experimental results, therefore, show that mobility via quantum tunnelling between physisorbed sites on realistic surfaces is not as important as it was calculated by Hollenbach & Salpeter (Hollenbach & Salpeter, 1970; Hollenbach & Salpeter, 1971). These experimental works confirmed theoretical calculations by Smoluchowski (1983) who studied the tunnelling diffusion for a non-periodic amorphous structure. This author showed that an amorphous structure decreases the tunnelling rate compared to a crystalline ice, essentially because of the large width of energy barriers (see also Cazaux & Tielens, 2004).

2.4.2 Diffusion energy to binding energy ratio

The energy barrier to diffusion, or diffusion energy, E_d is believed to follow a distribution, as for binding energies. Indeed, it varies considerably along the surface due to the irregular nature of real surfaces which show defects, steps, or irregularities. Figure 2.5 shows a schematic view of the influence of surface irregularity on the evolution of E_d. A perfectly smooth surface would display a regular evolution of energy whereas holes and steps generate increases in E_b.

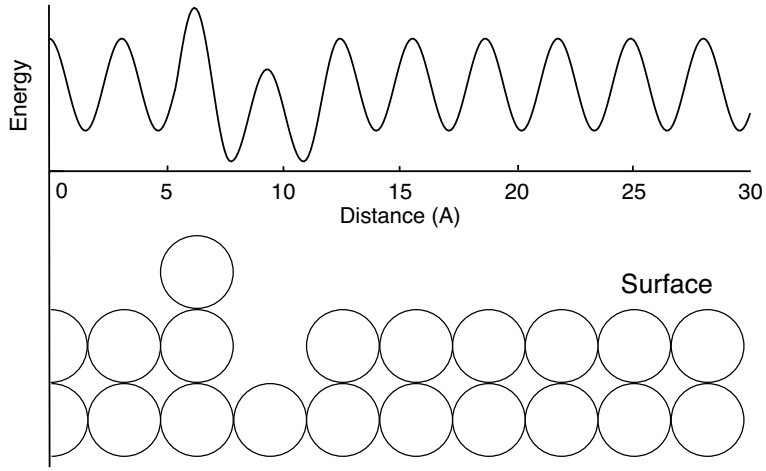

Figure 2.5: Evolution of the energy barrier between physisorbed sites. A perfectly regular surface induces a regular evolution of the energy while an irregularity in the surface increases the energy barrier between sites.

Theoretical calculations of barriers to diffusion for physical adsorption E_d on perfectly smooth surfaces have been carried out by Jaycock & Parfitt (1986). They showed that E_d is typically about 30 % of the binding energy E_b. However, “real" irregular surfaces tend to increase this ratio (Ehrlich & Hudda, 1966). Accordingly, several experimental studies have been carried out to constrain the diffusion barrier on astrophysically relevant surfaces. By fitting the experimental formation of molecular hydrogen on refractory bare surfaces and on amorphous water ices with a rate equation model, Katz et al. (1999) and Perets et al. (2005) found high E_d/E_b ratios (0.77 and $\sim$ 0.85 respectively). However, Collings et al. (2003a), Ulbricht et al. (2002), and Matar et al. (2008) estimated lower energy ratios (of about 0.5) for CO and D on water ice, and for atomic oxygen on carbon nanotubes. Clearly, the energy E_d/E_b ratio is highly uncertain and strongly depends on the composition and the structure of the substrate.

2.4.3 Bulk-diffusion

It is possible that light particles penetrate within ices, via the so-called bulk-diffusion. Again, the bulk-diffusion rate depends on ice morphology and composition. Bulk-diffusion is favoured compared to surface-diffusion in porous and amorphous low-density ices which allow the formation of cracks. However, estimating the bulk-diffusion rate is not an easy task. Several experimental works attempted to measure the penetration depth of H atoms into astrophysically relevant ices by measuring the influence of ice thickness on the formation of several molecules.

The Watanabe's group (Hokkaido University, Japan) has extensively studied the formation of formaldehyde and methanol occurring via hydrogenation reactions of solid CO (see next section for more details about the chemical network). In particular, they conducted experiments in which solid CO is irradiated by H atoms for a sample of temperatures, ice thicknesses and ice chemical compositions in order to constrain the dependence of various parameters on the chemical reactions. Watanabe et al. (2003) and Watanabe et al. (2004) showed that the saturation of solid CO consumption $\Delta N_f(\mathrm{CO})/N_i(\mathrm{CO})$ decreases with ice thickness, either for a pure solid CO ice or for a H_2O:CO mixture. Thin ices (< 5 monolayers) show a high CO saturation value of about 70 % at 12 K while this value dramatically decreases at higher thicknesses. These experiments suggest that CO hydrogenation occurs only in a few monolayers (ML) from the surface and a very low fraction of H atoms are able to react with deeply buried CO molecules. Watanabe et al. (2004) also observed an increase of the saturation value between 8 and 12 K, implying that the bulk-diffusion rate increases with the temperature. Furthermore, the bulk-diffusion seems to depend on the chemical composition of ice. Mixed H_2O:CO ices show lower CO saturation values, by a factor of two, and it appears that H atoms can diffuse into 1.5 MLs of pure H_2CO ice. Finally, no formation of formaldehyde and methanol was observed when water ice was deposited onto a pure CO ice, suggesting that H atoms barely diffuse within water ice.

Ioppolo et al. (2010) experimentally studied the dependence of ice thickness on water and hydrogen peroxide formation by irradiating a pure O_2 ice with H atoms at several temperatures and several thicknesses. These authors show that the saturation of solid O_2 consumption $\Delta N_f(O_2)/N_i(O_2)$ is thickness independent for thin ices. However, the saturation value of O_2 destruction starts to decrease above a threshold which depends on the temperature. At 25 K, $\Delta N_f(\mathrm{O_2})/N_i(\mathrm{O_2})$ starts to decrease at 15 MLs, suggesting that H atoms penetrate into the first 15 MLs of the surface. However, the overall formation of hydrogen peroxide and water, and therefore the bulk-diffusion of H atoms into O_2 ice, decrease with decreasing temperature (by a factor of 6 between 25 and 15 K, giving a penetration depth of 3 MLs).

In conclusion, it is believed that the bulk-diffusion of light particles accreting on interstellar ices is very limited because i) interstellar ices are generally cold in molecular clouds ($T_d < 20$ K) decreasing the diffusion rate, ii) most of ices are composed of ASW ices limiting the possibility of penetration, iii) H and D atoms accrete on an ice in formation in parallel with other reactive particles, increasing the reaction probability on the surface.

2.5 Chemical reaction pathways

Infrared observations of interstellar ices have revealed a rich complexity of molecules. Water is the main ice constituent but CO, CO_2, CH_3OH, CH_4, and NH_3 can also be found in significant abundances while other molecules, such as H_2CO, HCOOH, or OCN^- are potentially detected. In this section, we review the experimental evidence of the formation of these molecules on cold surfaces, as well as complementary theoretical calculations which provide a quantitative evaluation of the rate of these chemical pathways.

2.5.1 Reaction processes

Species can react on grain surfaces via three chemical mechanisms: the Langmuir-Hinshelwood, the Eley-Rideal, or the hot-atom. Figure 2.6 gives a schematic description of the three mechanisms.

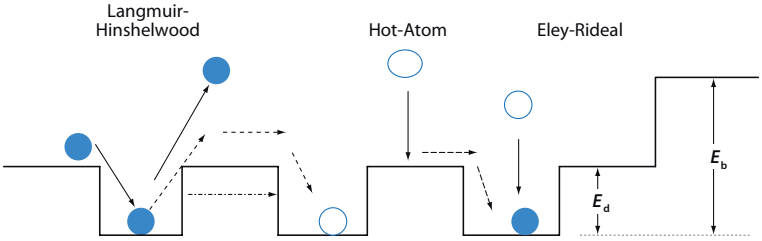

Figure 2.6: Schematic description of the three mechanisms for grain surface reactions on a regular grain surface. E_d is the energy barrier to diffusion, E_b is the binding energy. Figure adapted from Herbst & van Dishoeck (2009)

The Langmuir-Hinshelwood mechanism is the most common surface reaction mechanism. It involves the reaction between two adsorbed reactants which collide in the same potential well, or site. This mechanism, therefore, strongly depends on the surface coverage and the collision rate of particles. The reaction rate is function of adsorption, diffusion, and desorption. Once two particles are in the same potential well, they can react with a probability which depends on the activation energy and the width of the reaction barrier, and the mass of the reactants. The activation barrier can be approximated by a rectangular barrier of height E_a and width a. In this case, the tunnelling probability through this rectangular barrier is given by

$$P_r = \exp\left(-\frac{2a}{\hbar}\sqrt{2\mu E_a}\right) \tag{2.7}$$

where μ is the reduced mass of the reactants. The reaction probability strongly depends on the width of the activation barrier a. Although a is poorly constrained and depends on each considered reaction, astrochemical models generally assume a width of 1 Å.

The Eley-Rideal (ER) mechanism refers to the reaction involving a gas phase particle which strikes directly an adsorbed species. In this case, if the reaction occurs, the product escapes directly into the gas phase. The products should be highly energetic because the chemical energy of the exothermic reaction has not been released to the surface before desorption. Although this reaction mechanism is less understood than the LH mechanism, it is believed that reactions proceeding via the Eley-Rideal mechanism must be barrierless and exothermic, implying that they involve only radicals (Weinberg, 1991). Otherwise, the reactions occur via the Langmuir-Hinshelwood mechanism.

The Hot Atom (HA) mechanism proceeds on a surface when two particles, that are adsorbed in their neighbourhood of the surface but have not thermalized yet, react together. However, this mechanism involves chemisorbed species and is not relevant for ice formation (Harris & Kasemo, 1981).

2.5.2 Formation and deuteration of water ice

2.5.2.1 Chemical pathways on interstellar ice analogues

Water is the main constituent of interstellar ices. 30 years ago, Tielens & Hagen (1982) proposed a chemical network for the formation of H_2O by the sequential hydrogenation of atomic and molecular oxygen. Sophisticated experiments applied on astrophysically relevant surface have been carried out during the last 15 years to confirm this chemical network.

The simplest formation pathway towards solid water is the sequential hydrogenation of atomic oxygen:

$$O + H \rightarrow OH \tag{2.8}$$

$$OH + H \rightarrow H_2O \tag{2.9}$$

Deuterated isotopologues are also thought to form via similar reactions, involving OH, OD, H, and D. This reaction channel was experimentally claimed to occur in cold conditions, probably via barrierless reactions (Hiraoka et al., 1998; Dulieu et al., 2010; Jing et al., 2011). Dulieu et al. (2010) and Jing et al. (2011) codeposited O with D atoms on ASW ice and bare silicate surface at low temperatures (10 to 25 K). During the TPD process, they observed the desorption of HDO and D_2O, suggesting that water forms with high efficiencies at low temperatures when H atoms are allowed to stay stuck to the surface. Reactions (2.8) and (2.9) would occur, therefore, with negligible activation barriers. Dulieu et al. (2010) could not distinguish the water formation during the exposure at low temperature or during the heating, but Jing et al. (2011) observed a peak in the 1207 cm^{-1} absorption band attributed to water, via reflection absorption infrared spectrum (RAIRS) measurements at 15 K. The slightly higher temperature (15 and 25 K) used in the experiments by Jing et al. (2011) also allows the formation of ozone as well as hydrogen peroxide. The formation of water could also come from different channels involving O_2 or O_3.

Water and its deuterated isotopologues HDO and D_2O can also be formed from molecular oxygen, either directly coming from the gas phase or formed on interstellar grains following the reaction channels:

$$O_2 + H \rightarrow HO_2 \tag{2.10}$$

$$HO_2 + H \rightarrow H_2O_2 \tag{2.11}$$

$$H_2O_2 + H \rightarrow H_2O + OH \tag{2.12}$$

These pathways have been experimentally demonstrated by Miyauchi et al. (2008); Ioppolo et al. (2008); Matar et al. (2008); Ioppolo et al. (2010) and Cuppen et al. (2010c) at very low temperatures ($\sim$ 10 K). All these authors irradiated O_2 ice by H (and/or D) atoms and observed an efficient formation of water as well as hydrogen peroxide. By fitting their experimental results with a kinematic model, Miyauchi et al. (2008) deduced reaction rates for the reactions (2.10) and (2.12) involved in these experiments at 10 K. They showed that the rate of reaction (2.12) is lower than that of reaction (2.10). Furthermore, unlike reaction (2.10), the rate of reaction (2.12) appears to be lower for the reaction involving deuterated isotopologues, suggesting an isotope effect in the formation of water from hydrogen peroxide. Therefore, this reaction displays a significant activation barrier and occurs via quantum tunnelling. Ioppolo et al. (2008, 2010) and Cuppen et al. (2010c) extended this experimental study by investigating the influence of surface temperature and H/O_2 ratio on water and hydrogen peroxide formations. As described previously, diffusion and more particularly bulk-diffusion increases with the temperature, allowing a more efficient destruction of O_2 with increasing temperature and H/O_2 ratios.

Relative to the chemical network proposed by Tielens & Hagen (1982), Cuppen et al. (2010c) added several chemical reactions deduced from the variation of H and O_2 fluxes in their experiments. In particular, they claimed that the reaction between HO_2 and H does not only yield H_2O_2 but also

$$HO_2 + H \rightarrow 2OH \tag{2.13}$$

$$HO_2 + H \rightarrow H_2O + O \tag{2.14}$$

with a branching ratio of 1.6 and < 0.2 relative to reaction (2.11), respectively. However, Mousavipour & Saheb (2007) showed that reaction (2.13) is not a direct route. Instead, H_2O_2 should be formed as an intermediate. Oba et al. (2012) showed that if the intermediate H_2O_2 dissipates its excess energy through a cold surface upon formation, it is stabilized and does not further dissociate into OH because the latter part of the sequential process is endothermic. Therefore, it is not obvious that the OH formation occurs on the surface through this process, and it should depend on the rate of dissipation of excess energy to the surface.

Water and its isotopologues can also be formed from ozone, directly formed on interstellar grains (Cuppen & Herbst, 2007) because of its inefficient formation in the gas phase of cold dark clouds, following this reaction:

$$O_3 + H \rightarrow O_2 + OH \tag{2.15}$$

O_2 and OH can then continue to react to form water via the reactions described above. Mokrane et al. (2009) and Romanzin et al. (2011) experimentally showed the efficiency of this reaction by observing the presence of water (HDO, D_2O) after the irradiation of solid O_3 on water ice by D atoms either using a TPD method or Reflection-Absorption InfraRed Spectroscopy (RAIRS). The efficient formation of water from ozone hydrogenation suggests that this reaction has a negligible activation barrier.

With their microscopic Monte Carlo model, Cuppen & Herbst (2007) have claimed that molecular hydrogen plays a key role in the formation of water ice in molecular clouds. When hydrogen is mostly in its molecular form, $\sim 70\%$ of all of the water is formed by the reaction

$$OH + H_2 \rightarrow H_2O + H \tag{2.16}$$

Oba et al. (2012) have recently demonstrated that water can indeed be formed from molecular hydrogen at low temperatures. These authors co-deposited H_2 isotopologues and cold OH (or OD) radicals at 10 K and observed the formation of water via Fourier transform infrared (FTIR) spectroscopy. They also deduced the reaction rates of all the deuterated counterparts of reaction (2.16). They showed that HDO formation, from reaction OH + D_2, is ten times less efficient that the formation of H_2O from reaction (2.16), implying an isotope effect and therefore the possibility of tunnelling through an activation barrier in this reaction.

OH radicals can also recombine together if the ice temperature is high enough to allow their mobility. Oba et al. (2011) experimentally determined the branching ratios for the reactions

$$OH + OH \rightarrow H_2O + O \tag{2.17}$$

$$OH + OH \rightarrow H_2O_2 \tag{2.18}$$

of 0.2 and 0.8, respectively.

2.5.2.2 Quantum chemical calculations

Quantum chemical calculations provide an important theoretical framework for the interpretation of the experimental works previously described. The formation and the deuteration of solid water includes two reaction channels which have an activation barrier: reactions (2.12) and (2.16).

Reaction (2.12) has been theoretically studied by Koussa et al. (2006) and Ellingson et al. (2007) but only for the reaction including the main isotopologues. Ellingson et al. (2007) benchmarked this reaction by carrying out a variety of single-reference level calculations which have

been compared with gas phase experiments. This reaction displays a significant activation barrier of about 2500 K.

The activation energies and rates of all the deuterated counterparts of reaction (2.16) have been computed by Nguyen et al. (2011) who conducted semiclassical transition-state theory (SCTST) calculations. These authors show that reaction (2.16) has indeed a high activation barrier, between 2700 and 3000 K depending on the deuteration of the reactants. Furthermore, the reaction rate tends to decrease with the deuteration level of its reactants, induced by their higher mass.

2.5.3 Formation and deuteration of formaldehyde and methanol

2.5.3.1 Chemical pathways on interstellar ice analogues

By irradiating H atoms on a mixed CO:H_2O surface, Watanabe & Kouchi (2002) experimentally showed the efficient formation of formaldehyde and methanol in the solid state via the sequential hydrogenation of CO:

$$H + CO \rightarrow HCO \tag{2.19}$$

$$HCO + H \rightarrow H_2CO \tag{2.20}$$

$$H_2CO + H \rightarrow CH_3O \tag{2.21}$$

$$CH_3O + H \rightarrow CH_3OH \tag{2.22}$$

Watanabe et al. (2003); Hidaka et al. (2004); Watanabe et al. (2004) then extended their study by varying the surface temperature (8 to 15 K), ice composition (mixed CO:H_2O ice, pure CO ice, pure H_2CO ice, CO capped ice), and ice thickness (from 1 to 30 MLs). At low temperatures, the increase of the formation rate with increasing temperature is due the increase in the mobility of H atoms on the surface and in the bulk. Formaldehyde and methanol formations reach a maximum at a temperature where thermal desorption of H becomes too significant to allow H atoms to stay adsorbed on the surface. For a pure CO ice, the formation of formaldehyde and methanol initially increases with the temperature between 8 and 12 K and decreases at higher temperatures. For a mixed CO:H_2O ice, H_2CO and CH_3OH show a peak of their formation rate at $T = 15$ K. The different temperature-dependent formation rates between pure CO and mixed CO:H_2O ices are due to the increase of binding energy relative to water ice. By hydrogenating formaldehyde ice, Hidaka et al. (2004) estimated the conversion from H_2CO to CH_3OH, which is about half the conversion from CO to H_2CO.

Hidaka et al. (2007) conducted the same type of experiments, and showed that deuterated formaldehyde and methanol are also formed via the sequential deuteration of CO. They compared its efficiency with CO hydrogenation, and they deduced that the effective rate of CO hydrogenation is about ten times more efficient than that of CO deuteration ($k_D/k_H = 0.08$).

Unlike water which does not experience any reactions with D atoms after its formation, formaldehyde and methanol can also be deuterated via abstraction and substitution reactions as shown by the experimental works by Nagaoka et al. (2005), Nagaoka et al. (2007), and Hidaka et al. (2009). Indeed, Hidaka et al. (2009) detected the formation of HDCO, D_2CO, and CD_3OD after the irradiation of H_2CO monolayers on ASW by D atoms. The formation of these molecules implies that formaldehyde deuteration occurs via abstraction reactions

$$H_2CO + D \rightarrow HCO + HD \tag{2.23}$$

$$HCO + D \rightarrow HDCO \tag{2.24}$$

$$HDCO + D \rightarrow DCO + HD \tag{2.25}$$

$$DCO + D \rightarrow D_2CO \tag{2.26}$$

or via direct exchanges between H and D, namely by a substitution process

$$H_2CO + D \rightarrow CH_2DO^* \rightarrow HDCO + H \tag{2.27}$$

$$HDCO + D \rightarrow CHD_2O^* \rightarrow D_2CO + H \tag{2.28}$$

The non-detection of methanol isotopologues other than CD_3OD implies that the addition reactions on H_2CO and HDCO are negligible compared to abstraction and substitution reactions. The exposition of D_2CO molecules to H atoms leads to the formation of HDCO, H_2CO, CH_3OH, and CHD_2OH, implying that deuterium abstraction reactions in D_2CO and HDCO are also possible via the reactions

$$D_2CO + H \rightarrow DCO + HD \tag{2.29}$$

$$DCO + H \rightarrow HDCO \tag{2.30}$$

$$HDCO + H \rightarrow HCO + HD \tag{2.31}$$

$$HCO + H \rightarrow H_2CO \tag{2.32}$$

The presence of CHD_2OH in the experiments shows that the effective rates of the addition and abstraction reactions on D_2CO are similar.

By exposing CH_3OH ice to D atoms at 15 K, Nagaoka et al. (2005) showed that methanol can be efficiently deuterated. They observed the formation of CH_2DOH, CHD_2OH, and CD_3OH while no isotopologues containing D atom in the hydroxyl group were detected. Deuteration must occur via H abstraction on CH_3OH and subsequent additions of D on radicals:

$$CH_3OH + D \rightarrow CH_2OH + HD \tag{2.33}$$

$$CH_2OH + D \rightarrow CH_2DOH \tag{2.34}$$

$$CH_2DOH + D \rightarrow CHDOH + HD \tag{2.35}$$

$$CHDOH + D \rightarrow CHD_2OH \tag{2.36}$$

$$CHD_2OH + D \rightarrow CD_2OH + HD \tag{2.37}$$

$$CD_2OH + D \rightarrow CD_3OH \tag{2.38}$$

A spontaneous exchange between hydrogen and deuterium atoms in an intimate H_2O:CD_3OD ice mixture has been observed by Ratajczak et al. (2009) at 120 K. It appears the the H/D exchange occurs only on the hydroxyl functional group of methanol, suggesting a lower abundance of CH_3OD compared to CH_2DOH in ices.

2.5.3.2 Quantum chemical calculations

A variety of quantum chemical calculations focusing on the sequential hydrogenation and deuteration of CO as well as abstraction reactions in the gas phase have been performed during the last decade.

The addition of H and D atoms on the CO molecule has been theoretically studied in the gas phase by Woon (2002), Andersson et al. (2011) and Peters et al. (2012). Addition reactions studied with these calculations show a high and uncertain energy barrier of 2000 - 3000 K depending on the level of theory. Theoretical predictions are two times higher than the value experimentally measured by Wang et al. (1973) in the gas phase (1200 K). Woon (2002) conducted ab-initio calculations to study the influence of water on CO hydrogenation and deuteration by explicitly adding four water molecules in the surroundings of the CO and H species. It was found that the presence of water does not influence significantly the formation of HCO. Woon (2002) also showed that ZPE corrections favour deuteration additions relative to hydrogenation whereas

Andersson et al. (2011) deduced a rate ratio between the deuteration and hydrogenation reactions k_D/k_H of 0.004, with their Harmonic Quantum Transition State Theory (HQTST) calculations. The latter value is 20 times lower than the isotope effect experimentally deduced by Hidaka et al. (2007).

Woon (2002), Goumans (2011), and Peters et al. (2012) also studied the addition reactions of H and D on formaldehyde with similar methods. Again, the activation barriers deduced from these calculations are highly uncertain, between less than 2000 K to 3000 K. Peters et al. (2012) performed the first high level ab initio calculations of the CO hydrogenation reaction and deduced an activation barrier of 1960 K. Woon (2002) showed that the presence of water molecules tends to decrease the energy barrier by a few percent, depending on the level of theory. Abstraction reactions on (deuterated) formaldehyde have also been studied by Woon (2002) and Goumans (2011). The ZPE-corrected energy barriers of H and abstraction on formaldehyde deduced by Goumans (2011) are in good agreement with the experimental results by Oehlers et al. (2000), which are about 1900 - 2200 K. Furthermore, they also showed an isotope effect in which reactions involving D are less efficient than reactions involving H, due to the higher mass. These calculations therefore validate the experimental results by Hidaka et al. (2009).

Osamura et al. (2004) showed that a direct H-H exchange in methanol is unlikely to occur in cold conditions since this reaction has a huge energy barrier ($\sim$ 20000 K). Instead, deuteration of methanol occurs via abstraction reactions of H on methanol. By computing the potential energy surface (PES) of abstraction reactions of H and D on methanol via ab-initio calculations, Kerkeni & Clary (2004) deduced activation barriers of these reactions. H and D abstraction reactions on the methyl group display an energy barrier of 4300 and 3900 K while D abstraction reaction on the hydroxyl group shows an energy barrier of 6100 K. These calculations, therefore, confirm experimental surface results by Nagaoka et al. (2005), who showed that abstraction reactions occur only on the methyl group of methanol. Goumans & Kästner (2011) extended this work by studying the reactions involving deuterated isotopologues using HQTST theory down to 30 K. Their results are in good agreement with previous theoretical and experimental works and confirm that this reaction displays an inverse kinetic isotope effect ($k_H/k_D < 1$) induced by the lower ZPE-corrected activation barrier for D abstraction reactions.

2.5.4 Formation of carbon dioxide

2.5.4.1 Chemical pathways on interstellar ice analogues

The accretion of CO and O particles onto interstellar grains can lead to the formation of carbon dioxide (CO_2) mainly via three reaction channels (Ruffle & Herbst, 2001b)

$$HCO + O \rightarrow CO_2 + H \tag{2.39}$$

$$CO + O \rightarrow CO_2 \tag{2.40}$$

$$CO + OH \rightarrow CO_2 + H \tag{2.41}$$

Gas phase experiments have shown that reaction (2.39) is barrierless (e.g. Baulch et al., 2005) although it has never been studied on astrophysically relevant surfaces so far.

Laboratory experiments showed that solid carbon dioxide can be formed from reaction (2.40) at cold temperature (Roser et al., 2001; Raut & Baragiola, 2011). In the two experiments, the co-deposition of CO with atomic O on a cold surface leads to the formation of CO_2, detected either by TPD and infrared spectroscopy methods. However, the formation efficiency is very low. Raut & Baragiola (2011) measured an abundance CO_2:CO ratio equal to 10^{-3} which is at least two orders of magnitude smaller than the observed ratio found in interstellar ices (see previous chapter). Therefore, this formation pathway should be negligible.

Formation of solid carbon dioxide, from non-energetic OH radicals and CO molecules, has been observed at very low temperatures (10-20 K, Oba et al., 2010; Ioppolo et al., 2011; Noble et al., 2011), suggesting that reaction (2.41) has little barrier (380 K Noble et al., 2011). Oba et al. (2010) also observed the appearance of a band attributed to the HOCO radical. This experiment, therefore, confirms that CO_2 forms via the following pathway

$$CO + OH \rightarrow \text{trans-HOCO} \tag{2.42}$$

$$\text{trans-HOCO} \rightarrow \text{cis-HOCO} \tag{2.43}$$

$$\text{cis-HOCO} \rightarrow CO_2 + H \tag{2.44}$$

HOCO radicals could also react with H atoms via barrierless reactions to form three pairs of products: H_2 + CO_2, H_2O + CO, or HCOOH (Goumans et al., 2008). The presence of H atoms combined with the non-detection of HCOOH suggests that HOCO radicals are destroyed preferentially to form CO_2. Using a different method, Ioppolo et al. (2011) observed the formation of carbon dioxide from the irradiation of a mixed CO:O_2 ice with H atoms. The appearance of solid CO_2 along with icy water clearly suggests that these two molecules form in parallel.

2.5.4.2 Quantum chemical calculations

As described previously, the formation of carbon dioxide includes two reactions having an activation barrier. Theoretical chemistry calculations by Talbi et al. (2006); Goumans et al. (2008) and Goumans & Andersson (2010) have shown that reaction (2.40) has an activation barrier of 2500 - 3000 K. Furthermore, because this reaction involves two "heavy" species, the probability of quantum tunnelling through this barrier is very low, lower than 5×10^{-23} (Goumans & Andersson, 2010; Garrod & Pauly, 2011).

The profile of the potential energy of reaction (2.43) has been computed by Yu et al. (2001). They showed that the electronic energy of the intermediate radicals (t-HOCO, c-HOCO) and the products (CO_2 + H) are low compared to that of the reactants (CO + OH). Reactions involving t-HOCO and c-HOCO possess high activation barriers and/or are endothermic. Therefore, t-HOCO radicals continue to react only if their excess energy released by the chemical energy of reaction (2.42) are sufficient to overcome the high activation barriers of reactions (2.43) and (2.44).

In fact, the energy released by reaction (2.42) absorbed by HOCO radicals can be transferred to the surface before reacting. However, the dissipation rate of the chemical energy to the surface is very uncertain. The absence of formic acid HCOOH, and the low abundance of HOCO radicals observed in the experiments by Oba et al. (2010) suggests that CO_2 is readily formed from excited HOCO molecules. Therefore, most HOCO radicals continue to react before relaxing to their stable state.

Goumans & Andersson (2010) performed gas phase O-CO potential energy surface calculations, showing that O and CO can form a loosely bound O..CO van der Waals complex, allowing O atoms to stay bound to CO for some time. Following these results, Goumans & Andersson (2010) proposed a pathway in which H atoms which subsequently meet this O..CO complex react via a barrierless reaction to form an excited HO...CO* complex. If the time for energy transfer to the surface is long enough, the complex can yield OH + CO, CO_2 + H, or a stabilized t-HOCO radical via barrierless reactions.

2.5.5 Formation of other interstellar ices

It is believed that methane and ammonia are formed through sequential hydrogenations of atomic carbon and nitrogen via reactions with negligible activation energies, respectively (Allen & Robinson, 1977; D'Hendecourt et al., 1985).

The formation of methane on astrophysically relevant surfaces has been experimentally demonstrated to occur by Hiraoka et al. (1998). In their experiment, H atoms irradiate a CO surface containing trapped C atoms at 12 K. After the irradiation, the sample was heated, and desorption of species attributed to CH_4 was observed via TPD mass spectrometry. However, the deduction of reaction rates or activation energy barriers was not possible.

2.6 Non-photolytic desorption

2.6.1 Thermal desorption

An adsorbed species can desorb thermally, with a desorption rate given by

$$K_{ev} = \nu_0 \exp\left(-\frac{E_b}{kT_d}\right) \tag{2.45}$$

where ν_0 is the vibrational frequency of the adsorbed species on the surface (see section 2.4), E_b is the binding energy of the species, and T_d is the surface temperature. This rate corresponds to the inverse of the typical timescale for a species to acquire sufficient energy from thermal fluctuations to evaporate.

In addition to "normal" thermal desorption, several other desorption processes have been invoked to explain the presence of gaseous molecules in cold and dense clouds. We give here two examples which are considered to be as the most efficient non-thermal processes.

2.6.2 CR induced thermal desorption

Energetic cosmic-ray particles transfer energy to interstellar grains upon collisions. The collisions induce an increase of the grain temperature, allowing the desorption of volatile solid species, as suggested by Leger et al. (1985) to explain the presence of CO gas in molecular clouds. The grain heating depends both on the energy of cosmic ray particles and on the grain size.

Hasegawa & Herbst (1993a) estimated the average desorption rate induced by collisions between cosmic-rays and grains. Following Leger et al. (1985), they considered the collisions between relativistic Fe nuclei with energies 20-70 MeV / nucleon and "big" grains ($r = 0.1$ μm). These collisions allow a deposition of 0.4 MeV, increasing the grain temperature up to 70 K instantaneously. Hasegawa & Herbst (1993a) integrated the desorption rate when the grain cools down until its initial temperature (10-15 K for dense clouds) and deduced a simple estimation for the CR-induced desorption rate

$$K_{ev,CR} = f(70\text{K})K_{ev}(70\text{K}) \tag{2.46}$$

where $f(70\text{K})$ is defined as the ratio of the timescale for cooling via desorption of volatiles to the time interval between successive heatings to 70 K, and $K_{ev}(70\text{K})$ is the thermal desorption rate at 70 K. The CR-induced desorption rate of CO is about 10^{-14} s^{-1} which is 9 orders of magnitude larger than the thermal desorption rate at 10 K. This rate allows CO to desorb, giving gaseous CO abundances of 10^{-9} at long timescales.

2.6.3 Desorption via surface reactions

Adsorbed species can desorb upon formation thanks to the chemical energy release of the reaction. Garrod et al. (2006) and Garrod et al. (2007) estimated the desorption rate via exothermic surface reactions by considering the Rice-Ramsperger-Kessel (RRK) theory. They estimated the fraction f of desorbed molecules upon formation by modelling the competition between energy absorption

by the adsorbed molecule and energy transfer to the surface. f is given by

$$f = \frac{\nu P}{\nu_s + \nu P} = \frac{aP}{1 + aP} \tag{2.47}$$

where ν is the vibrational frequency of the bond between the adsorbed molecule and the surface, ν_s is the dissipation rate of the chemical energy to the surface, and $a = \nu/\nu_s$. P is the probability for an energy $E > E_b$ to be present in the bond, from the chemical energy E_{reac}

$$P = (1 - \frac{E_b}{E_{reac}})^{s-1} \tag{2.48}$$

s is equal to 2 for a diatomic species, and $s = 3N - 5$ otherwise. Generally, the binding energy is much lower than the chemical energy, P is, therefore, close to unity. The value of a is poorly constrained by theoretical calculations as well as experimental works. Garrod et al. (2007) estimated a by comparing observed abundances in molecular clouds with theoretical predictions. Observed abundance of methanol toward L134N is reproduced with $a = 0.03$ if the assumption that the observed gaseous methanol is due to this process.

2.7 Photolytic processes

As shown in 2.1, UV photons have a significant flux inside molecular clouds between $10^8 - 10^{10}$ photons cm^{-2} s^{-1} at the edge and 10^4 photons cm^{-2} s^{-1} in deeper regions due to the cosmic rays induced UV field (see Shen et al., 2004).

UV photons which irradiate interstellar ices can be absorbed by solid molecules, depending on their absorption band, allowing photodissociation or photodesorption.

2.7.1 Experimental evidence of UV photolytic processes in ices

A variety of experimental works studying the effect of UV irradiation on ices has been carried out during the last three decades. An exhaustive overview of all of these works is, therefore, not possible, and I will focus on a few main results by distinguishing the effect of UV photons both on ice photodesorption and ice photodissociation although these two processes are strongly correlated.

2.7.1.1 Photodissociation of ices

The effect of UV photolysis on ices has been studied first by considering "dirty" ices, ices including several species (Hagen et al., 1979; D'Hendecourt et al., 1986; Grim et al., 1989), aiming at reproducing the composition of interstellar ices. These authors followed the change of infrared spectra of ice mixtures with time when they are exposed to microwave excited hydrogen lamps, simulating ISRF radiation.

They showed that UV photolysis strongly affects the chemical composition of ices since new absorption band features attributed to the formation of new species are observed. For example, by irradiating two mixtures composed of H_2O, CO, O_2, CH_4, NH_3, and N_2 at 10 K, D'Hendecourt et al. (1986) observed the formation of CO_2, H_2CO but also O_3, NO, N_2O, and NO_2. The formation of these new molecules clearly shows the efficient photodissociation of the main ice constituents, allowing the formation of excited radicals, such as OH* or O*. These excited radicals can then react to form the new products via efficient chemical pathways.

Some ice components can exist in relatively pure states (Tielens et al., 1991) while irradiation of ice mixtures do not allow chemists to constrain directly the photoproducts of each ice component, systematic studies of pure ice irradiation have, therefore, also been performed (e.g.

Gerakines et al., 1996; Öberg et al., 2009c). Gerakines et al. (1996) performed UV photolysis experiments at 10 K on nine pure ices: H_2O, NH_3, CH_4, CO, CO_2, O_2, N_2, H_2CO, and CH_3OH. For each of these pure ices, ice mixtures of different complexities and including several photoproducts have been observed, confirming previous results of ice mixture photolysis as well as gas phase experiments (Okabe, 1978). In particular, water irradiation leads to the formation of hydrogen peroxide H_2O_2 as well as OH, and HO_2 radicals confirming that water is photodissociated in excited OH*, and H*. CO irradiation leads to the observation of CO_2 whose formation is due to the excitation of CO molecules. Methanol shows the most complex photoprocessed ice mixture. Methanol irradiation leads to the formation of more than 8 different species including formaldehyde, carbon dioxide, or methyl formate. These authors have succeeded to deduce destruction cross sections for most of the considered species, showing similar values of about 10^{-19} cm^2.

The high abundance of a variety of complex organic molecules observed around high-mass and low-mass protostars cannot be explained by gas phase chemistry (Horn et al., 2004; Garrod et al., 2006) and could be the consequence of an efficient photodissociation of ices. This is the reason why Öberg et al. (2009c) performed a comprehensive study of the effect of photolysis on methanol-rich ice mixtures. For this purpose, several ices (pure CH_3OH, or CH_3OH mixed with CH_4 or CO) have been irradiated with a broad-band UV hydrogen microwave-discharge lamp at 20-70 K and then heated until 200 K. The photoproducts have been observed by infrared spectroscopy (RAIRS) and TPD techniques. Methanol photodissociation leads to a rich chemistry since several complex organic molecules such as methyl formate, glycolaldehyde, acetaldehyde, ethanol, or dimethyl ether have been observed in at least one experiment. The exact chemical composition is shown to depend on the UV fluence as well as the temperature since the mobility of radicals formed via photodissociation increases with the temperature. Methanol photodissociation can, therefore, lead to the formation of COMs observed around protostars. However, since the UV flux used in experiments is much higher than the interstellar flux induced by cosmic rays, the formation efficiency of interstellar COMs remains unknown. More quantitative photodissociation rates are still needed to use them in astrochemical models and to confirm the formation of interstellar COMs via such photolytic processes.

2.7.1.2 Photodesorption of ices

In addition to photodissociation, UV photolysis also allows the desorption of adsorbed species whose rates depend on the adsorbate (absorption cross section), substrate (binding energy) as well as the energy of UV photons.

Öberg et al. (2007, 2009a,b) and Muñoz Caro et al. (2010) have conducted a series of experiments in order to quantify the photodesorption of CO, N_2, CO_2, and water. For this purpose, these authors have irradiated a sample of ices with a hydrogen discharge lamp, emitting UV photons at 7 - 10 eV. First experiments with solid CO confirms that CO only photodesorbs without significant photodissociation (Öberg et al., 2007, 2009a; Muñoz Caro et al., 2010). The photodesorption rate decreases with ice temperature caused by ice re-structuring to a more compact configuration at higher temperatures. Photodesorption rate increases with ice thickness between 1 and 5 monolayers and remains constant for thicker ices, confirming that molecules only photodesorb in the top layers. At low temperatures (15 K), Öberg et al. (2007) deduced a CO photodesorption rate of 3×10^{-3} molecules photon^{-1} while Muñoz Caro et al. (2010) deduced a higher value, by one order of magnitude. The discrepancy is probably caused by the use of different infrared spectroscopy techniques used for measuring ice absorbance. Unlike Öberg et al. (2007), the technique used by Muñoz Caro et al. (2010) provides a direct measurement of the ice absorbance and their yield would, therefore, be more accurate. In spite of their similarities (similar binding energies and ice structures), N_2 shows a lower photodesorption rate, $< 2 \times 10^{-4}$ molecules photon^{-1}. This is due to the fact that CO has an electric dipole allowed transition in

the 7 - 10 eV band while N_2 does not. After absorbing a UV photon, the excited CO molecule is allowed to relax via energetic transfer of its intramolecular energy to its weak intermolecular bond.

CO_2 and H_2O both photodesorb through dissociation and subsequent recombinations in the 10 top layers. Öberg et al. (2009a) and Öberg et al. (2009b) have been able to deduce an empirical photodesorption rate for CO_2 and H_2O (and D_2O) which are function of ice temperature and ice thickness. It should be noted that, unlike for CO, the CO_2 and H_2O photodesorption rates increase with ice temperature because of the increase of diffusion within ices.

These experiments are based on ice irradiation using a broad UV lamp which does not necessarily reproduce the interstellar UV spectrum found in molecular clouds. Indeed, as shown in Figure 2.7, the UV spectrum is not necessarily constant with the wavelength. Therefore, one needs to characterize ice photodesorption as function of the wavelength of UV photons. A wavelength-dependent study has been performed by Fayolle et al. (2011) for CO photodesorption. These authors have used a similar method as Öberg et al. (2007) but they used a tunable synchrotron radiation instead of the broad hydrogen discharge lamp, allowing them to irradiate a pure 10 ML CO ice at 18 K with a monochromatic photon beam scanning the 7 - 13.6 eV with a constant rate.

As it can be seen in Figure 2.7, showing the photodesorption spectrum of CO , CO photodesorption is highly wavelength-dependent. The photodesorption rate is high in the 7 - 10 eV energy band (1300 - 1600 nm) considered by previous authors (Öberg et al., 2007; Muñoz Caro et al., 2010) since CO displays photodesorption bands at 8 - 9 eV. These photodesorption bands match well the absorption spectrum of pure CO ice by Lu et al. (2005) and confirm that CO molecules are excited from the ground state to the first allowed electronic state and undergo a further relaxation which allows photodesorption. The photodesorption spectrum can be convolved with UV field profiles of interstellar (ISRF) or cosmic-ray induced (CRH2RF) radiation fields in order to deduce a photodesorption yield integrated over the FUV band (7 - 13.6 eV). Fayolle et al. (2011) deduced a photodesorption yield of 1.2×10^{-2} and 9.4×10^{-3} for ISRF and CRH2RF fields, respectively. These yields are comparable to those found by Muñoz Caro et al. (2010) and are higher than those deduced by Öberg et al. (2007) by a factor of ~ 3.

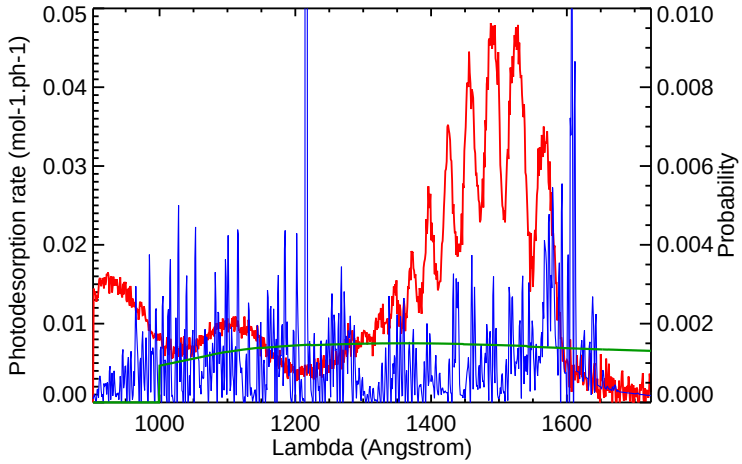

Figure 2.7: Photodesorption spectrum of a 10 ML pure CO ice (in red) measured by Fayolle et al. (2011) overplotted with the cosmic ray induced radiation field (in blue) computed by Gredel et al. (1987) and the interstellar radiation field (in green) by Mathis et al. (1983).

2.7.2 MD calculations of water photodissociation

So far, ice photodissociation rates have been considered in astrochemical models by analogy with gas phase chemistry. Astrochemists used the same photodissociation cross sections and branching ratios as those computed for gaseous species. Molecular dynamics simulations provide us a tool to investigate in more details the behaviour of ices when they are irradiated by UV photons, at a microscopic scale. We will see in this section that the analogy with gas phase chemistry is not necessarily realistic.

Andersson et al. (2006); Andersson & van Dishoeck (2008); Arasa et al. (2010) and Arasa et al. (2011) have studied the behaviour of the outer layers of compact amorphous and crystalline ices irradiated by FUV photons at several temperatures using classical dynamics calculations. Even if UV photons can penetrate deeper in the mantles (up to $\sim$ 100 monolayers, see Gerakines et al., 2000), photolytic effects are significant in the 5-6 outermost layers only while photoproducts burried at deeper layers usually recombine as soon as they form. These authors therefore study the behaviour of the 5-6 outermost layers undergoing UV irradiation.

The UV absorption spectra of amorphous and crystalline ices have been computed by Andersson & van Dishoeck (2008). Figure 2.8 shows the UV absorption spectrum of an amorphous ice overplotted with interstellar and cosmic-ray induced radiation fields. The theoretical absorption spectrum showing a 1-2 eV narrow band peaked at $\sim$ 8.5 eV reproduces well the experimental spectrum by Kobayashi (1983) and is blue-shifted with respect to that of gaseous water.

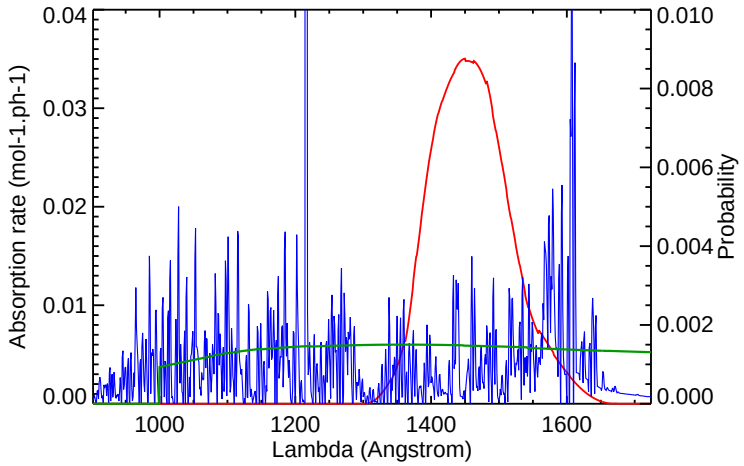

Figure 2.8: Spectrum of the first UV absorption band in ASW ice (in red) computed by Andersson & van Dishoeck (2008) overplotted with the cosmic ray induced radiation field (in blue) computed by Gredel et al. (1987) and the interstellar radiation field (in green) by Mathis et al. (1983).

Furthermore, these authors also followed the main outcomes of the photoproducts (OH and H) when water is photodissociated upon UV photon absorption. For this purpose, they deduced the yield of the different outcomes of the photofragments as function of the monolayer. Figure 2.9 shows the yield of the detailed outcome after water photodissociation as function of the monolayer. The direct photodesorption yield of H atoms decreases with the monolayer, between 0.9 at the surface to 0.1 at the 6^{th} monolayer while OH and H trapping and water recombination increase. H_2O direct desorption refers to water photodesorption after recombination of H and OH radicals. The rightmost three categories refer to the "kick-out" mechanism in which a H photoproduct transfers its kinetic energy to another water molecule, or when the chemical energy released by the formation of water is transferred to another molecule. OH and water can photodesorb only in the three outermost layers since they do not have enough kinetic energy to diffuse through more than three layers. The probability of total photodesorption of "intact" water integrated over the layers is estimated to be 1.4×10^{-4} molecules photon^{-1} which is lower

than the experimental values by Öberg et al. (2009b).

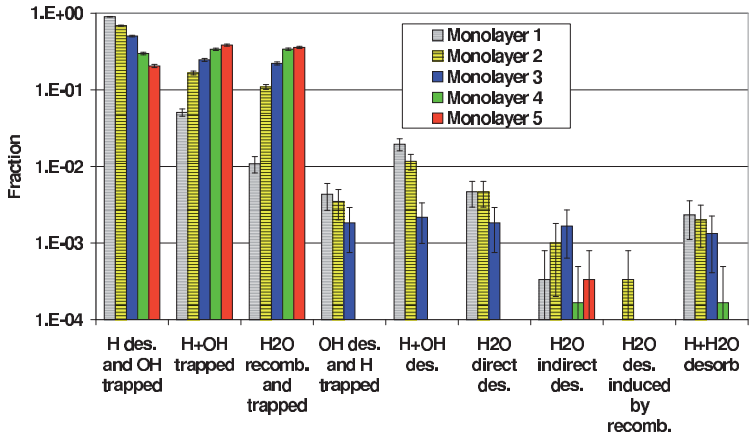

Figure 2.9: Yield of the detailed outcome after water photodissociation as function of the monolayer, taken from Andersson & van Dishoeck (2008).

Arasa et al. (2010, 2011) have investigated the influence of the temperature and the isotope effect by computing MD simulations for a wide range of temperatures ($10 < T < 90$ K) and for a D_2O ice. It is found that the temperature slightly influences the outcomes of the photoproducts, by increasing water and OH photodesorption by 30 % in the range of studied temperatures. D_2O photodesorption is found to be more efficient by a factor of 2 because the kick-out mechanism becomes more efficient with D atoms which have more momentum to transfer to water than H.

Unfortunately, MD studies have been performed on water ices only. More comprehensive MD calculations are needed to characterise the absorption spectrum of other ices such as solid methanol of mixed ices. These works will help us to fully understand the detailed outcome of the photoproducts in order to investigate the formation of complex organic molecules induced by photolytic processes.

2.7.3 Experimental evidence of CR photolytic processes in ices

Upon collisions with interstellar grains, cosmic rays have a direct impact on grain surface chemistry by photodissociating solid species in ices. A large set of experiments can be found in the literature, we will therefore focus on the main results published during the last decade which are the most relevant in the scientific context of this thesis.

Gerakines et al. (2000) and Gerakines et al. (2001) have studied the effect of UV photolysis and ion bombardment using the same experimental set-up. For this purpose, they irradiated 10 eV UV photons and 0.8 MeV protons on several ice mixtures, composed of water, carbon dioxide, methane, or methanol at 18 K. In the two experiments, they observed the apparition of new bands attributed to the same molecules: CO, H_2CO, or C_2H_6. Furthermore, these authors have been able to measure the normalised yields (formation/destruction yields per 100 eV) of products for the two experiments. The similar yields suggest that cosmic ray particles also have a significant effect on the ice photodissociation and the subsequent formation of secondary molecules.

More recent experimental works have shown that complex organic molecules can be formed via ice irradiation by cosmic ray particles. Bennett & Kaiser (2007) observed the formation of glycol aldehyde and methyl formate via infrared spectroscopy during the irradiation of a cold (10 K) solid CO:CH_3OH mixture by energetic (5 keV) electrons. Modica & Palumbo (2010) only observed the formation of methyl formate during the irradiation of a solid CO:CH_3OH mixture by energetic (200 keV) protons, reaching a methyl formate to methanol abundance ratio of 0.1 %. These experiments suggest that COMs can also be formed from the recombination

between energetic radicals (HCO, CH_3O, CH_2OH) formed via dissociation of methanol by cosmic rays. However, by scaling their experimental conditions to astrophysical scales, Modica & Palumbo (2010) estimated a timescale of 20 millions years to form methyl formate with a $HCOOCH_3/CH_3OH$ of 0.1 %. More quantitative efforts are needed to investigate these effects in astrophysical conditions.

2.8 Numerical methods

A variety of astrochemical models coupling gas and grain surface chemistry have been developed since more than three decades. These models are based on several numerical methods: ab-initio (Allen & Robinson, 1977), macroscopic Monte-Carlo (Tielens & Hagen, 1982; Charnley, 2001b; Vasyunin et al., 2009), rate equations (Hasegawa et al., 1992; Garrod, 2008), Master Equation (Biham et al., 2001; Green et al., 2001), moment equations (Lipshtat & Biham, 2003; Du & Parise, 2011), or microscopic "Continuous-Time-Random-Walk" Monte-Carlo (Chang et al., 2005; Cuppen et al., 2009), etc. In this section, I will describe the main numerical methods which are currently used in the state-of-the-art astrochemical models by highlighting their advantages and drawbacks.

2.8.1 Rate equations

2.8.1.1 Gas phase chemical modelling

Statistic rate equations were first used for time-dependent calculations of astrochemical modelling by Pickles & Williams (1977) and Prasad & Huntress (1980a,b). Here, the evolution of abundances is followed by calculating the time derivatives of the density of each species i from the rates of reactions forming and destroying i. The rate equations are given by

$$\frac{dn(i)}{dt} = \sum_l \sum_j K_{l,j} n(l) n(j) - n(i) \sum_k K_{i,k} n(k) \tag{2.49}$$

where $K_{l,j}$ and $K_{i,k}$ are the rate coefficients of the reactions of formation and destruction, respectively, $n(j)$ and $n(l)$ are the densities (cm^{-3}) of the reactants of reactions forming i, and $n(k)$ is the density of the reactants of reactions destroying i. The rate coefficients are expressed in cm^3 s^{-1} and refer to a variety of gas phase chemical reactions: direct cosmic ray processes, photoprocesses by interstellar and cosmic rays induced radiation fields (in this case, expressed in s^{-1}), bimolecular reactions, charge exchange reactions, radiative associations, associative detachments, electronic recombinations.

The computation of the density of a set of N chemical species as function of time is carried out through the solving of N "stiff" coupled differential equations by sophisticated algorithms. The solving of one differential equation for each chemical species allows the use of complex chemical networks including several hundreds of species, and several thousands of reactions. Nowadays, several chemical databases provide state-of-the-art chemical networks, such as:
- the Ohio State University (OSU) database [1]
- the UMIST Database For Astrochemistry (UDFA) [2]
- the KInetic Database for Astrochemistry (KIDA) [3].

2.8.1.2 Gas-grain chemical modelling

Hasegawa et al. (1992) incorporated a treatment of gas-grain chemical modelling in the rate

[1] http://www.physics.ohio-state.edu/ eric/research.html
[2] http://www.udfa.net
[3] http://kida.obs.u-bordeaux1.fr

equations method by linking gas phase and grain surfaces through the accretion and desorption rates, described in sections 2.3 and 2.6. The times derivatives, governing the evolution of the density of each species i in both phases, are given by

$$\frac{dn_g(i)}{dt} = \sum_l \sum_j K_{l,j} n_g(l) n_g(j) - n_g(i) \sum_k K_{i,k} n_g(k) - K_{acc}(i) n_g(i) + n_m(i) \sum K_{ev}(i) \quad (2.50)$$

$$\frac{dn_m(i)}{dt} = \sum_l \sum_j K'_{l,j} n_m(l) n_m(j) - n_m(i) \sum_k K'_{i,k} n_m(j) + K_{acc}(i) n_g(i) - \sum K_{ev}(i) n_m(i) \quad (2.51)$$

where $n_g(i)$ and $n_m(i)$ are the density (in cm^{-3}) of the species i in the gas phase and on the grain surfaces, respectively. The gas-phase and the grain-surface chemistry are linked through the accretion and the evaporation rates K_{acc} and K_{ev}. The formation and the destruction of solid species via surface reactions are included via the reaction rate coefficients $K'_{i,j}$ and $K'_{l,k}$.

Although interstellar grain particles follow size distributions, astrochemical models usually consider one constant grain size corresponding to the upper limit of the distributions. Therefore, interstellar grains display a specified number of sites N_s on their surface given by the ratio between the grain surface and the size of a site. Grain surface reactions are assumed to proceed via the Langmuir-Hinshelwood mechanism in which two particles react when they meet in the potential well (see section 2.5.1). The rate coefficient $K'_{i,j}$ of the surface reaction between two species i and j is defined by the product between the transmission probability of reaction P_r and the collision rate (in s^{-1}) between the two species on the grain surface. The collision rate is defined as the ratio between the sum of the hopping rates of the two reactants and the number of sites on the surfaces. $K'_{i,j}$ is therefore given by

$$K'_{i,j} = P_r \times \frac{K_{hop,i} + K_{hop,j}}{N_s} \times \frac{1}{n_d} \quad (2.52)$$

where n_d is the density of interstellar grains.

2.8.1.3 Modified-rate approaches

Rate equations are based on average variables, since they consider the evolution of homogeneous densities. This approach is accurate for gas phase chemistry and it represents a simple approach to link gas phase and grain surfaces. However, this approach becomes inaccurate for interstellar grain surface chemistry, because it does not take into account the discrete nature of microscopic grain surfaces. On such surfaces, the population of some surface species may become very low, and even lower than one particle per grain, in the so-called "accretion limit" when reaction rates are higher than accretion rates. Therefore, computing average populations from individual populations of 0 or 1 on grains becomes inaccurate and the production rate of a species can become faster than it is physically possible. Stochastic effects need to be taken into account, by modifying the reaction rates or by considering stochastic approaches, realistic for finite grain surfaces, such as the Monte-Carlo of the Master Equation approaches.

From a mathematical point of view, the production rate of the molecule AB formed via the reaction between A et B is given by

$$R_{AB} = K_{AB} < N(A) >< N(B) > \quad (2.53)$$

where K_{AB} is the rate coefficient of the reaction between A and B, and $< N(A) >$ and $< N(B) >$ are the average populations of surface species A and B over a large ensemble of grains or on the same grain but over a large statistic time. Average populations of species i can be expressed as

$$< N(i) >= \sum_{N=0}^{\infty} N \cdot P_N(i) \quad (2.54)$$

where P_N(i) is the probability that N species of i are on the grain. In fact, the product $< N(A) >< N(B) >$ is an approximation of $< N(A)N(B) >$ when surface populations are high and not strongly correlated . But when populations become low, this approximation is not accurate anymore because the probabilities $P_N(A)$ and $P_N(B)$ become correlated.

Modified rate approaches have been developed in a few papers. Caselli et al. (1998); Shalabiea et al. (1998) and Stantcheva et al. (2001) modified the reaction rate coefficients by considering a set of simple rules. Caselli et al. (2002) included a more sophisticated modification scheme for reactions involving activation energy barriers, such as the H + CO reaction. Garrod (2008) went further in this way, not only by modifying reaction rate coefficients but also by substituting the product of average populations.

2.8.2 Master equation and Moment equations

In order to solve the problems that appear at low surface abundance with the use of statistic rate equations, Biham et al. (2001) and Green et al. (2001) introduced a stochastic method based on the resolution of the Master Equation for the hydrogen recombination system, which has been extended by Stantcheva et al. (2002) and Stantcheva & Herbst (2003) for more complex systems.

2.8.2.1 Master equation

As described previously, the product of two average populations $< N(A) >< N(B) >$ is an approximation of the average of the population product $< N(A).N(B) >$, true for high populations but which tends to be wrong at low populations because the probabilities of populations of A and B become correlated.

Instead of computing average populations of species i, Biham et al. (2001) and Green et al. (2001) proposed to substitute the rates equations by the master equation for species whose populations are low. The master equation allows the computation of differential equations governing the joint probabilities of populations.

Stantcheva et al. (2002) and Stantcheva & Herbst (2003) succeeded to couple rate equations with the master equation for the H, O, CO and the H, D, O, CO systems. For the H, O, CO system, 5 species are considered as very reactive and will show low surface abundances (H, O, OH, HCO, CH_3O). Therefore, these abundances must to be studied stochastically with the Master Equation approach by solving the time derivatives of the joint probability P(i_1, i_2, i_3, i_4, i_5) that there are i_1, i_2, i_3, i_4, i_5 numbers of particles of minor species on the grain (1: H, 2: O, 3: OH, 4: HCO, 5: CH_3O). Initially, the joint probability is assumed to be P(0, 0, 0, 0, 0). X and Y are the j^{th} and k^{th} reactive elements of the set of species {H, O, OH, HCO, and H_3CO}. The time

derivatives of the joint probability is given by

$$\begin{aligned}\frac{dP(i_1,i_2,i_3,i_4,i_5)}{dt} &= \sum_{\{X\}} R_{acc}(X)n(X)[P(...,i_j-1,...)-P(...,i_j,...)] \\ &+ \sum_{\{X\}} R_{ev}(X)[(i_j+1)P(...,i_j+1,...)-i_jP(...,i_j...)] \\ &+ \sum_{\{X,Y\}} k_{X,Y}(i_j+1)(i_k+1)P(...,i_j+1,...,i_k+1,...) \\ &- \sum_{\{X,Y\}} k_{X,Y}(i_j)(i_k)P(...,i_j,...,i_k,...) \\ &+ \sum_{\{X,X\}} k_{X,X}\frac{(i_j+2)(i_j+1)}{2}P(...,i_j+2,...) \\ &- \sum_{\{X,X\}} k_{X,X}\frac{i_j(i_j-1)}{2}P(...,i_j,...) \\ &+ \sum_{\{X,Z\}} <N_Z> k_{X,Z}(i_j+1)P(...,i_j+1,...) \\ &- \sum_{\{X,Z\}} <N_Z> k_{X,Z}i_j\cdot i_kP(...,i_j,...)\end{aligned} \tag{2.55}$$

where $n(X)$ is the density of the species X in the gas phase, and $< N_Z >$ is the average abundance on the surface of the main abundant species Z. The first and the second terms of the equation represent the effect of the accretion and the desorption flux on the probability, adding the contribution of each species. The third and the fourth terms represent the effect of the reaction between two different species X and Y on the joint probability. The fifth and the sixth terms represent the effect of recombination of species X, and the seventh and the eighth terms the effect of the reaction between the abundant species Z and the minor species X.

Once the probabilities are computed, average populations and correlation terms (or moments) which are included in the rate equations are deduced as they are function of the joint probability. For example,

$$< N_{\rm H} >= \sum_{i_1,i_2,i_3,i_4,i_5}^{N} i_1P(i_1,i_2,i_3,i_4,i_5) \tag{2.56}$$

$$< N_{\rm H}^k >= \sum_{i_1,i_2,i_3,i_4,i_5}^{N} i_1^kP(i_1,i_2,i_3,i_4,i_5) \tag{2.57}$$

$$< N_{\rm H}\cdot N_{\rm O} >= \sum_{i_1,i_2,i_3,i_4,i_5}^{N} i_1\cdot i_2P(i_1,i_2,i_3,i_4,i_5) \tag{2.58}$$

Average surface abundances which depend on correlation terms can now be deduced. For example, the stable formaldehyde is formed via the reaction between two minor species (H and HCO) and is destructed via the reaction with H (a main and a minor species)

$$\frac{d< N_{\rm H_2CO} >}{dt} = k_{\rm H,HCO} < N_{\rm H}N_{\rm HCO} > -k_{\rm H,H_2CO} < N_{\rm H_2CO} >< N_{\rm H} > \tag{2.59}$$

The probability that there exists a high number of particles of minor species is very low. Thus, the maximal number of considered particles (=cut-off) $N_{max,i}$ for species i can be reasonably assumed to be low. However, even if the chosen cut-off is low, one needs to solve a

high number of differential equations since the number of equations increases exponentially with the number of considered species. If we choose a cut-off of 3 for each species, one needs to solve $3^5 = 243$ equations for only 5 species. Investigations were performed in order to reduce the number of differential equations to solve. Biham et al. (2001) suggested a decoupling of the probabilities, assuming that the probability of a species does not depend on the probability of others. Stantcheva et al. (2002) explored this approach, but comparisons with exact master equation results show that this approximation is not always justified and may produce inaccurate results.

Comparisons between several approaches allowed these authors to show the good accuracy of this method. However, extending this approach to sophisticated chemical networks is not possible because of the high number of differential equations which require to be solved.

2.8.2.2 Moment equations

Lipshtat & Biham (2003) and Barzel & Biham (2007) have presented a new method deduced from the master equation and which is based on the time derivatives of moments. Briefly, the differential equations of average populations are function of the moments which are function of the joint probabilities of populations, presented in the previous section. Coupling the time derivatives of joint probabilities with the moments allow these authors to deduce time derivatives for all the moments needed for solving average populations. With the use of a diagrammatic approach, the number of equations is reduced to $N_{species} + N_{reactions}$. Barzel & Biham (2007) applied this method on limited chemical networks forming water and methanol and show that these systems can be accurately and easily solved.

However, these authors have encountered numerical issues in incorporating this method into sophisticated chemical networks including several thousands reactions. These issues have not been fixed so far (O. Biham, private communication).

Du & Parise (2011) succeeded to overcome this problem by developing the so-called Hydrid Moment Equations (HME). At each iteration, their code selects the species showing abundances as low as 1 particle which need to be solved with the moment equations. Furthermore, they restricted the cut-off of moments at a low order, usually two. The comparisons of their method with the Monte Carlo approach by Vasyunin et al. (2009) showed that this method accurately reproduces exact methods.

2.8.3 Monte Carlo approaches

2.8.3.1 Mascroscopic Monte Carlo approaches

The first Monte Carlo method applied on grain surface chemistry was developed by Tielens & Hagen (1982). This method follows the evolution of individual species on grain surfaces, by computing the relative accretion of each species, and the probability that each species undergoes reaction, desorption, or does nothing before a new particle lands. Then, the Monte Carlo algorithm generates random numbers allowing a selection of accreting species and reactions which proceed. This process is repeated until the equilibrium is reached. This method gives accurate results but does not provide time-dependent calculations.

Exact resolutions of the Master Equation are possible through Monte-Carlo methods, via the Gillespie's stochastic simulation algorithm (SSA) (Gillespie, 1976). SSA was applied for interstellar gas phase chemistry by Charnley (1998) and then for grain surface chemistry by Charnley (2001b). Vasyunin et al. (2009) succeeded to unify gas and grain surface chemistry with sophisticated chemical networks and for a wide range of physical conditions. Unlike previous models by Tielens & Hagen (1982), the SSA also allows time-dependent calculations of chemical evolutions although this method is very time consuming.

Detailed comparisons between these exact Monte-Carlo methods and with "normal" (RE) or "modified" (MRE) rate equations have been carried out by Caselli et al. (2002), Garrod (2008), Vasyunin et al. (2009) and Garrod et al. (2009). In particular, Vasyunin et al. (2009) and Garrod et al. (2009) have performed a comprehensive comparison of their two types of methods for a wide range of densities (2×10^2 to 2×10^5 cm^{-3}) and temperatures (10 to 50 K). The results have been compared via the global agreement level, i.e the fraction of chemical abundances reproduced by the RE or MRE methods to within an order of magnitude of the MC value. Garrod et al. (2009) showed that the new MRE developed by Garrod (2008) fits well the MC method. Indeed, for almost all the range of physical conditions explored in this work, the global agreement level is higher than 95 %. Furthermore, the comparison of the MC method with the"normal" RE also showed that the latter method provides an acceptable modelling of grain surface chemistry since the global agreement level remains higher than 0.75 for most of the physical conditions (except where the density and the temperatures are high) at long timescales.

2.8.3.2 Microscopic Monte-Carlo Continuous-Time-Random-Walk

Chang et al. (2005) and Cuppen & Herbst (2005) introduced a new approach based on the Monte-Carlo algorithm, called the Continous-Time Random-Walk (CTRW). This method considers the actual diffusion of a number of particles from site to site. Furthermore, unlike previous Monte Carlo methods, it also takes into account the actual position of atoms so that the spatial distribution is also included in the simulation. Therefore, this method has some advantages compared to others. Since the physical and chemical processes of adsorbed species on the grain surfaces can be studied microscopically, the structure of the grain and the distribution of binding energies along the surface can be incorporated in the model. Moreover, the progressive formation of grain mantles, allowing the formation of heterogeneous ices, can be followed with time. However, a direct link with the gas-phase chemistry via the rate equations is barely possible and only simple systems have be studied so far because of the CPU time required by the Monte-Carlo algorithm.

Chang et al. (2005) used this approach to study the effect of energy distributions and the grain sizes on the formation of the molecular hydrogen on grains. Cuppen & Herbst (2005) introduced different types of grain surfaces and compared their effect on the H_2 formation efficiency. Cuppen & Herbst (2007) extended this approach to the water network and studied the growth of interstellar ices in diffuse to dark conditions. Chang et al. (2007) tried to link grain surface chemistry treated with the CRTW approach with gas phase chemistry using rate equations, for the H, O, CO system. Finally, Cuppen et al. (2009) studied in more details the formation of methanol and explained the observed ratio between methanol and formaldehyde abundances. The same CTRW model was also applied by Fuchs et al. (2009) to fit experimental results in order to characterise surface chemistry and to constrain the reaction probabilities of the sequential hydrogenation reactions of CO.

Chapter 3

GRAINOBLE: a multilayer macroscopic model

Contents

GRAINOBLE: un modèle multicouche macroscopique

Le travail principal de ma thèse a consisté au développement d'un modèle astrochimique gaz-grain appelé GRAINOBLE. Dans ce chapitre, je décris en détail ce modèle. Après une description générale des principaux processus en phase gazeuse et à la surface des grains interstellaires, je m'attarde sur les principales hypothèses introduites durant cette thèse.

Ce modèle prend en compte l'influence de la structure poreuse des grains sur la chimie de surface en considérant deux types de surface. Une approche multicouche a également été introduite. Elle distingue la surface réactive du manteau inerte, et permet de suivre la composition chimique au sein de la glace. Cette méthode permet d'effectuer un traitement plus réaliste de la photolyse sur la glace puisque l'influence des photons reste cantonnée à la surface. Enfin nous avons développé une approche multiparamètre qui nous permet d'étudier l'influence de chaque paramètre physique, chimique, ou de surface sur la chimie de surface.

Ce chapitre décrit également les réseaux chimiques introduits durant cette thèse. Ceux-ci reposent à la fois sur les résultats récents de travaux expérimentaux étudiant la chimie de surface ainsi que sur des calculs théoriques. Comme nous les verrons dans les chapitres ultérieurs, ils nous permettront d'étudier la formation et la deutération des principaux constituents des glaces interstellaires (eau, formaldehyde, methanol, dioxyde de carbone notamment).

Abstract

The main work of my thesis was the development of a gas-grain astrochemical model, called GRAINOBLE. In this chapter, I describe in details this model. After giving a general description of the main processes considered in the gas phase and on grain surfaces, I present the main assumptions introduced in this thesis.

This model takes the influence of the porous structure of grains on surface chemistry into account by considering two types of surfaces. A multilayer approach is also introduced. It allows us to distinguish the chemically reactive surface and the inert mantle, and to follow the chemical composition inside the ices. This approach allows us to treat more realistically the photolysis on ices because the influence of UV photons is limited to the surface. Finally, we also developed a multi-parameter approach which allows us to study the influence of each physical, chemical, and surface parameter on surface chemistry.

This chapter also describes the chemical networks introduced during this thesis. They are based on recent results from experimental works focusing on surface chemistry and on theoretical calculations. As we will see in the following chapters, these chemical networks will allow us to study the formation and the deuteration of the main interstellar ice components (water, formaldehyde, methanol, carbon dioxide).

3.1 General description

GRAINOBLE is an astrochemical model that couples the chemistry in the gas phase and on interstellar grain surfaces, following the method developed by Hasegawa et al. (1992). In this section, we give a general description of all the chemical processes, based on previous works.

3.1.1 Chemical processes in the gas phase

GRAINOBLE allows the computation of gas phase chemistry with the use of sophisticated gas phase chemical networks including a variety of chemical processes.

3.1.1.1 Cosmic-ray induced processes

Cosmic ray particles are energetic particles, mainly protons, electrons, or alpha particles, with energies above 1 MeV. The interactions of cosmic rays with gaseous species onset the gas phase chemistry in dark clouds. Indeed, they ionize a few key species, and in particular H_2, allowing ion-neutral reactions to occur. Electrons produced by the ionization process can also ionize neutral species, or electronically excite molecular and atomic hydrogen. H_2 subsequently relaxes to produce a secondary flux of UV photons, that ionizes or dissociates molecules (Prasad & Tarafdar, 1983).

The rate coefficient of the cosmic-ray induced processes (in s^{-1}) is proportional to the ionization rate of H_2, ζ,

$$k_{CR}(i) = A_i \zeta \tag{3.1}$$

where A_i is a constant that depends on each photolytic reaction i. The rate of each reaction is simply given by the product of the rate coefficient and the density of the reactant.

3.1.1.2 Photolytic processes

Gaseous particles can also be ionized or dissociated by UV photons coming from the interstellar radiation field (ISRF). The rate coefficient for these photo-processes (in s^{-1}) is function of A_V

because the flux of the ISRF decreases with the visual extinction A_V due to the dust extinction,

$$k_{photo}(i) = A_i \exp(-C_i A_V) \tag{3.2}$$

where A_i is the unattenuated photodissociation rate in a reference radiation field while $\exp(-C_i A_V)$ represents the extinction of the ISRF flux. Most rates considered in chemical networks are computed for the ISRF by Draine (1978) although other ISRF exist (see Mathis et al., 1983).

3.1.1.3 Self-shielding

In addition to the shielding induced by interstellar dust, the flux of UV photons is absorbed in discrete lines due to the photodissociation of abundant species such as H_2, CO, or HD. Indeed. these molecules are photodissociated in several transitions in the FUV domain. For example, H_2 photodissociates through FUV absorption in the Lyman and Werner transitions in the 912-1100 Å range. When the column density of these molecules is sufficiently high, the FUV absorption lines become optically thick and the self-shielding becomes important. The photodissociation rates depend on the abundances and level population distributions of the species as a function of depth in the cloud.

The self-shielding of H_2 and HD are taken from the Meudon PDR code (Le Petit et al., 2006) while the self-shielding of CO is taken from Lee et al. (1996). The Meudon PDR code self-consistently computes the excitation and photodissociation of H_2 and HD as function of their rotational levels. The code does not give directly the self-shielding function of H_2 and HD but their photodissociation rate $k_{photo,i}(A_V)$ as function of the visual extinction. We deduced the self-shielding $f(i)$ (where i refers to H_2 and HD) as function of A_V from $k_{photo,i}(A_V)$ by removing the dust contribution to the total shielding

$$f_i(A_V) = \frac{k_{photo,i}(A_V)}{k_{photo,i}(0)\exp(-\beta A_V)} \tag{3.3}$$

where $\beta = 2.5$ for H_2 and HD. For the visual extinction considered in this thesis ($A_V > 2$), we assumed that the abundances of H_2 and HD remain constant with A_V and the H_2 column density $N(H_2)$ (in cm^{-2}) is proportional to A_V,

$$N(H_2) = 1.9 \times 10^{21} A_V \tag{3.4}$$

Figure 3.1 shows the evolution of the H_2 and HD self-shieldings deduced from the Meudon PDR code, assuming a total density $n_H = 10^4$ cm^{-3}. We also verified that the variation of density does not influence significantly the self-shielding at $A_V > 1$.

We incorporated the self-shielding function of CO from Table 11 of Lee et al. (1996). To deduce the value of the CO self-shielding at a given A_V, we assumed a linear relation between $N(CO)$ and A_V,

$$N(CO) = 1.9 \times 10^{21} A_V X(CO) \tag{3.5}$$

where $X(CO)$ is the CO abundance relative to H nuclei.

3.1.1.4 Bimolecular reactions

Bimolecular reactions refer to reactions involving two species:
- neutral-neutral reactions of the type A + B → C + D
- ion-neutral reactions of the type A^+ + B → C^+ + D
- anion-cation reactions of the type A^+ + B^- → C + D
- associative ionization reactions of the type A + B → AB^+ + e^-
- charge exchange reactions of the type A^+ + B → A + B^+

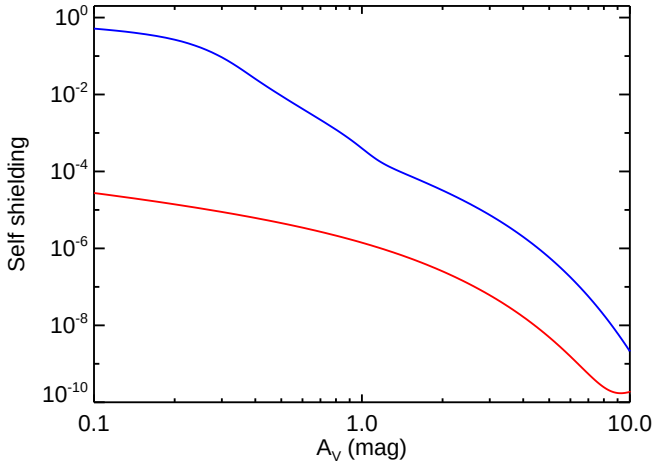

Figure 3.1: Self-shielding functions of H_2 (red) and HD (blue) with the visual extinction A_V deduced from the Meudon PDR code at $n_H = 10^4$ cm^{-3} (see text).

- radiative association reactions of the type A + B → AB + photon
- associative detachment reactions of the type A^- + B → AB + e^-
- electronic recombination and attachment reactions of the type $AB^+ + e^- \rightarrow A + B$ or $AB^+ + e^- \rightarrow AB$ + photon.

The rate coefficients (in cm^{-3} s^{-1}) are generally deduced from gas phase experiments, and fit the Arrhenius formula

$$k_{ij}(i) = A_i(T/300)^{\beta_i} \exp(-C_i/T) \tag{3.6}$$

where A_i, B_i, and C_i are parameters that depend on each reaction.

3.1.1.5 Electronic charging of grains

Interactions between electrons or photons with interstellar grains can lead to an electronic grain charging (see Flower & Pineau des Forêts, 2003).

First, electrons (or positive ions) can attach to neutral grains with an "electronic attachment" rate coefficient (s^{-1}) simply given by the number of collisions between grains and electrons (or ions)

$$k_{att} = sv(\sigma n_{g,0}) \tag{3.7}$$

where s is the sticking coefficient of electrons (or ions) on grains, equal to 0.5 (Weingartner & Draine, 2001), v is the thermal velocity of electrons (or ions), while σ and n_{g0} are the cross section and density of neutral grains, respectively.

Electrons can come off the grains due to the grain photoionization induced by the secondary UV photons, with a rate depending on the ionization rate of H_2 (governing the UV flux), the fraction of UV photons absorbed by the grains, and the detachment probability. Following Walmsley et al. (2004), the rate coefficients (in s^{-1}) have the same expression as the "direct cosmic ray induced" processes

$$k_{det}(i) = A_i\zeta \tag{3.8}$$

where A_i is equal to 6.3×10^7 and 4.1×10^8 for electron detachment on neutral and negatively charged grains, respectively.

Electrons can attach to positively charged grains with the same rate coefficient (in s^{-1}) as the rate with neutral grains, enhanced by the attractive long-range Coulomb potential at low temperature. Le Bourlot et al. (1995) derived an approximate expression for the enhancement factor: $(1+450/T_e)$. Neutralization between positive ions and negative grains are also considered using the same rate coefficient.

3.1.2 Chemical processes on grain surfaces

Four main processes are taken into account on grain surfaces. Here, we only give the rates associated to each process, and the equations needed to compute the main parameters along with a very brief description. For more details, we refer the reader to the previous chapter.

3.1.2.1 Accretion

Gas-phase particles can accrete onto the grains considered as spherical. Although it is known that interstellar grains follow grain size distributions, we assumed one constant grain size. For a given gas-phase species i, the accretion rate is function of:
- the thermal velocity $v(i) = \sqrt{8k_bT/(\pi m(i))}$;
- the cross section of interstellar grains $\sigma_d = \pi(a_d/2)^2$, where a_d is the grain diameter;
- the density of interstellar grains $n_d = 6m_H R_{dg}/(\pi\rho_d a_d^3)$ where m_H is the proton mass, R_{dg} is the dust-to-gas mass ratio (equal to 1%), ρ_d is the volumic mass of grains (equal to 3 g cm^{-3});
- the sticking coefficient $S(i)$. We assumed the sticking coefficient estimated by Tielens (2005) and given in chapter 2 for atomic hydrogen and a sticking coefficient equal to 1 for heavier particles.
The accretion rate of i (in s^{-1}) is given by

$$K_{acc}(i) = S(i)\sigma_d(a_d)v(i)n_d(a_d) \tag{3.9}$$

For dark cloud conditions, particles constituting the ice are bound via the physisorption interactions.

3.1.2.2 Diffusion

Once a particle i is stuck onto the grains, it can diffuse along the surface via thermal hopping according to the Boltzmann law, which gives the hopping rate K_{hop} (in s^{-1})

$$K_{hop}(i) = \nu_0 \exp\left(-\frac{E_d}{k_bT_d}\right) \tag{3.10}$$

where ν_0 is the vibrational frequency of the adsorbed species along the surface (see previous chapter). Several experimental works have emphasized the low efficiency of diffusion via quantum tunnelling. We, therefore, neglect tunnelling diffusion.

3.1.2.3 Reaction

Physisorbed particles can react only via the Langmuir-Hinshelwood (Hinshelwood, 1940) process, in which two species i and j can react when they meet in the same site. The reaction rate K_{reac} (in cm^3 s^{-1}) is given by

$$K_{reac}(i,j) = P_r \times \frac{K_{hop,i} + K_{hop,j}}{N_s(a_d)} \times \frac{1}{n_d(a_d)} \tag{3.11}$$

where P_r is the transmission probability of the reactant, $N_s(a_d)$ is the number of sites at the grain surface given by the ratio between the surface area and the site area.

3.1.2.4 Desorption

Surface species can desorb via several processes:
- the “classic" thermal process caused by the thermal balance of the grain;
- the cosmic ray induced desorption process in which cosmic rays heat the grains, as suggested by Leger et al. (1985), whose rate was computed by Hasegawa & Herbst (1993a);
- the chemical desorption induced by the release of chemical energy of exothermic reactions.

3.2 Porosity treatment

To model the impact of the porous structures of interstellar grains, we introduced two types of sites: the *non-porous*, and the *porous* sites, following Perets & Biham (2006). The *non-porous*

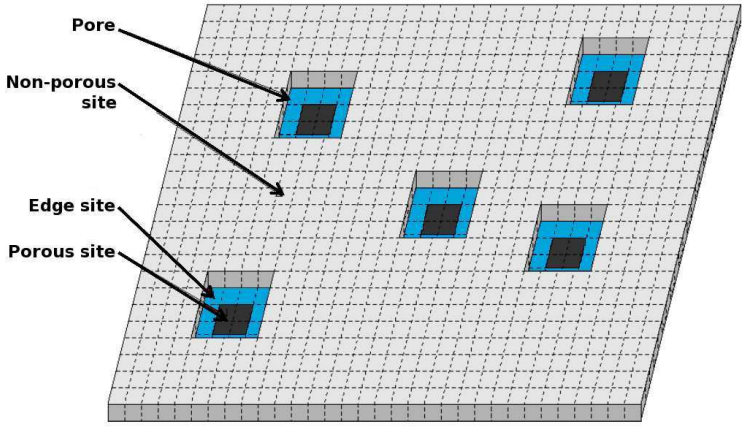

Figure 3.2: Schematic view of a portion of the mantle layer as modelled by GRAINOBLE. All pores are assumed to be square, to have the same size, and no walls (see text). The edges sites, that connect the non-porous surface and the pores are depicted in blue. In this example, each pore is constituted by 16 sites, of which the 12 blue sites are edge sites, and the fraction of area occupied by the pores is 0.1.

sites form a smooth surface that is perfectly regular, where particles interact directly with the gas phase. The gas phase species can accrete onto the grain, and the adsorbates can desorb into the gas phase. The *porous sites* correspond to sites where no direct accretion and desorption are possible. They are filled up only by diffusion from non-porous sites at the edge of the pores. The porous sites cover a fraction F_{por} of the grain surface. For the sake of simplicity, all the pores are assumed to be square and to have the same size, constituted by N_{pore} sites, where $N_{pore} \geq 4$. The fraction of the grain surface occupied by the pores, F_{por}, is poorly constrained. Therefore we ran models with four values for F_{por}: 0, 0.3, 0.6, and 0.9, to cover a large range of possibilities.

The fraction of the edge porous sites, F_{ed}, on the grain depends then on F_{por} and N_{pore} as follows:

$$F_{ed} = 4 \cdot F_{por} \frac{\sqrt{N_{pore}} - 1}{N_{pore}}. \tag{3.12}$$

A posteriori, the actual value of N_{pore} does not influence the results significantly because what matters is mostly the fraction of area occupied by the pores and not the size or the number of pores. In the following, we assumed $N_{pore} = 9$.

The approach that we used for modelling the grain porosity is sketched in Fig. 3.2.

3.3 Multilayer approach

As described in the previous chapter, the bulks of cold ices appear to be inert, and the chemical processes mostly occur on ice surfaces. In order to distinguish the chemistry on the surface and in the bulk of the mantle, we introduced a multilayer approach. In practice, the code follows the chemical processes on a single layer, the one at the surface of the mantle.

In this layer, particles can accrete, diffuse, react with each other and desorb, depending on whether they are on non-porous or porous sites. The growth of the mantle layer is treated at the same time as the chemistry. Specifically, at each time t, the chemistry is followed by solving the set of differential equations described in section 3.9 between t and $t + \Delta t$ and a new number

of particles on the grain is computed at $t + \Delta t$. The layer is considered chemically inert as soon as the number of particles that are on the layer is equal to the number $N_s(a_d)$ of (porous plus non-porous) sites of the layer.

The pores fill up more slowly than the non-porous sites because the porous sites are populated only via diffusion (§3.2). It is, therefore, possible that the layer is considered inert when some pores are still empty. In this case, the number of non-porous sites is "artificially" increased to counterbalance the porous sites that are free. When the considered layer is frozen, the final number of non-porous sites N_{np} can, therefore, be higher than the *a priori* number of non-porous sites $F_{np}N_s(a_d)$ computed at the beginning of the considered layer. Although this is somewhat arbitrary, a posteriori this assumption has almost no impact on the results.

When the layer becomes inert, the code memorizes its composition and a new and reactive layer is started. Note that no chemical exchange is allowed between layers. Finally, the code also takes into account the growth of the grain size and of the number of sites of the new layer by assuming that the thickness of the layer is equal to the site size d_s. All layers have, therefore, the same thickness, equal to the site size. Figure 3.3 gives a schematic view of this approach.

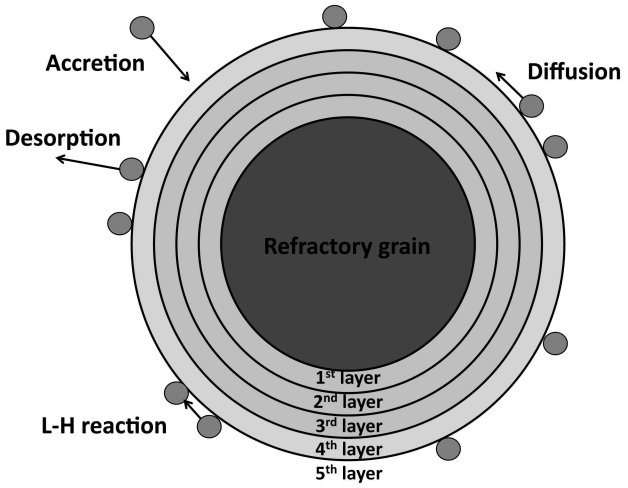

Figure 3.3: Schematic view of the multilayer approach adopted by the GRAINOBLE code. The inner layers of the mantle are chemically inert, whereas the layer at the surface is chemically reactive (see text).

In order to accurately follow the chemical composition of each layer, the timestep depends on the growth rate of ices. At each timestep t, the code evaluates the change of number of particles dN/dt on the surface by computing the number of accreting and desorbing particles. The timestep Δt is then given by

$$\Delta t = (\frac{dN/dt}{N_s} \times N_{steps})^{-1} \tag{3.13}$$

where N_{steps} is the number of timesteps desired for each layer (= 100 in this work).

3.4 Binding energies

Comparisons between the observed absorption 3 μm band of water and laboratory experiments have shown that grain mantles are mainly composed of high-density amorphous solid water (ASW) (Smith et al., 1989; Jenniskens et al., 1995). Therefore, binding energies of adsorbed species relative to ASW must be considered. The binding energies used in this model are listed in Table 2.1.

H_2 is, by about 4 orders of magnitude, the most abundant molecule in molecular clouds. Most of particles that accrete onto the surface are, therefore, H_2 molecules. At low temperatures, H_2 would become the most abundant icy molecule if binding energies were computed relative to a water ice substrate only.

However, microscopic models by Cuppen & Herbst (2007) and Cuppen et al. (2009) have shown that the total binding energy of an adsorbate relative to a substrate is given by the additive energy contribution of the occupied neighbouring sites. Therefore, a H_2O:H_2 mixture must be considered for computing the effective E_b. As described in the previous chapter, Pierre et al. (1985) theoretically estimated the binding energy of H on a H_2 ice, which is about 45 K at 10 K. We applied the same scaling factor than for atomic hydrogen ($E_{b,\mathrm{H2}}(\mathrm{H})/E_{b,\mathrm{ASW}}(\mathrm{H})$) to deduce $E_{b,\mathrm{H2}}$ of species other than H.

Following Garrod & Pauly (2011), we computed the effective binding energy $E_b(i)$ of each species i from the fractional coverage of H_2 on the surface, $P(H_2)$

$$E_b(i) = (1 - P(\mathrm{H_2})) \cdot E_{b,\mathrm{wat}}(i) + P(\mathrm{H_2}) \cdot E_{b,\mathrm{H2}}(i) \tag{3.14}$$

where $E_{b,\mathrm{wat}}(i)$ is the binding energy of the species i relative to water ice. The increase of the H_2 abundance in the mantle tends to decrease the effective binding energy $E_b(i)$ of physisorbed species i.

3.5 Chemical network

The chemical network incorporated in this thesis has been developed following a stepwise process. At first, no chemistry in the gas was considered while a restrictive chemical network on grain surfaces was used to investigate the effect of the multilayer approach as well as other parameters on ice chemistry. Then, a small chemical network producing the main gaseous isotopologues in the gas phase was added while the chemical network producing deuterated isotopologues of solid formaldehyde and methanol is proposed. Finally, full networks coupling gas phase and grain surface chemistry were used to study the formation of water. This section details the three chemical networks.

3.5.1 Formation of simple ices: chemical network (1)

3.5.1.1 Gas phase chemistry

The (observed and predicted) gas-phase abundance of atomic carbon is much lower than CO or atomic oxygen abundances. Therefore, we first considered only the accretion of gaseous H, O, and CO onto the grain mantles.

In dark cloud conditions, the abundance of atomic hydrogen in the gas phase results from a balance between the cosmic rays ionization of H_2 on the one hand and the accretion on dust grains (which react to form H_2 or heavier icy species) on the other hand. At steady state, the density of H is, therefore, given by the ratio between these two processes (Tielens, 2005), as follows:

$$n(H) = \frac{2.3 \cdot \zeta_{CR} \cdot n(H_2)}{2 \cdot v(H) \cdot \sigma_d \cdot X_d \cdot n(H_2)} \tag{3.15}$$

where $v(H)$ is the thermal velocity of atomic hydrogen. The resulting H density is independent of the density and equal to 1.2 $\mathrm{cm^{-3}}$ at 10 K, for a cosmic rays ionization rate ζ of $3 \cdot 10^{-17}$ $\mathrm{s^{-1}}$ (Caselli et al., 1998), a grain abundance X_d of $1.33 \cdot 10^{-12}$ relative to H nuclei and for a grain radius r_d of 0.1 μm ($\sigma_d = \pi \cdot r_d^2$), giving $n_d \cdot \sigma_d / n_H = 4.2 \cdot 10^{-22}$ $\mathrm{cm^2}$. Observations and astrochemical models show that CO is a very stable species and the most abundant molecule after H_2 in dark clouds. Following the estimates by Frerking et al. (1982), we assumed an initial

abundance of CO of $4.75 \cdot 10^{-5}$ with respect to H nuclei. This abundance decreases with time because of the freeze-out onto the grain mantles. Finally, the abundance of atomic oxygen in the gas phase remains poorly constrained. Observations of the [OI] 63 μm line obtained by Caux et al. (1999); Vastel et al. (2000); Lis et al. (2001) with the Infrared Space Observatory (ISO) have measured abundances higher than 10^{-4}, suggesting that most of the gaseous oxygen is in atomic form. But astrochemical models predict an atomic oxygen abundances of $6 \cdot 10^{-5}$ or less. The initial abundance of O is therefore considered as a free parameter and can vary between $2 \cdot 10^{-5}$ and $2 \cdot 10^{-4}$.

3.5.1.2 Grain surface chemistry

We first adopted a small network based on the work by Allen & Robinson (1977) and Tielens & Hagen (1982), and adapted to model the formation of water, formaldehyde, and methanol. As described in chapter 1, observations of ices have shown that grain mantles are mainly composed of O- and CO- bearing molecules such as water, CO, CO_2, or methanol. Molecules such as NH_3 and CH_4 produced by the hydrogenation of N and C can also be found, but only in smaller quantities. In this first chemical network, we therefore neglected the formation of ammonia and methane. In addition, we also did not consider photolytic processes. Our network considers the formation of stable species (e.g, formaldehyde and methanol) and radicals (e.g, HCO, and CH_3O) via hydrogenation of frozen CO. Note that we did not consider CH_2OH because, in absence of photolytic processes, it is formed via the hydrogenation of H_2CO. Theoretical studies have shown that the reaction $H_2CO + H \rightarrow CH_2OH$ has an activation barrier (10.5 kcal/mol) more than twice the activation barrier leading to CH_3O (4–6 kcal/mol) (Sosa & Schlegel, 1986; Walch, 1993; Woon, 2002). We, therefore, neglected CH_2OH in the present study.

For the H_2O formation, we adopted the new reaction scheme based on the experimental works by Dulieu et al. (2010), Ioppolo et al. (2010) and Cuppen et al. (2010c), who estimated the energy barriers of several reactions.

The recombination reaction of hydrogen atoms, forming molecular hydrogen, is also taken into account. Since H_2 has a low binding energy with respect to water ice, and since its reaction of formation releases chemical energy (Hollenbach & Salpeter, 1970), we assumed that the H_2 molecules are desorbed in the gas phase as soon as they are formed.

Finally, we neglect CO_2 formation because its formation pathways, either by a direct surface route or by UV photolysis, in cold conditions are still not well understood.

Red arrows of Figures 3.5 and 3.4 list the surface reactions along with activation barriers considered in this chemical network.

3.5.2 Deuteration of formaldehyde and methanol: chemical network (2)

3.5.2.1 Gas phase chemistry

The second chemical network was developed to study the deuteration of formaldehyde and methanol on ices. Since ice deuteration depends on the atomic gas phase D/H ratio, we are here particularly interested in the chemical network leading to the formation of atomic deuterium in the gas phase. We used the fractionation reactions introduced by Roberts & Millar (2000); Roberts et al. (2003, 2004) to study the formation of H_3^+ isotopologues and atomic deuterium. The gas phase chemical network is shown in Figure 3.5 and the main processes of deuteration in the gas phase have already been described in the introduction chapter.

Briefly, the deuterium is assumed to be initially located in HD. The reaction between H_3^+ and HD and the subsequent reactions are exothermic and allow the formation of H_3^+ isotopologues. Because CO is the main destroyer of H_3^+, its freeze-out onto grains enhances the reactivity of the reaction involving H_3^++HD and, therefore, the abundance of H_3^+ isotopologues. Atomic deu-

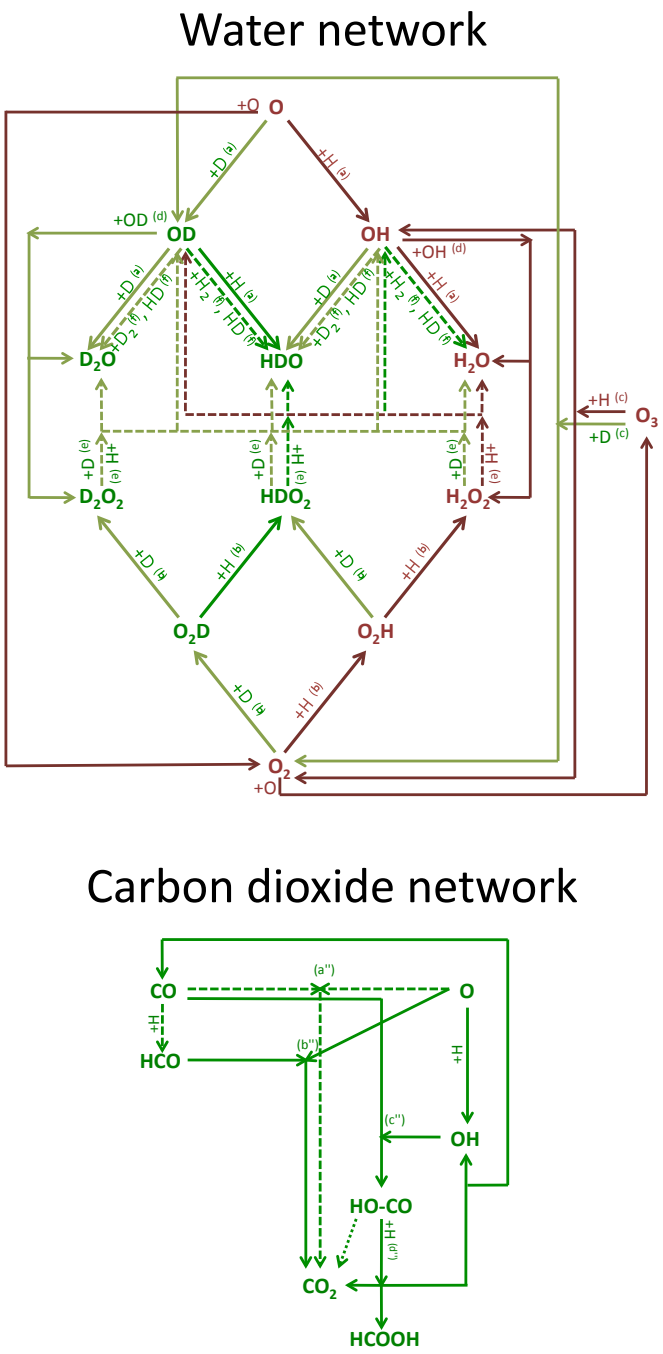

Figure 3.4: Schematic picture of the water and carbon dioxide chemical networks introduced in this work. Red: reactions introduced in chemical network (1), blue:reactions introduced in chemical network (2), green: reactions introduced in chemical network (3). For grain surface networks: dark arrows refer to hydrogenation reactions, light arrows refer to deuteration reactions, solid arrows refer to barrierless reactions, dashed arrows represent reactions with activation barrier.

References. Water network: (a) $E_a = 0$ K (Dulieu et al., 2010; Jing et al., 2011), (b) $E_a = 0$ K (Miyauchi et al., 2008; Cuppen et al., 2010a), (c) $E_a = 0$ K Mokrane et al. (2009); Romanzin et al. (2011), (d) $E_a = 0$ K, Branching ratio: $R = 0.2$ (H_2O) and 0.8 (H_2O_2) (Oba et al., 2011), (e) $E_a = 1400$ K (Klemm et al., 1975, for networks (1) and (2)), $E_a = 2300 - 2500$ K (Ellingson et al., 2007; Miyauchi et al., 2008; Cuppen et al., 2010a, and this work, for network (3)), (f) $E_a = 2700 - 3000$ K (Nguyen et al., 2011; Oba et al., 2012). Carbon dioxide network: (a") $E_a = 2500$ K (Talbi et al., 2006; Raut & Baragiola, 2011), (b") $E_a = 0$ K Baulch et al. (2005), (c") $E_a = 300$ K (Yu et al., 2001; Oba et al., 2010), (d") $E_a = 0$ K (Goumans et al., 2008).

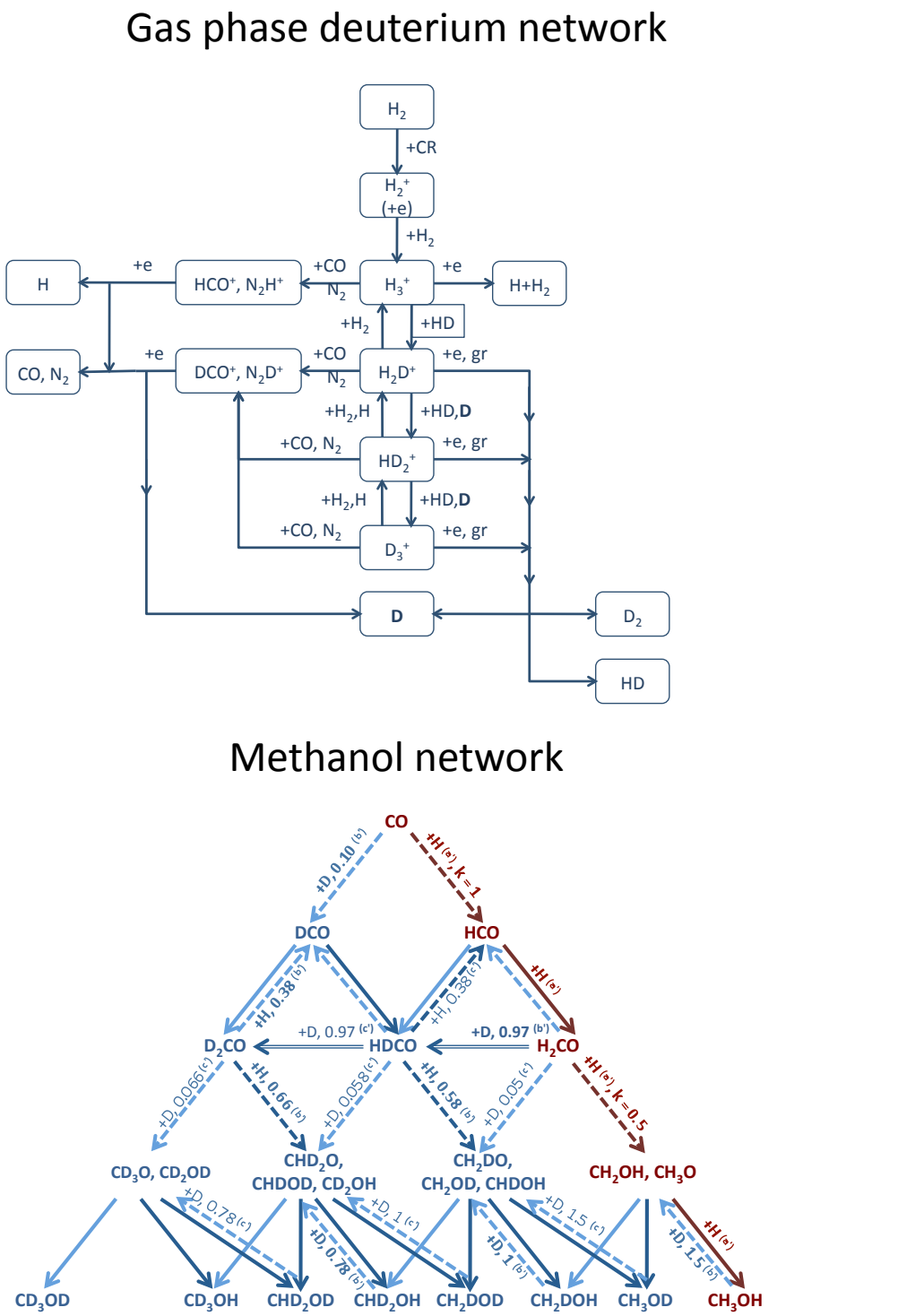

Figure 3.5: Schematic picture of the gas phase and methanol chemical networks introduced in this work. Red: reactions introduced in chemical network (1), blue:reactions introduced in chemical network (2), green: reactions introduced in chemical network (3). For grain surface networks: dark arrows refer to hydrogenation reactions, light arrows refer to deuteration reactions, solid arrows refer to barrierless reactions, dashed arrows represent reactions with activation barrier.

References. Methanol network: (a') For the CO+H and H_2CO+H reactions: $E_a = 400 - 2500$ K (Watanabe & Kouchi, 2002; Watanabe et al., 2004; Watanabe, 2006; Woon, 2002; Fuchs et al., 2009; Andersson et al., 2011, for networks (1) and (2)) and $E_a = 1980$ K (Peters et al., 2012, for network (3)), for other reactions: $E_a = 0$ K, (b'): Rates deduced from Nagaoka et al. (2007); Hidaka et al. (2009) (see text), (c'): This work.

terium is formed via electronic recombinations (or recombinations on grains) of H_3^+ isotopologues. In addition, the abundance of atomic hydrogen is self-consistently computed by considering its formation via H_2 dissociation by cosmic rays.

As shown by Flower et al. (2006), the ortho/para ratio (opr) of H_2 can influence the deuteration of H_3^+ and consequently the atomic D/H ratio, but only when it is $\geq 10^{-3}$. The available measures in cold gas indicate low H_2 opr values ($< 10^{-3} - 10^{-2}$, Dislaire et al., 2012, and references therein). We, therefore, did not consider this effect in the second chemical network.

The abundance relative to H nuclei of the deuterium and CO reservoirs are 1.5×10^{-5} and 4.75×10^{-5}. As for the chemical network (1), the abundance of atomic oxygen is considered as a free parameter.

3.5.2.2 Grain surface chemistry

We considered the accretion of gaseous H, D, H_2, HD, D_2, O, and CO onto grains to focus on the deuteration of solid formaldehyde and methanol.

First, we assumed that formaldehyde, methanol and their deuterated isotopologues are formed via hydrogenation and deuteration addition reactions on molecules initiated by the accretion of CO. Based on experimental and theoretical works (Hidaka et al., 2007; Watanabe & Kouchi, 2008; Andersson et al., 2011), the energy barriers of the D and H addition reactions involving CO and formaldehyde are very similar, so we assumed them to be identical ($= E_a$). Note that, however, given the high uncertainty in the value of E_a (see previous chapter), this is taken as a free parameter. In contrast, reactions involving a radical are barrierless.

Subsequently, we also included the abstraction and substitution reactions of H and D on formaldehyde and methanol following the experimental works by Hidaka et al. (2009) and Nagaoka et al. (2007), according to the scheme proposed by Watanabe & Kouchi (2008) and Hidaka et al. (2009), and shown in Fig. 3.5. We adopted the probability of each reaction following the rates relative to the CO+H reaction deduced experimentally when they are available, as marked in the Figure. For the reactions that have not been derived by the experiments, we adopted the probability measured for the same isotopologue by analogy. For example, the reaction D_2CO + D $\rightarrow$ CD_3O has a reaction rate equal to the H + CO rate multiplied by 0.1 (D + CO) and 0.66 (D_2CO + H).

Even if most of water is likely formed during the translucent phase and, therefore, before H_2CO and CH_3OH, we also took into account its formation, as it is in competition with formaldehyde and methanol formation. With respect to chemical network (1), we added the deuteration reactions and the reaction

$$H_2 + OH \rightarrow H_2O + H$$

which seems to be the most efficient reaction in molecular clouds, as suggested by Cuppen & Herbst (2007).

3.5.3 Water deuteration: chemical network (3)

3.5.3.1 Gas phase chemistry

We considered the gas-phase chemical network from the KIDA database (Wakelam et al., 2012) for seven elements: H, He, C, N, O, S, and Fe, giving a total of 258 gaseous species. Sulphur and iron were introduced to consistently study ion chemistry. Reactions involving atomic Fe and S play a significant role in the destruction of H^+ and H_3^+ whilst S^+, and to a lesser extent Fe^+, is believed to be one of the most abundant ions before the CO depletion (see Flower et al., 2005). Relative to the KIDA network, we modified the rate coefficient of the cosmic-ray dissociation of H_2 yielding H+H. Following Dalgarno et al. (1999), we assumed $\gamma = 0.5$, where the rate k_{diss}

(in s^{-1}) of cosmic ray dissociation reactions is given by $k_{diss} = \gamma\zeta$ (ζ is the cosmic-ray ionization rate). Before ice formation, bare grains are considered. The recombination efficiency of atomic hydrogen and deuterium are assumed to be unity, following the theoretical works by Cazaux & Tielens (2004) and Cuppen et al. (2010b), who considered chemisorption interactions. The initial elemental abundances in the gas phase considered in this work are listed in Table 3.1 and follows the work by Wakelam et al. (2010) and Linsky (2003). To model the water formation at low visual extinctions (see Introduction), we considered the depth-dependent self-shielding of H_2, HD, and CO, using the Meudon PDR code (Le Petit et al., 2002, 2006).

Since standard gas-phase models overpredict the O_2 abundance with respect to what is observed (see Goldsmith et al., 2011; Liseau et al., 2012) we also ran a grid of models by artificially decreasing the formation rate of O_2 by a factor of 10. We checked that the $[O_2]/[O]$ abundance ratio remains indeed ten times lower than the "standard" case throughout the whole calculation.

Deuteration of water and other molecules formed on interstellar grains strongly depend on the gas phase abundances of H, D, H_2, HD, and D_2. In turn, the abundance of these gaseous species, and D in particular, depends mainly on the deuteration of H_3^+ which is function of the degree of CO and N_2 freeze-outs onto the grain surfaces (see Roberts & Millar, 2000; Roberts et al., 2003). The deuterium gas phase chemical network is based on chemical network 2. The major differences with respect to it are the inclusion of the ortho-to-para (hereinafter opr) H_2 ratio and reactions involving N_2.

Reactions between H_3^+ isotopologues and H_2, reducing the deuterium fractionation, are endothermic. Therefore, these reactions cannot occur in cold-cloud conditions if para-H_2 only is considered. However, H_2 is also believed to exist in the ortho spin state, higher in energy (170 K), since H_2 probably forms on grains with an ortho-to-para ratio (opr) of 3. Reactions between ortho-H_2 and ortho-H_2D^+ (ortho-HD_2^+, ortho-D_3^+) can reduce the degree of deuteration of H_3^+ significantly at low temperatures. Flower et al. (2006) have shown that the fractionation of H_3^+, hence, the abundance of atomic D are strongly reduced when the H_2 opr is higher than 10^{-4}. Consequently, we enlarged the chemical network, relative to chemical network 2, by considering the H_3^+-H_2 system whose new reaction rate coefficients have been computed by Hugo et al. (2009). Ion-neutral reactions between H_3^+ isotopologues (including their different spin states) and CO or N_2, electronic recombinations, and recombinations on electronegative charged grains have also been included following Roberts & Millar (2000); Roberts et al. (2003, 2004); Walmsley et al. (2004) and Pagani et al. (2009).

The actual opr of H_2 in molecular clouds is still highly uncertain. The initial value of H_2 opr formed on grain surfaces is most likely 3, as recently confirmed by the experiment by Watanabe et al. (2010) conducted on amorphous solid water. Proton-exchange reactions in the gas phase would then convert ortho-H_2 to para-H_2, decreasing the opr of H_2 towards the Boltzmann value ($\sim 3\times10^{-7}$ at 10 K, see Flower et al., 2006). Recent experimental studies have also demonstrated that H_2 undergoes a nuclear spin conversion from the ortho to the para spin state on amorphous solid water (ASW) (Sugimoto & Fukutani, 2011; Chehrouri et al., 2011; Hama et al., 2012). The influence of the H_2 opr on absorption lines of formaldehyde has been observed by Troscompt et al. (2009) who deduce that the H_2 opr is much lower than 1. Indirect estimates of H_2 based on the comparison with chemical models suggest values of about $10^{-3} - 10^{-2}$ (Pagani et al., 2009; Dislaire et al., 2012). Given the relative uncertainty in this value and its importance in the molecular deuteration process, in this work we assumed the H_2 opr as a free parameter constant with time.

3.5.3.2 Grain surface chemistry

To study the formation and the deuteration of water, we considered a chemical network based on the work by Tielens & Hagen (1982) modified following the results of several experimental

Table 3.1: Elemental abundances with respect to hydrogen nuclei for the chemical network (3).

Species	Abundance
H_2	0.5
HD	1.6×10^{-5}
He	0.09
C	1.2×10^{-4}
N	7.6×10^{-5}
O	2.6×10^{-4}
S	8.0×10^{-8}
Fe	1.5×10^{-8}

works as described in the previous chapter. We also enlarged the water-formation network by including the deuterated counterparts to follow the formation of deuterated water. Barrierless reactions have the same rate coefficients, the decrease of the reaction rates are only due to the lower mobility of deuterated species, induced by their higher mass. A careful treatment of the transmission probabilities (i.e. probability of tunnelling through the activation barrier) of all reactions possessing a barrier is described in section 3.6. Figure 3.4 gives a schematic picture of the chemical network producing deuterated water from O, O_2, and O_3.

In addition to water, formaldehyde, and methanol, we also considered the formation (and the deuteration) of carbon dioxide, methane, and ammonia. Deuterated methane and ammonia are formed via barrierless addition reactions of solid atomic carbon and nitrogen.

The accretion of CO and O particles onto interstellar grains can lead to the formation of carbon dioxide (CO_2) mainly via three reaction channels as described in the previous chapter, and shown in Figure 3.4. Following Oba et al. (2010) who observed a weak band attributed to the HOCO radical and other theoretical works, we proposed a reaction pathway for the CO_2 formation from CO and OH, described below.

CO_2 is thought to be formed via the following pathway

$$\mathrm{CO + OH \rightarrow trans\text{-}HOCO} \tag{3.16}$$

$$\mathrm{trans\text{-}HOCO \rightarrow cis\text{-}HOCO} \tag{3.17}$$

$$\mathrm{cis\text{-}HOCO \rightarrow CO_2 + H} \tag{3.18}$$

The electronic energy of the intermediate radicals (t-HOCO, c-HOCO) and the products (CO_2 + H) are low compared to that of the reactants (CO + OH). Reactions involving t-HOCO and c-HOCO possess high activation barriers and/or are endothermic (Yu et al., 2001). Therefore, t-HOCO radicals continue to react only if their excess energy released by the chemical energy of reaction (3.16) are sufficient to overcome the high activation barriers of reactions (3.17) and (3.18). Following Goumans et al. (2008), HOCO radicals can also react with H atoms via barrierless reactions to form three pairs of products: H_2 + CO_2, H_2O + CO, or HCOOH. Due to the lack of more quantitative data, we assumed a branching ratio of 1/3 for every pair of product.

In fact, the energy released by reaction (3.16) absorbed by HOCO radicals can be transferred to the surface before reacting. However, the transfer rate of the chemical energy to the surface is very uncertain. The absence of formic acid HCOOH, and the low abundance of HOCO radicals observed in the experiments of Oba et al. (2010) suggests that CO_2 is readily formed from excited HOCO molecules. Therefore, most HOCO radicals continue to react before relaxing to their stable state. To reproduce these experiments, we assumed that 99 % of HOCO radicals are sufficiently excited to form CO_2 while 1% of them are stabilized.

Goumans & Andersson (2010) performed gas phase O-CO potential energy surface calculations, showing that O and CO can form a van der Waals complex, allowing O atoms to stay bound to CO for a long time. Following these results, we considered that O atoms which meet CO molecules (via direct accretion from gas phase or surface diffusion) form a loosely bound O...CO complex. H atoms which meet these O..CO complexes react via a barrierless reaction to form an excited HO...CO* complex. If the time for energy transfer to the surface is long enough, the complex can yield OH + CO, or t-HOCO* radical via barrierless reactions. Otherwise, the complex forms the t-HOCO radical through quantum tunnelling. We considered that 99% of HO...CO* complexes continue to react without activation barriers.

In total, our chemical network consists of 341 (gaseous and solid) species and 3860 (gas phase and grain surface) reactions. A full list of surface reactions considered in this work is presented in the Appendix.

3.6 Transmission probabilities

3.6.1 Square barriers

For the chemical networks (1) and (2), the transmission probabilities of reactions displaying activation barriers have been computed by assuming a rectangular barrier of height E_a and width a. In this case, the tunnelling probability is given by

$$P_r = \exp\left(-\frac{2a}{\hbar}\sqrt{2\mu E_a}\right) \tag{3.19}$$

where μ is the reduced mass of the reactants. However, this approach has two main limitations:
i) it does not fit correctly the potential energy profile of reactions;
ii) the width a is unknown. In most astrochemical models, it is arbitrarly fixed to 1 Å (Tielens & Hagen, 1982; Hasegawa et al., 1992). Garrod & Pauly (2011) reproduced the value of the transmission probability of a few reactions computed with HQTST theory (Andersson et al., 2009; Goumans & Andersson, 2010), with square potential barriers and deduced a width of about 2 Å. However, the width has been deduced from poorly constrained activation barriers or other activation energies.

3.6.2 Eckart model

Square potential barriers do not allow us to accurately deduce the values of the transmission probabilities. Therefore, we computed the transmission probabilities of the reactions included in the chemical network (3) and involved in the formation of water, carbon dioxide, formaldehyde, and methanol with the Eckart model (Eckart, 1930; Johnston & Heicklen, 1962). This approach allowed us to deduce the transmission probability by fitting an approximate potential energy surface. A full description of the Eckart model, the quantum chemistry calculations carried out by our collaborators from the PhLAM laboratory (Lille, France) and the computations of the transmission probabilities is given in the Appendix.

Briefly, the formation of deuterated water includes two reaction channels which have an activation barrier: reactions (2.12) and (2.16). Reaction (2.12) has been theoretically studied by Koussa et al. (2006) and Ellingson et al. (2007) but only for the main isotopologues. Therefore, quantum chemistry calculations were conducted for all the reactions (2.12) including deuterated isotopologues. Concerning reaction (2.16), the transmission probabilities of all the deuterated counterparts have been deduced from the theoretical work by Nguyen et al. (2011).

Figure 3.6 shows the Eckart and the symmetric rectangular potentials as function of reaction coordinates for the reaction (2.12) computed in this work. As suggested previously, it can be seen

that the Eckart potential is far to be symmetric. Furthermore, the reaction profile is thinner than the square barrier. Since the quantum tunnelling probability of transmission through this barrier depends on the area of the potential energy profile, the Eckart model gives higher probability of transmission than the square barrier (1.4×10^{-7} versus 1.2×10^{-8}).

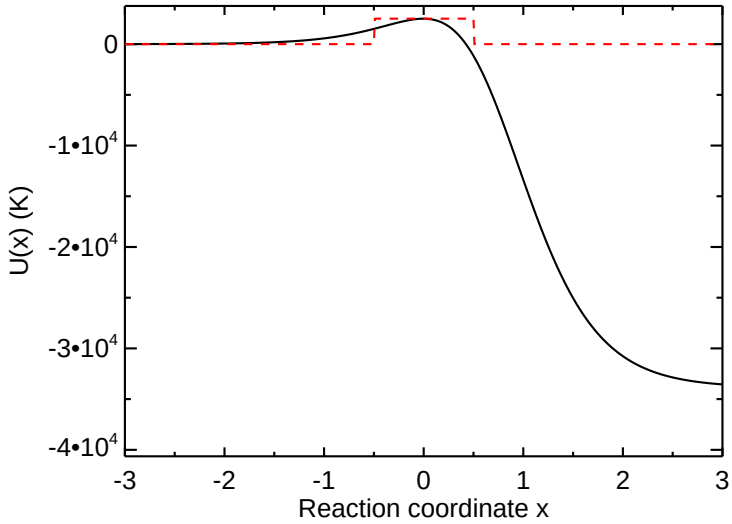

Figure 3.6: Potential energy profile as function of the reaction coordinate of the $H_2O_2 + H \rightarrow H_2O + OH$ reaction computed with the Eckart model (black solid curve) and adopting a symmetric square barrier of a width of 1 Å (red dashed curve). See the Appendix for more details on the calculations.

The formation of carbon dioxide includes two reactions having an activation barrier. Quantum calculations by Talbi et al. (2006); Goumans et al. (2008) and Goumans & Andersson (2010) showed that reaction (2.40) has an activation barrier of 2500 - 3000 K, leading to a transmission probability of 5×10^{-23} (Goumans & Andersson, 2010; Garrod & Pauly, 2011). Assuming an activation energy of 2500 K and considering a square barrier, we reproduce this transmission probability with a barrier width of 0.8 Å. The transmission probabilities of the reaction pathways involved in reaction (2.41), and including the HOCO radicals, the van der Waals complex HO...CO, and their deuterated isotopologues, have been deduced from the potential energy surface computed by Yu et al. (2001).

Table 3.2 lists the reactions displaying an activation barrier as well as the input parameters needed for computing the transmission probabilities. It also compares the transmission probability computed with the Eckart model and with a symmetric square potential barrier of the same activation energy and adopting a width of 1 Å (the value commonly used in most gas-grain astrochemical models). Comparisons between the two approaches show that the assumption of a square barrier width of 1 Å tends to underestimate the reaction probabilities for all the reactions, since $P_{r,Eckart}$ is higher than $P_{r,square}$ between 1 and 7 orders of magnitude.

Table 3.2: List of reactions having a barrier, with the forward, backward activation barriers, the imaginary frequency of the transition state, the transmission probabilities computed with the Eckart model and the square barrier method (using a barrier width of 1 Å). The probability type refers to the method used for computing the probability. "Experiments" mean that the transmission probability is deduced from the rate relative to the CO+H reaction deduced experimentally (see text).

Reactions							Probability type	V_f (K)	V_b (K)	ν_S	$P_{r,Eckart}$	"$P_{r,square}$	Reference
OH	+	H_2	→	H_2O	+	H	Eckart	2935	10209	-1293	4.07(-07)	1.49(-13)	1
OH	+	HD	→	H_2O	+	D	Eckart	2855	9396	-1259	3.62(-07)	7.91(-16)	1
OH	+	HD	→	HDO	+	H	Eckart	3051	10508	-970.4	1.00(-09)	2.44(-16)	1
OH	+	D_2	→	HDO	+	D	Eckart	3026	9556	-955.3	8.07(-10)	8.02(-18)	1
OD	+	H_2	→	HDO	+	H	Eckart	2789	10246	-1293	8.74(-07)	2.88(-13)	1
OD	+	HD	→	D_2O	+	H	Eckart	2900	10871	-970.1	2.81(-09)	5.2(-16)	1
OD	+	HD	→	HDO	+	D	Eckart	2703	9736	-1258	7.99(-07)	1.76(-15)	1
OD	+	D_2	→	D_2O	+	D	Eckart	2870	10338	-955.1	2.26(-09)	7.03(-18)	1
H_2O_2	+	H	→	H_2O	+	OH	Eckart	2508	36358	-1054	1.37(-07)	1.18(-08)	2
H_2O_2	+	D	→	HDO	+	OH	Eckart	2355	37118	-843.7	5.54(-09)	8.83(-12)	2
HDO_2	+	H	→	HDO	+	OH	Eckart	2523	36239	-1053	1.23(-07)	1.17(-08)	2
HDO_2	+	H	→	H_2O	+	OD	Eckart	2524	36063	-1053	1.22(-07)	1.17(-08)	2
HDO_2	+	D	→	HDO	+	OD	Eckart	2369	36822	-846.6	5.28(-09)	8.66(-12)	2
HDO_2	+	D	→	D_2O	+	OH	Eckart	2367	37023	-846.1	5.29(-09)	8.66(-12)	2
D_2O_2	+	H	→	HDO	+	OD	Eckart	2540	35938	-1052	1.08(-07)	1.17(-08)	2
D_2O_2	+	D	→	D_2O	+	OD	Eckart	2384	36721	-842.9	4.28(-09)	8.49(-12)	2
CO	+	H	→	HCO			Eckart	1979	8910	-793.6	1.92(-07)	1.83(-08)	3
CO	+	D	→	DCO			Experiments				1.92(-08)	1.83(-09)	4
H_2CO	+	H	→	CH_3O			Experiments				9.60(-08)	9.15(-09)	4
H_2CO	+	D	→	CH_2DO			Experiments				9.60(-09)	9.15(-10)	5
H_2CO	+	D	→	HCO	+	HD	Experiments				9.31(-08)	8.88(-09)	4
H_2CO	+	D	→	HDCO	+	H	Experiments				9.31(-08)	8.88(-09)	4
HDCO	+	H	→	CH_2DO			Experiments				1.11(-07)	1.06(-09)	4
HDCO	+	D	→	CHD_2O			Experiments				1.11(-07)	1.06(-09)	5
HDCO	+	H	→	HCO	+	HD	Experiments				1.54(-07)	1.46(-08)	5
HDCO	+	D	→	DCO	+	HD	Experiments				9.31(-08)	8.87(-09)	5
HDCO	+	D	→	D_2CO	+	H	Experiments				9.31(-08)	8.87(-09)	5
D_2CO	+	H	→	CH_2DO			Experiments				1.27(-07)	1.21(-08)	4

D_2CO	+	D	→	CD_3O			Experiments				1.27(-08)	1.21(-09)	5
D_2CO	+	H	→	DCO	+	HD	Experiments				7.30(-08)	6.95(-09)	4
CH_3OH	+	D	→	CH_2OH	+	HD	Experiments				2.88(-07)	2.75(-08)	4
CH_2DOH	+	D	→	CHDOH	+	HD	Experiments				1.92(-07)	1.83(-08)	4
CHD_2OH	+	D	→	CD_2OH	+	HD	Experiments				1.50(-07)	1.43(-08)	4
CH_3OD	+	D	→	CH_2OD	+	HD	Experiments				2.88(-07)	2.75(-08)	5
CH_2DOD	+	D	→	CHDOD	+	HD	Experiments				1.92(-07)	1.83(-08)	5
CHD_2OD	+	D	→	CD_2OD	+	HD	Experiments				1.50(-07)	1.43(-08)	5
CO	+	O	→	CO_2			Square (a= 0.8)	2500			/	4.80(-23)	6-7
CO	+	OH	→	t-HOCO			Eckart	285	13050	261	3.61(-03)	1.91(-10)	8
CO	+	OH	→	c-HOCO			Eckart	2128	14047	379	5.81(-17)	2.79(-27)	8
HO...CO			→	t-HOCO			Eckart	775	13050	261	9.46(-09)	9.44(-17)	8
HO...CO			→	c-HOCO			Eckart	2618	14047	379	8.17(-21)	3.53(-30)	8
HO...CO* [a]			→	t-HOCO			Eckart	775	13050	261	1	1	8
HO...CO* [a]			→	c-HOCO			Eckart	2618	14047	261	1	1	8
t-HOCO			→	CO	+	OH	Eckart	13050	285	261	0	6.04(-21)	8
t-HOCO			→	c-HOCO			Eckart	4114	3272	584	0	4.44(-12)	8
c-HOCO			→	t-HOCO			Eckart	3272	4114	584	1.19(-17)	7.51(-11)	8
c-HOCO			→	CO_2	+	H	Eckart	12440	12900	2053	2.94(-21)	1.81(-20)	8
t-HOCO* [b]			→	CO	+	OH	Eckart	13050	285	261	1.63(-10)	1.91(-10)	8
t-HOCO* [b]			→	c-HOCO*			Eckart	4114	3272	584	1	1	8
c-HOCO* [c]			→	t-HOCO*			Eckart	3272	4114	584	1	1	8
c-HOCO* [c]			→	CO_2	+	H	Eckart	12440	12900	2053	2.63(-01)	9.20(-05)	8
CO	+	OD	→	t-DOCO			Eckart	121	13220	260	1.65(-01)	4.65(-07)	8
CO	+	OD	→	c-DOCO			Eckart	1964	14171	260	9.57(-16)	3.08(-26)	8
DO...CO			→	t-DOCO			Eckart	727	13220	260	2.97(-08)	3.01(-16)	8
DO...CO			→	c-DOCO			Eckart	2769	14171	260	1.60(-20)	5.12(-31)	8
DO...CO* [a]			→	t-DOCO			Eckart	121	13220	260	1	1	8
DO...CO* [a]			→	c-DOCO			Eckart	1964	14171	260	1	1	8
t-DOCO			→	CO	+	OD	Eckart	13220	121	260	0	4.46(-21)	8
t-DOCO			→	c-DOCO			Eckart	4238	3343	463	0	3.00(-12)	8
c-DOCO			→	t-DOCO			Eckart	3343	4238	463	1.51(-22)	5.81(-11)	8

c-DOCO	→	CO_2	+	D	Eckart	13230	12670	1632	0	4.38(-21)	8
t-DOCO* [d]	→	CO	+	OD	Eckart	13220	121	260	9.27(-02)	1.13(-02)	8
t-DOCO* [d]	→	c-DOCO*			Eckart	4238	3343	463	1	1	8
c-DOCO* [e]	→	t-DOCO*			Eckart	3343	4238	463	1	1	8
c-DOCO* [e]	→	CO_2	+	D	Eckart	13230	12670	1632	6.18(-02)	2.16(-06)	8

Notes. Excess energies [a]: E* = 49200 K, [b]: E* = 12765 K, [c]: E* = 11920 K, [d]: E* = 13100 K, [e]: E* = 12205 K.
References. 1: Nguyen et al. (2011), 2: This work. 3: Peters et al. (2012), 4: Hidaka et al. (2009), 5: This work, 6: Talbi et al. (2006), 7: Goumans & Andersson (2010), 8: Yu et al. (2001).

3.7 Photodissociation and photodesorption of ices

For chemical network (3), we also considered the effect of FUV (6 - 13.6 eV) photons on interstellar ices following the results of molecular dynamics simulations carried out by Andersson et al. (2006) and Andersson & van Dishoeck (2008). As described in the previous chapter, they studied the behaviour of the five outermost layers of a compact amorphous ice irradiated by FUV photons at 10 K. The wavelength-dependent UV absorption by ices gives absorption probabilities P_{abs} of each monolayer integrated along the 6 - 13.6 eV band of 1.51×10^{-3} for ISRF and 1.03×10^{-3} for CRH2RF. The yield of the different outcomes of the photofragments, OH and H, as function of the monolayer is also computed. Our model only considers one chemically reactive layer (the outermost), we, therefore, deduced the yield of each trajectory by averaging the yields computed by Andersson & van Dishoeck (2008) on each layer. The list of trajectories as well as their averaged yield Y are given in Table 3.3. The rate of each trajectory can, therefore, be deduced, via the following equation

$$R_{photo,i}(s^{-1}) = Y_i \times F_{UV} \times \sigma(a_d) \times 5 \times P_{abs} \times 1/N_s \tag{3.20}$$

where F_{UV} (cm^{-2} s^{-1}) is the photon flux of the 6 - 13.6 eV UV band which is absorbed by the amorphous ice, $\sigma(a_d)$ (cm^2) is the cross section of interstellar grains ($= \pi(a_d/2)^2$ where a_d is the grain diameter), 5 refers to the absorption of the 5 outermost layers to scale with the effective absorption measured in experiments, and N_s is the number of sites on the grain surface. Due to the lack of quantitative data on the photodissociation of other molecules, we analogously considered the same treatment for other hydrogenated molecules, by considering the same absorption and outcome probabilities.

Table 3.3: List of outcomes after H_2O photodissociation with their probability averaged on the 5 outermost layers (deduced from Andersson & van Dishoeck, 2008).

Outcome	Probability
$H_2O_{ice} \rightarrow H_{gas} + OH_{ice}$	0.5
$H_2O_{ice} \rightarrow H_{ice} + OH_{ice}$	0.2
$H_2O_{ice} \rightarrow H_{ice} + OH_{gas}$	2.2×10^{-3}
$H_2O_{ice} \rightarrow H_{gas} + OH_{gas}$	6.8×10^{-3}
$H_2O_{ice} \rightarrow H_2O_{gas}$	4.0×10^{-3}
$H_2O_{ice} \rightarrow H_2O_{ice}$	0.28

We followed the experimental results by Fayolle et al. (2011) for wavelength-dependent CO photodesorption between 7.5 and 13 eV. The convolution of the CO photodesorption spectrum with the ISRF and CRH2RF fields gives integrated photodesorption yields of 1.2×10^{-2} and 9.4×10^{-3} photon^{-1} molecule $^{-1}$ respectively. Due to the lack of data on the wavelength-dependent photodesorption of other molecules, we considered the same photodesorption rates for O_2, and N_2.

3.8 Multiparameter approach

The two previous chapters have emphasized that interstellar ices form within a wide range of physical conditions, while several key surface and chemical parameters are poorly constrained. In spite of their limited accuracy, the rate equations allow an easy and fast computation of sophisticated gas-grain chemistry. A multi-parameter approach is developed in which several thousands of models can be run by varying several physical, chemical, and surface input parameters. This approach allowed us to study their influence on the chemical composition of interstellar ices. Table 3.4 lists the free input parameters along with their range of values explored in this thesis.

Interstellar ices form from translucent and sparse regions of molecular clouds ($n_H \sim 10^3$ cm^{-3}, $T \sim 20$ K, $A_V \sim 2$ mag) to the center of cold dark cores ($n_H > 10^6$ cm^{-3}, $T < 8$ K, $A_V > 15$ mag). The total density, the temperature, and the visual extinction are, therefore, considered as free parameters.

As described in the previous chapter, the coagulation of grains occurring in molecular clouds and in prestellar cores tend to increase their size. In this work, all interstellar grains are assumed to have the same diameter a_d, and display several values between 0.1 and 0.4 μm.

Surface parameters, such as the diffusion to binding energy ratio E_d/E_b, the binding energy E_b of volatile species, and the surface density of sites (or the site size d_s) are known to depend on the morphology and composition of ices. Their values vary within a range given by experimental and theoretical works, and described in the previous chapter. The porosity factor F_{por} varies between 0 (perfectly smooth grain) and 0.9 (highly porous grain).

Several chemical parameters are believed to play a key role in the chemical composition of ices. This is the case of the activation energies of the sequential hydrogenation reactions of CO whose values vary between 400 to $\sim 2000 - 3000$ K in the literature. The abundance of atomic oxygen in the gas phase, before its freeze-out onto interstellar grains, shows uncertain abundances in molecular clouds that might affect the formation of water ice. The ortho to para ratio (opr) of H_2 is known to vary by several orders of magnitude in molecular clouds. As described in section 3.5, it strongly affects the deuteration of gaseous and solid species.

For each model grid considered in this thesis, we analysed the impact of each input parameter on ice chemistry via two methods:
- *abundance distribution.* At selected timesteps, we compute the distributions of abundances on grain mantles $X_m(i)$ of selected species , namely the number of results giving $X_m(i)$ in each abundance interval, when all parameters are varied, except the parameter under consideration. The comparisons between abundance distributions induced by the studied parameter and other parameters allowed us to estimate if and by how much the considered parameter influences the results.
- *mean value and standard deviation.* For each parameter in consideration, we computed the mean abundance (and fractionation) of each species with its 1 sigma standard deviation induced by the variation of other parameters. At each timestep, and for N models, the mean abundances (of fractionations) in logarithmic units are computed following the expression

$$\overline{X} = 10^{\overline{\log(X)}} \tag{3.21}$$

while the logarithmic standard deviation is defined by

$$\sigma = \sqrt{\frac{1}{N}\sum_{1}^{N}\left(\log(X_n) - \overline{\log(X)}\right)^2} \tag{3.22}$$

Note that, in the model grids, some of the parameter values are inconsistent together and do not necessarily reflect realistic physical models. We used them in order to systematically study the influence of each parameter on the formation and/or the deuteration of interstellar ices.

3.9 Computational aspects

The code solves three sets of differential equations: the first one describes the evolution of the densities of species in the gas phase, the other two describe the chemical composition of the mantle outermost layer on the non-porous surface and within the pores (when considered). The equations are the following:

Table 3.4: List of the free input parameters and the range of values explored in this work.

Input parameters	Values
Physical conditions	
n_H	10^3 - 5×10^6 cm^{-3}
$T_g = T_d$	8 - 20 K
A_v	0 - 10 mag
Grain surface parameters	
a_d	0.1 - 0.4 μm
F_{por}	0 - 0.9
E_b(H)	400 - 600 K
E_d/E_b	0.5 - 0.8
d_s	1.4 - 7 Å
Chemical parameters	
E_a(CO)	400 - 2500 K
X(O)	10^{-8} - 10^{-4}
H_2 o/p ratio	3×10^{-6} - 3

$$\begin{aligned}\frac{dn_g(i)}{dt} = & \sum_l \sum_j k_{l,j} n_g(l) n_g(j) - n_g(i) \sum_k k_{i,k} n(k) \\ & - K_{acc}(i) n_g(i) + K_{ev}(i) n_{np}(i) \\ & + \frac{n_g(i)}{n_H} \frac{dn_H}{dt}\end{aligned} \tag{3.23}$$

$$\begin{aligned}\frac{dn_{np}(i)}{dt} = & K_{acc}(i) n_g(i) - K_{ev}(i) n_{np}(i) \\ & - \frac{F_{ed}}{F_{np}} K_{hop}(i) n_{np}(i) + \frac{F_{ed}}{F_{por}} K_{hop}(i) n_{por}(i) \\ & + \sum_l \sum_j K_{l,j} n_{np}(l) n_{np}(j) - n_{np}(i) \sum_k K_{i,k} n_{np}(k) \\ & + \frac{n_{np}(i)}{n_H} \frac{dn_H}{dt}\end{aligned} \tag{3.24}$$

$$\begin{aligned}\frac{dn_{por}(i)}{dt} = & + \frac{F_{ed}}{F_{np}} K_{hop}(i) n_{np}(i) - \frac{F_{ed}}{F_{por}} K_{hop}(i) n_{por}(i) \\ & + \sum_l \sum_j K_{l,j} n_{por}(l) n_{por}(j) - n_{por}(i) \sum_k K_{i,k} n_{por}(k) \\ & + \frac{n_{por}(i)}{n_H} \frac{dn_H}{dt}\end{aligned} \tag{3.25}$$

where $n_{np}(i)$ and $n_{por}(i)$ are the densities of surface species i (in cm^{-3}) on the non-porous surface and within the pores respectively, and $n_g(i)$ the gas-phase density of i. The first and second terms in equation 3.23 describe the formation and destruction rates by gas phase reactions. The third and fourth terms describe the accretion rate and the evaporation rate. The fifth term describes the evolution of density of i due to the evolution of the total density. The first and second terms of equation 3.24 describe the accretion and the evaporation rates. The third and fourth terms describe the exchange rate between the non-porous surface and the pores via diffusion. The

fifth and sixth terms describe the production and the destruction rates of i via reactions on the non-porous surface. The seventh term describes the evolution of density of i due to the evolution of the total density. Similarly, the first and second terms of equation 3.25 describe the exchange rate between the non-porous surface and the pores via diffusion. The third and fourth terms describe the production and the destruction rates of i via reactions in the pores. Note that the evolution of composition within all the pores can be treated with a single equation because all pores are assumed to have the same size. The equations giving the evolution of each pore can be deduced from equation 3.25 by multiplying it with a simple factor of proportionality.

At each timestep, the set of differential equations is solved with the DVODE equation solver. It uses variable-coefficient Adams-Moulton and BDF methods in Nordsieck form, as taken from the older solvers EPISODE and EPISODEB (Brown et al., 1989). Unlike the older codes, VODE has a highly flexible user interface that is nearly identical to that of the ODEPACK solver LSODE. The options chosen for solving the set of differential equations are the following:
- the stiff BDF method is used with a dense, internally generated jacobian matrix.
- a relative error tolerance of 10^{-5} is considered, determining the number of digits of accuracy (in this case: 5)
- an absolute error tolerance of 10^{-20} is chosen, predicting accurate species abundances down to $10^{-20}/n_H$.

Chapter 4

Benchmarking of the GRAINOBLE code

Contents

Analyse comparative du code GRAINOBLE

Ce chapitre décrit les tests effectués qui ont permis de valider notre code. Afin de valider la résolution des équations différentielles, nous avons comparé les résultats d'un réseau chimique complexe en phase gazeuse avec le modèle publique NAHOON. Nous avons ensuite validé l'introduction des paramètres de chimie de surface en appliquant un réseau simple et en le comparant avec des résultats publiés. La modélisation de la porosité a été validée en comparant les résultats de Perets & Biham (2006) pour le système de recombinaison de l'hydrogène.

Notre approche multicouche a ensuite été comparée avec une autre approche multicouche développée par Hasegawa & Herbst (1993b) qui diffère par le piègeage des particules dans le manteau qui est introduit dans les équations différentielles elles-meme. Les abondances prédites par les deux approches pour un réseau simple sont similaires, avec des différences d'abondance absolue d'un facteur deux au maximum. Les deux approches sont donc équivalentes. Nous avons ensuite comparé GRAINOBLE avec le modèle Monte-Carlo de Cuppen et al. (2009) qui permet de suivre l'évolution d'un manteau de glace de manière microscopique. En introduisant un facteur de porosité, nous avons été capable de reproduire les memes compositions chimiques pour différentes conditions physiques, validant notre approche multicouche.

Abstract

This chapter describes the several tests that have been performed in order to validate our code. First, we have compared the results of a sophisticated gas phase chemical network with the public NAHOON code in order to validate the solving of the differential equations. Then, we validated the use of grain surface parameters by applying a simple surface chemical network and by comparing the results with published data. Porosity modelling has been validated by comparing the results for a hydrogen recombination system with the model of Perets & Biham (2006).

Our multilayer approach has been then compared with another multilayer approach developed by Hasegawa & Herbst (1993b) which differs from ours because the trapping of particles inside the bulk is treated in the differential equations. The abundances predicted by the two approaches for a simple network are very similar, showing differences by a factor of two at maximum. The two approaches are, therefore, equivalent. Finally, we compared GRAINOBLE with the Monte-Carlo model by Cuppen et al. (2009) which microscopically follows the evolution of ice mantles. By introducing a porosity factor, we were able to reproduce the same chemical compositions for different physical conditions, validating our approach.

4.1 Validation of the rate equations

4.1.1 Complex gas phase chemistry

We compared the gas phase chemistry computed by GRAINOBLE with the NAHOON model developed by V. Wakelam (see Wakelam et al., 2005). For this purpose, we considered the same chemical network taken from the KIDA database and we computed the chemistry for typical dark cloud conditions ($n_H = 10^4$ cm^{-3}, $T = 10$ K, $A_V = 10$ mag) with the two models. The chemical abundances of most abundant species at 10^7 yr have found to be very similar. Indeed, the differences of abundances are within the relative error tolerances given by the DVODE solver.

4.1.2 Simple surface chemistry

GRAINOBLE has been compared with the results by Stantcheva et al. (2002) and Garrod (2008) for a small chemical network. The chemical network considers the formation of water, formaldehyde, methanol, and carbon dioxide and includes 10 reactions. We compared the chemical abundances at 10^3 yr for three densities $n_H = 10^3$, 10^4, 10^5 cm^{-3} and 10 K. In general, the chemical compositions do not perfectly match with those of Stantcheva et al. (2002) and Garrod (2008). However, the chemical abundances of the main species (water, formaldehyde, methanol) give similar values within $\sim 10\%$ for the three physical cases. Note that the results given by Stantcheva et al. (2002) and Garrod (2008) are not in perfect agreement neither. Tables 6, 7, 8 from Stantcheva et al. (2002) and Tables 4, 5, 6 from Garrod (2008) do not show exactly the same chemical compositions with the same typical error of 10%. Grain surface chemistry is based on a variety of rates that depend exponentially on many input parameters. Therefore, the weak differences between the models are probably due to a small difference of one or a few input parameters.

4.1.3 Porosity modelling

The porosity treatment has been validated by comparisons with the model by Perets & Biham (2006). For this purpose, we adapted GRAINOBLE to follow the H_2 formation via rate equations that compute the evolution of the abundances in terms of monolayers. We are able to reproduce the populations of H atoms in the internal and external surfaces of Figure 4 from Perets & Biham

(2006) for several temperatures. These comparisons, therefore, validate the use of exchange terms between internal and external surfaces.

4.2 Benchmarking of the multilayer approach

4.2.1 Comparisons with the three-phase model by Hasegawa & Herbst (1993b)

In this section, we compared the multilayer approach introduced in the previous chapter with the three-phase model developed by Hasegawa & Herbst (1993b). For this purpose, we introduced in our code the method suggested by Hasegawa & Herbst (1993b) in which three sets of differential equations are considered: one for gas phase species, one for surface species, and one for bulk species. The equations governing chemical abundances on the surface and in the bulk are linked via an additional term, proportional to the rate of growth of the grain mantle. In this manner, surface species are continuously trapped into the bulk induced by the accretion of new particles, unlike our approach in which the trapping is carried out once at a time. The advantage of this method is that the code continuously computes during all the growth of the mantle whereas our code needs to restart the calculation for each layer. The drawback is the complexification of the differential equations compared to the equations used in our method.

We computed the grain surface chemistry with the two methods for a "reference" model ($n_H = 10^5$ cm^{-3}, $T = 15$ K, $a_d = 0.2$ μm) and by considering the chemical network (1) presented in the previous chapter. Figure 4.1 shows the absolute abundances of solid species integrated over all the ice computed with the two methods. We can see that the two models predict very similar abundances for all species. The largest difference is found for methanol which shows a difference of 50 %. As we will see in Part III, a difference of 50% is negligible compared to the abundance evolution induced by the variation of input parameters. As the two models require similar computation time, we can, therefore, assert that the two methods are equivalent.

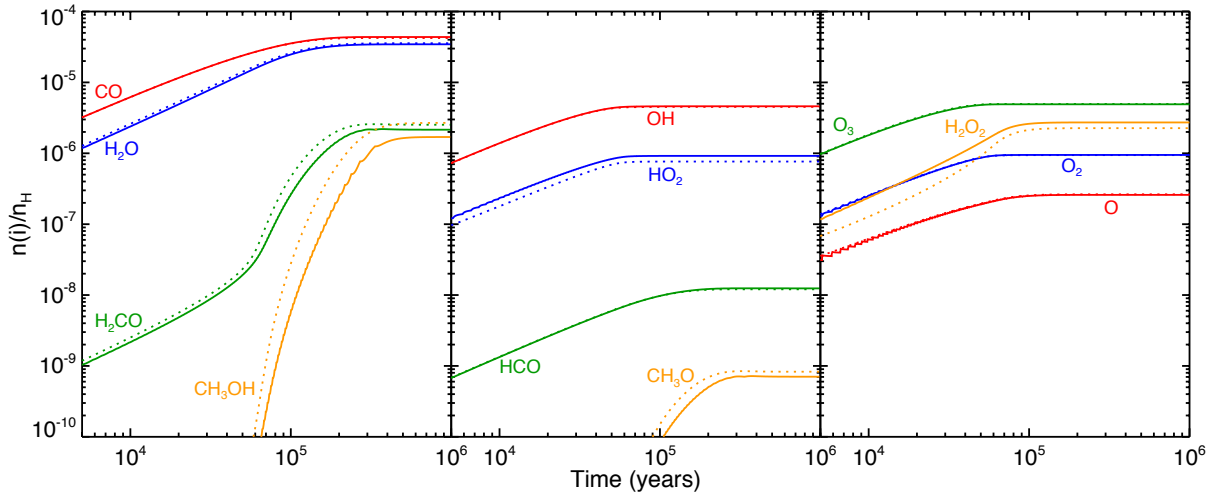

Figure 4.1: Abundances of species in interstellar grain mantles as function of time computed with GRAINOBLE (solid) and the three-phase model by Hasegawa & Herbst (1993b).

4.2.2 Comparisons with the microscopic CTRW model

The Monte-Carlo continuous time random walk (CTRW) method was introduced by Chang et al. (2005) and Cuppen & Herbst (2005) for the hydrogen recombination system, and was then extended to more complex networks in Chang et al. (2007), Cuppen & Herbst (2007), Cuppen et al. (2009). The natural output of this model is the multilayer structure of the mantle. This

section compares our results with the model of Cuppen et al. (2009) with the twofold aim of validating the GRAINOBLE code and of highlighting the differences between the two models.

4.2.2.1 Validation of the GRAINOBLE code

Cuppen et al. (2009) considered the accretion of H, CO, and H_2 on smooth surfaces as described by Cuppen & Herbst (2005), leading to the formation of formaldehyde, methanol, and their associated radicals HCO and CH_3O via the Langmuir-Hinshelwood and the Eley-Rideal mechanisms. A major difference between GRAINOBLE and the Cuppen et al. model is that they consider an α-CO ice, whereas we assumed that the bulk of the mantle is formed by iced water. To reproduce the interactions of molecules within an α-CO ice, we modified the set of binding energies in our model accordingly. Second, the CTRW model takes into account the individual interaction energies between each particle, while our model only considers the total binding energy between the adsorbate and the substrate. To simulate their approach, we assumed for each species i a binding energy equal to fourteen times the interaction between the species i and a CO molecule ($E_b(i) = 14E_{i-CO}$), corresponding to the interaction between an adsorbate and a porous multilayered CO ice. The binding energy of H is equal to 450 K, while the binding energy of CO is 880 K. The diffusion to desorption energy ratio is assumed to be 0.8, as in Cuppen et al. (2009) for a layer that is initially smooth. The activation energies for CO and H_2CO hydrogenation reactions are those measured by Fuchs et al. (2009), and slightly depend on the grain temperature.

To validate our code with respect to the model of Cuppen et al. (2009), we ran our model with a density of 10^5 cm^{-3} and considered the results at 2×10^5 yr, for the following four cases (as in Part 3.3 of Cuppen et al. (2009)): a) grain temperature 12 K, $n(H)/n(CO)$=1 and $n_d = 2 \times 10^{-12} n_{\rm H}$; b) as a) but $n_d = 1 \times 10^{-12} n_{\rm H}$; c) as a) but a temperature of 15 K; d) as b) but $n(H)/n(CO)$=0.5. Figure 4.2 shows the chemical composition of each monolayer for the four cases, for porous grains ($F_{por} = 0.7$: this is the value that agrees best for our and Cuppen's model). The comparison between the two sets of predictions shows that the two codes give very similar results, which validates our code.

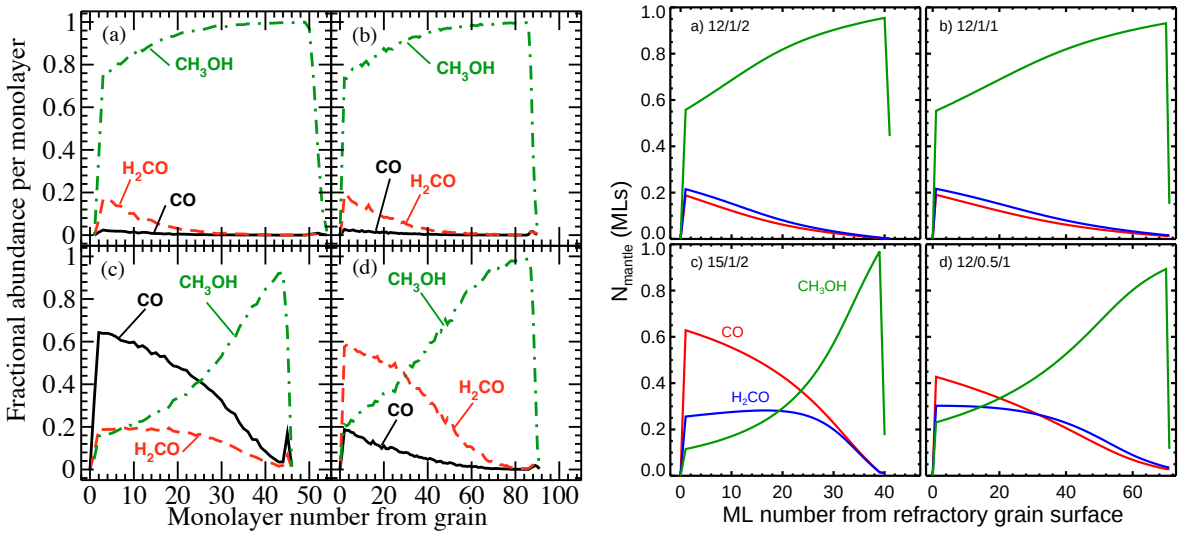

Figure 4.2: Chemical composition of the mantle layers as a function of the monolayers at a time of $2 \cdot 10^5$ years, for a density $n_H = 10^5$ cm^{-3} computed by Cuppen et al. (2009) (left) and by GRAINOBLE (right): CO (red), formaldehyde (blue) and methanol (green). The four panels refer to different cases: a) grain temperature 12 K, n(H)/n(CO)=1 and $n_d = 2 \times 10^{-12} n_{\rm H}$; b) as a) but $n_d = 1 \times 10^{-12} n_{\rm H}$; c) as a) but temperature 15 K; d) as b) but n(H)/n(CO)=0.5.

4.2.2.2 Differences between the two approaches

We highlight a few critical differences between the model of Cuppen and ours.

Unlike our multilayer approach, the CTRW method allows us to model the segregation effects. Heavier particles can agglomerate together to form islands where they can be fixed onto the grains more efficiently. Our multilayer method is a macroscpic approach where segregation effects are not taken into account. However, the pores can play the same role as the islands, because particles that enter into the pores cannot desorb either. This is supported by the fact that our porous grains case agrees best with Cuppen's model.

An important difference between ours and Cuppen et al.'s model is the inclusion of the water ice formation described in the previous chapter. Because Cuppen et al. did not consider the formation of water, their ices are formed by pure α-CO ice. Consequently, the interaction energies are lower than those used in our model. Therefore in Cuppen's model, ices can form only at temperatures lower than 16-18 K, whereas in our model iced CO can still survive until 21-23 K. In our model, then, the formation of formaldehyde and methanol can occur in a wider range of temperatures than in Cuppen et al. (2009). Consequently, the abundance of formaldehyde and methanol formed on grain mantles decreases much more efficiently with the increase of the temperature in Cuppen et al.'s model than in ours. For example, between 15 and 16.5 K using the same physical parameters, the CTRW model predicts a decrease of the mantle thickness of 85 % ($\sim$ 40 to 6 monolayers), whereas our model does not predict any thickness decreases. .

Part II

Ice formation and deuteration: Comparisons with observations

Chapter 5

Multilayer formation of interstellar ices

Contents

Formation multicouche des glaces interstellaires

Les manteaux de glace d'eau mélangés avec du monoxyde de carbon, du formaldehyde et du methanol se forment durant la phase prestellaire. De plus, les radicaux pourraient également se former à la surface des grains, et réagiraient ensuite pour former des molécules organiques complexes durant la phase de réchauffement de l'évolution prestellaire. Dans ce chapitre, nous étudions la formation des manteaux de glace se formant durant la phase de coeur prestellaire et l'abondance du formaldehyde, et du methanol, ainsi que des radicaux piégés dans les manteaux.

Nous avons utilisé le modèle GRAINOBLE pour étudier la formation des glaces interstellaires. Le modèle utilisé un réseau de H, O, et CO formant des espèces neutres telles que l'eau, CO, le formaldehyde, le methanol, ainsi que plusieurs radicaux. Nous avons lancé une grille de modèles pour étudier l'impact de la nature multicouche des manteaux et de la structure poreuse des grains. De plus, nous avons exploré l'influence de l'incertitude d'autres paramètres clés sur la composition des manteaux.

Notre modèle prédit des abondances relativement élevées de radicaux, et plus particulièrement de HCO et CH_3O ($10^{-9} - 10^{-7}$). De plus, l'approche multicouche nous a permis de suivre la differenciation chimique au sein des manteaux de glace, montrant que les manteaux sont loins d'etre uniformes. Par exemple, le methanol est principalement présent dans les couches externes des manteaux alors que le CO et d'autres espèces réactives sont piégés dans les couches internes. La composition intégrée du manteau dépend de la densité et de l'age du coeur prestellaire ainsi que de paramètres microscopiques, tels que l'énergie de diffusion et l'énergie d'activation des réactions d'hydrogénation. Des comparaisons avec les observations de glace nous ont permis de contraindre la value des deux derniers paramètres (0.5-0.65 et 1500 K, respectivement) et nous fournissent des indications sur les conditions physiques pendant la formation des glaces.

Ce chapitre est tiré de la publication: **V. Taquet,** C. Ceccarelli, C. Kahane 2012, *Multilayer modeling of grain porous surface chemistry I. The GRAINOBLE code*, A&A, 538, 42.

Abstract

Mantles of icy water mixed with carbon monoxyde, formaldehyde, and methanol are formed during the so-called prestellar core phase. In addition, radicals are also thought to be formed on the grain surfaces, and to react to form complex organic molecules later on, during the so-called warm-up phase of the protostellar evolution. We aim to study the formation of the grain mantles during the prestellar core phase and the abundance of formaldehyde, methanol, and radicals trapped in them.

We have used the GRAINOBLE model to study the formation of interstellar ices. The model considers a network of H, O, and CO forming neutral species such as water, CO, formaldehyde, and methanol, plus several radicals. We ran a large grid of models to study the impact of the mantle multilayer nature and grain porous structure. In addition, we explored how the uncertainty of other key parameters influences the mantle composition.

Our model predicts relatively high abundances of radicals, especially of HCO and CH_3O ($10^{-9} - 10^{-7}$). In addition, the multilayer approach enables us to follow the chemical differentiation within the grain mantle, showing that the mantles are far from being uniform. For example, methanol is mostly present in the outer layers of the mantles, whereas CO and other reactive species are trapped in the inner layers. The overall mantle composition depends on the density and age of the prestellar core as well as on some microscopic parameters, such as the diffusion energy and the hydrogenation reactions activation energy. Comparison with observations allows us to constrain the value of the last two parameters (0.5-0.65 and 1500 K, respectively) and provide some indications on the physical conditions during the formation of the ices.

This chapter is taken from the publication: **V. Taquet,** C. Ceccarelli, C. Kahane 2012, *Multilayer modeling of grain porous surface chemistry I. The GRAINOBLE code*, A&A, 538, 42.

5.1 Introduction

Among the 150 molecules that have been detected in the interstellar medium (ISM) so far, a significant number are complex organic molecules (here-after COMs), carbon bearing molecules with more than five atoms. Several COMs have been observed in large quantities for two decades in the warm and dense hot cores of massive protostars (Blake et al., 1987). They have received renewed interest in the last few years after the detection of abundant COMs in solar-type protostars, specifically in hot corinos (Cazaux et al., 2003; Bottinelli et al., 2007), and in the clouds of the Galactic Center (Requena-Torres et al., 2006).

Although the abundances of the simplest COMs, such as formaldehyde (H_2CO) or methanol (CH_3OH), are now quite well predicted, astrochemical models still fail to reproduce the abundance of more complex ones, such as methyl formate ($HCOOCH_3$), for example. This molecule is assumed to be mainly formed on grains via the reaction between HCO and CH_3O during the warm-up phase (Allen & Robinson, 1977; Garrod & Herbst, 2006), a reaction in competition with the hydrogenation reaction of CH_3O, which leads to methanol. As described in chapter 1, state-of-art astrochemical models underestimate the methyl formate to methanol abundance ratios and always predict a decreasing ratio with increasing methanol abundance (because methyl formate is in competition with methanol formation).

In this chapter, we focus on the dense and cold phase of the pre-collapse, the prestellar core phase. One possibility, explored by the above models, is that the radicals are formed by the UV photodissociation of frozen species. However, since the impact of the UV photons on the surface chemistry is poorly understood, we explored here the possibility that radicals are synthesized even without photolysis and are trapped in the grain mantles, thanks to the multilayer mantle treatment.

The chapter is structured as follows. In section 5.2 we briefly summarize what is assumed

in the model used in this chapter. Section 5.3 reports the results of the new computations, discussing a reference set of parameters and a large grid of runs where several input parameters are varied. Section 5.4 compares the GRAINOBLE predictions with the observations of ices and discusses the constraints on the various parameters of the model. Finally, §5.5 concludes the chapter, emphasising the main results and perspectives.

5.2 Model

In this work, we followed the formation of interstellar ices with a limited version of GRAINOBLE, which takes into account the following processes:
- No gas phase chemistry was allowed, the density of atomic H in the gas phase is kept as constant, following eq. (3.15).
- H, O, and CO accrete on grain surfaces.
- The formation of water, formaldehyde, methanol as well as other species (OH, HO_2, H_2O_2, HCO, CH_3O, O_2, O_3) was followed on grain surfaces with chemical network (1) described in chapter 3. No photolytic processes are considered.
- The reaction probabilities were computed by assuming a square barrier of a width $a = 1$Å.
- We assumed that H_2, formed from the recombinations between H atoms, desorb upon formation. No H_2 is present in ices and does not influence the binding energies of solid species.
- The thermal and cosmic ray induced desorption processes were taken into account.
- We considered the variation of eight parameters, listed in Table 5.1 with their range of values. The free activation energy E_a refers to the activation energy of the CO and H_2CO hydrogenation reactions.

Table 5.1: List of the free parameters and the value range considered in this chapter.

Parameter	Values
Density n_H	10^4 - $\mathbf{10^5}$ - 10^6 cm^{-3}
Temperature $T_g = T_d$	10 - **15** - 20 K
Initial oxygen abundance $X(\mathrm{O})_{ini}$	$2 \cdot 10^{-5}$ - $\mathbf{6 \cdot 10^{-5}}$ - $2 \cdot 10^{-4}$
Grain size a_d	0.1 - **0.2** - 0.3 μm
Energy ratio E_d/E_b	0.5 - **0.65** - 0.8
Porosity factor F_{por}	**0** - 0.3 - 0.6 - 0.9
Site size d_s	1.4 - **4.2** - 7 Å
Activation energy E_a	**400** - 1450 - 2500 K

Note. Bold values mark the values adopted in the reference model.

5.3 Multilayer formation of ices

We ran a grid of 17496 models, varying the eight free parameters listed in Table 3.4. In this section, we describe the results of our model. We start by describing the results relative to the reference model, and then we describe how the results change when each of the parameters changes. The analysis is based on the distribution of the obtained mantle abundances when all parameters are varied, except for the parameter under consideration. This allowed us to understand if and by how much the considered parameter influences the results. The plot of the multilayer and bulk distributions is shown in section 5.3.2, while the distributions of other parameters (using the multilayer approach only) are shown in Figures 5.7 and 5.8. Finally, Table 5.2 summarises the main effects on the resulting mantle abundances caused by each parameter.

5.3.1 The reference model

This section describes the results obtained using the reference set of parameters (the boldface values in Table 3.4). Below we refer to it as the "reference model". Figure 5.1 presents the evolution with time of the abundance of each species in the gas phase and in the grain mantles.

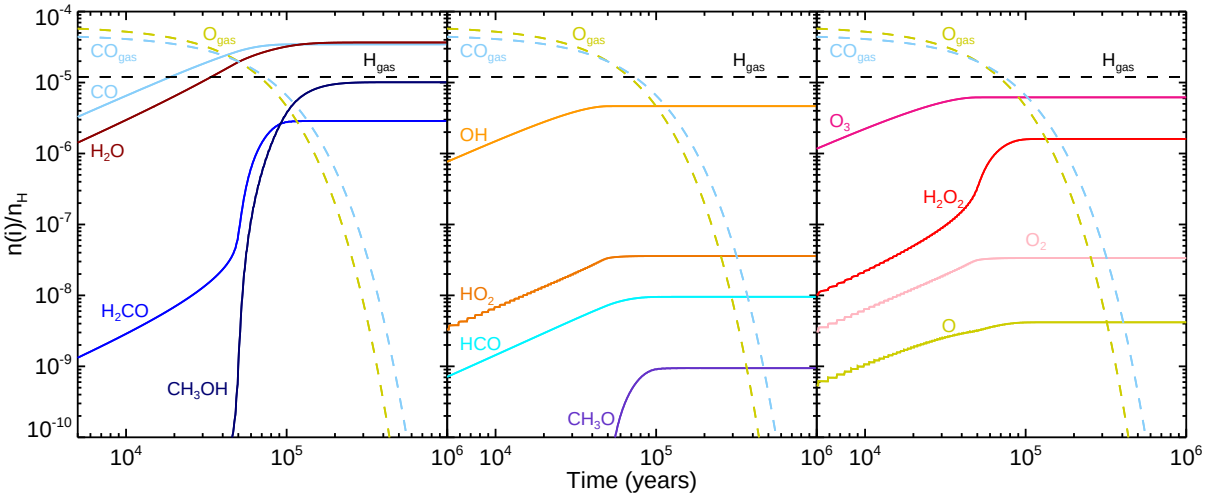

Figure 5.1: Abundance of species in interstellar grain mantles (solid) and in gas phase (dashed) as a function of time for the reference model (boldface values in Table 3.4). *Left panel:* the most abundant stable species. *Middle panel:* reactive species. *Right panel:* less abundant stable species.

The evolution of the chemical composition of the mantle depends on the initial gas phase abundances. In the reference model, O and CO abundances are approximately five times higher than the H abundance. Consequently, H atoms cannot hydrogenate all O and CO molecules that accrete onto the mantles. Besides, H atoms react preferentially with O and its products via barrierless reactions, ending up in water molecules, because the CO hydrogenation reaction has a barrier of 400 K. In $2 \cdot 10^5$ years, 80 % of the CO reservoir is trapped within the mantle bulk, whereas $\sim$ 60 % of O atoms are contained in water. The remaining O atoms are shared between O_3 (ozone), OH and H_2O_2 (hydrogen peroxyde). Indeed, the high O to H initial gas phase abundance ratio ($\sim$ 6) and the relatively high temperature (15 K) allow a significant amount of O atoms to diffuse on the surface and to react with each other before meeting hydrogen atoms.

However, gas phase CO and O abundance ratios relative to H gradually decrease with time (because they freeze-out onto the mantles), increasing the possibility of hydrogenation reactions. After $\sim 5 \cdot 10^4$ years, the formation rates of formaldehyde and methanol start to increase while the formation of ozone stops, corresponding to the time when H, O, and CO have similar abundances. The percentage of ozone, formaldehyde, and methanol in the ices therefore strongly depends on the age of the core. Young cores would show high abundances of ozone and of hydrogen peroxyde with respect to water, whereas older ones would show high abundances of formaldehyde and methanol.

Another important result of the model is that a significant amount of radicals is trapped in the bulk because of the multilayer treatment. Radicals assumed to be the precursors of COMs such as OH, HCO or CH_3O, reach abundances between $\sim 5 \cdot 10^{-6}$ and 10^{-9}. OH is more abundant because of its barrierless formation reaction, and its formation mostly occurs at shorter times.

The evolution of the chemical composition can also be studied "spatially". Indeed, our multilayer approach allows us to study the composition of each monolayer within the grain mantle. Figure 5.2 shows the evolution of the formation time of each layer and the evolution of the mantle thickness with time. In the reference model, a grain mantle of 77 layers is formed in $2 - 3 \cdot 10^5$ yr. Assuming that the layer thickness is equal to the site size (here 4.2 Å), it gives a total mantle

thickness of ~ 0.04 μm, namely 32 % of the grain radius. The first 60 layers are created in less than 10^5 yr because they have a fast formation rate (each layer is formed in less than $\sim 2 \cdot 10^3$ yr). The formation time of layers increases sharply at $\sim 10^5$ yr, because of the drop of the gas phase abundances.

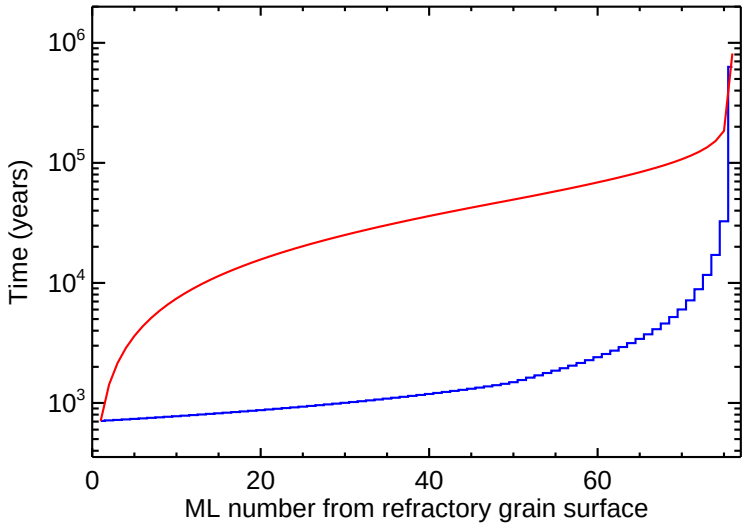

Figure 5.2: Formation time of each monolayer (blue line) and mantle formation time (red line) versus its thickness expressed in monolayers for the reference model (boldface values in Table 3.4).

The differentiation of the composition between the inner and the outer layers of the mantle can also be seen in Fig. 5.3. Indeed, "intermediate" molecules such as O_3, which is created from atomic oxygen, are rapidly formed and are therefore abundant in the inner layers of the mantle (the first 50 layers), whereas formaldehyde and methanol are mostly formed later, their fractional composition showing significant abundances only in the 20 outermost layers. The abundances of the two main species, CO and H_2O, remain relatively constant throughout the mantle up to the last outermost layers, where they decrease in favour of H_2CO and CH_3OH. The composition of radicals within the mantle follows the same evolution as their precursor molecules: the HCO abundance stays relatively constant until the drop in the last layers like CO, while the OH abundance decreases following the O abundance behaviour. Finally, the CH_3O abundance increases when approaching the surface, as H_2CO.

5.3.2 Multilayer versus bulk approach

The introduction of the multilayer approach modifies the chemical behaviour of grain mantles and thus their overall chemical composition. Figure 5.4 shows the evolution of the mantle composition with time for the reference model, adopting a multilayer (described in sec. 3.3) or a bulk (old method described in chapter 1) approach, respectively. The figure shows that at short timescales ($\leq 5 \times 10^4$ yr), both approaches give similar abundances for the main species because the H abundance is initially low compared to the CO and O abundances (§5.3.1). In contrast, O and its associated "intermediate" molecules (OH, O_2, and HO_2) are more efficiently burned in O_3, H_2O_2, and H_2O in the bulk method compared to the multilayer approach.

At later times ($\geq 5 \times 10^4$ yr), reactive species, which are trapped by the multilayer approach, continue to react in the bulk method. Consequently, in the bulk approach, radicals (OH, HCO, HO_2, CH_3O) and "intermediate" stable species (O, O_3, H_2O_2, O_2) are totally burned in less than $\sim 10^6$ yr. In contrast, the abundances of these species do not evolve after $\sim 3 \cdot 10^5$ yr with the multilayer approach. Finally, the predicted methanol and formaldehyde abundances substantially diverge in the two approaches at times longer than $\sim 10^5$ yr, namely the presumed

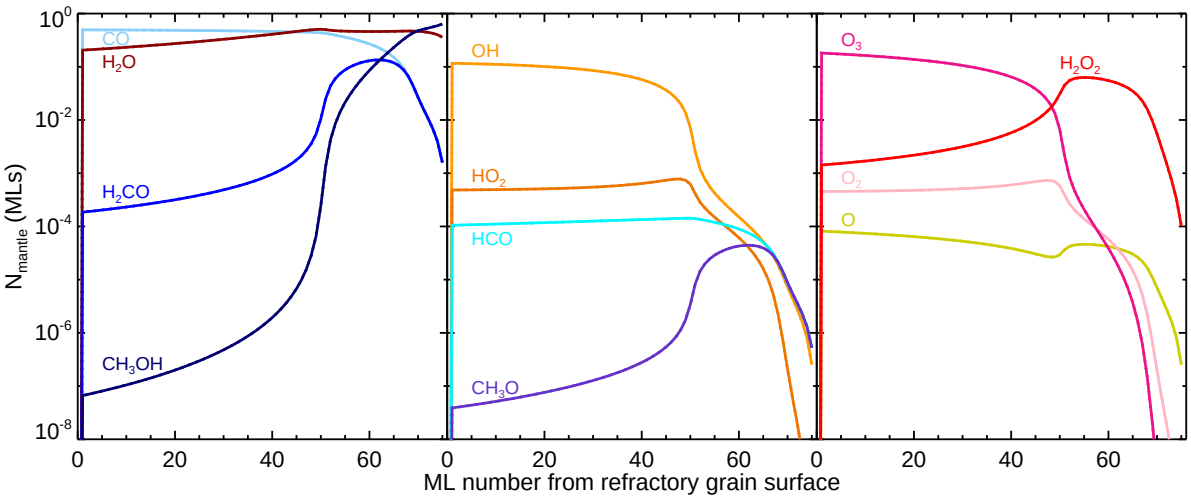

Figure 5.3: Fractional composition of each mantle monolayer for the reference model (boldface values in Table 3.4).

ages of the prestellar cores. The bulk method predicts a final (at 10^6 yr) methanol abundance higher by factor 6 compared to the multilayer approach, and a formaldehyde abundance lower by a factor higher than 10^4.

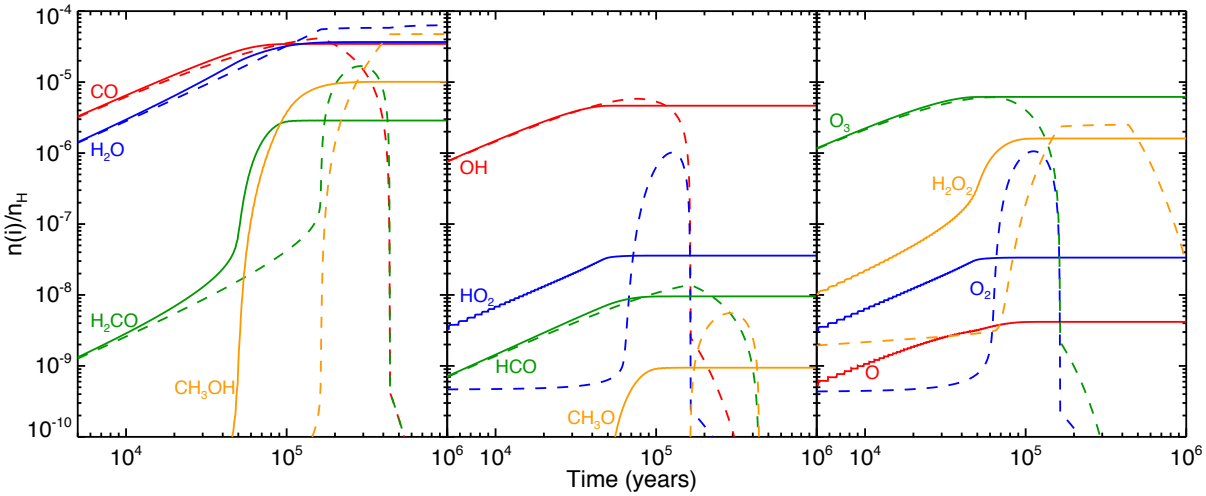

Figure 5.4: Abundance of species in interstellar grain mantles as a function of time for the reference model (solid lines), and the bulk approach model (§5.3.2; dashed lines). *Left panel:* the most abundant stable species. *Middle panel:* reactive species. *Right panel:* less abundant stable species.

To understand how robust these results are, we considered the whole grid of models described in §5.2 and built the distribution of the predicted abundances. Figure 5.5 shows this distribution for key stable species (CO, H_2O, H_2CO, and CH_3OH) and the radicals (OH, HCO, and CH_3O) for the bulk and multilayer approaches for two times (10^5 and 10^6 yrs). The plots of Fig. 5.5 tell us that at short times (10^5 yr) the predicted species abundance distributions are quite similar in the bulk and multilayer approaches, with the exceptions of H_2CO and CH_3O, for which the distribution are slightly different. In contrast, at long times (10^6 yr), the distribution of all radicals are substantially different in the two approaches, demonstrating that the age is a key parameter. The plots also provide another important information. For example, considering the multilayer approach results, CO and OH have quite peaked distributions and their predicted abundances depend slightly if at all, on the assumed values of the input parameters: they are

robust predictions. On the contrary, H_2CO, CH_3OH, HCO and CH_3O have broad abundance distributions implying that their predicted abundances are very sensitive to the values of the other model parameters.

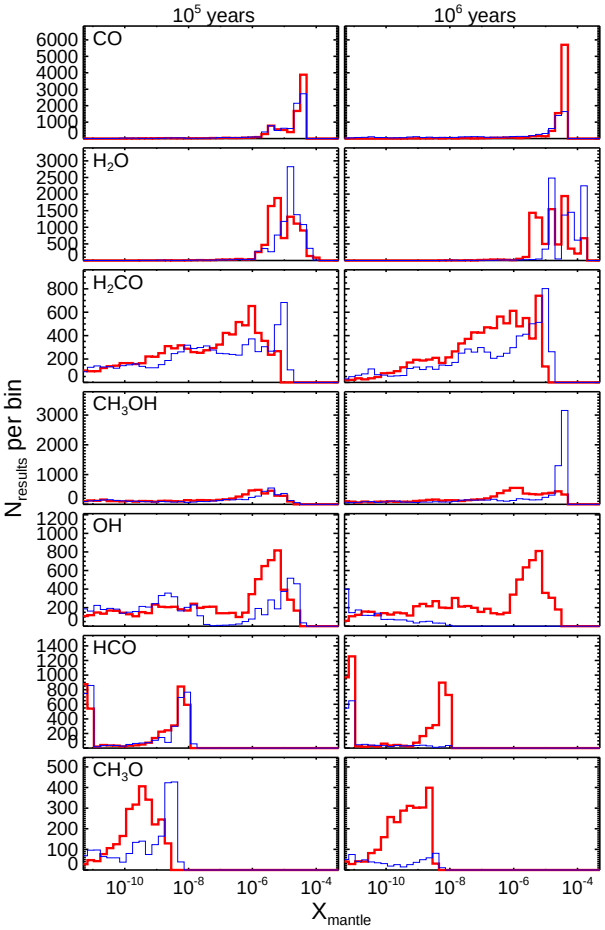

Figure 5.5: Distribution of the predicted mantle abundance X_{mantle} of the key species at 10^5 (left panels) and 10^6 yr (right panels). The thin blue and thick red lines refer to the bulk and multilayer approach. The distribution has been built by considering all the ∼18000 runs of the grid (§5.2).

.

Table 5.2: Summary of the effect of each free parameter on the surface chemistry and on the distribution of results (shown in the Figures 5.7 and 5.8).

Parameter	Effect on the surface chemistry	Distributions of abundances for stable species	Distributions of abundances for radicals
Multilayer versus bulk approach	The multilayer approach - decreases the formation of stable species - traps reactive species into the mantle	- $X(\mathrm{CO}) > 10^{-5}$ for 88% (ML), 50% (bulk) cases - $X(\mathrm{H_2O}) > 10^{-5}$ for 60% (ML), 93% (bulk) cases - $X(\mathrm{CH_3OH}) > 10^{-5}$ for 15% (ML), 55% (bulk) cases	- $\mathrm{X(OH)} > 10^{-9}$ for 75% (ML), 1% (bulk) cases - $X(\mathrm{HCO}) > 10^{-9}$ for 25% (ML), 2% (bulk) cases
Porosity	The increase of porosity - traps volatile and diffusing particles - increases the formation rate of stable species	- $X(\mathrm{H_2CO}) > 10^{-7}$ for 52% (smooth), 61% (porous) cases - $X(\mathrm{CH_3OH}) > 10^{-7}$ for 51% (smooth), 61% (porous) cases	- $\mathrm{X(OH)} > 10^{-6}$ for 55% (smooth), 20% (porous) cases
Density	The increase of density - decreases the formation of stable species formed by hydrogenation reactions	- $X(\mathrm{H_2O}) > 10^{-5}$ for 2% (dense) , 85% (sparse) cases with $X(\mathrm{H_2O}) \rightarrow 2 \cdot 10^{-4}$ - $X(\mathrm{CH_3OH}) > 10^{-5}$ for 0% (dense) , 35% (sparse) cases with $X(\mathrm{CH_3OH}) \rightarrow 9 \cdot 10^{-5}$	- $X(\mathrm{OH}) > \cdot 10^{-6}$ for 0% (sparse), 75% (dense) cases
Temperature	The increase of temperature - strongly increases the desorption of H and O - decreases the rates of hydrogenation reactions - decreases the abundance of stable species formed by these reactions	- $X(\mathrm{CH_3OH}) > 10^{-7}$ for 65% (cold), 45% (warm) cases - $X(\mathrm{H_2CO}) > 10^{-7}$ for 60% (cold), 45% (warm) cases	- $X(\mathrm{OH}) > 10^{-6}$ for 55% (cold), 48% (warm) cases
Grain size a_d	The increase of the grain size - increases the mantle thickness - does not influence the integrated mantle composition	Same evolution of distributions for all stable species	Same evolution of distributions for all radicals

Initial abundance of atomic oxygen	The increase of X_{ini}(O): - increases the formation of water (and other molecules formed from reactions involving O) - slightly decreases the formation of molecules formed from CO	- $X(H_2O) > 2 \cdot 10^{-5}$ for 0% (low-O), 65% (high-O) cases with $X(H_2O) \rightarrow 2 \cdot 10^{-4}$ - No influence is seen for CO, H_2CO and CH_3OH	- $X(OH) > 4 \cdot 10^{-6}$ for 0% (low-O), 50% (high-O) cases with $X(OH) \rightarrow 4 \cdot 10^{-5}$
Diffusion energy	The increase of the diffusion energy - decreases the diffusion rate of mobile species - decreases the formation rate of stable species - slightly increases the survival of radicals	- $X(H_2O) > 5 \cdot 10^{-6}$ for 87% (fast), 74% (slow) cases - $X(CH_3OH) > 10^{-7}$ for 80% (fast), 30% (slow) cases - $X(H_2CO) > 10^{-7}$ for 75% (fast), 40% (slow) cases	Same evolution of distributions for all radicals
Activation energies	The increase of activation energies - strongly decreases the formation rate of H_2CO and CH_3OH - strongly decreases the survival of radicals HCO and CH_3O - slightly increases the reaction rates of reactions involving O - slightly increases the formation of water	- $X(CO) > 10^{-5}$ for 35% (low-Ea), 98% (high-Ea) cases - $X(H_2CO) > 10^{-7}$ for 83% (low-Ea), 25% (high-Ea) cases - $X(CH_3OH) > 10^{-6}$ for 80% (low-Ea), 5% (high-Ea) cases	- $X(HCO) > 10^{-10}$ for 90% (low-Ea), 0% (high-Ea) cases - $X(CH_3O) > 10^{-10}$ for 70% (low-Ea), 0% (high-Ea) cases
Site size	The increase of the site sizes - decreases the formation time of layers - increases the mantle thickness - does not influence the integrated mantle composition	Same evolution of distributions for all stable species	Same evolution of distributions for all radicals

5.3.3 Porous versus non-porous grains

The influence of the grain porosity (§3.2) is shown in Figure 5.6 for the reference set of parameters. The presence of the porosity in the grain has the effect of slightly speeding up and increasing (by less than a factor 4) the formation of formaldehyde, methanol, and CH_3O, as well as to increase the destruction of HO_2, O_2 and O. The reason is that porous grains trap H atoms more efficiently, increasing their number on the grains, but in the end, the H atom numbers is still limited by their low gas phase abundance (Fig. 5.4). Furthermore, the porosity only slightly modifies the distribution of the results shown in Fig. 5.7. Therefore, the porosity only enhances the formation of hydrogenated molecules by a few factors at most, regardless of the values of other parameters.

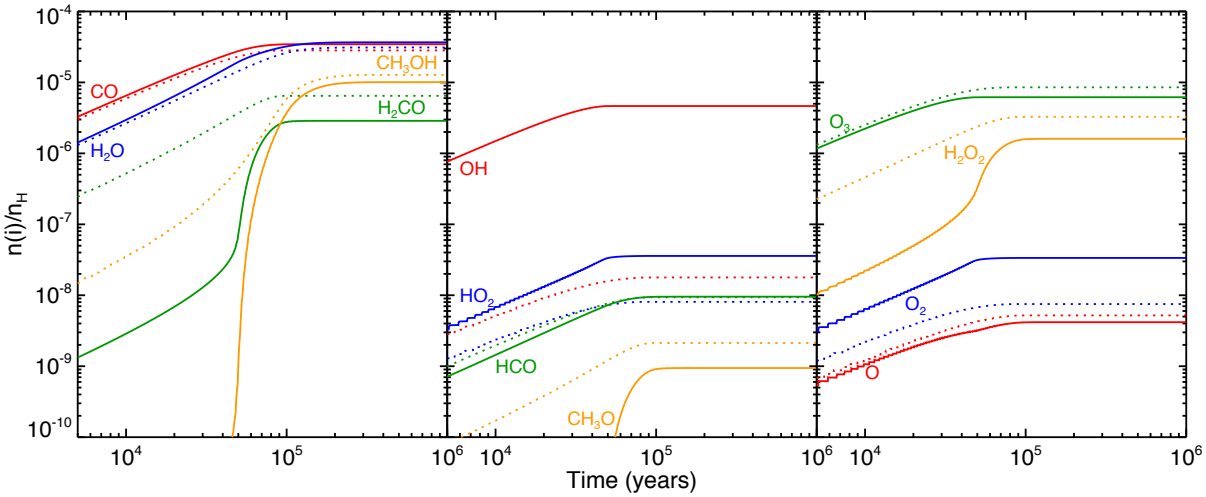

Figure 5.6: Abundance of species in interstellar grain mantles as a function of time for the reference model (solid lines), and the porous grain model (§5.3.3; dotted lines). *Left panel:* the most abundant stable species. *Middle panel:* reactive species. *Right panel:* less abundant stable species.

5.3.4 Influence of physical conditions

Density n_H

The density plays an important role for two reasons. First, increasing the density reduces the time needed to form each monolayer (because the accretion rate is proportional to the square of the density). Second, the ratio between the number of H atoms and the number of heavy particles (CO and O) that land on the grain is inversely proportional to the density. Indeed, the density of atomic H remains constant regardless of n_H (see eq. 3.15) whereas the density of atomic O and CO increase linearly with n_H. As a consequence, the higher the density, the lower the abundance of stable species (H_2O, H_2CO, CH_3OH) created by the hydrogenation reactions, especially at long times ($\geq 10^5$ yr) (see Fig. 5.7). In contrast and for the same reasons, mantle CO and OH are more abundant for higher density.

Temperature $T_g = T_d$

The grain temperature has a moderate influence on the predicted mantle composition, although the diffusion (and thus the reaction) and the desorption rates depend exponentially on it. However, the desorption rate increases much more quickly than the diffusion rate with temperature (by factors of $10^2 - 10^6$ depending on the E_d/E_b ratio). Consequently, with increasing grain temperature, H atoms have a higher probability to desorb into the gas phase before encountering another particle. The final mantle abundance of molecules created by hydrogenation reactions (H_2CO and CH_3OH) is therefore lower at any time at higher temperatures, as shown by Fig. 5.7.

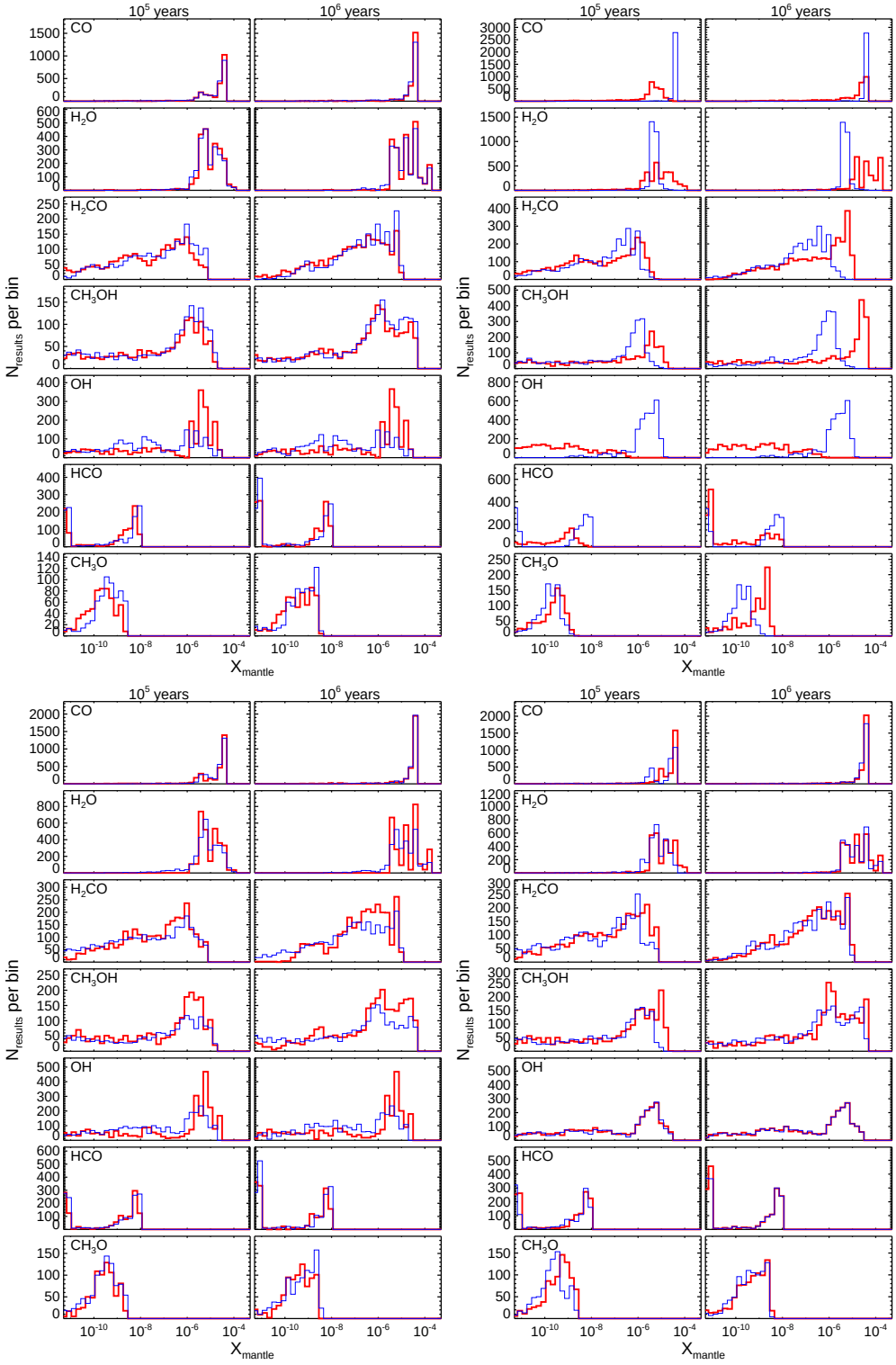

Figure 5.7: Distribution of abundances on grain mantles at $t = 10^5$ and 10^6 years for two porosity values (top left): $F_{por} = 0$ (thick red) and 0.9 (thin blue), two total density values (top right): $n_H = 10^4$ (thick red) and 10^6 (thin blue) cm^{-3}, two temperature values (bottom left): $T = 10$ (thick red) and 20 (thin blue) K, two grain sizes (bottom right): $a_d = 0.1$ (thick red) and 0.3 (thin blue) μm.

The mantle abundance of radicals, on the other hand, is not affected by the grain temperature.

Grain size a_d

While the mantle thickness depends roughly quadratically on the grain size, the final mantle composition depends very little on it. The reason is that the particle accretion rate (inversely proportional to the grain size square) and the formation time of each layer compensate each other. The result is that the mantle composition does not depend on the assumed grain size, whether 0.1 or 0.3 μm (see Fig. 5.7).

5.3.5 Influence of other key parameters of GRAINOBLE

Initial abundance of atomic oxygen $X(O)_{ini}$

Not surprisingly, the initial gas phase abundance of atomic oxygen is an important parameter for the final mantle water abundance. The higher the O abundance, the higher the iced H_2O. Less evidently, oxygenation is in competition with hydrogenation. The initial O abundance also affects the final mantle abundance of formaldehyde and, even more, methanol, because the elemental C/O ratio decreases between 0.7 and 0.2 when $X(O)_{ini}$ increases between $2 \cdot 10^{-5}$ and $2 \cdot 10^{-4}$. At 10^5 yr, the predicted methanol abundance is a factor of ten higher when the O abundance is a factor ten lower (see Fig. 5.8).

Diffusion energy to binding energy ratio E_d/E_b

The diffusion energy is an important parameter in the predicted mantle abundance of formaldehyde and methanol. The diffusion rates depend exponentially on the diffusion energy, the mantle abundance of stable species, like formaldehyde and methanol, therefore decreases with increasing E_d. Conversely, the diffusion energy does not affect the mantle abundance of radicals, because their formation and destruction rates compensate each other.

Activation energy E_a

The activation energy of CO and H_2CO hydrogenation reactions strongly influences the formation rates of formaldehyde and methanol because their reaction rates depend exponentially on E_a. As seen in Fig. 5.8 most of the runs with a low value of E_a (400 K) predict mantle abundances of formaldehyde and methanol higher than 10^{-6} at $\geq 10^5$ yr. Conversely, higher values of E_a give uniform distributions of H_2CO and CH_3OH abundances, between 10^{-18} and 10^{-6}. Only $\sim$ 5% of the runs using an activation energy equal to 2500 K predict formaldehyde and methanol abundances higher than 10^{-6}. The final abundances of formaldehyde and methanol, consequently strongly depend on the other model parameters for high E_a values. A significant amount of radicals, like HCO and CH_3O, can survive in the mantle only if the activation energies are low. Runs with activation energies of 400 K predict radical mantle abundances between 10^{-10} and 10^{-8} for both radicals, while runs with $E_a = 2500$ K predict abundances less than $\sim 10^{-11}$. Not surprisingly, the activation energy of CO and H_2CO hydrogenation reactions are, therefore, critical parameters for the survival of radicals in the mantle.

Site size d_s

The reaction rates and the formation time of each monolayer are both functions of the site size d_s: the former is proportional to d_s^2, whereas the latter is proportional to d_s^{-2}. Therefore, the two processes, which are in competition, cancel each other. Consequently, the total mantle abundance of stable species and radicals do not sensitively depend on the size of sites.

However, the thickness of the grain mantle strongly depends on the site size. Indeed, the maximum number of monolayers is given by the ratio between the number of particles on the grain N_{part} and the number of grain sites N_s (proportional to d_s^{-2}). Furthermore, if we assume

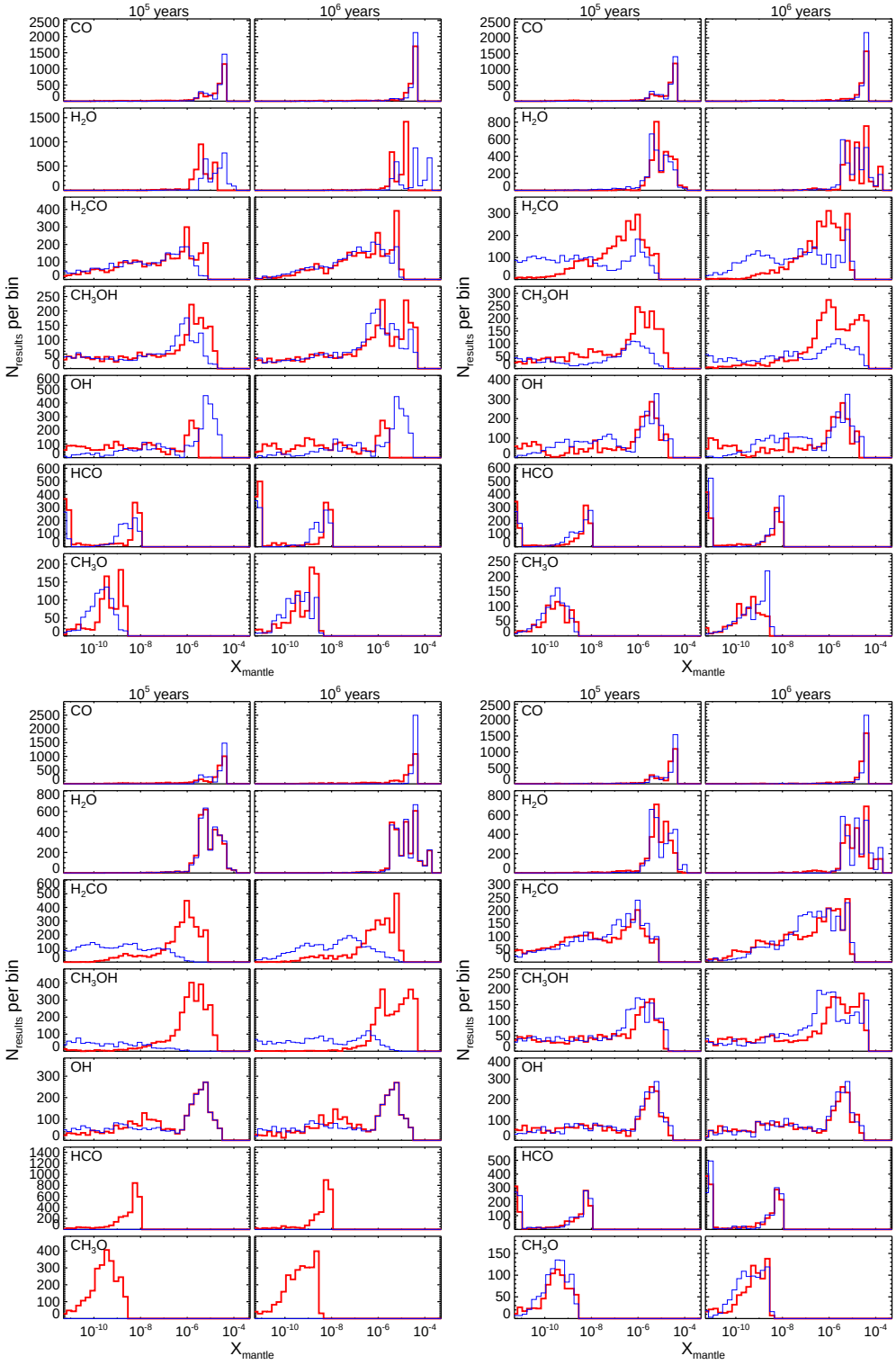

Figure 5.8: Distribution of abundances on grain mantles at $t = 10^5$ and 10^6 years for two initial oxygen abundances (top left): $X_{ini}(\mathrm{O}) = 2 \times 10^{-5}$ (thick red) and 2×10^{-4} (thin blue), two E_d/E_b values (top right): $E_d/E_b = 0.5$ (thick red) and 0.8 (thin blue), two E_a values (bottom left): 400 (thick red) and 2500 (thin blue) K, two site sizes (bottom right): 1.4 (thick red) and 7 (thin blue) Å.

that the thickness of a layer is equal to the distance between two sites, the thickness of the mantle is proportional to d_s^3. Thus, the bigger the sites, the faster the grains grow. Consequently, the depletion is more efficiently on grains with big sites, increasing the abundance of methanol and decreasing the abundance of CO for example (as seen in Fig. 5.8).

5.3.6 Concluding remarks

Based on the previous paragraphs, we can identify three classes of parameters, depending on their influence on the results:

- 1) The parameters that have a *strong* influence on the mantle composition are the approach to model the chemical behaviour (multilayer versus bulk), the density, the diffusion energy and the activation energy of CO and H_2CO hydrogenation reactions. Modifying the values of these parameters within their chosen range drastically changes the distribution of the predicted mantle abundances, both in the shape and in the extremal values.
- 2) The grain porosity and the temperature as well as the initial abundance of atomic oxygen have only a *moderate* impact on the predicted mantle composition.
- 3) The grain and the site sizes have a *negligible* influence on the total mantle composition. However, these parameters strongly modify the ice thickness, which could have an impact on photolytic processes and for the desorption time of the mantle during the warm-up phase in protostar envelopes.

5.4 Comparisons with observations

5.4.1 The observations

In order to compare our model predictions with observations, we used the data pertaining to the ices only, because the abundance of the sublimated mantle species does not necessarily reflect the chemical composition of their precursor ices. First, it can be altered by reactions in the gas phase. Second, the different sublimation temperatures may introduce errors when comparing the abundance ratios of different species, because they may refer to different regions.

Unfortunately, solid CO, H_2CO, and CH_3OH have been observed simultaneously only towards a very small sample of high- and intermediate-mass protostars (Gibb et al., 2004; Pontoppidan et al., 2004). To increase the statistics and to include low-mass protostars, too, we, therefore, restricted the comparison of our model to the observed solid CO and CH_3OH abundances only. Fortunately, *a posteriori*, when considering the model predictions, we found that using the H_2CO would not provide (substantially) more constraints. Table 5.3 reports the compilation of observations that we used for the comparison.

5.4.2 Constraining the activation and diffusion energies

As a first step, we compared the model predictions with the observations with the goal to constrain the two microphysics parameters, which have a high impact on the model predictions, namely E_d/E_b and E_a. Figure 5.9 shows the CH_3OH/CO abundance ratio as a function of time obtained assuming reference parameters (and more particularly a density 10^5 cm^{-3}) and for different values of the activation energy E_a and diffusion energy E_d. The comparison of the model predictions with the values observed towards intermediate- and high- mass protostars clearly excludes an activation energy higher than 1450 K and a diffusion energy higher than 0.65 times the binding energy E_b. More stringently, if E_a = 1450 K, E_d/E_b has to be equal to 0.5. The analysis of a similar plot for a density of 10^4 cm^{-3} gives similar constraints: E_a=1450 K

Table 5.3: Mantle abundances of CO and CH_3OH with respect to water along with the relative CH_3OH/CO abundance ratio, as observed towards low- (LM), intermediate- (IM), and high-mass (HM) protostars.

Source	X(CO) % wrt H_2O	X(CH_3OH) % wrt H_2O	X(CH_3OH) % wrt to CO
Low-Mass			
L1448 IRS 1	45.5 [a–e]	< 14.9 [d]	< 32.7
L1455 SMM 1	5.6 [a–e]	< 13.5 [d]	< 241.1
RNO 15	13.6 [a–e]	< 5.0 [d]	< 36.8
IRAS 03254	13.6 [a–e]	< 4.6 [d]	< 33.8
IRAS 03271	8.2 [a–e]	< 5.6 [d]	< 68.3
B1-a	13 [a–e]	< 1.9 [d]	< 14.6
B1-c	28.6 [a–e]	< 7.1 [d]	< 24.8
L1489	15.2 [a–e]	4.9 [d]	32.3
DG Tau B	20.5 [a–e]	< 5.7 [d]	< 27.8
IRAS 12553	12.6 [a–e]	< 3.0 [d]	< 23.8
IRAS 13546	22.7 [a–e]	< 3.9 [d]	< 17.2
IRAS 15398	40.3 [a–e]	10.3 [d]	25.6
CRBR 2422.8-3423	11.2 [a–e]	< 9.3 [d]	< 83.0
RNO 91	19.0 [a–e]	< 5.6 [d]	< 29.5
IRAS 23238	4.0 [a–e]	< 3.6 [d]	90.0
Intermediate-Mass			
AFGL989	19.0 [b]	1.7 [b]	8.9
SMM4	30.0 [c]	28.0 [c]	93.3
High-Mass			
W33A	7.4 [a–e]	14.7 [d]	198.6
GL 2136	10.2 [a–e]	8.5 [d]	83.3
S140	16.6 [a–e]	< 3.0 [d]	< 18.1
NGC 7538 IRS 9	16.5 [a–e]	7.5 [d]	45.5
AFGL2136	5.0 [b]	5.0 [b]	100.0
AFGL7009	16.0 [b]	33.0 [b]	206.3

References. [(a)] Pontoppidan et al. (2003); [(b)] Gibb et al. (2004); [(c)] Pontoppidan et al. (2004); [(d)] Boogert et al. (2008); [(e)] Pontoppidan et al. (2008).

implies E_d/E_b=0.5 and E_a=400 K, $E_d/E_b \sim 0.65$. The case 10^6 cm^{-3} does not provide more constraints, it is indeed excluded by the observations (see below).

5.4.3 Constraining the pre-collapse phase duration and density

Once we limited the range of possible values of E_a and E_b consistent with the observations, we can attempt to constrain the duration of the pre-collapse phase and the density. To this end, Figure 5.10 shows the curves of the CH_3OH/CO abundance ratio versus time for three different densities (10^4, 10^5 and 10^6 cm^{-3}) and computed for the two following sets of E_a and E_d values: 1) E_a=400 K and E_d/E_b=0.65 (and the reference parameters) ; 2) E_a=1450 K and E_d/E_b=0.5 (and the reference parameters). The comparison between the predicted and observed CH_3OH/CO abundance ratio in intermediate- and high-mass protostars suggests that the bulk of methanol has been formed when the pre-collapse condensation had densities between 10^4 and 10^5 cm^{-3}. Higher densities would produce an insufficiently CH_3OH/CO abundance ratio compared to the values observed in intermediate- and high- mass protostars. If the densities are around 10^5

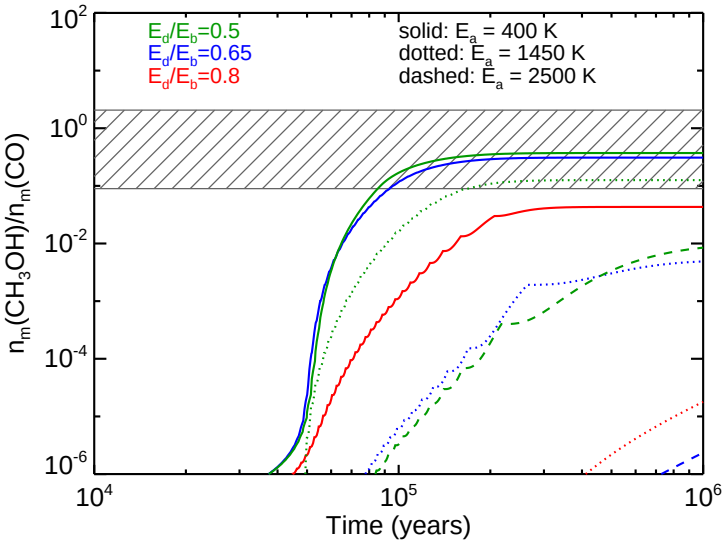

Figure 5.9: Mantle CH_3OH/CO abundance ratio versus time. The blue, green, and red lines refer to E_d/E_b=0.65, 0.5, and 0.8, respectively. Solid, dotted, and dashed lines refer to E_a=400 K, 1450 K, and 2500 K, respectively. In these computations the density is 10^5 cm^{-3}. The box with hatching shows the interval of CH_3OH/CO abundance ratio observed towards intermediate- and high- mass protostars (Table 5.3). Because low-mass protostars provide only less stringent upper limits, they are not reported in the plot.

cm^{-3}, the duration of the pre-collapse phase must have lasted at least 10^5 yr. Lower densities would allow shorter pre-collapse duration times. But densities higher than 10^5 cm^{-3} are not ruled out for the condensations that produce the low-mass protostars. In that case, the duration of the pre-collapse phase lasted more than 5×10^4 yr.

One important result is that the CH_3OH/CO abundance ratio does not provide an estimate of the duration of the pre-collapse phase, but only a lower limit to it. It neither provides an estimate of the density at the time of the collapse but only a range of possible densities for any given observed CH_3OH/CO abundance ratio. Note that the CH_3OH/H_2CO abundance ratio does not allow us to arrive at better constraints, because the theoretical curves are very similar to those of Fig. 5.10.

5.4.4 Chemical differentiation within grain mantles

As described in chapter 1, IR observations suggest a chemical differentiation of the grain mantles with a polar matrix formed already at $A_V \sim 3$ mag (Whittet et al., 1988), and a non-polar CO matrix formed at higher densities (Tielens et al., 1991). In between, CO can be mixed either with water, methanol, or both at the same time (Bisschop et al., 2007), as well as mixed with O_2, O_3, N_2, or CO_2 (Pontoppidan, 2006). Actually, this observational fact is one of the motivations of our work. As discussed in §5.3 and, for example, shown in Fig. 5.3, our code predicts inhomogeneous grain mantle composition. For the reference model, for example, CO is mixed with water in the inner layers while a mixture between CO and methanol is predicted in the outer layers. Given the lack of a dataset to compare our results with, it is difficult to carry out quantitative comparisons between observations and predictions. However, it is worth noticing that the exact grain mantle composition and stratification depends on the overall evolution and structure of the pre-collapse condensation, because the chemical differentiation depends on the density, the temperature and time.

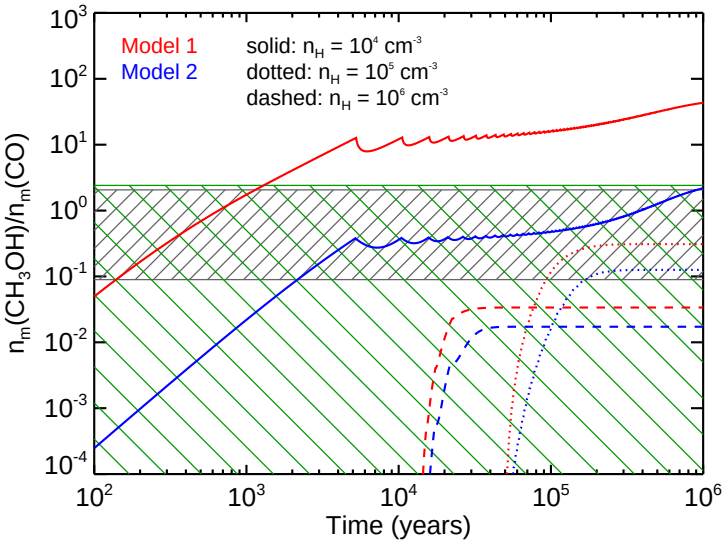

Figure 5.10: Mantle CH_3OH/CO abundance ratio versus time. The red lines refer to Model 1 (E_a=400 K and E_d/E_b=0.65), the blue lines refer to Model 2 (E_a=1450 K and E_d/E_b=0.5) (see text). Solid, dotted and dashed lines refer to densities 10^4, 10^5 and 10^6 cm^{-3} respectively. The grey box with hatching shows the interval of CH_3OH/CO abundance ratio observed towards high- and intermediate- mass protostars, while the green dashed box shows the values (upper limits) observed in low-mass protostars (Table 5.3).

5.5 Conclusions and perspectives

We ran GRAINOBLE for a large set of parameters, which are either unconstrained (density, temperature and grain size of the prestellar condensation) or poorly known (gas atomic oxygen abundance, diffusion energy, activation energy of hydrogenation reactions, grain site size) . We obtained a grid of about 18000 models and built distribution plots of the predicted mantle abundances. This allowed us to study the influence of each of these parameters on the predicted abundances and, consequently, the robustness of the predictions.

The most important results of the GRAINOBLE model are the following

1) The multilayer treatment shows a differentiation of the species within the mantle, with the innermost layers being rich in CO, the intermediate layers in formaldehyde, and the outermost layers in methanol, reflecting the different formation time of each species in the mantle. This differentiation will likely lead to a differentiation in the deuteration of formaldehyde and methanol on the ices. The deuteration increases with the CO depletion in the gas phase (Roberts et al., 2003; Ceccarelli & Dominik, 2005), methanol will, therefore, likely be more deuterated than formaldehyde, as indeed observed in Parise et al. (2006). The next chapter will focus on the detailed modeling of the deuteration process.

2) The multilayer treatment predicts a relatively high abundance of radicals trapped in the mantle. For example, HCO and CH_3O show abundances of $10^{-9} - 10^{-7}$ with respect to H nuclei if a low activation energy (400 K) is considered). As suggested by Garrod & Herbst (2006), these radicals can react to form COMs when the grain temperature increases during the formation of the protostar. At this stage, we cannot say whether the predicted radical abundances are sufficient to explain the present observations (e.g. Fig. 1.9), and, unfortunately, comparisons with previous models are not possible because of the lack of specific information.

3) The presence of porosity in the grains only moderately influences the mantle chemical composition, causing an enhanced abundance of formaldehyde and methanol by less than a factor four.

4) The chemical composition of grain mantles strongly depends on the physical conditions of the prestellar condensation, particularly on its density as well as its age. Therefore, it will be

important to model the evolution of the condensation for realistic predictions of the mantle composition. Conversely, the observed mantle composition can provide valuable information on the past history of protostars. Comparisons of the present predictions with the ices observations (specifically the CH_3OH/CO abundance ratio) suggest that intermediate- and high- mass protostars evolved from condensations less dense than about 10^5 cm^{-3}, while no stringent constraints can be put on the prestellar condensations of low-mass protostars.
5) The predicted mantle composition critically depends on the values of the diffusion energy and activation energy of the hydrogenation reactions. Comparing our model predictions with observations of ices allows to constrain the values of these two important parameters: the diffusion to binding energy ratio has to be around 0.5–0.65, and the activation energy has to be less than 1450 K.
6) Other parameters of the GRAINOBLE model, like the gas atomic oxygen abundance and the site size, do not substantially influence the predicted mantle abundances of H_2CO and CH_3OH.

In summary, GRAINOBLE is a versatile and fast code to model the grain surface chemistry. It predicts that the mantles are indeed stratified and that radicals are trapped inside the mantles. Because it is not expensive from the point of view of computing time, modeling of complex and more realistic cases, like the evolution of a prestellar core, are now feasible.

Chapter 6

Deuteration of formaldehyde and methanol ices

Contents

Deutération des glaces de formaldehyde et de methanol

Une deutération extrememement élevée de plusieurs molécules a été observée autour des étoiles de faible masse depuis une décennie. Parmis elles, le formaldehyde et le methanol présente une deutération particulièrement élevée, avec des observations d'isotopes doublement et triplement deutérées très abondantes. Les deux espèces se formeraient probablement sur les grains interstellaires durant la phase froide et dense de pré-effondrement par des réactions d'addition d'atomes d'hydrogène et de deutérium sur la glace de CO.

Nous présentons ici une étude théorique de la deutération du formaldehyde et du methanol obtenue avec notre modèle gaz-grain, GRAINOBLE. Avec ce modèle, nous considèrons la nature multicouche des manteaux de glace et nous explorons la robustesse des résultats sur l'incertitude de paramètres chimiques et de surface qui sont peu contraints.

La comparaison de nos prédictions avec les observations aboutit à deux résultats importants: i) la haute deutération observée est obtenue durant la phase tardive de pré-effondrement, lorsque la densité atteint $\sim 5 \times 10^6$ cm^{-3}, et cette phase est rapide, puisqu'elle ne dure que quelques milliers d'années. ii) les réactions d'abstraction et de substitution de D et de H sont d'une importance cruciale pour reproduire les rapports de deutération observés. Ce travail montre la capacité de l'analyse de la composition chimique à reconstruire l'histoire des protoétoiles.

Abstract

Extremely high deuteration of several molecules has been observed around low mass protostars since a decade. Among them, formaldehyde and methanol present particularly high deuteration, with observations of abundant doubly and triply deuterated forms. Both species are thought to be mainly formed on interstellar grains during the low temperature and dense pre-collapse phase by H and D atom additions on the iced CO.

We present here a theoretical study of the formaldehyde and methanol deuteration obtained with our gas-grain model, GRAINOBLE. With this model, we considered the multilayer nature of the mantle and explores the robustness of the results against the uncertainties of poorly constrained chemical and surface model parameters.

The comparison of the model predictions with the observations leads to two major results: i) the observed high deuteration is obtained during the last phase of the pre-collapse stage, when the density reaches $\sim 5 \times 10^6$ cm^{-3}, and this phase is fast, lasting only several thousands years. ii) D and H abstraction and substitution reactions are crucial in making up the observed deuteration ratios. This work shows the power of chemical composition as a tool to reconstruct the past history of protostars.

This chapter is taken from the publication: **V. Taquet**, C. Ceccarelli, C. Kahane 2012, *Formaldehyde and methanol deuteration in protostars: fossiles from a past fast high density pre-collapse phase*, ApJL, 748, L3.

6.1 Introduction

Although the deuterium elemental abundance is 1.5×10^{-5} relative to hydrogen (Linsky, 2003), observations carried out during the last decade have revealed high abundances of singly, doubly, and even triply deuterated molecules in low mass pre-stellar cores and Class 0 protostars (Ceccarelli et al., 2007). In this work, we focused on formaldehyde and methanol, both species likely synthesized on the grain surfaces (Tielens & Hagen, 1982; Watanabe & Kouchi, 2002) as gas phase reactions are unable to reproduce the large observed abundances (Roberts et al., 2004; Maret et al., 2005).

As described in chapter 1, the observed deuterium fractionations of formaldehyde and methanol increase with the increasing CO depletion up to 10% (Bacmann et al., 2003, 2007; Bergman et al., 2011), suggesting that the latter is a key parameter. Analogously, several formaldehyde and methanol isotopologues have been detected in Class 0 low mass protostars (Ceccarelli et al., 1998, 2001; Parise et al., 2002, 2004, 2006). However, unlike in pre-stellar cores, no correlation between the CO depletion and deuterium fractionation is observed, so that the deuteration process is thought to occur in the previous pre-collapse phase.

Recent experimental works have confirmed the synthesis of formaldehyde and methanol by hydrogenation of iced CO (Watanabe & Kouchi, 2002; Hidaka et al., 2007; Fuchs et al., 2009) and also highlighted the complex chemical evolution of H_2O-CO ices when they are exposed to D and H atoms (Nagaoka et al., 2005; Nagaoka et al., 2007).Formaldehyde and methanol can be efficiently deuterated into HDCO, D_2CO, CH_2DOH, CHD_2OH and CD_3OH, when they are irradiated by D atoms. Conversely, abstractions of D can only occur on formaldehyde, and not on methanol. Therefore, formaldehyde isotopologues only can be hydrogenated to form back HDCO and H_2CO if they are exposed to H atoms. The relative reaction rates deduced from these works show that H and D abstractions and substitutions on formaldehyde and methanol are as efficient as addition reactions (see also the theoretical calculations by Goumans, 2011; Goumans & Kästner, 2011). These processes could, therefore, largely increase the deuterium fractionations of formaldehyde and methanol after the complete depletion of CO and their formation on the surfaces.

In this chapter, we re-consider the problem of the formaldehyde and methanol deuteration, using our gas-grain coupled model, GRAINOBLE, that takes into account D and H atoms addition, but also abstraction and substitution reactions. Our goal is to simultaneously reproduce the formaldehyde and methanol deuteration observed towards Class 0 protostars by considering their formation on interstellar grains only. Note that, once sublimated from ices, the abundance of these species is only slightly affected by gas phase reactions, as the typical chemical timescale ($\sim 10^5$ yr, Charnley et al., 1997) is larger than the typical age of these objects ($\sim 10^4$ yr, Andre et al., 2000). We will show that understanding how and when the observed deuteration occurs will also provide us with hints on the process itself and on the past history of the protostars.

6.2 Model

6.2.1 Chemical processes

In this work, we studied the deuteration of solid formaldehyde and methanol with a second version of GRAINOBLE, which takes into account the following processes:
- The deuterium chemistry in the gas phase was studied, following chemical network (2) presented in Fig. 3.5.
- We considered the accretion of gaseous H, D, H_2, HD, D_2, O, and CO onto grains.
- The formation and the deuteration of formaldehyde, and methanol was studied on grain surfaces with chemical network (2) described in chapter 3. No photolytic processes were considered.
- The reaction probabilities were computed by assuming a square barrier of a width $a = 1$Å.
- The effect of H_2 abundance in ices on the binding energies of solid species was taken into account, following eq. 3.14.
- The thermal and cosmic ray induced desorption processes were taken into account.
- We considered the variation of seven parameters, listed in Table 6.1 with their range of values. The free activation energy E_a refers to the activation energy of the CO and H_2CO hydrogenation (and deuteration) reactions.

Table 6.1: List of the free parameters and the value range considered in this chapter.

Parameter	Values
Density n_H	10^4 - 10^5 - 10^6 - 5×10^6 cm^{-3}
Temperature $T_g = T_d$	8 - 10 - 12 K
Grain size a_d	0.1 - 0.2 - 0.3 μm
Energy ratio E_d/E_b	0.5 - 0.65 - 0.8
Binding energy $E_{b,wat}$(H)	400 - 500 - 600 K
Activation energy E_a	400 - 900 - 1400 K
Initial oxygen abundance $X(O)_{ini}$	10^{-8} - 10^{-6} - 10^{-4}

6.2.2 Physical model

Rather than simulating the evolution from the diffuse cloud state to the pre-stellar core, we focused on the last stage of the evolution, when the material is already molecular and the density reaches the value n_H. The initial abundance of gas phase species (H, D, HD, D_2, H_3^+ isotopologues, ...) are given by the steady-state abundance, obtained solving the gas phase chemical network of chemical network (2) and considering the recombination of H and D onto grains. The abundance relative to H nuclei of the deuterium and CO reservoirs are 1.5×10^{-5} and 4.75×10^{-5}.

We followed, then, the formation and evolution of the grain mantles during this phase, keeping

the gas density n_H constant. Briefly, as the time passes, CO freezes out onto the grain mantles, where it forms H_2CO and CH_3OH and their deuterated isotopologues. Therefore, the deuteration of the formaldehyde and methanol on the mantle primarily depends on the gaseous atomic D/H ratio.

6.3 Results

6.3.1 The D/H gas phase ratio

At first approximation, the steady state densities of H and D, assumed as initial conditions, are roughly constant regardless the total density and their abundance relative to H nuclei, therefore, decrease with increasing n_H. At low densities, a significant fraction (∼30%) of the deuterium reservoir is already in atomic form before the depletion of CO: the increase of the atomic D/H ratio with the CO depletion will therefore be low. On the contrary, at high densities, only a negligible fraction of deuterium is in the atomic form at the beginning, so that the atomic D/H ratio strongly increases with the CO depletion. The larger the density, the larger the gaseous atomic D/H ratio increase with the CO depletion, as highlighted in Figure 6.1 which shows the evolution of the atomic D/H as function of CO depletion, for n_H equal to 10^5 and 5×10^6 cm^{-3} respectively.

6.3.2 Model with addition reactions only

In this section, only addition reactions are considered on grain mantles (see chapter 3). In this case, the deuteration of formaldehyde and methanol primarily depends on two factors, as illustrated in Fig. 6.1: i) *The increase of the gas phase atomic D/H ratio with the CO depletion:* the ratio increases with increasing CO depletion, namely with time, and with increasing density (see above); ii) *When formaldehyde and methanol are formed:* as explained in detail in the previous chapter, the increase of n_H delays the formation of formaldehyde and methanol. In general, the two effects result in a larger deuteration of formaldehyde and methanol for larger densities and larger evolutionary times.

This is illustrated in the left panel of Fig. 6.2, which shows the temporal evolution of the mean deuterium fractionations of iced formaldehyde and methanol along with their uncertainty, for different densities. The high density cases ($n_H \geq 10^6$ cm^{-3}) show large enhancements of the CH_2DOH/CH_3OH and $HDCO/H_2CO$ ratios with time, reaching the unity for the singly deuterated forms. No increase of the deuterium fractionation is, on the contrary, observed at low densities ($n_H = 10^4 - 10^5$ cm^{-3}), the deuteration ratios never exceeding 0.02. On the same figure, we reported the range of observed values (from Parise et al., 2006). No model can reproduce the full set of observations. Indeed, the high density cases predict CH_2DOH/CH_3OH and $HDCO/H_2CO$ ratios in agreement with observations for times between 5×10^3 and 10^6 yr. However, they cannot predict the observed high abundances of the doubly deuterated molecules. In addition, observations show that methanol is three times more deuterated than formaldehyde whereas the models of the left panel of Fig. 6.2 predict a factor 1.5 at most. We concluded that this class of models fails to reproduce the observations.

6.3.3 Abstraction and substitution reactions

The right panel of Figure 6.2 shows the temporal evolutions of formaldehyde and methanol deuterium fractionations when abstraction and substitution reactions are included. From the right panel of Fig. 6.2 it is clear that the inclusion of the addition and substitution reactions strongly increase the deuterium fractionations, especially at high densities. For densities $\sim 5 \times 10^6$ cm^{-3}, the model predicts fractionations of doubly-deuterated molecules compatible with observations,

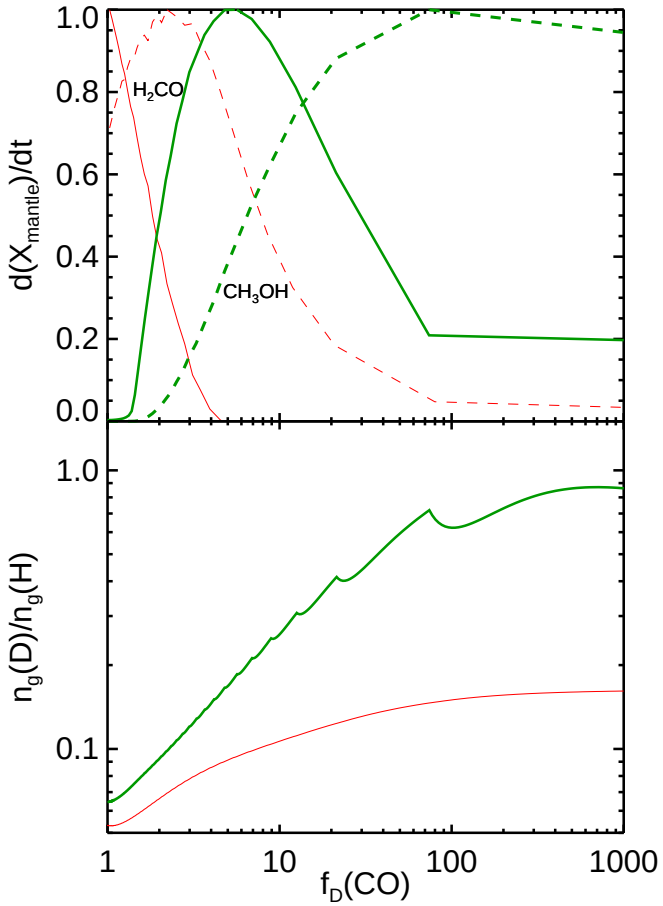

Figure 6.1: Normalized H_2CO (solid lines) and CH_3OH (dashed lines) formation rates (top panel) and gaseous atomic D/H ratio (bottom panel) as function of the CO depletion factor $f_D(\mathrm{CO}) = n_{g,ini}(\mathrm{CO})/n_g(\mathrm{CO})$, for $n_H = 10^5$ (thin red lines), and 5×10^6 (thick green lines) cm^{-3}. The spikes are caused by the multilayer nature of the mantle.

at time $\sim 5 \times 10^3$ yr. Unlike CH_2DOH, which shows an increase of deuteration compared to the left panel of Fig. 6.2 and more particularly at longer timescales, the HDCO deuteration is not enhanced. This is due to the efficiency of deuterium abstraction on HDCO which allows the formation of H_2CO whereas deuterium abstraction reactions on CH_2DOH, leading to CH_3OH formation, are negligible. The observed [CH_2DOH]/[HDCO] ratio of 3 can now be predicted. Finally, the [CH_2DOH]/[CH_3OD] ratio is enhanced because the abstraction reactions can only occur significantly on the methyl group of methanol and not on its hydroxyl group. The observed ratio of 10-20 can also be predicted but at a larger time, $5 - 10 \times 10^4$ yr. We concluded that this class of models succeeds to reproduce all the observations simultaneously for a density of about 5×10^6 cm^{-3} and at a time of 5000 yr, with the exception of the [CH_2DOH]/[CH_3OD] ratio which is reproduced at longer timescales.

6.4 Discussion and conclusions

Although multiply deuterated molecules in low mass protostars have been discovered and observed for a decade, published models have had difficulties in reproducing the observed abundances, especially those of formaldehyde and methanol (Parise et al., 2006). Both species are believed to be mainly synthesised and to be observed on the grain surfaces during the cold and dense pre-collapse phase (see Öberg et al., 2011a) and that they are observed in the gas when

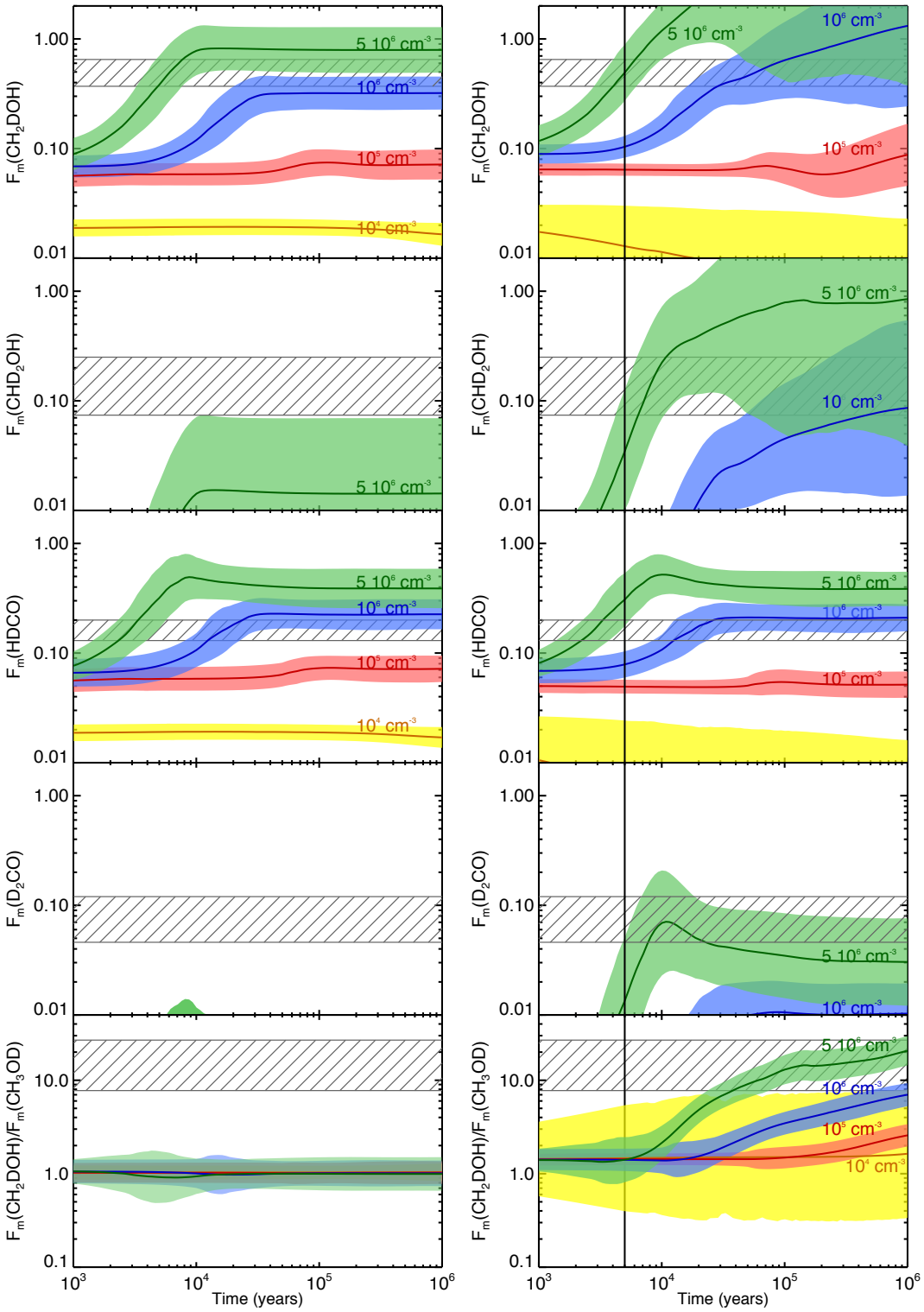

Figure 6.2: Mean deuterium fractionation of methanol and formaldehyde (solid lines) with their 1 sigma standard deviation (color levels) with time, obtained considering addition reactions only (left), and abstraction and substitution reactions (right). The hatched zones give the range of observed values (Parise et al., 2006).

they sublimate off the grain mantles upon heating from the central star. On the grains, H_2CO and CH_3OH are thought to be the result of the hydrogenation of iced CO. Their deuteration, therefore, depends on when exactly the two species are formed and how. We have shown that, based on our grain surface model GRAINOBLE, formation of H_2CO and CH_3OH from addition reactions alone fails to predict the observed deuterium fractionation. In contrast, if D and H abstraction and substitution reactions are added, the GRAINOBLE model can reproduce *simultaneously* the observed values. Therefore, these processes are crucial and more laboratory experiments and theoretical computations are needed to better constrain their rates on the ices. Reproducing the observed $[CH_2DOH]/[CH_3OD]$ ratio remains a challenge, as it is still underestimated by the model for a short timescale. Previous studies have suggested that this may be caused by D and H exchanges on the ices during the sublimation phase (Ratajczak et al., 2009) or activated by photolysis processes (Weber et al., 2009) or on the gas phase (Osamura et al., 2004), all processes that would be inefficient in altering the other isotopologues (see Ratajczak et al., 2011, and chapter 5 of this thesis for a detailed discussion).

With the above exception, our model predicts the observed abundance ratios for high densities ($\sim 5 \times 10^6$ cm^{-3}) and for relatively short times ($\sim$ 5000 yr). We emphasise that this time corresponds only to the final stage at high density and not to the age of the condensation, which can be considerably larger. In fact, it is possible and even likely that the pre-stellar cores spend a long time in a less dense phase (e.g. Bergin & Tafalla, 2007). However, the comparison of the observed H_2CO and CH_3OH deuteration with our model predictions suggests that the last phase at high density is short, just a few thousands years. In other words, soon after the central density reaches $\sim 5 \times 10^6$ cm^{-3} the protostellar collapse starts. This is a nice illustration of how chemistry can help us to understand the past history of the protostar.

In conclusion, our work leads to two important results:
1) The pre-collapse phase may last hundred thousands of years: however, when the central density reaches $\sim 5 \times 10^6$ cm^{-3}, the collapse starts in about a few thousands years. 2) D and H atoms abstraction and substitution reactions are crucial in the grain surface chemistry and should be incorporated into models. Thus, more experimental and theoretical works are therefore needed to better contrain their efficiency and, therefore, the timescale needed to reproduce the observations.

Chapter 7

Deuteration of water ice

Contents

Deutération de la glace d'eau

Des observations millimétriques ont mesuré des forts degrés de deutération moléculaire dans différentes espèces autour de protoétoiles de faible masse. Le *Télescope Spatial Herschel*, lancé en 2009, fournit actuellement des nouvelles mesures du fractionement de deutération de l'eau, le principal constituent des glaces interstellaires. Dans ce chapitre, nous étudions la formation et la deutération de l'eau qui doit se former à la surface des grains interstellaires dans les nuages moléculaires.

Nous avons utilisé notre modèle astrochimique gaz-grain GRAINOBLE dépendant du temps et qui suit la formation multicouche des glaces interstellaires. Nous avons également considéré la variation de plusieurs paramètres d'entrée pour étudier leur impact sur la deutération de l'eau. Nous avons inclu le traitement des états de spin ortho et para d'espèces clés, et notamment de H_2, qui affectent la deutération des molécules. Le modèle inclut également les résultats de travaux expérimentaux et théoriques sur la formation et la deutération de l'eau à la surface des grains. Nous avons notamment calculé les probabilités de transmission des réactions de surface en utilisant le modèle d'Eckart et nous avons considéré la photodissociation de la glace en utilisant des résultats de simulations de dynamique moléculaire.

L'utilisation d'une approche multicouche nous a permis d'étudier l'influence de plusieurs parametres sur l'abondance et la deutération de l'eau. La deutération de l'eau est très sensible au rapport ortho/para de H_2 et à la densité totale, mais dépend également de la température du gaz et des grains ainsi que de l'extinction visuelle dans le nuage. La comparaison avec des observations sub-millimétriques vers la protoétoile de faible masse IRAS 16293 nous permet de proposer un scénario dans lequel la glace d'eau se forme avec le CO_2 dans les nuages moléculaires avec des densités limitées tandis que le formaldehyde et le methanol se forment dans une phase plus tardive, lorsque la condensation devient plus dense et plus froide. La deutération est très sensible aux conditions physiques et peut donc etre utilisée pour estimer le moment de formation de n'importe quelle espèce solide.

Ce chapitre est tiré de la publication: **V. Taquet**, P. Peters, C. Kahane, C. Ceccarelli, D. Duflot, C. Toubin, L. Wiesenfeld 2012, *Modelling of deuterated water ice formation*, A&A, accepté.

Abstract

Millimetric observations have measured high degrees of molecular deuteration in several species seen around low-mass protostars. The *Herschel Space Telescope*, launched in 2009, is now providing new measures of the deuterium fractionation of water, the main constituent of interstellar ices. We aim at theoretically studying the formation and the deuteration of water, which is believed to be formed on interstellar grain surfaces in molecular clouds.

We used our gas-grain astrochemical model GRAINOBLE, which considers the multilayer formation of interstellar ices. We varied several input parameters to study their impact on water deuteration. We included the treatment of ortho- and para-states of key species, including H_2, which affects the deuterium fractionation of all molecules. The model also includes relevant laboratory and theoretical works on the water formation and deuteration on grain surfaces. In particular, we computed the transmission probabilities of surface reactions using the Eckart model, and we considered ice photodissociation following molecular dynamics simulations.

The use of a multilayer approach allowed us to study the influence of various parameters on the abundance and the deuteration of water. Deuteration of water is found to be very sensitive to the ortho-to-para ratio of H_2 and to the total density, but it also depends on the gas/grain temperatures and the visual extinction of the cloud. Since the deuteration is very sensitive to the physical conditions, the comparison with sub-millimetric observation towards the low-mass protostar IRAS 16293 allows us to suggest that water ice is formed together with CO_2 in molecular clouds with limited density, whilst formaldehyde and methanol are mainly formed in a later phase, where the condensation becomes denser and colder.

This chapter is taken from the publication: **V. Taquet**, P. Peters, C. Kahane, C. Ceccarelli, D. Duflot, C. Toubin, L. Wiesenfeld 2012, *Water ice deuteration: a tracer of the chemical history of protostars*, A&A, accepted.

7.1 Introduction

Understanding the formation of water is crucial, not only because of its primordial importance for life on Earth, but also because it is thought to be one of the most abundant oxygen-bearing species and also one of the main gas coolants (Ceccarelli et al., 1996; Kaufman & Neufeld, 1996; van Dishoeck et al., 2011).

H_2O, but also H_2S, H_2CO, CH_3OH (and $HCOOCH_3$) are thought to be mainly formed on grain surfaces, via hydrogenation of accreted O (or O_2), S, and CO from the gas phase. Cold gas phase chemistry produces water vapour with low abundances (a few 10^{-7}; Bergin et al., 2000) while endothermic reactions producing warm water are efficient at $T > 250$ K. In contrast, water ice desorbs into the gas phase in the envelope of Class 0 protostars in large quantities at $T \sim 100$ K. Therefore, the deuteration of water measured by millimetric observations likely reflects the deuteration of its icy precursor governed by the accretion of gas phase H and D atoms. Indeed, the timescale needed to alter significantly the deuteration after evaporation in warm gas is longer than the typical age of Class 0 protostars ($\sim 10^5$ versus $\sim 10^4$ yr, Charnley et al., 1997; Andre et al., 2000).

As described in chapter 1, infrared observations show that water ice can be mixed with several other species. Consequently, one needs to include the formation of all other solid molecules in order to correctly study the formation of deuterated water ice.

In this chapter, we extend our study to the formation and the deuteration of interstellar water ice formed in molecular clouds and in prestellar cores, using the multilayer GRAINOBLE model. Our goal is to explore the influence of the physical conditions (representative of different typical cloud stages) on ice formation and water deuteration. This is the first time that such a systematic study is done. Besides, it includes the crucial influence of the H_2 ortho/para ratio

on the water deuteration. We briefly remind the chemical processes considered in this chapter in Sect. 7.2. In Sect. 10.3, we study the formation of typical grain mantles and show the influence of several physical and chemical parameters on the deuteration of water ice. In each section, we summarise the main ideas with headings and conclusive remarks. In Sect. 7.4, we compare our with previous model predictions and in Sect. 7.5 with published observations of water, formaldehyde, and methanol.

7.2 Model

7.2.1 Chemical processes

In this work, we followed the formation of interstellar ices and the deuteration of water with a expanded version of GRAINOBLE, which takes into account the following processes:
- We followed the gas phase chemistry with chemical network 3 described in chapter 3. The chemical network is taken from the KIDA database for 7 elements (H, He, C, N, O, S, Fe), including the effect of the H_2 ortho/para ratio on the deuterium chemistry.
- All neutral species were allowed to accrete on grain surfaces.
- The formation/deuteration of water, formaldehyde, methanol as well as carbon dioxide and other solid species was followed on grain surfaces with chemical network (3) described in chapter 3.
- Ice photodissociation and photodesorption were considered, with the method described in chapter 3.
- The reaction probabilities were computed with the Eckart model with data presented in chemical network (3) in chapter 3. The transmission probability of the CO+H reaction deduced with the Eckart model is in good agreement with the range of values we deduced in chapter 5. In chapter 5, we varied the transmission probability P_r of this reaction and found that a transmission probability higher than 2×10^{-7} was needed to reproduce the solid [CH_3OH]/[CO] ratio observed toward high-mass protostars.
- The effect of the H_2 abundance in ices on the binding energies of solid species is taken into account, following eq. 3.14.
- All the desorption processes described in chapter 3 were taken into account.
- We considered the variation of seven parameters, listed in Table 7.1 with their range of values. All the parameters are fixed and constant with time.

7.2.2 Physical model

As described in chapter 1, water ice is formed at visual extinctions A_V higher than 3 mag (Whittet et al., 1988, 2001) while gas phase CO is detected above a visual extinction threshold of 2 mag (Frerking et al., 1982) and PDR models show that hydrogen is already mainly molecular at $A_V < 1$ mag. Water ice is, therefore, thought to be formed when the gas is already molecular.

We considered a two-step model. For each set of input parameters, we first computed the abundances of gas phase species assuming the element abundances shown in Table 3.1 and considering the gas phase network described in section 3.5.3. For this, we assumed the steady state values, which are reached after 5×10^6 yr when the density is 10^3 cm^{-3} and after 10^6 yr at 10^4 cm^{-3}. This first step is meant to describe the molecular cloud and the initial pre-collapse phase before the formation of the ice bulk. In practice, we assumed that the timescale to reach the chemical equilibrium is shorter than the dynamical timescale for the gas to reach the prestellar core conditions. These gas phase abundances are then considered as the initial abundances for the gas-grain modeling. In the second step, we allowed gas and grain surface chemistry to evolve while physical conditions (density, temperature, visual extinction) remain

Table 7.1: List of the input parameters and the values range explored in this chapter. Bold values mark the values adopted in the reference models (see text).

Input parameters	Values
Physical conditions	
$n_{H,ini}$	10^3 - 10^4 - 10^5 - 10^6 cm^{-3}
$T_g = T_d$	10 - 15 - 20 K
A_V	0 - 1 - 2 - 3 - 4 - 5 - 6 - 7 - 8 - 9 - 10 mag
ζ	3×10^{-17} s^{-1}
ISRF	1×10^8 photons cm^{-2} s^{-1}
G_0	20
Grain surface parameters	
a_d	0.1 - **0.2** - 0.3 μm
E_b(H)	400 - **500** - 600 K
E_d/E_b	0.5 - **0.65** - 0.8
d_s	3.1
Chemical parameters	
H_2 o/p ratio	3×10^{-6} - 3×10^{-4} - 3×10^{-2} - 3

constant.

7.3 Results

In this section, we present the results in two steps. First, we consider the formation of water and other major ice species, and second, we focus on the deuteration.

Specifically, in section 7.3.1, we validate our model. For this purpose, i) we compare our predicted gas phase abundances as function of the visual extinction with PDR model predictions; ii) we compare the predicted abundances of gaseous and solid water as function of the visual extinction with published observations; iii) we discuss the multilayer formation of interstellar ices for a set of three reference physical conditions. We emphasize that our approach does not pretend to describe the whole evolution of the cloud. The reference models are meant to quantify the influence of specific physical conditions, which are likely to describe different evolutionary stages, on the ice chemistry.

Second, after validating the model, we focus on the water deuteration. In section 7.3.2, we emphasize the importance of the CO depletion on the deuterium fractionation of the reference models. Then, in section 7.3.3, we perform a multiparameter study that allows us to evaluate the influence of each model parameter on the deuterium fractionation of water. Comparing the model predictions with the observations allows us to constrain a range of values for the chemical and physical parameters.

7.3.1 Validation of the model

7.3.1.1 Initial gas phase abundances

As described in section 7.2.2, we adopted a two-step model. The ice formation phase is followed by considering initial abundances that are computed from steady-state calculations of gas phase chemistry. These initial abundances depend on the density and the temperature, but mainly on the visual extinction A_V (hereafter, A_V means the edge-to-centre visual extinction, half of the observed visual extinction), because photolytic processes play a significant role at low visual extinctions. In fact, the abundance of most gas phase species weakly depends on the density and the temperatures (in the range of values considered in this work) but are essentially a function

of the visual extinction. Therefore, we compared the gas-phase abundances of key molecules for ice formation (H, D, C, O, CO, O_2) between our model and the Meudon PDR code (Le Petit et al., 2006) for a total density $n_H = 10^4$ cm^{-3}.

Figure 7.1 shows the depth-dependent chemical abundances of gas phase H, D, O, C, O_2, and CO, for $n_H = 10^4$ cm^{-3} computed by the PDR code in the low visual extinction regime. These abundance profiles are in relative good agreement with the initial abundances computed with our model. The abundances differ by 20% for most abundant species and within one order of magnitude when species display low abundances (C and O_2). This validates the use of the H_2, HD, and CO self-shieldings in our code. The other differences are due to the different chemical networks and physical conditions between the two codes (the PDR and ours). The decrease in UV flux with increasing A_V increases the abundance of molecules such as H_2, HD, and CO, and decreases the abundances of H, D, and then C, and O. D abundance is governed by the high photodissociation of HD at low A_V and by the formation of H_3^+ isotopologues at higher A_V, and shows an abundance minimum at $A_V = 1$ mag.

Molecular oxygen is formed at higher visual extinction, and it reaches its maximal abundance at $A_V > 5$ mag. Our chemical network predicts a high O_2/O abundance ratio ($\sim 1-1.5$). In fact, the O_2 abundance is highly uncertain because it depends on 1) the rate coefficients of some key reactions displaying high uncertainties, and 2) the elemental abundances of carbon and oxygen (see Wakelam et al., 2010; Hincelin et al., 2011). Moreover, observations carried out with the *SWASS*, *Odin*, and *Herschel* space telescopes have revealed that O_2 is not abundant in molecular clouds ($X(O_2) \lesssim 10^{-7}$, see Goldsmith et al., 2011; Liseau et al., 2012). Modelling the formation of ices with high O_2 abundances is not necessarily realistic, and we, therefore, investigate the influence of the gas phase O_2/O abundance ratio on the formation of ices in section 7.3.1.3.

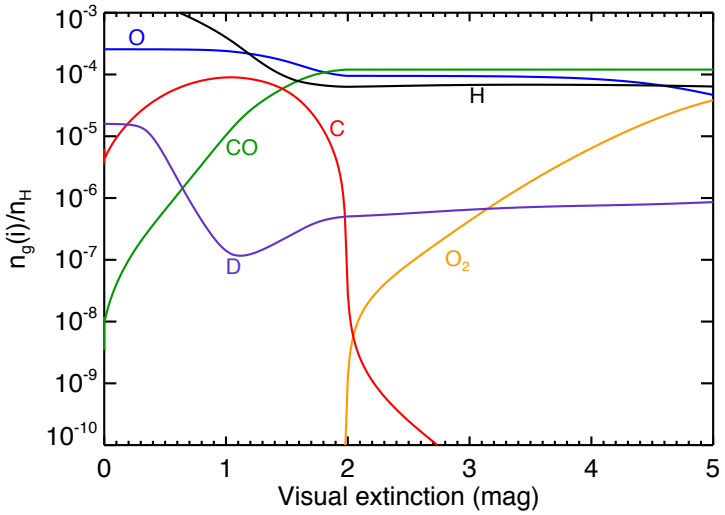

Figure 7.1: Initial abundances of C, O, CO, and O_2 as function of the visual extinction computed with the Meudon PDR code at $n_H = 10^4$ cm^{-3}, $G_0 = 20$.

Concluding remarks. As shown in Fig. 7.1, the chemistry in the gas phase is known to strongly depend on the visual extinction A_V. The steady-state gas phase abundances computed with our model are in good agreement with the results of PDR simulations. The use of a two-step model might overestimate the abundance of gaseous O_2 affecting ice formation. Therefore, the influence of the O_2/O ratio on ice formation needs to be investigated.

7.3.1.2 Depth-dependent water abundances

Figure 7.2 shows the final (at 10^7 yr) abundances of water ice and vapour as functions of visual extinction A_V for physical condition representative of molecular clouds (e.g. $n_H = 10^4$ cm^{-3}, $T_g = T_d = 15$ K). The final abundances can be divided into two zones:

i) a photon-dominated layer ($A_V < 2$ mag) where gas phase molecules are photodissociated and ices are photodesorbed. At very low visual extinctions, interstellar ices are efficiently photodesorbed and show a low abundance of $\sim 10^{-7}$ relative to H nuclei corresponding to less than one monolayer. The abundance of water vapour, given by the balance between its formation in gas phase, its photodesorption from interstellar grains, and its photodissociation, reaches steady state values of $10^{-8} - 10^{-7}$ (see also Hollenbach et al., 2009).

ii) a darker region ($A_V > 2$ mag) where the decrease in UV flux allows the formation of interstellar ices, mainly composed of water. At $A_V = 2 - 4$, water ice is mainly formed from the accretion of O atoms via the barrierless reaction (2.9). Most of the oxygen reservoir not trapped in CO is easily converted into water ice, reaching abundances up to 2×10^{-4}. The increase in gas-phase O_2 initial abundance with A_V slightly decreases the final abundance of water ice. Indeed, water ice is also formed via the accretion of O_2 including the formation of hydrogen peroxide. These formation pathways involve reactions possessing significant activation energies and low transmission probabilities (see Table 3.2). Finally, water formation also depends on the grain surface parameters E_d/E_b and E_b(H). A highly porous case (high E_d/E_b ratio combined with a high binding energy of H) strongly decreases the diffusion rate of mobile H species, decreasing the final abundance of water ice by one order of magnitude ($\sim 10^{-5}$).

Gas phase abundance of water is mainly governed by the balance between photodesorption and accretion. The decrease in UV flux with increasing A_v decreases water ice photodesorption and therefore the final abundance of water vapour from 10^{-7} at $A_V = 2$ to less than 10^{-9} at $A_V = 5$. We can note that the multilayer nature of grain mantles and the use of a wavelength-dependent absorption of UV photons from ices give similar results to theoretical PDR studies (e.g. Hollenbach et al., 2009).

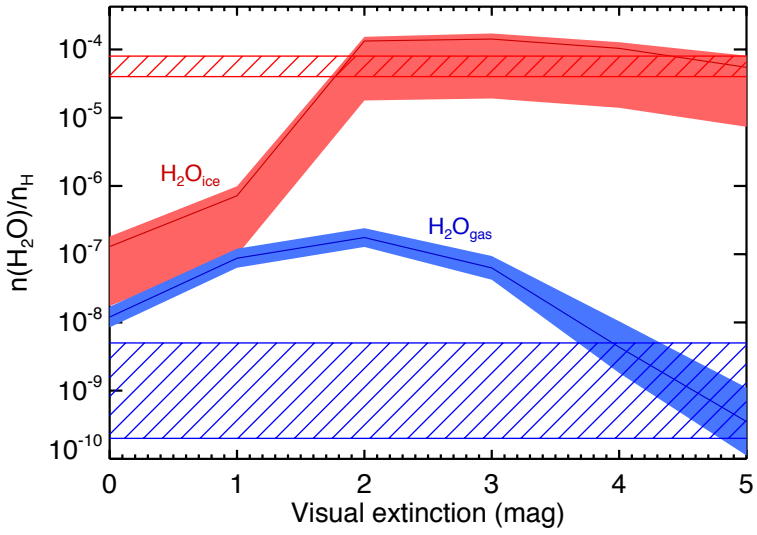

Figure 7.2: Final abundances (10^7 yr) of water ice (H_2O_{ice}, red) and water vapour (H_2O_{gas}, blue) as function of the visual extinction A_v for typical molecular cloud conditions ($n_H = 10^4$ cm^{-3}, $T = 15$ K) and including the variation of all other input parameters. Hatched boxes refer to water ice observed by Pontoppidan et al. (2004) towards the Serpens SMM4 regions and water vapour observed by Caselli et al. (2010) towards the L1544 prestellar core (the upper limit represents water abundance in the external part while the lower value represents water abundance in the central region).

In spite of the inevitable approximations of our modelling, our predictions are in good agreement with observations of water ice and water vapour, as shown in Fig. 7.2.

Concluding remarks. For typical conditions representative of a molecular cloud, we are able to reproduce the observed A_V threshold ($A_V \sim 1.5$ mag, $A_{V,obs} \sim 3$ mag) and the high abundance of water ice ($X \sim 10^{-4}$). The low abundance of water vapour observed in molecular clouds is reproduced at higher visual extinctions (4-5 mag).

7.3.1.3 Reference models

Very likely, the different ice components and their relative deuteration are the result of a long history where the physical conditions evolve. Therefore, a model aiming at reproducing the whole set of observations should take this evolution into account. However, before embarking on such a complicated modelling, it is worth while and even important to make clear what the characteristics (specifically, solid species and deuteration)are at each evolutionary step. To this end, we considered three "reference" models in the following: i) translucent cloud model, forming H_2O and CO_2 ices; ii) dark cloud model, allowing the formation of CO ice; iii) dark core model, showing high depletion of CO. The chemical composition of grain mantles for these reference models are shown in Figure 7.3 for the two sets of runs with different $[O_2]/[O]$ abundance ratios (see chapter 3).

i) *Translucent cloud model* where ices are mainly composed of H_2O and CO_2: $n_H = 10^4$ cm^{-3}, T = 15 K, $A_V = 2$ mag (corresponding to an observed visual extinction of 4 mag). For the conditions considered in this model, grain mantles are mainly composed of water and carbon dioxide. After H_2, the most abundant species that accrete onto grain surfaces are H, O, and CO. For these conditions, the initial O_2/O abundance ratio is low (5×10^{-4}). The decrease in the O_2/O ratio, therefore, does not affect the ice composition significantly. O_2 is involved in the formation of O and CO in the gas phase, and its artificial decrease favours O instead of CO and increases the formation of water ice by 25%, increasing the ice thickness. The relatively high grain temperature (15 K) allows accreted particles to diffuse efficiently and form H_2O and CO_2. At this visual extinction, the UV flux irradiating grain surfaces is high, and volatile species, such as atoms or light stable molecules (CO), are efficiently photodesorbed.

Water is the main ice component because it is formed from the barrierless reactions (2.8) and (2.9) whilst its other reaction routes are negligible (less than 0.1 %). Carbon dioxide is mainly formed from the hydrogenation of the O...CO complex and not by the direct reaction between CO and OH. Indeed, the grain temperature is not high enough to allow a high diffusion of CO and OH, because of their high binding energy. Instead, O atoms that are less attractively bound can meet CO atoms to form the O...CO van der Waals complex. In turn, O...CO readily reacts with H to form a hot HO...CO* complex that forms CO_2 + H. The accretion of CO and O also allow the formation of formaldehyde and methanol, but only in low abundances, lower than 1 % compared to solid water whilst a low fraction of hydrogen peroxide is predicted for a "normal" O_2/O ratio. Indeed, they are formed by reactions involving either heavy atoms or significant activation barriers.

The overall abundance of CO_2 relative to H_2O decreases with time, varying from 30% at the beginning to less than 1% at the end. The decrease in the CO_2 abundance is due to the increase in H abundance once interstellar ices start to form, because of the high photodesorption.

Although H_2O and CO_2 are formed in high abundances, O and CO are not totally depleted on grains. They still show high gas-phase abundances (about 5×10^{-5} relative to H nuclei) at the end of the ice formation. The predicted CO_2 abundance relative to water ice is lower than the observations. However, CO_2 formation is very sensitive to the grain temperature (governing the diffusion of O atoms) and to the hydrogen abundance (governing the reaction rate between O and H atoms). A higher temperature, higher visual extinction, and/or higher density would,

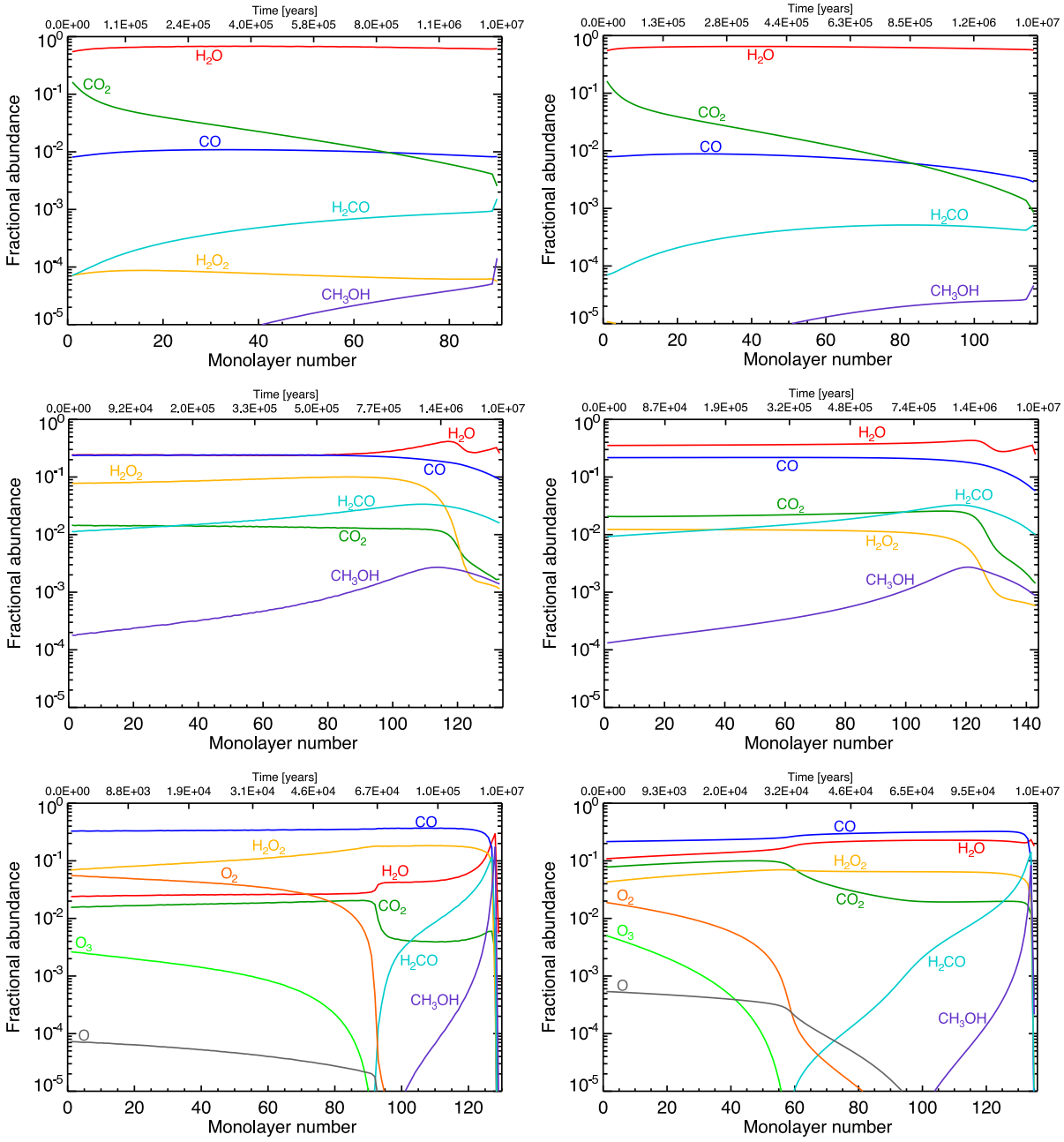

Figure 7.3: Fractional ice abundances of main species formed from O, O_2, and CO for three reference models with "normal" gas phase abundances computed with the chemical network presented in section 3.5.3 (left), and for a gas phase $[O_2]/[O]$ abundance ratio decreased by a factor of 10 (right): top) $n_H = 10^4$ cm^{-3}, $T = 15$ K, $A_V = 2$ mag, middle) $n_H = 1 \times 10^4$ cm^{-3}, $T = 10$ K, $A_V = 4$ mag, bottom) $n_H = 10^5$ cm^{-3}, $T = 10$ K, $A_V = 10$ mag. Values of other parameters are bold values of Table 3.4.

therefore, tend to increase the abundance of CO_2 relative to water.

ii) *Dark cloud model* where CO ice starts to form with water, forming a CO:H_2O mixture: $n_H = 1 \times 10^4$ cm^{-3}, T = 10 K, $A_V = 4$ mag (corresponding to an observed visual extinction of 8 mag), $t = 10^6$ yr. The low temperature limits the diffusion of O atoms and heavier species whilst the higher visual extinction allows CO molecules to stay bound on grain surfaces even if they do not react to form CO_2. Therefore, the main components of grain mantles are H_2O, mainly formed via the reaction (2.9), and CO.

CO shows an overall abundance relative to water of about 80 %, which is more than two times higher than observed abundance ratios of ices (10-30 %, Whittet et al., 2007; Öberg et al., 2011a). This is due to the high O_2/O abundance ratio (~ 0.5 throughout the calculation) that allows the formation of H_2O_2, via barrierless hydrogenation reactions, instead of water. H_2O_2 is easily trapped within grain mantles before reacting because the reaction destroying hydrogen peroxide has a low transmission probability (see Table 3.2). The decrease in the O_2/O ratio by one order of magnitude increases the formation of water, giving a CO/H_2O abundance ratio of 30%, whilst the H_2O_2 abundance decreases by one order of magnitude. Hydrogen peroxide has recently been observed by Bergman et al. (2011) towards the ρ Oph A dark cloud, confirming its formation in ices and its subsequent sublimation via non-photolytic processes. The low grain temperature favours the formation of formaldehyde and methanol via CO hydrogenation, compared to the formation of CO_2. Formaldehyde shows an unexpected abundance higher than 8 % compared to water ice. Again, the formation efficiency of formaldehyde and methanol strongly depends on the grain temperature and on the total density. For example, a higher temperature and/or higher density would favour CO_2 formation instead of H_2CO and CH_3OH.

A visual extinction of 4 mag decreases the final gas-phase abundances of O and CO, compared to $A_V = 2$ mag. Indeed, gas-phase CO reaches an abundance of 5×10^{-6} whilst O abundance decreases to 10^{-7} at 10^7 yr. The difference in the two abundances is due to the efficient destruction of O atoms forming solid water, whilst most CO molecules do not react and are still able to photodesorb.

iii) *Dark core model* where most of CO is depleted, allowing the formation of pure CO ice and solid formaldehyde and methanol: $n_H = 10^5$ cm^{-3}, T = 10 K, $A_V = 10$ mag (corresponding to an observed A_V of 20 mag). The low temperature, the high visual extinction, and the high density allow a significant trapping of CO molecules in the inner part of grain mantles whilst the formation efficiency of CO_2 is low owing to the low temperature. H_2CO and CH_3OH are formed via hydrogenation reactions that have high activation barriers. They are, therefore, mainly formed in the outer part of the ice when the CO depletion is high, which allows an efficient hydrogenation (see chapter 5).

At this visual extinction, solid water is less abundant than hydrogen peroxide because the initial gas-phase O_2 abundance is higher than the abundance of atomic oxygen (O_2/O between $1 \sim 3$ throughout the calculation). Water formation is mainly formed through the formation of H_2O_2, which involves reactions having high activation barriers. Hydrogen peroxide is most likely trapped in the bulk before forming water owing to the relatively high density. In this case, solid CO reaches an absolute abundance relative to H nuclei of 10^{-4}, water and CO_2 show lower abundances (10^{-5} and 4×10^{-6}), whilst formaldehyde and methanol show an abundance of 2×10^{-6} and 8×10^{-7}, respectively. Decreasing the O_2/O abundance ratio to 0.3 strongly increases the formation efficiency of water and CO_2 instead of hydrogen peroxide. For this case, water is almost as abundant as CO. Gas-phase abundances of O, O_2, and CO decrease with time and show high depletions (with final abundances lower than 10^{-10}), whereas H abundance remains constant.

Concluding remarks. The chemical composition of ices is very sensitive to the physical conditions and to the initial abundances. Most of the observed ice features are reproduced by the reference models: the water-rich ice seen at low visual extinctions is also composed of abundant

CO_2, whilst the abundances of solid CO (and H_2CO and CH_3OH) gradually increase with the visual extinction and the density. The increase in the O_2/O ratio decreases the abundance of water because its formation from O_2 involves reactions that have significant activation barriers (see Table 3.2). However, since it is likely that O_2 abundance remains low in dark clouds, water formation seems to be efficient in a wide range of physical conditions. Therefore, the study of the water deuteration needs to include the variation of several physical parameters.

7.3.2 CO depletion and molecular deuteration

As discussed in the previous chapter, the deuteration of solid species strongly depend on the values of the CO depletion and the density at the moment of their formation. The initial densities of H and D are roughly constant regardless of the total density. Their abundance relative to H nuclei decreases with increasing $n_{\rm H}$. At low densities, the increase in D abundance is limited by the weak deuterium reservoir, whilst the D/H ratio is able to strongly increase at higher densities. The gas and grain temperatures, as well as the visual extinction, also affect the evolution of the D/H ratio because they influence the desorption rate of H and D. In summary, since all these quantities vary with time, deuteration is not necessarily constant within grain mantles.

The influence of the CO depletion, the density, the temperatures, and the visual extinction on the water deuteration is shown in Figure 7.4 for the three "reference" models described in the previous section. At the beginning of the gas-grain calculation, CO has already reached its maximal abundance ($\sim 10^{-4}$, see Fig. 7.1). With time, the CO molecules freeze-out onto grains, decreasing the gas-phase CO abundance and increasing the CO depletion factor. The decrease in the temperatures from 15 to 10 K and the increase in the visual extinction from 2 to 4 mag increase the gas-phase D/H ratio from 0.1 % to 0.4 % at $f_D(\mathrm{CO}) = 1$. The increase in total density from 10^4 to 10^5 cm^{-3} increases the final D/H ratio from 1 % to 10 %. The decrease in the gas-phase O_2/O abundance ratio does not modify the water deuteration for the two low-density cases. However, it slightly decreases the HDO/H_2O ratio for the dense core model by a factor of two because water is more efficiently formed at low CO depletion (see Fig. 7.3) when the D/H ratio is low.

Concluding remarks. As previously noted, water deuteration is largely influenced by the gas D/H atomic ratio. Consequently, the largest deuteration is obtained where the CO depletion and the gas-phase D/H ratio are high, namely in the latest and less efficient phases of water formation, represented by the reference model iii). Comparison with the observed deuterium fractionation towards IRAS 16293 shows that a part of water ice should have formed during a dark and/or dense phase. In the following section, we investigate the impact of key parameters on water deuteration.

7.3.3 Physical/chemical parameters and water deuteration

In this section, we study the influence on ice deuteration of several physical and chemical parameters which play a key role. Each figure presented in this section shows the influence of one (or two) parameter(s) at a time. For each value of the studied parameters, mean value and standard deviation of absolute abundances and deuterations induced by the variation in other input parameters are computed. Comparisons between the evolution of the mean deuteration induced by the variation in the studied parameter and the standard deviation caused by other parameters allow us to deduce the importance of that parameter on water ice deuteration.

The predicted deuteration levels of water ice are compared with the observed HDO/H_2O and D_2O/H_2O ratios towards the hot corino of IRAS 16293 (Coutens et al., 2012) to constrain the input parameters that reproduce the observations best. For this purpose, we assume that the entire bulk of interstellar ices desorbed in the hot corino and the observed deuteration reflects

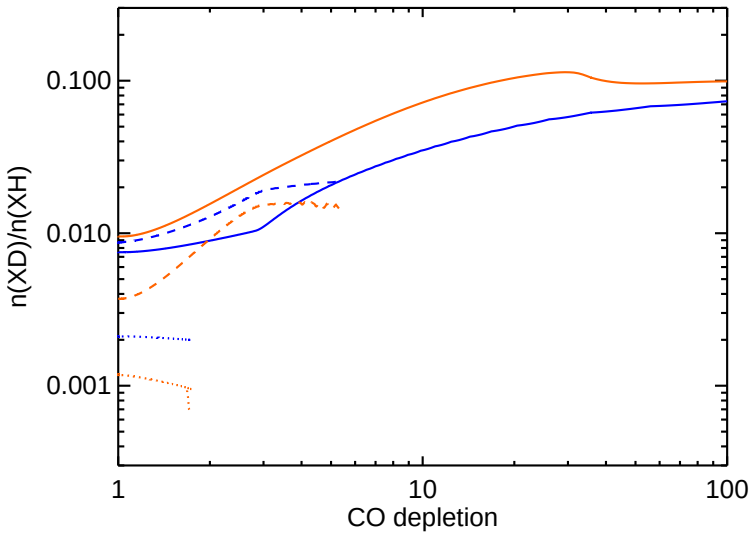

Figure 7.4: Solid HDO/H_2O (blue) and gaseous D/H ratio (orange) as function of the CO depletion factor $f_D(\mathrm{CO}) = n_g(\mathrm{CO})/n_{g,ini}(\mathrm{CO})$, which increases with time, for the three reference models: translucent cloud region (dotted), dark cloud region (dashed), dark core region (solid).

the deuteration in ices (see Introduction).

7.3.3.1 Influence of the H_2 o/p ratio

As described in chapter 3, the H_2 opr influences the deuteration of gas-phase species (including atomic D) (Walmsley et al., 2004; Flower et al., 2006; Pagani et al., 2009), thereby affecting the deuteration of solid water. Figure 7.5 shows the HDO/H_2O and D_2O/H_2O ratios in grain mantles as a function of time for four values of H_2 opr, including the variation in all other parameters, except the visual extinction range, which is limited to 2 - 10 mag (where most of water is believed to form, see Fig. 7.2). As anticipated, the H_2 opr governs the deuteration of water ice via its influence on the abundance of H_3^+ isotopologues and atomic D, for values higher than about 3×10^{-4}. An increase in H_2 opr between 3×10^{-4} and 3 decreases the HDO/H_2O and D_2O/H_2 ratios by 2.5 orders and 5.5 orders of magnitude, respectively. Furthermore, the ortho/para ratio of H_2 is a key, even the most important, parameter for water deuteration. The decrease in the deuteration due to the increase in the H_2 opr is much greater than the standard deviation induced by the variation in other parameters.

Comparisons with the observations by Coutens et al. (2012) clearly suggest that a low opr of H_2, lower than 3×10^{-4}, is needed to reproduce the observed deuterium fractionation.

7.3.3.2 Influence of the total density

As discussed in section 7.3.2, the gas-phase D/H ratio is a function of the total density n_H because high densities allow the gas-phase D/H ratio to increase with the CO depletion. Figure 7.6 shows the deuteration of HDO and D_2O for the four considered densities, using an H_2 opr of 3×10^{-6}, two temperatures (10 and 20 K), and a high visual extinction (10 mag), including the variation in grain surface parameters.

At low densities ($n_H \leq 10^4$ cm^{-3}), water deuteration is constant and low with time because a significant part of HD is already trapped in atomic D, before the CO depletion. At higher densities ($n_H > 10^5$ cm^{-3}), the efficient increase in the gaseous D/H ratio allows an increase in the deuteration of water up to 10%. In these cases, HDO is mostly located in the outer part of grain mantles, and D_2O is only located in the outermost layers, whilst H_2O is present throughout

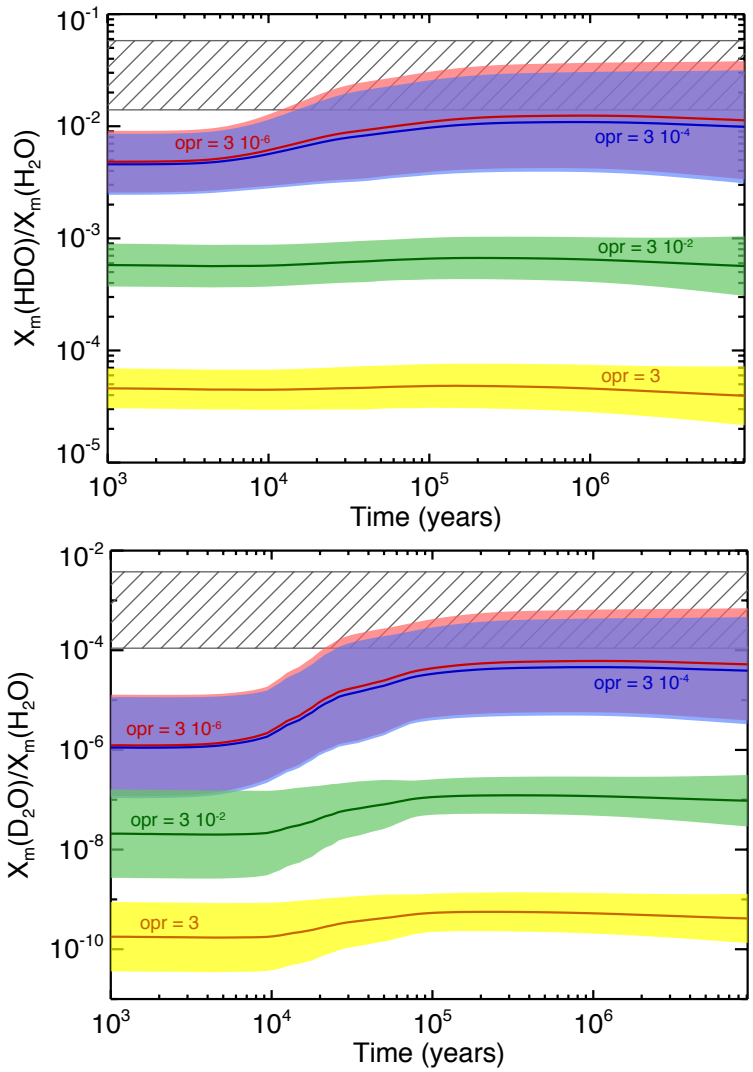

Figure 7.5: Deuteration of water ice for four values of H_2 ortho/para ratios: 3×10^{-6} (red), 3×10^{-4} (blue), 3×10^{-2} (green), and 3 (yellow) including the variation in all other input parameters, except the visual extinction range that is limited to 2 - 10 mag. Hatched boxes refer to water deuteration observed by Coutens et al. (2012) towards IRAS 16293.

the mantle bulk. For this reason, the HDO/H_2O is limited and cannot reach the final gas-phase D/H ratio (up to 50 % at $n_H = 10^6$ cm^{-3}).

In summary, the total density plays a key role in the deuteration of water. Indeed, the variation in the total density n_H between 10^3 and 10^6 cm^{-3} influences the HDO/H_2O and D_2/H_2O ratios by 2 and 3.5 orders of magnitude, respectively.

The two observed deuteration ratios can be predicted with total densities n_H between 10^4 and 10^5 cm^{-3} at 10 K and between 10^5 and 10^6 cm^{-3} at 20 K, regardless of other grain surface parameters. In the following section, we study the case $n_H = 10^4$ cm^{-3} in more detail to investigate the effect of the temperature and the visual extinction on water deuteration.

7.3.3.3 Influence of the temperature and visual extinction

Temperatures either in the gas-phase and on grain surfaces also influence the deuteration of water. First, an increase in the gas-phase temperature enhances the reactivity of endothermic reactions, which can hydrogenate back H_3^+ isotopologues, decreasing the abundance of gaseous

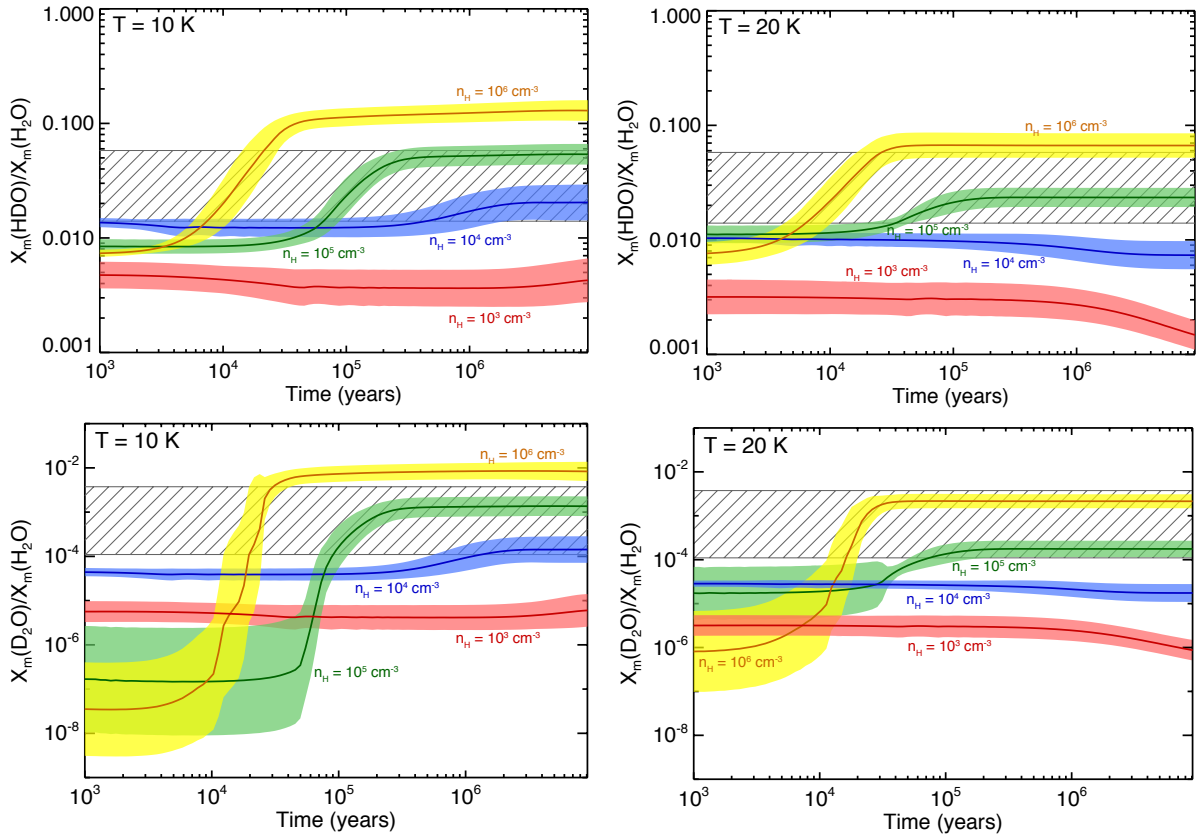

Figure 7.6: Deuteration of water ice for four values of total density 10^3 (red), 10^4 (blue), 10^5 (green), 10^6 (yellow) cm^{-3}, and two temperatures: 10 K (left panels), 20 K (right panels), using an H_2 opr of 3×10^{-6}, a visual extinction of 10 mag, including the variation of all other input parameters. Hatched boxes refer to water deuteration observed by Coutens et al. (2012) towards IRAS 16293.

D atoms. Second, an increase in the grain temperature severely increases the desorption rate of volatile species, such as atomic H or D. The abundance of gaseous D is limited by the low deuterium reservoir, whereas the abundance of atomic hydrogen can increase up to two orders of magnitude, decreasing the gaseous D/H ratio. Water is mainly produced via reactions involving atomic H and D, increasing gas and dust temperatures, hence, decreasing the water deuteration on grain surfaces.

Figure 7.7 shows this effect by presenting the final HDO/H_2O and D_2O/H_2O ratios (at 10^7 yr) with the visual extinction, for the three temperatures, considering an H_2 opr of 3×10^{-6}, a total density of 10^4 cm^{-3}, and including the variation in grain surface parameters. The increase in the (gas and grain) temperatures between 10 and 20 K slightly decreases the water deuteration approximately by a factor of 3 for HDO and of 10 for D_2O at visual extinctions higher than 2 mag. The evolution of deuteration is the same order of magnitude as the standard deviations induced by the variation of other parameters.

The H and CO abundances in the gas-phase increase with decreasing A_V because of the increase in the photodesorption rate, decreasing the gaseous D/H ratio. Visual extinction, therefore, influences water deuteration at low visual extinctions where water starts to form (2mag $< A_V <$ 5 mag). As can be seen in Fig. 7.7, HDO/H_2O and D_2O/H_2O ratios increase by one and two orders of magnitude respectively, between $A_V = 2$ and 5 mag, .

Comparison with observations shows that observed HDO and D_2O fractionations are reproduced for a low temperature of 10 K and for visual extinctions A_V higher than 4 mag ($A_{V,obs} = 8$ mag), implying that deuterated water needs to be formed in dark regions if $n_H = 10^4$ cm^{-3}.

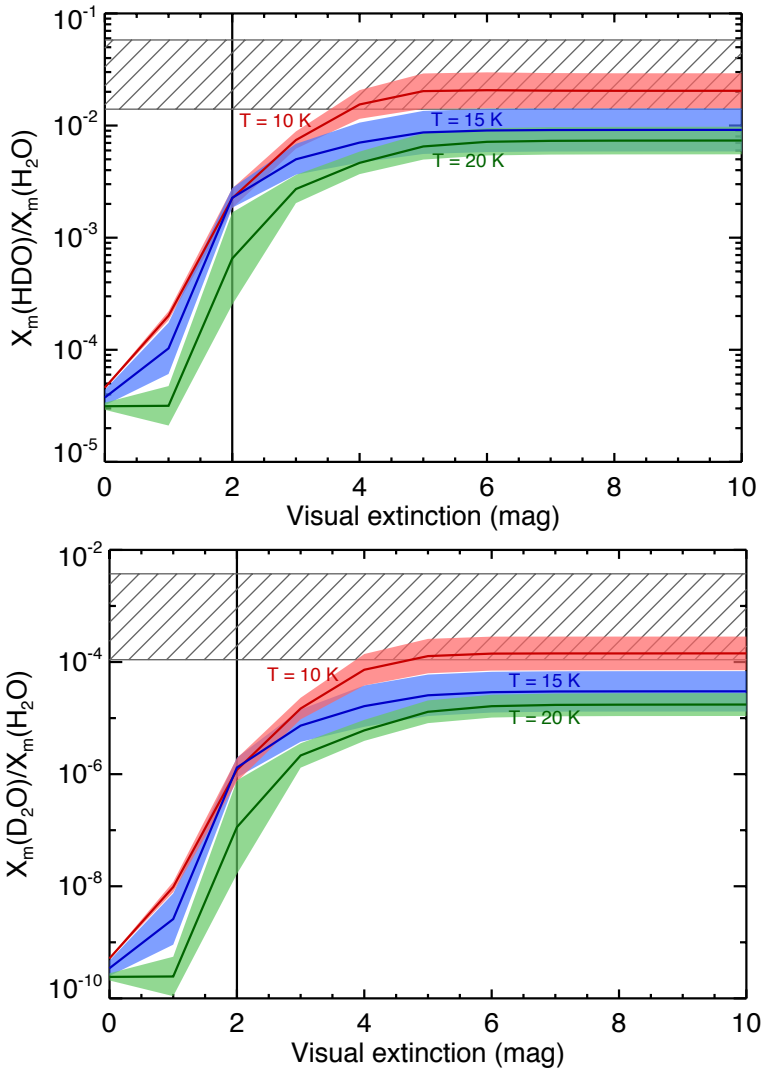

Figure 7.7: Final deuteration of water ice (at $t > 10^6$ yr: representative of a typical molecular cloud age) as function of visual extinction for three values of temperatures: 10 (red), 15 (blue), 20 (green) K, using a total density of 10^4 cm^{-3}, an H_2 opr of 3×10^{-6} and including the variation of all other input parameters. The vertical line refers to the A_V threshold of water ice observed by Whittet et al. (1988). Hatched boxes refer to water deuteration observed by Coutens et al. (2012) towards IRAS 16293.

7.3.3.4 Influence of grain surface parameters

The grain surface parameters ($a_d, E_d/E_b, E_b$(H)) can also influence the formation of interstellar ices. As discussed in chapter 5, the absolute abundance of the main ice constituents formed on grain surfaces (water, formaldehyde, methanol for instance) decrease with E_d/E_b whilst the grain size does not affect the overall abundance (but only the ice thickness). Moreover, it is also seen that the absolute abundance of water slightly decreases with the binding energy of volatile species.

The water deuteration is slightly affected by the variation of the grain surface parameters. As shown in Fig. 7.7, the standard deviations given by the variation of the grain surface parameters remain lower than the evolution of the water deuteration lead by the variation in the temperature and the visual extinction. The water deuteration slightly decreases with the grain size due to the decrease in the CO depletion efficiency (since the accretion rate is inversely proportional to the grain size), limiting the increase in the deuterium fractionation. On the other hand, the water deuteration slightly increases with E_d/E_b and E_b(H) because the formation efficiency of H_2O

decreases with the diffusion energy of volatile species, increasing the overall fractionation.

7.3.3.5 Concluding remarks

Comparing the average value of the deuterium fractionation with the standard deviation induced by the variation of other parameters allowed us to claim that the H_2 opr is the most important parameter for water deuteration, followed by the total density. The visual extinction and the temperature also influence water deuteration but more weakly.

The comparison of our model predictions with observations allows us to constrain some parameters involved in the formation of deuterated water seen towards IRAS 16293. The observations are reproduced for
- a H_2 opr lower than 3×10^{-4};
- a density lower than 10^5 cm^{-3} if $T = 10$ K and $A_V > 4$ mag;
- a higher density $n_{\rm H}$ between $\sim 5 \times 10^4$ cm^{-3} and 10^6 cm^{-3} if $T = 20$ K.

7.4 Comparisons with previous models

In this section, we compare our model predictions for the gas-phase deuteration and for water ice deuteration with previous models. The atomic D/H ratio in the gas-phase depends on the deuteration of H_3^+. We compare our predictions from steady state models with those by Flower et al. (2006), specifically their Fig. 5. We obtain the same influence of the H_2 opr on the deuteration of H_3^+, with similar fractionation values.

To our knowledge, the only comprehensive theoretical study focused on the deuterated water formation on grain surfaces was performed by Cazaux et al. (2011), even if other works also included the deuteration of water ice in their astrochemical model (i.e. Tielens, 1983; Caselli et al., 2002; Stantcheva & Herbst, 2003; Bell et al., 2011). Cazaux et al. (2011) considered a static stage followed by a free-fall collapse phase. However, in their model, the deuterated water is practically formed only during the first static phase. Thus, it is worth comparing their predictions with ours.

The main difference is that they found that the water deuteration is highly temperature-dependent and lower than our predictions at low (< 15 K) temperatures (Fig. 7.6 of this work versus Fig. 3.c of Cazaux et al., 2011). This is due to a different approach in the reaction probability computation and the use of the endothermic O+H_2 reaction in the chemical network. Cazaux et al. (2011) assumed a competition between the reaction and the diffusion. In their model, if the diffusion timescale of the reactants is larger than the transmission timescale of the reaction, the reaction occurs regardless of its activation barrier. Thus, at low temperatures, the mobility is low and the reaction always occurs. In contrast, in our work, the reaction rate is given by the product of the collision rate of the two reactants and the reaction probability P_r (see Sec. 2.1 and 2.4), giving a much smoother dependence on the temperature. As a consequence, in Cazaux et al. (2011), H_2O is formed, at low temperatures, via reactions involving H_2 because of its large abundance, whilst HDO is formed via reactions involving atomic D. The solid HDO/H_2O ratio, therefore, scales with the gaseous [D]/[H_2] ratio ($\sim 10^{-5}$). In our work, water is always mostly formed via the O+H and OH+H reactions, and the deuteration scales with the [D]/[H] ratio (up to 10^{-1}). At higher temperatures (> 15 K), both models agree since water is formed via the same reactions, namely O+H and OH+H (and their deuterated counterparts). This comparison shows that the chemical route for the water formation is the major actor in the game, whilst other differences in the two models, including the physical evolution treatment, play a minor role in the water deuteration. However, we should point out that the O+H_2 reaction cannot occur at low temperatures given its endothermicity. Therefore, it is unlikely that water deuteration shows a such strong temperature dependence.

7.5 Discussion

In the previous paragraphs, we have shown that the deuteration of water and other molecules strongly depends on the H_2 opr and the total density, but also on the visual extinction and the temperature where solid molecules are formed. The high deuteration of water ($HDO/H_2O > 1$ % and $D_2O/H_2O > 0.01$ %) observed towards the low-mass protostar IRAS 16293 (Coutens et al., 2012) can only be reproduced with an H_2 opr that is lower than 3×10^{-4}, suggesting that most of deuterated water is formed at low H_2 opr. The ortho-para ratio reaches its steady-state value on a timescale proportional to the total density, of about 10^7 yr at $n_H = 10^4$ cm^{-3} (Flower et al., 2006). If the H_2 molecule has an initial opr value of 3 upon its formation on grain surfaces, the high deuteration observed around IRAS 16293 would suggest that water observed in this envelope has been formed in an "old" molecular gas, i.e. a gas old enough to show a low H_2 opr at the moment of the formation of interstellar ices. However, it is possible that the ortho-to-para conversion also occurs on grain surfaces (Le Bourlot, 2000) but with an uncertain rate (see Sugimoto & Fukutani, 2011; Chehrouri et al., 2011; Hama et al., 2012). The decrease in the H_2 opr could occur, therefore, faster and the molecular cloud age of 10^7 yr deduced from the estimate by Flower et al. (2006) should only be used as an upper limit.

The observed deuterium fractionation of water is only reproduced for dark conditions (high visual extinctions and low temperatures if $n_H = 10^4$ cm^{-3} or higher densities). Therefore, although IR observations of ices show that water ice starts to form at low visual extinctions, the deuterated water observed in IRAS 16293 should instead be formed in darker regions. Consequently, H_2O would be present in the inner part of ice mantles, whilst most of HDO and D_2O molecules should be located in the outer layers. A physical evolution, modelling the accumulation of matter from diffuse molecular clouds to dense cores, would allow us to directly confirm this result. The high observed deuteration of water also confirms that water is mostly formed from reactions involving atomic H and D and not by molecular hydrogen (see Sec. 7.4).

Observations of water, formaldehyde, and methanol vapours towards low-mass protostars show that these species have different deuterium fractionations. Figure 9.2 overplots the observed deuteration towards IRAS 16293 with mean theoretical deuteration values reached at $t = 3 \times 10^5$ yr (i.e., the upper limit of the age of prestellar cores, see Bergin & Tafalla, 2007) as function of the density, for two temperatures, a low H_2 opr of 3×10^{-6} and only considering dark regions ($A_v = 10$ mag). The comparison of our predictions with observations shows that
i) our model reproduces the observed HDO/H_2O and D_2O/H_2O ratios for densities between 1×10^4 and 1×10^5 cm^{-3} at 10 K and between and 2×10^4 and 3×10^5 cm^{-3} at 20 K. Therefore, water deuteration is reproduced within a wide range of physical conditions representative of molecular clouds but not in the too-translucent cloud phase with too low density, too low visual extinctions and too high temperatures.
ii) the observed $HDCO/H_2CO$ can be reproduced at higher densities ($3 \times 10^5 - 10^6$ cm^{-3}) and lower temperatures ($\sim$ 10 K) as seen in the central regions of prestellar cores. The D_2CO/H_2CO ratio is reproduced at densities higher than 10^6 cm^{-3} (at $\sim 5 \times 10^6$ cm^{-3}, chapter 6).
iii) methanol deuteration (CH_2DOH/CH_3OH and CHD_2OH/CH_3OH ratios) proceeds in the outer parts of grain mantles when the prestellar core condensation reached high densities ($> 5 \times 10^5$ cm^{-3}) and low temperatures (10 K).

In summary, the difference in the deuterium fractionation of molecules seen in IRAS 16293 can be explained by different periods of formation. Water is mainly formed first in regions showing intermediate densities representative of molecular clouds ($n_H = 10^4 - 10^5$ cm^{-3} where the CO depletion is limited. Formaldehyde and methanol are formed subsequently, at higher CO depletions when the gas is denser and colder. These predictions are in good agreement with infrared observations of interstellar ices presented in the introduction which also show that water ice is formed first, at low visual extinctions, whilst solid methanol forms later on at visual

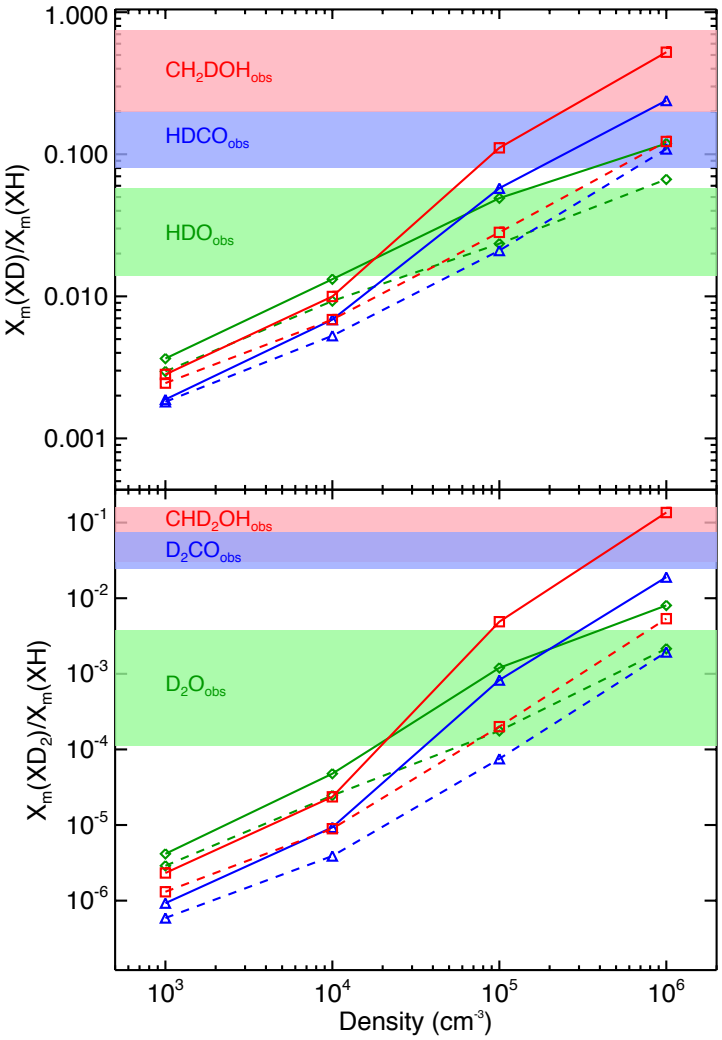

Figure 7.8: Averaged deuterations of water (green diamonds), formaldehyde (blue triangles), and methanol (red squares) at 3×10^5 yr (representative of a typical prestellar core age) as function of the total density (abscissa) and temperature (10 K: solid, 20 K: dashed) considering an H_2 opr of 3×10^{-6} and $A_V = 10$ mag and considering grain surface parameters as free. Solid boxes refer to observations by Coutens et al. (2012) towards IRAS 16293 for water, and by Parise et al. (2006) (and references therein) towards a sample of low-mass protostars for formaldehyde and methanol.

extinctions higher than 15 mag (Whittet et al., 2011).

More generally, the deuterium fractionation of any species, believed to be formed mainly in ices, can be used as a tracer to estimate the physical conditions at the moment of its formation. As shown in Fig. 9.2, the D/H ratio increases with increasing density and with decreasing temperature. A low deuteration, similar to the deuteration of water, implies that the solid species is mainly formed in regions with relatively low densities, even if its deuterated isotopologues could be formed mainly in a later phase. In contrast, a high deuteration level suggests that the solid species is mostly formed in the dense and cold phase where the deuteration in the gas-phase (and in particular the atomic D/H ratio) is high. Extremely high deuteration, such as methanol deuteration, would also imply the existence of abstraction reactions or other processes enhancing the formation of deuterated isotopologues with respect to the main isotopologue (chapter 6). H/D exchange reactions between solid methanol and water, for example, can also lead to a selective deuteration of functional groups (Ratajczak et al., 2009).

7.6 Conclusions

We have presented a comprehensive study of the formation and the deuteration of interstellar water ice carried out with our astrochemical model GRAINOBLE. In addition to the multilayer formation of grain mantles presented in chapters 3 and 5 and the use of abstraction reactions for the deuteration of formaldehyde and methanol (chapter 6), we introduced a better treatment for computing the transmission probabilities of surface reactions based on the Eckart model. We also considered wavelength-dependent UV photodesorption of ices following molecular dynamics (MD) simulations and new experimental works.

The main results of this work are the following:

1) Our model reproduces the abundance of water ice and the visual extinction threshold observed by Whittet et al. (1988), as well as the different ice components seen in different molecular clouds regions.

2) Water deuteration strongly depends on the ortho-to-para ratio of H_2 and the total density, but also, even though more weakly, on the gas and grain temperatures and on the visual extinction.

3) The deuteration of water observed towards the low-mass protostar IRAS 16293 can only be reproduced by considering a H_2 opr lower than 3×10^{-4} and a total density between 8×10^3 and 5×10^5 cm^{-3}. If a low density (10^4 cm^{-3}) is considered, a low temperature (10 K) and a visual extinction higher than 4 mag are necessary. Dark regions (high densities or high visual extinctions) are, therefore, needed to reproduce the observations.

4) Comparison between the observed deuteration of water, formaldehyde, and methanol and our theoretical predictions allowed us to propose the following scenario. Water ice is formed first within relatively wide ranges of physical conditions: H_2O is allowed to start its formation at low densities and low visual extinctions, but HDO and D_2O are instead formed in darker (higher $n_{\rm H}$ and/or A_V) regions. Formaldehyde and then methanol are mainly formed subsequently, in the dense and cold prestellar cores.

5) Deuterium fractionation can be used to estimate the values of the density and temperature at the moment of formation of solid species because of its sensitivity to the physical conditions. Low deuteration, similar to water deuteration, implies that the species is formed in a wide range of physical conditions, whilst a high deuteration suggests an efficient formation in the centre of dense and cold prestellar cores.

With this work, we have explored the influence of a wide range of parameters values on the formation of deuterated ices. Now that the influence of the various parameters is clarified, our next step will be a more sophisticated model, based on a realistic physical evolution of a cloud.

Part III

Millimetric observations

Chapter 8

Selective deuteration of methanol in low- to high-mass protostars

Contents

Deuteration sélective du methanol dans les étoiles de faibles masses et de masses élevées

La théorie actuelle de la deutération du methanol sur les grains interstellaires prédit que le rapport d'abondance des isotopologues simplement deutérés [CH_2DOH]/[CH_3OD] doit etre de 3. Dans les régions chaudes où les manteaux de glace se subliment, les vapeurs de methanol sont détectables par transitions rotationnelles. Dans des études précédentes, le rapport [CH_2DOH]/[CH_3OD] gazeux mesuré est bien supérieur à 3 dans les étoiles de faible masse et proche de 1 dans le coeur chaud massif de Orion IRc2.

Nous présentons des nouvelles mesures du rapport [CH_2DOH]/[CH_3OD] gazeux dans deux nouvelles proto-étoiles massives, ainsi que dans deux proto-étoiles de masse intermediaire afin de confirmer ou d'exclure la dépendence du rapport avec la masse de la proto-étoile. Les observations ont été effectuées avec le telescope 30m de l'IRAM. Plusieures raies rotationnelles de chaque isotopologue ont été mesurées vers les proto-étoiles de masse intermediaire, alors que seulement des raies de CH_3OD ont été détectées vers les coeurs chauds massifs. Le rapport [CH_2DOH]/[CH_3OD] (ou sa limite supérieure) a été calculé á la fois par les densités de colonne moyennées et directement du rapport de flux des raies.

Nos résultats confirment que le rapport [CH_2DOH]/[CH_3OD] est inférieur d'un ordre de grandeur dans les coeurs chauds massives que dans les proto-étoiles de faible masse. De plus, ces résultats suggérent que les masses intermédiaires présentent des propriétés similaires aux proto-étoiles de faible masse. Les rapports [CH_2DOH]/[CH_3OD] mesurés ne sont pas corrélés avec la théorie de deuteration du methanol qui ne dépend pas de la masse de la source. Bien que les rapports élevés mesurés dans les proto-étoiles de faible masse et de masse intermédiaire peuvent etre expliqués par différents mécanismes de dépletion sélective, les faibles rapports (< 2) mesurés dans les coeurs chauds massives demeurent inexpliqués. Une révision de la chimie du deuterium est donc proposée.

Ce chapitre est tiré de la publication: A. Ratajczak, **V. Taquet**, C. Kahane, C. Ceccarelli, A. Faure, E. Quirico 2011, *The puzzling deuteration of methanol in low- to high- mass protostars*, A&A, 528, 13.

Abstract

The current theory of methanol deuteration on interstellar grains predicts that the abundance ratio of the singly deuterated isotopologues [CH_2DOH]/[CH_3OD] should always be 3. In warm regions where grain mantles have sublimated, gaseous methanol is detectable via its rotational transitions. In previous observational studies, the gas-phase [CH_2DOH]/[CH_3OD] ratio was measured and found to be significantly larger than 3 in low-mass protostars and close to 1 in the Orion IRc2 massive hot core.

We present new measurements of the gas-phase [CH_2DOH]/[CH_3OD] ratio in two additional high-mass protostars, as well as in two intermediate-mass protostars, to either confirm or exclude the dependence of this ratio on the mass of the protostar. The observations were carried out using the IRAM-30m telescope. Several rotational lines of each isotopologue were detected toward the intermediate-mass protostars, while only CH_3OD lines were detected in the massive hot cores. The ratio [CH_2DOH]/[CH_3OD] (or its upper limit) was computed from both the averaged column densities and directly from line flux ratios.

Our results confirm that the [CH_2DOH]/[CH_3OD] ratio is substantially lower in massive hot cores than in (low-mass) hot- corinos, by typically one order of magnitude. Furthermore, they suggest that intermediate-mass protostars have similar properties to low-mass protostars. The measured [CH2DOH]/[CH3OD] ratios are inconsistent with the current theory of methanol deuteration, independently of the mass of the source. While the large ratios measured in low- and intermediate-mass sources can be explained qualitatively by various selective depletion mechanisms, the small ratios (<2) measured toward massive hot cores are puzzling. A revision of the deuterium chemistry in hot cores is suggested.

This chapter is taken from the publication: A. Ratajczak, **V. Taquet**, C. Kahane, C. Ceccarelli, A. Faure, E. Quirico 2011, *The puzzling deuteration of methanol in low- to high- mass protostars*, A&A, 528, 13.

8.1 Introduction

Since the first detection of a deuterated isotopologue in space (DCN, Jefferts et al., 1973)), molecular deuteration has been considered as a powerful diagnostic tool for studying the physical conditions and past history of the interstellar gas (see for example the reviews by Roueff & Gerin, 2003; Ceccarelli et al., 2007). Among the various molecules with high degrees of deuteration, methanol is a particularly interesting one, for several reasons. First the detection of the (gaseous) triply deuterated methanol with an abundance of a few percent with respect to the hydrogenated counterpart makes it the most deuterium-enriched molecule so far known (Parise et al., 2004). Second, theoretical and experimental studies predict that methanol is formed on the grain surfaces rather than in the gas-phase (Garrod et al., 2006). Thus, the measurements of methanol deuteration permit us to study, almost unambiguously (see below), the process(es) on the grain surfaces. The link with observations is however complicated. This is firstly because there are at least two ways to form methanol on the surfaces: either by addition of hydrogen atoms on iced CO (e.g. Nagaoka et al., 2005) or by the photolysis or radiolysis of an iced mixture of methane, CO, and water (e.g. Hudson & Moore, 1999; Wada et al., 2006). Deuteration is expected to be very different in the two cases and, specifically, much higher in the first case. Secondly, the alteration of the deuteration degree can occur on the grain surfaces via H/D atom exchanges both because of thermal activation (Ratajczak et al., 2009) or, again, photolysis (Weber et al., 2009). In addition, when solid methanol sublimates, it can undergo chemical reactions in the gas phase, which may again alter the original deuteration degree set on the grain surfaces (Charnley et al., 1997; Osamura et al., 2004). Despite the complications and thanks to them, deuterated methanol is a tool rich in information.

Previous studies toward low mass protostars have shown that the singly deuterated methanol CH_2DOH can be almost as abundant as CH_3OH (e.g. Parise et al., 2006), a property observed in several other deuterated molecules in low mass protostars, although to a lesser extent (Ceccarelli et al., 2007). This large deuteration very likely implies that, in low mass protostars, methanol was formed during the pre-collapse, cold, and dense phase. Surprisingly, however, the other form of singly deuterated methanol, CH_3OD, is much less abundant, by more than a factor of 10. According to the grain chemistry statistical model of Charnley et al. (1997), if the deuterated isotopologues of methanol are formed by H/D atoms addition to CO on the grain surfaces, the abundance of CH_2DOH should always be only a factor of $\sim$3 larger than the CH_3OD one. To make the situation even more puzzling, the same $[CH_2DOH]/[CH_3OD]$ ratio is close to 1 in the high-mass protostar Orion IRc2 (Jacq et al., 1993). This difference between high- and low-mass protostars might reflect different deuteration degrees and/or ice compositions, as suggested by Ratajczak et al. (2009). On the other hand, no other measurement of the $[CH_2DOH]/[CH_3OD]$ ratio exists in high-mass protostars other than Orion IRc2, so that the measured low $[CH_2DOH]/[CH_3OD]$ ratio may be peculiar to this source, itself peculiar in many other aspects.

In this chapter, we present new measurements of the $[CH_2DOH]/[CH_3OD]$ ratio in two additional high-mass protostars, which confirm the low value measured in Orion IRc2. In addition, we present observations of deuterated methanol in intermediate mass protostars. As shown by Crimier et al. (2010a), intermediate mass protostars are in several aspects also intermediate in the characteristics between low- and high-mass protostars. Their case can therefore help us to understand why the $[CH_2DOH]/[CH_3OD]$ ratio is so different at the two extremes of the mass range.

8.2 Observations and data reduction

The observations were carried out using the IRAM-30 m telescope in June 2010. Two frequency ranges were observed simultaneously with the new broad-band EMIR receivers, one centered at 110.2 GHz, the other at 134.0 GHz. At these frequencies, the 30 m telescope HPBW is, respectively, 22 " and 18 " and the main beam efficiency is close to 0.78. Each receiver was equipped with two channels corresponding to orthogonal linear polarizations and showed image rejections higher than 20 dB when operating in single sideband mode. The broad-band autocorrelator WILMA, divided into four parts, each providing a spectral resolution of 2 MHz and a frequency coverage of 3.7 GHz, was associated with the four channels. In addition, a high resolution autocorrelator, VESPA, was divided into two parts, one centered at 110.2 GHz covering 140 MHz with a spectral resolution of 80 kHz, the second centered at 134.0 GHz with a coverage of 290 MHz and a resolution of 310 kHz. The system temperatures were between 95 K and 115 K at 134 GHz and between 155 K and 180 K at 110 GHz. Observations were performed in wobbler-switch mode, with a 90" throw at a rate of 0.5 Hz. The temperature scale was calibrated every 15 min using two absorbers at different temperatures and the calibration uncertainty (1σ) is about 15% of the line flux at both frequency ranges. The pointing and focus were checked every two hours on planets and continuum radio sources close to the targets. Effective on-source integration times were 45 min for G24.78, 140 min for OMC2, and 210 min for CepE and W3(H2O), where both polarisation channels were added (after checking that the line intensities were identical).

The deuterated methanol lines detected in the high resolution spectra were fitted with gaussian profiles using the `CLASS` tool[1] and the frequencies given in Parise et al. (2002). For the CH_3OH lines detected in the broad-band spectra, we used the `CASSIS` package[2] and the spectro-

[1] *http://www.iram.fr/IRAMFR/GILDAS*
[2] *http://cassis.cesr.fr*

scopic data from the CDMS database to perform the line identification and the gaussian fit. In both cases, only linear baselines were subtracted from the spectra.

Table 8.1: Parameters of the observed CH_3OH, CH_2DOH, and CH_3OD transitions.

Transition	Frequency (GHz)	Spectroscopic parameter $\mu^2 S$ (Deb^2)	E_{up} (cm^{-1})	$\int T_{mb} dv$ OMC2FIR4	CepheusE	W3(H_2O)	G24.78+0.08
CH_3OH				K km s^{-1}			
$0_{(+0),0} - 1_{(-1),1}$ E	108.8939	1.0	9.03	1.43 ± 0.01	0.49 ± 0.01	4.68 ± 0.03	9.45 ± 0.02
$14_{(+5),10} - 15_{(+4),11}$ E	109.1387	3.4	264	(0.04)	(0.03)	1.09 ± 0.03	0.82 ± 0.02
$16_{(-2),15} - 16_{(+1),15}$ E	109.1531	3.7	238	(0.04)	(0.03)	0.92 ± 0.03	0.77 ± 0.03
$7_{2,5} - 8_{1,8}$ A	111.2896	2.3	71.6	0.25 ± 0.01	(0.03)	3.97 ± 0.03	2.16 ± 0.04
$6_{2,5} - 7_{1,6}$ A	132.6219	2.0	59.6	0.48 ± 0.02	0.07 ± 0.01	6.80 ± 0.19	2.54 ± 0.05
$6_{(-1),6} - 5_{(+0),5}$ E	132.8907	3.7	37.5	11.30 ± 0.04	2.81 ± 0.01	11.09 ± 0.10	21.03 ± 0.04
$5_{(-2),4} - 6_{(-1),6}$ E	133.6055	1.6	42.4	0.62 ± 0.03	(0.03)	4.77 ± 0.03	2.58 ± 0.02
$12_{(-3),10} - 13_{(-2),12}$ E	134.2311	3.9	170	(0.03)	0.09 ± 0.01	3.61 ± 0.03	1.50 ± 0.02
$8_{2,7} - 7_{3,4}$ A	134.8970	1.8	84.1	0.93 ± 0.01	0.21 ± 0.01	4.55 ± 0.04	2.69 ± 0.03
$8_{2,6} - 7_{3,5}$ A	135.3768	1.8	84.1	0.33 ± 0.01	(0.03)	4.14 ± 0.07	2.20 ± 0.02
CH_2DOH				mK km s^{-1}			
$9_{18} - 9_{09}$ o1	110.1054	3.3	83.4	(32)	(46)	(73)	(103)
$3_{03} - 2_{02}$ e1	133.8473	1.1	18.3	24 ± 9	(35)	(90)	(95)
$3_{03} - 2_{02}$ o1	133.8729	1.1	21.7	(27)	35 ± 7	(25)	(41)
$3_{22} - 2_{21}$ o1	133.8818	0.6	33.6	(27)	(25)	(29)	(57)
$3_{22} - 2_{21}$ e1	133.8929	0.6	27.4	(27)	(25)	(29)	(57)
$3_{21} - 2_{20}$ o1	133.8974	0.6	33.6	41 ± 8	(24)	(29)	(57)
$3_{21} - 2_{20}$ e1	133.9302	0.6	27.4	(28)	37 ± 6	(37)	(48)
$3_{03} - 2_{02}$ e0	134.0655	1.2	8.90	66 ± 7	89 ± 4	(27)	(49)
$3_{22} - 2_{21}$ e0	134.1124	0.7	20.2	(28)	(19)	(24)	(54)
$3_{21} - 2_{20}$ e0	134.1854	0.7	20.2	25 ± 9	(29)	(72)	(69)
CH_3OD				mK km s^{-1}			
$1_1 - 1_0$	110.1889	1.6	7.8	(40)	(40)	(40)	(94)
$2_1 - 2_0$	110.2626	2.7	10.8	57 ± 11	(45)	93 ± 18	(95)
$3_1 - 3_0$	110.4758	3.8	15.4	(55)	(43)	(67)	(108)
$1_{1-} - 1_{0+}$	133.9254	3.2	6.00	28 ± 6	17 ± 4	116 ± 12	141 ± 16*

Notes. Fluxes are expressed in main-beam temperature unit. Upper limits (in parentheses) are given at 3 σ and include both statistical and calibration uncertainties. In contrast, for the detected lines, only 1 σ statistical uncertainties are given; total uncertainties are given by the quadratic sum of these statistical uncertainties and of 15% calibration uncertainties. According to the detected CH_3OH lines, upper limits for both isotopologues were estimated using linewidths of 5 km.s^{-1}, except for low resolution spectra (velocity resolution of ∼5 km.s^{-1}) where linewidths of 9 km.s^{-1} were assumed. We have also checked that the relative intensities of the detected lines and the upper limits on the other lines from CH_2DOH and CH_3OD are consistent with predictions at local thermodynamic equilibrium to within a factor two.
The asterisk denotes the uncertain identification of the CH_3OD line (133.9254 GHz) in G24.78+0.08.

8.3 Data analysis

Table 8.1 presents the results of gaussian fits to our observations for CH_3OH and its two isotopologues CH_2DOH and CH_3OD. The spectra of the CH_2DOH $3_{03} - 2_{02}$ e_0 and the CH_3OD $1_{1-} - 1_{0+}$ transitions are plotted in Fig. 8.1.

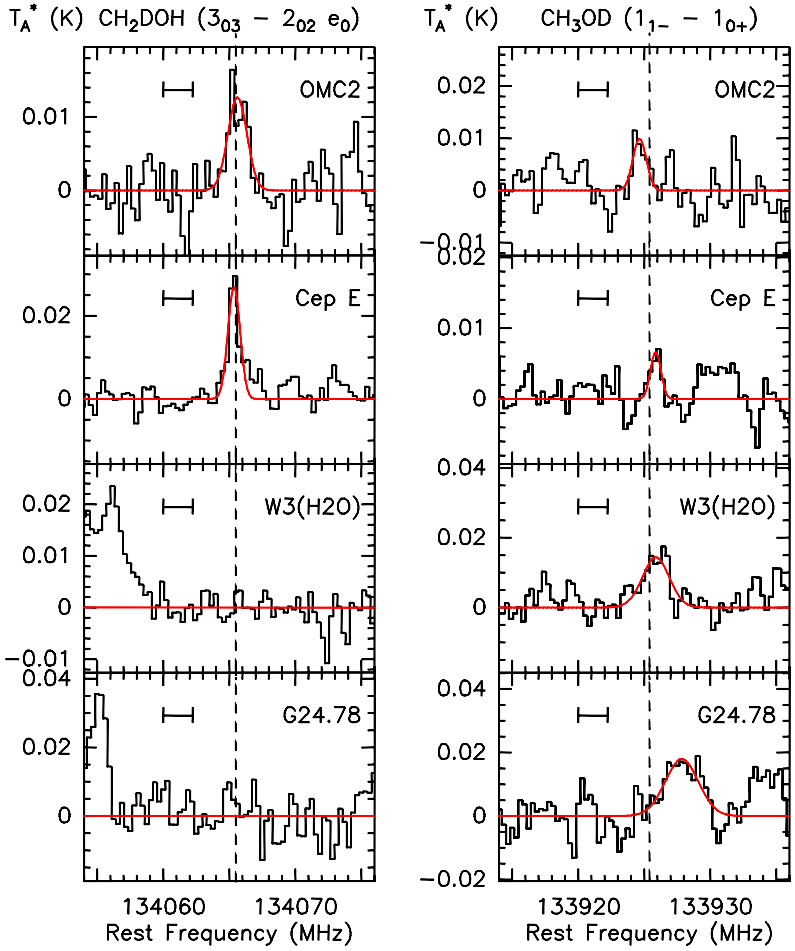

Figure 8.1: CH_2DOH and CH_3OD spectra towards the four sources. The observed positions and the assumed v_{LSR} rest velocities are the following: OMC2 FIR4 (05:35:26.7, -05:09:59), 10.5 km.s^{-1}; CepheusE (23:03:12.7, +61:42:27), -11.4 km.s^{-1} ; W3(H_2O) (02:27:04.6, +61:52:26), -48.0 km.s^{-1}; G24.78+0.08 (18:36:12.6, -07:12:11), 111.0 km.s^{-1}. The line intensities are expressed in antenna temperature scale. The curves are gaussian fits to the detected lines and the dashed lines indicate the expected frequencies of the lines. The small horizontal segment has a width of 5 km.s^{-1}. The broad feature right to the CH_3OD line in Cep E includes the CH_2DOH line ($3_{21} - 2_{20}$ e1) at 133930.2 GHz. The CH_3OD line in G24.78+0.08 appears at a significantly velocity shift so that its identification must be considered as uncertain.

Assuming that the spatial distribution of both isotopologues is the same in the region probed by the observations, the [CH_2DOH]/[CH_3OD] abundance ratio is simply equal to the column density ratio. In addition, if the lines are optically thin and the populations of all molecular energy levels in thermodynamical equilibrium are at the same rotational temperature T_{rot}, then for each isotopologue (i) the total column density N_i can be derived from the line flux W_i of any of its transitions by the relation:

$$N_i = \left(\frac{3k_b W_i}{8\pi^3 \nu_i (\mu^2 S)_i} \right) Z_i(T_{rot}) \exp \left[\frac{E_{u,i}}{k_b T_{rot}} \right], \tag{8.1}$$

where $Z_i(T_{rot})$ is the partition function and ν_i the frequency of the transition from the upper level of energy $E_{u,i}$, corresponding to the effective line strength $(\mu^2 S)_i$. Thus, the [CH_2DOH]/[CH_3OD] ratio can be derived directly from any line flux ratio using

$$\frac{N_1}{N_2} = \left(\frac{W_1}{W_2}\right) \frac{Z_1(T_{rot})\nu_2(\mu^2 S)_2}{Z_2(T_{rot})\nu_1(\mu^2 S)_1} \exp\left[\frac{E_{u,1} - E_{u,2}}{k_b T_{rot}}\right], \tag{8.2}$$

where Eqs. (1) and (2) refer respectively to CH_2DOH and CH_3OD. The rotational partition functions were computed within the rigid-rotor approximation, assuming that the rotational temperature is much higher than the largest rotational constant (here $A(CH_3OH)\sim$6 K). The corresponding expression for CH_3OH and CH_3OD, neglecting the energy difference between the A and E symmetry species, is simply twice the normal asymmetric rotor function

$$Z(T) = 2\sqrt{\frac{\pi}{ABC}\left(\frac{k_b T}{h}\right)^3}. \tag{8.3}$$

We thus obtain $Z(T)$=$1.23T^{3/2}$ for CH_3OH and $Z(T)$=$1.42T^{3/2}$ for CH_3OD. In the case of CH_2DOH, the energy difference between the e_0, e_1, and o_1 symmetry species cannot be neglected and the partition function is given by (Parise et al., 2004):

$$Z(T) = 0.75T^{3/2}\left[1 + \exp(-13.4/T) + \exp(-18.3/T)\right]. \tag{8.4}$$

Thus, the estimate of the abundance ratio depends on the assumed rotational temperature. In practice, however, this ratio was found to be essentially insensitive to rotational temperatures in the range 20−220 K. As the number of detected lines for the deuterated species is too small to get a reliable estimate of T_{rot} using the rotational diagram method, the rotational temperature was derived from the lines of the main isotopologue CH_3OH, assuming that the rotational temperature is similar for all three isotopologues. For each source, the rotational temperature and the CH_3OH column density are reported in Table 8.2.

Once the rotational temperature of methanol isotopologues is known, the [CH_2DOH]/[CH_3OD] ratio can be computed via two methods: *i)* total column densities of CH_2DOH and CH_3OD can be estimated from each of the detected lines using equation (8.1). The ratio of the averaged column densities provides a first measure of the [CH_2DOH]/[CH_3OD] ratio. This method however requires us to take into account the calibration uncertainty in each line, since data coming from both frequency ranges are used. The results are shown in column 7 of Table 8.2. *ii)* Using equation (8.2), we can obtain as many abundance ratios as there are pairs formed with CH_2DOH and CH_3OD lines. However, some of these pairs allow us to achieve a better precision than others. They have to satisfy two criteria: the upper levels must be close in energy and the lines must belong to the same frequency band to be able to ignore the calibration uncertainty. In practice, in our data, a single pair of lines satisfies both criteria and the ratios derived by this method are given in column 6 of Table 8.2. It is observed that both methods give essentially the same result, within the estimated uncertainties, suggesting the reliability of the derived ratios. These results clearly show that in the two observed intermediate-mass protostars, the [CH_2DOH]/[CH_3OD] ratio is larger than 3 and much higher than the ratios in high-mass protostars. For these latter, only upper limits of the ratio were derived because no line of CH_2DOH was detected. Implications of these results are discussed in detail below.

Table 8.2: Isotopologue ratios $[CH_2DOH]/[CH_3OD]$ in low-, intermediate- and high-mass protostars. The luminosities and distances of the sources are given, as well as the column densities ($\times 10^{15}$ cm^{-2}) and rotational temperatures of CH_3OH. References for luminosities and distances: [a] Parise et al. (2006); [b] Crimier et al. (2009, 2010a); [c] Robberto et al. (2005); [d] Bisschop et al. (2007); [e] Moscadelli et al. (2007).

Source	Luminosity ($L_\odot$)	Distance (pc)	$N_{tot}(CH_3OH)$	$T_{rot}(CH_3OH)$ (K)	$[CH_2DOH]/[CH_3OD]$	$<[CH_2DOH]>/<[CH_3OD]>$
IRAS 4A[a]	6	2.2×10^2	0.7 ± 0.1	38 ± 3		14^{+6}_{-4}
IRAS 4B[a]	6	2.2×10^2	0.8 ± 0.3	85 ± 17		26^{+9}_{-6}
IRAS 2[a]	16	2.2×10^2	1.1 ± 0.4	207 ± 48		> 5.5
IRAS 16293[a]	27	1.6×10^2	3.5 ± 0.4	85 ± 6		21^{+25}_{-9}
Cepheus E[b]	1×10^2	7.3×10^2	$0.5^{+0.8}_{-0.3}$	44 ± 31	20 ± 5	18 ± 5
OMC2FIR4[b]	1×10^3	4.4×10^2	$1.4^{+2}_{-0.8}$	48 ± 24	9 ± 3	8 ± 7
Orion IRc2[c]	5×10^3	4.5×10^2	84 ± 8.0	112 ± 11		$1.1 - 1.5$
W3(H2O)[d]	2×10^4	2×10^3	13^{+3}_{-2}	133 ± 17	< 0.9	
G24.78+0.08[e]	$\leq 7 \times 10^4$	7.7×10^3	9.3^{+7}_{-4}	113 ± 44	$< 1.4^*$	

Notes. The column $[CH_2DOH]/[CH_3OD]$ contains abundance ratios derived from the line pair 134.0655 GHz (for CH_2DOH) and 133.9254 GHz (for CH_3OD), which shows similar E_{up} ($\Delta E_{up} \sim 4.2$ K); the column $<[CH_2DOH]>/<[CH_3OD]>$) contains ratios derived from averaged column densities (see text). Data for low-mass protostars (IRAS 16293, IRAS 4a, IRAS 4b and IRAS 2) and Orion IRc2 were taken respectively from Parise et al. (2002, 2006) and Jacq et al. (1993), and references therein.
The asterisk refers to the uncertain identification of the CH_3OD line (133.9254 GHz) in G24.78+0.08.

8.4 Discussion and conclusions

In Fig. 8.2, we have plotted the $[CH_2DOH]/[CH_3OD]$ ratio as a function of the luminosity of the protostars for all the sources (except G24.78+0.08) where this ratio has been measured so far. In addition to the present observations, we have thus included a sample of low-mass protostars (Parise et al., 2006), as well as the hot-core Orion IRc2 (Jacq et al., 1993). Our results confirm that the $[CH_2DOH]/[CH_3OD]$ ratio is substantially lower in massive hot cores than in (low-mass) hot-corinos, by typically one order of magnitude. Furthermore, they suggest that intermediate-mass protostars have similar properties to low-mass protostars. We have also found that in all sources, the observed $[CH_2DOH]/[CH_3OD]$ ratio significantly differs from the value of 3 predicted by the grain chemistry models of Charnley et al. (1997) and Osamura et al. (2004). In low- and intermediate- mass protostars, this ratio is much greater than 3, while in high-mass protostars it is significantly lower. As a result, whatever the mass of the source, the observed gas-phase $[CH_2DOH]/[CH_3OD]$ ratio is inconsistent with the current theory of methanol deuteration in the grain mantles, that is via additions of H/D atoms on solid CO. Alternative or additional processes in solid-state and/or in the post-evaporative gas-phase must be at play in the hot cores/corinos. We now discuss the different possibilites based on theoretical and laboratory works.

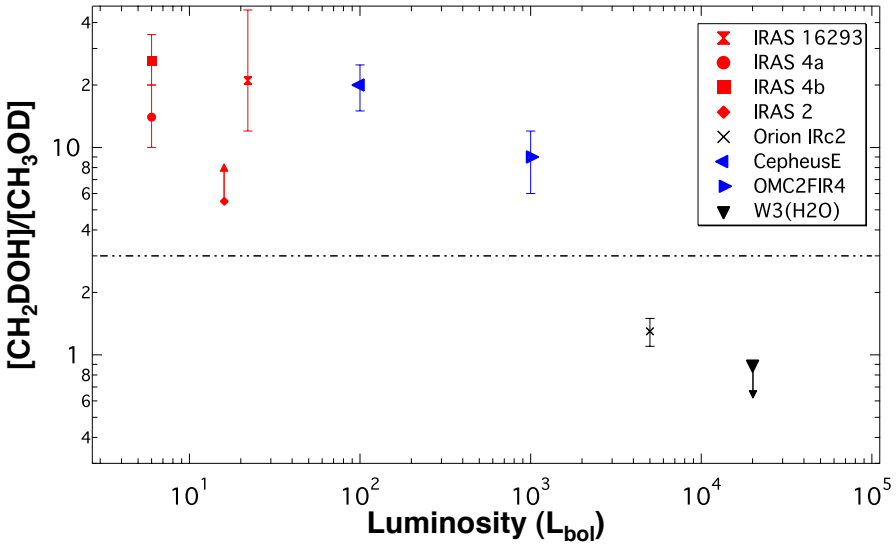

Figure 8.2: $[CH_2DOH]/[CH_3OD]$ ratio as a function of the protostar luminosity. Low-mass data (IRAS 16293, IRAS 4a, IRAS 4b and IRAS 2) were taken from Parise et al. (2006), while the data for Orion IRc2 is from Jacq et al. (1993). The upper limit reported in Table 1 for G24.78+0.08 is not plotted because of the uncertain identification of the CH_3OD line at 133.9254 GHz. The horizontal dashed line refers to the value predicted by grain chemistry models (Charnley et al., 1997).

For low- and intermediate-mass protostars, various mechanisms have been suggested to explain the much lower abundance of CH_3OD compared to CH_2DOH. First, CH_3OD could be selectively destroyed in the gas-phase via protonation reactions because the dissociative recombination (DR) of CH_2DOH^+ reforms CH_2DOH, while the DR of CH_3ODH^+ leads to both CH_3OD and CH_3OH (Charnley et al., 1997; Osamura et al., 2004). Second, laboratory experiments have suggested that H/D exchange reactions in solid state might contribute to reducing the CH_3OD abundance. Thus, in the experiment of Nagaoka et al. (2005), the deuterium enrichment was found to proceed via H/D substitution in solid CH_3OH leading to the formation of methyl-deuterated methanol isotopologues, but no CH_3OD. An alternative solid-state depletion mechanism was proposed by Ratajczak et al. (2009): in their experiment, rapid H/D exchanges between CD_3OD and H_2O ices were found to occur at T ∼120 K on the hydroxyl (-OD) functional

group of methanol, resulting in CD_3OH and HDO molecules.

All the previous mechanisms can thus *qualitatively* explain a much lower abundance of CH_3OD compared to CH_2DOH, as observed in low- and intermediate-mass protostars. The reverse behavior, as observed unambiguously in W3(H_2O) and Orion IRc2, is more difficult to understand. We note, however, that the gas temperature in massive hot cores may be significantly higher than in low- and intermediate-mass protostars, as suggested for example by the CH_3OH rotational temperatures reported in Table 8.2 (with the exception of the value measured in IRAS 2). Temperature effects might thus explain the difference in the measured $[CH_2DOH]/[CH_3OD]$ ratios. Following the pioneering work of Charnley et al. (1997), Osamura et al. (2004) investigated the impact of increasing the gas temperature from 50 to 100 K, using a hot core chemistry network. The $[CH_2DOH]/[CH_3OD]$ ratio was found to decrease from greater than 3 at 50 K to $\sim$1 at 100 K. This effect was attributed to the reaction between CH_3OH and H_2DO^+ (which is the major deuteron donor at 100 K)

$$H_2DO^+ + CH_3OH \rightarrow CH_3OHD^+ + H_2O, \tag{8.5}$$

followed by dissociative recombination. However, an unrealistically large initial abundance ratio $[HDO]/[H_2O]\sim0.1$ was necessary to decrease the $[CH_2DOH]/[CH_3OD]$ ratio below 3. Isomerization processes were finally proposed by Charnley et al. (1997) to explain the finding that $[CH_2DOH]\sim[CH_3OD]$ in Orion IRc2. The quantum calculations of Osamura et al. (2004) demonstrated, however, that internal rearrangements of energized methanol (in the neutral, ionized, or protonated forms) cannot occur efficiently.

We are thus compelled to conclude that the deuteration of methanol in massive hot cores, where the abundance of CH_2DOH is at most similar to that of CH_3OD, remains enigmatic. It is possibly related to the lower deuterium enrichment of massive protostars compared to low-mass sources (Ceccarelli et al., 2007). We also note that since the distances of the high-mass protostars are significantly larger than those of low- and intermediate-mass sources, the region probed by the observations is much larger in the high-mass objects. This may affect the measurements of the $[CH_2DOH]/[CH_3OD]$ ratio if the (large-scale) spatial distribution of both isotopologues is different. In any case, additional laboratory and theoretical studies are needed, in particular on H/D exchange processes in ices. A revision of the deuterium chemistry in hot cores also seems necessary. In this context, we note that Thi et al. (2010) demonstrated that a high $[HDO]/[H_2O]$ ratio ($> 10^{-2}$) can be obtained in dense ($n_H > 10^6$ cm^{-3}) and warm gas ($T = 100-1000$ K) owing to photodissociation and neutral-neutral reactions. In addition to modeling efforts, new observations are also crucial to assessing whether the methanol deuteration is peculiar or whether a similar selective deuteration affects other interstellar species with various functional groups, e.g. $HCOOCH_3$, $HCONH_2$, and CH_3NH_2. The detection of new multiply deuterated species (e.g. CH_2DOD) is also fundamental to helping us to discriminate between the different classes of fractionation/depletion processes.

Chapter 9

Water deuteration in low-mass protostars

Contents

Deutération de l'eau dans des étoiles de faible masse

Le rapport d'abondance [HDO]/[H_2O] est un paramètre clé pour sonder la formation de l'eau et son éventuelle évolution durant la formation des étoiles. Cependant, des valeurs précises de la deutération de l'eau ont été estimées vers une seule protoétoile de Classe 0 pour le moment: IRAS 16293-2422. Nous examinons la deutération de l'eau vers deux autres protoétoiles de faible masse, IRAS2A et IRAS4A, situées dans la région NGC1333, via des observations de la raie $4_{2,2} - 4_{2,3}$ de HDO à 143.727 GHz effectuées avec l'interférométre du Plateau de Bure.

L'émission de la raie de HDO n'est pas résolue avec le beam de l'interféromètre, et provient de la région compacte centrée sur les sources. Les comparaisons avec les observations interférométriques de $H_2^{18}O$ par Persson et al. (2012) suggérent clairement que HDO et H_2O proviennent majoritairement de la meme région. Une analyse LVG de l'émission de HDO et de $H_2^{18}O$ provenant de ce travail ainsi que d'autres observations publiées single-dish et interférométriques nous a permis montre que l'eau présente un rapport [HDO]/[H_2O] de 0.3 - 8 % dans IRAS2A et de 0.5 - 3 % dans IRAS4A. Ces valeurs sont similaires au fractionement mesuré dans IRAS 16293. En utilisant notre modele astrochimique GRAINOBLE, nous montrons que l'eau observée autour de ces deux protoétoiles de faible masse s'est formée pour des conditions typiques de nuage moléculaire, présentant des densités ($10^3 - 10^5$ cm^{-3}) et des températures (10 - 20 K) modérées.

Ce chapitre est tiré de la publication: **V. Taquet**, A. López-Sepulcre, C. Ceccarelli, R. Neri, C. Kahane 2012, *Arcsecond resolution observations of deuterated water towards low-mass protostars*, ApJL, soumis.

Abstract

The [HDO]/[H_2O] ratio is thought to be a key parameter to probe the formation of water and its eventual reprocessing during the formation of stars. However, accurate values of this ratio have been estimated towards one Class 0 protostar so far: IRAS 16293-2422. We investigate the deuteration of water towards two other low-mass protostars, IRAS2A and IRAS4A located in the NGC1333 region, via observations of the HDO $4_{2,2} - 4_{2,3}$ line at 143.727 GHz performed with the Plateau de Bure interferometer.

The emission of the HDO line is not resolved, and originates from the compact region centered on the sources. Comparison with interferometric observations of the $H_2^{18}O$ $3_{1,3} - 2_{2,0}$ line at 203 GHz by Persson et al. (2012) clearly suggests that HDO and H_2O mostly originate from the same region. LVG analysis of the HDO and $H_2^{18}O$ emissions combined with published single-dish and interferometric observations shows that water presents a [HDO]/[H_2O] ratio of 0.3-8 % in IRAS2A and 0.5-3 % in IRAS4A. These values are similar to the deuterium fractionation found in IRAS 16293. By using our astrochemical model GRAINOBLE, we show that water observed around these two low-mass protostars has been formed for typical molecular cloud conditions, with moderate densities ($10^3 - 10^5$ cm^{-3}) and temperatures (10 - 20 K).

This chapter is taken from the publication: **V. Taquet**, A. López-Sepulcre, C. Ceccarelli, R. Neri, C. Kahane, A. Coutens, C. Vastel 2012, *Arcsecond resolution observations of deuterated water towards low-mass protostars*, ApJL, submitted.

9.1 Introduction

Water is the main component of interstellar ices. As described in the first chapter, ices are formed in cold molecular clouds and prestellar cores and they likely desorb in the surroundings of low-mass protostars during the Class 0 phase. The formation pathways of water in the gas phase either by cold ion-neutral reactions or warm endothermic reactions are not sufficiently efficient to produce a high abundance of water in the quiescent envelopes of low-mass protostars. Most of the water observed around low-mass protostars should, therefore, has been formed in ices.

The deuterium fractionation of water can help us to probe its formation pathways on ices because of its sensitivity to the physical conditions. Unlike formaldehyde and methanol whose deuteration has been estimated in several low-mass protostars (see Parise et al., 2006), so far the water deuteration has been precisely constrained toward one protostar only. The main isotopologue (via $H_2^{18}O$) as well as its simply and doubly deuterated isotopologues have been observed several times toward IRAS 16293 via ground-based and space telescopes (Ceccarelli et al., 2000; Parise et al., 2005; Butner et al., 2007; Vastel et al., 2010; Coutens et al., 2012). The more recent work by Coutens et al. (2012) reports a [HDO]/[H_2O] ratio of ~ 3 % in the hot corino, ~ 0.5 % in the cold envelope, and ~ 5 % in the photodesorption layer of the foreground cloud. Observations of D_2O by Butner et al. (2007) and Vastel et al. (2010) give a D_2O/H_2O ratio of $\sim 10^{-3}$. Although these values are much higher than the cosmic elemental abundance of deuterium (1.5×10^{-5}, Linsky, 2003), water seems to be less deuterated than formaldehyde and methanol. Observations toward other protostars have given lower or upper limits. Jørgensen & van Dishoeck (2010) deduced a [HDO]/[H_2O] ratio lower than 0.04% in NGC1333-IRAS4B while Liu et al. (2011) gave a lower limit to the [HDO]/[H_2O] in the warm envelope of NGC1333-IRAS2A ($> 1\%$).

In this chapter, we present interferometric observations of the HDO $4_{2,2}$-$4_{2,3}$ line transition toward two Class 0 protostars: IRAS2A and IRAS4A performed with the Plateau de Bure interferometer. These sources are located in the Perseus complex, specifically in the NGC1333 cloud, whose distance is about 220 pc (Cernis, 1990). They were selected because they are

the two brightest protostars after IRAS 16293 due to their distance and their luminosity. In addition, their hot corinos have been already studied in details (see Maret et al., 2004; Bottinelli et al., 2004a, 2007) and interferometric observations of $H_2^{18}O$ have been recently performed by Persson et al. (2012) toward these two protostars. They, therefore, allowed us to estimate the [HDO]/[H_2O] ratio in their warm quiescent envelopes. Estimates of the [HDO]/[H_2O] ratio will be greatly valuable to constrain the formation of water ice because the deuteration of water around protostars likely reflects the deuteration of its icy precursor. Indeed, the timescale needed to alter significantly the deuteration after evaporation in the warm gas is longer than the typical age of Class 0 protostars ($\sim 10^5$ versus $\sim 10^4$ yr, Charnley et al., 1997; Andre et al., 2000).

9.2 Observations and results

The two low-mass Class 0 protostars NGC1333-IRAS2A and IRAS4A have been observed with the IRAM Plateau de Bure Interferometer on 2010 August 1, August 3 and 2011 March 10 in the C and D configurations of the array. The $4_{2,2}$ - $4_{2,3}$ HDO transition at 143.727 GHz and the 2 mm continuum emission have been obtained simultaneously using the WIDEX correlator, with a 1.8 GHz bandwidth centered at 143.5 GHz, and providing a spectral resolution of 1.95 MHz (4 km s^{-1}). Phase and amplitude were calibrated by performing regular observations of the nearby point sources 3C454.3, 3C84, and 0333+321. The amplitude calibration uncertainty is estimated to be $\sim 30\%$.

The data calibration and imaging were performed using the CLIC, and MAPPING packages of the GILDAS software[1]. Continuum images were produced by averaging line-free channels in the WIDEX correlator before the Fourier transformation of the data. The coordinates of the sources, and the size of the synthesized beams are reported in Table 9.1.

Table 9.1: Coordinates, synthesized beams, continuum fluxes, and sizes of the observed low-mass protostars.

Source	NGC1333 IRAS2A	NGC1333 IRAS4A
RA	03:28:55.56	03:29:10.45
Dec	31:14:37.05	31:13:31.18
Synthesized beam ($''$)	2.16 x 1.73	2.18 x 1.76
Continuum flux (Jy) [a]	0.13	1.08
Source size ($''$) [a]	1.75 x 1.69	2.13 x 1.72

Note. [a] Continuum fluxes and sizes are obtained from elliptical Gaussian fits in the (u,v) plane (i.e., deconvolved full width at half-maximum (FWHM) size).

Figure 9.1 shows the maps of the continuum emission at 2mm of NGC1333-IRAS2A and -IRAS4A obtained after natural weighted cleaning. Parameters of the continuum emission (flux and deconvolved FWHM size), obtained from elliptical Gaussian fits, are given in Table 1. The FWHM size of the continuum emission is very similar to the size of the synthesized beam. The continuum emission is, therefore, not resolved for the two sources. In particular, IRAS4A is known to be a binary system with a $1.8''$ separation (Looney et al., 2000), as depicted in Fig. 9.1. Although the continuum emission of IRAS4A is peaked at the southeast (SE) position rather than at the northwest (NW) position, we cannot distinguish the two structures.

Figure 9.1 shows the maps of the integrated HDO $4_{2,2}$ - $4_{2,3}$ line towards the two sources obtained after natural weighted cleaning. For both sources, the FWHM size of the HDO line is very similar to the size of the synthesized beam, as shown in Fig. 9.1. The emission clearly originates from compact regions, that are confined within the synthesized beam of the telescope.

[1]The GILDAS package is available at http://www.iram.fr/IRAMFR/GILDAS

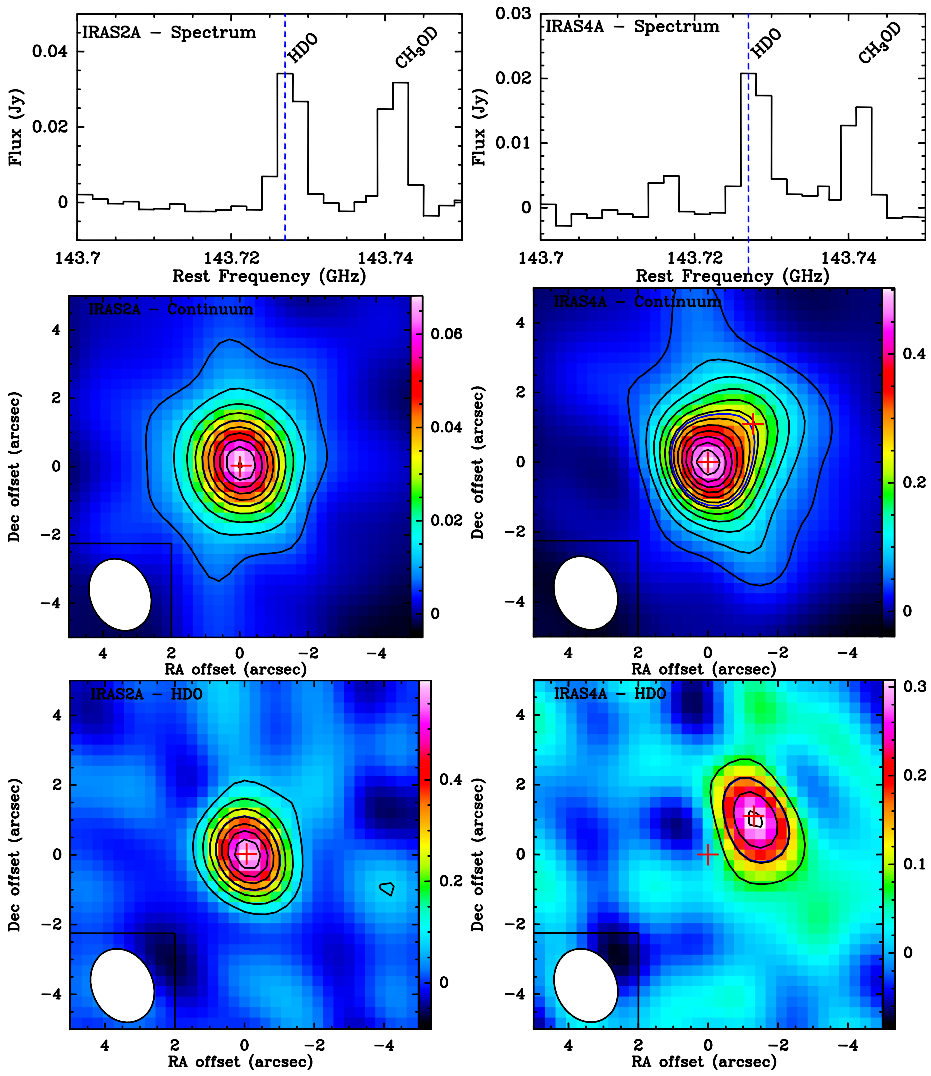

Figure 9.1: Maps and spectra towards IRAS2A (left) and IRAS4A (right). Upper panels: HDO spectra towards the two-low mass protostars integrated over the emission regions of the sources. The velocity resolution is 4 km s^{-1}. The V_{LSR} is assumed to be 7 km s^{-1} (dashed blue line). Middle panels: Continuum maps at 143 GHz in IRAS2A (with a rms of 1.7 mJy/beam, contour levels are in steps of 4 σ), and in IRAS4A (with a rms of 9.6 mJy/beam, contour levels are in steps of 4 σ). Blue contours depict the deconvolved full width at half-maximum size. Bottom panels: Line maps of HDO integrated over the $4_{2,2}$ - $4_{2,3}$ transition in IRAS2A (with a rms of 2.9 mJy/beam km s^{-1}, contour levels are in steps of 3 σ) and in IRAS4A (with a rms of 2.8 mJy/beam km s^{-1}, contour levels are in steps of 3 σ). Green contours depict the region showing a flux at half maximum of the line peak. The red crosses mark the source positions measured by Looney et al. (2000). The bottom-left ellipses represent the beam sizes.

In particular, although the SE position of IRAS4A is the brightest in the continuum, the HDO line emission comes from the NW position. The spectra of the HDO transition integrated within the FWHM size are shown in Fig. 9.1 assuming $V_{LSR} = 7$ km s^{-1} for the two sources. Table 9.2 gives the flux and the brightness temperature of the HDO line transition integrated inside the FWHM size.

Table 9.2: Parameters of the HDO and $H_2^{18}O$ lines observed towards IRAS2A and IRAS4A.

Transition	Frequency (GHz)	E_{up} (K)	A_{ij} (s^{-1})	Flux (Jy km s^{-1})	$(\int T_B dv)_{obs}$ (K km s^{-1})	Beam ($''$)	Δv (km s^{-1})	Ref.
				NGC1333 IRAS2A				
HDO $4_{2,2}$ - $4_{2,3}$	143.727	319.2	3.5×10^{-6}	0.43	6.8 ± 1.4	2.2 x 1.8	7	1
HDO $1_{1,0}$-$1_{1,1}$	80.578	46.8	1.3×10^{-6}	0.37	0.07 ± 0.02	31.2	3.9	2
HDO $2_{1,1}$-$2_{1,2}$	241.561	95.3	1.2×10^{-5}	2.2	0.43 ± 0.05	10.4	4.1	2
HDO $3_{1,2}$-$2_{2,1}$	225.896	167.7	1.3×10^{-5}	2.6	0.50 ± 0.03	11.1	4.2	2
$H_2^{18}O$ $3_{1,3} - 2_{2,0}$	203.408	203.7	4.8×10^{-6}	0.98	46 ± 9	0.9 x 0.7	4.0	3
				NGC1333 IRAS4A				
HDO $4_{2,2}$ - $4_{2,3}$	143.727	319.2	3.5×10^{-6}	0.21	3.2 ± 0.6	2.2 x 1.8	6	1
$H_2^{18}O$ $3_{1,3} - 2_{2,0}$	203.408	203.7	4.8×10^{-6}	0.27	13 ± 3	0.9 x 0.7	2.9	3

References. 1: This work, 2: Liu et al. (2011), 3: Persson et al. (2012).

Comparison with maps of the $H_2^{18}O$ $3_{1,3}$-$2_{2,0}$ line transition by Persson et al. (2012) shows that most of the HDO and H_2O emissions originate from the same region, although our beam is two times larger. In IRAS2A, even if the bulk of the $H_2^{18}O$ emission is associated with the central warm envelope, an outflow component towards southwest is also observed (see Fig. 2 of Persson et al., 2012) whereas the HDO line only originates from the compact envelope located within the synthesized beam. Persson et al. (2012) estimated the FWHM size of the $H_2^{18}O$ emission, from Gaussian fit in the (u, v) plane, and they found that most of the emission originates from a $0.8''$ ellipse, similar to their synthesized beam. Observational data (flux, brightness temperature) derived by Persson et al. (2012) is given in Table 9.2. Our maps are in good agreement with previous single-dish observations of IRAS2A which have shown that H_2O also traces the outflow whereas HDO only traces the central envelope. Using the *Herschel Space Telescope*, Kristensen et al. (2010) observed a broad outflow component for the 987 GHz H_2O line. However, Liu et al. (2011) were able to fit the observed HDO line observed with ground-based facilities by assuming a jump profile for the HDO abundance in a spherical quiescent envelope. For IRAS4A, the HDO and $H_2^{18}O$ emissions come from the same NW position and their FWHM sizes are similar to the respective synthesized beams suggesting that the emission originates from the central protostellar region. Therefore, it is meaningful to compare the flux of the HDO and $H_2^{18}O$ lines originating from the FWHM regions, similar to the synthesized beams. The fluxes are given in Table 9.2 and are used in the next section to deduce the [HDO]/[H_2O] ratio.

9.3 Deuterium fractionation of water

9.3.1 Presentation of the LVG analysis

A single transition line of HDO and $H_2^{18}O$ does not allow us to deduce an accurate estimate of the HDO and H_2O column densities towards the two protostars and, therefore, of the [HDO]/[H_2O] abundance ratio. In order to derive the physical conditions of the line emitting gas and the relevant column densities, we used a non-LTE LVG code (Ceccarelli et al., 2003) using our observations and the observations by Liu et al. (2011) of HDO lines towards IRAS2A carried out with the IRAM 30m, JCMT, and APEX telescopes. We considered the collisional coefficients

from Faure et al. (2007) and Daniel et al. (2011) for $H_2^{18}O$ and from Faure et al. (2012) for HDO, respectively. The Einsten coefficients are from the Jet Propulsion Laboratory molecular database (Pickett et al., 1998).

We ran a grid of models covering a large parameter space in kinetic temperature (15 values from 70 to 220 K), density (15 values from 1×10^6 to 1×10^9 cm^{-3}), column density (15 values from 8×10^{14} to 1×10^{17} cm^{-2}), and source size (30 values from 0.1 to 200 arcsec). In addition, we considered three values for the ortho to para ratio (opr) of H_2: 10^{-2} (namely all H_2 molecules are in the para state), 1, and 3 (namely most of the H_2 molecules are in the ortho state). To find the best fit to the data, we excluded the 464 GHz line observed by Liu et al. (2011) as it may be contaminated by the cold envelope emission given its low energy level (22 K).

9.3.2 Results

We ran the grid of models to reproduce the emission of the HDO lines towards IRAS2A only. The H_2 ortho/para ratio has a low influence on the column densities deduced from the observations. The variation of the opr(H_2) between 0.1 and 3 induces a small variation of the results not more than 20%, namely within the incertitudes of the observations. In the following, we consider an opr(H_2) of 3. We are able to reproduce the flux of all the HDO lines, with a reduced χ^2 lower than 0.5, for a kinetic temperature of 75-80 K, a source size of 0.4 $''$, and a wide range of total densities $n_{\rm H}$ between 6×10^5 and 10^8 cm^{-3}. The deduced HDO column density, N(HDO), varies between 5×10^{17} and 1^{19} cm^{-2} and decreases with $n_{\rm H}$. To evaluate the [HDO/[H_2O] ratio, we consider three physical cases that reproduce the emission of the HDO lines. Table 9.3 lists the parameter values obtained with each solution. The total density used in Case 1 (6×10^5 cm^{-3}) is similar to the density used by Maret et al. (2004) for reproducing the H_2CO emission with a similar LVG analysis. The densities used in Cases 2 and 3 are slightly lower than the density found in the hot corino following the density profile of IRAS2A derived by Jørgensen et al. (2002).

Using the same three physical cases as for HDO, we are able to reproduce the emission flux of the $H_2^{18}O$ line at 203 GHz using the column density given in Table 9.3. Regardless of the density, the deduced column density of $H_2^{18}O$ is equal to $6 - 7 \times 10^{16}$ cm^{-2}. Note that at $n_{\rm H} = 6 \times 10^5$ cm$^{[}-3|$, the line weakly masers (see also Neufeld & Melnick, 1991). These values are slightly higher, by a factor of two, than the column density deduced by Persson et al. (2012) who used a LTE model by assuming an optically thin emission but with a higher excitation temperature than the value derived in this work. The column density of the main water isotope H_2O can then be deduced by assuming an isotopic abundance ratio $^{16}O/^{18}O$ of 560 (Wilson & Rood, 1994) and an ortho/para ratio of 3 (see Emprechtinger et al., 2010). Depending on $n_{\rm H}$, we deduce an [HDO]/[H_2O] abundance ratio between 0.3 and 8 % (see Table 9.3.

For IRAS4A, no other HDO lines but the line observed in this work is available. The flux of the HDO and $H_2^{18}O$ lines are, therefore, predicted by using the same set of physical conditions as for IRAS2A. Another set of parameters presenting a higher source size θ_s of 0.8$''$, consistent with the upper limit given by Persson et al. (2012) for the $H_2^{18}O$ transition, is also used. The increase in θ_s decreases the column density of HDO and $H_2^{18}O$ by approximately the same factor (2-3). θ_s does not influence significantly the water fractionation since the [HDO]/[H_2O] ratio decreases by a factor of two, at maximum. For both sets of physical conditions, we predict an [HDO]/[H_2O] abundance ratio between 0.5 and 3 %.

9.4 Discussion and conclusions

The deuterium fractionation of water deduced in this work is found to be around 1 % in IRAS2A and IRAS4A. The value of 0.3-8 % in IRAS2A is compatible with the water fractionation found

Table 9.3: LVG best fit parameters for HDO and $H_2^{18}O$ emissions.

Case	1	2	3
Density (cm^{-3})	6×10^5	2×10^7	1×10^8
IRAS2A ($T = 80$ K, $\theta_s = 0.4\,''$)			
N(HDO) (cm^{-2})	1×10^{19}	1×10^{18}	6×10^{17}
τ(HDO)	23	2	1
N(p-$H_2^{18}O$) (cm^{-2})	6×10^{16}	7×10^{16}	7×10^{16}
τ(p-$H_2^{18}O$)	-0.4	0.8	1.5
$N(H_2O)$ (cm^{-2})	1.3×10^{20}	1.6×10^{20}	1.6×10^{20}
HDO/H_2O	0.08	0.006	0.003
IRAS4A			
	$\theta_s = 0.4\,''$		
N(HDO) (cm^{-2})	1.5×10^{18}	3×10^{17}	2×10^{17}
τ(HDO)	3	0.8	0.4
N(p-$H_2^{18}O$) (cm^{-2})	2.5×10^{16}	1.5×10^{16}	1.5×10^{16}
τ(p-$H_2^{18}O$)	-0.4	0.05	0.15
$N(H_2O)$ (cm^{-2})	5×10^{19}	3×10^{19}	3×10^{19}
HDO/H_2O	0.03	0.01	0.007
	$\theta_s = 0.8\,''$		
N(HDO) (cm^{-2})	5×10^{17}	1×10^{17}	6×10^6
τ(HDO)	0.8	0.3	0.2
N(p-$H_2^{18}O$) (cm^{-2})	1.5×10^{16}	6×10^{15}	5.5×10^{15}
τ(p-$H_2^{18}O$)	-0.2	-0.02	0.08
$N(H_2O)$ (cm^{-2})	3×10^{19}	1.3×10^{19}	1.3×10^{19}
HDO/H_2O	0.016	0.008	0.005

by Liu et al. (2011) in the warm envelope of IRAS2A ([HDO]/[H_2O] > 1%) from single-dish observations. The deuteration of water and other molecules has been evaluated towards a sample of a few low-mass protostars. Figure 9.2 summarizes the deuteration of water, formaldehyde, and methanol (three main constituents of interstellar ices) observed towards a protostellar shock (L1157-B1), the protostellar prototype IRAS 16293, the two protostars observed in this work, IRAS2A and IRAS4A, as well as the protostar IRAS4B, located in the NGC1333 region, $\sim 15\,''$away from IRAS4A (Sandell et al., 1991). The deuterium fractionation found in IRAS2A and IRAS4A appears to be similar to the fractionation in IRAS 16293 where the [HDO]/[H_2O] ratio is 3 % according to Coutens et al. (2012). We used the value deduced by Coutens et al. (2012) instead of that derived in the recent work by Persson et al. (2013) because Persson et al. (2013) deduced the [HDO]/[H_2O] ratio by assuming LTE conditions from tentatively detected lines showing a low signal/noise ratio. The same tendency is observed for formaldehyde and methanol whose fractionations are slightly higer in IRAS2A and IRAS4A than in IRAS 16293 and IRAS4B but their differences remain within the uncertainties. However, our values present a surprising discrepancy, by at least one order of magnitude, with the low [HDO]/[H_2O] ratio estimated by Jørgensen & van Dishoeck (2010) in IRAS4B ($< 6 \times 10^{-4}$).

As first proposed by Roberts & Millar (2000) and Roberts et al. (2003), the deuteration of gaseous species increases with the density n_H because i) the decrease of the electronic abundance with n_H tends to increase the H_3^+ isotopologues with respect to H_3^+, ii) the CO depletion is more efficient at high densities, increasing the efficiency of the deuteration reactions. Hydrogenated species of interstellar ices are mainly formed via addition reactions involving atomic H and D. Their fractionation, therefore, tends to increase with n_H. In our previous papers (Taquet et al., 2012b,c), we have investigated the influence of various parameters on the ice deuteration with

our astrochemical model GRAINOBLE. Fig. 9.2 shows the predicted deuterium fractionations of water, formaldehyde, and methanol for different densities and temperatures computed with this model. Comparison between these observations and the theoretical predictions shows that the [HDO]/[H_2O] ratio derived in IRAS2A and IRAS4A is reproduced for moderated densities $n_H \sim 10^3 - 10^5$ cm^{-3} depending on the temperature. Although subsequent processes might affect the [HDO]/[H_2O] ratio (partial ice desorption, warm gas phase reactions), this comparison suggests that water observed in IRAS2A and IRAS4A should have been formed on grain surfaces for typical molecular cloud conditions, before formaldehyde and methanol which may have been formed later, during the prestellar core phase.

NGC1333 is a very active star-forming region undergoing the compression by various outflows coming from first-generation stars (Liseau et al., 1988; Warin et al., 1996; Lefloch et al., 1998; Knee & Sandell, 2000) whereas ρ-Ophiucus, containing IRAS 16293, is a more quiescent cloud (Mizuno et al., 1990) . Neverthless, the similar deuterium fractionation derived in IRAS2A, IRAS4A, and IRAS 16293 suggest that these protostars have followed a similar chemical history although they are located in very different environments.

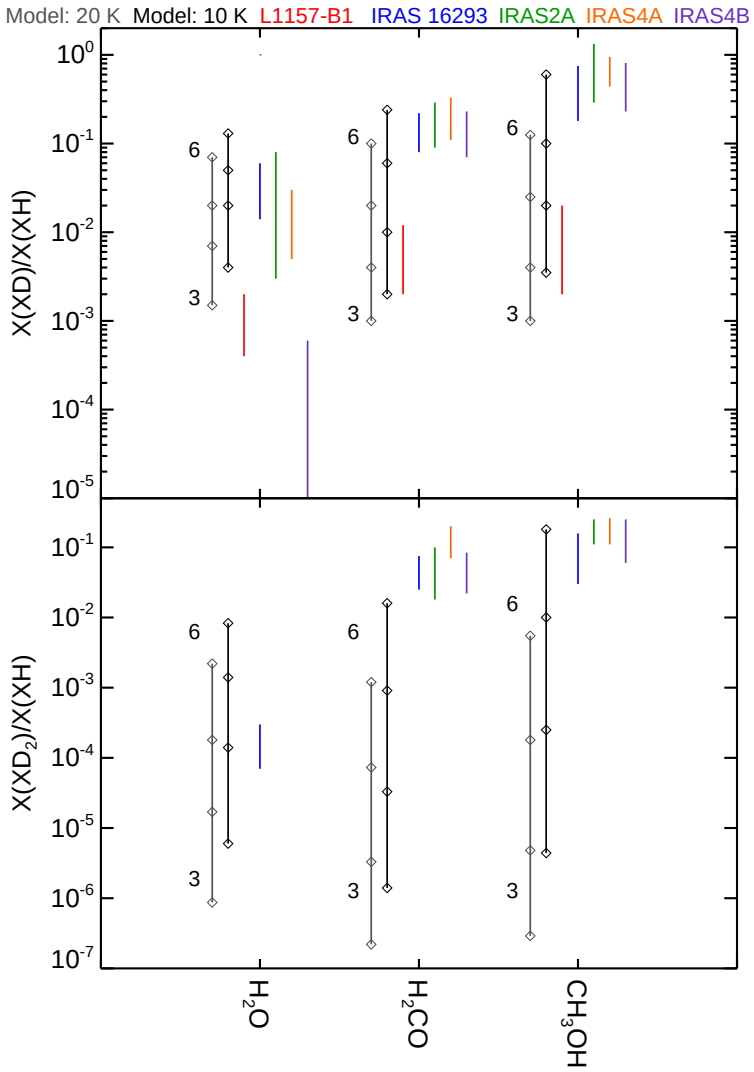

Figure 9.2: Deuterium fractionation of water, formaldehyde, methanol of simply (top) and doubly (bottom) deuterated species. and From left to right: deuterium fractionation computed by our astrochemical model (Taquet et al., 2012b,c) at 20 K (grey) and 10 K (black), and observed towards L1157-B1 (red, from Codella et al., 2012), IRAS 16293 (blue, from Loinard et al., 2001; Parise et al., 2002, 2004; Vastel et al., 2010; Coutens et al., 2012), IRAS2A (green, from this work, for water, and Parise et al., 2006, for formaldehyde and methanol), IRAS4A (green, from this work, for water, and Parise et al., 2006, for formaldehyde and methanol), and IRAS4B (purple, from Parise et al., 2006; Jørgensen & van Dishoeck, 2010).

Chapter 10

Detection of complex organic molecules in a prestellar core

Contents

Détection de molécules organiques complexes dans un coeur prestellaire

Les molécules organiques complexes (COMs) ont été détectées depuis plusieurs décennies dans le milieu interstellaire, and plus particulièrement dans les coeurs chauds des étoiles massives et de faible masse. Leurs mécanismes de formation demeurent néanmoins incertains. La chimie tiède en phase gazeuse ou à la surface des grains a été invoquée pour expliquer leur présence autour des protoétoiles de faible masse. Dans ce dernier scénario, les COMs proviennent de réactions entre radicaux sur les grains lorsque ceux-ci deviennent mobiles durant le réchauffement de l'enveloppe par la protoétoile. Les molécules formées sont évaporées par la suite en phase gazeuse à plus hautes températures.

Les coeurs prestellares sont les précurseurs directes des protoétoiles de faible masse et offrent une opportunité unique d'étudier la formation des COMs avant la phase de réchauffement. Leur faible température (< 10 K) et l'absence de source de chauffage ou de jets protostellaires excluent tout type de chimie tiède en phase gazeuse ou sur les grains. La présence de COMs dans les coeurs prestellaires proviendrait donc de processus chimiques non thermiques.

Nous avons utilisé le télescope 30m de l'IRAM pour rechercher quatre molécules organiques complexes oxygénées (acetaldehyde CH_3CHO, dimethyl ether CH_3OCH_3, formate de methyle CH_3OCHO, et ketene CH_2CO) dans le coeur prestellar L1689B. Nous reportons la détection des quatre molécules dans le gaz froid de L1689B sans aucune ambiguité. Ces détections appuyent le role joué par certains processus non-thermiques (probablement photolytiques) impliqués dans la formation et la désorption de ces COMs. Les données montrent sans équivoque que la synthèse de COMs a déjà commencé durant la phase prestellaire et suggèrent qu'une part de ces COMs détectées dans les hot corinos ont une origine prestellaire.

Ce chapitre est tiré de la publication: : A. Bacmann, **V. Taquet**, A. Faure, C. Kahane, C. Ceccarelli 2012, *Detection of complex organic molecules in a prestellar core: a new challenge for astrochemical models*, A&A, 541, L12.

Abstract

Complex organic molecules (COMs) have long been detected in the interstellar medium, especially in hot cores and in the hot corinos of low-mass protostars. Their formation routes however remain uncertain. Both warm gas-phase reactions and warm grain-surface reactions have been invoked to account for their presence in low-mass protostars. In this latter scheme, COMs result from radical-radical reactions on the grains as radicals become mobile when the nascent protostar warms up its surroundings and the resulting molecules are subsequently desorbed into the gas phase at higher temperatures.

Prestellar cores are the direct precursors of low-mass protostars and offer a unique opportunity to study the formation of COMs before the warm-up phase. Their very low temperatures (≤ 10 K) and the absence of any heating source or outflow exclude any efficient warm gas phase or warm dust chemistry, so that the presence of COMs in prestellar cores would have to originate from non-thermal chemical processes.

We used the IRAM 30 m telescope to look for four O-bearing complex organic molecules (acetaldehyde CH_3CHO, dimethyl ether CH_3OCH_3, methyl formate CH_3OCHO, and ketene CH_2CO) in the prestellar core L1689B. We report the unambiguous detection of all four molecules in the cold gas phase of L1689B. These detections support the role played by non-thermal (possibly photolytic) processes in COM formation and desorption. The data show univocally that COM synthesis has already started at the prestellar stage and suggests at least part of the COMs detected in hot corinos have a prestellar origin.

This chapter is taken from the publication: A. Bacmann, **V. Taquet**, A. Faure, C. Kahane, C. Ceccarelli 2012, *Detection of complex organic molecules in a prestellar core: a new challenge for astrochemical models*, A&A, 541, L12.

10.1 Introduction

Complex organic molecules (COMs) have long been detected in the hot cores of massive star-forming regions such as Sgr B2 (Cummins et al., 1986) or OMC-1 (Blake et al., 1987). The warm central regions of low-mass protostars have been shown to harbour the same organic molecules (van Dishoeck et al., 1995; Cazaux et al., 2003), which led them to be called "hot corinos" (Bottinelli et al., 2004a). In these regions, O- and N- bearing species like methyl formate (CH_3OCHO), dimethyl ether (CH_3OCH_3) or acetonitrile (CH_3CN) are abundant, so that these molecules have been designated as "hot core tracers". The mechanisms leading to COM formation in star forming regions are however still debated. COMs were first thought to be the result of warm gas-phase chemistry between ice mantle constituents, sometimes called primary species or parent molecules, which are evaporated in the gas phase in the vicinity of the nascent protostar (Charnley et al., 1992). In this scheme, primary molecules are formed on the grain ice mantles via successive hydrogenation of atoms or simple molecules like CO. When they are injected into the gas phase via thermal desorption, they can react and form secondary species like, e.g., CH_3OCHO. The gas-phase scenario has been however challenged by experimental results showing that gas-phase formation pathways were much less efficient than originally thought (Horn et al., 2004, for methyl formate). Alternative scenarios have been proposed in which radicals are formed by ultraviolet (UV) irradiation of grain mantle molecules (e.g., Garrod & Herbst, 2006) or trapped within the bulk of ice mantles of dust grains (Taquet et al., 2012a, chapter 5 of this thesis). Following Garrod & Herbst (2006), the radicals can react on the grain mantles once the protostar starts heating its immediate surroundings and the grains reach a temperature of around 30–40 K, and form complex species on the grain, before they are being desorbed and released into the gas phase. Laboratory experiments however have shown the possibility to synthesize COMs such as methyl formate by irradiation (with UV photons

or energetic particles) of methanol ices at temperatures as low as 10 K (Gerakines et al., 1996; Bennett & Kaiser, 2007).

In contrast to warm star-forming regions such as hot cores or hot corinos, little research has been carried out to investigate the contents of cold gas. Studies of the dark cloud TMC-1 have revealed the presence of acetaldehyde (Matthews et al., 1985), ketene (Irvine et al., 1989), and methanol (Friberg et al., 1988). Evidence of COMs in prestellar cores is similarly scarce: Matthews et al. (1985) reported the detection of acetaldehyde in L183 (L134N), but searches for dimethyl ether (Friberg et al., 1988), ketene (Irvine et al., 1989) and methyl formate (Requena-Torres et al., 2007) only yielded upper limits. Despite their very low temperatures ($\sim$ 10 K), prestellar cores are however an important piece of the puzzle, as they represent the stage immediately before the gravitational collapse leading to protostar formation. They thus offer the opportunity to study the initial conditions of the star formation process. The relative simplicity of their structure (shallow temperature gradients, absence of inner heating source, absence of shocks or outflows, environment shielded from external radiation fields) makes them ideal targets to study chemical processes in cold gas at the very early stages of star formation.

We present here the first detection of the COMs dimethyl ether and methyl formate in a prestellar core, as well as the detection of the two other COMs acetaldehyde and ketene, in the gas phase at a temperature of $\sim$ 10 K.

10.2 Observations

The target of our observation is the prestellar core L1689B. This source is a typical core characterised by low dust temperatures around 11$-$12 K (Kirk et al., 2007), high central densities of 10^5-10^6 cm^{-2}, and a high central column density of $\sim 10^{23}$ cm^{-2} (Bacmann et al., 2000; Dapp & Basu, 2009). It was selected based on the assumption that the gas-phase abundances of C-bearing molecules such as formaldehyde (Bacmann et al., 2003) or methanol (Bacmann et al., in prep) were relatively large with respect to other cores. Therefore, it can be hypothesised that complex organic molecules are more likely to be detected in this object than in more depleted ones.

Observations were carried out in March 2011 at the IRAM 30 m telescope. We used the E090 receiver tuned to a frequency of 99.325 GHz (close to low energy transitions of CH_3OCH_3) to which we connected both the high resolution autocorrelator VESPA and the low resolution Fourier Transform Spectrometer (FTS). The spectral resolution and bandwidth of VESPA were 20 kHz (corresponding to a velocity resolution of $\sim$ 0.06 km/s) and 100 MHz, respectively. The FTS covered the whole 4 GHz receiver band (from 97.6 to 101.6 GHz in this case) with a spectral resolution of 192 kHz, corresponding to a velocity resolution of $\sim$ 0.6 km/s. The observations were carried out in the frequency switching mode with a frequency switch of 7.5 MHz to reduce standing waves. Pointing was checked every two hours on a nearby quasar and was found to be accurate to within 1 $''$. The weather conditions were very good and system temperatures were typically 100$-$120 K despite the low elevation of the source. We integrated on the dust peak of the core L1689B, at $\alpha_{2000} = 16^{\rm h}34^{\rm m}48\overset{\rm s}{.}30, \delta_{2000} = -24°38'04.0''$. The size of the telescope beam at the observing frequency was $\sim 25''$, and the forward and beam efficiencies were $\eta_{\rm fwd} = 0.95$ and $\eta_{\rm beam} = 0.80$, respectively.

The data were reduced using the IRAM CLASS/GILDAS package[1]. The scans were coadded, deconvolved from the frequency switching procedure, and a low order (typically 3) polynomial was then fitted over line-free regions to correct for baseline oscillations. The spectra were converted from T_a^* to the $T_{\rm mb}$ scale, using the values of the efficiencies given above.

[1] http://www.iram.fr/IRAMFR/GILDAS

Table 10.1: Parameters of detected lines. The frequencies, upper energy levels, upper level degeneracies and Einstein coefficients of the observed transitions were taken from the JPL spectroscopic database.

Species	Transition	Frequency (MHz)	$E_{\rm up}$ (K)	$g_{\rm up}$	$A_{\rm ul}$ (s−1)
AA-CH_3OCH_3	$4_{14} - 3_{03}$	99326.072	10.2	90	$5.533\ 10^{-6}$
EE-CH_3OCH_3	$4_{14} - 3_{03}$	99325.217	10.2	144	$5.533\ 10^{-6}$
EA-CH_3OCH_3	$4_{14} - 3_{03}$	99324.362	10.2	36	$5.533\ 10^{-6}$
AE-CH_3OCH_3	$4_{14} - 3_{03}$	99324.364	10.2	54	$5.533\ 10^{-6}$
E-CH_3CHO	$5_{14} - 4_{13}$	98863.328	16.6	22	$3.104\ 10^{-5}$
A-CH_3CHO	$5_{14} - 4_{13}$	98900.948	16.5	22	$3.108\ 10^{-5}$
A-CH_3OCHO	$8_{17} - 7_{16}$	100490.682	22.8	34	$1.435\ 10^{-5}$
E-CH_3OCHO	$8_{17} - 7_{16}$	100482.241	22.8	34	$1.434\ 10^{-5}$
A-CH_3OCHO	$9_{09} - 8_{08}$	100683.368	24.9	38	$1.472\ 10^{-5}$
E-CH_3OCHO	$9_{09} - 8_{08}$	100681.545	24.9	38	$1.472\ 10^{-5}$
A-CH_3OCHO	$9_{19} - 8_{18}$	100080.542	25.0	38	$1.444\ 10^{-5}$
E-CH_3OCHO	$9_{19} - 8_{18}$	100078.608	25.0	38	$1.444\ 10^{-5}$
o-CH_2CO	$5_{15} - 4_{14}$	100094.514	27.5	33	$1.031\ 10^{-5}$
p-CH_2CO	$5_{05} - 4_{04}$	101036.630	14.6	11	$1.104\ 10^{-5}$

10.3 Results

The high spectral resolution spectrum obtained close to 99.325 GHz is shown in Fig.10.1. The *rms* noise in the spectra is ~ 7 mK. The frequencies and spectroscopic parameters of the detected species are listed in Table 10.1. Three spectral lines are clearly detected (to the $7-12\,\sigma$ level), corresponding to the $4_{14} - 3_{03}$ transitions of the four symmetry substates (AA-, EE-, AE-, and EA-) of CH_3OCH_3. The EA- and AE- transitions are only 2 kHz apart and therefore are indistinguishable in our spectrum. The lines are very narrow, $\simeq 0.4$ km/s wide, as expected for lines originating from cold gas at around 10 K. These spectra show the unambiguous presence in the cold gas of dimethyl ether, which is detected for the first time in a cold dark core.

The low-resolution spectrum covers the 97.6 GHz to 101.6 GHz region. Within this bandwidth, we also detect six lines of CH_3OCHO (three lines of the A- and three lines of the E-substates), which had so far never been detected in a prestellar core. In addition, two lines of CH_2CO (one ortho line and one para line) and two lines of CH_3CHO (one of the A- and one of the E-substates) were also detected. Figures 10.2, 10.3, and 10.4 present the spectra of CH_3OCHO, CH_3CHO, and CH_2CO, respectively. Again, the detection of more than one line of each species at the measured catalog frequencies (see figures) is clear evidence of these three species in the gas phase of L1689B.

Table 10.2: Line fluxes[a] and column densities.

Species	Transition	$T_{\rm mb}$ (mK)	rms (mK)	Integrated area (K km/s)	Column density[c] ($\rm cm^{-2}$) $T_{\rm ex} = 5\,\rm K$	Column density[c] ($\rm cm^{-2}$) $T_{\rm ex} = 4\,\rm K$	Column density[c] ($\rm cm^{-2}$) $T_{\rm ex} = 8\,\rm K$
AA-CH_3OCH_3	$4_{14} - 3_{03}$	55	7	0.026 ± 0.005	(3.32 ± 0.74) 10^{12}	(5.08 ± 1.12) 10^{12}	(2.49 ± 0.55) 10^{12}
EE-CH_3OCH_3	$4_{14} - 3_{03}$	90	7	0.037 ± 0.005	(6.81 ± 0.92) 10^{12}	(10.4 ± 1.40) 10^{12}	(5.11 ± 0.69) 10^{12}
EA-CH_3OCH_3	$4_{14} - 3_{03}$	36[b]	7	0.014 ± 0.003	(1.65 ± 0.55) 10^{12}	(2.53 ± 0.84) 10^{12}	(1.24 ± 0.41) 10^{12}
AE-CH_3OCH_3	$4_{14} - 3_{03}$	22[b]	7	0.009 ± 0.003	(1.67 ± 0.37) 10^{12}	(2.55 ± 0.56) 10^{12}	(1.25 ± 0.28) 10^{12}
E-CH_3CHO	$5_{14} - 4_{13}$	125	3	0.149 ± 0.015	(9.12 ± 0.92) 10^{12}	(2.67 ± 0.27) 10^{13}	(2.12 ± 0.21) 10^{12}
A-CH_3CHO	$5_{14} - 4_{13}$	110	4	0.137 ± 0.014	(8.26 ± 0.84) 10^{12}	(1.73 ± 0.18) 10^{13}	(3.86 ± 0.39) 10^{12}
A-CH_3OCHO	$8_{17} - 7_{16}$	20	3	0.025 ± 0.005	(2.01 ± 0.40) 10^{13}	(5.73 ± 1.15) 10^{13}	(5.91 ± 1.18) 10^{12}
A-CH_3OCHO	$9_{09} - 8_{08}$	12	2	0.016 ± 0.005	(1.73 ± 0.54) 10^{13}	(5.50 ± 1.71) 10^{13}	(4.33 ± 1.35) 10^{12}
E-CH_3OCHO	$8_{17} - 7_{16}$	19	3	0.024 ± 0.005	(1.90 ± 0.40) 10^{13}	(5.44 ± 1.15) 10^{13}	(5.59 ± 1.18)10^{12}
E-CH_3OCHO	$9_{09} - 8_{08}$	12	2	0.016 ± 0.003	(1.72 ± 0.32) 10^{13}	(5.47 ± 1.03) 10^{13}	(4.32 ± 0.81) 10^{12}
o-CH_2CO	$5_{15} - 4_{14}$	140	3	0.171 ± 0.018	(1.50 ± 0.16) 10^{13}	(3.09 ± 0.33) 10^{13}	(6.75 ± 0.71) 10^{12}
p-CH_2CO	$5_{05} - 4_{04}$	82	2	0.096 ± 0.010	(4.54 ± 0.47) 10^{12}	(9.64 ± 1.00) 10^{12}	(1.95 ± 0.20) 10^{12}

[a] The fluxes were derived by fitting Gaussians to the lines using the dedicated CLASS routine. The uncertainty was calculated as $\sqrt{\sigma_{\rm stat} + \sigma_{\rm cal}}$, where $\sigma_{\rm stat}$ is the statistical uncertainty in the Gaussian fit (given by the CLASS routine) and $\sigma_{\rm cal}$ is the calibration uncertainty taken as 10%.

[b] Both EA- and AE- CH_3OCH_3 lines are so close in frequency that they are indistinguishable in our spectra. In the table, we assume that the ratio of their intensities was equal to the ratio of their upper level degeneracy because the transitions have nearly equal frequencies, Einstein coefficients, and equal level energies. This hypothesis is supported by it also applying to the EE- and AA- transitions (the ratio of their respective intensities is consistent with the ratio of their respective upper level degeneracies).

[c] The column densities in columns (6), (7), and (8) are those of the corresponding substates listed in column (1), as derived from the line fluxes given in column (5).

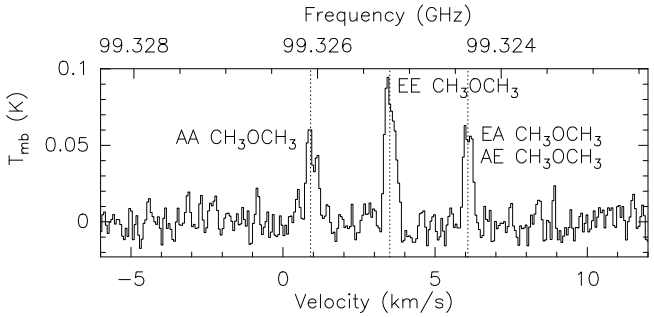

Figure 10.1: CH_3OCH_3 spectrum at 99.325 GHz in the prestellar core L1689B. Three lines corresponding to the AA, EE, EA, and AE symmetry substates (AE and EA being at the same frequency) are clearly detected at the $>7\sigma$ level. The vertical dotted lines indicate the rest frequencies measured in the laboratory and listed in the CDMS database.

At these low temperatures, the different substates have to be considered separately. Since we only have one line for each substate (except for methyl formate), the excitation conditions are poorly constrained and estimates of the column densities can only be given by assuming an excitation temperature. In the case of methyl formate, all detected lines have similar upper level energies and Einstein coefficients, so that having more than one line per substate does not bring supplementary constraints for the excitation. As these data are a subset of a larger ongoing observing project targetting several lines for each molecule and substate, we postpone the detailed analysis[2] of the column densities and abundances to a future paper and give here only preliminary estimates of the column densities. At densities around 10^5–10^6 cm^{-3} (similar to the critical density of 10^6 cm^{-3}), and gas temperatures of 7–10 K (Redman et al., 2004), it is reasonable to assume excitation temperatures of around 5 K. Because this value is uncertain, the column densities are also given for more extreme values of the excitation temperature, 4 K and 8 K.

The total column densities of the species were derived from the integrated line intensities assuming local thermodynamic equilibrium. The derived column densities are given in Table 10.2. The difference between the column density values at $T_{\rm ex} = 4$ K and $T_{\rm ex} = 8$ K varies between a factor of two for CH_3OCH_3 and an order of magnitude for CH_3OCHO. It is reasonable to expect the same excitation temperature for the A- and E- substates of CH_3CHO and CH_3OCHO, as these have similar upper level energies, Einstein coefficients, frequencies, and upper level degeneracies. We find that both A- and E- substates are equally abundant in those two molecules. For CH_3OCH_3, we find the abundance ratio of the EE- to AA- substates to be equal to the statistical ratio of two, although no conclusion can be drawn about the AE- and EA- substates, as these are too close in values of frequency to be spectrally resolved, so we simply assumed that the ratio of their intensities was equal to the ratio of their upper level degeneracies (which leads to equal column densities in AE- and EA-, each equal to half that of the AA- substate - see note to Table 10.2). For CH_2CO, we find an ortho-to-para ratio of ~ 3.3, which is similar to the value of 3.5 found in TMC-1 (Ohishi et al., 1991), consistent with the statistical ratio of 3. Assuming a H_2 column density of 10^{23} cm^{-2} (Dapp & Basu, 2009), we find abundances of a few 10^{-10} for the four species. This is a factor of ~ 100 lower than in hot corinos (e.g. in NGC1333-IRAS4A – Bottinelli et al., 2004a), similar to the formaldehyde abundance ratio between prestellar cores (Bacmann et al., 2003) and hot corinos (Bottinelli et al., 2004a).

[2]Note that collisional rates for methyl formate have been obtained by Faure et al. (2011)

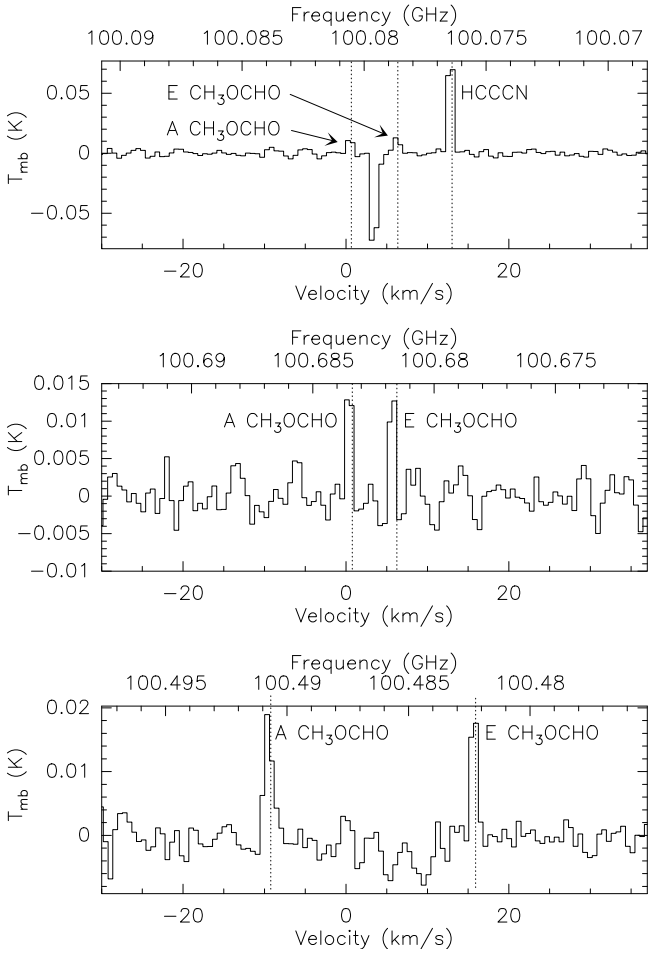

Figure 10.2: CH_3OCHO spectra of the $8_{17} - 7_{11}$ transitions at 100.48 GHz (A and E substates, bottom panel), of the $9_{09} - 8_{08}$ transitions at 100.68 GHz (A and E substates, middle panel), and of the $9_{19} - 8_{18}$ transitions at 100.08 GHz (A and E substates, top panel) in L1689B. The vertical dotted lines indicate the rest frequencies measured in the laboratory and listed in the JPL database. The CH_3OCHO spectrum in the top panel also shows a HC_3N line. The negative spectral feature between both CH_3OCHO lines results from the frequency switching procedure and the folding of the ortho-CH_2CO line shown in Fig. 10.4.

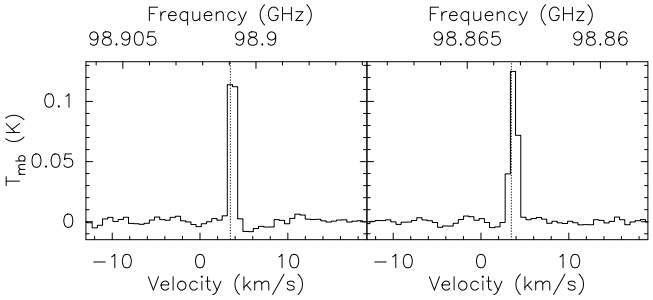

Figure 10.3: CH_3CHO spectra of the $5_{14} - 4_{13}$ transitions at 98.9009 GHz (A substate, left) and at 98.8633 GHz (E substate, right) in L1689B. The vertical dotted lines indicate the rest frequencies measured in the laboratory and listed in the JPL database.

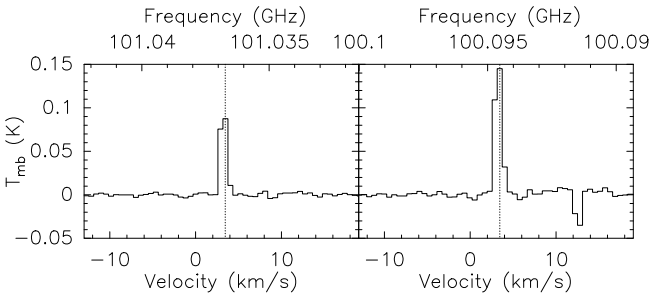

Figure 10.4: CH_2CO spectra of the $5_{05} - 4_{04}$ (para) transition at 101.0367 GHz (left) and of the $5_{15} - 4_{14}$ (ortho) transition (right) at 100.0945 GHz in L1689B. The vertical dotted lines indicate the laboratory rest frequencies listed in the CDMS database.

10.4 Discussion and conclusions

The detection of CH_3OCH_3, CH_3OCHO, CH_2CO, and CH_3CHO in the gas phase of a prestellar core at temperatures of around 10 K sheds new light on COM formation in the interstellar medium. Grain-surface chemistry models such as those of Garrod & Herbst (2006) require temperatures of around 30 K to ensure that the radicals present in the ice mantle have sufficient mobility to recombine and form COMs. This scenario cannot, however, explain the presence of COMs in the gas phase of this prestellar core. Pure gas-phase scenarios assuming that COMs result from warm ($\sim$ 100 K) gas-phase reactions between grain mantle constituents after their evaporation from the grains (Charnley et al., 1992) are also excluded by the low temperature in prestellar cores.

According to the hypothesis of a grain mantle formation scenario, the COMs that we detected in the gas phase have been desorbed from the ices by non-thermal processes such as secondary UV photon (originating from cosmic rays impacting on H_2 molecules) heating, or direct cosmic-ray impacts. It is therefore possible that radical mobility on the grains is also provided by the energy brought to the grains by UV photons. Similar mechanisms were invoked by Öberg et al. (2010) who detected methyl formate in the protostar B1-b, possibly desorbed by UV originating from the protostar through an outflow cavity. In the case of L1689B, the gas is significantly colder than in B1-b, and the core is well-shielded from external UV, as there is no nearby protostar and no outflow cavity so that the core is not exposed to a direct UV field. In Galactic center clouds, the detection of COMs by Requena-Torres et al. (2006) in the gas phase has been interpreted as the result of the ejection of ice mantle molecules by either shocks or supersonic turbulence. This scheme does not apply to the prestellar core L1689B, in which there are no shocks and the levels of turbulence are very low, as demonstrated by the narrow linewidths. If COMs form on grains, the most likely mechanisms to bring radical mobility and lead to molecular desorption are thus secondary UVs, cosmic rays, or the release of chemical energy due to exothermic reactions on the grains (e.g. chemical explosions, Garrod et al., 2007).

The simultaneous detection of CH_3OCH_3 and CH_3OCHO in very cold gas is particularly interesting. According to Öberg et al. (2011b), COMs could form sequentially and CH_3OCHO and CH_3CHO are formed by UV irradiation of cold CO-rich ices and CH_3OCH_3 forms in warmer (CH_3OH-rich) ice after CO has evaporated (see also Öberg et al., 2009c). Our observations do not support this scenario, and show that either CH_3OCH_3 forms in the same ice as CH_3OCHO (since prestellar core have rather uniform temperature and do not undergo temperature changes similar to those of protostars) or that the formation mechanisms of both types of molecules are different with, e.g., CH_3OCH_3 forming in the gas phase, as suggested by Peeters et al. (2006), though this idea is disputed by Requena-Torres et al. (2006).

The main conclusion of this paper is the detection of methyl formate and dimethyl ether for the first time in a very cold ($\sim$ 10 K) dark core, here the prestellar core L1689B. Acetaldehyde

and ketene, which were previously detected in TMC-1, are also detected. The detection of these species is also further evidence that they do not specifically trace hot core or hot corino regions, but that they are also present in the cold and dense ISM. Since prestellar cores are thought to be the precursors of low-mass protostars, the presence of COMs at the prestellar stage means that we have to re-investigate COM formation scenario in protostars, especially in the case of dimethyl ether, which is not expected to form in similar ices as methyl formate. Following our results, it is likely that at least part of the COM contents in young protostars originates from the prestellar phase.

Conclusions and Perspectives

Chapter 11

Conclusions and Perspectives

11.1 Conclusions

In the introduction, I presented the main items of this thesis, focused on the central role of interstellar dust in the chemical evolution during star formation, and here listed again: ice formation, high deuteration, formation of complex organic molecules. I summarize here the results presented in this thesis for each of these items.

Ice formation The multilayer formation of interstellar ices, introduced in chapter 3, strongly modifies the chemical composition of mantles compared to the "bulk" treatment, commonly used in previous astrochemical models. This result is in disagreement with the conclusions by Hasegawa & Herbst (1993b) who applied a three-phase model with low binding and diffusion energies and used quantum tunneling diffusion. Meanwhile, more recent experiments have readjusted the binding and diffusion energies to higher values while the diffusion via quantum tunneling does not seem to proceed efficiently on astrophysical relevant surfaces (see chapter 2). This results in a decrease of the rates of several key reactions increasing the trapping induced by the multilayer approach. Studies of the chemical abundance distributions, presented in chapter 8, show that the chemical composition of ices strongly depends on the total density which governs the hydrogenation efficiency on grain surfaces, but also on a few grain surface parameters (diffusion and binding energies) governing the mobility of H and D atoms and, therefore, the formation of polar ices. The porosity factor introduced in this work does not seem to influence significantly the ice chemistry. Some chemical parameters (activation energies, H_2 ortho/para ratio) also play a crucial role in the ice composition.The formation of formaldehyde and methanol are very sensitive to the activation barriers of the CO and H_2CO hydrogenation reactions.

The multilayer treatment allowed us to show that ices are very heterogeneous. Their chemical differentiation depend on the evolution of the gas phase abundances of species with time. Although we did not consider any physical evolution from diffuse molecular clouds to dense prestellar cores, we were able to reproduce the main ice features observed in protostellar envelopes: water rich ice showing a significant abundance of CO_2 in translucent regions (low density and visual extinction, high temperature), CO-rich ice in darker regions (higher density and visual extinction, lower temperature), while formaldehyde and methanol are formed in the outer part of ice mantles during the denser phases. Other species can be formed in significant quantities, depending on the physical conditions. We predicted the formation of hydrogen peroxide in dark regions where the abundance of gaseous O_2 is significant and the density is high. It is in good agreement with the recent observation of H_2O_2 in the ρ Oph A cloud by Bergman et al. (2011). Ozone is also predicted to have significant abundances if the density and the temperature are

sufficiently high. Solid and gaseous ozone cannot be detected from the ground. Consequently, we performed a search for ozone toward the low-mass protostar IRAS 16293 with the *Herschel Space Telescope* but we could not detected ozone (results not presented in this thesis). The upper limit deduced from our observations is easily explained by its efficient destruction after its desorption in the gas phase. No quantitative constraints on solid ozone abundance can, therefore, be deduced from these observations.

High deuteration It has been known for a decade that several species found in low-mass protostar envelopes display a high deuteration. Among these molecules, methanol is the more enriched in deuterium and shows deuterium fractionation values up to 50%. Moreover, the deuteration of methanol occurs more efficiently on the methyl group rather than on the hydroxyl group since CH_2DOH/CH_3OD abundance ratios higher than 10 have been measured (Parise et al., 2006). We investigated the evolution of this ratio with the protostar luminosity by performing new observations of CH_2DOH and CH_3OD toward intermediate- and high-mass protostars presented in chapter 5. We confirmed a similar CH_2DOH/CH_3OD ratio, higher than 10, around intermediate-mass protostars while high-mass protostars show a low ratio, close to unity.

The *Herschel Space Telescope* provided precise constraints of the deuteration of water toward the low-mass protostar IRAS 16293 (Coutens et al., 2012). As already suspected, water shows a lower deuteration than other icy species (formaldehyde and methanol) with HDO/H_2O and D_2O/H_2O abundance ratios of 3% and 10^{-3} in the hot corino. New observations of HDO were performed with the PdB interferometer toward two low-mass protostars NGC1333-IRAS2A and -IRAS4A, presented in chapter 6. The HDO emission comes from a confined region not resolved by the interferometer beam. By comparing the HDO emission with $H_2^{18}O$ observations by Persson et al. (2012) and with other HDO lines observed by Liu et al. (2011), we showed that the two molecules originate from the same region and water has a similar deuterium fractionation as in IRAS 16293. It is in agreement with the similar deuteration of methanol and formaldehyde in IRAS2A, IRAS4A, and in IRAS 16293 (Parise et al., 2006) altough these protostars are located in different clouds, showing different star-formation activity.

The deuteration of water, formaldehyde, and methanol have been theoretically investigated with our astrochemical model GRAINOBLE in chapters 10 and 11. The very high deuteration of formaldehyde and methanol can be predicted at high densities ($> 10^6$ cm^{-3}) and low temperatures ($\sim$ 10 K) and by considering abstraction reactions recently emphasized in experimental studies (e.g. Hidaka et al., 2009). For such conditions, the timescale needed to reproduce the observations is short (a few thousands years). Abstraction reactions efficiently occur on the methyl group of methanol rather than of the hydroxyl group, the high CH_2DOH/CH_3OD, therefore, increases with time, reaching the values of 10-20 observed toward low-mass (and intermediate-mass) protostars for a longer timescale (a few 10^4 yr). The different timescale involved in the formation of low-mass and high-mass protostars could explain then the different ratios observed by Parise et al. (2006) and in chapt. 5 of this work.

Water ice is believed to form in a wide range of conditions. In chapter 11, we studied the influence of the density, temperature, visual extinction as well as the H_2 ortho/para ratio on the water deuteration. It was found that a low H_2 opr ($\leq 3 \times 10^{-4}$) is needed to reproduce the observed water deuteration. We predicted the observations for lower densities (between 10^4 and $\sim 10^5$ cm^{-3}). If $n_H = 10^4$ cm^{-3}, only low temperatures and high visual extinctions are able to reproduce the observations. Although water ice is observed in translucent regions, deuterated water should be rather formed subsequently in a darker phase. The different deuterium fractionation of icy molecules observed in low-mass protostars should be, therefore, due to a different moment of formation. Water should be formed first in molecular clouds with low density where the deuteration degree is limited, while formaldehyde and methanol are rather formed in cold and dense regions in prestellar cores where the CO depletion and the D/H ratio are high.

Complex organic molecules Radicals, such as HCO or CH_3O, are believed to be important for the subsequent formation of complex organic molecules during the protostellar phase. In chapter 8, we studied the trapping of radicals into the bulk of grain mantles induced by the multilayer approach to assess whether a significant part of radicals can survive during the ice formation. The study of chemical abundance distributions shows that radical abundances are significant if the activation energies of CO and H_2CO hydrogenation reactions are low ($\sim$ 400 K). However, the use of new quantum calculations in our model with the Eckart model shows that these reactions display a low transmission probability, implying that integrated abundances of radicals in the ice mantles are negligible (less than 10^{-10}). Therefore, given the larger abundances of COMs measured in hot cores/corinos, another mechanism must be at work. In addition, the detection of four complex organic molecules toward the cold prestellar core L1689B, presented in chapter 7, suggests that COMs are formed even at low temperatures. Radicals trapped into the bulk cannot recombine together at the surface without energetic support. In addition, due to their low abundance, photolytic processes are believed to be responsible for the formation of cold COMs in spite of the low flux of UV photons in prestellar cores. Charnley (2001a) also proposed a formation of cold COMs by the sequential addition reactions of C and H from CO at cold temperatures.

11.2 Perspectives

Physical evolution and ice formation In this thesis, we followed the formation and the deuteration of interstellar ices only for constant physical conditions. We could not, therefore, predict all the ice features and the overall ice chemical composition observed toward protostar envelopes. To predict the formation of interstellar ices during the physical evolution from sparse molecular clouds to dense prestellar cores, one needs to couple dynamical models with astrochemical models, that can be easily achieved with the rate equation method. Dynamical models of collapsing cores have already been coupled with astrochemical models treating homogeneous grain mantles (e.g. Aikawa et al., 2005, 2008) while Garrod & Pauly (2011) applied his multilayer model on a simple free-fall collapse model. However, no multilayer models have been coupled with realistic dynamical models of collapsing cores so far. We aim at coupling the hydrodynamic model by Keto & Caselli (2008, 2010) with GRAINOBLE to predict realistic chemical composition of ices, including the deuteration.

As an illustration, Figure 11.1 shows the fractional abundance and deuteration of ices during a typical collapse: the total density n_H evolves with time from 3×10^3 to 10^7 cm^{-3} in 10^6 yr following a power-law function with a power index of 2. The visual extinction A_V has an initial value $A_{V,0}$ of 1 mag and evolves as $A_V = A_{V,0}(n_H/n_{H,0})^{2/3}$. The temperature decreases with A_V from 18 K to 9 K following a power-law function. A simple evolution allowed us to reproduce all the main ice features described in this thesis: H_2O is the main component throughout the ice, CO_2 is mainly formed in the inner part, CO is trapped in the outer part, while formaldehyde and methanol are mainly formed in the outermost layers although they can also be present in inner regions. Not surprisingly, the deuterium fractionation of all species increases with the ice monolayer because of the progressive depletion of CO. Formaldehyde and methanol are mainly formed in the outer part, their final deuteration are, therefore, slightly higher than that of water.

Grain porosity We investigated the influence of grain porosity on ice chemistry by considering two types of sites, following the method by Perets & Biham (2006). This treatment only allowed us to study the effect of the trapping induced by the grain pores and did not take the increase of the grain surface into account. We are currently developing a three-dimensional treatment of the grain porosity which follows the increase of the grain surface following the estimation of the vacuum fraction inside grains by observational and numerical studies. This approach will be

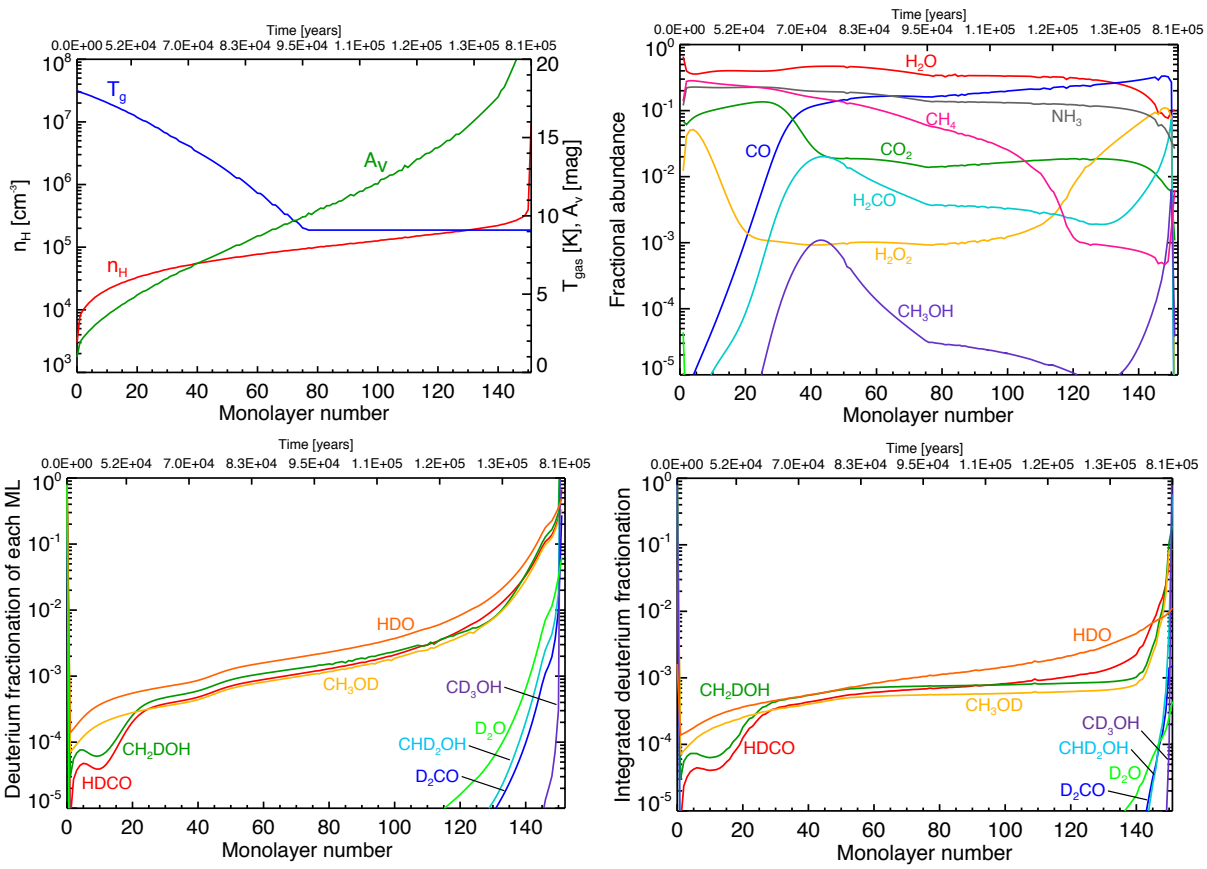

Figure 11.1: Evolution of physical conditions (top left), fractional abundance (top right) and deuterium fractionation (bottom left) in each layer, and integrated deuterium fractionation (bottom right) during a typical evolution from diffuse molecular cloud to dense prestellar core conditions.

applied on ice desorption during the protostellar stage to investigate the effect of grain porosity on the sublimation temperature of water ice. Indeed, the difference of water abundance observed in cold ices ($\sim 10^{-4}$) and in the warm gas of quiescent envelopes around low-mass protostars (a few 10^{-6}) could be due to an efficient trapping of ices in interstellar grains, limiting the thermal desorption. This is supported by higher water abundances observed toward protostellar outflows where an efficient desorption occurs via grain sputtering.

Experimental validation of models and quantum calculations The quantum calculations used in this work have been performed for gas phase conditions and they did not take the effect of neighbour solid species into account. Furthermore, astrochemical models are based on numerous assumptions which can be of strong importance for the formation of ices. Experimental studies on interstellar ice analogues provide an in-situ laboratory to test the assumptions of the models and to validate the use of theoretical calculations in grain surface models. We are modelling the experimental studies by the group of Prof. Watanabe, who focused on the sequential hydrogenation of CO, by using recent theoretical calculations by Peters et al. (2012) in a modified version of GRAINOBLE. For this purpose, we are running grids of models which consider the variation of a few free parameters: binding energy of H atoms, diffusion to binding energy ratio, and the bulk diffusion rate, to reproduce the time-dependent formation of formaldehyde and methanol. This comparison will help us to validate our astrochemical model and the use of theoretical calculations, and eventually to constrain the values of free surface parameters.

Methyl formate and methanol emissions In the introduction, we presented a sample of observational data showing that the methyl formate/methanol abundance ratio tends to be higher in hot corinos than in high-mass hot cores. However, no data were available for intermediate-mass protostars at the beginning of this thesis. Moreover, the ratios observed in low-mass hot corinos were deduced from single dish observations whose beams are larger than the size of hot corinos. They, therefore, encompass other components such as the cold envelope which is also believed to display low abundances of methanol and methyl formate. We are performing interferometric mapping of methyl formate and methanol toward two low-mass (NGC-IRAS2A and -IRAS4A) and two intermediate-mass (Cepheus E and OMC2-FIR4) protostars to compare the emission of these two molecules and constrain the abundance ratio in the hot core region. These observations will help us to confirm (or infirm) the abundance ratios deduced from single-dish observations and to investigate the dependence of this ratio with the mass of the protostar.

Deuteration of other complex organic molecules Several complex organic molecules have been detected around low-mass protostars with similar abundances and similar origins than methanol, believed to play a precursor role in their formation. The high deuteration of methanol would, therefore, imply a high deuteration of COMs. Several spectral survey programs have been or are being performed. With the use of new spectroscopical laboratory data, they will allow us to investigate the deuteration of COMs. These observations will help us to confirm the high deuteration and to constrain their formation pathways. High deuteration of COMs has a strong importance for the subsequent formation of amino-acids in protoplanetary disks and planetary systems. Laboratory analyses of meteoritic samples have revealed that several amino acids are enriched in deuterium, reflecting molecule formation at low temperatures, and, therefore, some memory of interstellar heritage. Comparison with the deuterium fractionation of amino-acids could provide new clues for the interstellar origin of amino-acids found in the Solar System.

Conclusive remarks This thesis has emphasized the strong dependence of the grain surface chemistry on the physical conditions of the studied object and on the microphysics of the problem, namely on several surface parameters. However, in spite of its inevitable limitations, our model has shown that the study of interstellar ices can be used as a powerful tool to retrace the chemical history of astronomical objects (chapters 5, 6, 7). Much more can be done, on many more situations and objects. For example, the physical conditions of high-mass protostars are thought to be quite different from that of low-mass protostars. The study of the ice deuteration could then help us to understand the different history of the two types of stars, their physical conditions and their evolutions. The use of the multilayer model developed in this thesis could also be of great interest for the study of protostellar outflows, in their history and present conditions. In fact, the molecular shocks at the interface of the outflows and quiescent gas show a particular chemical enrichment due to the sublimation of icy mantles via specific desorption processes, such as sputtering. GRAINOBLE has already been applied to the outflow of L1157-B1 to give an estimation in the density of the pre-shocked gas (article by Codella et al. submitted to ApJL and listed in Appendix C). Last, but not least, the pristine material of comets and meteorites in the Solar System might reflect an interstellar origin. The GRAINOBLE model could be used in prototoplanetary disk conditions to investigate the eventual reprocessing of ices and COMs during the protoplanetary disk phase. This will allow us to estimate the chemical evolution of comets and meteorites during the solar nebula.

In conclusion, the model I developed during my thesis can be applied to a variety of astrophysical problems from galactic protostars and outflows, to solar system objects and even, in the near future, to extragalactic objects, whose molecular studies will no doubt see a huge advance thanks to the new generation of telescopes like ALMA and NOEMA, and to the new generation of receivers and correlators like those now at the IRAM 30m.

Bibliography

Adamo, C. & Barone, V. 1999, J. Chem. Phys., 110, 6158

Adams, F. C., Lada, C. J., & Shu, F. H. 1987, The Astrophysical Journal, 312, 788

Aikawa, Y., Herbst, E., Roberts, H., & Caselli, P. 2005, The Astrophysical Journal, 620, 330

Aikawa, Y., Wakelam, V., Garrod, R. T., & Herbst, E. 2008, The Astrophysical Journal, 674, 984

Al-Halabi, A., Fraser, H. J., Kroes, G. J., & van Dishoeck, E. F. 2004, Astronomy & Astrophysics, 422, 777

Al-Halabi, A., Kleyn, A. W., van Dishoeck, E. F., & Kroes, G. J. 2002, The Journal of Physical Chemistry B, 106, 6515

Al-Halabi, A. & van Dishoeck, E. F. 2007, Monthly Notices of the Royal Astronomical Society, 382, 1648

Allen, M. & Robinson, G. W. 1977, The Astrophysical Journal, 212, 396

Amiaud, L., Fillion, J. H., Baouche, S., et al. 2006, The Journal of Chemical Physics, 124, 094702

Andersson, S., Al-Halabi, A., Kroes, G.-J., & van Dishoeck, E. F. 2006, Journal of Chemical Physics, 124, 064715

Andersson, S., Goumans, T., & Arnaldsson, A. 2011, Chemical Physics Letters, 513, 31

Andersson, S., Nyman, G., Arnaldsson, A., Manthe, U., & Jonsson, H. 2009, The Journal of Physical Chemistry A, 113, 4468

Andersson, S. & van Dishoeck, E. F. 2008, Astronomy & Astrophysics, 491, 907

André, P. 1994, in The Cold Universe, ed. T. Montmerle, C. J. Lada, I. F. Mirabel, & J. Tran Thanh Van, 179

Andre, P., Ward-Thompson, D., & Barsony, M. 2000, Protostars and Planets IV, 59

Arasa, C., Andersson, S., Cuppen, H. M., van Dishoeck, E. F., & Kroes, G.-J. 2010, Journal of Chemical Physics, 132, 184510

Arasa, C., Andersson, S., Cuppen, H. M., van Dishoeck, E. F., & Kroes, G. J. 2011, Journal of Chemical Physics, 134, 164503

Bacmann, A., André, P., Puget, J.-L., et al. 2000, Astronomy & Astrophysics, 361, 555

Bacmann, A., Caux, E., Hily-Blant, P., et al. 2010, Astronomy & Astrophysics, 521, L42

Bacmann, A., Lefloch, B., Ceccarelli, C., et al. 2002, Astronomy & Astrophysics, 389, L6

Bacmann, A., Lefloch, B., Ceccarelli, C., et al. 2003, The Astrophysical Journal Letters, 585, L55

Bacmann, A., Lefloch, B., Parise, B., Ceccarelli, C., & Steinacker, J. 2007, in Molecules in Space and Laboratory

Barzel, B. & Biham, O. 2007, The Journal of Chemical Physics, 127, 144703

Baulch, D. L., Bowman, C. T., Cobos, C. J., et al. 2005, Journal of Physical and Chemical Reference Data, 34, 757

Beichman, C. A., Myers, P. C., Emerson, J. P., et al. 1986, The Astrophysical Journal, 307, 337

Bell, T. A., Willacy, K., Phillips, T. G., Allen, M., & Lis, D. C. 2011, The Astrophysical Journal, 731, 48

Bennett, C. J. & Kaiser, R. I. 2007, The Astrophysical Journal, 661, 899

Bergeron, H., Rougeau, N., Sidis, V., et al. 2008, The Journal of Physical Chemistry A, 112, 11921

Bergin, E. A., Alves, J., Huard, T., & Lada, C. J. 2002, The Astrophysical Journal Letters, 570, L101

Bergin, E. A., Melnick, G. J., Stauffer, J. R., et al. 2000, The Astrophysical Journal Letters, 539, L129

Bergin, E. A. & Tafalla, M. 2007, Annual Review of Astronomy & Astrophysics, 45, 339

Bergman, P., Parise, B., Liseau, R., & Larsson, B. 2011, Astronomy & Astrophysics, 527, A39

Beuther, H., Zhang, Q., Bergin, E. A., & K., S. T. 2009, The Astrophysical Journal, 137, 406

Biham, O., Furman, I., Pirronello, V., & Vidali, G. 2001, The Astrophysical Journal, 553, 595

Bisschop, S. E., Fraser, H. J., Öberg, K. I., van Dishoeck, E. F., & Schlemmer, S. 2006, Astronomy & Astrophysics, 449, 1297

Bisschop, S. E., Jørgensen, J. K., van Dishoeck, E. F., & de Wachter E. B. M. 2007, Astronomy & Astrophysics, 465, 913

Blake, G. A., Sutton, E. C. ., Masson, C. R., & Phillips, T. G. 1987, The Astrophysical Journal, 315, 621

Bockelée-Morvan, D., Lis, D. C., Wink, J. E., et al. 2000, Astronomy & Astrophysics, 353, 1101

Boley, A. C., Payne, M. J., Corder, S., et al. 2012, The Astrophysical Journal Letters, 750, L21

Bonnor, W. B. 1956, Monthly Notices of the Royal Astronomical Society, 116, 351

Boogert, A. C. A., Pontoppidan, K. M., Knez, C., et al. 2008, The Astrophysical Journal, 678, 985

Bottinelli, S., Ceccarelli, C., Lefloch, B., et al. 2004a, The Astrophysical Journal, 615, 354

Bottinelli, S., Ceccarelli, C., Neri, R., et al. 2004b, The Astrophysical Journal Letters, 617, L69

Bottinelli, S., Ceccarelli, C., Williams, J. P., & Lefloch, B. 2007, Astronomy & Astrophysics, 463, 601

Brown, P. N., Byrne, G. D., & Hindmarsh, A. C. 1989, SIAM Journal on Scientific Computing, 10, 1038

Buch, V. 1990, The Journal of Chemical Physics, 93, 2631

Buch, V. 1992, The Journal of Chemical Physics, 96, 3814

Butner, H. M., Charnley, S. B., Ceccarelli, C., et al. 2007, The Astrophysical Journal Letters, 659, L137

Cambrésy, L. 1999, Astronomy & Astrophysics, 345, 965

Caselli, P., Hasegawa, T. I., & Herbst, E. 1993, The Astrophysical Journal, 408, 548

Caselli, P., Hasegawa, T. I., & Herbst, E. 1998, The Astrophysical Journal, 495, 309

Caselli, P., Keto, E., Pagani, L., et al. 2010, Astronomy & Astrophysics, 521, L29

Caselli, P., Stantcheva, T., Shalabiea, O., Shematovich, V. I., & Herbst, E. 2002, Planetary and Space Science, 50, 1257

Caselli, P., Walmsley, C. M., Tafalla, M., Dore, L., & Myers, P. C. 1999, The Astrophysical Journal Letters, 523, L165

Caselli, P., Walmsley, C. M., Terzieva, R., & Herbst, E. 1998, The Astrophysical Journal, 499, 234

Caux, E., Ceccarelli, C., Castets, A., et al. 1999, Astronomy & Astrophysics, 347, L1

Cazaux, S., Caselli, P., & Spaans, M. 2011, The Astrophysical Journal Letters, 741, L34

Cazaux, S. & Tielens, A. G. G. M. 2004, The Astrophysical Journal, 604, 222

Cazaux, S., Tielens, A. G. G. M., Ceccarelli, C., et al. 2003, The Astrophysical Journal Letters, 593, L51

Ceccarelli, C., Caselli, P., Herbst, E., Tielens, A. G. G. M., & Caux, E. 2007, Protostars and Planets V, 47

Ceccarelli, C., Castets, A., Caux, E., et al. 2000, Astronomy & Astrophysics, 355, 1129

Ceccarelli, C., Castets, A., Loinard, L., Caux, E., & Tielens, A. G. G. M. 1998, Astronomy & Astrophysics, 338, L43

Ceccarelli, C. & Dominik, C. 2005, Astronomy & Astrophysics, 440, 583

Ceccarelli, C., Hollenbach, D. J., & Tielens, A. G. G. M. 1996, The Astrophysical Journal, 471, 400

Ceccarelli, C., Loinard, L., Castets, A., et al. 2001, Astronomy & Astrophysics, 372, 998

Ceccarelli, C., Maret, S., Tielens, A. G. G. M., Castets, A., & Caux, E. 2003, Astronomy & Astrophysics, 410, 587

Cernis, K. 1990, Astrophysics and Space Science, 166, 315

Chang, Q., Cuppen, H. M., & Herbst, E. 2005, Astronomy & Astrophysics, 434, 599

Chang, Q., Cuppen, H. M., & Herbst, E. 2007, Astronomy & Astrophysics, 469, 973

Charnley, S. 2001a, in The Bridge Between the Big Bang and Biology: Stars, Planetary Systems, Atmospheres, Volcanoes: Their Link to Life, ed. F. Giovannelli, 139

Charnley, S. B. 1998, The Astrophysical Journal Letters, 509, L121

Charnley, S. B. 2001b, The Astrophysical Journal Letters, 562, L99

Charnley, S. B., Tielens, A. G. G. M., & Millar, T. J. 1992, The Astrophysical Journal Letters, 399, L71

Charnley, S. B., Tielens, A. G. G. M., & Rodgers, S. D. 1997, The Astrophysical Journal Letters, 482, L203

Chehrouri, M., Fillion, J.-H., Chaabouni, H., et al. 2011, Phys. Chem. Chem. Phys., 13, 2172

Codella, C., Ceccarelli, C., Lefloch, B., et al. 2012, The Astrophysical Journal Letters, 757, L9

Collings, M. P., Anderson, M. A., Chen, R., et al. 2004, Monthly Notices of the Royal Astronomical Society, 354, 1133

Collings, M. P., Dever, J. W., Fraser, H. J., & McCoustra, M. R. S. 2003a, Astrophysics and Space Science, 285, 633

Collings, M. P., Dever, J. W., Fraser, H. J., McCoustra, M. R. S., & Williams, D. A. 2003b, The Astrophysical Journal, 583, 1058

Coutens, A., Vastel, C., Caux, E., & Ceccarelli, C. 2012, Astronomy & Astrophysics, 539, A132

Crapsi, A., Caselli, P., Walmsley, C. M., et al. 2005, The Astrophysical Journal, 619, 379

Crimier, N., Ceccarelli, C., Alonso-Albi, T., et al. 2010a, Astronomy & Astrophysics, 516, A102

Crimier, N., Ceccarelli, C., Lefloch, B., & Faure, A. 2009, Astronomy & Astrophysics, 506, 1229

Crimier, N., Ceccarelli, C., Maret, S., et al. 2010b, Astronomy & Astrophysics, 519, A65

Cummins, S. E., Linke, R. A., & Thaddeus, P. 1986, The Astrophysical Journal Supplement Series, 60, 819

Cuppen, H. M. & Herbst, E. 2005, Monthly Notices of the Royal Astronomical Society, 361, 565

Cuppen, H. M. & Herbst, E. 2007, The Astrophysical Journal, 668, 294

Cuppen, H. M., Ioppolo, S., Romanzin, C., & Linnartz, H. 2010a, Physical Chemistry Chemical Physics (Incorporating Faraday Transactions), 12, 12077

Cuppen, H. M., Kristensen, L. E., & Gavardi, E. 2010b, Monthly Notices of the Royal Astronomical Society, 406, L11

Cuppen, H. M., Kristensen, L. E., & Gavardi, E. 2010c, Monthly Notices of the Royal Astronomical Society, 406, L11

Cuppen, H. M., van Dishoeck, E. F., Herbst, E., & Tielens, A. G. G. M. 2009, Astronomy & Astrophysics, 508, 275

Dalgarno, A., Yan, M., & Liu, W. 1999, The Astrophysical Journal Supplement Series, 125, 237

Daniel, F., Dubernet, M.-L., & Grosjean, A. 2011, Astronomy & Astrophysics, 536, A76

Dapp, W. B. & Basu, S. 2009, Monthly Notices of the Royal Astronomical Society, 395, 1092

Demyk, K., Bottinelli, S., Caux, E., et al. 2010, Astronomy & Astrophysics, 517, A17

D'Hendecourt, L. B., Allamandola, L. J., & Greenberg, J. M. 1985, Astronomy & Astrophysics, 152, 130

D'Hendecourt, L. B., Allamandola, L. J., Grim, R. J. A., & Greenberg, J. M. 1986, Astronomy & Astrophysics, 158, 119

di Francesco, J., Evans, II, N. J., Caselli, P., et al. 2007, Protostars and Planets V, 17

Di Francesco, J., Johnstone, D., Kirk, H., MacKenzie, T., & Ledwosinska, E. 2008, The Astrophysical Journal Supplement Series, 175, 277

Dislaire, V., Hily-Blant, P., Faure, A., et al. 2012, Astronomy & Astrophysics, 537, A20

Draine, B. T. 1978, The Astrophysical Journal Supplement Series, 36, 595

Du, F. & Parise, B. 2011, Astronomy & Astrophysics, 530, A131

Dulieu, F., Amiaud, L., Congiu, E., et al. 2010, Astronomy & Astrophysics, 512, A30+

Dunning Jr, T. H. 1989, J. Chem. Phys., 90, 1007

Ebert, R. 1955, Zeitschrift für Astrophysik, 37, 217

Eckart, C. 1930, Physical Review, 35, 1303

Ehrlich, G. & Hudda, F. G. 1966, Journal of Chemical Physics, 44, 1039

Ellingson, B. A., Theis, D. P., Tishchenko, O., Zheng, J., & Truhlar, D. G. 2007, The Journal of Physical Chemistry A, 111, 13554

Emprechtinger, M., Lis, D. C., Bell, T., et al. 2010, Astronomy & Astrophysics, 521, L28

Evans, II, N. J., Allen, L. E., Blake, G. A., et al. 2003, Publications of the Astronomical Society of the Pacific, 115, 965

Evans, II, N. J., Dunham, M. M., Jørgensen, J. K., et al. 2009, The Astrophysical Journal Supplement Series, 181, 321

Faure, A., Crimier, N., Ceccarelli, C., et al. 2007, Astronomy & Astrophysics, 472, 1029

Faure, A., Szalewicz, K., & Wiesenfeld, L. 2011, Journal of Chemical Physics, 135, 024301

Faure, A., Wiesenfeld, L., Scribano, Y., & Ceccarelli, C. 2012, Monthly Notices of the Royal Astronomical Society, 420, 699

Fayolle, E. C., Bertin, M., Romanzin, C., et al. 2011, The Astrophysical Journal Letters, 739, L36

Fillion, J.-H., Amiaud, L., Congiu, E., et al. 2009, Phys. Chem. Chem. Phys., 11, 4396

Flower, D. R. & Pineau des Forêts, G. 2003, Monthly Notices of the Royal Astronomical Society, 343, 390

Flower, D. R., Pineau Des Forêts, G., & Walmsley, C. M. 2005, Astronomy & Astrophysics, 436, 933

Flower, D. R., Pineau Des Forêts, G., & Walmsley, C. M. 2006, Astronomy & Astrophysics, 449, 621

Fraser, H. J., Collings, M. P., McCoustra, M. R. S., & Williams, D. A. 2001, Monthly Notices of the Royal Astronomical Society, 327, 1165

Frerking, M. A., Langer, W. D., & Wilson, R. W. 1982, The Astrophysical Journal, 262, 590

Friberg, P., Hjalmarson, A., Madden, S. C., & Irvine, W. M. 1988, Astronomy & Astrophysics, 195, 281

Frisch, M. J., Trucks, G. W., Schlegel, H. B., et al. 2009, Gaussian 09 Revision A. 02, *

Fuchs, G. W., Cuppen, H. M., Ioppolo, S., et al. 2009, Astronomy & Astrophysics, 505, 629

Galli, D., Walmsley, M., & Gonçalves, J. 2002, Astronomy & Astrophysics, 394, 275

Garrod, R., Park, I. H., Caselli, P., & Herbst, E. 2006, Faraday Discussions, 133, 51

Garrod, R. T. 2008, Astronomy & Astrophysics, 491, 239

Garrod, R. T. & Herbst, E. 2006, Astronomy & Astrophysics, 457, 927

Garrod, R. T. & Pauly, T. 2011, The Astrophysical Journal, 735, 15

Garrod, R. T., Vasyunin, A. I., Semenov, D. A., Wiebe, D. S., & Henning, T. 2009, The Astrophysical Journal Letters, 700, L43

Garrod, R. T., Wakelam, V., & Herbst, E. 2007, Astronomy & Astrophysics, 467, 1103

Garrod, R. T., Weaver, S. L. W., & Herbst, E. 2008, The Astrophysical Journal, 682, 283

Gerakines, P. A., Moore, M. H., & Hudson, R. L. 2000, Astronomy & Astrophysics, 357, 793

Gerakines, P. A., Moore, M. H., & Hudson, R. L. 2001, Journal of Geophysical Research, 106, 33381

Gerakines, P. A., Schutte, W. A., & Ehrenfreund, P. 1996, Astronomy & Astrophysics, 312, 289

Gibb, E., Nummelin, A., Irvine, W. M., Whittet, D. C. B., & Bergman, P. 2000, The Astrophysical Journal, 545, 309

Gibb, E. L., Whittet, D. C. B., Boogert, A. C. A., & Tielens, A. G. G. M. 2004, The Astrophysical Journal Supplement Series, 151, 35

Gillespie, D. T. 1976, Journal of Computational Physics, 22, 403

Goldsmith, P. F., Heyer, M., Narayanan, G., et al. 2008, The Astrophysical Journal, 680, 428

Goldsmith, P. F., Liseau, R., Bell, T. A., et al. 2011, The Astrophysical Journal, 737, 96

Goumans, T. P. M. 2011, Monthly Notices of the Royal Astronomical Society, 262

Goumans, T. P. M. & Andersson, S. 2010, Monthly Notices of the Royal Astronomical Society, 406, 2213

Goumans, T. P. M. & Kästner, J. 2011, The Journal of Physical Chemistry A, 115, 10767

Goumans, T. P. M., Uppal, M. A., & Brown, W. A. 2008, Monthly Notices of the Royal Astronomical Society, 384, 1158

Gredel, R., Lepp, S., & Dalgarno, A. 1987, The Astrophysical Journal Letters, 323, L137

Gredel, R., Lepp, S., Dalgarno, A., & Herbst, E. 1989, The Astrophysical Journal, 347, 289

Green, N. J. B., Toniazzo, T., Pilling, M. J., et al. 2001, Astronomy & Astrophysics, 375, 1111

Grim, R. J. A., Greenberg, J. M., de Groot, M. S., et al. 1989, Astronomy & Astrophysics, 78, 161

Hagen, W., Allamandola, L. J., & Greenberg, J. M. 1979, Astrophysics and Space Science, 65, 215

Hama, T., Kuwahata, K., Watanabe, N., et al. 2012, The Astrophysical Journal, 757, 185

Hamberg, M., Österdahl, F., Thomas, R. D., et al. 2010, Astronomy & Astrophysics, 514, A83

Harris, J. & Kasemo, B. 1981, Surface Science, 105, L281

Hasegawa, T. I. & Herbst, E. 1993a, Monthly Notices of the Royal Astronomical Society, 261, 83

Hasegawa, T. I. & Herbst, E. 1993b, Monthly Notices of the Royal Astronomical Society, 263, 589

Hasegawa, T. I., Herbst, E., & M., L. C. 1992, The Astrophysical Journal Supplement Series, 82, 167

Herbst, E. & Klemperer, W. 1973, The Astrophysical Journal, 185, 505

Herbst, E. & van Dishoeck, E. F. 2009, Annual Reviews of Astronomy & Astrophysics, 47, 427

Hidaka, H., Kouchi, A., & Watanabe, N. 2007, J. Chem. Phys., 126, 204707

Hidaka, H., Watanabe, M., Kouchi, A., & Watanabe, N. 2009, The Astrophysical Journal, 702, 291

Hidaka, H., Watanabe, N., Shiraki, T., Nagaoka, A., & Kouchi, A. 2004, The Astrophysical Journal, 614, 1124

Hincelin, U., Wakelam, V., Hersant, F., et al. 2011, Astronomy & Astrophysics, 530, A61

Hinshelwood, C. N. 1940, The Kinetics Of Chemical Change (The Clarendon Press)

Hiraoka, K., Miyagoshi, T., Takayama, T., Yamamoto, K., & Kihara, Y. 1998, The Astrophysical Journal, 498, 710

Hollenbach, D., Kaufman, M. J., Bergin, E. A., & Melnick, G. J. 2009, The Astrophysical Journal, 690, 1497

Hollenbach, D. & Salpeter, E. E. 1970, The Astrophysical Journal, 163, 155

Hollenbach, D. & Salpeter, E. E. 1971, The Astrophysical Journal, 163, 155

Horn, A., Møllendal, H., Sekiguchi, O., et al. 2004, The Astrophysical Journal, 611, 605

Hornekær, L., Baurichter, A., Petrunin, V. V., Field, D., & Luntz, A. C. 2003, Science, 302, 1943

Hornekær, L., Baurichter, A., Petrunin, V. V., et al. 2005, Journal of Chemical Physics, 122

Hudson, R. L. & Moore, M. H. 1999, Icarus, 140, 451

Hugo, E., Asvany, O., & Schlemmer, S. 2009, Journal of Chemical Physics, 130, 164302

Ikeda, M., Ohishi, M., Nummelin, A., et al. 2001, The Astrophysical Journal, 560, 792

Ioppolo, S., Cuppen, H. M., Romanzin, C., van Dishoeck, E. F., & Linnartz, H. 2008, The Astrophysical Journal, 686, 1474

Ioppolo, S., Cuppen, H. M., Romanzin, C., van Dishoeck, E. F., & Linnartz, H. 2010, Physical Chemistry Chemical Physics (Incorporating Faraday Transactions), 12, 12065

Ioppolo, S., van Boheemen, Y., Cuppen, H. M., van Dishoeck, E. F., & Linnartz, H. 2011, Monthly Notices of the Royal Astronomical Society, 413, 2281

Irvine, W. M., Friberg, P., Kaifu, N., et al. 1989, The Astrophysical Journal, 342, 871

Jacq, T., Walmsley, C. M., Mauersberger, R., et al. 1993, Astronomy & Astrophysics, 271, 276

Jaycock, M. J. & Parfitt, G. D. 1986, Chemistry of Interfaces (Wiley and Sons, New York)

Jefferts, K. B., Penzias, A. A., & Wilson, R. W. 1973, The Astrophysical Journal Letters, 179, L57

Jenniskens, P., Blake, D. F., Wilson, M. A., & Pohorille, A. 1995, The Astrophysical Journal, 455, 389

Jing, D., He, J., Brucato, J., et al. 2011, The Astrophysical Journal Letters, 741, L9

Johnston, H. S. & Heicklen, J. 1962, The Journal of Physical Chemistry, 66, 532

Jones, A. P. 2011, Astronomy & Astrophysics, 528, A98+

Jørgensen, J. K., Bourke, T. L., Myers, P. C., et al. 2005a, The Astrophysical Journal, 632, 973

Jørgensen, J. K., Schöier, F. L., & van Dishoeck, E. F. 2002, Astronomy & Astrophysics, 389, 908

Jørgensen, J. K., Schöier, F. L., & van Dishoeck, E. F. 2005b, Astronomy & Astrophysics, 435, 177

Jørgensen, J. K. & van Dishoeck, E. F. 2010, The Astrophysical Journal Letters, 725, L172

Jørgensen, J. K., van Dishoeck, E. F., Visser, R., et al. 2009, Astronomy & Astrophysics, 507, 861

Katz, N., Furman, I., Biham, O., Pirronello, V., & Vidali, G. 1999, The Astrophysical Journal, 522, 505

Kaufman, M. J. & Neufeld, D. A. 1996, The Astrophysical Journal, 456, 611

Kendall, R. A., Dunning Jr, T. H., & Harrison, R. J. 1992, J. Chem. Phys., 96, 6796

Kerkeni, B. & Clary, D. C. 2004, The Journal of Physical Chemistry A, 108, 8966

Keto, E. & Caselli, P. 2008, The Astrophysical Journal, 683, 238

Keto, E. & Caselli, P. 2010, Monthly Notices of the Royal Astronomical Society, 402, 1625

Kirk, J. M., Ward-Thompson, D., & André, P. 2007, Monthly Notices of the Royal Astronomical Society, 375, 843

Klemm, R. B., Payne, W. A., & Stief, L. J. 1975

Knee, L. B. G. & Sandell, G. 2000, Astronomy & Astrophysics, 361, 671

Kobayashi, K. 1983, The Journal of Physical Chemistry, 87, 4317

Kolasinski, K. W. 2002, Surface Science: Fondations of Catalysis and Nanoscience, ed. Wiley

Koussa, H., Bahri, M., Jaidane, N., & Ben Lakhdar, Z. 2006, Journal of Molecular Structure: THEOCHEM, 770, 149

Kristensen, L. E., Amiaud, L., Fillion, J.-H., Dulieu, F., & Lemaire, J.-L. 2011, Astronomy & Astrophysics, 527, A44

Kristensen, L. E., Visser, R., van Dishoeck, E. F., et al. 2010, Astronomy & Astrophysics, 521, L30

Kuan, Y.-J., Huang, H. C., Charnley, S. B., et al. 2004, The Astrophysical Journal, 616, 27

Lada, C. J. & Wilking, B. A. 1984, The Astrophysical Journal, 287, 610

Landau, L. & Lifshitz, E. 1960, Course of Theoretical Physics. Mechanics., Vol. 1 (Pergamon Press)

Le Bourlot, J. 2000, Astronomy & Astrophysics, 360, 656

Le Bourlot, J., Pineau des Forets, G., Roueff, E., & Flower, D. R. 1995, Astronomy & Astrophysics, 302, 870

Le Petit, F., Nehmé, C., Le Bourlot, J., & Roueff, E. 2006, The Astrophysical Journal Supplement Series, 164, 506

Le Petit, F., Roueff, E., & Le Bourlot, J. 2002, Astronomy & Astrophysics, 390, 369

Lee, H.-H., Herbst, E., Pineau des Forets, G., Roueff, E., & Le Bourlot, J. 1996, Astronomy & Astrophysics, 311, 690

Lefloch, B., Castets, A., Cernicharo, J., Langer, W. D., & Zylka, R. 1998, Astronomy & Astrophysics, 334, 269

Leger, A., Jura, M., & Omont, A. 1985, Astronomy & Astrophysics, 144, 147

Linsky, J. L. 2003, Space Science Reviews, 106, 49

Lipshtat, A. & Biham, O. 2003, Astronomy & Astrophysics, 400, 585

Lis, D. C., Keene, J., Phillips, T. G., et al. 2001, The Astrophysical Journal, 561, 823

Liseau, R., Goldsmith, P. F., Larsson, B., et al. 2012, Astronomy & Astrophysics, 541, A73

Liseau, R., Sandell, G., & Knee, L. B. G. 1988, Astronomy & Astrophysics, 192, 153

Liu, F.-C., Parise, B., Kristensen, L., et al. 2011, Astronomy & Astrophysics, 527, A19

Loinard, L., Castets, A., Ceccarelli, C., Caux, E., & Tielens, A. G. G. M. 2001, The Astrophysical Journal Letters, 552, L163

Looney, L. W., Mundy, L. G., & Welch, W. J. 2000, The Astrophysical Journal, 529, 477

Lu, H.-C., Chen, H.-K., Cheng, B.-M., Kuo, Y.-P., & Ogilvie, J. F. 2005, Journal of Physics B Atomic Molecular Physics, 38, 3693

MacDonald, G. H., Gibb, A. G., Habing, R. J., & Millar, T. J. 1996, Astronomy & Astrophysics, 119

Manicò, G., Ragunì, G., Pirronello, V., Roser, J. E., & Vidali, G. 2001, The Astrophysical Journal Letters, 548, L253

Maret, S., Ceccarelli, C., Caux, E., et al. 2004, Astronomy & Astrophysics, 416, 577

Maret, S., Ceccarelli, C., Tielens, A. G. G. M., et al. 2005, Astronomy & Astrophysics, 442, 527

Matar, E., Bergeron, H., Dulieu, F., et al. 2010, Journal of Chemical Physics, 133, 104507

Matar, E., Congiu, E., Dulieu, F., Momeni, A., & Lemaire, J. L. 2008, Astronomy & Astrophysics, 492, L17

Mathis, J. S. 1996, The Astrophysical Journal, 472, 643

Mathis, J. S., Mezger, P. G., & Panagia, N. 1983, Astronomy & Astrophysics, 128, 212

Mathis, J. S., Rumpl, W., & Nordsieck, K. H. 1977, The Astrophysical Journal, 217, 425

Matthews, H. E., Friberg, P., & Irvine, W. M. 1985, The Astrophysical Journal, 290, 609

Maury, A. J., André, P., Men'shchikov, A., Könyves, V., & Bontemps, S. 2011, Astronomy & Astrophysics, 535, A77

Mehringer, D. M. & Snyder, L. E. 1996, The Astrophysical Journal, 471, 897

Millar, T. J., Bennett, A., & Herbst, E. 1989, The Astrophysical Journal, 340, 906

Millar, T. J., Herbst, E., & Charnley, S. B. 1991, The Astrophysical Journal, 369, 147

Miyauchi, N., Hidaka, H., Chigai, T., et al. 2008, Chemical Physics Letters, 456, 27

Mizuno, A., Fukui, Y., Iwata, T., Nozawa, S., & Takano, T. 1990, The Astrophysical Journal, 356, 184

Modica, P. & Palumbo, M. E. 2010, Astronomy & Astrophysics, 519, A22+

Mokrane, H., Chaabouni, H., Accolla, M., et al. 2009, The Astrophysical Journal Letters, 705, L195

Moscadelli, L., Goddi, C., Cesaroni, R., Beltrán, M. T., & Furuya, R. S. 2007, Astronomy & Astrophysics, 472, 867

Motte, F., Andre, P., & Neri, R. 1998, Astronomy & Astrophysics, 336, 150

Mousavipour, S. H. & Saheb, V. 2007, Bulletin of the Chemical Society of Japan, 80, 1901

Muñoz Caro, G. M., Jiménez-Escobar, A., Martín-Gago, J. Á., et al. 2010, Astronomy & Astrophysics, 522, A108

Mumma, M. J. & Charnley, S. B. 2011, Annual Reviews of Astronomy & Astrophysics, 49, 471

Nagaoka, A., Watanabe, N., & Kouchi, A. 2005, The Astrophysical Journal Letters, 624, L29

Nagaoka, A., Watanabe, N., & Kouchi, A. 2007, J. Phys. Chem. A, 111, 3016

Neufeld, D. A. & Melnick, G. J. 1991, The Astrophysical Journal, 368, 215

Nguyen, T. K., Ruffle, D. P., Herbst, E., & Williams, D. A. 2002, Monthly Notices of the Royal Astronomical Society, 329, 301

Nguyen, T. L., Stanton, J. F., & Barker, J. R. 2011, The Journal of Physical Chemistry A, 115, 5118

Noble, J. A., Dulieu, F., Congiu, E., & Fraser, H. J. 2011, The Astrophysical Journal, 735, 121

Nummelin, A., Bergman, P., Hjalmarson, A., et al. 2000, The Astrophysical Journal Supplement Series, 128, 213

Oba, Y., Watanabe, N., Hama, T., et al. 2012, The Astrophysical Journal, 749, 67

Oba, Y., Watanabe, N., Kouchi, A., Hama, T., & Pirronello, V. 2010, The Astrophysical Journal Letters, 712, L174

Oba, Y., Watanabe, N., Kouchi, A., Hama, T., & Pirronello, V. 2011, Physical Chemistry Chemical Physics (Incorporating Faraday Transactions), 13, 15792

Öberg, K. I., van Dishoeck, E. F., & Linnartz, H. 2009a, Astronomy & Astrophysics, 496, 281

Öberg, K. I., Linnartz, H., Visser, R., & van Dishoeck, E. F. 2009b, The Astrophysical Journal, 693, 1209

Öberg, K. I., Boogert, A. C. A., Pontoppidan, K. M., et al. 2011a, The Astrophysical Journal, 740, 109

Öberg, K. I., Bottinelli, S., Jørgensen, J. K., & van Dishoeck, E. F. 2010, The Astrophysical Journal, 716, 825

Öberg, K. I., Fuchs, G. W., Awad, Z., et al. 2007, The Astrophysical Journal Letters, 662, L23

Öberg, K. I., Garrod, R. T., van Dishoeck, E. F., & Linnartz, H. 2009c, Astronomy & Astrophysics, 504, 891

Öberg, K. I., van der Marel, N., Kristensen, L. E., & van Dishoeck, E. F. 2011b, The Astrophysical Journal, 740, 14

Oehlers, C., Wagner, H. G., Ziemer, H., Temps, F., & Dóbé, S. 2000, The Journal of Physical Chemistry A, 104, 10500

Ohishi, M., Kawaguchi, K., Kaifu, N., et al. 1991, in Astronomical Society of the Pacific Conference Series, Vol. 16, Atoms, Ions and Molecules: New Results in Spectral Line Astrophysics, ed. A. D. Haschick & P. T. P. Ho, 387

Okabe, H. 1978, Photochemistry of small molecules

Ormel, C. W., Paszun, D., Dominik, C., & Tielens, A. G. G. M. 2009, Astronomy & Astrophysics, 502, 845

Osamura, Y., Roberts, H., & Herbst, E. 2004, Astronomy & Astrophysics, 421, 1101

Ossenkopf, V. 1993, Astronomy & Astrophysics, 280, 617

Padovani, M., Galli, D., & Glassgold, A. E. 2009, Astronomy & Astrophysics, 501, 619

Pagani, L., Vastel, C., Hugo, E., et al. 2009, Astronomy & Astrophysics, 494, 623

Parise, B., Castets, A., Herbst, E., et al. 2004, Astronomy & Astrophysics, 416, 159

Parise, B., Caux, E., Castets, A., et al. 2005, Astronomy & Astrophysics, 431, 547

Parise, B., Ceccarelli, C., Tielens, A. G. G. M., et al. 2006, Astronomy & Astrophysics, 453, 949

Parise, B., Ceccarelli, C., Tielens, A. G. G. M., et al. 2002, Astronomy & Astrophysics, 393, L49

Peeters, Z., Rodgers, S. D., Charnley, S. B., et al. 2006, Astronomy & Astrophysics, 445, 197

Perdew, J. P., Burke, K., & Ernzerhof, M. 1996a, Physical Review Letters, 78, 1396

Perdew, J. P., Burke, K., & Ernzerhof, M. 1996b, Physical Review Letters, 77, 3865

Perets, H. B. & Biham, O. 2006, Monthly Notices of the Royal Astronomical Society, 365, 801

Perets, H. B., Biham, O., Manicó, G., et al. 2005, The Astrophysical Journal, 627, 850

Persson, M. V., Jørgensen, J. K., & van Dishoeck, E. F. 2012, Astronomy & Astrophysics, 541, A39

Persson, M. V., Jørgensen, J. K., & van Dishoeck, E. F. 2013, Astronomy & Astrophysics, 549, L3

Peters, P. S., Duflot, D., Faure, A., et al. 2011, The Journal of Physical Chemistry A, 115, 8983

Peters, P. S., Duflot, D., Monnerville, M., et al. 2012, The Journal of Physical Chemistry A, submitted

Pickett, H. M., Poynter, R. L., Cohen, E. A., et al. 1998, Journal of Quantitative Spectroscopy and Radiative Transfer, 60, 883

Pickles, J. B. & Williams, D. A. 1977, Astrophysics and Space Science, 52, 443

Pierre, L., Guignes, H., & Lhuillier, C. 1985, The Journal of Chemical Physics, 82, 496

Pirronello, V., Biham, O., Liu, C., Shen, L., & Vidali, G. 1997a, The Astrophysical Journal Letters, 483, L131

Pirronello, V., Liu, C., Roser, J. E., & Vidali, G. 1999, Astronomy & Astrophysics, 344, 681

Pirronello, V., Liu, C., Shen, L., & Vidali, G. 1997b, The Astrophysical Journal Letters, 475, L69

Pizzarello, C. U. P. 2011, Origins and Evolution of Life - Cambridge University Press

Pontoppidan, K. M. 2006, Astronomy & Astrophysics, 453, L47

Pontoppidan, K. M., Boogert, A. C. A., Fraser, H. J., et al. 2008, The Astrophysical Journal, 678, 1005

Pontoppidan, K. M., Fraser, H. J., Dartois, E., et al. 2003, Astronomy & Astrophysics, 408, 981

Pontoppidan, K. M., van Dishoeck, E. F., & Dartois, E. 2004, Astronomy & Astrophysics, 426, 925

Prasad, S. S. & Huntress, Jr., W. T. 1980a, The Astrophysical Journal Supplement Series, 43, 1

Prasad, S. S. & Huntress, Jr., W. T. 1980b, The Astrophysical Journal, 239, 151

Prasad, S. S. & Tarafdar, S. P. 1983, The Astrophysical Journal, 267, 603

Qin, S., Wu, Y., Huang, M., et al. 2010, The Astrophysical Journal, 711, 399

Ratajczak, A., Quirico, E., Faure, A., Schmitt, B., & Ceccarelli, C. 2009, Astronomy & Astrophysics, 496, L21

Ratajczak, A., Taquet, V., Kahane, C., et al. 2011, Astronomy & Astrophysics, 528, L13

Raut, U. & Baragiola, R. A. 2011, The Astrophysical Journal Letters, 737, L14

Redman, M. P., Keto, E., Rawlings, J. M. C., & Williams, D. A. 2004, Monthly Notices of the Royal Astronomical Society, 352, 1365

Remijan, A., Shiao, Y., Friedel, D. N., Meier, D. S., & Snyder, L. E. 2004, The Astrophysical Journal, 617, 384

Requena-Torres, M. A., Marcelino, N., Jiménez-Serra, I., et al. 2007, The Astrophysical Journal Letters, 655, L37

Requena-Torres, M. A., Martín-Pintado, J., Martín, S., & Morris, M. R. 2008, The Astrophysical Journal, 672, 352

Requena-Torres, M. A., Martín-Pintado, J., Rodríguez-Franco, A., et al. 2006, Astronomy & Astrophysics, 455, 971

Robberto, M., Beckwith, S. V. W., Panagia, N., et al. 2005, Astronomical Journal, 129, 1534

Roberts, H., Herbst, E., & Millar, T. J. 2003, The Astrophysical Journal Letters, 591, L41

Roberts, H., Herbst, E., & Millar, T. J. 2004, Astronomy & Astrophysics, 424, 905

Roberts, H. & Millar, T. J. 2000, Astronomy & Astrophysics, 361, 388

Rodgers, S. D. & Charnley, S. B. 2003, The Astrophysical Journal, 585, 355

Romanzin, C., Ioppolo, S., Cuppen, H. M., van Dishoeck, E. F., & Linnartz, H. 2011, Journal of Chemical Physics, 134, 084504

Roser, J. E., Vidali, G., Manicò, G., & Pirronello, V. 2001, The Astrophysical Journal Letters, 555, L61

Roueff, E. & Gerin, M. 2003, Space and Science Review, 106, 61

Roueff, E., Lis, D. C., van der Tak, F. F. S., Gerin, M., & Goldsmith, P. F. 2005, Astronomy & Astrophysics, 438, 585

Ruffle, D. & Herbst, E. 2001a, Monthly Notices of the Royal Astronomical Society, 322, 770

Ruffle, D. & Herbst, E. 2001b, Monthly Notices of the Royal Astronomical Society, 324, 1054

Ruffle, D. P. & Herbst, E. 2001, Monthly Notices of the Royal Astronomical Society, 324, 1054

Sandell, G., Aspin, C., Duncan, W. D., Russell, A. P. G., & Robson, E. I. 1991, The Astrophysical Journal Letters, 376, L17

Sandford, S. A. & Allamandola, L. J. 1990, The Astrophysical Journal, 355, 357

Shalabiea, O. M., Caselli, P., & Herbst, E. 1998, The Astrophysical Journal, 502, 652

Shen, C. J., Greenberg, J. M., Schutte, W. A., & van Dishoeck, E. F. 2004, Astronomy & Astrophysics, 415, 203

Shu, F. H. 1977, The Astrophysical Journal, 214, 488

Smith, R. G., Sellgren, K., & Tokunaga, A. T. 1989, The Astrophysical Journal, 344, 413

Smoluchowski, R. 1983, The Journal of Physical Chemistry, 87, 4229

Sosa, A. & Schlegel, B. H. 1986, International Journal of Quantum Chemistry, 29, 1001

Speedy, R. J., Debenedetti, P. G., Scott Smith, R., Huang, C., & Kay, B. D. 1996, The Journal of Chemical Physics, 105, 240

Stantcheva, T., Caselli, P., & Herbst, E. 2001, Astronomy & Astrophysics, 375, 673

Stantcheva, T. & Herbst, E. 2003, Monthly Notices of the Royal Astronomical Society, 340, 983

Stantcheva, T., Shematovich, V. I., & Herbst, E. 2002, Astronomy & Astrophysics, 391, 1069

Sternberg, A., Dalgarno, A., & Lepp, S. 1987, The Astrophysical Journal, 320, 676

Sugimoto, T. & Fukutani, K. 2011, Nat Phys, 7, 307

Sutton, E. C., Peng, R., Danchi, W. C., et al. 1995, The Astrophysical Journal Supplement Series, 97, 455

Tafalla, M., Myers, P. C., Caselli, P., & Walmsley, C. M. 2004, Astronomy & Astrophysics, 416, 191

Takahashi, J. & Williams, D. A. 2000, Monthly Notices of the Royal Astronomical Society, 314, 273

Talbi, D., Chandler, G., & Rohl, A. 2006, Chemical Physics, 320, 214

Taquet, V., Ceccarelli, C., & Kahane, C. 2012a, Astronomy & Astrophysics, 538, A42

Taquet, V., Ceccarelli, C., & Kahane, C. 2012b, The Astrophysical Journal Letters, 748, L3

Taquet, V., Peters, P., Kahane, C., et al. 2012c, åsubmitted

Thi, W.-F., Woitke, P., & Kamp, I. 2010, Monthly Notices of the Royal Astronomical Society, 407, 232

Tielens, A. G. G. M. 1983, Astronomy & Astrophysics, 119, 177

Tielens, A. G. G. M. 2005, The Physics and Chemistry of the Interstellar Medium (Cambridge University Press)

Tielens, A. G. G. M. & Allamandola, L. J. 1987, in Interstellar Processes, ed. D. J. Hollenbach & H. A. Thronson, 397–469

Tielens, A. G. G. M. & Hagen, W. 1982, Astronomy & Astrophysics, 114, 245

Tielens, A. G. G. M., Tokunaga, A. T., Geballe, T. R., & Baas, F. 1991, The Astrophysical Journal, 381, 181

Troscompt, N., Faure, A., Maret, S., et al. 2009, Astronomy & Astrophysics, 506, 1243

Ulbricht, H., Moos, G., & Hertel, T. 2002, Physical Review B, 66

van der Tak, F. F. S., Schilke, P., Müller, H. S. P., et al. 2002, Astronomy & Astrophysics, 388, L53

van Dishoeck, E. F., Blake, G. A., Jansen, D. J., & Groesbeck, T. D. 1995, The Astrophysical Journal, 447, 760

van Dishoeck, E. F., Kristensen, L. E., Benz, A. O., et al. 2011, Publications of the Astronomical Society of the Pacific, 123, 138

Vastel, C., Caux, E., Ceccarelli, C., et al. 2000, Astronomy & Astrophysics, 357, 994

Vastel, C., Ceccarelli, C., Caux, E., et al. 2010, Astronomy & Astrophysics, 521, L31

Vastel, C., Phillips, T. G., & Yoshida, H. 2004, The Astrophysical Journal Letters, 606, L127

Vasyunin, A. I., Semenov, D. A., Wiebe, D. S., & Henning, T. 2009, The Astrophysical Journal, 691, 1459

Visser, R. 2009, PhD thesis, Leiden Observatory

Visser, R., Doty, S. D., & van Dishoeck, E. F. 2011, Astronomy & Astrophysics, 534, A132

Visser, R., van Dishoeck, E. F., Doty, S. D., & Dullemond, C. P. 2009, Astronomy & Astrophysics, 495, 881

Wada, A., Mochizuki, N., & Hiraoka, K. 2006, The Astrophysical Journal, 644, 300

Wakelam, V., Herbst, E., Le Bourlot, J., et al. 2010, Astronomy & Astrophysics, 517, A21

Wakelam, V., Herbst, E., Loison, J.-C., et al. 2012, The Astrophysical Journal Supplement Series, 199, 21

Wakelam, V., Selsis, F., Herbst, E., & Caselli, P. 2005, Astronomy & Astrophysics, 444, 883

Walch, S. P. 1993, Journal of Chemical Physics, 98, 3076

Walmsley, C. M., Flower, D. R., & Pineau des Forêts, G. 2004, Astronomy & Astrophysics, 418, 1035

Wang, H., Eyre, J. A., & Dorfman, L. M. 1973, J Chem Phys, 59, 5199

Warin, S., Castets, A., Langer, W. D., Wilson, R. W., & Pagani, L. 1996, Astronomy & Astrophysics, 306, 935

Watanabe, N. 2006, in Astrochemistry: Recent Successes And Current Challenges: Proceedings of the 231st Symosium of the International Astronomical Union, ed. D. Lis, G. A. Blake, & E. Herbst

Watanabe, N., Kimura, Y., Kouchi, A., et al. 2010, The Astrophysical Journal Letters, 714, L233

Watanabe, N. & Kouchi, A. 2002, The Astrophysical Journal, 567, 651

Watanabe, N. & Kouchi, A. 2008, Progress in Surface Science, 83, 439

Watanabe, N., Nagaoka, A., Shiraki, T., & Kouchi, A. 2004, The Astrophysical Journal, 616, 638

Watanabe, N., Shiraki, T., & Kouchi, A. 2003, The Astrophysical Journal Letters, 588, L121

Watson, W. D. 1976, Reviews of Modern Physics, 48, 513

Weber, A. S., Hodyss, R., Johnson, P. V., Willacy, K., & Kanik, I. 2009, The Astrophysical Journal, 703, 1030

Weinberg, W. H. 1991, Kinetics of Surface Reactions (Wiley)

Weingartner, J. C. & Draine, B. T. 2001, The Astrophysical Journal Supplement Series, 134, 263

Whittet, D. C. B., Bode, M. F., Longmore, A. J., et al. 1988, Monthly Notices of the Royal Astronomical Society, 233, 321

Whittet, D. C. B., Cook, A. M., Herbst, E., Chiar, J. E., & Shenoy, S. S. 2011, The Astrophysical Journal, 742, 28

Whittet, D. C. B., Gerakines, P. A., Hough, J. H., & Shenoy, S. S. 2001, The Astrophysical Journal, 547, 872

Whittet, D. C. B., Shenoy, S. S., Bergin, E. A., et al. 2007, The Astrophysical Journal, 655, 332

Williams, J. P., de Geus, E. J., & Blitz, L. 1994, The Astrophysical Journal, 428, 693

Wilson, T. L. & Rood, R. 1994, Annual Reviews of Astronomy & Astrophysics, 32, 191

Woon, D. E. 2002, The Astrophysical Journal, 569, 541

Yu, H.-G., Muckerman, J. T., & Sears, T. J. 2001, Chemical Physics Letters, 349, 547

Zhang, Q. & Buch, V. 1990, The Journal of Chemical Physics, 92, 5004

Appendix

Chapter A

Eckart model and quantum chemical calculations

A.1 The Eckart model

We computed the transmission probabilities of all the reactions involved in the water-producing and the methanol-producing networks by using the Eckart model (Eckart, 1930; Johnston & Heicklen, 1962). In this approach, an approximate potential energy surface (PES) is fitted as a function of the zero point energies (ZPEs) of the stationary points. The parameters needed for computing the transmission probability are the zero-point-corrected barrier heights of the forward and reverse reactions V_f and V_r, the frequency of the imaginary mode of the transition state ν_S, and the reduced mass of the reactants μ.

The Eckart potential can be parametrised as

$$U_x = \frac{A \exp\left(\frac{x-x_0}{l}\right)}{1+\exp\left(\frac{x-x_0}{l}\right)} + \frac{B \exp\left(\frac{x-x_0}{l}\right)}{\left(1+\exp\left(\frac{x-x_0}{l}\right)\right)^2} \tag{A.1}$$

where

$$A = V_f - V_r \tag{A.2}$$

$$B = \left(\sqrt{V_f} + \sqrt{V_r}\right)^2 \tag{A.3}$$

$$l = \frac{2\pi}{|\nu_S|}\sqrt{\frac{2}{\mu}}\left(\frac{1}{\sqrt{V_f}} + \frac{1}{\sqrt{V_r}}\right)^{-1}. \tag{A.4}$$

Once one has fitted the potential then the transmission probability, P_r, may be calculated using

$$P_r = \frac{\cosh(\alpha+\beta) - \cosh(\alpha-\beta)}{\cosh(\alpha+\beta) + \cosh(\delta)} \tag{A.5}$$

where

$$\alpha = \frac{4\pi}{|\nu_S|}\left(\frac{1}{\sqrt{V_f}} + \frac{1}{\sqrt{V_r}}\right)^{-1}\sqrt{E} \tag{A.6}$$

$$\beta = \frac{8\pi^2}{h|\nu_S|}\left(\frac{1}{\sqrt{V_f}} + \frac{1}{\sqrt{V_r}}\right)^{-1}\sqrt{E - V_f + V_r} \tag{A.7}$$

$$\delta = 4\pi\sqrt{\frac{V_f V_r 2\pi}{(h|\nu_S|)^2} - \frac{1}{16}}. \tag{A.8}$$

When the reactants are considered as excited by their formation involving an exothermic reaction, E refers to the excess energy of this reaction of formation. Otherwise, E is the thermal energy of the particles.

The Eckart model provides a significant improvement over square barriers but it can underpredict (or overpredict) the transmission probabilities of some reactions at low temperatures compared to more exact methods (see Peters et al., 2011). However, given the number of surface reactions considered in this work, exact quantum chemical computations for all reactions are not feasible.

A.2 Quantum chemical calculations

The OH + H_2 reaction system has been theoretically studied by Nguyen et al. (2011). These authors have computed the forward and reverse reactions, the imaginary frequency of the transition states, and the rate constants of the eight reactions involving H_2, HD, D_2, OH, and OD using the semiclassical transition-state theory (SCTST).

The H_2O_2 + H reaction has been studied by Koussa et al. (2006) and Ellingson et al. (2007). However, data for the reactions involving deuterated isotopologues was not available. Therefore, to obtain the data required for the model, quantum chemistry calculations have been conducted with the Gaussian 09 (Frisch et al., 2009) program. For these calculations, the PBE0 (Perdew et al., 1996b,a; Adamo & Barone, 1999) functional and the aug-cc-pVTZ (Dunning Jr, 1989; Kendall et al., 1992) basis set were used because this combination produced results that are in good agreement with the experimentally determined values for the process in gas-phase (Klemm et al., 1975, who measured an activation barrier of 4.6 kcal/mol = 2300 K) .

The CO + H reaction has been theoretically studied by several authors (Woon, 2002; Andersson et al., 2011; Peters et al., 2012). We decided to use the work of Peters et al. (2012) because they used the most accurate methodology and obtained a value for the activation energy for the formation of HCO that best agrees the gas-phase experiment (Wang et al., 1973). The transmission probabilities of all the reactions producing deuterated formaldehyde and methanol are computed from this reaction and relative rates measured by Nagaoka et al. (2007) and Hidaka et al. (2009) or deduced in this work (see chapter 3).

The formation of carbon dioxide includes two reactions having an activation barrier. Quantum calculations of Talbi et al. (2006); Goumans et al. (2008), and Goumans & Andersson (2010) showed that reaction (2.40) has an activation barrier of 2500 - 3000 K, leading to a transmission probability of 5×10^{-23} (Goumans & Andersson, 2010; Garrod & Pauly, 2011). Assuming an activation energy of 2500 K and considering a square barrier, we reproduce this transmission probability with a barrier width of 0.8 . The transmission probabilities of the reaction pathways involved in reaction (2.41), and including HOCO radicals, the van der Waals complex HO...CO, and their deuterated isotopologues, were deduced from the potential energy surface computed by Yu et al. (2001). These authors computed the stationary points of the potential energy surface of this reaction using an extrapolated full coupled cluster/complete basis set (FCC/CBS) method.

Chapter B

List of grain surface chemical reactions

Table B.1: List of grain surface chemical reactions considered in this work along with their activation barriers and transmission probabilities computed with the Eckart model.

Reaction							E_a (K)	P_r
H	+	H	→	(o)H_2			0	0.75
H	+	H	→	(p)H_2			0	0.25
H	+	D	→	HD			0	1
D	+	D	→	(o)D_2			0	0.66
D	+	D	→	(p)D_2			0	0.33
CO	+	H	→	HCO			1763	1.92(-07)
CO	+	D	→	DCO			/	1.92(-08)
HCO	+	H	→	H_2CO			0	1
HCO	+	D	→	HDCO			0	1
DCO	+	H	→	HDCO			0	1
DCO	+	D	→	D_2CO			0	1
H_2CO	+	H	→	CH_3O			/	9.60(-08)
H_2CO	+	D	→	CH_2DO			/	9.60(-09)
H_2CO	+	D	→	HCO	+	HD	/	9.31(-08)
H_2CO	+	D	→	HDCO	+	H	/	9.31(-08)
HDCO	+	H	→	CH_2DO			/	1.11(-07)
HDCO	+	D	→	CHD_2O			/	1.11(-07)
HDCO	+	H	→	HCO	+	HD	/	1.54(-07)
HDCO	+	D	→	DCO	+	HD	/	9.31(-08)
HDCO	+	D	→	D_2CO	+	H	/	9.31(-08)
D_2CO	+	H	→	CHD_2O			/	1.27(-07)
D_2CO	+	D	→	CD_3O			/	1.27(-08)
D_2CO	+	H	→	DCO	+	HD	/	7.30(-08)
CH_3O	+	H	→	CH_3OH			0	1
CH_3O	+	D	→	CH_3OD			0	1
CH_2OH	+	H	→	CH_3OH			0	1
CH_2OH	+	D	→	CH_2DOH			0	1
CH_2OD	+	H	→	CH_3OD			0	1
CH_2OD	+	D	→	CH_2DOD			0	1
CH_2DO	+	H	→	CH_2DOH			0	1
CH_2DO	+	D	→	CH_2DOD			0	1

CHDOH	+	H	→	CH_2DOH			0	1
CHDOH	+	D	→	CHD_2OH			0	1
CHDOD	+	H	→	CH_2DOD			0	1
CHDOD	+	D	→	CHD_2OD			0	1
CHD_2O	+	H	→	CHD_2OH			0	1
CHD_2O	+	D	→	CHD_2OD			0	1
CD_2OH	+	H	→	CHD_2OH			/	1
CD_2OH	+	D	→	CD_3OH			0	1
CD_2OD	+	H	→	CHD_2OD			0	1
CD_2OD	+	D	→	CD_3OD			0	1
CD_3O	+	H	→	CD_3OH			0	1
CD_3O	+	D	→	CD_3OD			0	1
CH_3OH	+	D	→	CH_2OH	+	HD	/	2.88(-07)
CH_2DOH	+	D	→	CHDOH	+	HD	/	1.92(-07)
CHD_2OH	+	D	→	CD_2OH	+	HD	/	1.50(-07)
CH_3OD	+	D	→	CH_2OD	+	HD	/	2.88(-07)
CH_2DOD	+	D	→	CHDOD	+	HD	/	1.92(-07)
CHD_2OD	+	D	→	CD_2OD	+	HD	/	1.50(-07)
O	+	O	→	O_2			0	1
O_2	+	O	→	O_3			0	1
O	+	H	→	OH			0	1
O	+	D	→	OD			0	1
OH	+	H	→	H_2O			0	1
OH	+	D	→	HDO			0	1
OD	+	H	→	HDO			0	1
OD	+	D	→	D_2O			0	1
OH	+	OH	→	H_2O_2			0 (R= 0.8)	1
OD	+	OH	→	HDO_2			0 (R= 0.8)	1
OD	+	OD	→	D_2O_2			0 (R= 0.8)	1
OH	+	OH	→	H_2O	+	O	0 (R=0.2)	1
OD	+	OH	→	HDO	+	O	0 (R=0.2)	1
OD	+	OD	→	D_2O	+	O	0 (R=0.2)	1
OH	+	H_2	→	H_2O	+	H	2935	4.07(-07)
OD	+	H_2	→	HDO	+	H	2855	3.62(-07)
OD	+	HD	→	D_2O	+	H	3051	1.00(-09)
OD	+	HD	→	HDO	+	D	3026	8.07(-10)
OH	+	HD	→	H_2O	+	D	2789	8.74(-07)
OH	+	HD	→	HDO	+	H	2900	2.81(-09)
OH	+	D_2	→	HDO	+	D	2703	7.99(-07)
OD	+	D_2	→	D_2O	+	D	2870	2.26(-09)
O_2	+	H	→	HO_2			0	1
O_2	+	D	→	DO_2			0	1
HO_2	+	H	→	H_2O_2			0	1
HO_2	+	D	→	HDO_2			0	1
DO_2	+	H	→	HDO_2			0	1
DO_2	+	D	→	D_2O_2			0	1
H_2O_2	+	H	→	H_2O	+	OH	2508	1.37(-07)
H_2O_2	+	D	→	HDO	+	OH	2355	5.54(-09)
HDO_2	+	H	→	HDO	+	OH	2523	1.23(-07)

HDO_2	+	H	→	H_2O	+	OD	2524	1.22(-07)
HDO_2	+	D	→	D_2O	+	OH	2369	5.28(-09)
HDO_2	+	D	→	HDO	+	OD	2367	5.29(-09)
D_2O_2	+	H	→	D_2O	+	OH	2540	1.08(-07)
D_2O_2	+	D	→	D_2O	+	OD	2384	4.28(-09)
O_3	+	H	→	O_2	+	OH	0	1
O_3	+	D	→	O_2	+	OD	0	1
N	+	H	→	NH			0	1
N	+	D	→	ND			0	1
NH	+	H	→	NH_2			0	1
NH	+	D	→	NHD			0	1
ND	+	H	→	NHD			0	1
ND	+	D	→	ND_2			0	1
NH_2	+	H	→	NH_3			0	1
NH_2	+	D	→	NH_2D			0	1
NHD	+	H	→	NH_2D			0	1
NHD	+	D	→	NHD_2			0	1
ND_2	+	H	→	NHD_2			0	1
ND_2	+	D	→	ND_3			0	1
C	+	H	→	CH			0	1
C	+	D	→	CD			0	1
CH	+	H	→	CH_2			0	1
CH	+	D	→	CHD			0	1
CD	+	H	→	CHD			0	1
CD	+	D	→	CD_2			0	1
CH_2	+	H	→	CH_3			0	1
CH_2	+	D	→	CH_2D			0	1
CHD	+	H	→	CH_2D			0	1
CHD	+	D	→	CHD_2			0	1
CD_2	+	H	→	CHD_2			0	1
CD_2	+	D	→	CD_3			0	1
CH_3	+	D	→	CH_3D			0	1
CH_2D	+	H	→	CH_3D			0	1
CH_2D	+	D	→	CH_2D_2			0	1
CHD_2	+	H	→	CH_2D_2			0	1
CHD_2	+	D	→	CHD_3			0	1
CD_3	+	H	→	CHD_3			0	1
CD_3	+	D	→	CD_4			0	1
HCO	+	O	→	CO_2	+	H	0	1
DCO	+	O	→	CO_2	+	D	0	1
CO	+	O	→	CO_2			2500	4.80(-23)
CO	+	OH	→	t-HOCO			285	3.50(-03)
CO	+	OD	→	t-DOCO			121	1.63(-01)
CO	+	OH	→	c-HOCO			2128	5.81(-17)
CO	+	OD	→	c-DOCO			1964	9.57(-16)
t-HOCO*	+		→	CO	+	OH	13050	1.63(-10)
t-HOCO*	+		→	c-HOCO			4114	1
t-HOCO	+	H	→	CO_2	+	H_2	0	1
t-HOCO	+	H	→	H_2O	+	CO	0	1

t-HOCO	+	H	→	HCOOH			0	1
t-HOCO	+	D	→	CO_2	+	HD	0	1
t-HOCO	+	D	→	HDO	+	CO	0	1
t-HOCO	+	D	→	HCOOD			0	1
c-HOCO*	+		→	t-HOCO			3272	1
c-HOCO*	+		→	CO_2	+	H	12440	2.63(-01)
c-HOCO	+		→	t-HOCO			3272	1.19(-17)
c-HOCO	+		→	CO_2	+	H	12440	2.94(-21)
c-HOCO	+	H	→	CO_2	+	H_2	0	1
c-HOCO	+	H	→	H_2O	+	CO	0	1
c-HOCO	+	H	→	HCOOH			0	1
c-HOCO	+	D	→	CO_2	+	HD	0	1
c-HOCO	+	D	→	HDO	+	CO	0	1
c-HOCO	+	D	→	HCOOD			0	1
t-DOCO*	+		→	CO	+	OD	13220	9.27(-02)
t-DOCO*	+		→	c-DOCO			4238	1
t-DOCO	+	H	→	CO_2	+	HD	0 (R=0.33)	1
t-DOCO	+	H	→	HDO	+	CO	0 (R=0.33)	1
t-DOCO	+	H	→	DCOOH			0 (R=0.33)	1
t-DOCO	+	D	→	CO_2	+	D_2	0 (R=0.33)	1
t-DOCO	+	D	→	D_2O	+	CO	0 (R=0.33)	1
t-DOCO	+	D	→	DCOOD			0 (R=0.33)	1
c-DOCO*	+		→	t-DOCO			3343	1
c-DOCO*	+		→	CO_2	+	D	13230	6.18(-02)
c-DOCO	+		→	t-DOCO			3343	1.51(-22)
c-DOCO	+	D	→	CO_2	+	D_2	0 (R=0.33)	1
c-DOCO	+	D	→	D_2O	+	CO	0 (R=0.33)	1
c-DOCO	+	D	→	DCOOD			0 (R=0.33)	1
c-DOCO	+	H	→	CO_2	+	HD	0 (R=0.33)	1
c-DOCO	+	H	→	HDO	+	CO	0 (R=0.33)	1
c-DOCO	+	H	→	DCOOH			0 (R=0.33)	1
O	+	CO	→	O...CO			0	1
O...CO	+	H	→	HO...CO			0	1
HO...CO			→	t-HOCO			775	9.46(-09)
HO...CO			→	c-HOCO			2618	8.17(-21)
HO...CO*			→	t-HOCO			775	1
HO...CO*			→	c-HOCO			2618	1
DO...CO			→	t-DOCO			727	2.97(-18)
DO...CO			→	c-DOCO			2769	1.60(-20)
DO...CO*			→	t-DOCO			727	1
DO...CO*			→	c-DOCO			2769	1

Chapter C

Publications

List of publications

[10] **V. Taquet**, C. Ceccarelli, E. Caux, S. Bottinelli, A. Coutens, C. Kahane, A. López-Sepulcre, C. Vastel 2012, *Herschel CHESS search of ozone in the solar type protostar IRAS16293-2422*, ApJL, in preparation

[9] A. López-Sepulcre, **V. Taquet**, A. Sánchez-Monge, C. Ceccarelli, C. Dominik, F. Fontani, P.T.P. Ho, C. Kahane, M. Kama, R. Neri 2012, *High angular resolution observations towards OMC-2 FIR 4: Dissecting an intermediate-mass protocluster*, A&A, submitted

[8] **V. Taquet**, A. Lopez-Sepulcre, C. Ceccarelli, R. Neri, C. Kahane, A. Coutens, C. Vastel 2012, *Arcsecond resolution observations of deuterated water towards low-mass protostars*, ApJL, submitted

[7] **V. Taquet**, P. Peters, C. Kahane, C. Ceccarelli, D. Duflot, C. Toubin, L. Wiesenfeld 2012, *Water ice deuteration: a tracer of the chemical history of protostars*, A&A, accepted

[6] C. Codella, C. Ceccarelli, B. Lefloch, F. Fontani, G. Busquet, P. Caselli, C. Kahane, D. Lis, **V. Taquet**, M. Vasta, S. Viti, L. Wiesenfeld 2012, *Fossile deuteration in the protostellar shock L1157-B1*, ApJL, 757, L9 [URL]

[5] A. Bacmann, **V. Taquet**, A. Faure, C. Kahane, C. Ceccarelli 2012, *Detection of complex organic molecules in a prestellar core: a new challenge for astrochemical models*, A&A, 541, L12 [URL]

[4] **V. Taquet**, C. Ceccarelli, C. Kahane 2012, *Formaldehyde and methanol deuteration in protostars: fossiles from a past fast high density pre-collapse phase*, ApJL, 748, L3 [URL]

[3] **V. Taquet,** C. Ceccarelli, C. Kahane 2012, *Multilayer modeling of grain porous surface chemistry I. The GRAINOBLE code*, A&A, 538, 42 [URL]

[2] A. Ratajczak, **V. Taquet**, C. Kahane, C. Ceccarelli, A. Faure, E. Quirico 2011, *The puzzling deuteration of methanol in low- to high- mass protostars*, A&A, 528, 13 [URL]

[1] F. Pignatale, S. Maddison, **V. Taquet**, G. Brooks, K. Liffman 2011, *The effect of the regular solution model in the condensation of protoplanetary dust*, MNRAS, 506 [URL]

Published or submitted publications are shown in the following pages.

A&A 528, L13 (2011)
DOI: 10.1051/0004-6361/201016402

Astronomy & Astrophysics

L E

The puzzling deuteration of methanol in low- to high-mass protostars⋆

A. Ratajczak, V. Taquet, C. Kahane, C. Ceccarelli, A. Faure, and E. Quirico

UJF-Grenoble 1/CNRS, Institut de Planétologie et d'Astrophysique de Grenoble (IPAG) UMR 5274, 38041 Grenoble, France
e-mail: afaure@obs.ujf-grenoble.fr

Received 23 December 2010 / Accepted 16 February 2011

ABSTRACT

Context. The current theory of methanol deuteration on interstellar grains predicts that the abundance ratio of the singly deuterated isotopologues [CH_2DOH]/[CH_3OD] should always be ∼3. In warm regions where grain mantles have sublimated, gaseous methanol is detectable via its rotational transitions. In previous observational studies, the gas-phase [CH_2DOH]/[CH_3OD] ratio was measured and found to be significantly larger than 3 in low-mass protostars and close to 1 in the Orion IRc2 massive hot core.
Aims. We present new measurements of the gas-phase [CH_2DOH]/[CH_3OD] ratio in two additional high-mass protostars, as well as in two intermediate-mass protostars, to either confirm or exclude the dependence of this ratio on the mass of the protostar.
Methods. The observations were carried out using the IRAM-30 m telescope. Several rotational lines of each isotopologue were detected toward the intermediate-mass protostars, while only CH_3OD lines were detected in the massive hot cores. The ratio [CH_2DOH]/[CH_3OD] (or its upper limit) was computed from both the averaged column densities and directly from line flux ratios.
Results. Our results confirm that the [CH_2DOH]/[CH_3OD] ratio is substantially lower in massive hot cores than in (low-mass) hot-corinos, by typically one order of magnitude. Furthermore, they suggest that intermediate-mass protostars have similar properties to low-mass protostars.
Conclusions. The measured [CH_2DOH]/[CH_3OD] ratios are inconsistent with the current theory of methanol deuteration, independently of the mass of the source. While the large ratios measured in low- and intermediate-mass sources can be explained qualitatively by various selective depletion mechanisms, the small ratios (<2) measured toward massive hot cores are puzzling. A revision of the deuterium chemistry in hot cores is suggested.

Key words. molecular processes – stars: protostars – ISM: molecules

1. Introduction

Since the first detection of a deuterated isotopologue in space (DCN, Jefferts et al. 1973), molecular deuteration has been considered as a powerful diagnostic tool for studying the physical conditions and past history of the interstellar gas (see for example the reviews by Roueff & Gerin 2003 and Ceccarelli et al. 2007). Among the various molecules with high degrees of deuteration, methanol is a particularly interesting one, for several reasons. First the detection of the (gaseous) triply deuterated methanol with an abundance of a few percent with respect to the hydrogenated counterpart makes it the most deuterium-enriched molecule so far known (Parise et al. 2004). Second, theoretical and experimental studies predict that methanol is formed on the grain surfaces rather than in the gas-phase (Garrod et al. 2006). Thus, the measurements of methanol deuteration permit us to study, almost unambiguously (see below), the process(es) on the grain surfaces. The link with observations is however complicated. This is firstly because there are at least two ways to form methanol on the surfaces: either by addition of hydrogen atoms on iced CO (e.g. Nagaoka et al. 2005) or by the photolysis or radiolysis of an iced mixture of methane, CO, and water (e.g. Hudson & Moore 1999; Wada et al. 2006). Deuteration is expected to be very different in the two cases and, specifically, much higher in the first case. Secondly, the alteration of the deuteration degree can occur on the grain surfaces via H/D atom exchanges both because of thermal activation (Ratajczak et al. 2009) or, again, photolysis (Weber et al. 2009). In addition, when solid methanol sublimates, it can undergo chemical reactions in the gas phase, which may again alter the original deuteration degree set on the grain surfaces (Charnley et al. 1997; Osamura et al. 2004). Despite the complications and thanks to them, deuterated methanol is a tool rich in information.

Previous studies toward low mass protostars have shown that the singly deuterated methanol CH_2DOH can be almost as abundant as CH_3OH (e.g. Parise et al. 2006), a property observed in several other deuterated molecules in low mass protostars, although to a lesser extent (Ceccarelli et al. 2007). This large deuteration very likely implies that, in low mass protostars, methanol was formed during the pre-collapse, cold, and dense phase. Surprisingly, however, the other form of singly deuterated methanol, CH_3OD, is much less abundant, by more than a factor of 10. According to the grain chemistry statistical model of Charnley et al. (1997), if the deuterated isotopologues of methanol are formed by H/D atoms addition to CO on the grain surfaces, the abundance of CH_2DOH should always be only a factor of ∼3 larger than the CH_3OD one. To make the situation even more puzzling, the same [CH_2DOH]/[CH_3OD] ratio is close to 1 in the high-mass protostar Orion IRc2 (Jacq et al. 1993). This difference between high- and low-mass protostars

⋆ Table A.1 is only available in electronic form at http://www.aanda.org

might reflect different deuteration degrees and/or ice compositions, as suggested by Ratajczak et al. (2009). On the other hand, no other measurement of the [CH_2DOH]/[CH_3OD] ratio exists in high-mass protostars other than Orion IRc2, so that the measured low [CH_2DOH]/[CH_3OD] ratio may be peculiar to this source, itself peculiar in many other aspects.

In this Letter, we present new measurements of the [CH_2DOH]/[CH_3OD] ratio in two additional high-mass protostars, which confirm the low value measured in Orion IRc2. In addition, we present observations of deuterated methanol in intermediate mass protostars. As shown by Crimier et al. (2010), intermediate mass protostars are in several aspects also intermediate in the characteristics between low- and high-mass protostars. Their case can therefore help us to understand why the [CH_2DOH]/[CH_3OD] ratio is so different at the two extremes of the mass range.

2. Observations and data reduction

The observations were carried out using the IRAM-30 m telescope in June 2010. Two frequency ranges were observed simultaneously with the new broad-band EMIR receivers, one centered at 110.2 GHz, the other at 134.0 GHz. At these frequencies, the 30 m telescope HPBW is, respectively, 22″ and 18″ and the main beam efficiency is close to 0.78. Each receiver was equipped with two channels corresponding to orthogonal linear polarizations and showed image rejections higher than 20 dB when operating in single sideband mode. The broad-band autocorrelator WILMA, divided into four parts, each providing a spectral resolution of 2 MHz and a frequency coverage of 3.7 GHz, was associated with the four channels. In addition, a high resolution autocorrelator, VESPA, was divided into two parts, one centered at 110.2 GHz covering 140 MHz with a spectral resolution of 80 kHz, the second centered at 134.0 GHz with a coverage of 290 MHz and a resolution of 310 kHz. The system temperatures were between 95 K and 115 K at 134 GHz and between 155 K and 180 K at 110 GHz. Observations were performed in wobbler-switch mode, with a 90″ throw at a rate of 0.5 Hz. The temperature scale was calibrated every 15 min using two absorbers at different temperatures and the calibration uncertainty (1σ) is about 15% of the line flux at both frequency ranges. The pointing and focus were checked every two hours on planets and continuum radio sources close to the targets. Effective on-source integration times were 45 min for G24.78, 140 min for OMC2, and 210 min for CepE and W3(H2O), where both polarisation channels were added (after checking that the line intensities were identical).

The deuterated methanol lines detected in the high resolution spectra were fitted with Gaussian profiles using the CLASS tool[1] and the frequencies given in Parise et al. (2002). For the CH_3OH lines detected in the broad-band spectra, we used the CASSIS package[2] and the spectroscopic data from the CDMS database (Müller et al. 2001, 2004, and references therein) to perform the line identification and the Gaussian fit. In both cases, only linear baselines were subtracted from the spectra.

3. Data analysis

Table A.1 presents the results of Gaussian fits to our observations for CH_3OH and its two isotopologues CH_2DOH and CH_3OD.

[1] http://www.iram.fr/IRAMFR/GILDAS
[2] http://cassis.cesr.fr

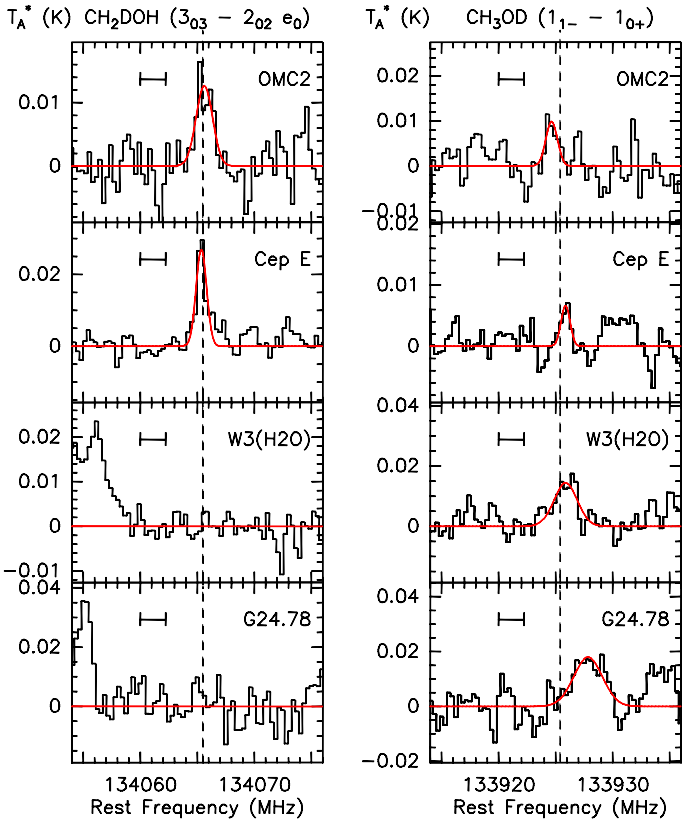

Fig. 1. CH_2DOH and CH_3OD spectra towards the four sources. The observed positions and the assumed v_{LSR} rest velocities are the following: OMC2 FIR4 (05:35:26.7, –05:09:59), 10.5 km s^{-1}; CepheusE (23:03:12.7, +61:42:27), –11.4 km s^{-1}; W3(H_2O) (02:27:04.6, +61:52:26), –48.0 km s^{-1}; G24.78+0.08 (18:36:12.6, –07:12:11), 111.0 km s^{-1}. The line intensities are expressed in antenna temperature scale. The curves are Gaussian fits to the detected lines and the dashed lines indicate the expected frequencies of the lines. The small horizontal segment has a width of 5 km s^{-1}. The broad feature right to the CH_3OD line in Cep E includes the CH_2DOH line (3_{21}–2_{20} e1) at 133930.2 GHz. The CH_3OD line in G24.78+0.08 appears at a significantly velocity shift so that its identification must be considered as uncertain.

The spectra of the CH_2DOH 3_{03}–2_{02} e_0 and the CH_3OD 1_{1-}–1_{0+} transitions are plotted in Fig. 1.

Assuming that the spatial distribution of both isotopologues is the same in the region probed by the observations, the [CH_2DOH]/[CH_3OD] abundance ratio is simply equal to the column density ratio. In addition, if the lines are optically thin and the populations of all molecular energy levels in thermodynamical equilibrium are at the same rotational temperature T_{rot}, then for each isotopologue (i) the total column density N_i can be derived from the line flux W_i of any of its transitions by the relation:

$$N_i = \left(\frac{3k_b W_i}{8\pi^3 \nu_i (\mu^2 S)_i}\right) Z_i(T_{rot}) \exp\left[\frac{E_{u,i}}{k_b T_{rot}}\right], \quad (1)$$

where $Z_i(T_{rot})$ is the partition function and ν_i the frequency of the transition from the upper level of energy $E_{u,i}$, corresponding to the effective line strength $(\mu^2 S)_i$. Thus, the [CH_2DOH]/[CH_3OD] ratio can be derived directly from any line flux ratio using

$$\frac{N_1}{N_2} = \left(\frac{W_1}{W_2}\right) \frac{Z_1(T_{rot})\nu_2(\mu^2 S)_2}{Z_2(T_{rot})\nu_1(\mu^2 S)_1} \exp\left[\frac{E_{u,1} - E_{u,2}}{k_b T_{rot}}\right], \quad (2)$$

where Eqs. (1) and (2) refer respectively to CH_2DOH and CH_3OD. The rotational partition functions were computed within the rigid-rotor approximation, assuming that the rotational temperature is much higher than the largest rotational constant (here $A(CH_3OH) \sim 6$ K). The corresponding expression for CH_3OH and CH_3OD, neglecting the energy difference between the A and E symmetry species, is simply twice the normal asymmetric rotor function

$$Z(T) = 2\sqrt{\frac{\pi}{ABC}\left(\frac{k_b T}{h}\right)^3}. \quad (3)$$

We thus obtain $Z(T) = 1.23T^{3/2}$ for CH_3OH and $Z(T) = 1.42T^{3/2}$ for CH_3OD. In the case of CH_2DOH, the energy difference between the e_0, e_1, and o_1 symmetry species cannot be neglected and the partition function is given by (Parise 2004):

$$Z(T) = 0.75T^{3/2}\left[1 + \exp(-13.4/T) + \exp(-18.3/T)\right]. \quad (4)$$

Thus, the estimate of the abundance ratio depends on the assumed rotational temperature. In practice, however, this ratio was found to be essentially insensitive to rotational temperatures in the range 20−220 K. As the number of detected lines for the deuterated species is too small to get a reliable estimate of T_{rot} using the rotational diagram method, the rotational temperature was derived from the lines of the main isotopologue CH_3OH, assuming that the rotational temperature is similar for all three isotopologues. For each source, the rotational temperature and the CH_3OH column density are reported in Table 1.

Once the rotational temperature of methanol isotopologues is known, the $[CH_2DOH]/[CH_3OD]$ ratio can be computed via two methods: *i)* total column densities of CH_2DOH and CH_3OD can be estimated from each of the detected lines using Eq. (1). The ratio of the averaged column densities provides a first measure of the $[CH_2DOH]/[CH_3OD]$ ratio. This method however requires us to take into account the calibration uncertainty in each line, since data coming from both frequency ranges are used. The results are shown in Col. 7 of Table 1. *ii)* Using Eq. (2), we can obtain as many abundance ratios as there are pairs formed with CH_2DOH and CH_3OD lines. However, some of these pairs allow us to achieve a better precision than others. They have to satisfy two criteria: the upper levels must be close in energy and the lines must belong to the same frequency band to be able to ignore the calibration uncertainty. In practice, in our data, a single pair of lines satisfies both criteria and the ratios derived by this method are given in column 6 of Table 1. It is observed that both methods give essentially the same result, within the estimated uncertainties, suggesting the reliability of the derived ratios. These results clearly show that in the two observed intermediate-mass protostars, the $[CH_2DOH]/[CH_3OD]$ ratio is larger than 3 and much higher than the ratios in high-mass protostars. For these latter, only upper limits of the ratio were derived because no line of CH_2DOH was detected. Implications of these results are discussed in detail below.

4. Discussion and conclusions

In Fig. 2, we have plotted the $[CH_2DOH]/[CH_3OD]$ ratio as a function of the luminosity of the protostars for all the sources (except G24.78+0.08) where this ratio has been measured so far. In addition to the present observations, we have thus included a sample of low-mass protostars (Parise et al. 2006), as well as the hot-core Orion IRc2 (Jacq et al. 1993). Our results confirm that the $[CH_2DOH]/[CH_3OD]$ ratio is substantially

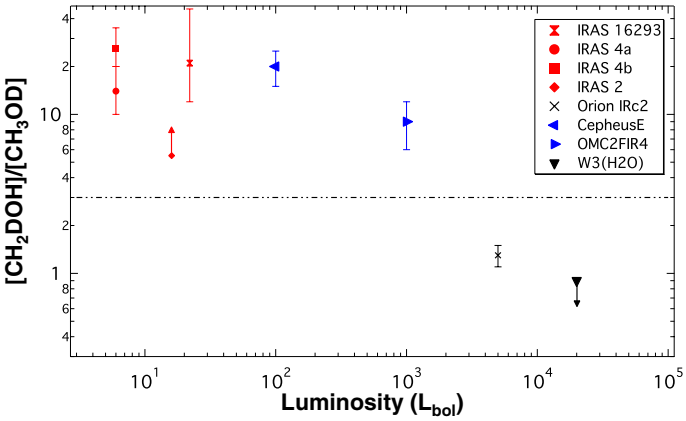

Fig. 2. $[CH_2DOH]/[CH_3OD]$ ratio as a function of the protostar luminosity. Low-mass data (IRAS 16293, IRAS 4a, IRAS 4b and IRAS 2) were taken from Parise et al. (2006), while the data for Orion IRc2 is from Jacq et al. (1993). The upper limit reported in Table 1 for G24.78+0.08 is not plotted because of the uncertain identification of the CH_3OD line at 133.9254 GHz. The horizontal dashed line refers to the value predicted by grain chemistry models (Charnley et al. 1997).

lower in massive hot cores than in (low-mass) hot-corinos, by typically one order of magnitude. Furthermore, they suggest that intermediate-mass protostars have similar properties to low-mass protostars. We have also found that in all sources, the observed $[CH_2DOH]/[CH_3OD]$ ratio significantly differs from the value of 3 predicted by the grain chemistry models of Charnley et al. (1997) and Osamura et al. (2004). In low- and intermediate- mass protostars, this ratio is much greater than 3, while in high-mass protostars it is significantly lower. As a result, whatever the mass of the source, the observed gas-phase $[CH_2DOH]/[CH_3OD]$ ratio is inconsistent with the current theory of methanol deuteration in the grain mantles, that is via additions of H/D atoms on solid CO. Alternative or additional processes in solid-state and/or in the post-evaporative gas-phase must be at play in the hot cores/corinos. We now discuss the different possibilites based on theoretical and laboratory works.

For low- and intermediate-mass protostars, various mechanisms have been suggested to explain the much lower abundance of CH_3OD compared to CH_2DOH. First, CH_3OD could be selectively destroyed in the gas-phase via protonation reactions because the dissociative recombination (DR) of CH_2DOH^+ reforms CH_2DOH, while the DR of CH_3ODH^+ leads to both CH_3OD and CH_3OH (Charnley et al. 1997; Osamura et al. 2004). Second, laboratory experiments have suggested that H/D exchange reactions in solid state might contribute to reducing the CH_3OD abundance. Thus, in the experiment of Nagaoka et al. (2005), the deuterium enrichment was found to proceed via H/D substitution in solid CH_3OH leading to the formation of methyl-deuterated methanol isotopologues, but no CH_3OD. An alternative solid-state depletion mechanism was proposed by Ratajczak et al. (2009): in their experiment, rapid H/D exchanges between CD_3OD and H_2O ices were found to occur at $T \sim 120$ K on the hydroxyl (-OD) functional group of methanol, resulting in CD_3OH and HDO molecules.

All the previous mechanisms can thus *qualitatively* explain a much lower abundance of CH_3OD compared to CH_2DOH, as observed in low- and intermediate-mass protostars. The reverse behavior, as observed unambiguously in W3(H_2O) and Orion IRc2, is more difficult to understand. We note, however, that the gas temperature in massive hot cores may be significantly higher than in low- and intermediate-mass protostars, as

Table 1. Isotopologue ratios $[CH_2DOH]/[CH_3OD]$ in low-, intermediate- and high-mass protostars, luminosities and distances of the sources, column densities ($\times 10^{15}$ cm^{-2}) and rotational temperatures of CH_3OH.

Source	Luminosity ($L_\odot$)	Distance (pc)	$N_{tot}(CH_3OH)$	$T_{rot}(CH_3OH)$ (K)	$[CH_2DOH]/[CH_3OD]$	$\langle[CH_2DOH]\rangle/\langle[CH_3OD]\rangle$
IRAS 4A[a]	6	2.2×10^2	0.7 ± 0.1	38 ± 3		14^{+6}_{-4}
IRAS 4B[a]	6	2.2×10^2	0.8 ± 0.3	85 ± 17		26^{+9}_{-6}
IRAS 2[a]	16	2.2×10^2	1.1 ± 0.4	207 ± 48		> 5.5
IRAS 16293[a]	27	1.6×10^2	3.5 ± 0.4	85 ± 6		21^{+25}_{-9}
Cepheus E[b]	1×10^2	7.3×10^2	$0.5^{+0.8}_{-0.3}$	44 ± 31	20 ± 5	18 ± 5
OMC2FIR4[b]	1×10^3	4.4×10^2	$1.4^{+2}_{-0.8}$	48 ± 24	9 ± 3	8 ± 7
Orion IRc2[c]	5×10^3	4.5×10^2	84 ± 8.0	112 ± 11		$1.1 - 1.5$
W3(H2O)[d]	2×10^4	2×10^3	13^{+3}_{-2}	133 ± 17	<0.9	
G24.78+0.08[e]	$\leq 7 \times 10^4$	7.7×10^3	9.3^{+7}_{-4}	113 ± 44	$<1.4^*$	

Notes. The column $[CH_2DOH]/[CH_3OD]$ contains abundance ratios derived from the line pair 134.0655 GHz (for CH_2DOH) and 133.9254 GHz (for CH_3OD), which shows similar E_{up} ($\Delta E_{up} \sim 4.2$ K); the column $\langle[CH_2DOH]\rangle/\langle[CH_3OD]\rangle$ contains ratios derived from averaged column densities (see text). Data for low-mass protostars (IRAS 16293, IRAS 4a, IRAS 4b and IRAS 2) and Orion IRc2 were taken respectively from Parise et al. (2002, 2006) and Jacq et al. (1993), and references therein. The asterisk refers the uncertain identification of the CH_3OD line (133.9254 GHz) in G24.78+0.08.

References. For luminosities and distances: [a] Parise et al. (2006); [b] Crimier et al. (2009, 2010); [c] Robberto et al. (2005); [d] Bisschop et al. (2007); [e] Moscadelli et al. (2007).

suggested for example by the CH_3OH rotational temperatures reported in Table 1 (with the exception of the value measured in IRAS 2). Temperature effects might thus explain the difference in the measured $[CH_2DOH]/[CH_3OD]$ ratios. Following the pioneering work of Charnley et al. (1997), Osamura et al. (2004) investigated the impact of increasing the gas temperature from 50 to 100 K, using a hot core chemistry network. The $[CH_2DOH]/[CH_3OD]$ ratio was found to decrease from greater than 3 at 50 K to ~1 at 100 K. This effect was attributed to the reaction between CH_3OH and H_2DO^+ (which is the major deuteron donor at 100 K)

$$H_2DO^+ + CH_3OH \rightarrow CH_3OHD^+ + H_2O, \quad (5)$$

followed by dissociative recombination. However, an unrealistically large initial abundance ratio $[HDO]/[H_2O] \sim 0.1$ was necessary to decrease the $[CH_2DOH]/[CH_3OD]$ ratio below 3. Isomerization processes were finally proposed by Charnley et al. (1997) to explain the finding that $[CH_2DOH] \sim [CH_3OD]$ in Orion IRc2. The quantum calculations of Osamura et al. (2004) demonstrated, however, that internal rearrangements of energized methanol (in the neutral, ionized, or protonated forms) cannot occur efficiently.

We are thus compelled to conclude that the deuteration of methanol in massive hot cores, where the abundance of CH_2DOH is at most similar to that of CH_3OD, remains enigmatic. It is possibly related to the lower deuterium enrichment of massive protostars compared to low-mass sources (Ceccarelli et al. 2007). We also note that since the distances of the high-mass protostars are significantly larger than those of low- and intermediate-mass sources, the region probed by the observations is much larger in the high-mass objects. This may affect the measurements of the $[CH_2DOH]/[CH_3OD]$ ratio if the (large-scale) spatial distribution of both isotopologues is different. In any case, additional laboratory and theoretical studies are needed, in particular on H/D exchange processes in ices. A revision of the deuterium chemistry in hot cores also seems necessary. In this context, we note that Thi et al. (2010) demonstrated that a high $[HDO]/[H_2O]$ ratio ($>10^{-2}$) can be obtained in dense ($n_H > 10^6$ cm^3) and warm gas ($T = 100-1000$ K) owing to photodissociation and neutral-neutral reactions. In addition to modeling efforts, new observations are also crucial to assessing whether the methanol deuteration is peculiar or whether a similar selective deuteration affects other interstellar species with various functional groups, e.g. $HCOOCH_3$, $HCONH_2$, and CH_3NH_2. The detection of new multiply deuterated species (e.g. CH_2DOD) is also fundamental to helping us to discriminate between the different classes of fractionation/depletion processes.

Acknowledgements. We are deeply thankful to the IRAM staff for assistance during remote observations at the IRAM-30 m telescope. We thank an anonymous referee for constructive comments, which have contributed to improve this manuscript. This work has been supported by l'Agence Nationale pour la Recherche (ANR), France (contract ANR-08-BLAN-022).

References

Bisschop, S. E., Jørgensen, J. K., van Dishoeck, E. F., & de Wachter, E. B. M. 2007, A&A, 465, 913
Ceccarelli, C., Caselli, P., Herbst, E., Tielens, A. G. G. M., & Caux, E. 2007, Protostars and Planets V, 47
Charnley, S. B., Tielens, A. G. G. M., & Rodgers, S. D. 1997, ApJ, 482, L203
Crimier, N., Ceccarelli, C., Lefloch, B., & Faure, A. 2009, A&A, 506, 1229
Crimier, N., Ceccarelli, C., Alonso-Albi, T., et al. 2010, A&A, 516, A102
Garrod, R., Park, I. H., Caselli, P., & Herbst, E. 2006, Faraday Discussions, 133, 51
Hudson, R. L., & Moore, M. H. 1999, Icarus, 140, 451
Jacq, T., Walmsley, C. M., Mauersberger, R., et al. 1993, A&A, 271, 276
Jefferts, K. B., Penzias, A. A., & Wilson, R. W. 1973, ApJ, 179, L57
Moscadelli, L., Goddi, C., Cesaroni, R., Beltrán, M. T., & Furuya, R. S. 2007, A&A, 472, 867
Müller, H. S. P., Thorwirth, S., Roth, D. A., & Winnewisser, G. 2001, A&A, 370, L49
Müller, H. S. P., Menten, K. M., & Mäder, H. 2004, A&A, 428, 1019
Nagaoka, A., Watanabe, N., & Kouchi, A. 2005, ApJ, 624, L29
Osamura, Y., Roberts, H., & Herbst, E. 2004, A&A, 421, 1101
Parise, B. 2004, PhD Thesis, Université Toulouse III, France
Parise, B., Ceccarelli, C., Tielens, A. G. G. M., et al. 2002, A&A, 393, L49
Parise, B., Castets, A., Herbst, E., et al. 2004, A&A, 416, 159
Parise, B., Ceccarelli, C., Tielens, A. G. G. M., et al. 2006, A&A, 453, 949
Ratajczak, A., Quirico, E., Faure, A., Schmitt, B., & Ceccarelli, C. 2009, A&A, 496, L21
Robberto, M., Beckwith, S. V. W., Panagia, N., et al. 2005, AJ, 129, 1534
Roueff, E., & Gerin, M. 2003, Space Sci. Rev., 106, 61
Thi, W., Woitke, P., & Kamp, I. 2010, MNRAS, 407, 232
Wada, A., Mochizuki, N., & Hiraoka, K. 2006, ApJ, 644, 300
Weber, A. S., Hodyss, R., Johnson, P. V., Willacy, K., & Kanik, I. 2009, ApJ, 703, 1030

Table A.1. Parameters of the observed CH_3OH, CH_2DOH, and CH_3OD transitions.

Transition	Frequency (GHz)	Spectroscopic parameter $\mu^2 S$ (Deb^2)	E_{up} (cm^{-1})	$\int T_{mb} dv$ OMC2FIR4	CepheusE	W3(H_2O)	G24.78+0.08
CH_3OH					K km s^{-1}		
$0_{(+0),0}-1_{(-1),1}$ E	108.8939	1.0	9.03	1.43 ± 0.01	0.49 ± 0.01	4.68 ± 0.03	9.45 ± 0.02
$14_{(+5),10}-15_{(+4),11}$ E	109.1387	3.4	264	(0.04)	(0.03)	1.09 ± 0.03	0.82 ± 0.02
$16_{(-2),15}-16_{(+1),15}$ E	109.1531	3.7	238	(0.04)	(0.03)	0.92 ± 0.03	0.77 ± 0.03
$7_{2,5}-8_{1,8}$ A	111.2896	2.3	71.6	0.25 ± 0.01	(0.03)	3.97 ± 0.03	2.16 ± 0.04
$6_{2,5}-7_{1,6}$ A	132.6219	2.0	59.6	0.48 ± 0.02	0.07 ± 0.01	6.80 ± 0.19	2.54 ± 0.05
$6_{(-1),6}-5_{(+0),5}$ E	132.8907	3.7	37.5	11.30 ± 0.04	2.81 ± 0.01	11.09 ± 0.10	21.03 ± 0.04
$5_{(-2),4}-6_{(-1),6}$ E	133.6055	1.6	42.4	0.62 ± 0.03	(0.03)	4.77 ± 0.03	2.58 ± 0.02
$12_{(-3),10}-13_{(-2),12}$ E	134.2311	3.9	170	(0.03)	0.09 ± 0.01	3.61 ± 0.03	1.50 ± 0.02
$8_{2,7}-7_{3,4}$ A	134.8970	1.8	84.1	0.93 ± 0.01	0.21 ± 0.01	4.55 ± 0.04	2.69 ± 0.03
$8_{2,6}-7_{3,5}$ A	135.3768	1.8	84.1	0.33 ± 0.01	(0.03)	4.14 ± 0.07	2.20 ± 0.02
CH_2DOH					mK km s^{-1}		
$9_{18}-9_{09}$ o1	110.1054	3.3	83.4	(32)	(46)	(73)	(103)
$3_{03}-2_{02}$ e1	133.8473	1.1	18.3	24 ± 9	(35)	(90)	(95)
$3_{03}-2_{02}$ o1	133.8729	1.1	21.7	(27)	35 ± 7	(25)	(41)
$3_{22}-2_{21}$ o1	133.8818	0.6	33.6	(27)	(25)	(29)	(57)
$3_{22}-2_{21}$ e1	133.8929	0.6	27.4	(27)	(25)	(29)	(57)
$3_{21}-2_{20}$ o1	133.8974	0.6	33.6	41 ± 8	(24)	(29)	(57)
$3_{21}-2_{20}$ e1	133.9302	0.6	27.4	(28)	37 ± 6	(37)	(48)
$3_{03}-2_{02}$ e0	134.0655	1.2	8.90	66 ± 7	89 ± 4	(27)	(49)
$3_{22}-2_{21}$ e0	134.1124	0.7	20.2	(28)	(19)	(24)	(54)
$3_{21}-2_{20}$ e0	134.1854	0.7	20.2	25 ± 9	(29)	(72)	(69)
CH_3OD					mK km s^{-1}		
1_1-1_0	110.1889	1.6	7.8	(40)	(40)	(40)	(94)
2_1-2_0	110.2626	2.7	10.8	57 ± 11	(45)	93 ± 18	(95)
3_1-3_0	110.4758	3.8	15.4	(55)	(43)	(67)	(108)
$1_{1-}-1_{0+}$	133.9254	3.2	6.00	28 ± 6	17 ± 4	116 ± 12	141 ± 16*

Notes. Fluxes are expressed in main-beam temperature unit. Upper limits (in parentheses) are given at 3σ and include both statistical and calibration uncertainties. In contrast, for the detected lines, only 1σ statistical uncertainties are given; total uncertainties are given by the quadratic sum of these statistical uncertainties and of 15% calibration uncertainties. According to the detected CH_3OH lines, upper limits for both isotopologues were estimated using linewidths of 5 km s^{-1}, except for low resolution spectra (velocity resolution of ~5 km s^{-1}) where linewidths of 9 km s^{-1} were assumed. We have also checked that the relative intens ities of the detected lines and the upper limits on the other lines from CH_2DOH and CH_3OD are consistent with predictions at local thermodynamic equilibrium to within a factor two. The asterisk denotes the uncertain identification of the CH_3OD line (133.9254 GHz) in G24.78+0.08.

A&A 538, A42 (2012)
DOI: 10.1051/0004-6361/201117802

Astronomy & Astrophysics

Multilayer modeling of porous grain surface chemistry

I. The GRAINOBLE model

V. Taquet, C. Ceccarelli, and C. Kahane

UJF-Grenoble 1/CNRS-INSU, Institut de Planétologie et d'Astrophysique de Grenoble (IPAG) UMR 5274, 38041 Grenoble, France
e-mail: vianney.taquet@obs.ujf-grenoble.fr

Received 1 August 2011 / Accepted 10 November 2011

ABSTRACT

Context. Mantles of iced water mixed with carbon monoxyde, formaldehyde, and methanol are formed during the so-called prestellar core phase. In addition, radicals are also thought to be formed on the grain surfaces, and to react to form complex organic molecules later on, during the so-called warm-up phase of the protostellar evolution.
Aims. We aim to study the formation of the grain mantles during the prestellar core phase and the abundance of formaldehyde, methanol, and radicals trapped in them.
Methods. We have developed a macrosopic statistic multilayer model that follows the formation of grain mantles with time and that includes two effects that may increase the number of radicals trapped in the mantles: i) during the mantle formation, only the surface layer is chemically active and not the entire bulk; and ii) the porous structure of grains allows the trapping reactive particles. The model considers a network of H, O, and CO forming neutral species such as water, CO, formaldehyde, and methanol, plus several radicals. We ran a large grid of models to study the impact of the mantle multilayer nature and grain porous structure. In addition, we explored how the uncertainty of other key parameters influences the mantle composition.
Results. Our model predicts relatively high abundances of radicals, especially of HCO and CH_3O (10^{-9}–10^{-7}). In addition, the multilayer approach enables us to follow the chemical differentiation within the grain mantle, showing that the mantles are far from being uniform. For example, methanol is mostly present in the outer layers of the mantles, whereas CO and other reactive species are trapped in the inner layers. The overall mantle composition depends on the density and age of the prestellar core as well as on some microscopic parameters, such as the diffusion energy and the hydrogenation reactions activation energy. Comparison with observations allows us to constrain the value of the last two parameters (0.5–0.65 and 1500 K, respectively) and provide some indications on the physical conditions during the formation of the ices.

Key words. astrochemistry – ISM: abundances – ISM: clouds – ISM: molecules – molecular processes – stars: formation

1. Introduction

Among the 150 molecules that have been detected in the interstellar medium (ISM) so far, a significant number are complex organic molecules (COMs), carbon bearing molecules with more than five atoms. Several COMs have been observed in large quantities for two decades in the warm and dense hot cores of massive protostars (Blake et al. 1987). They have received renewed interest in the last few years after the detection of abundant COMs in solar-type protostars, specifically in hot corinos (Cazaux et al. 2003; Bottinelli et al. 2007), and in the clouds of the Galactic Center (Requena-Torres et al. 2006).

Astrochemical models have shown that many COMs cannot be produced efficiently in the gas phase. Horn et al. (2004), for example, predicted methyl formate abundances to be less than 10^{-10} by considering formation pathways only in the gas phase, but this molecule has been detected with abundances up to 10^{-6} (see references in the caption of Fig. 1). On the other hand, several observational and experimental works have highlighted the catalytic behaviour of interstellar grains for chemical reactions. First, infrared (IR) observations of protostellar sources carried out with space or ground-based telescopes have shown that formaldehyde and methanol can be significant components of the grain mantles with fractional abundances up to 30% with respect to water in some cases (Gibb et al. 2004; Boogert et al. 2008). These mantles are believed to be formed during the cold and dense prestellar core phase mainly via hydrogenation and oxydation of CO and O. Second, several laboratory experiments simulating cold cloud conditions have confirmed the efficiency of the hydrogenation processes. Watanabe & Kouchi (2002) for instance have succeeded in producing solid formaldehyde and methanol at low temperature (∼10 K) via CO hydrogenation reactions in a CO-H_2O ice mixture.

Modelling the chemistry on the grain surfaces is therefore crucial if we aim to understand the formation of COMs on the interstellar grains. Over the past 30 years, several numerical methods based on ab initio (Allen & Robinson 1977), Monte Carlo (Tielens & Hagen 1982; Charnley et al. 1992), or rate equations (Hasegawa et al. 1992; Caselli et al. 1998a) approaches have been developed. All these methods give a macroscopic description of the problem, meaning that they follow the overall behaviour of the mantle rather than the single particle. This method, based on the rate equations, though the least precise from a physical point of view, is the fastest and allows studies of the chemical evolution in objects with varying physical conditions as a function of the time. In this context, time-dependent models have been developed that predict the abundance of many COMs in hot cores/corinos by considering two phases: a dense and cold pre-collapse phase during which the grain mantles with simple hydrogenated species are formed, and a warm-up phase, caused by the collapse, during which heavier species, and particularly radicals, can react together on the grain surfaces before sublimating into the gas phase (Garrod & Herbst 2006; Garrod et al. 2008; Aikawa et al. 2008). A key point of these models is

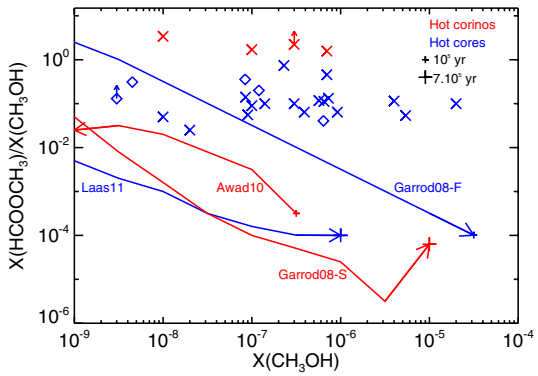

Fig. 1. Gas phase methyl formate to methanol abundance ratio as function of the gas phase abundance of methanol. Observations of hot corinos with single-dish telescopes are represented by red crosses: NGC 1333-4A by Bottinelli et al. (2004), IRAS16293 by Cazaux et al. (2003), NGC 1333-2A and –4B by Bottinelli et al. (2007). Observations of hot cores with single-dish telescopes are represented by blue crosses: G34.3+0.15 by Mehringer & Snyder (1996), SgrB2(N) and SgrB2(M) by Nummelin et al. (2000), G327.3-0.6 by Gibb et al. (2000), OMC1 by Sutton et al. (1995), G34.3+0.2, SgrB2(N), DR23(OH), W51, Orion Hot-Core by Ikeda et al. (2001), AFGL2591, G24.78, G75.78, NGC 6334, NGC 7538, W3(H2O), W33A by Bisschop et al. (2007). Observations of hot cores with interferometers are represented by blue diamonds: G34.3+0.15 by MacDonald et al. (1996), G19.61-0.23 by Qin et al. (2010), Orion KL, G29.96 by Beuther et al. (2009), and G47.47+0.05 by Remijan et al. (2004). The red curves report the predictions of the methyl formate to methanol abundance ratio appropriate to the hot corinos case by Garrod et al. (2008, their Fig. 6) and Awad et al. (2010, their Fig. 5). The blue curves report the predictions appropriate to the hot cores case by Garrod et al. (2008, their Fig. 4) and Laas et al. (2011, their Fig. 5). The arrows represent the direction of the time in each model and the ticks refer to timescales.

therefore the presence of radicals (OH, HCO, CH_3O) trapped in the cold mantles. In these models, the radicals are assumed to be mainly produced by the UV photodissociation of the neutral species in the grain mantles. Garrod & Herbst (2006) tested this assumption by introducing reactions between OH, HCO, CH_3, CH_3O to produce methyl formate, dimethyl ether, and formic acid. Garrod et al. (2008) then expanded the chemical network of reactions between radicals to form other COMs such as ethanol, glycolaldehyde, or acetic acid. Finally, Aikawa et al. (2008) and Awad et al. (2010) have included the spatial distribution and evolution of a collapsing cloud with the aim to estimate the size of typical hot corinos such as the well-known source IRAS16293-2422.

Although the abundances of the simplest COMs, such as formaldehyde (H_2CO) or methanol (CH_3OH), are now quite well predicted, astrochemical models still fail to reproduce the abundance of more complex ones, such as methyl formate ($HCOOCH_3$), for example. This molecule is assumed to be mainly formed on grains via the reaction between HCO and CH_3O during the warm-up phase (Allen & Robinson 1977; Garrod & Herbst 2006), a reaction in competition with the hydrogenation reaction of CH_3O, which leads to methanol. Figure 1 shows the observed and the predicted methyl formate to methanol gas phase abundance ratios as function of the gas phase methanol abundance. The plotted observations refer to the abundance values estimated in the articles cited in the figure caption, where the sizes are either directly estimated by interferometric observations or indirectly by other considerations for single-dish observations. The plotted model predictions refer to gas phase abundances. The curves "Garrod-F" and "Garrod-S" have been obtained from Figs. 4 and 6 of Garrod et al. (2008) respectively, the curve "Awad10" comes from Fig. 5 of Awad et al. (2010), and the curve "Laas11" from Fig. 5 of Laas et al. (2011). Each point of the curves represents a different time or temperature (depending on the model). In these models, the methanol abundance increases with time, except in Awad et al. (2010) who considered the destruction of the species in the gas phase. We remark that while the methanol abundances may suffer of the uncertainty on the source size and H_2 column density, the methanol to methyl formate abundance ratios are almost unaffected by these uncertainties. Therefore, unless the observed methanol abundance is always lower than 10^{-7}, which is certainly not the case, no model can reproduce the totality of observations. Specifically, the observed ratios are roughly independent of the methanol abundance and are about 0.1 and 1 in hot cores and hot corinos respectively, regardless of the telescope used for the observations. State-of-art astrochemical models consequently underestimate the methyl formate to methanol abundance ratios and always predict a decreasing ratio with increasing methanol abundance (because methyl formate is in competition with methanol formation).

Motivated by this unsatisfactory situation, we developed a new model, called GRAINOBLE, whose ultimate goal is to simulate the synthesis of COMs on the grain surfaces. In this article, we focus on the first phase, namely the formation of the mantle during the dense and cold phase of the pre-collapse, the prestellar core phase. Our model differs from most previous published models because it treats the multilayer and porous structure of the iced mantles. In the mentioned previous models (Garrod & Herbst 2006; Garrod et al. 2008; Aikawa et al. 2008; Awad et al. 2010; Laas et al. 2011), COMs are synthesized during the warm-up phase thanks to the increased mobility of radicals, formed on the grain surfaces during the previous cold phase. The abundance of radicals in the mantles during the cold phase is, therefore, a key point. One possibility, explored by the above models, is that the radicals are formed by the UV photodissociation of frozen species. However, since the impact of the UV photons on the surface chemistry is poorly understood (see the detailed discussion in Sect. 2.1), we explore here the possibility that radicals are synthesized even without photolysis and are trapped in the grain mantles, thanks to the multilayer mantle treatment.

The article is structured as follows. In the next section, we review the models available in the literature, outlining their limits and pointing out possible improvement. The concluding paragraph of the section describes the improvements proposed by our new model GRAINOBLE. In Sect. 3 we describe the technical details of GRAINOBLE. Section 4 reports the results of the new computations, discussing a reference set of parameters and a large grid of runs where several input parameters are varied. In Sect. 5 we compare the obtained results with previous models with the twofold goal to validate our code and discuss the different results from the different adopted physical models and conditions. Section 6 compares the GRAINOBLE predictions with the observations of ices and discusses the constraints on the various parameters of the model. Finally, Sect. 7 concludes the article, emphasising the main results and perspectives.

2. Limits of the existing models and need for improvement

2.1. The physics of grain surface chemistry

a) Multilayer vers bulk chemistry

One of the main limits of many published models is that they do not distinguish the chemical processes that occur in the

mantle bulk and on the surface. In these models, species that are buried in the mantle can keep diffusing in the mantle and reacting with others even if they are covered by new layers. Furthermore, particles landing on the surface on top of the grain mantle can react with all particles, regardless of their depth within the mantle. Thus, heavy reactive particles such as radicals can continue to react with landing hydrogen atoms even though the radicals are buried deep in the mantle bulk. The "bulk chemistry method" may therefore (grossly) underestimate the abundance of radicals in grain mantles.

In contrast, the difference in the chemical behaviour of the mantle and of the surface may lead to the formation of non-homogeneous grain ices as suggested by the IR observations. Tielens et al. (1991), for instance, by observing two features in the CO bands, suggested a polar mixture enriched by water in the bottom of the mantle covered by a non-polar one mainly composed of CO located on the outermost layers. In addition, experiments have shown that UV and cosmic rays irradiation can alter the chemistry of astrophysically relevant ices composed of water, methanol, and other CO-bearing molecules even in dark cold cloud conditions (Gerakines et al. 1996; Bennett & Kaiser 2007). However, unlike highly energetic cosmic rays, which can cross through the entire grain mantle, UV photons only penetrate a limited number of monolayers, depending on the absorption cross-section of molecules that constitute the ice (see Gerakines et al. 2001, for an illustrative discussion). Modelling the photolytic processes in ices requires, therefore, a distinction between the surface and the bulk of the mantle.

The desorption of grain mantles during the warm-up phase depends on their chemical composition. By carrying out temperature programmed desorption (TPD) experiments, Collings et al. (2004) demonstrated that CO ices desorb at ~20 K, whereas methanol and water ices desorb at temperatures higher than 100 K, for instance. Numerical values of desorption energies were deduced from these experiments and were incorporated in macroscopic rate equation models. Consequently, the model of Garrod et al. (2008) predicts a total desorption of the CO reservoir at 25 K, whereas more refractory species are desorbed at temperatures higher than 100 K. Actually, a significant amount of volatile ices can be trapped with highly polar molecules, such as water, in the mantle bulk. Thus, the desorption of such species is limited by the gradual evaporation of the mantle main matrix, which depends on other molecules.

The continuous time random walk (CTRW) Monte-Carlo method, introduced by Chang et al. (2005) and Cuppen & Herbst (2005), strongly differs from the macroscopic methods described above. This "microscopic" model considers the actual hopping of a discrete number of particles from one site to another but, unlike previous Monte Carlo methods, it takes into account the actual position of particles so that the spatial distribution is also included in the simulation. Cuppen & Herbst (2007) and Cuppen et al. (2009) have explained the growth of ice monolayers in dense clouds and showed a differentiation of the chemical composition in the mantle. More particularly, Cuppen et al. (2009) showed that under dense cloud conditions, CO can be trapped in the mantle by the accretion of new species above it before reacting with other particles. They also highlighted the survivability of very reactive particles in the mantle bulk by this process. Unfortunately, this method can only study simple chemical systems because of the CPU time required by the Monte-Carlo algorithm, and a direct link with the gas phase is not possible at present.

Hasegawa & Herbst (1993b) have attempted to treat separately the chemical processes within the bulk and on the surface with a three-phase model. They considered the formation of an inert mantle caused by the accretion of particles onto it. They found that the differences between the three-phase and the two-phase models are small for stable species but become non-negligible for reactive species at long ($\geq 10^5$ yr) timescales. Furthermore, the values of desorption and diffusion energies used in 1993 are lower than the values measured by the experiments carried out during the past decade. Because higher desorption and diffusion energies values tend to decrease the rate of the chemical processes on grain surfaces, the impact of the three-phase model on the frozen radical abundances would be significantly higher with the new values. However, at the time of the submission of this article, this three-phase model has not been pursued in other works.

b) Porous grain surfaces

Astrochemical models used for predicting the COM formation have so far only considered perfectly spherical and smooth grains. However, observations (Mathis 1996), theoretical studies (Ossenkopf 1993; Ormel et al. 2009), and analyses of solar system bodies have provided evidence for the fluffy and porous structure of interstellar grains. For example, Mathis (1996) needed to use interstellar grains with a substantial fraction of vacuum to fit the observed extinction curves. Numerical simulations of dust coagulations carried out by Ossenkopf (1993) from a MRN-like grain size distribution have shown an increase of the size and the porosity of the dust in molecular cloud conditions. This fluffy structure of interstellar grains may alter the surface chemistry because grains can have micro-pores of small apertures compared to their volume in which species can be trapped. Thus, porous grains can increase the reactivity of chemical reactions by trapping volatile particles such as atomic hydrogen in their pores.

c) Photolysis

As described in the introduction, the new generation of COMs formation models predicts that COMs are synthesized during the warm-up phase thanks to the increased mobility of radicals, formed on the grain surfaces during the previous cold phase (Garrod & Herbst 2006; Garrod et al. 2008; Aikawa et al. 2008; Awad et al. 2010; Laas et al. 2011). The abundance of radicals in the mantles during the cold phase is, therefore, a key point. In these works, UV photons from cosmic rays play a major role in synthesising radicals during this phase. However, as for any model, a series of inevitable assumptions are adopted to treat the process.

The first important assumption regards the photodissociation rates on the ices. They are assumed to be the same as those in the gas phase, computed by Sternberg et al. (1987); Gredel et al. (1989). However, there are various reasons to think that this may be a serious overestimate. First, grain surfaces could absorb part of the UV photon energy, ending up with a lower dissociation rate. Second, once the molecule is broken, if it is broken, being not in the gas phase but on a surface with almost no mobility, the photoproducts may recombine almost instantaneously. In addition, some products can even have enough energy to sublimate (see for example Andersson et al. 2006). Thus, the products of the photodissociation are likely different from those in the gas phase, and the overall formation rate of the assumed products (and radicals) may be severely lower than assumed.

A second point is related to the flux of CR induced UV photons in dense clouds. The exact value is fairly uncertain, because it largely depends on the primary cosmic ray energy spectrum, and on the grain extinction cross section, which are also

uncertain (see for example Padovani et al. 2009). For example, Shen et al. (2004) have shown that the typical uncertainty on the low-energy cosmic ray spectrum leads to a variation of the UV flux of more than one order of magnitude.

Another important assumption regards the penetration of the UV photons through the bulk of the mantle. Unfortunately, there exists almost no observational or theoretical ground for that, and it is not obvious how realistic this assumption is. Indeed, the experimental work by Gerakines et al. (2000) suggests that the UV photons can only penetrate a limited number of layers, depending on the optical properties of the ice.

Finally, even the branching ratios of species caused by the photodissociation in the gas phase are very poorly known (e.g., Laas et al. 2011). In this context, various authors omit the photolysis in their model (e.g., Chang et al. 2007; Cuppen et al. 2009).

2.2. The computational methods

The rate equations method allows us to study the evolution of the chemical composition of grain mantles via one temporal differential equation for each species. This approach allows us the use of complex chemical networks that include photolytic processes involving hundreds of species, and allows us to directly link the gas phase and the grain surfaces. However, rate equations are based on the evolution of densities of species in gas-phase and on grain surfaces, which are average values. Therefore this approach can be inaccurate when the number of particles on the grain becomes low because of the finite surface of grains. Caselli et al. (1998a) took into account the discrete nature of the individual composition of grain mantles by modifiying the reaction rate coefficients, while Garrod et al. (2008) went further by modifying the functional form of the reaction rates. Biham et al. (2001) and Green et al. (2001) introduced a stochastic method based on the resolution of the master equations (ME), in which the system solves the time derivatives of the probability of each discrete mantle composition. In spite of its good accuracy for grain surfaces, this method can only be used for small chemical networks since the number of equations grows exponentially with the number of species. Lipshtat & Biham (2003) have thus introduced another method based on the time derivatives of the moments to study the formation of molecular hydrogen, while Barzel & Biham (2007) have extended this method for more complex chemical networks. The comparisons between the methods introduced here show that the rate equations method tends to overestimate the reaction rates and the abundance of the reactants, especially when they are in low quantities.

2.3. Need for improvement: the GRAINOBLE model

Although the past few years have seen a huge improvement in the modelling of grain surface chemistry, models are not yet able to accurately reproduce observations (e.g. Fig. 1). Therefore, something is still missing in those models. In the following, we review what are, in our opinion, the areas where improvements are needed and possible. Our new grain surface model, GRAINOBLE, has been developed to include the improvements described below.

a) Multilayer structure of the ices

The first obvious limitation of the Herbst, Garrod, and collaborators class of models, the present state of the art, is that they do not take into account the multilayering formation of the ices, which leads to the differentiation observed in the interstellar ices (Tielens et al. 1991; Pontoppidan et al. 2003) that is also predicted by the microscopic Monte-Carlo (MC) models of Cuppen and collaborators, and to the potential survival of reactive particles in the mantle bulk. On the other hand, the microscopic MC treatment is too cumbersome in computer time and difficult, if not impossible, to apply to model realistic cases. GRAINOBLE uses the rate equation method developed by Herbst and collaborators (which is at the base of the Garrod models) in a way that permits us to follow the multilayering structure of the ice. Therefore, it benefits from the advantages of the rate equation method (computer speed) and of the microscopic MC (multilayer) approach.

b) Porosity of the grains

Laboratory experiments, numerical simulations of grain coagulation, mantle formation, and astronomical observations all demonstrate that interstellar grains are porous (Jones 2011). As previously discussed, the presence of pores creates traps for the molecules and atoms on the grain surfaces, leading to an enhancement of reactivity on the grains. GRAINOBLE includes pores, following the treatment of Perets & Biham (2006). The number and area of the pores are treated as parameters (Sect. 3).

c) Multiparameter approach

Many parameters in the microphysics of the problem have highly uncertain values, like the various activation barriers of key chemical reactions, or the barriers against diffusion of adsorbed particules. Additionally, several macroscopic parameters are also either uncertain or vary depending on the astronomical object. In particular, it is worth mentioning that the densities and the temperatures of the prestellar cores depend on their age and their surroundings.

3. The GRAINOBLE model

3.1. General description

Following the work of Hasegawa et al. (1992), four main processes occuring on grains are taken into account.

1) Gas-phase particles can accrete onto the grains, which are considered spherical. For a given gas-phase species i, the accretion rate is a function of the thermal velocity of the gas-phase species $v(i)$, of the cross section of the grains $\sigma(a_{\rm d})$, of the density of the grains $n_{\rm d}(a_{\rm d})$ where $a_{\rm d}$ is the grain diameter, and of the sticking coefficient $S(i)$. We assumed the sticking coefficient estimated by Tielens (2005) for atomic hydrogen and a sticking coefficient equal to 1 for heavier particles, based on the TPD experimental work of Bisschop et al. (2006). For dark cloud conditions, particles constituting the ice are bound mainly via the physisorbed van de Waals interactions.
2) Once the particles are stuck onto the grains, they can diffuse along the surface via thermal hopping according to the Boltzmann law, which gives the hopping rate $R_{\rm hop}$. Following experimental work of Katz et al. (1999), we neglected tunelling diffusion.
3) Physisorbed particles can react only via the Langmuir-Hinshelwood (Hinshelwood 1940) process, in which two species can react when they meet in the same site. The reaction rate $R_{\rm r}$ is given by the product between the diffusion rate (i.e., the number of times per second that a species sweeps over a number of sites equal to the number of sites of the layer) and the probability of the chemical reaction, which is a function of its activation energy.

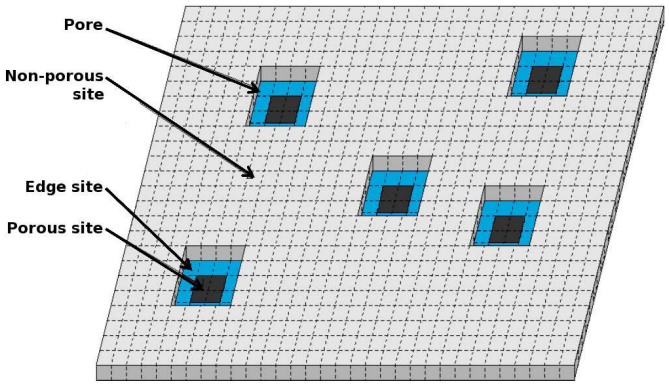

Fig. 2. Schematic view of a portion of the mantle layer as modelled by GRAINOBLE. All pores are assumed to be square, to have the same size, and no walls (see text). The edges sites, that connect the non-porous surface and the pores are depicted in blue. In this example, each pore is constituted by 16 sites, of which the 12 blue sites are edge sites, and the fraction of area occupied by the pores is 0.1.

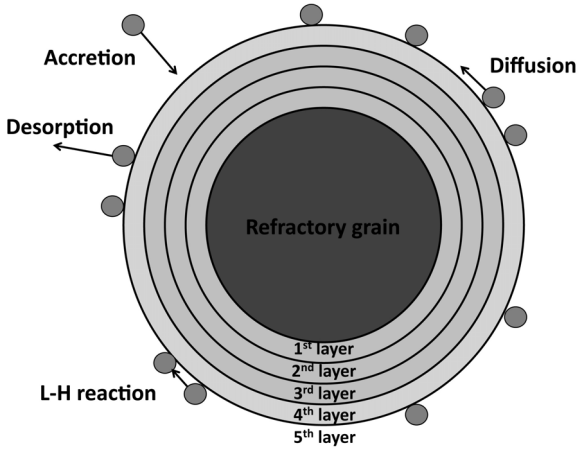

Fig. 3. Schematic view of the multilayer approach adopted by the GRAINOBLE code. The inner layers of the mantle are chemically inert, whereas the layer at the surface is chemically reactive (see text).

4) Surface species can desorb only via thermal processes, i) the "classic" thermal process caused by the thermal balance of the grain; ii) the cosmic ray induced desorption process in which cosmic rays heat the grains, as suggested by Leger et al. (1985), whose heating rate was computed by Hasegawa & Herbst (1993a). The sum of these two thermal desorption rates gives the total evaporation rate R_{ev}.

A full list of the symbols used in this work is provided in the Appendix.

3.2. Porosity

To model the impact of the porous structures of interstellar grains, we introduce two types of sites: the *non-porous*, and the *porous* sites, following Perets & Biham (2006). The *non-porous* sites form a smooth surface that is perfectly regular, where particles interact directly with the gas phase. The gas phase species can accrete onto the grain, and the adsorbates can desorb into the gas phase. The *porous sites* correspond to sites where no direct accretion and desorption are possible. They are filled up only by diffusion from non-porous sites at the edge of the pores. The porous sites cover a fraction F_{por} of the grain surface. For the sake of simplicity, all the pores are assumed to be square and to have the same size, constituted by N_{pore} sites, where $N_{pore} \geq 4$. The fraction of the grain surface occupied by the pores, F_{por}, is poorly known because, to date, no experimental measurements or numerical estimates have been attempted. Therefore we ran models with four values for F_{por}: 0, 0.3, 0.6, and 0.9, to cover a large range of possibilities,

The fraction of the edge porous sites, F_{ed}, on the grain depends then on F_{por} and N_{pore} as follows:

$$F_{ed} = 4 \times F_{por} \frac{\sqrt{N_{pore}} - 1}{N_{pore}}. \quad (1)$$

A posteriori, the actual value of N_{pore} does not influence the results significantly because what matters is mostly the fraction of area occupied by the pores and not the size or the number of pores. In the following, we assumed $N_{pore} = 9$.

The approach that we used for modelling the grain porosity is sketched in Fig. 2.

3.3. Multilayer approach

In order to distinguish the chemistry on the surface and in the bulk of the mantle, we used a multilayer approach. In practice, the code follows the chemical processes on a single layer, the one at the surface of the mantle. In this layer, particles can accrete, diffuse, react with each other and desorb, depending on whether they are on non-porous or porous sites. The mantle layer growth is treated at the same time as the chemistry. Specifically, at each time t, the chemistry is followed by solving the set of differential equations described in Sect. 3.9 between t and $t + \Delta t$ and a new number of particles on the grain is computed at $t + \Delta t$. The layer is considered chemically inert as soon as the number of particles that are on the layer is equal to the number $N_s(a_d)$ of (porous plus not-porous) sites of the layer, where $N_s(a_d)$ is given by the ratio between the grain surface area and the site area d_s^2 (see Sect. 3.7). Because the porous sites are populated only via diffusion (Sect. 3.2), they fill up more slowly than the non-porous sites. It is therefore possible that the layer is considered inert when some pores are still empty. In this case, the number of non-porous sites is artificially increased. Although this is somewhat arbitrary, a posteriori this assumption has almost no impact on the results, as described in Sect. 4.3. When the layer becomes inert, the code memorizes its composition and a new and reactive layer is started. Note that no chemical exchange is allowed between layers. Finally, the code also takes into account the growth of the grain size and of the number of sites of the new layer by assuming that the thickness of the layer is equal to the site size d_s. All layers have, therefore, the same thickness, equal to the site size. Figure 3 gives a schematic view of this approach.

3.4. Chemical network

We adopted the network based on the work by Allen & Robinson (1977) and Tielens & Hagen (1982), updated for the new theoretical and experimental results and adapted to model the formation of the main constituents of intestellar ices. As previously mentioned in the introduction, observations of ices have shown that grain mantles are mainly composed of O- and CO- bearing molecules such as water, CO, CO_2, or methanol. Molecules such as NH_3 and CH_4 produced by the hydrogenation of N and C can also be found, but only in smaller quantities (Gibb et al. 2004). In this work, we therefore neglected the formation of ammonia and

Table 1. Species and binding energies, assuming that the ice matrix is mainly water ice.

Species	E_b(water ice) (K)
H	450[a]
O	800[b]
CO	1150[c]
OH	2820[d]
H_2O	5640[e]
O_2	1000[c]
O_3	1800[f]
HO_2	5570[c]
H_2O_2	6300[f]
HCO	1600[f]
H_2CO	2050[f]
CH_3O	5080[f]
CH_3OH	5530[c]

Notes. [(a)] Hollenbach & Salpeter (1970); [(b)] Tielens & Hagen (1982); [(c)] Collings et al. (2004); [(d)] Avgul & Kiselev (1970); [(e)] Speedy et al. (1996); [(f)] Garrod & Herbst (2006).

Table 2. Surface reactions and activation energies.

Number	Reaction	E_a (K)
1	$O + O \longrightarrow O_2$	0
2	$O + O_2 \longrightarrow O_3$	0
3	$H + H \longrightarrow H_{2,gas}$	0
4	$H + O \longrightarrow OH$	0
5	$H + OH \longrightarrow H_2O$	0
6	$H + O_2 \longrightarrow HO_2$	0
7	$H + HO_2 \longrightarrow H_2O_2$	0 (36%)[a]
8	$H + HO_2 \longrightarrow OH + OH$	0 (57%)[a]
9	$H + H_2O_2 \longrightarrow H_2O + OH$	1400[b]
10	$OH + OH \longrightarrow H_2O_2$	0
11	$H + O_3 \longrightarrow O_2 + OH$	0
12	$H + CO \longrightarrow HCO$	$400^c < E_a < 2500^d$
13	$H + HCO \longrightarrow H_2CO$	0
14	$H + H_2CO \longrightarrow CH_3O$	$400^c < E_a < 2500^d$
15	$H + CH_3O \longrightarrow CH_3OH$	0

Notes. [(a)] Branching ratios measured by Cuppen et al. (2010); [(b)] Klemm et al. (1975); [(c)] Fuchs et al. (2009); [(d)] Woon (2002).

methane. In addition, for the reasons explained in Sect. 2.1, we also do not consider photolytic processes. Our model, therefore, considers the formation of stable species (e.g., formaldehyde and methanol) and radicals (e.g., HCO, and CH_3O) via hydrogenation of frozen CO. Note that we did not consider CH_2OH because, in absence of photolytic processes, it is formed via the hydrogenation of H_2CO. Theoretical studies have shown that the reaction $H_2CO + H \rightarrow CH_2OH$ has an activation barrier (10.5 kcal/mol) more than twice the activation barrier leading to CH_3O (4–6 kcal/mol) (Sosa & Schlegel 1986; Walch 1993; Woon 2002). We therefore neglected CH_2OH in the present study. For the H_2O formation, we adopted the new reaction scheme based on the experimental works by Dulieu et al. (2010), Ioppolo et al. (2010) and Cuppen et al. (2010), who estimated the energy barriers of several reactions. The recombination reaction of hydrogen atoms, forming molecular hydrogen, is also taken into account. Since H_2 has a low binding energy with respect to water ice (Tielens & Allamandola 1987; Perets et al. 2005), and since its reaction of formation releases chemical energy (Hollenbach & Salpeter 1970), we assumed that the H_2 molecules are desorbed in the gas phase as soon as they are formed. Finally, IR observations have shown that CO_2 may be a major component of ices with abundances reaching 30% with respect to to water in some cases (Dartois et al. 1999; Pontoppidan et al. 2008). However, the formation pathways of carbon dioxide, either by a direct surface route or by UV photolysis, in such cold conditions are still not well understood. Accordingly, we decided to neglect the formation of this molecule.

Table 1 lists the chemical species considered in our network with their binding energies relative to an amorphous water ice substrate. Indeed, interstellar grains located in prestellar-cores are already covered by a polar ice mainly composed of water, formed during an earlier phase when atomic abundances are still high, before the depletion of CO. The network used for the grain surface chemistry is reported in Table 2.

3.5. Gas phase initial abundances

The observed and predicted gas-phase abundance of atomic carbon is much lower than CO or atomic oxygen abundances. Therefore, we considered only the accretion of gaseous H, O, and CO onto the grain mantles.

In dark cloud conditions, the abundance of atomic hydrogen in the gas phase results from a balance between the cosmic rays ionization of H_2 on the one hand and the accretion on dust grains (which react to form H_2 or heavier iced species) on the other hand. At steady state, the density of H is therefore given by the ratio between these two processes (Tielens 2005), as follows:

$$n(H) = \frac{2.3\zeta_{CR} n(H_2)}{2v(H)\sigma_d X_d n(H_2)} \quad (2)$$

where $v(H)$ is thermal velocity of atomic hydrogen. The resulting H density is independent of the density and equal to 1.2 cm^{-3} at 10 K, for a cosmic rays ionization rate ζ of 3×10^{-17} (Caselli et al. 1998b), a grain abundance X_d of 1.33×10^{-12} relative to H nuclei and for a grain radius r_d of 0.1 μm ($\sigma_d = \pi r_d^2$), giving $n_d\sigma_d/n_H = 4.2 \times 10^{-22}$ cm^2. Observations and astrochemical models show that CO is a very stable species and the most abundant molecule after H_2 in dark clouds. Following the estimates of Frerking et al. (1982), we assumed an initial abundance of CO of 4.75×10^{-5} with respect to H nuclei. This abundance decreases with time because of the freeze-out onto the grain mantles. Finally, the abundance of atomic oxygen in the gas phase remains poorly constrained. Observations of the [OI] 63 μm line obtained by Caux et al. (1999); Vastel et al. (2000); Lis et al. (2001) with the Infrared Space Observatory (ISO) have measured abundances higher than 10^{-4}, suggesting that all the gaseous oxygen is in atomic form. But astrochemical models predict an atomic oxygen abundances of 6×10^{-5} or less. The initial abundance of O is therefore considered as a free parameter and can vary between 2×10^{-4} and 2×10^{-5}.

3.6. Physical conditions

As supported by observational and theoretical arguments, the physical properties of prestellar cores vary substantially with the age and the mass of the object (see di Francesco et al. 2007; Bergin & Tafalla 2007). The densities n_H evolve typically from $\sim 10^4$ to $\sim 10^6$ cm^{-3}, while the gas kinetic temperature (equal to the grain temperature in most cases) varies between 7 and 20 K,

depending on the type of the object. Indeed, massive stars are suspected to be formed from warmer prestellar cores than low mass ones. Consequently, we included several values of the density and the temperature, listed in Table 3, in our parameter grid.

Additionally, as shown by numerical simulations (Ossenkopf 1993; Ormel et al. 2009) and observations (Stepnik et al. 2003; Steinacker et al. 2010), the coagulation of grains occuring in molecular clouds and in prestellar cores tend to increase their size. That is why the grain size distribution, which is assumed to follow a broad nearly power-law in diffuse interstellar clouds (Mathis et al. 1977), tends to evolve with time, the bigger grains dominating most of the dust mass. We assumed all interstellar grains to have the same diameter a_d, and we considered three values: 0.1, 0.2, and 0.3 μm respectively. The grain abundance X_d changes in accordance with the grain size, to keep a dust-to-gas mass ratio of 1%.

Table 3. Key free parameters of GRAINOBLE and value range.

Parameter	Values
Density n_H	10^4 – $\mathbf{10^5}$ – 10^6 cm^{-3}
Temperature $T_g = T_d$	10 – **15** – 20 K
Initial oxygen abundance $X(O)_{ini}$	2×10^{-5} – $\mathbf{6\times10^{-5}}$ – 2×10^{-4}
Grain size a_d	0.1 – **0.2** – 0.3 μm
Energy ratio E_d/E_b	0.5 – **0.65** – 0.8
Porosity factor F_{por}	**0** – 0.3 – 0.6 – 0.9
Site size d_s	1.4 – **4.2** – 7 Å
Activation energy E_a	**400** – 1450 – 2500 K

Notes. Bold values mark the values adopted in the reference model (see text, Sect. 4).

3.7. Other key parameters of GRAINOBLE

In addition to the above described parameters, astrochemical models of grain chemistry are based on several other parameters related to the particle-surface, surface particle-particle interaction and surface properties. We list below three additional key parameters of the GRAINOBLE model whose values are poorly constrained because of the difficulties involved in measuring or computing them. We considered them as free parameters in a range defined by the different values found in the literature.

a) Diffusion energy to binding energy ratio E_d/E_b

Theoretical calculations of barriers against diffusion for physical adsorption E_d on perfectly smooth surfaces have been carried out by Jaycock & Parfitt (1986) and have shown that E_d is typically about 30% of the binding energy E_b. However, "real" surfaces, which show defects, irregularities, or steps, tend to increase this ratio (Ehrlich & Hudda 1966). Accordingly, several experimental studies have been carried out to constrain the diffusion barrier on astrophysically relevant surfaces. By fitting experimental formation of molecular hydrogen on refractory bare surfaces and on amorphous water ices with a rate equation model, Katz et al. (1999) and Perets et al. (2005) experimentally found high E_d/E_b ratios (0.77 and ~0.85 respectively). However, Collings et al. (2003), Ulbricht et al. (2002), and Matar et al. (2008) estimated lower energy ratios (of about 0.5) for CO and D on water ice, and for atomic oxygen on carbon nanotubes. Clearly, the energy E_d/E_b ratio is highly uncertain and strongly depends on the composition and the structure of the substrate. Three values of the E_d/E_b energy ratio have been considered here: 0.5, 0.65, and 0.8.

b) Activation energy E_a

The activation energy values of the CO and H_2CO hydrogenation reactions are also very uncertain. Theoretical studies of these reactions on an icy mantles via calculations of quantum chemistry carried out by Woon (2002) and Goumans (2011), showed that the activation energies are about 2000–2500 K, and depend slightly on the presence of water molecules around the reactants. In contrast to these theoretical values, experiments show that these reactions take place at low temperature (Watanabe & Kouchi 2002). Fuchs et al. (2009), by modelling the experiments of a hydrogen deposition on a CO ice with a CTRW method, found values of about 400–500 K for both reactions. We therefore consider these barriers as a free parameter. Three values of activation energies, assumed to be equal for the H+CO and H+H_2CO reactions, have been considered: E_a = 400, 1450, 2500 K.

c) Site size d_s

The surface density of sites s, i.e. the number of sites per surface unit given in sites x cm^{-2}, depends on the structure of the surface and its composition. Most astrochemical models assume a value of $s = 10^{15}$ cm^{-2} which has been measured experimentally by Jenniskens et al. (1995) for a high-density amorphous water ice. By assuming that the distance between two sites d_s is constant along the surface, d_s can be easily deduced from the surface density s ($d_s = 1/\sqrt{s}$), and is equal to 3.2 Å. However, Biham et al. (2001) found a value of $s = 5\times10^{13}$ cm^{-2} (d_s = 14 Å) for an amorphous carbon surface and Perets & Biham (2006) assumed a value of $s = 5\times10^{15}$ cm^{-3} (d_s = 1.4 Å) in their model of porous grains. We therefore treat d_s as a free parameter, with values equal to 1.4, 4.2 and 7 Å.

3.8. Multi-parameter approach

To summarize, the GRAINOBLE model depends on eight key parameters presented in the previous paragraphs and listed in Table 3 along with the range and values considered in this study for each of them. The values reported in bold are used in the "reference" model (Sect. 4). They correspond to the average physical conditions of prestellar cores (density, temperature, and grain size), to the average values found in the litterature (site size, diffusion energy to binding energy ratio, initial abundance of atomic oxygen), to the values of parameters used by most of previous astrochemical models (porosity factor) or to the most recent values measured by experiments (activation energy).

In total, we ran a grid of 17 496 models varying these eight free parameters.

3.9. Computational aspects

The code solves three sets of differential equations: the first one describes the evolution of the densities of species (other than H, whose density is given by Eq. (2)) in the gas phase, the other two describe the chemical composition of the mantle outermost layer on the non-porous surface and within the pores. The equations giving the evolution of the chemical composition of the mantle layer do not depend on the grain size and are expressed in monolayers/sec (MLs/s) where a monolayer is given by the number of particles of the considered species divided by the number of sites

of a layer. The equations are the following:

$$\frac{dn_g(i)}{dt} = -S(i)v(i)n_g(i)\sigma(a_d)n_d(a_d) + R_{ev}(i)P_{np}(i)N_s(a_d)n_d(a_d) \quad (3)$$

$$\frac{dP_{np}(i)}{dt} = \frac{1}{4}S(i)d_s^2 v(i)n_g(i) - R_{ev}(i)P_{np}(i) - \frac{F_{ed}}{F_{np}}R_{hop}(i)P_{np}(i) + \frac{F_{ed}}{F_{por}}R_{hop}(i)P_{por}(i) + \sum_{i_f} R_{r,ext}(i_f)P_{np}(i_{r1})P_{np}(i_{r2}) - \sum_{i_d} R_{r,ext}(i_d)P_{np}(i_{r1})P_{np}(i_{r2}) \quad (4)$$

$$\frac{dP_{por}(i)}{dt} = +\frac{F_{ed}}{F_{np}}R_{hop}(i)\cdot P_{np}(i) - \frac{F_{ed}}{F_{por}}R_{hop}(i)P_{por}(i) + \sum_{i_f} R_{r,in}(i_f)P_{por}(i_{r1})P_{por}(i_{r2}) - \sum_{i_d} R_{r,in}(i_d)P_{por}(i_{r1})P_{por}(i_{r2}) \quad (5)$$

where $P_{np}(i)$ and $P_{por}(i)$ are the surface populations of the species i (in MLs) on the non-porous surface and within the pores respectively, and $n_g(i)$ its gas-phase density. The first and second terms in Eq. (3) describe the accretion rate and the evaporation rate. The first and second terms of Eq. (4) describe the accretion and the evaporation rates. The third and fourth terms describe the exchange rate between the non-porous surface and the pores via diffusion. The fifth and sixth terms describe the production and the destruction rates of i via reactions on the non-porous surface. Similarly, the first and second terms of Eq. (5) describe the exchange rate between the non-porous surface and the pores via diffusion. The third and fourth terms describe the production and the destruction rates of i via reactions in the pores. Note that the evolution of composition within all the pores can be treated with a single equation because all pores are assumed to have the same size. The equations giving the evolution of each pore can be deduced from Eq. (5) by multiplying it with a simple factor of proportionality.

3.10. What the model does not consider

We aim to study the impact of the multilayer behaviour and the porous structure of the grains on the mantle formation and its chemical composition. To this end, we considered thermal processes only. Therefore we did not consider the desorption processes caused by exothermic surface reactions (Garrod et al. 2007), and the photolytic desorption (Öberg et al. 2009b,a; Arasa et al. 2010) in spite of their relative possible importance. Neither did we account for the photodissociation processes on the ice in this version of GRAINOBLE owing to the reasons given in Sect. 2.1.

4. Results

We ran a grid of 17 496 models, varying the eight free parameters listed in Table 3. In this section, we describe the results of our model. We start by describing the results relative to the reference model, and then we describe how the results change when each of the parameters changes. The analysis is based on the distribution of the obtained mantle abundances when all parameters are varied, except for the parameter under consideration. This allows us to understand if and by how much the considered parameter influences the results. The plot of the multilayer and bulk distributions is shown in Sect. 4.2, while the distributions of other parameters (using the multilayer approach only) are shown in the Appendix. Finally, Table 4 summarises the main effects on the resulting mantle abundances caused by each parameter.

4.1. The reference model

This section describes the results obtained using the reference set of parameters (the boldface values in Table 3). Below we refer to it as the "reference model". Figure 4 presents the evolution with time of the abundance of each species in the gas phase and in the grain mantles.

The evolution of the chemical composition of the mantle depends on the initial gas phase abundances. In the reference model, O and CO abundances are approximately five times higher than the H abundance. Consequently, H atoms cannot hydrogenate all O and CO molecules that accrete onto the mantles. Besides, because the CO hydrogenation reaction has a barrier of 400 K, H atoms react preferentially with O and its products via barrierless reactions, ending up in water molecules. In 2×10^5 years, 80% of the CO reservoir is trapped within the mantle bulk, whereas ~60% of O atoms are contained in water. The remaining O atoms are shared between O_3 (ozone), OH and H_2O_2 (hydrogen peroxyde). Indeed, the high O to H initial gas phase abundance ratio (~6) and the relatively high temperature (15 K) allow a significant amout of O atoms to diffuse on the surface and to react with each other before meeting hydrogen atoms.

However, gas phase CO and O abundance ratios relative to H gradually decrease with time (because they freeze-out onto the mantles), increasing the possibility of hydrogenation reactions. After $\sim 5 \times 10^4$ years, the formation rates of formaldehyde and methanol start to increase while the formation of ozone stops, corresponding to the time when H, O, and CO have similar abundances. The percentage of ozone, formaldehyde, and methanol in the ices therefore strongly depends on the age of the core. Young cores would show high abundances of ozone and of hydrogen peroxyde with respect to water, whereas older ones would show high abundances of formaldehyde and methanol.

Another important result of the model is that a significant amount of radicals is trapped in the bulk because of the multilayer treatment. Radicals assumed to be the precursors of COMs such as OH, HCO or CH_3O, reach abundances between $\sim 5 \times 10^{-6}$ and 10^{-9}. OH is more abundant because of its barrierless formation reaction, and its formation mostly occurs at shorter times.

The evolution of the chemical composition can also be studied "spatially". Indeed, our multilayer approach allows us to study the composition of each monolayer within the grain mantle. Figure 5 shows the evolution of the formation time of each layer and the evolution of the mantle thickness with time. In the reference model, a grain mantle of 77 layers is formed in $2–3 \times 10^5$ yr. Assuming that the layer thickness is equal to the site size (here 4.2 Å), it gives a total mantle thickness of ~0.04 μm, namely 32% of the grain radius. The first 60 layers are created in less than 10^5 yr because they have a fast formation rate (each layer is formed in less than $\sim 2 \times 10^3$ yr). The formation time of layers increases sharply at $\sim 10^5$ yr, because of the drop of the gas phase abundances.

The differentiation of the composition between the inner and the outer layers of the mantle can also be seen in Fig. 6.

Table 4. Summary of the effect of each free parameter on the surface chemistry and on the distribution of results (shown in the Appendix).

Parameter	Effect on the surface chemistry	Distributions of abundances for stable species	Distributions of abundances for radicals
Multilayer versus bulk approach	The multilayer approach – decreases the formation of stable species – traps reactive species in the mantle	– $X(CO) > 10^{-5}$ for 88% (ML), 50% (bulk) cases – $X(H_2O) > 10^{-5}$ for 60% (ML), 93% (bulk) cases – $X(CH_3OH) > 10^{-5}$ for 15% (ML), 55% (bulk) cases	– $X(OH) > 10^{-9}$ for 75% (ML), 1% (bulk) cases – $X(HCO) > 10^{-9}$ for 25% (ML), 2% (bulk) cases
Porosity	The increase of porosity – traps volatile and diffusing particles – increases the formation rate of stable species	– $X(H_2CO) > 10^{-7}$ for 52% (smooth), 61% (porous) cases – $X(CH_3OH) > 10^{-7}$ for 51% (smooth), 61% (porous) cases	– $X(OH) > 10^{-6}$ for 55% (smooth), 20% (porous) cases
Density	The increase of density – decreases the formation of stable species formed by hydrogenation reactions	– $X(H_2O) > 10^{-5}$ for 2% (dense), 85% (sparse) cases with $X(H_2O) \rightarrow 2 \times 10^{-4}$ – $X(CH_3OH) > 10^{-5}$ for 0% (dense), 35% (sparse) cases with $X(CH_3OH) \rightarrow 9 \times 10^{-5}$	– $X(OH) > \times 10^{-6}$ for 0% (sparse), 75% (dense) cases
Temperature	The increase of temperature – strongly increases the desorption of H and O – decreases the rates of hydrogenation reactions – decreases the abundance of stable species formed by these reactions	– $X(CH_3OH) > 10^{-7}$ for 65% (cold), 45% (warm) cases – $X(H_2CO) > 10^{-7}$ for 60% (cold), 45% (warm) cases	– $X(OH) > 10^{-6}$ for 55% (cold), 48% (warm) cases
Grain size a_d	The increase of the grain size – increases the mantle thickness – does not influence the integrated mantle composition	Same evolution of distributions for all stable species	Same evolution of distributions for all radicals
Initial abundance of atomic oxygen	The increase of $X_{ini}(O)$: – increases the formation of water (and other molecules formed from reactions involving O) – slightly decreases the formation of molecules formed from CO	– $X(H_2O) > 2 \times 10^{-5}$ for 0% (low-O), 65% (high-O) cases with $X(H_2O) \rightarrow 2 \times 10^{-4}$ – No influence is seen for CO, H_2CO and CH_3OH	– $X(OH) > 4 \times 10^{-6}$ for 0% (low-O), 50% (high-O) cases with $X(OH) \rightarrow 4 \times 10^{-5}$
Diffusion energy	The increase of the diffusion energy – decreases the diffusion rate of mobile species – decreases the formation rate of stable species – slightly increases the survival of radicals	– $X(H_2O) > 5 \times 10^{-6}$ for 87% (fast), 74% (slow) cases – $X(CH_3OH) > 10^{-7}$ for 80% (fast), 30% (slow) cases – $X(H_2CO) > 10^{-7}$ for 75% (fast), 40% (slow) cases	Same evolution of distributions for all radicals
Activation energies	The increase of activation energies – strongly decreases the formation rate of H_2CO and CH_3OH – strongly decreases the survival of radicals HCO and CH_3O – slightly increases the reaction rates of reactions involving O – slightly increases the formation of water	– $X(CO) > 10^{-5}$ for 35% (low-Ea), 98% (high-Ea) cases – $X(H_2CO) > 10^{-7}$ for 83% (low-Ea), 25% (high-Ea) cases – $X(CH_3OH) > 10^{-6}$ for 80% (low-Ea), 5% (high-Ea) cases	– $X(HCO) > 10^{-10}$ for 90% (low-Ea), 0% (high-Ea) cases – $X(CH_3O) > 10^{-10}$ for 70% (low-Ea), 0% (high-Ea) cases
Site size	The increase of the site sizes – decreases the formation time of layers – increases the mantle thickness – does not influence the integrated mantle composition	Same evolution of distributions for all stable species	Same evolution of distributions for all radicals

Indeed, "intermediate" molecules such as O_3, which is created from atomic oxygen, are rapidly formed and are therefore abundant in the inner layers of the mantle (the first 50 layers), whereas formaldehyde and methanol are mostly formed later, their fractional composition showing significant abundances only in the 20 outermost layers. The abundances of the two main species, CO and H_2O, remain relatively constant throughout the mantle up to the last outermost layers, where

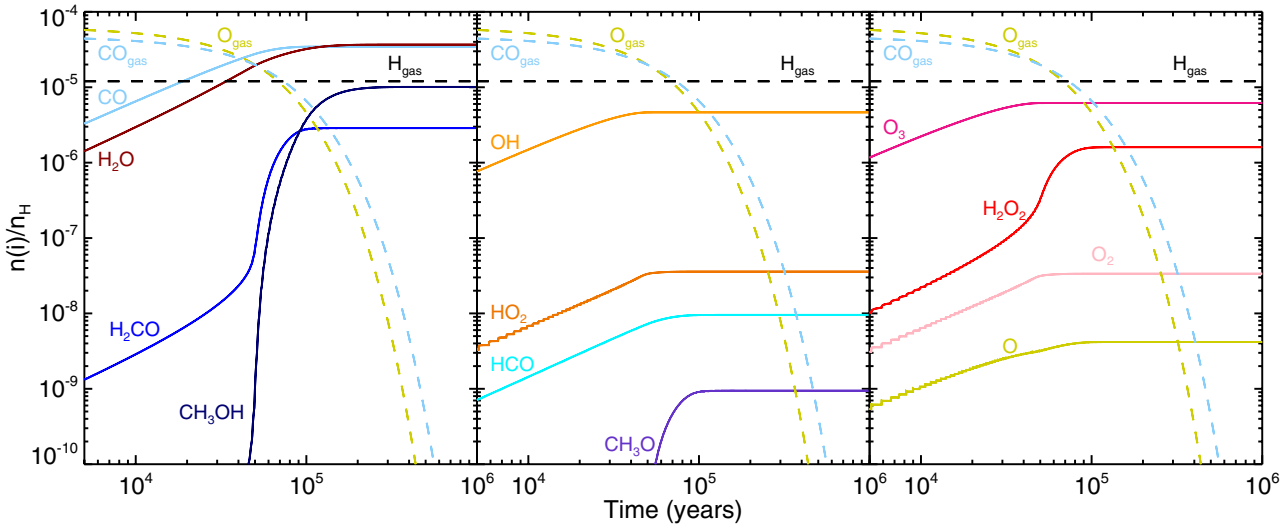

Fig. 4. Abundance of species in interstellar grain mantles (solid) and in gas phase (in dashed) as a function of time for the reference model (boldface values in Table 3). *Left panel*: the most abundant stable species. *Middle panel:* reactive species. *Right panel*: less abundant stable species.

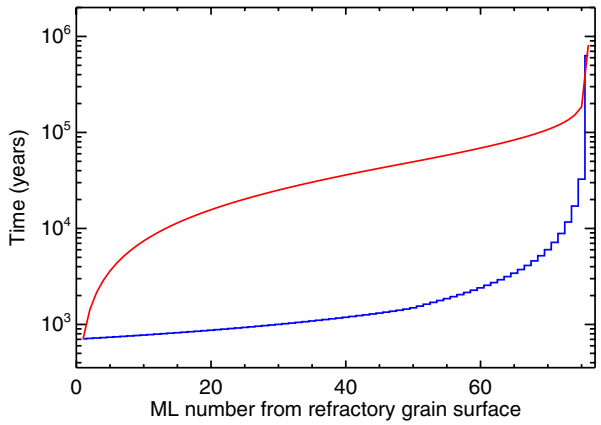

Fig. 5. Formation time of each monolayer (blue line) and mantle formation time versus its thickness expressed in monolayers (red line) for the reference model (boldface values in Table 3).

they decrease in favour of H_2CO and CH_3OH. The composition of radicals within the mantle follows the same evolution as their precursor molecules: the HCO abundance stays relatively constant until the drop in the last layers like CO, while the OH abundance decreases following the O abundance behaviour. Finally, the CH_3O abundance increases approaching the surface, as H_2CO.

4.2. Multilayer versus bulk approach

The introduction of the multilayer approach modifies the chemical behaviour of grain mantles and thus their overall chemical composition. Figure 7 shows the evolution of the mantle composition with time for the reference model, adopting a multilayer (described in Sect. 3.3) or a bulk (old method described in 2.1) approach, respectively. The figure shows that at short timescales ($\leq 5 \times 10^4$ yr), both approaches give similar abundances for the main species because the H abundance is initially low compared to the CO and O abundances (Sect. 4.1). In contrast, O and its associated "intermediate" molecules (OH, O_2, and HO_2) are more efficiently burned in O_3, H_2O_2, and H_2O in the bulk compared to the multilayer approach.

At later times ($\geq 5 \times 10^4$ yr), reactive species, which are trapped by the multilayer approach, continue to react in the bulk method. Consequently, in the bulk approach, radicals (OH, HCO, HO_2, CH_3O) and "intermediate" stable species (O, O_3, H_2O_2, O_2) are totally burned in less than $\sim 10^6$ yr. In contrast, the abundances of these species do not evolve after $\sim 3 \times 10^5$ yr with the multilayer approach. Finally, the predicted methanol and formaldehyde abundances substantially diverge in the two approaches at times longer than $\sim 10^5$ yr, namely the presumed ages of the prestellar cores. The bulk method predicts a final (at 10^6 yr) methanol abundance higher by factor 6 compared to the multilayer approach, and a formaldehyde abundance lower by a factor higher than 10^4.

To understand how robust these results are, we considered the whole grid of models described in Sect. 3.8 and built the distribution of the predicted abundances. Figure 8 shows this distribution for key stable species (CO, H_2O, H_2CO, and CH_3OH) and the radicals (OH, HCO, and CH_3O) for the bulk and multilayer approaches for two times (10^5 and 10^6 yrs). The plots of Fig. 8 tell us that at short times (10^5 yr) the predicted species abundance distributions are quite similar in the bulk and multilayer approaches, with the exceptions of H_2CO and CH_3O, for which the distribution are slightly different. In contrast, at long times (10^6 yr), the distribution of all radicals are substantially different in the two approaches, demonstrating that the age is a key parameter. The plots also provide another important information. For example, considering the multilayer approach results, CO and OH have quite peaked distributions and their predicted abundances depend slightly if at all, on the assumed values of the parameters: they are robust predictions. On the contrary, H_2CO, CH_3OH, HCO and CH_3O have broad abundance distributions implying that their predicted abundances are very sensitive to the values of the other model parameters.

4.3. Porous versus non-porous grains

The influence of the grain porosity (Sect. 3.2) is shown in Fig. 7 for the reference set of parameters. The presence of the porosity in the grain has the effect of slightly speeding up and increasing (by less than a factor 4) the formation of formaldehyde, methanol, and CH_3O, as well as to increase the destruction of

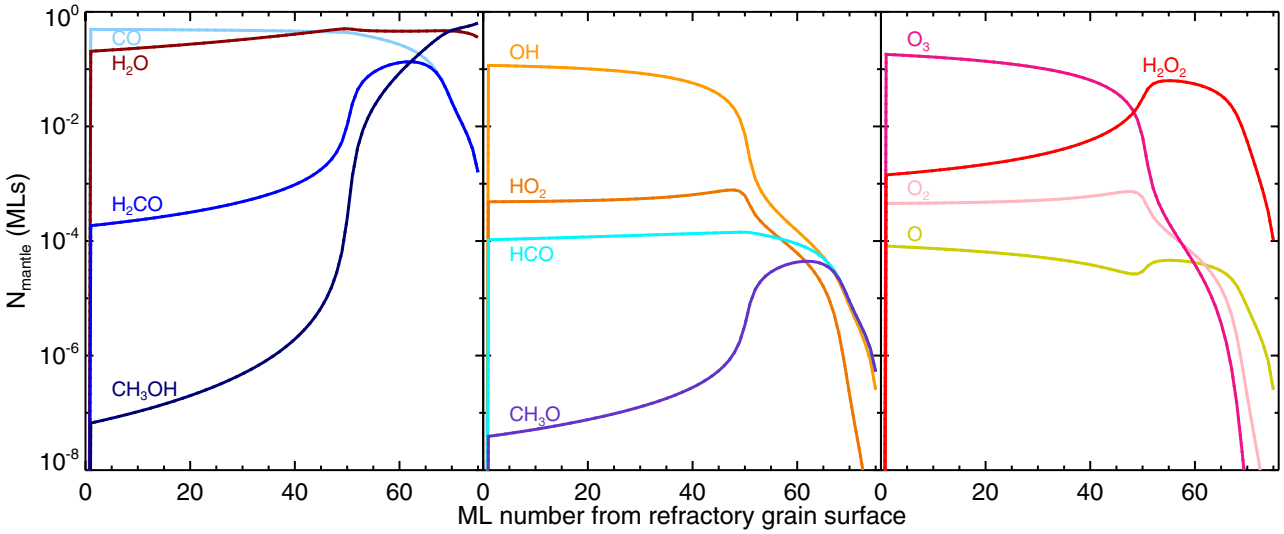

Fig. 6. Fractional composition of each mantle monolayer for the reference model (boldface values in Table 3).

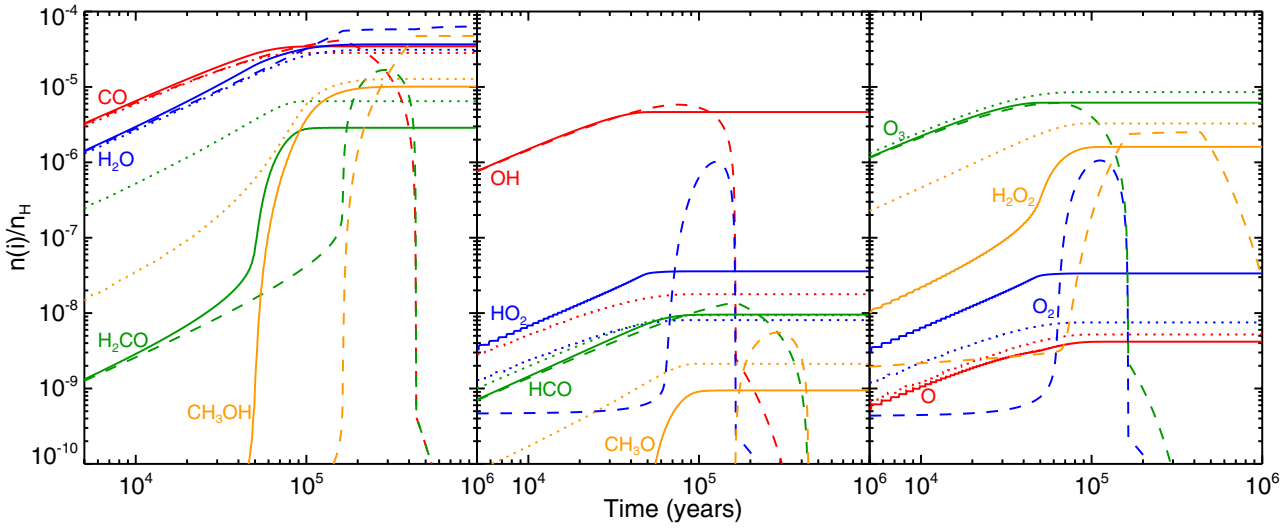

Fig. 7. Abundance of species in interstellar grain mantles as a function of time for the reference model (solid lines), the bulk approach model (Sect. 4.2; dashed lines), and the porous grain model (Sect. 4.3; dotted lines). *Left panel*: the most abundant stable species. *Middle panel*: reactive species. *Right panel*: less abundant stable species.

HO_2, O_2 and O. The reason is that porous grains trap H atoms more efficiently, increasing their number on the grains, but in the end, the H atom numbers is still limited by their low gas phase abundance (Fig. 7). Furthermore, the porosity only slightly modifies the distribution of the results shown in Fig. A.1. Therefore, the porosity only enhances the formation of hydrogenated molecules by a few factors at most, regardless of the values of other parameters.

4.4. Influence of physical conditions

Density n_H

The density plays an important role for two reasons. First, increasing the density reduces the time needed to form each monolayer (because the accretion rate is proportional to the square of the density). Second, the ratio between the number of H atoms and the number of heavy particles (CO and O) that land on the grain is inversely proportional to the density (see Sect. 3.5). As a consequence, the higher the density, the lower the abundance of stable species (H_2O, H_2CO, CH_3OH) created by the hydrogenation reactions, especially at long times ($\geq 10^5$ yr) (Fig. A.2). In contrast and for the same reasons, mantle CO and OH are more abundant for higher density.

Temperature $T_g = T_d$

The grain temperature has a moderate influence on the predicted mantle composition, although the diffusion (and thus the reaction) and the desorption rates depend exponentially on it. However, the desorption rate increases much more quickly than the diffusion rate with temperature (by factors of 10^2–10^6 depending on the E_d/E_b ratio). Consequently, with increasing grain temperature, H atoms have a higher probability to desorb into the gas phase before encountering another particle. The final mantle abundance of molecules created by hydrogenation reactions (H_2CO and CH_3OH) is therefore lower at any time at higher temperatures, as shown by Fig. A.3. The mantle abundance of radicals, on the other hand, is not affected by the grain temperature.

Grain size a_d

While the mantle thickness depends roughly quadratically on the grain size, the final mantle composition depends on it

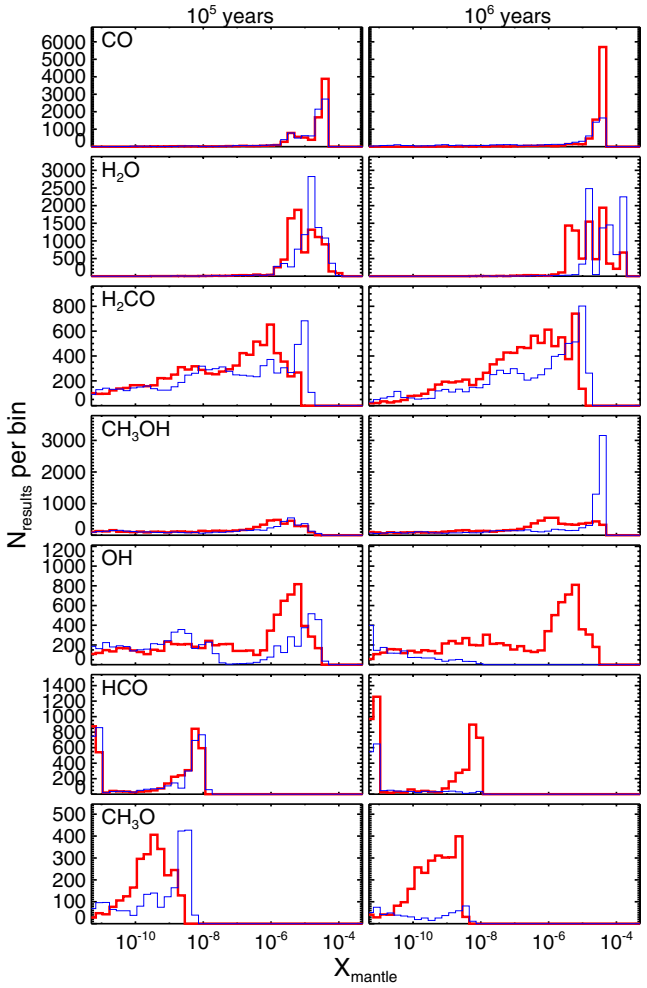

Fig. 8. Distribution of the predicted mantle abundance $X_{\rm mantle}$ of the key species at 10^5 (*left panels*) and 10^6 yr (*right panels*). The thin blue and thick red lines refer to the bulk and multilayer approach. The distribution has been built by considering all the ~18 000 runs of the grid (Sect. 3.8).

very little. The reason is that the particle accretion rate (inversely proportional to the grain size square) and the formation time of each layer compensate each other. The result is that the mantle composition does not depend on the assumed grain size, whether 0.1 or 0.3 μm.

4.5. Influence of other key parameters of GRAINOBLE

Initial abundance of atomic oxygen $X(O)_{\rm ini}$

Not surprisingly, the initial gas phase abundance of atomic oxygen is an important parameter for the final mantle water abundance. The higher the O abundance, the higher the iced H_2O. Less evidently, oxygenation is in competition with hydrogenation. The initial O abundance also affects the final mantle abundance of formaldehyde and, even more, methanol, because the elemental C/O ratio decreases between 0.7 and 0.2 when $X(O)_{\rm ini}$ increases between 2×10^{-5} and 2×10^{-4}. At 10^5 yr, the predicted methanol abundance is a factor ten higher when the O abundance is a factor ten lower.

Diffusion energy to binding energy ratio $E_{\rm d}/E_{\rm b}$

The diffusion energy is an important parameter in the predicted mantle abundance of formaldehyde and methanol. Because the diffusion rates depend exponentially on the diffusion energy, the mantle abundance of stable species, like formaldehyde and methanol, decreases with increasing $E_{\rm d}$. Conversely, the diffusion energy does not affect the mantle abundance of radicals, because their formation and destruction rates compensate each other.

Activation energy $E_{\rm a}$

The activation energy of CO and H_2CO hydrogenation reactions strongly influences the formation rates of formaldehyde and methanol because their reaction rates depend exponentially on $E_{\rm a}$. Most of the runs with a low value of $E_{\rm a}$ (400 K) predict mantle abundances of formaldehyde and methanol higher than 10^{-6} at $\geq 10^5$ yr. Conversely, higher values of $E_{\rm a}$ give uniform distributions of H_2CO and CH_3OH abundances, between 10^{-18} and 10^{-6}. Only ~5% of the runs using a activation energy equal to 2500 K predict formaldehyde and methanol abundances higher than 10^{-6}. The final abundances of formaldehyde and methanol, consequently strongly depend on the other model parameters for high $E_{\rm a}$ values. A significant amount of radicals, like HCO and CH_3O, can survive in the mantle only if the activation energies are low. Runs with activation energies of 400 K predict radical mantle abundances between 10^{-10} and 10^{-8} for both radicals, while runs with $E_{\rm a}$ = 2500 K predict abundances less than $\sim 10^{-11}$. Not surprisingly, the activation energy of CO and H_2CO hydrogenation reactions are, therefore, critical parameters for the survival of radicals in the mantle.

Site size $d_{\rm s}$

The reaction rates and the formation time of each monolayer are both functions of the site size $d_{\rm s}$: the former is proportional to $d_{\rm s}^2$, whereas the latter is proportional to $d_{\rm s}^{-2}$. Therefore, the two processes, which are in competition, cancel each other, and consequently, the total mantle abundance of stable species and radicals do not sensitively depend on the size of sites.

However, the thickness of the grain mantle strongly depends on the site size. Indeed, the maximum number of monolayers is given by the ratio between the number of particles on the grain N_{part} and the number of grain sites $N_{\rm s}$ (proportional to $d_{\rm s}^{-2}$). Furthermore, if we assume that the thickness of a layer is equal to the distance between two sites, the thickness of the mantle is proportional to $d_{\rm s}^3$. Thus, the bigger are the sites, the faster the grains grow. Consequently, the depletion is more efficiently on grains with big sites, increasing the abundance of methanol and decreasing the abundance of CO for example.

4.6. Concluding remarks

Based on the previous paragraphs, we can identify three classes of parameters, depending on their influence on the results:

- The parameters that have a *strong* influence on the mantle composition are the approach to model the chemical behaviour (multilayer versus bulk), the density, the diffusion energy and the activation energy of CO and H_2CO hydrogenation reactions. Modifying the values of these parameters within their chosen range drastically changes the distribution of the predicted mantle abundances, both in the shape and in the values.
- The grain porosity and the temperature as well as the initial abundance of atomic oxygen have only a *moderate* impact on the predicted mantle composition.
- The grain and the site sizes have a *negligible* influence on the total mantle composition. However, these parameters strongly modify the ice thickness, which could have an

impact on photolytic processes and for the desorption time of the mantle during the warm-up phase in protostar envelopes.

5. Comparisons with previous microscopic models

The Monte-Carlo continuous time random walk (CTRW) method was introduced by Chang et al. (2005) and Cuppen & Herbst (2005) for the hydrogen recombination system, and was then extended to more complex networks in Chang et al. (2007), Cuppen & Herbst (2007), Cuppen et al. (2009). The natural output of this model is the multilayer structure of the mantle. This section compares our results with the model of Cuppen et al. (2009) with the twofold aim of validating the GRAINOBLE code and of highlighting the differences between the two models.

5.1. Validation of the GRAINOBLE code

Cuppen et al. (2009) considered the accretion of H, CO, and H_2 on smooth surfaces as described by Cuppen & Herbst (2005), leading to the formation of formaldehyde, methanol, and their associated radicals HCO and CH_3O via the Langmuir-Hinshelwood and the Eley-Rideal mechanisms. A major difference between GRAINOBLE and the Cuppen et al. model is that they consider an α-CO ice, whereas we assumed that the bulk of the mantle is formed by iced water. To reproduce the interactions of molecules within an α-CO ice, we modified the set of binding energies in our model accordingly. Second, the CTRW model takes into account the individual interaction energies between each particle, while our model only considers the total binding energy between the adsorbate and the substrate. To simulate their approach, we assumed for each species i a binding energy equal to fourteen times the interaction between the species i and a CO molecule ($E_b(i) = 14E_{i-CO}$), corresponding to the interaction between an adsorbate and a porous multi-layered CO ice. The binding energy of H is equal to 450 K, while the binding energy of CO is 880 K. The diffusion to desorption energy ratio is assumed to be 0.8, as in Cuppen et al. (2009) for a layer that is initially smooth. The activation energies for CO and H_2CO hydrogenation reactions are those measured by Fuchs et al. (2009), and slightly depend on the grain temperature.

To validate our code with respect to the model of Cuppen et al. (2009), we run our model with a density of 10^5 cm^{-3} and considered the results at 2×10^5 yr, for the following four cases (as in Part 3.3 of Cuppen et al. 2009): a) grain temperature 12 K, n(H)/n(CO) = 1 and $n_d = 2 \times 10^{12} n_h$; b) as a) but $n_d = 1 \times 10^{12} n_h$; c) as a) but temperature 15 K; d) as b) but n(H)/n(CO) = 0.5. Figure 9 shows the chemical composition of each monolayer for the four cases, for porous grains ($F_{por} = 0.7$: this is the value that agrees best for our and Cuppen's model). The comparisons between Fig. 4 of Cuppen et al. (2009) and our Fig. 9 shows that the two codes give very similar results, which validates our code.

5.2. Differences between the two approaches

We highlight a few critical differences between the model of Cuppen and ours.

Unlike our multilayer approach, the CTRW method allows us to model the segregation effects. Heavier particles can agglomerate together to form islands where they can be fixed onto the grains more efficiently. Our multilayer method is a macroscpic approach where segration effects are not taken into account. However, the pores can play the same role as the islands, because particles that enter into the pores cannot desorb either. This is supported by the fact that our porous grains case agrees best with Cuppen's model.

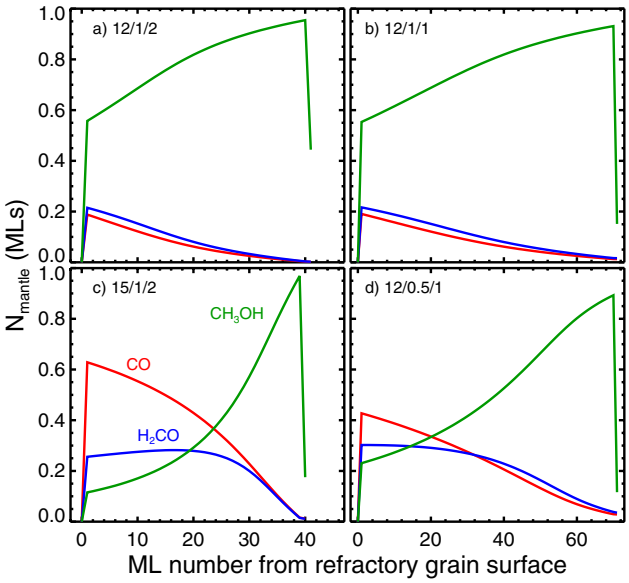

Fig. 9. Chemical composition of the mantle layers as a function of the monolayers at a time of 2×10^5 years, for a density $n_H = 10^5$ cm^{-3}, as in Cuppen et al. (2009) (see text): CO (red), formaldehyde (blue) and methanol (green). The four panels refer to the four cases of Fig. 4 of Cuppen et al. (2009) (see text): **a)** grain temperature 12 K, n(H)/n(CO) = 1 and $n_d = 2 \times 10^{12} n_h$; **b)** as **a)** but $n_d = 1 \times 10^{12} n_h$; **c)** as **a)** but temperature 15 K; **d)** as **b)** but n(H)/n(CO) = 0.5.

An important difference between ours and Cuppen et al.'s model is the inclusion of the water ice formation. Because Cuppen et al. did not consider the formation of water, their ices are formed by pure α-CO ice. Consequently, the interaction energies are lower than those used in our model. Therefore in Cuppen's model ices can form only at temperatures lower than 16–18 K, whereas in our model iced CO can still survive until 21–23 K. In our model, then, the formation of formaldehyde and methanol can occur in a wider range of temperatures than in Cuppen et al. (2009). Consequently, the abundance of formaldehyde and methanol formed on grain mantles decreases much more efficiently with the increase of the temperature in Cuppen et al.'s model than in ours. For example, using the same physical parameters, the CTRW model predicts a decrease of the mantle thickness of 85% (~40 to 6 monolayers), whereas our model does not predict any thickness decreases between 15 and 16.5 K.

6. Comparisons with observations

6.1. The observations

In order to compare our model predictions with observations, we used the data pertaining to the ices only, because the abundance of the sublimated mantle species does not necessarily reflect the chemical composition of their precursor ices. First, it can be altered by reactions in the gas phase. Second, the different sublimation temperatures may introduce errors when comparing the abundance ratios of different species, because they may refer to different regions.

Unfortunately, solid CO, H_2CO, and CH_3OH have been observed simultaneously only towards a very small sample of high- and intermediate-mass protostars (Gibb et al. 2004; Pontoppidan et al. 2004). To increase the statistics and to include low-mass

Table 5. Mantle abundances of CO and CH_3OH with respect to water along with the relative CH_3OH/CO abundance ratio, as observed towards low – (LM), intermediate – (IM), and high-mass (HM) protostars.

Source	X(CO) % wrt H_2O	X(CH_3OH) % wrt H_2O	X(CH_3OH) % wrt to CO
Low-Mass			
L1448 IRS 1	45.5^{a-e}	$<14.9^{d}$	<32.7
L1455 SMM 1	5.6^{a-e}	$<13.5^{d}$	<241.1
RNO 15	13.6^{a-e}	$<5.0^{d}$	<36.8
IRAS 03254	13.6^{a-e}	$<4.6^{d}$	<33.8
IRAS 03271	8.2^{a-e}	$<5.6^{d}$	< 68.3
B1-a	13^{a-e}	$<1.9^{d}$	<14.6
B1-c	28.6^{a-e}	$<7.1^{d}$	<24.8
L1489	15.2^{a-e}	4.9^{d}	32.3
DG Tau B	20.5^{a-e}	$<5.7^{d}$	<27.8
IRAS 12553	12.6^{a-e}	$<3.0^{d}$	<23.8
IRAS 13546	22.7^{a-e}	$<3.9^{d}$	<17.2
IRAS 15398	40.3^{a-e}	10.3^{d}	25.6
CRBR 2422.8-3423	11.2^{a-e}	$<9.3^{d}$	<83.0
RNO 91	19.0^{a-e}	$<5.6^{d}$	<29.5
IRAS 23238	4.0^{a-e}	$<3.6^{d}$	90.0
Intermediate-Mass			
AFGL989	19.0^{b}	1.7^{b}	8.9
SMM4	30.0^{c}	28.0^{c}	93.3
High-Mass			
W33A	7.4^{a-e}	14.7^{d}	198.6
GL 2136	10.2^{a-e}	8.5^{d}	83.3
S140	16.6^{a-e}	$<3.0^{d}$	<18.1
NGC 7538 IRS 9	16.5^{a-e}	7.5^{d}	45.5
AFGL2136	5.0^{b}	5.0^{b}	100.0
AFGL7009	16.0^{b}	33.0^{b}	206.3

References. [(a)] Pontoppidan et al. (2003); [(b)] Gibb et al. (2004); [(c)] Pontoppidan et al. (2004); [(d)] Boogert et al. (2008); [(e)] Pontoppidan et al. (2008).

protostars, too, we therefore restricted the comparison of our model to the observed solid CO and CH_3OH abundances only. Fortunately, a posteriori, when considering the model predictions, we found that using the H_2CO would not provide (substantially) more constraints. Table 5 reports the compilation of observations that we used for the comparison.

6.2. Constraining the activation and diffusion energies

As a first step, we compared the model predictions with the observations with the goal to constrain the two microphysics parameters, which have a high impact on the model predictions (Sect. 4.6), namely E_d/E_b and E_a. Figure 10 shows the CH_3OH/CO abundance ratio as a function of time obtained assuming reference parameters (and more particularly a density 10^5 cm^{-3}) and for different values of the activation energy E_a and diffusion energy E_d. The comparison of the model predictions with the values observed towards intermediate- and high-mass protostars clearly excludes an activation energy higher than 1450 K and a diffusion energy higher than 0.65 times the binding energy E_b. More stringently, if E_a = 1450 K, E_d/E_b has to be equal to 0.5. The analysis of a similar plot for a density of 10^4 cm^{-3} gives similar constraints: E_a = 1450 K implies E_d/E_b = 0.5 and E_a = 400 K, $E_d/E_b \sim 0.65$. The case 10^6 cm^{-3} does not provide more constraints, it is indeed excluded by the observations (see below).

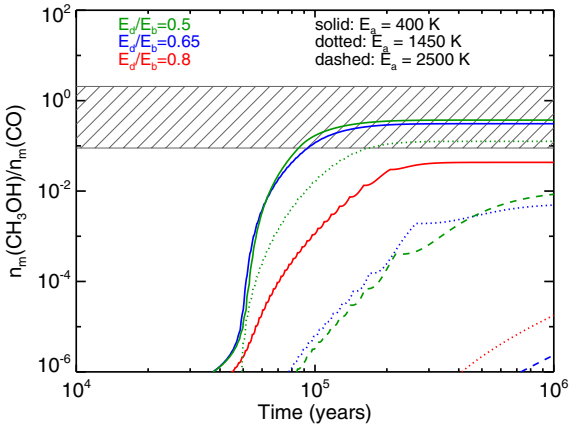

Fig. 10. Mantle CH_3OH/CO abundance ratio versus time. The blue, green, and red lines refer to E_d/E_b = 0.65, 0.5, and 0.8, respectively. Solid, dotted, and dashed lines refer to E_a = 400 K, 1450 K, and 2500 K, respectively. In these computations the density is 10^5 cm^{-3}. The box with hatching shows the interval of CH_3OH/CO abundance ratio observed towards intermediate- and high- mass protostars (Table 5). Because low-mass protostars provide only less stringent upper limits, they are not reported in the plot.

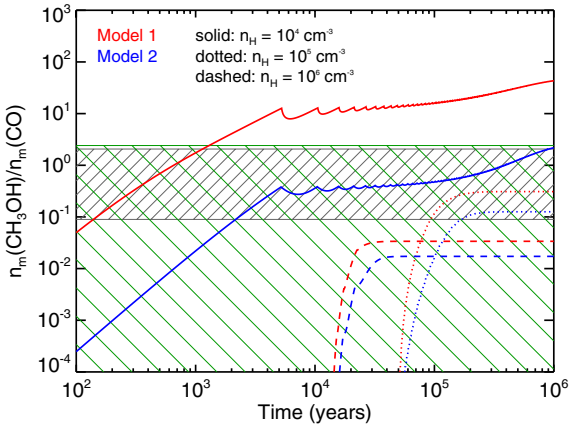

Fig. 11. Mantle CH_3OH/CO abundance ratio versus time. The red lines refer to Model 1 (E_a = 400 K and E_d/E_b = 0.65), the blue lines refer to Model 2 (E_a = 1450 K and E_d/E_b = 0.5) (see text). Solid, dotted and dashed lines refer to densities 10^4, 10^5 and 10^6 cm^{-3} respectively. The grey box with hatching shows the interval of CH_3OH/CO abundance ratio observed towards high- and intermediate- mass protostars, while the green dashed box shows the values (upper limits) observed in low-mass protostars (Table 5).

6.3. Constraining the pre-collapse phase duration and density

Once we limited the range of possible values of E_a and E_b consistent with the observations, we can attempt to constrain the duration of the pre-collapse phase and the density. To this end, Fig. 11 shows the curves of the CH_3OH/CO abundance ratio versus time for three different densities (10^4, 10^5 and 10^6 cm^{-3}) and computed for the two following sets of E_a and E_d values: 1) E_a = 400 K and E_d/E_b = 0.65 (and the reference parameters); 2) E_a = 1450 K and E_d/E_b = 0.5 (and the reference parameters). The comparison between the predicted and observed CH_3OH/CO abundance ratio in intermediate- and high-mass protostars suggests that the bulk of methanol has been formed when the pre-collapse condensation had densities between 10^4 and 10^5 cm^{-3}. Higher densities would produce an insufficiently CH_3OH/CO abundance ratio compared to the values observed in intermediate- and high- mass protostars. If the densities are

around 10^5 cm^{-3}, the duration of the pre-collapse phase must have lasted at least 10^5 yr. Lower densities would allow shorter pre-collapse duration times. But densities higher than 10^5 cm^{-3} are not ruled out for the condensations that produce the low-mass protostars. In that case, the duration of the pre-collapse phase lasted more than 5×10^4 yr.

One important result is that the CH_3OH/CO abundance ratio does not provide an estimate of the duration of the pre-collapse phase, but only a lower limit to it. It neither provides an estimate of the density at the time of the collapse but only a range of possible densities for any given observed CH_3OH/CO abundance ratio. Note that the CH_3OH/H_2CO abundance ratio does not allow us to arrive at better constraints, because the theoretical curves are very similar to those of Fig. 11.

6.4. Chemical differentiation within grain mantles

As briefly mentioned in Sect. 2, IR observations suggest a chemical differentiation of the grain mantles with a polar matrix formed already at $A_V \sim 3$ mag (Whittet et al. 1988), and a non-polar CO matrix formed at higher densities (Tielens et al. 1991). In between, CO can be mixed either with water, methanol, or both at the same time (Bisschop et al. 2007), as well as mixed with O_2, O_3, N_2, or CO_2 (Pontoppidan 2006). Actually, this observational fact is one of the motivations of our work. As discussed in Sect. 4 and, for example, shown in Fig. 6, our code predicts inhomogeneous grain mantle composition. For the reference model, for example, CO is mixed with water in the inner layers while a mixture between CO and methanol is predicted in the outer layers. Given the lack of a dataset to compare our results with, it is difficult to carry out quantitative comparisons between observations and predictions. However, it is worth noticing that the exact grain mantle composition and stratification depends on the overall evolution and structure of the pre-collapse condensation, because the chemical differentiation depends on the density, the temperature and time.

7. Conclusions and perspectives

We presented a new model, GRAINOBLE, which computes the chemical composition of interstellar grain mantles during the cold and dense phase of the pre-collapse. The model presents two main differences from most other published codes: 1) it assumes that only the outermost mantle layer is chemically active, while the mantle bulk is not; 2) it considers porous grains.

We run GRAINOBLE for a large set of parameters, which are either unconstrained (density, temperature and grain size of the prestellar condensation) or poorly known (gas atomic oxygen abundance, diffusion energy, hydrogenation reactions activation energy, grain site size). We obtained a grid of about 18 000 models and built distribution plots of the predicted mantle abundances. This allows us to study the influence of each of these parameters on the predicted abundances and, consequently, the robustness of the predictions.

Finally, we compared the GRAINOBLE predictions with those obtained by the microscopic CTRW model of Cuppen et al. (2009), obtaining a fair agreement between the two models. The comparison clearly validates our treatment and our code (Sect. 5). The most important results of the GRAINOBLE model are the following.

- The multilayer treatment shows a differentiation of the species within the mantle, with the innermost layers being rich in CO, the intermediate layers in formaldehyde, and the outermost layers in methanol, reflecting the different formation time of each species in the mantle. This differentiation will likely lead to a differentiation in the deuteration of formaldehyde and methanol on the ices. Because the deuteration increases with the CO depletion in the gas phase (Roberts et al. 2003; Ceccarelli & Dominik 2005), methanol will likely be more deuterated than formaldehyde, as indeed observed in Parise et al. (2006). A forthcoming paper will focus on the detailed modeling of the deuteration process.
- The multilayer treatment predicts a relatively high abundance of radicals trapped in the mantle. For example, HCO and CH_3O show abundances of 10^{-9}–10^{-7} with respect to H nuclei. As suggested by Garrod & Herbst (2006), these radicals can react to form COMs when the grain temperature increases during the formation of the protostar. At this stage, we cannot say whether the predicted radical abundances are sufficient to explain the present observations (e.g. Fig. 1), and, unfortunately, comparisons with previous models are not possible because of the lack of specific information. We will explore this aspect, the formation of COMs, in a forthcoming paper.
- The presence of porosity in the grains only moderately influences the mantle chemical composition, causing an enhanced abundance of formaldehyde and methanol by less than a factor four.
- The chemical composition of grain mantles strongly depends on the physical conditions of the prestellar condensation, particularly on its density as well as its age. Therefore, it will be important to model the evolution of the condensation for realistic predictions of the mantle composition. Conversely, the observed mantle composition can provide valuable information on the past history of protostars, and will be the focus of a forthcoming paper. Comparisons of the present predictions with the ices observations (specifically the CH_3OH/CO abundance ratio) suggest that intermediate – and high – mass protostars evolved from condensations less dense than about 10^5 cm^{-3}, while no stringent constraints can be put on the prestellar condensations of low-mass protostars.
- The predicted mantle composition critically depends on the values of the diffusion energy and activation energy of the hydrogenation reactions. Comparing our model predictions with observations of ices allows to constrain the values of these two important parameters: the diffusion to binding energy ratio has to be around 0.5–0.65, and the activation energy has to be less than 1450 K.
- Other parameters of the GRAINOBLE model, like the gas atomic oxygen abundance and the site size, do not substantially influence the predicted mantle abundances.

In summary, GRAINOBLE is a versatile and fast code to model the grain surface chemistry. Its main improvement with respect to previous similar models is the treatment of the layer-by-layer chemistry, which provides a more realistic stratified mantle composition. It predicts that the mantles are indeed stratified and that radicals are trapped inside the mantles. Because it is not expensive from the point of view of computing time, modeling of complex and more realistic cases, like the evolution of a prestellar core, are now feasible.

Acknowledgements. The authors would like to thank O. Biham, P. Caselli, T. Hasegawa, and V. Wakelam for useful exchanges on grain chemistry modelling, P. Peters and L. Wiesenfeld for discussions about the physical and chemical processes on grain surfaces, and X. Tielens for helpful discussions on the abundances in the gas phase. This work has been supported by l'Agence Nationale pour la Recherche (ANR), France (project FORCOMS, contracts ANR-08-BLAN-022).

Appendix A: Distributions of abundances

As introduced in Sect. 3.8, we have built a model grid in which eight input parameters vary. To study the results of this grid, we computed the distributions of selected species abundances on grain mantles $X_m(i)$, namely the number of results giving $X_m(i)$ in each abundance interval. The following figures show the distributions of abundances for each input parameter and for two extremal values, using the multilayer approach only.

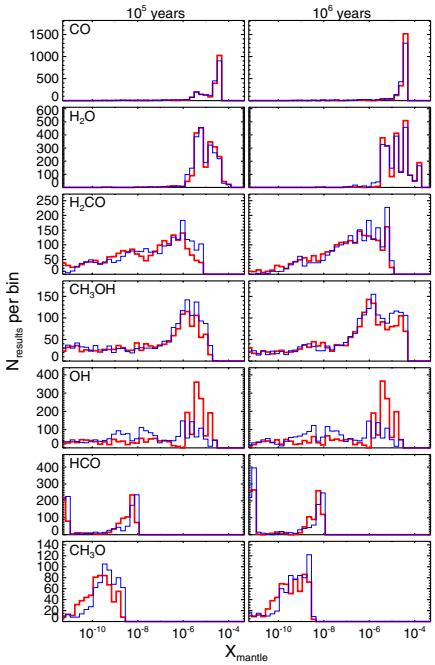

Fig. A.1. Distribution of abundances on grain mantles at $t = 10^5$ and 10^6 years for two porosity values: $F_{\rm por} = 0$ (thick red) and 0.9 (narrow blue).

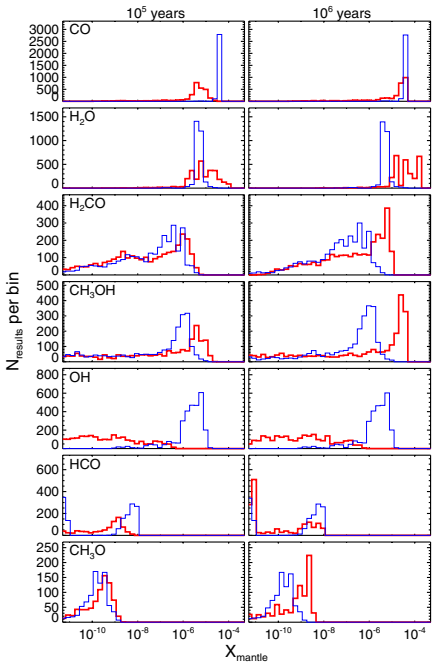

Fig. A.2. Distribution of abundances on grain mantles at $t = 10^5$ and 10^6 years for two densities: $n_{\rm H} = 10^4$ (thick red) and 10^6 cm^{-3} (narrow blue).

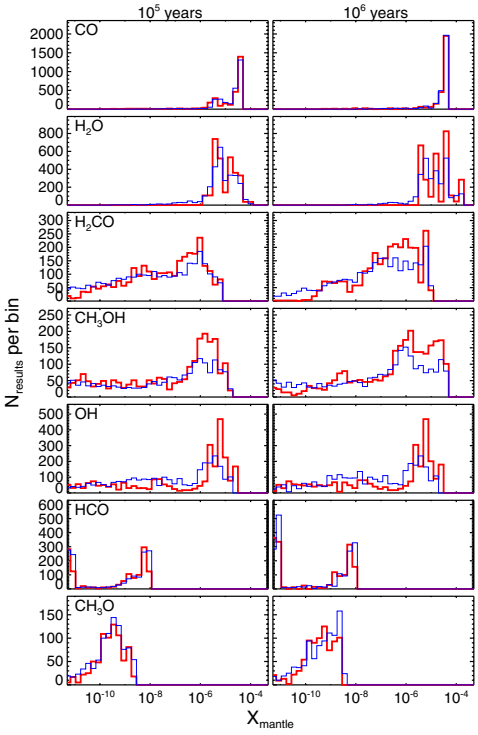

Fig. A.3. Distribution of abundances on grain mantles at $t = 10^5$ and 10^6 years for two temperatures: $T = 10$ (thick red) and 20 K (narrow blue).

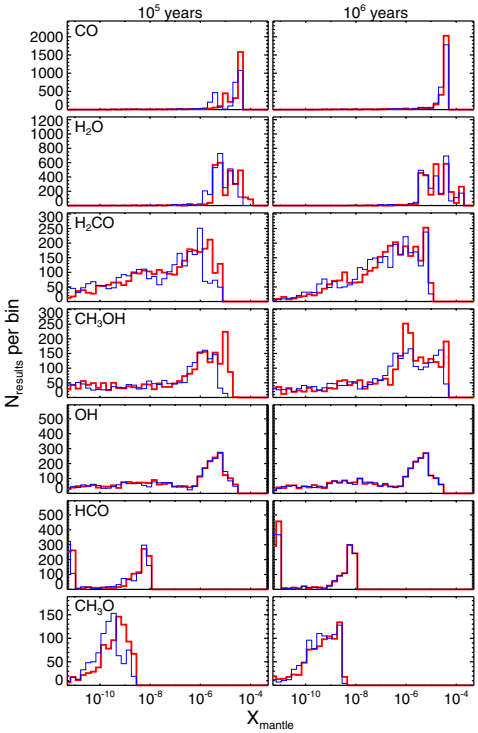

Fig. A.4. Distribution of abundances on grain mantles at $t = 10^5$ and 10^6 years for two grain sizes: $a_{\rm d} = 0.1$ (thick red) and 0.3 μm (narrow blue).

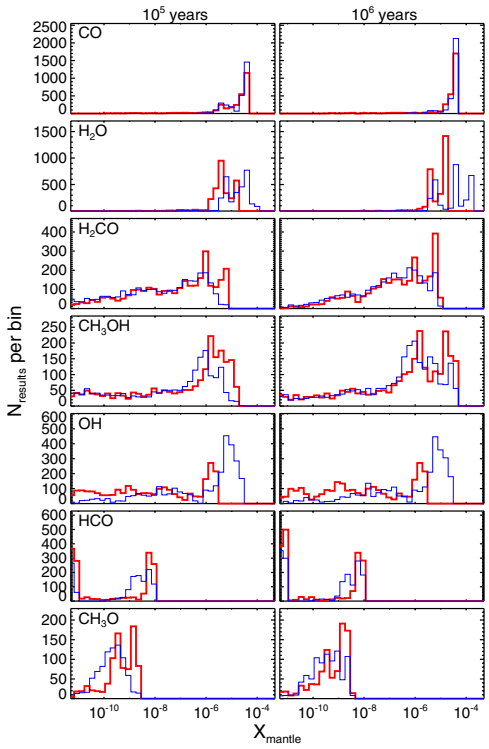

Fig. A.5. Distribution of abundances on grain mantles at $t = 10^5$ and 10^6 years for two initial oxygen abundances: $X_{\rm ini}$(O)= 2×10^{-5} (thick red) and 2×10^{-4} (narrow blue).

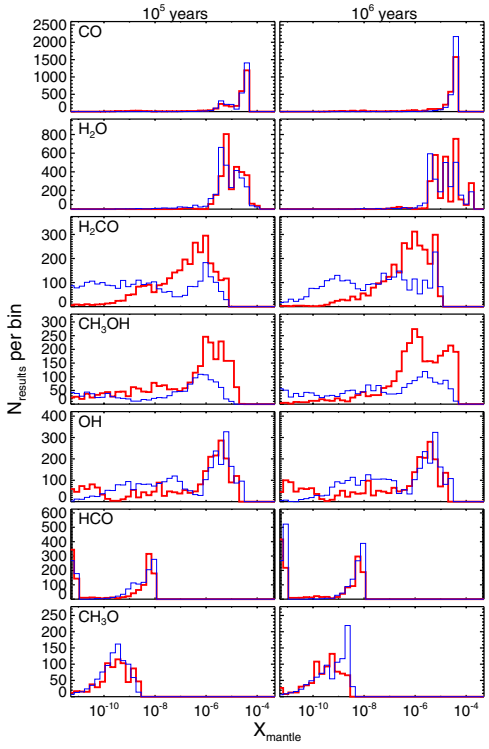

Fig. A.6. Distribution of abundances on grain mantles at $t = 10^5$ and 10^6 years for two energy ratios: $E_{\rm d}/E_{\rm b} = 0.5$ (thick red) and 0.8 (narrow blue).

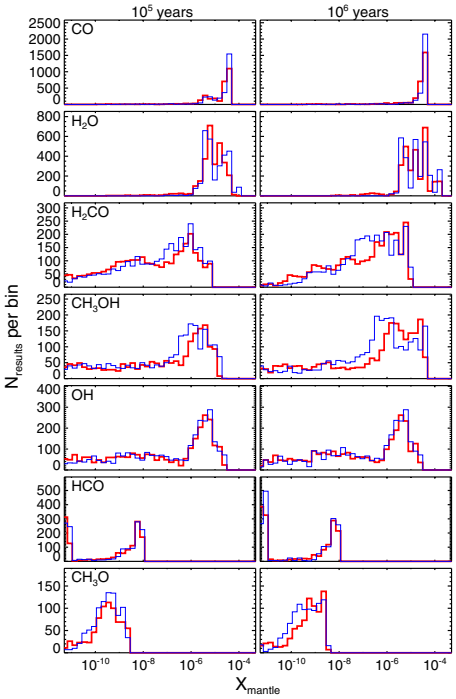

Fig. A.7. Distribution of abundances on grain mantles at $t = 10^5$ and 10^6 years for two site sizes: $d_{\rm s} = 1.4$ (thick red) and 7 Å (narrow blue).

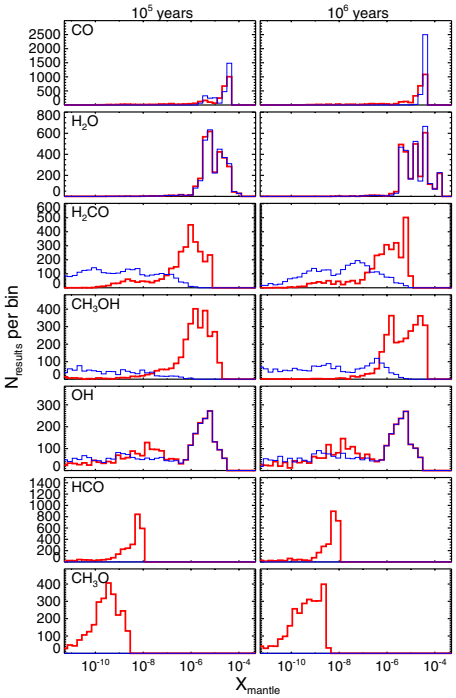

Fig. A.8. Distribution of abundances on grain mantles at $t = 10^5$ and 10^6 years for two CO and H_2CO hydrogenation reactions: $E_{\rm a} = 400$ (thick red) and 2500 K (narrow blue).

Appendix B: List of symbols used in this work

Table B.1. List of symbols and their explanation.

Symbol	Parameter
a_d	diameter of interstellar grains (in μm)
d_s	size of each site (in Å)
E_d	barrier energy against diffusion of a considered species (in K)
E_b	barrier energy against desorption of a considered species (in K)
E_a	activation energy of the CO and H_2CO hydrogenation reactions (in K)
F_{por}	fraction of the grain surface occupied by the pores
F_{np}	fraction of the grain surface occupied by the non-porous surface
F_{ed}	fraction of the grain surface occupied by the edge porous sites
r_d	radius of interstellar grains (in μm)
n_d	density of interstellar grains (in cm^{-3})
N_{pore}	number of sites occupied by each pore
N_s	number of sites of the considered layer
n_H	total density of H nuclei (in cm^{-3})
n_g	gas phase density of a considered species (in cm^{-3})
P_{np}	surface population of a considered species in the non-porous surface (in monolayers)
P_{por}	surface population of a considered species in the pores (in monolayers)
R_{acc}	accretion rate of a considered species (in s^{-1})
R_{hop}	hopping rate from site to site of a considered species (in s^{-1})
R_{diff}	diffusion rate of a considered species (in s^{-1})
$R_{r,np}$	reaction rate of a considered reaction in the non-porous surface (in s^{-1})
$R_{r,por}$	reaction rate of a considered reaction in the pores (in s^{-1})
R_{ev}	evaporation rate of a considered species (in s^{-1})
S	sticking coefficient of a considered species
σ_d	cross section of interstellar grains (in cm^2)
T_g	gas temperature (in K)
T_d	dust temperature (in K)
v	thermal velocity of a considered species in the gas phase (in $cm\,s^{-1}$)
X_d	abundance of interstellar grains relative to H nuclei
X_g	abundance relative to H nuclei of a considered species in the gas phase
X_m	abundance relative to H nuclei of a considered species on grain mantles
ζ	cosmic rays ionization rate (in s^{-1})

References

Aikawa, Y., Wakelam, V., Garrod, R. T., & Herbst, E. 2008, ApJ, 674, 984
Allen, M., & Robinson, G. W. 1977, ApJ, 212, 396
Andersson, S., Al-Halabi, A., Kroes, G.-J., & van Dishoeck, E. F. 2006, J. Chem. Phys., 124, 064715
Arasa, C., Andersson, S., Cuppen, H. M., van Dishoeck, E. F., & Kroes, G.-J. 2010, J. Chem. Phys., 132, 184510
Avgul, N. N., & Kiselev, A. V. 1970, Chem. Phys. Carbon, 6, 1
Awad, Z., Viti, S., Collings, M. P., & Williams, D. A. 2010, MNRAS, 407, 2511
Barzel, B., & Biham, O. 2007, J. Chem. Phys., 127, 144703
Bennett, C. J., & Kaiser, R. I. 2007, ApJ, 661, 899
Bergin, E. A., & Tafalla, M. 2007, ARA&A, 45, 339
Beuther, H., Zhang, Q., Bergin, E. A., & K., S. T. 2009, ApJ, 137, 406
Biham, O., Furman, I., Pirronello, V., & Vidali, G. 2001, ApJ, 553, 595
Bisschop, S. E., Fraser, H. J., Öberg, K. I., van Dishoeck, E. F., & Schlemmer, S. 2006, A&A, 449, 1297
Bisschop, S. E., Jrgensen, J. K., van Dishoeck, E. F., & de Wachter E. B. M. 2007, A&A, 465, 913
Blake, G. A., Sutton, E. C., Masson, C. R., & Phillips, T. G. 1987, ApJ, 315, 621
Boogert, A. C. A., Pontoppidan, K. M., Knez, C., et al. 2008, ApJ, 678, 985
Bottinelli, S., Ceccarelli, C., Lefloch, B., et al. 2004, ApJ, 615, 354
Bottinelli, S., Ceccarelli, C., Williams, J. P., & Lefloch, B. 2007, A&A, 463, 601
Caselli, P., Hasegawa, T. I., & Herbst, E. 1998a, ApJ, 495, 309
Caselli, P., Walmsley, C. M., Terzieva, R., & Herbst, E. 1998b, ApJ, 499, 234
Caux, E., Ceccarelli, C., Castets, A., et al. 1999, A&A, 347, L1
Cazaux, S., Tielens, A. G. G. M., Ceccarelli, C., et al. 2003, ApJ, 593, L51
Ceccarelli, C., & Dominik, C. 2005, A&A, 440, 583
Chang, Q., Cuppen, H. M., & Herbst, E. 2005, A&A, 434, 599
Chang, Q., Cuppen, H. M., & Herbst, E. 2007, A&A, 469, 973
Charnley, S. B., Tielens, A. G. G. M., & Millar, T. J. 1992, ApJ, 399, L71
Collings, M. P., Dever, J. W., Fraser, H. J., & McCoustra, M. R. S. 2003, Ap&SS, 285, 633
Collings, M. P., Anderson, M. A., Chen, R., et al. 2004, MNRAS, 354, 1133
Cuppen, H. M., & Herbst, E. 2005, MNRAS, 361, 565
Cuppen, H. M., & Herbst, E. 2007, ApJ, 668, 294
Cuppen, H. M., Ioppolo, S., Romanzin, C., & Linnartz, H. 2010, Phys. Chem. Chem. Phys. (Incorporating Faraday Transactions), 12, 12077
Cuppen, H. M., van Dishoeck, E. F., Herbst, E., & Tielens, A. G. G. M. 2009, A&A, 508, 275
Dartois, E., Schutte, W., Geballe, T. R., et al. 1999, A&A, 342, L32
di Francesco, J., Evans, II, N. J., Caselli, P., et al. 2007, Protostars and Planets V, 17
Dulieu, F., Amiaud, L., Congiu, E., et al. 2010, A&A, 512, A30
Ehrlich, G., & Hudda, F. G. 1966, J. Chem. Phys., 44, 1039
Frerking, M. A., Langer, W. D., & Wilson, R. W. 1982, ApJ, 262, 590
Fuchs, G. W., Cuppen, H. M., Ioppolo, S., et al. 2009, A&A, 505, 629
Garrod, R. T., & Herbst, E. 2006, A&A, 457, 927
Garrod, R. T., Wakelam, V., & Herbst, E. 2007, A&A, 467, 1103
Garrod, R. T., Weaver, S. L. W., & Herbst, E. 2008, ApJ, 682, 283
Gerakines, P. A., Schutte, W. A., & Ehrenfreund, P. 1996, A&A, 312, 289
Gerakines, P. A., Moore, M. H., & Hudson, R. L. 2000, A&A, 357, 793
Gerakines, P. A., Moore, M. H., & Hudson, R. L. 2001, J. Geophys. Res., 106, 33381
Gibb, E., Nummelin, A., Irvine, W. M., Whittet, D. C. B., & Bergman, P. 2000, ApJ, 545, 309
Gibb, E. L., Whittet, D. C. B., Boogert, A. C. A., & Tielens, A. G. G. M. 2004, ApJS, 151, 35
Goumans, T. P. M. 2011, MNRAS, 262
Gredel, R., Lepp, S., Dalgarno, A., & Herbst, E. 1989, ApJ, 347, 289
Green, N. J. B., Toniazzo, T., Pilling, M. J., et al. 2001, A&A, 375, 1111
Hasegawa, T. I., & Herbst, E. 1993a, MNRAS, 261, 83
Hasegawa, T. I., & Herbst, E. 1993b, MNRAS, 263, 589
Hasegawa, T. I., Herbst, E., & Leung, M. C. 1992, Ap&SS, 82, 167
Hinshelwood, C. N. 1940, The Kinetics Of Chemical Change (The Clarendon Press)
Hollenbach, D. & Salpeter, E. E. 1970, ApJ, 163, 155
Horn, A., Møllendal, H., Sekiguchi, O., et al. 2004, ApJ, 611, 605
Ikeda, M., Ohishi, M., Nummelin, A., et al. 2001, ApJ, 560, 792
Ioppolo, S., Cuppen, H. M., Romanzin, C., van Dishoeck, E. F., & Linnartz, H. 2010, Phys. Chem. Chem. Phys. (Incorporating Faraday Transactions), 12, 12065

Jaycock, M. J., & Parfitt, G. D. 1986, Chemistry of Interfaces (New York: Wiley and Sons)
Jenniskens, P., Blake, D. F., Wilson, M. A., & Pohorille, A. 1995, ApJ, 455, 389
Jones, A. P. 2011, A&A, 528, A98
Katz, N., Furman, I., Biham, O., Pirronello, V., & Vidali, G. 1999, ApJ, 522, 505
Klemm, R. B., Payne, W. A., & Stief, L. J. 1975, in Chemical kinetic data for the upper and lower atmosphere, ed. S. W. Benson (New York: Wiley)
Laas, J. C., Garrod, R. T., Herbst, E., & Widicus Weaver, S. L. 2011, ApJ, 728, 71
Leger, A., Jura, M., & Omont, A. 1985, A&A, 144, 147
Lipshtat, A., & Biham, O. 2003, A&A, 400, 585
Lis, D. C., Keene, J., Phillips, T. G., et al. 2001, ApJ, 561, 823
MacDonald, G. H., Gibb, A. G., Habing, R. J., & Millar, T. J. 1996, A&AS, 119, 333
Matar, E., Congiu, E., Dulieu, F., Momeni, A., & Lemaire, J. L. 2008, A&A, 492, L17
Mathis, J. S. 1996, ApJ, 472, 643
Mathis, J. S., Rumpl, W., & Nordsieck, K. H. 1977, ApJ, 217, 425
Mehringer, D. M., & Snyder, L. E. 1996, ApJ, 471, 897
Nummelin, A., Bergman, P., Hjalmarson, A., et al. 2000, ApJS, 128, 213
Öberg, K. I., Linnartz, H., Visser, R., & van Dishoeck, E. F. 2009a, ApJ, 693, 1209
Öberg, K. I., van Dishoeck, E. F., & Linnartz, H. 2009b, A&A, 496, 281
Ormel, C. W., Paszun, D., Dominik, C., & Tielens, A. G. G. M. 2009, A&A, 502, 845
Ossenkopf, V. 1993, A&A, 280, 617
Padovani, M., Galli, D., & Glassgold, A. E. 2009, A&A, 501, 619
Parise, B., Ceccarelli, C., Tielens, A. G. G. M., et al. 2006, A&A, 453, 949
Perets, H. B., & Biham, O. 2006, MNRAS, 365, 801
Perets, H. B., Biham, O., Manicó, G., et al. 2005, ApJ, 627, 850
Pontoppidan, K. M. 2006, A&A, 453, L47
Pontoppidan, K. M., Fraser, H. J., Dartois, E., et al. 2003, A&A, 408, 981
Pontoppidan, K. M., van Dishoeck, E. F., & Dartois, E. 2004, A&A, 426, 925
Pontoppidan, K. M., Boogert, A. C. A., Fraser, H. J., et al. 2008, ApJ, 678, 1005
Qin, S., Wu, Y., Huang, M., et al. 2010, ApJ, 711, 399
Remijan, A., Shiao, Y., Friedel, D. N., Meier, D. S., & Snyder, L. E. 2004, ApJ, 617, 384
Requena-Torres, M. A., Martín-Pintado, J., Rodríguez-Franco, A., et al. 2006, A&A, 455, 971
Roberts, H., Herbst, E., & Millar, T. J. 2003, ApJ, 591, L41
Shen, C. J., Greenberg, J. M., Schutte, W. A., & van Dishoeck, E. F. 2004, A&A, 415, 203
Sosa, A., & Schlegel, B. H. 1986, Int. J. Quant. Chem., 29, 1001
Speedy, R. J., Debenedetti, P. G., Scott Smith, R., Huang, C., & Kay, B. D. 1996, J. Chem. Phys., 105, 240
Steinacker, J., Pagani, L., Bacmann, A., & Guieu, S. 2010, A&A, 511, A9
Stepnik, B., Abergel, A., Bernard, J., et al. 2003, A&A, 398, 551
Sternberg, A., Dalgarno, A., & Lepp, S. 1987, ApJ, 320, 676
Sutton, E. C., Peng, R., Danchi, W. C., et al. 1995, Ap&SS, 97, 455
Tielens, A. G. G. M. 2005, Phys. Chem. Interstellar Medium (Cambridge University Press)
Tielens, A. G. G. M., & Hagen, W. 1982, A&A, 114, 245
Tielens, A. G. G. M., & Allamandola, L. J. 1987, in Interstellar Processes, ed. D. J. Hollenbach, & H. A. Thronson, 397
Tielens, A. G. G. M., Tokunaga, A. T., Geballe, T. R., & Baas, F. 1991, ApJ, 381, 181
Ulbricht, H., Moos, G., & Hertel, T. 2002, Phys. Rev. B, 66
Vastel, C., Caux, E., Ceccarelli, C., et al. 2000, A&A, 357, 994
Walch, S. P. 1993, J. Chem. Phys., 98, 3076
Watanabe, N., & Kouchi, A. 2002, ApJ, 567, 651
Whittet, D. C. B., Bode, M. F., Longmore, A. J., et al. 1988, MNRAS, 233, 321
Woon, D. E. 2002, ApJ, 569, 541

The Astrophysical Journal Letters, 748:L3 (6pp), 2012 March 20 doi:10.1088/2041-8205/748/1/L3

FORMALDEHYDE AND METHANOL DEUTERATION IN PROTOSTARS: FOSSILS FROM A PAST FAST HIGH-DENSITY PRE-COLLAPSE PHASE

V. Taquet, C. Ceccarelli, and C. Kahane
UJF-Grenoble 1/CNRS-INSU, Institut de Planétologie et d'Astrophysique de Grenoble (IPAG) UMR 5274, F-38041 Grenoble, France
Received 2011 December 21; accepted 2012 February 14; published 2012 February 27

ABSTRACT

Extremely high deuteration of several molecules has been observed around low-mass protostars for a decade. Among them, formaldehyde and methanol present particularly high deuteration, with observations of abundant doubly and triply deuterated forms. Both species are thought to be mainly formed on interstellar grains during the low-temperature and dense pre-collapse phase by H and D atom additions on the iced CO. We present here a theoretical study of the formaldehyde and methanol deuteration obtained with our gas–grain model, GRAINOBLE. This model takes into account the multilayer nature of the mantle and explores the robustness of the results against the uncertainties of poorly constrained chemical and surface model parameters. The comparison of the model predictions with the observations leads to two major results: (1) the observed high deuteration is obtained during the last phase of the pre-collapse stage, when the density reaches $\sim 5 \times 10^6$ cm^{-3}, and this phase is fast, lasting only several thousands years; and (2) D and H abstraction and substitution reactions are crucial in making up the observed deuteration ratios. This work shows the power of chemical composition as a tool to reconstruct the past history of protostars.

Key words: ISM: abundances – ISM: molecules – stars: abundances – stars: formation

Online-only material: color figures

1. INTRODUCTION

Although the deuterium elemental abundance is 1.5×10^{-5} relative to hydrogen (Linsky 2003), observations carried out during the last decade have revealed high abundances of singly, doubly, and even triply deuterated molecules in low-mass pre-stellar cores and Class 0 protostars (Ceccarelli et al. 2007). In this work, we focus on formaldehyde and methanol, both species likely synthesized on the grain surfaces (Tielens & Hagen 1982; Watanabe & Kouchi 2002) as gas phase reactions are unable to reproduce the large observed abundances (Roberts et al. 2004; Maret et al. 2005).

In pre-stellar cores, HDCO/H_2CO and D_2CO/H_2CO abundance ratios up to 10% have been observed (Bacmann et al. 2003; Bergman et al. 2011). The observed deuterium fractionations increase with the increasing CO depletion, suggesting that the latter is a key parameter. Analogously, several formaldehyde and methanol isotopologues have been detected in Class 0 low-mass protostars (Ceccarelli et al. 1998, 2001; Parise et al. 2002, 2004, 2006). However, unlike in pre-stellar cores, no correlation between the CO depletion and deuterium fractionation is observed, so that the deuteration process is thought to occur in the previous pre-collapse phase. In general, methanol is more enriched in deuterium than formaldehyde. In most of the observed sources, the simply deuterated molecule HDCO shows a deuterium fractionation between 13% and 20% whereas CH_2DOH shows a fractionation between 37% and 65% (Parise et al. 2006). CHD_2OH also shows a higher fractionation than D_2CO, by a factor of $\sim$2. Finally, the deuteration process occurs more efficiently on the methyl group than on the hydroxyl group of methanol, as the [CH_2DOH]/[CH_3OD] ratio has been observed to be between 10 and 20 in a sample of low- and intermediate-mass protostars by Parise et al. (2006) and Ratajczak et al. (2011).

Recent experimental works have confirmed the synthesis of formaldehyde and methanol by hydrogenation of iced CO (Watanabe & Kouchi 2002; Hidaka et al. 2007; Fuchs et al. 2009) and also highlighted the complex chemical evolution of H_2O–CO ices when they are exposed to D and H atoms. Indeed, Nagaoka et al. (2005, 2007) and Hidaka et al. (2009) have shown that formaldehyde and methanol can be efficiently deuterated into HDCO, D_2CO, CH_2DOH, CHD_2OH, and CD_3OH, when they are irradiated by D atoms. Conversely, abstractions of D can only occur on formaldehyde, and not on methanol. Therefore, formaldehyde isotopologues can only be hydrogenated to form back HDCO and H_2CO if they are exposed to H atoms. The relative reaction rates deduced from these works show that H and D abstractions and substitutions on formaldehyde and methanol are as efficient as addition reactions (see also the theoretical calculations by Goumans 2011; Goumans & Kaestner 2011). These processes could, therefore, largely increase the deuterium fractionations of formaldehyde and methanol after the complete depletion of CO and their formation on the surfaces.

In the past, astrochemical models have struggled to reproduce the observed deuteration ratios of formaldehyde and methanol. While it is now clear that CO depletion plays a major role in increasing the atomic D/H ratio of the gas landing on the grain surfaces (Roberts et al. 2004), a full model coupling the gas and grain chemistry that *simultaneously* reproduces the observed formaldehyde and methanol deuteration is still missing. A previous attempt was carried out by Caselli et al. (2002) and Stantcheva & Herbst (2003), who studied the formaldehyde and methanol deuteration as a function of the atomic D/H ratio, taken as a free parameter. However, as also emphasized by Parise et al. (2006), the use of a constant [D]/[H] ratio is (1) unable to predict all the deuterium fractionations at the same time and (2) is not necessarily correct, as formaldehyde and methanol may be formed on the grains at different times. Cazaux et al. (2011) have coupled gas phase and grain mantle chemical networks to study the deuteration of water and formaldehyde only (and not methanol).

In this Letter, we re-consider the problem of the formaldehyde and methanol deuteration, using our gas–grain coupled model,

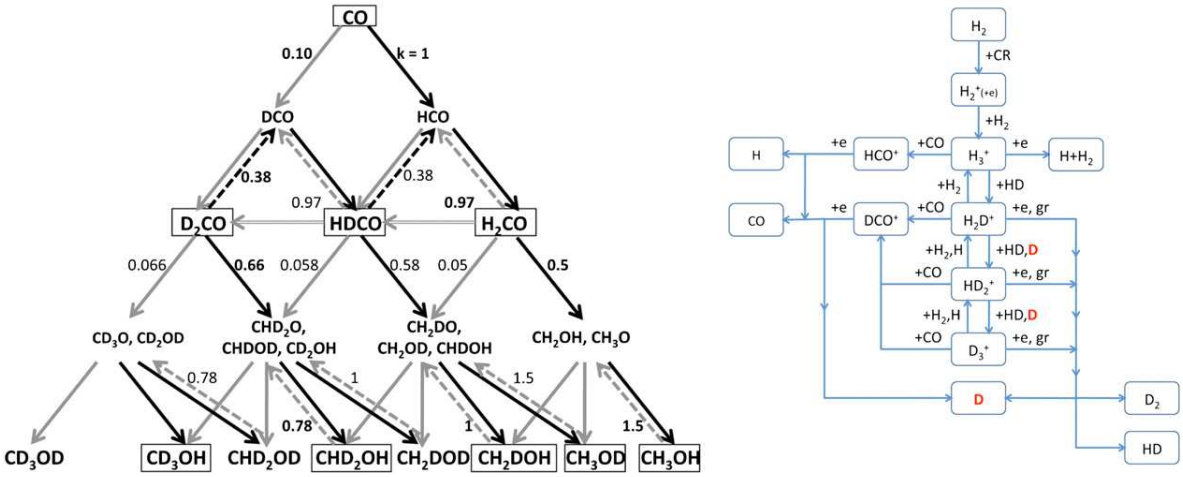

Figure 1. Left: chemical network on grain mantles focusing on the formation of formaldehyde and methanol. Solid, dashed, and open arrows refer to addition, abstraction, and substitution reactions. Black arrows refer to reactions involving H while gray arrows represent reactions involving D. Finally, the bold values refer to the rates relative to the H + CO reaction experimentally deduced by Nagaoka et al. (2007) and Hidaka et al. (2009) while non-bold values show the deduced relative rates by analogy with similar reactions. Right: chemical network in the gas phase leading to atomic deuterium formation.

(A color version of this figure is available in the online journal.)

GRAINOBLE, which takes into account D and H atoms addition, but also abstraction and substitution reactions. Our goal is to simultaneously reproduce the formaldehyde and methanol deuteration observed toward Class 0 protostars by considering their formation on interstellar grains only. Note that, once sublimated from ices, the abundance of these species is only slightly affected by gas phase reactions, as the typical chemical timescale ($\sim 10^5$ yr; Charnley et al. 1997) is larger than the typical age of these objects ($\sim 10^4$ yr; André et al. 2000). We will show that understanding how and when the observed deuteration occurs will also provide us with hints on the process itself and on the past history of the protostars.

2. MULTILAYER MODELING OF DEUTERATED ICES

2.1. Description of the GRAINOBLE Model

For this study we use the GRAINOBLE model (Taquet et al. 2012, hereafter TCK12). Briefly, it is a gas–grain chemical model, based on the rate equations approach introduced by Hasegawa et al. (1992) for time-dependent grain surface chemistry modeling. It considers the following four processes.

1. Accretion of gas phase species onto the grain surfaces as a function of time.
2. Thermal diffusion of adsorbed species. The hopping rate follows a Boltzmann function which depends on the diffusion energy E_d.
3. Surface reactions via the Langmuir–Hinshelwood mechanism. The probability of the reaction is given by the exponential portion of the quantum mechanical probability for tunneling through a square barrier and therefore depends on the activation energy E_a of the reaction.
4. Thermal evaporation caused by the thermal balance and by the cosmic-ray-induced heating of the grains (Hasegawa & Herbst 1993a). We ignored the photolytic process due to the cosmic-ray-induced UV photons because they have a negligible influence on the abundance of formaldehyde and methanol in dark clouds (5% at maximum; Cuppen et al. 2009).

We follow the mantle formation on grains with a multilayer approach in which the outermost layer only is reactive, while the mantle bulk remains inert. Unlike Hasegawa & Herbst (1993b) and Garrod & Pauly (2011) models, the trapping of particles into the bulk is performed one layer at a time, once the considered layer is filled.

2.2. Chemical Network

We consider the accretion of gaseous H, D, H_2, HD, D_2, O, and CO onto grains.

We assume that formaldehyde, methanol, and their deuterated isotopologues are formed via hydrogenation and deuteration addition reactions on molecules initiated by the accretion of CO. Based on experimental and theoretical works (Hidaka et al. 2007; Watanabe & Kouchi 2008; Andersson et al. 2011), the energy barriers of the D and H addition reactions involving CO and formaldehyde are very similar, so we assume them to be identical ($=E_a$). Note that, however, given the high uncertainty in the value of E_a (see TCK12), this is taken as a free parameter. In contrast, reactions involving a radical are barrierless.

Following the experimental works of Hidaka et al. (2009) and Nagaoka et al. (2007), we also include the abstraction and substitution reactions of H and D on formaldehyde and methanol according the scheme proposed by Watanabe & Kouchi (2008) and Hidaka et al. (2009), and as shown in Figure 1. We adopt the probability of each reaction following the relative rates deduced experimentally when they are available, as marked in the figure. For the reactions that have not been derived by the experiments, we adopt the probability measured for the same isotopologue by analogy. For example, the reaction $D_2CO + D \rightarrow CD_3O$ has a reaction rate equal to the H + CO rate multiplied by 0.1 (D + CO) and 0.66 (D_2CO + H).

Even if most of the water is likely formed during the translucent phase, and therefore before H_2CO and CH_3OH (see Öberg et al. 2011), our model also takes into account its formation, as it is in competition with formaldehyde and methanol formation according to TCK12. With respect to TCK12, we added the deuteration reactions and the path

$$H_2 + OH \rightarrow H_2O + H,$$

which seem to be the most efficient reaction in molecular clouds, as suggested by Cuppen & Herbst (2007).

Since the deuteration of formaldehyde and methanol on the grains depends on the atomic gas phase D/H ratio, we are here particularly interested in the chemical network leading to the formation of atomic deuterium in the gas phase. We use the fractionation reactions introduced by Roberts & Millar (2000) and Roberts et al. (2004) to study the formation of H_3^+ isotopologues and atomic deuterium. The gas phase chemical network is shown in Figure 1. As shown by Flower et al. (2006), the ortho/para ratio (opr) of H_2 can influence the deuteration of H_3^+ and consequently the atomic D/H ratio, but only when it is $\geqslant 10^{-3}$. The available measures in cold gas indicate low H_2 opr values ($<10^{-3}$ to 10^{-2}; Dislaire et al. 2012 and references therein). We, therefore, did not consider this effect in this work.

2.3. The Physical Model

Rather than simulating the evolution from the diffuse cloud state to the pre-stellar core, we focus on the last stage of the evolution, when the material is already molecular and the density reaches the value $n_{\rm H}$. The initial abundance of gas phase species (H, D, HD, D_2, H_3^+ isotopologues, ...) are given by the steady state abundance, obtained solving the gas phase chemical network presented in Section 2.2 and considering the recombination of H and D onto grains. The abundance relative to the H nuclei of the deuterium and CO reservoirs are 1.5×10^{-5} and 4.75×10^{-5}.

We follow, then, the formation and evolution of the grain mantles during this phase, keeping the gas density $n_{\rm H}$ constant. Briefly, as time passes, CO freezes out onto the grain mantles, where it forms H_2CO and CH_3OH and their deuterated isotopologues. Therefore, the deuteration of formaldehyde and methanol on the mantle primarily depends on the gaseous atomic D/H ratio.

2.4. Multi-parameter Approach

We use a multi-parameter approach as described in TCK12, to take into account the variation or the uncertainty of physical conditions and surface parameters.

Low-mass pre-stellar cores are the places where most of formaldehyde and methanol are assumed to be formed. These objects show spatial distributions of densities of H nuclei between 10^4 and 5×10^6 cm^{-3} and temperatures between 8 and 12 K (see Crapsi et al. 2007). Accordingly, we consider here four density values ($n_{\rm H} = 10^4$, 10^5, 10^6, 5×10^6 cm^{-3}) and three temperatures ($T_g = T_d = 8, 10, 12$ K). Besides, pre-stellar cores show an increase in the grain sizes caused by the coagulation process whose the efficiency increases with the density (Flower et al. 2005; Vastel et al. 2006). We adopt three grain sizes $a_d = 0.1, 0.2, 0.3$ μm, which affect the depletion rates and therefore the density of H and D in the gas phase.

As discussed in TCK12, the diffusion to desorption energy E_d/E_b ratio mainly depends on the ice properties. We, therefore, vary E_d/E_b between 0.5 and 0.8, as suggested by experimental studies. The activation energy E_a of the reactions involving CO and formaldehyde is also a free parameter. By comparing the model predictions with the observations of solid CO and methanol, we have deduced in TCK12 that E_a must be lower than 1500 K, so that we restrain the value of E_a between 400 and 1400 K. Light particles (H, D, H_2, HD, D_2) that accrete onto the ices have a binding energy distribution that depends on the ice properties, and the adsorption conditions of the adsorbate (see, for example, Hornekær et al. 2005). We therefore consider the binding energies relative to amorphous water ice of these light species as a free parameter whose values are: 400, 500, 600 K.

Table 1
List of Parameters and the Value Ranges Explored in This Work

Parameter	Values
Density $n_{\rm H}$	10^4–10^5–10^6–5×10^6 cm^{-3}
Temperature $T_g = T_d$	8–10–12 K
Grain size a_d	0.1–0.2–0.3 μm
Energy ratio E_d/E_b	0.5–0.65–0.8
Binding energy $E_{b,\rm wat}$(H)	400–500–600 K
Activation energy E_a	400–900–1400 K
Initial oxygen abundance $X(\rm O)_{ini}$	10^{-8}–10^{-6}–10^{-4}

As the abundance of the gaseous atomic oxygen in the pre-stellar cores is uncertain, we consider three values of oxygen abundance relative to the H nuclei $X(\rm O)_{ini}$: 10^{-8}, 10^{-6}, 10^{-4}.

Finally, in TCK12, we have shown that the site size d_s and the porosity factor $F_{\rm por}$ have a little impact on the chemical composition of the grain mantles, so we assume $d_s = 3.1$ Å (Jenniskens et al. 1995) and $F_{\rm por} = 0$.

We run a grid of 2916 models in which we vary the parameters described above and listed in Table 1. For each density $n_{\rm H}$, we compute the mean fractionation of each isotopologue with its 1σ standard deviation, following Wakelam et al. (2010).

3. RESULTS

3.1. The D/H Gas Phase Ratio

At first approximation, the steady state densities of H and D, assumed as initial conditions, are roughly constant regardless the total density and their abundance relative to H nuclei, therefore, decrease with increasing $n_{\rm H}$. At low densities, a significant fraction (~30%) of the deuterium reservoir is already in atomic form before the depletion of CO: the increase of the atomic D/H ratio with the CO depletion will therefore be low. On the contrary, at high densities, only a negligible fraction of deuterium is in atomic form at the beginning, so that the atomic D/H ratio strongly increases with the CO depletion. The larger the density, the larger the gaseous atomic D/H ratio increase is with the CO depletion, as highlighted in Figure 2 which shows the evolution of the atomic D/H as a function of CO depletion, for $n_{\rm H}$ equal to 10^5 and 5×10^6 cm^{-3}, respectively.

3.2. Model with Addition Reactions Only

In this section, only addition reactions are considered on grain mantles (see Section 2.2). In this case, the deuteration of formaldehyde and methanol primarily depends on two factors, as illustrated in Figure 2: (1) *the increase of the gas phase atomic D/H ratio with the CO depletion:* the ratio increases with increasing CO depletion, namely, with time, and with increasing density (see above) and (2) *when formaldehyde and methanol are formed:* as explained in detail in TCK12, the increase of $n_{\rm H}$ delays the formation of formaldehyde and methanol. In general, the two effects result in a larger deuteration of formaldehyde and methanol for larger densities and larger evolutionary times.

This is illustrated in Figure 3, which shows the temporal evolution of the mean deuterium fractionations of iced formaldehyde and methanol along with their uncertainty, for different densities. The high-density cases ($n_{\rm H} \geqslant 10^6$ cm^{-3}) show large enhancements of the CH_2DOH/CH_3OH and

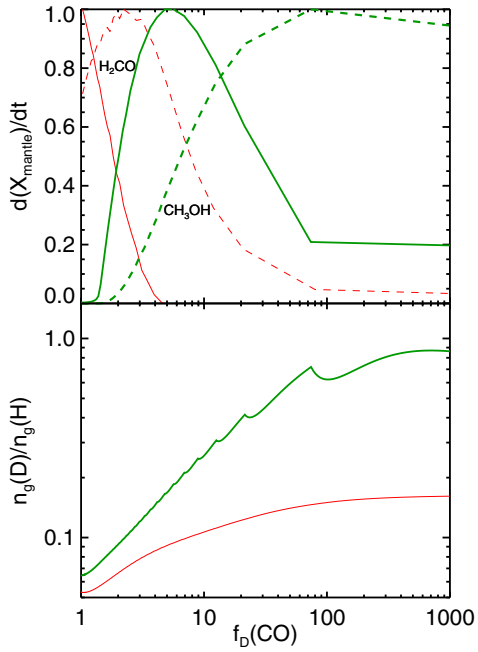

Figure 2. Normalized H_2CO (solid lines) and CH_3OH (dashed lines) formation rates (top panel) and gaseous atomic D/H ratio (bottom panel) as a function of the CO depletion factor $f_D(CO) = n_g(CO)/n_{g,ini}(CO)$, for $n_H = 10^5$ (thin red lines) and 5×10^6 (thick green lines) cm^{-3}. The spikes are caused by the multilayer nature of the mantle.

(A color version of this figure is available in the online journal.)

$HDCO/H_2CO$ ratios with time, reaching unity for the singly deuterated forms. No increase in the deuterium fractionation is, on the contrary, observed at low densities ($n_H = 10^4$–10^5 cm^{-3}); the deuteration ratios never exceed 0.02.

In the same figure, we report the range of observed values (from Parise et al. 2006). No model can reproduce the full set of observations. Indeed, the high-density cases predict CH_2DOH/CH_3OH and $HDCO/H_2CO$ ratios in agreement with observations for times between 5×10^3 and 10^6 yr. However, they cannot predict the observed high abundances of the doubly deuterated molecules. In addition, observations show that methanol is three times more deuterated than formaldehyde whereas the models of Figure 3 predict a factor of 1.5 at most. We conclude that this class of models fails to reproduce the observations.

3.3. Abstraction and Substitution Reactions

Figure 4 shows the temporal evolutions of formaldehyde and methanol deuterium fractionations when abstraction and substitution reactions are included. From Figure 4 it is clear that the inclusion of the addition and substitution reactions strongly increase the deuterium fractionations, especially at high densities. For densities $\sim 5 \times 10^6$ cm^{-3}, the model predicts fractionations of doubly deuterated molecules compatible with observations, at time $\sim 5 \times 10^3$ yr. Unlike CH_2DOH, which shows an increase of deuteration compared to Figure 3 and more particularly at longer timescales, the HDCO deuteration is not enhanced. This is due to the efficiency of deuterium abstraction on HDCO, which allows the formation of H_2CO, whereas deuterium abstraction reactions on CH_2DOH, leading to CH_3OH formation, are negligible. The observed

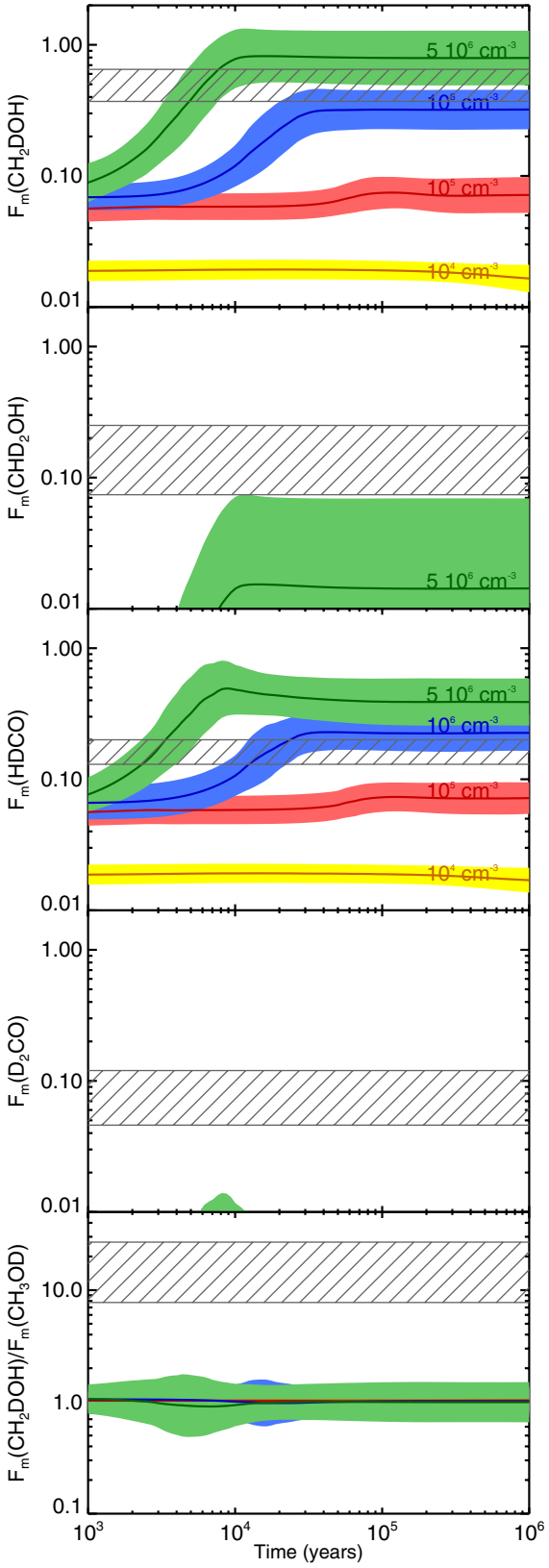

Figure 3. Mean deuterium fractionation of methanol and formaldehyde (solid lines) with their 1σ standard deviation (color levels) with time, obtained considering addition reactions only (Section 3.2). The hatched zones give the range of observed values (Parise et al. 2006).

(A color version of this figure is available in the online journal.)

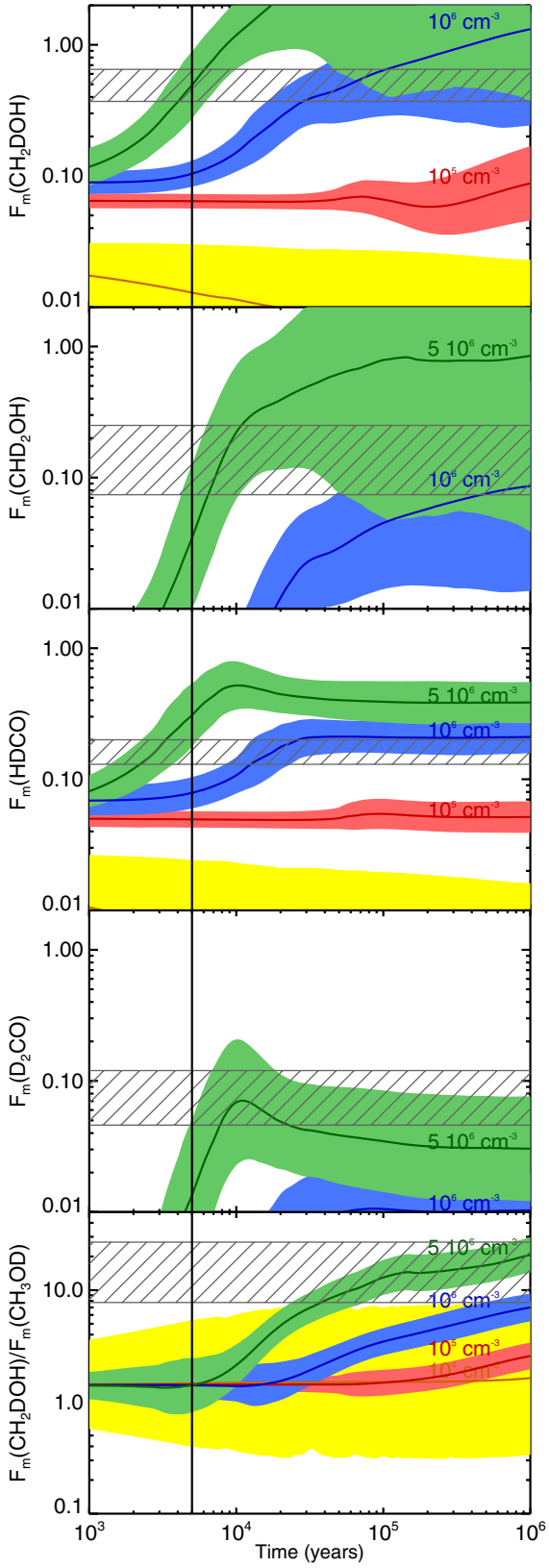

Figure 4. Mean deuterium fractionation of methanol and formaldehyde (solid lines) with their 1σ standard deviation (color levels) with time, obtained by adding the abstraction and substitution reactions (Section 3.3). The hatched zones give the range of observed values (Parise et al. 2006).

(A color version of this figure is available in the online journal.)

$[CH_2DOH]/[HDCO]$ ratio of 3 can now be predicted. Finally, because the abstraction reactions can only occur significantly on the methyl group of methanol and not on its hydroxyl group, the $[CH_2DOH]/[CH_3OD]$ ratio in enhanced. The observed ratio of 10–20 can also be predicted but at a larger time, 5–10 $\times$ 10^4 yr. We conclude that this class of models succeeds to reproduce all the observations simultaneously, with the exception of the $[CH_2DOH]/[CH_3OD]$ ratio, for a density of about 5×10^6 cm^{-3} and at a time of 5000 yr.

4. DISCUSSION AND CONCLUSIONS

Although multiply deuterated molecules in low-mass protostars have been discovered and observed for a decade, published models have had difficulties in reproducing the observed abundances, especially those of formaldehyde and methanol (Parise et al. 2006). Both species are believed to be mainly synthesized and to be observed on the grain surfaces during the cold and dense pre-collapse phase (see Öberg et al. 2011) and that they are observed in the gas when they sublimate off the grain mantles upon heating from the central star. On the grains, H_2CO and CH_3OH are thought to be the result of the hydrogenation of iced CO. Their deuteration, therefore, depends on when exactly the two species are formed and how. We have shown that, based on our grain surface model GRAINOBLE, formation of H_2CO and CH_3OH from addition reactions alone fails to predict the observed deuterium fractionation. In contrast, if D and H abstraction and substitution reactions are added, the GRAINOBLE model can reproduce *simultaneously* the observed values. Therefore, these processes are crucial and more laboratory experiments and theoretical computations are needed to better constrain their rates on the ices. Reproducing the observed $[CH_2DOH]/[CH_3OD]$ ratio remains a challenge, as it is still underestimated by the model. Previous studies have suggested that this may be caused by D and H exchanges on the ices during the sublimation phase (Ratajczak et al. 2009) or activated by photolysis processes (Weber et al. 2009) or on the gas phase (Osamura et al. 2004), all processes that would be inefficient in altering the other isotopologues (see Ratajczak et al. 2011 for a detailed discussion).

With the above exception, our model predicts the observed abundance ratios for high densities ($\sim 5 \times 10^6$ cm^{-3}) and for relatively short times ($\sim$5000 yr). We emphasize that this time corresponds only to the final stage at high density and not to the age of the condensation, which can be considerably larger. In fact, it is possible and even likely that the pre-stellar cores spend a long time in a less dense phase (e.g., Bergin & Tafalla 2007). However, the comparison of the observed H_2CO and CH_3OH deuteration with our model predictions suggests that the last phase at high density is short, just a few thousand years. In other words, soon after the central density reaches $\sim 5 \times 10^6$ cm^{-3}, the protostellar collapse starts. This is a nice illustration of how chemistry can help us to understand the past history of the protostar.

In conclusion, our work leads to two important results. (1) The pre-collapse phase may last hundreds of thousands of years: however, when the central density reaches $\sim 5 \times 10^6$ cm^{-3}, the collapse starts in about a few thousands years. (2) D and H atoms abstraction and substitution reactions are crucial in the grain surface chemistry and should be incorporated into models. Thus, more experimental and theoretical works are therefore needed to better constrain their efficiency and therefore the timescale needed to reproduce the observations.

This work has been supported by l'Agence Nationale pour la Recherche (ANR), France (project FORCOMS, contract ANR-08-BLAN-022).

REFERENCES

Andersson, S., Goumans, T. P. M., & Arnaldsson, A. 2011, Chem. Phys. Lett., 513, 31
André, P., Ward-Thompson, D., & Barsony, M. 2000, in Protostars and Planets IV, ed. V. Mannings, A. P. Boss, & S. S. Russell (Tucson, AZ: Univ. Arizona Press), 59
Bacmann, A., Lefloch, B., Ceccarelli, C., et al. 2003, ApJ, 585, L55
Bergin, E. A., & Tafalla, M. 2007, ARA&A, 45, 339
Bergman, p., Parise, B., Liseau, R., & Larsson, B. 2011, A&A, 527, 39
Caselli, P., Stantcheva, T., Shalabiea, O., Shematovich, V. I., & Herbst, E. 2002, Planet. Space Sci., 50, 1257
Cazaux, S., Caselli, P., & Spaans, M. 2011, ApJ, 741, L34
Ceccarelli, C., Caselli, P., Herbst, E., Tielens, A. G. G. M., & Caux, E. 2007, in Protostars and Planets V, ed. B. Reipurth, D. Jewitt, & K. Keil (Tocson, AZ: Univ. Arizona Press), 47
Ceccarelli, C., Castets, A., Loinard, L., Caux, E., & Tielens, A. G. G. M. 1998, A&A, 338, L43
Ceccarelli, C., Loinard, L., Castets, A., et al. 2001, A&A, 372, 998
Charnley, S. B., Tielens, A. G. G. M., & Rodgers, S. D. 1997, ApJ, 482, L203
Crapsi, A., Caselli, P., Walmsley, M. C., & Tafalla, M. 2007, A&A, 470, 221
Cuppen, H. M., & Herbst, E. 2007, ApJ, 668, 294
Cuppen, H. M., van Dishoeck, E. F., Herbst, E., & Tielens, A. G. G. M. 2009, A&A, 508, 275
Dislaire, V., Hily-Blant, P., Faure, A., et al. 2012, A&A, 537, A20
Flower, D. R., Pineau Des Forêts, G., & Walmsley, C. M. 2005, A&A, 436, 933
Flower, D. R., Pineau Des Forêts, G., & Walmsley, C. M. 2006, A&A, 449, 621
Fuchs, G. W., Cuppen, H. M., Ioppolo, S., et al. 2009, A&A, 505, 629
Garrod, R. T., & Pauly, T. 2011, ApJ, 735, 15
Goumans, T. P. M. 2011, MNRAS, 413, 2615
Goumans, T. P. M., & Kaestner, J. 2011, J. Phys. Chem. A, 115, 10767
Hasegawa, T. I., & Herbst, E. 1993a, MNRAS, 261, 83
Hasegawa, T. I., & Herbst, E. 1993b, MNRAS, 263, 589
Hasegawa, T. I., Herbst, E., & Leung, C. M. 1992, ApJ, 82, 167
Hidaka, H., Kouchi, A., & Watanabe, N. 2007, J. Chem. Phys., 126, 204707
Hidaka, H., Watanabe, M., Kouchi, A., & Watanabe, N. 2009, ApJ, 702, 291
Hornekær, L., Baurichter, A., Petrunin, V. V., et al. 2005, J. Chem. Phys., 122, 12
Jenniskens, P., Blake, D. F., Wilson, M. A., et al. 1995, ApJ, 455, 389
Linsky, J. L. 2003, Space Sci. Rev., 106, 49
Maret, S., Ceccarelli, C., Tielens, A. G. G. M., et al. 2005, A&A, 442, 527
Nagaoka, A., Watanabe, N., & Kouchi, A. 2005, ApJ, 624, L29
Nagaoka, A., Watanabe, N., & Kouchi, A. 2007, J. Phys. Chem. A, 111, 3016
Öberg, K. I., Boogert, A. C. A., Pontoppidan, K. M., et al. 2011, ApJ, 740, 109
Osamura, Y., Roberts, H., & Herbst, E. 2004, A&A, 421, 1101
Parise, B., Castets, A., Herbst, E., et al. 2004, A&A, 416, 159
Parise, B., Ceccarelli, C., Tielens, A. G. G. M., et al. 2002, A&A, 393, L49
Parise, B., Ceccarelli, C., Tielens, A. G. G. M., et al. 2006, A&A, 453, 949
Ratajczak, A., Quirico, E., Faure, A., Schmitt, B., & Ceccarelli, C. 2009, A&A, 496, L21
Ratajczak, A., Taquet, V., Kahane, C., et al. 2011, A&A, 528, L13
Roberts, H., Herbst, E., & Millar, T. J. 2004, A&A, 424, 905
Roberts, H., & Millar, T. J. 2000, A&A, 361, 388
Stantcheva, T., & Herbst, E. 2003, MNRAS, 340, 983
Taquet, V., Ceccarelli, C., & Kahane, C. 2012, A&A, 538, A42
Tielens, A. G. G. M., & Hagen, W. 1982, A&A, 114, 245
Vastel, C., Caselli, P., Ceccarelli, C., et al. 2006, ApJ, 645, 1198
Wakelam, V., Herbst, E., Le Bourlot, J., et al. 2010, A&A, 517, 21
Watanabe, N., & Kouchi, A. 2002, ApJ, 571, L73
Watanabe, N., & Kouchi, A. 2008, Prog. Surf. Sci., 83, 439
Weber, A. S., Hodyss, R., Johnson, P. V., Willacy, K., & Kanik, I. 2009, ApJ, 703, 10300

A&A 541, L12 (2012)
DOI: 10.1051/0004-6361/201219207

Astronomy & Astrophysics

Letter to the Editor

Detection of complex organic molecules in a prestellar core: a new challenge for astrochemical models⋆,⋆⋆

A. Bacmann[1], V. Taquet[1], A. Faure[1], C. Kahane[1], and C. Ceccarelli[1]

UJF-Grenoble 1 / CNRS-INSU, Institut de Planétologie et d'Astrophysique de Grenoble (IPAG) UMR 5274, 38041 Grenoble, France
e-mail: abacmann@ujf-grenoble.fr

Received 12 March 2012 / Accepted 29 March 2012

ABSTRACT

Context. Complex organic molecules (COMs) have long been detected in the interstellar medium, especially in hot cores and in the hot corinos of low-mass protostars. Their formation routes however remain uncertain. Both warm gas-phase reactions and warm grain-surface reactions have been invoked to account for their presence in low-mass protostars. In this latter scheme, COMs result from radical-radical reactions on the grains as radicals become mobile when the nascent protostar warms up its surroundings and the resulting molecules are subsequently desorbed into the gas phase at higher temperatures.

Aims. Prestellar cores are the direct precursors of low-mass protostars and offer a unique opportunity to study the formation of COMs before the warm-up phase. Their very low temperatures ($\leq$10 K) and the absence of any heating source or outflow exclude any efficient warm gas phase or warm dust chemistry, so that the presence of COMs in prestellar cores would have to originate from non-thermal chemical processes.

Methods. We used the IRAM 30 m telescope to look for four O-bearing COMs (acetaldehyde CH_3CHO, dimethyl ether CH_3OCH_3, methyl formate CH_3OCHO, and ketene CH_2CO) in the prestellar core L1689B.

Results. We report the unambiguous detection of all four molecules in the cold gas phase of L1689B. These detections support the role played by non-thermal (possibly photolytic) processes in COM formation and desorption, though the presence of dimethyl ether is so far unexplained by current grain formation scenarios. The data show univocally that COM synthesis has already started at the prestellar stage and suggests at least part of the COMs detected in hot corinos have a prestellar origin.

Key words. astrochemistry – molecular processes – ISM: molecules – stars: formation

1. Introduction

Complex organic molecules (COMs) have long been detected in the hot cores of massive star-forming regions such as Sgr B2 (Cummins et al. 1986) or OMC-1 (Blake et al. 1987). The warm central regions of low-mass protostars have been shown to harbour the same organic molecules (van Dishoeck et al. 1995; Cazaux et al. 2003), which led them to be called "hot corinos" (Bottinelli et al. 2004). In these regions, O- and N- bearing species like methyl formate (CH_3OCHO), dimethyl ether (CH_3OCH_3) or acetonitrile (CH_3CN) are abundant, so that these molecules have been designated as "hot core tracers". The mechanisms leading to COM formation in star-forming regions are however still debated. COMs were first thought to be the result of warm gas-phase chemistry between ice mantle constituents, sometimes called primary species or parent molecules, which are evaporated in the gas phase in the vicinity of the nascent protostar (Charnley et al. 1992). In this scheme, primary molecules are formed on the grain ice mantles via successive hydrogenation of atoms or simple molecules like CO. When they are injected into the gas phase via thermal desorption, they can react and form secondary species like, e.g., CH_3OCHO. The gas-phase scenario has been however challenged by experimental results showing that gas-phase formation pathways were much less efficient than originally thought (Horn et al. 2004, for methyl formate). Alternative scenarios have been proposed in which radicals are formed by ultraviolet (UV) irradiation of grain mantle molecules (e.g., Garrod & Herbst 2006) or trapped within the bulk of ice mantles of dust grains (Taquet et al. 2012). Following Garrod & Herbst (2006), the radicals can react on the grain mantles once the protostar starts heating its immediate surroundings and the grains reach a temperature of around 30–40 K, and form complex species on the grain, before they are being desorbed and released into the gas phase. Laboratory experiments however have shown the possibility to synthesize COMs such as methyl formate by irradiation (with UV photons or energetic particles) of methanol ices at temperatures as low as 10 K (Gerakines et al. 1996; Bennett & Kaiser 2007).

In contrast to warm star-forming regions such as hot cores or hot corinos, little research has been carried out to investigate the contents of cold gas. Studies of the dark cloud TMC-1 have revealed the presence of acetaldehyde (Matthews et al. 1985), ketene (Irvine et al. 1989), and methanol (Friberg et al. 1988). Evidence of COMs in prestellar cores is similarly scarce: Matthews et al. (1985) reported the detection of acetaldehyde in L183 (L134N), but searches for dimethyl ether (Friberg et al. 1988), ketene (Irvine et al. 1989) and methyl formate (Requena-Torres et al. 2007) only yielded upper limits. Despite their very low temperatures (~10 K), prestellar cores are however an important piece of the puzzle, as they represent the stage immediately before the gravitational collapse leading to protostar formation. They thus offer the opportunity to study the initial conditions of the star formation process. The relative simplicity

⋆ Based on observations carried out with the IRAM 30 m Telescope. IRAM is supported by INSU/CNRS (France), MPG (Germany), and IGN (Spain).

⋆⋆ Appendices are available in electronic form at http://www.aanda.org

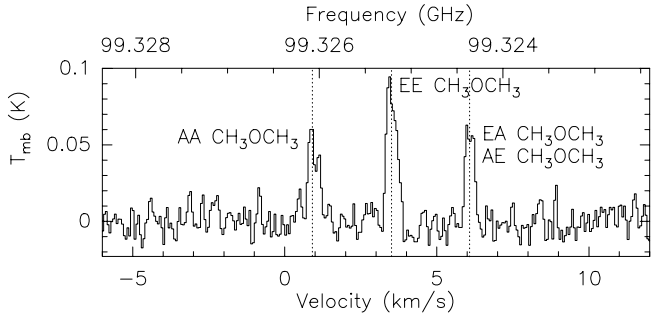

Fig. 1. CH_3OCH_3 spectrum at 99.325 GHz in the prestellar core L1689B. Three lines corresponding to the AA, EE, EA, and AE symmetry substates (AE and EA being at the same frequency) are clearly detected at the $>7\sigma$ level. The vertical dotted lines indicate the rest frequencies measured in the laboratory and listed in the CDMS database (Müller et al. 2001).

of their structure (shallow temperature gradients, absence of inner heating source, absence of shocks or outflows, environment shielded from external radiation fields) makes them ideal targets to study chemical processes in cold gas at the very early stages of star formation.

We present here the first detection of the COMs dimethyl ether and methyl formate in a prestellar core, as well as the detection of the two other COMs acetaldehyde and ketene, in the gas phase at a temperature of ∼10 K.

2. Observations

The target of our observation is the prestellar core L1689B. This source is a typical core characterised by low dust temperatures around 11−12 K (Kirk et al. 2007), high central densities of 10^5–10^6 cm^{-2}, and a high central column density of $\sim 10^{23}$ cm^{-2} (Bacmann et al. 2000; Dapp & Basu 2009). It was selected based on the assumption that the gas-phase abundances of C-bearing molecules such as formaldehyde (Bacmann et al. 2003) or methanol (Bacmann et al., in prep.) were relatively large with respect to other cores. Therefore, it can be hypothesised that COMs are more likely to be detected in this object than in more depleted ones.

Observations were carried out in March 2011 at the IRAM 30 m telescope. We used the E090 receiver tuned to a frequency of 99.325 GHz (close to low energy transitions of CH_3OCH_3) to which we connected both the high resolution autocorrelator VESPA and the low resolution Fourier transform spectrometer (FTS). The spectral resolution and bandwidth of VESPA were 20 kHz (corresponding to a velocity resolution of ∼0.06 km s^{-1}) and 100 MHz, respectively. The FTS covered the whole 4 GHz receiver band (from 97.6 to 101.6 GHz in this case) with a spectral resolution of 192 kHz, corresponding to a velocity resolution of ∼0.6 km s^{-1}. The observations were carried out in the frequency switching mode with a frequency switch of 7.5 MHz to reduce standing waves. Pointing was checked every two hours on a nearby quasar and was found to be accurate to within 1″. The weather conditions were very good and system temperatures were typically 100−120 K despite the low elevation of the source. We integrated on the dust peak of the core L1689B, at $\alpha_{2000} = 16^h34^m48\overset{s}{.}30, \delta_{2000} = -24°38'04.0''$. The size of the telescope beam at the observing frequency was ∼25″, and the forward and beam efficiencies were $\eta_{fwd} = 0.95$ and $\eta_{beam} = 0.80$, respectively.

The data were reduced using the IRAM CLASS/GILDAS package[1]. The scans were coadded, deconvolved from the frequency switching procedure, and a low order (typically 3) polynomial was then fitted over line-free regions to correct for baseline oscillations. The spectra were converted from T_a^* to the T_{mb} scale, using the values of the efficiencies given above.

3. Results

The high spectral resolution spectrum obtained close to 99.325 GHz is shown in Fig. 1. The *rms* noise in the spectra is ∼7 mK. The frequencies and spectroscopic parameters of the detected species are listed in Table A.1. Three spectral lines are clearly detected (to the 7−12σ level), corresponding to the 4_{14}−3_{03} transitions of the four symmetry substates (AA-, EE-, AE-, and EA-) of CH_3OCH_3. The EA- and AE- transitions are only 2 kHz apart and therefore are indistinguishable in our spectrum. The lines are very narrow, ≃0.4 km s^{-1} wide, as expected for lines originating from cold gas at around 10 K. These spectra show the unambiguous presence in the cold gas of dimethyl ether, which is detected for the first time in a cold dark core.

The low-resolution spectrum covers the 97.6 GHz to 101.6 GHz region. Within this bandwidth, we also detect six lines of CH_3OCHO (three lines of the A- and three lines of the E- substates), which had so far never been detected in a prestellar core. In addition, two lines of CH_2CO (one ortho line and one para line) and two lines of CH_3CHO (one of the A- and one of the E-substates) are also detected. Figures 2–4 present the spectra of CH_3OCHO, CH_3CHO, and CH_2CO, respectively. Again, the detection of more than one line of each species at the measured catalog frequencies (see figures) is clear evidence of these three species in the gas phase of L1689B.

At these low temperatures, the different substates have to be considered separately. Since we only have one line for each substate (except for methyl formate), the excitation conditions are poorly constrained and estimates of the column densities can only be given by assuming an excitation temperature. In the case of methyl formate, all detected lines have similar upper level energies and Einstein coefficients, so that having more than one line per substate does not bring supplementary constraints for the excitation. As these data are a subset of a larger ongoing observing project targetting several lines for each molecule and substate, we postpone the detailed analysis[2] of the column densities and abundances to a future paper and give here only preliminary estimates of the column densities. At densities around 10^5–10^6 cm^{-3} (similar to the critical density of 10^6 cm^{-3}), and gas temperatures of 7–10 K (Redman et al. 2004), it is reasonable to assume excitation temperatures of around 5 K. Because this value is uncertain, the column densities are also given for more extreme values of the excitation temperature, 4 K and 8 K.

The total column densities of the species were derived from the integrated line intensities assuming local thermodynamic equilibrium (see Appendix B for more details). The derived column densities are given in Table 1. The difference between the column density values at $T_{ex} = 4$ K and $T_{ex} = 8$ K varies between a factor of two for CH_3OCH_3 and an order of magnitude for CH_3OCHO. It is reasonable to expect the same excitation temperature for the A- and E- substates of CH_3CHO and CH_3OCHO, as these have similar upper level energies, Einstein coefficients, frequencies, and upper level degeneracies. We find

[1] http://www.iram.fr/IRAMFR/GILDAS

[2] Note that collisional rates for methyl formate have been obtained by Faure et al. (2011).

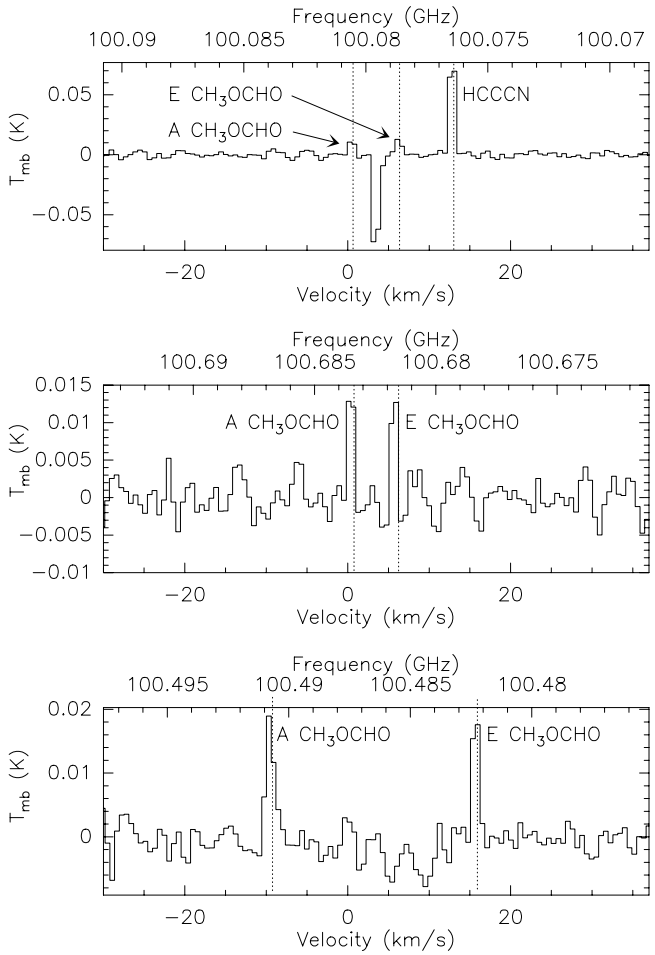

Fig. 2. CH_3OCHO spectra of the $8_{17}-7_{11}$ transitions at 100.48 GHz (A and E substates, *bottom panel*), of the $9_{09}-8_{08}$ transitions at 100.68 GHz (A and E substates, *middle panel*), and of the $9_{19}-8_{18}$ transitions at 100.08 GHz (A and E substates, *top panel*) in L1689B. The vertical dotted lines indicate the rest frequencies measured in the laboratory and listed in the JPL database (Pickett et al. 1998). The CH_3OCHO spectrum in the top panel also shows a HC_3N line. The negative spectral feature between both CH_3OCHO lines results from the frequency switching procedure and the folding of the ortho-CH_2CO line shown in Fig. 4.

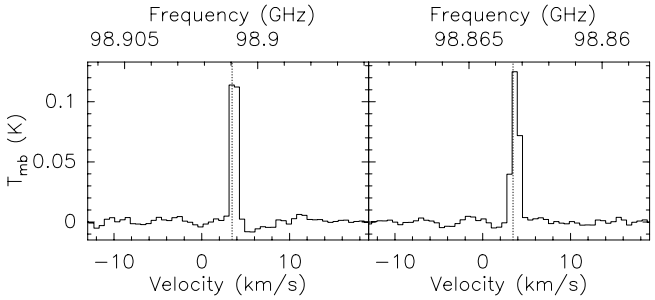

Fig. 3. CH_3CHO spectra of the $5_{14}-4_{13}$ transitions at 98.9009 GHz (A substate, *left*) and at 98.8633 GHz (E substate, *right*) in L1689B. The vertical dotted lines indicate the rest frequencies measured in the laboratory and listed in the JPL database (Pickett et al. 1998).

that both A- and E- substates are equally abundant in those two molecules. For CH_3OCH_3, we find the abundance ratio of the EE- to AA- substates to be equal to the statistical ratio of two, although no conclusion can be drawn about the AE- and

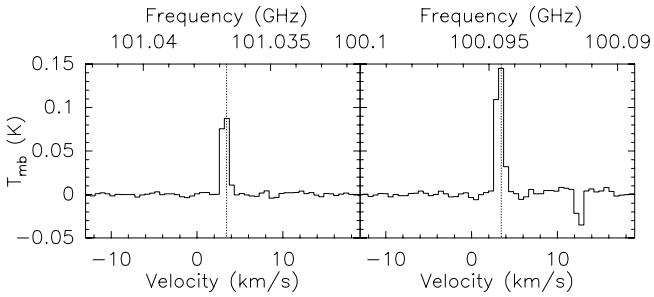

Fig. 4. CH_2CO spectra of the $5_{05}-4_{04}$ (para) transition at 101.0367 GHz (*left*) and of the $5_{15}-4_{14}$ (ortho) transition (*right*) at 100.0945 GHz in L1689B. The vertical dotted lines indicate the laboratory rest frequencies listed in the CDMS database (Müller et al. 2001).

EA- substates, as these are too close in values of frequency to be spectrally resolved, so we simply assumed that the ratio of their intensities was equal to the ratio of their upper level degeneracies (which leads to equal column densities in AE- and EA-, each equal to half that of the AA- substate – see note to Table 1). For CH_2CO, we find an ortho-to-para ratio of ∼3.3, which is similar to the value of 3.5 found in TMC-1 (Ohishi et al. 1991), consistent with the statistical ratio of 3. Assuming a H_2 column density of 10^{23} cm^{-2} (Dapp & Basu 2009), we find abundances of a few 10^{-10} for the four species. This is a factor of ∼100 lower than in hot corinos (e.g. in NGC1333-IRAS4A – Bottinelli et al. 2004), similar to the formaldehyde abundance ratio between prestellar cores (Bacmann et al. 2003) and hot corinos (Bottinelli et al. 2004).

4. Discussion and conclusions

The detection of CH_3OCH_3, CH_3OCHO, CH_2CO, and CH_3CHO in the gas phase of a prestellar core at temperatures of around 10 K sheds new light on COM formation in the interstellar medium. Grain-surface chemistry models such as those of Garrod & Herbst (2006) require temperatures of around 30 K to ensure that the radicals present in the ice mantle have sufficient mobility to recombine and form COMs. This scenario cannot, however, explain the presence of COMs in the gas phase of this prestellar core. Pure gas-phase scenarios assuming that COMs result from warm (∼100 K) gas-phase reactions between grain mantle constituents after their evaporation from the grains (Charnley et al. 1992) are also excluded by the low temperature in prestellar cores.

According to the hypothesis of a grain mantle formation scenario, the COMs that we detect in the gas phase have been desorbed from the ices by non-thermal processes such as secondary UV photon (originating from cosmic rays impacting on H_2 molecules) heating, or direct cosmic-ray impacts. It is therefore possible that radical mobility on the grains is also provided by the energy brought to the grains by UV photons. Similar mechanisms were invoked by Öberg et al. (2010) who detected methyl formate in the protostar B1-b, possibly desorbed by UV originating from the protostar through an outflow cavity. In the case of L1689B, the gas is significantly colder than in B1-b, and the core is well-shielded from external UV, as there is no nearby protostar and no outflow cavity so that the core is not exposed to a direct UV field. In Galactic center clouds, the detection of COMs by Requena-Torres et al. (2006) in the gas phase has been interpreted as the result of the ejection of ice mantle molecules by either shocks or supersonic turbulence. This scheme does not apply to the prestellar core L1689B, in which there are no shocks and the levels of turbulence are very low, as demonstrated by

Table 1. Line fluxes[a] and column densities.

Species	Transition	T_{mb} (mK)	rms (mK)	Integrated area (K km s^{-1})	Column density[c] (cm^{-2}) T_{ex} = 5 K	Column density[c] (cm^{-2}) T_{ex} = 4 K	Column density[c] (cm^{-2}) T_{ex} = 8 K
AA-CH_3OCH_3	4_{14}–3_{03}	55	7	0.026 ± 0.005	(3.32 ± 0.74) 10^{12}	(5.08 ± 1.12) 10^{12}	(2.49 ± 0.55) 10^{12}
EE-CH_3OCH_3	4_{14}–3_{03}	90	7	0.037 ± 0.005	(6.81 ± 0.92) 10^{12}	(10.4 ± 1.40) 10^{12}	(5.11 ± 0.69) 10^{12}
EA-CH_3OCH_3	4_{14} – 3_{03}	36[b]	7	0.014 ± 0.003	(1.65 ± 0.55) 10^{12}	(2.53 ± 0.84) 10^{12}	(1.24 ± 0.41) 10^{12}
AE-CH_3OCH_3	4_{14}–3_{03}	22[b]	7	0.009 ± 0.003	(1.67 ± 0.37) 10^{12}	(2.55 ± 0.56) 10^{12}	(1.25 ± 0.28) 10^{12}
E-CH_3CHO	5_{14}–4_{13}	125	3	0.149 ± 0.015	(9.12 ± 0.92) 10^{12}	(2.67 ± 0.27) 10^{13}	(2.12 ± 0.21) 10^{12}
A-CH_3CHO	5_{14}–4_{13}	110	4	0.137 ± 0.014	(8.26 ± 0.84) 10^{12}	(1.73 ± 0.18) 10^{13}	(3.86 ± 0.39) 10^{12}
A-CH_3OCHO	8_{17}–7_{16}	20	3	0.025 ± 0.005	(2.01 ± 0.40) 10^{13}	(5.73 ± 1.15) 10^{13}	(5.91 ± 1.18) 10^{12}
A-CH_3OCHO	9_{09}–8_{08}	12	2	0.016 ± 0.005	(1.73 ± 0.54) 10^{13}	(5.50 ± 1.71) 10^{13}	(4.33 ± 1.35) 10^{12}
E-CH_3OCHO	8_{17}–7_{16}	19	3	0.024 ± 0.005	(1.90 ± 0.40) 10^{13}	(5.44 ± 1.15) 10^{13}	(5.59 ± 1.18)10^{12}
E-CH_3OCHO	9_{09}–8_{08}	12	2	0.016 ± 0.003	(1.72 ± 0.32) 10^{13}	(5.47 ± 1.03) 10^{13}	(4.32 ± 0.81) 10^{12}
o-CH_2CO	5_{15}–4_{14}	140	3	0.171 ± 0.018	(1.50 ± 0.16) 10^{13}	(3.09 ± 0.33) 10^{13}	(6.75 ± 0.71) 10^{12}
p-CH_2CO	5_{05}–4_{04}	82	2	0.096 ± 0.010	(4.54 ± 0.47) 10^{12}	(9.64 ± 1.00) 10^{12}	(1.95 ± 0.20) 10^{12}

Notes. [(a)] The fluxes were derived by fitting Gaussians to the lines using the dedicated CLASS routine. The uncertainty was calculated as $\sqrt{\sigma_{stat} + \sigma_{cal}}$, where σ_{stat} is the statistical uncertainty in the Gaussian fit (given by the CLASS routine) and σ_{cal} is the calibration uncertainty taken as 10%. [(b)] Both EA- and AE- CH_3OCH_3 lines are so close in frequency that they are indistinguishable in our spectra. In the table, we assume that the ratio of their intensities was equal to the ratio of their upper level degeneracy because the transitions have nearly equal frequencies, Einstein coefficients, and equal level energies. This hypothesis is supported by it also applying to the EE- and AA- transitions (the ratio of their respective intensities is consistent with the ratio of their respective upper level degeneracies). [(c)] The column densities in Cols. (6)–(8) are those of the corresponding substates listed in Col. (1), as derived from the line fluxes given in Col. (5).

the narrow linewidths. If COMs form on grains, the most likely mechanisms to bring radical mobility and lead to molecular desorption are thus secondary UVs, cosmic rays, or the release of chemical energy due to exothermic reactions on the grains (e.g. chemical explosions, Garrod et al. 2007).

The simultaneous detection of CH_3OCH_3 and CH_3OCHO in very cold gas is particularly interesting. According to Öberg et al. (2011), COMs could form sequentially and CH_3OCHO and CH_3CHO are formed by UV irradiation of cold CO-rich ices and CH_3OCH_3 forms in warmer (CH_3OH-rich) ice after CO has evaporated (see also Öberg et al. 2009). Our observations do not support this scenario, and show that either CH_3OCH_3 forms in the same ice as CH_3OCHO (since prestellar core have rather uniform temperature and do not undergo temperature changes similar to those of protostars) or that the formation mechanisms of both types of molecules are different with, e.g., CH_3OCH_3 forming in the gas phase, as suggested by Peeters et al. (2006), though this idea is disputed by Requena-Torres et al. (2006).

The main conclusion of this paper is the detection of methyl formate and dimethyl ether for the first time in a very cold (~10 K) dark core, here the prestellar core L1689B. Acetaldehyde and ketene, which were previously detected in TMC-1, are also detected. The detection of these species is also further evidence that they do not specifically trace hot core or hot corino regions, but that they are also present in the cold and dense ISM. Since prestellar cores are thought to be the precursors of low-mass protostars, the presence of COMs at the prestellar stage means that we have to re-investigate COM formation scenario in protostars, especially in the case of dimethyl ether, which is not expected to form in similar ices as methyl formate. Following our results, it is likely that at least part of the COM contents in young protostars originates from the prestellar phase.

Acknowledgements. This work has been supported by l'Agence Nationale pour la Recherche (ANR), France (contract ANR-08-BLAN-022).

References

Bacmann, A., André, P., Puget, J.-L., et al. 2000, A&A, 361, 555
Bacmann, A., Lefloch, B., Ceccarelli, C., et al. 2003, ApJ, 585, L55
Bennett, C. J., & Kaiser, R. I. 2007, ApJ, 661, 899
Blake, G. A., Sutton, E. C., Masson, C. R., & Phillips, T. G. 1987, ApJ, 315, 621
Bottinelli, S., Ceccarelli, C., Lefloch, B., et al. 2004, ApJ, 615, 354
Cazaux, S., Tielens, A. G. G. M., Ceccarelli, C., et al. 2003, ApJ, 593, L51
Charnley, S. B., Tielens, A. G. G. M., & Millar, T. J. 1992, ApJ, 399, L71
Cummins, S. E., Linke, R. A., & Thaddeus, P. 1986, ApJS, 60, 819
Dapp, W. B., & Basu, S. 2009, MNRAS, 395, 1092
Faure, A., Szalewicz, K., & Wiesenfeld, L. 2011, J. Chem. Phys., 135, 024301
Friberg, P., Hjalmarson, A., Madden, S. C., & Irvine, W. M. 1988, A&A, 195, 281
Garrod, R. T., & Herbst, E. 2006, A&A, 457, 927
Garrod, R. T., Wakelam, V., & Herbst, E. 2007, A&A, 467, 1103
Gerakines, P. A., Schutte, W. A., & Ehrenfreund, P. 1996, A&A, 312, 289
Horn, A., Møllendal, H., Sekiguchi, O., et al. 2004, ApJ, 611, 605
Irvine, W. M., Friberg, P., Kaifu, N., et al. 1989, ApJ, 342, 871
Kirk, J. M., Ward-Thompson, D., & André, P. 2007, MNRAS, 375, 843
Matthews, H. E., Friberg, P., & Irvine, W. M. 1985, ApJ, 290, 609
Müller, H. S. P., Thorwirth, S., Roth, D. A., & Winnewisser, G. 2001, A&A, 370, L49
Öberg, K. I., Garrod, R. T., van Dishoeck, E. F., & Linnartz, H. 2009, A&A, 504, 891
Öberg, K. I., Bottinelli, S., Jørgensen, J. K., & van Dishoeck, E. F. 2010, ApJ, 716, 825
Öberg, K. I., van der Marel, N., Kristensen, L. E., & van Dishoeck, E. F. 2011, ApJ, 740, 14
Ohishi, M., Kawaguchi, K., Kaifu, N., et al. 1991, in Atoms, Ions and Molecules: New Results in Spectral Line Astrophysics, ed. A. D. Haschick, & P. T. P. Ho, ASP Conf. Ser., 16, 387
Peeters, Z., Rodgers, S. D., Charnley, S. B., et al. 2006, A&A, 445, 197
Pickett, H. M., Poynter, R. L., Cohen, E. A., et al. 1998, JQSRT, 60, 883
Redman, M. P., Keto, E., Rawlings, J. M. C., & Williams, D. A. 2004, MNRAS, 352, 1365
Requena-Torres, M. A., Martín-Pintado, J., Rodríguez-Franco, A., et al. 2006, A&A, 455, 971
Requena-Torres, M. A., Marcelino, N., Jiménez-Serra, I., et al. 2007, ApJ, 655, L37
Taquet, V., Ceccarelli, C., & Kahane, C. 2012, A&A, 538, A42
van Dishoeck, E. F., Blake, G. A., Jansen, D. J., & Groesbeck, T. D. 1995, ApJ, 447, 760

Appendix A: Spectroscopic line parameters

The frequencies, upper energy levels, upper level degeneracies, and Einstein coefficients of the observed transitions were taken from the JPL spectroscopic database (Pickett et al. 1998) and are summed up here in Table A.1.

Table A.1. Parameters of detected lines.

Species	Transition	Frequency (MHz)	E_{up} (K)	g_{up}	A_{ul} (s−1)
AA-CH_3OCH_3	$4_{14}-3_{03}$	99 326.072	10.2	90	5.533×10^{-6}
EE-CH_3OCH_3	$4_{14}-3_{03}$	99 325.217	10.2	144	5.533×10^{-6}
EA-CH_3OCH_3	$4_{14}-3_{03}$	99 324.362	10.2	36	5.533×10^{-6}
AE-CH_3OCH_3	$4_{14}-3_{03}$	99 324.364	10.2	54	5.533×10^{-6}
E-CH_3CHO	$5_{14}-4_{13}$	98 863.328	16.6	22	3.104×10^{-5}
A-CH_3CHO	$5_{14}-4_{13}$	98 900.948	16.5	22	3.108×10^{-5}
A-CH_3OCHO	$8_{17}-7_{16}$	100 490.682	22.8	34	1.435×10^{-5}
E-CH_3OCHO	$8_{17}-7_{16}$	100 482.241	22.8	34	1.434×10^{-5}
A-CH_3OCHO	$9_{09}-8_{08}$	100 683.368	24.9	38	1.472×10^{-5}
E-CH_3OCHO	$9_{09}-8_{08}$	100 681.545	24.9	38	1.472×10^{-5}
A-CH_3OCHO	$9_{19}-8_{18}$	100 080.542	25.0	38	1.444×10^{-5}
E-CH_3OCHO	$9_{19}-8_{18}$	100 078.608	25.0	38	1.444×10^{-5}
o-CH_2CO	$5_{15}-4_{14}$	100 094.514	27.5	33	1.031×10^{-5}
p-CH_2CO	$5_{05}-4_{04}$	101 036.630	14.6	11	1.104×10^{-5}

Appendix B: Column density determination

The column densities were determined within the LTE approximation, using

$$N = \frac{8\pi\nu^3}{c^3}\frac{Q(T_{ex})}{g_{up}A_{ul}}\frac{e^{E_{up}/kT_{ex}}}{e^{h\nu/kT_{ex}}-1}\frac{1}{J_\nu(T_{ex})-J_\nu(T_{bg})}\int T_{mb}\mathrm{d}v, \quad \text{(B.1)}$$

where ν is the frequency of the transition, c the velocity of light, h and k the Planck and Boltzman constants, respectively, g_{up} the upper level degeneracy, A_{ul} the spontaneous emission Einstein coefficient, T_{ex} the excitation temperature, $Q(T_{ex})$ the partition function at T_{ex}, E_{up} the upper level energy, and $J_\nu(T)$ is the radiation temperature that is defined as

$$J_\nu(T) = \frac{h\nu}{k}\frac{1}{e^{h\nu/kT}-1}. \quad \text{(B.2)}$$

Equation (B.1) assumes that the lines are optically thin. We note that since the temperatures are very low, $J_\nu(T_{bg})$ is not negligible with respect to $J_\nu(T_{ex})$.

Astronomy & Astrophysics manuscript no. deutwat˙submission˙v4
December 13, 2012

Water ice deuteration: a tracer of the chemical history of protostars

V. Taquet[1], P. S. Peters[1,2], C. Kahane[1], C. Ceccarelli[1], A. López-Sepulcre[1], C. Toubin[2], D. Duflot[2], and L. Wiesenfeld[1]

[1] UJF-Grenoble 1 / CNRS-INSU, Institut de Planétologie et d'Astrophysique de Grenoble (IPAG) UMR 5274, Grenoble, F-38041, France
[2] Laboratoire de Physique des Lasers, Atomes et Molecules (PhLAM), UMR CNRS 8523, Universite Lille 1, Villeneuve d'Ascq Cedex 59655, France

Received / Accepted

ABSTRACT

Context. Millimetric observations have measured high degrees of molecular deuteration in several species seen around low-mass protostars. The *Herschel Space Telescope*, launched in 2009, is now providing new measures of the deuterium fractionation of water, the main constituent of interstellar ices.
Aims. We aim at theoretically studying the formation and the deuteration of water, which is believed to be formed on interstellar grain surfaces in molecular clouds.
Methods. We used our gas-grain astrochemical model GRAINOBLE, which considers the multilayer formation of interstellar ices. We varied several input parameters to study their impact on water deuteration. We included the treatment of ortho- and para-states of key species, including H_2, which affects the deuterium fractionation of all molecules. The model also includes relevant laboratory and theoretical works on the water formation and deuteration on grain surfaces. In particular, we computed the transmission probabilities of surface reactions using the Eckart model, and we considered ice photodissociation following molecular dynamics simulations.
Results. The use of a multilayer approach allowed us to study the influence of various parameters on the abundance and the deuteration of water. Deuteration of water is found to be very sensitive to the ortho-to-para ratio of H_2 and to the total density, but it also depends on the gas/grain temperatures and the visual extinction of the cloud. Since the deuteration is very sensitive to the physical conditions, the comparison with sub-millimetric observation towards the low-mass protostar IRAS 16293 allows us to suggest that water ice is formed together with CO_2 in molecular clouds with limited density, whilst formaldehyde and methanol are mainly formed in a later phase, where the condensation becomes denser and colder.

Key words. Astrochemistry, ISM: abundances, ISM: clouds, ISM: molecules, Molecular processes, Stars: formation

1. Introduction

Understanding the formation of water is crucial, not only because of its primordial importance for life on Earth, but also because it is thought to be one of the most abundant oxygen-bearing species and also one of the main gas coolants (Ceccarelli et al. 1996; Kaufman & Neufeld 1996; van Dishoeck et al. 2011). Interstellar water is believed to be formed mainly via three main mechanisms: 1) cold gas-phase chemistry, starting from the ionization of H_2 by cosmic rays, eventually leading to H_3O^+ via ion-neutral reactions that then recombine with electrons to form H_2O (Bates 1986; Hollenbach et al. 2009); 2) on the surface of interstellar dust particles, via the hydrogenation of accreted atomic and molecular oxygen occurring at cold temperatures (Tielens & Hagen 1982; Cuppen & Herbst 2007; Miyauchi et al. 2008); 3) warm gas chemistry, initiated by a few endothermic reactions involving H_2 in warm gas ($T > 250$ K) (Ceccarelli et al. 1996; Kaufman & Neufeld 1996).

The advent of space telescopes, combined with ground-based observatories, has allowed astronomers to observe vapours and ices of water in several phases of star formation. Water vapour is present in cold molecular clouds and prestellar cores but only with low abundances ($X_{gas}(H_2O) \sim 10^{-8} - 10^{-9}$ relative to H nuclei, see Bergin & Snell 2002; Klotz et al. 2008; Caselli et al. 2010). In cold clouds, water is likely condensed in ices ($X_{ice}(H_2O) \sim 5 \times 10^{-5} - 10^{-4}$, Whittet & Duley 1991; Pontoppidan et al. 2004). Hot corinos and outflows of low-mass Class 0 protostars show higher abundances of gas phase water, with abundances of a few 10^{-6} in hot corinos (Ceccarelli et al. 2000; Coutens et al. 2012; Kristensen et al. 2012), whilst protostar outflows show higher abundances up to a few 10^{-5} (Liseau et al. 1996; Lefloch et al. 2010; Kristensen et al. 2010, 2012). Water ice has also been observed towards cold protostellar envelopes with similar abundances to molecular clouds ($\sim 10^{-4}$, Pontoppidan et al. 2004; Boogert et al. 2008). Recent infrared observations have also shown the presence of water in protoplanetary disks in different states: water ice (Terada et al. 2007) and hot and cold water vapour (Carr & Najita 2008; Hogerheijde et al. 2011, with abundances of 10^{-4} and lower than 10^{-7}, respectively). Analysis of debris disks show that dust particles are covered by ice mixtures (e.g. Li & Greenberg 1998; Lebreton et al. 2012).

To summarise, it is now accepted that water is present during all phases of the star formation process. However, its evolution from molecular cloud to planetary system still remains unclear. The deuterium fractionation can help us constrain its formation and its evolution. First, it can probe the formation pathways of water observed in the early stages because of its sensitivity to the physical conditions. Second, it allows us to investigate its reprocessing in protoplanetary disks, and eventually to determine whether water on Earth has an interstellar origin. Comparing the HDO/H_2O ratio in comets and Earth is, for example, important for evaluating the possible contribution of comets for transfer-

Send offprint requests to: V. Taquet: vianney.taquet@obs.ujf-grenoble.fr

ring water in Earth's oceans (Owen & Bar-Nun 1995). Recent Herschel observations have reported a D/H ratio of water (0.014 %) in the Jupiter family comet 103P/Hartley2 originating in the Kuiper Belt, very similar to the value for the Earth's oceans, supporting the hypothesis that a part of water comes from comets (Hartogh et al. 2011).

The HDO/H_2O ratio has recently been evaluated in the gas phase of low-mass Class 0 protostar envelopes with values varying from less than 10^{-4} in NGC1333-IRAS4B (Jørgensen & van Dishoeck 2010) to more than 10^{-2} in NGC1333-IRAS2A (Liu et al. 2011). The low-mass Class 0 protostar IRAS 16293-2422 seems to have the most reliable value since the main isotopologue (via $H_2^{18}O$) and its simply and doubly deuterated isotopologues have been observed several times via ground-based and space telescopes (Ceccarelli et al. 2000; Parise et al. 2005; Butner et al. 2007; Vastel et al. 2010; Coutens et al. 2012). The most recent work by Coutens et al. (2012) reports an HDO/H_2O ratio of $\sim$ 3 % in the hot corino, $\sim$ 0.5 % in the cold envelope, and $\sim$ 5 % in the photodesorption layer of the foreground cloud. Observations of D_2O by Butner et al. (2007) and Vastel et al. (2010) give a D_2O/H_2O ratio of $\sim 10^{-3}$. Using the 4.1 μm OD stretch band, solid HDO has been observed towards a sample of low- and high-mass stars by (Dartois et al. 2003) and Parise et al. (2003). These observations provide an upper limit for the solid abundance ratio between 0.2 and 2 %. Although these values are much higher than the cosmic elemental abundance of deuterium (1.5×10^{-5} Linsky 2003), water seems to be less deuterated than the other molecules also mainly formed on grain surfaces, such as formaldehyde and methanol. Figure 1 graphically shows that water possesses a lower level of deuteration, with a mean HDO/H_2O ratio of $\sim$ 3 %, whereas other molecules have a fractionation of their singly deuterated isotopologue higher than 10 %.

H_2O, but also H_2S, H_2CO and CH_3OH (and $HCOOCH_3$) are thought to be mainly formed on grain surfaces via the hydrogenation of accreted O (or O_2), S, and CO from the gas phase. Cold gas-phase chemistry produces water vapour with low abundances (a few 10^{-7}; Bergin et al. 2000), whilst endothermic reactions producing warm water are efficient at $T > 250$ K. In contrast, water ice desorbs into the gas phase in the envelope of Class 0 protostars in large quantities at $T \sim 100$ K. Therefore, the deuteration of water measured by millimetric observations likely reflects the deuteration of its icy precursor governed by the accretion of gas phase H and D atoms. Indeed, the timescale needed to significantly alter the deuteration after evaporation in warm gas is longer than the typical age of Class 0 protostars ($\sim 10^5$ versus $\sim 10^4$ yr, Charnley et al. 1997; Andre et al. 2000). Roberts et al. (2003) showed that the gas phase atomic D/H ratio increases with the CO depletion. Molecules that are formed in the earlier stages of star formation, when the CO depletion is low, would, therefore, show lower deuteration. Based on our astrochemical model GRAINOBLE (Taquet et al. 2012a, hereafter TCK12a), we theoretically confirmed this hypothesis by successfully reproducing the observed formaldehyde and methanol deuterations (Taquet et al. 2012b, hereafter TCK12b). The difference in deuteration between these two molecules is explained by the earlier formation of formaldehyde compared to methanol, when the D/H is lower. We also demonstrated the necessity to introduce the abstraction reactions experimentally shown by Nagaoka et al. (2007) and Hidaka et al. (2009). Similarly, Cazaux et al. (2011) showed the possibility that water is formed through reactions involving H_2. According to these authors, instead of reflecting the atomic D/H ratio, water deuteration should scale with the gas phase HD/H_2 ratio ($\sim 10^{-5}$) at low temperatures.

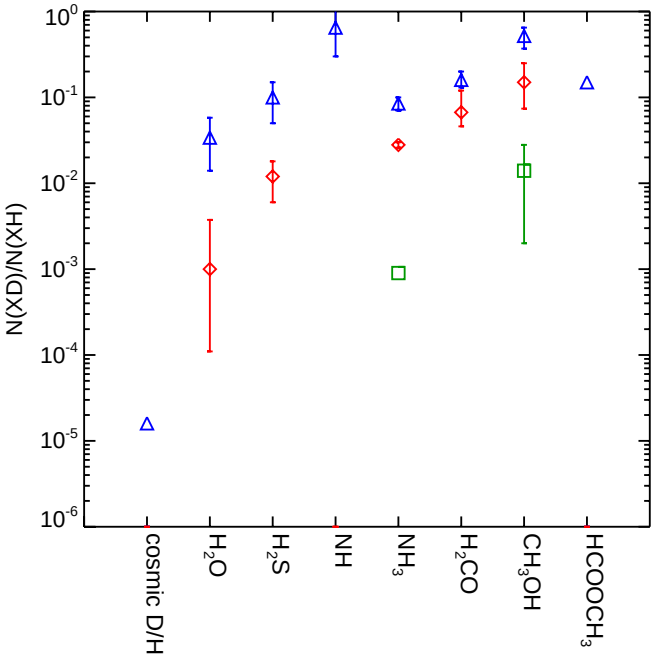

Fig. 1: Deuterium fractionation of several molecules assumed to be partly (or mainly) formed on interstellar grain surfaces and observed around low-mass Class 0 protostars. Blue triangles: simple deuteration; red diamonds: double deuteration; green squares: triple deuteration.

References.
(a) Cosmic D/H: Linsky (2003)
(b) H2O: HDO/H_2O by Coutens et al. (2012), D_2O/H_2O by Vastel et al. (2010) towards IRAS 16293.
(c) H2S: HDS/H_2S by van Dishoeck et al. (1995) towards IRAS 16293, D_2S/H_2S by Vastel et al. (2003) towards IRAS4A.
(d) NH: ND/NH by Bacmann et al. (2010) towards IRAS 16293.
(e) NH3: NH_2D/NH_3 by van Dishoeck et al. (1995) towards IRAS 16293; NHD_2/NH_3 by Loinard et al. (2001) towards IRAS 16293, and ND_3/NH_3 by van der Tak et al. (2002) towards IRAS 4A.
(f) H2CO: $HDCO/H_2CO$ by van Dishoeck et al. (1995) towards IRAS 16293 and by Parise et al. (2006) towards seven low-mass protostars; D_2CO/H_2CO by Ceccarelli et al. (1998) and Ceccarelli et al. (2001) towards IRAS 16293 and by Parise et al. (2006) and Roberts & Millar (2007) towards a sample of low-mass protostars.
(g) CH3OH: CH_2DOH/CH_3OH and CHD_2OH/CH_3OH by Parise et al. (2006) towards seven low-mass protostars, CD_3OH/CH_3OH by Parise et al. (2004) towards IRAS 16293.
(h) HCOOCH3: $DCOOCH_3/HCOOCH_3$ by Demyk et al. (2010) towards IRAS 16293.

The linear relationship between the observed column density of water ice and the visual extinction, above the threshold of $A_V \sim 3.2$ mag found by Whittet et al. (1988), suggests that water ice starts to form significantly at low visual extinctions. Other solid compounds are believed to form along with water ice. The linear relationship between carbon dioxide and water column densities, with a column density ratio $N(CO_2)/N(H_2O)$ of 18 %, suggests that these two molecules form in parallel (Whittet et al. 2007). This conclusion is supported by comparisons between observed and laboratory band profiles showing that CO_2 is mainly located in a polar water-rich mixture whilst a non-polar component (pure CO_2, or $CO:CO_2$) exist in very

low quantities (Gerakines et al. 1999; Pontoppidan et al. 2008). Other solid organic compounds, such as CO or CH_3OH, have also been observed in large quantities ($\sim$ 30 % for CO, and up to 20% for methanol) but at higher visual extinctions, above A_V thresholds of 8-9 and 15 mag respectively (Whittet et al. 2007, 2011). Consequently, one needs to include the formation of all other solid molecules in order to correctly study the formation of deuterated water ice.

In this article, we extend our study to the formation and the deuteration of the interstellar water ice formed in molecular clouds and in prestellar cores, using the multilayer GRAINOBLE model. Our goal is to explore the influence of the physical conditions (representative of different typical cloud stages) on ice formation and water deuteration. This is the first time that such a systematic study has been done. Besides that, it includes the crucial influence of the H_2 ortho/para ratio on the water deuteration. The astrochemical model is presented in Sect. 2. In Sect. 3, we study the formation of typical grain mantles and show the influence of several physical and chemical parameters on the deuteration of water ice. In each section, we summarise the main ideas with headings and concluding remarks. In Sect. 4, we compare our with previous model predictions and in Sect. 5 with published observations of water, formaldehyde, and methanol.

2. Modelling

2.1. Overview of the GRAINOBLE model

GRAINOBLE is a gas-grain astrochemical model based on the rate equations approach introduced by Hasegawa et al. (1992). A detailed presentation of GRAINOBLE can be found in TCK12a. Briefly, GRAINOBLE couples gas-phase and grain-surface chemistry. In total, our chemical network consists of 341 (gaseous and solid) species and 3860 (gas phase and grain surface) reactions. The gas phase chemistry is described in detail in section 2.2. The grain surface chemistry processes are the following:

i) The accretion of gas phase species onto the grain surfaces, assumed to be spherical.

ii) The diffusion of adsorbed species via thermal hopping.

iii) The reaction between two particles via the Langmuir-Hinshelwood mechanism, once they meet in the same site. The reaction rate is the product of the number of times that the two reactants meet each other and the transmission probability P_r of reaction.

iv) The desorption of adsorbed species into the gas phase via several processes:

- thermal desorption;
- cosmic-ray induced heating of grains;
- chemical desorption caused by the energy release of exothermic reactions.

This last process is an upgrade with respect to TCK12a. Following Garrod et al. (2007), we assume a value of 0.012 for the factor *a* (the ratio of the surface-molecule bond frequency to the frequency at which energy is lost to the grain surface) since it seems to be the most consistent value given by molecular dynamics simulations (Kroes & Andersson 2005).

In addition, in the present work, we take the effect of the UV photolysis on the ices into account (see section 2.5), because this is important for the formation of H_2O at low visual extinctions. As suggested by laboratory experiments, cold mantle bulks are mostly inert (see Watanabe et al. 2004; Fuchs et al. 2009; Ioppolo et al. 2010). Therefore, we follow the formation of grain mantles with a multilayer approach in which the outermost only layer is reactive, whilst the mantle bulk remains inert (see TCK12a for more details).

2.2. Gas-phase chemical network

We consider the gas-phase chemical network from the KIDA database (Wakelam et al. 2012) for seven elements: H, He, C, N, O, S, and Fe, giving a total of 258 gaseous species. Sulphur and iron are introduced to consistently study ion chemistry. Reactions involving atomic Fe and S play a significant role in the destruction of H^+ and H_3^+ whilst S^+, and to a lesser extent Fe^+, is believed to be one of the most abundant ions before the CO depletion (see Flower et al. 2005). Relative to the KIDA network, we modify the rate coefficient of the cosmic-ray dissociation of H_2 yielding H+H. Following Dalgarno et al. (1999), we assume $\gamma = 0.5$, where the rate k_{diss} (in s^{-1}) of cosmic ray dissociation reactions is given by $k_{diss} = \gamma\zeta$ (ζ is the cosmic-ray ionization rate). Before ice formation, bare grains are considered. The recombination efficiency of atomic hydrogen and deuterium are assumed to be unity, following the theoretical works by Cazaux & Tielens (2004) and Cuppen et al. (2010b), who considered chemisorption interactions. The initial elemental abundances in the gas phase considered in this work are listed in Table 1 and follows the work by Wakelam et al. (2010) and Linsky (2003). To model the water formation at low visual extinctions (see Introduction), we consider the depth-dependent self-shielding of H_2, HD, and CO, using the Meudon PDR code (Le Petit et al. 2002, 2006).

Since standard gas-phase models overpredict the O_2 abundance with respect to what is observed (see Goldsmith et al. 2011; Liseau et al. 2012) we also ran a grid of models by artificially decreasing the formation rate of O_2 by a factor of 10. We checked that the $[O_2]/[O]$ abundance ratio remains indeed ten times lower than the "standard" case throughout the whole calculation.

Deuteration of water and other molecules formed on interstellar grains strongly depend on the gas phase abundances of H, D, H_2, HD, and D_2. In turn, the abundance of these gaseous species, and more particularly D, depends mainly on the deuteration of H_3^+ which is function of the degree of CO and N_2 freeze-outs onto the grain surfaces (see Roberts & Millar 2000; Roberts et al. 2003). The deuterium gas phase chemical network is based on that of TCK12b. The major differences with respect to TCK12b are the inclusion of the ortho-to-para (hereinafter opr) H_2 ratio and reactions involving N_2.

Reactions between H_3^+ isotopologues and H_2, reducing the deuterium fractionation, are endothermic. Therefore, these reactions cannot occur in cold-cloud conditions if para-H_2 only is considered. However, H_2 is also believed to exist in the ortho spin state, higher in energy (170 K), since H_2 probably forms on grains with an ortho-to-para ratio (opr) of 3. Reactions between ortho-H_2 and ortho-H_2D^+ (ortho-HD_2^+, ortho-D_3^+) can reduce the degree of deuteration of H_3^+ significantly at low temperatures. Flower et al. (2006) have shown that the fractionation of H_3^+, hence, the abundance of atomic D are strongly reduced when the H_2 opr is higher than 10^{-4}. Consequently, we enlarge the chemical network, relative to TCK12b, by considering the H_3^+-H_2 system whose new reaction rate coefficients have been computed by Hugo et al. (2009). Ion-neutral reactions between H_3^+ isotopologues (including their different spin states) and CO or N_2, electronic recombinations, and recombinations on electronegative charged grains have also been included following

Roberts & Millar (2000); Roberts et al. (2003, 2004); Walmsley et al. (2004) and Pagani et al. (2009).

The actual opr of H_2 in molecular clouds is still highly uncertain. The initial value of H_2 opr formed on grain surfaces is most likely 3, as recently confirmed by the experiment by Watanabe et al. (2010) conducted on amorphous solid water. Proton-exchange reactions in the gas phase would then convert ortho-H_2 to para-H_2, decreasing the opr of H_2 towards the Boltzmann value ($\sim 3 \times 10^{-7}$ at 10 K, see Flower et al. 2006). Recent experimental studies have also demonstrated that H_2 undergoes a nuclear spin conversion from the ortho to the para spin state on amorphous solid water (ASW) (Sugimoto & Fukutani 2011; Chehrouri et al. 2011; Hama et al. 2012). The influence of the H_2 opr on absorption lines of formaldehyde has been observed by Troscompt et al. (2009) who deduce that the H_2 opr is much lower than 1. Indirect estimates of H_2 based on the comparison with chemical models suggest values of about 10^{-3} – 10^{-2} (Pagani et al. 2009; Dislaire et al. 2012). Given the relative uncertainty in this value and its importance in the molecular deuteration process, in this work we assume the H_2 opr as a free parameter constant with time.

Table 1: Initial elemental abundances in the gas phase with respect to hydrogen nuclei (from Linsky 2003; Wakelam et al. 2010).

Species	Abundance
H_2	0.5
HD	1.6×10^{-5}
He	0.09
C	1.2×10^{-4}
N	7.6×10^{-5}
O	2.6×10^{-4}
S	8.0×10^{-8}
Fe	1.5×10^{-8}

2.3. Chemical network on grain surfaces

2.3.1. Formation and deuteration of water ice

We consider a chemical network based on the work by Tielens & Hagen (1982) modified following the results of several recent experimental works as described below. The simplest formation pathway towards solid water is the sequential hydrogenation of atomic oxygen:

$$O + H \rightarrow OH \quad (1)$$

$$OH + H \rightarrow H_2O. \quad (2)$$

This reaction channel was experimentally measured to occur in cold conditions, probably via barrierless reactions (Hiraoka et al. 1998; Dulieu et al. 2010; Jing et al. 2011).

In addition, water can also be formed from different channels involving O_2 or O_3 as follows. First, water can be formed from molecular oxygen, either from the gas phase or formed on grains, following the reaction channels:

$$O_2 + H \rightarrow HO_2 \quad (3)$$

$$HO_2 + H \rightarrow H_2O_2 \quad (4)$$

$$H_2O_2 + H \rightarrow H_2O + OH. \quad (5)$$

These pathways have been experimentally demonstrated by Miyauchi et al. (2008); Ioppolo et al. (2010) and Cuppen et al. (2010a) at temperatures of 10 K. Miyauchi et al. (2008) also showed an isotope effect in the formation of water from hydrogen peroxide, implying the possibility of tunnelling through an activation barrier for this reaction.

Second, water can be formed from ozone on interstellar grains (Cuppen & Herbst 2007; Taquet et al. 2012a) following the reaction

$$O_3 + H \rightarrow O_2 + OH \quad (6)$$

Then, O_2 and OH can continue to react to form water via the reactions described above. Mokrane et al. (2009) and Romanzin et al. (2011) experimentally showed the efficiency of this reaction by observing the presence of water (HDO, D_2O) after the irradiation of solid O_3 on water ice by H (D) atoms. We treat this reaction as barrierless.

With their microscopic Monte Carlo model, Cuppen & Herbst (2007) have concluded that molecular hydrogen plays a key role in the formation of water ice in molecular clouds. When hydrogen is mostly in its molecular form, water is formed at $\sim$ 70% by the reaction

$$OH + H_2 \rightarrow H_2O + H. \quad (7)$$

Oba et al. (2012) experimentally showed that HDO formation from OH is ten times less efficient than the formation of H_2O from OH, implying an isotope effect and therefore the possibility of tunnelling through an activation barrier in this reaction.

OH radicals can also recombine if the ice temperature is high enough (40 K in their experiment) to allow their mobility. Oba et al. (2011) experimentally determined branching ratios for the reactions

$$OH + OH \rightarrow H_2O + O \quad (8)$$

$$OH + OH \rightarrow H_2O_2 \quad (9)$$

of 0.2 and 0.8, respectively.

Unlike Cazaux et al. (2010, 2011), we do not include the O+H_2 reaction since it is unlikely to proceed at low temperatures (10-20 K) given its high endothermicity (960 K; Baulch et al. 1992). Oba et al. (2012) confirmed that the co-deposition of cold O atoms with H_2 at 10 K does not result in the formation of water but only of O_2.

We enlarge the water-formation network by including the deuterated counterparts of all reactions mentioned above. Due to the higher mass of deuterated species with respect to their main isotopologue, the reaction rates of barrierless reactions involving deuterated species are decreased. A careful treatment of the transmission probabilities (i.e. probability of tunnelling through the activation barrier) of all reactions possessing a barrier is described in section 2.4.

2.3.2. Formation and deuteration of other ices

The accretion of CO and O particles onto interstellar grains can lead to the formation of carbon dioxide (CO_2) mainly via three reaction channels (Ruffle & Herbst 2001)

$$HCO + O \rightarrow CO_2 + H \quad (10)$$

$$CO + O \rightarrow CO_2 \quad (11)$$

$$CO + OH \rightarrow CO_2 + H \quad (12)$$

Gas phase experiments have shown that reaction (10) is barrierless (e.g. Baulch et al. 2005) although it has never been studied on interstellar ice analogues so far.

Reaction (11) is thought to have a high activation energy (Talbi et al. 2006). Laboratory experiments have shown that solid carbon dioxide can be formed from this reaction with low efficiency, at least two orders of magnitude lower than astronomical observations (Roser et al. 2001; Raut & Baragiola 2011).

Formation of solid carbon dioxide, from OH radicals and CO molecules, has been observed even at very low temperatures (10-20 K, Oba et al. 2010; Ioppolo et al. 2011; Noble et al. 2011). However, the exact pathway of the formation of CO_2 is still uncertain. Following Oba et al. (2010) who observed a weak band attributed to the HOCO radical and other theoretical works, we propose a reaction pathway for the CO_2 formation from CO and OH, as described in Appendix A.2.

The chemical network presented in TCK12b, with the same relative rates, is used to study the formation and the deuteration of formaldehyde and methanol. We also consider the formation of deuterated methane and ammonia from barrierless addition reactions of solid atomic carbon and nitrogen. A full list of surface reactions considered in this work is presented in Appendix B.

2.4. Eckart model and reaction probabilities

In previous gas-grain astrochemical models, the transmission probability of exothermic surface reactions has been approximated by the exponential portion of the quantum mechanical probability for tunnelling through a square potential barrier of width *a*. However, this approach has two main limitations:
i) it does not fit the potential energy profile of reactions correctly;
ii) the width *a* is unknown, although in most astrochemical models it is arbitrarily fixed to 1Å (Tielens & Hagen 1982; Hasegawa et al. 1992). Garrod & Pauly (2011) reproduced the value of the transmission probability of a few reactions with square potential barriers and deduced a width of about 2Å. However, the deduction of this width is based on poorly constrained activation barriers.

Since square potential barriers do not allow us to accurately estimate the values of the transmission probabilities, we compute the transmission probabilities of all the reactions using the Eckart model (Eckart 1930; Johnston & Heicklen 1962), which fits an approximate potential energy surface. A full description of the Eckart model, our quantum chemistry calculations and the computations of the transmission probabilities are given in Appendix A.

Briefly, the formation of deuterated water includes two reaction channels which have an activation barrier: reactions (5) and (7). Reaction (5) has been theoretically studied by Koussa et al. (2006) and Ellingson et al. (2007) but only for the main isotopologues. Therefore, quantum chemistry calculations are conducted for all the reactions (5) including deuterated isotopologues (see Appendix A for more details on the calculations). Concerning reaction (7), the transmission probabilities of all the deuterated counterparts have been deduced from the theoretical work by Nguyen et al. (2011).

Figure 2 shows the Eckart and the symmetric square potentials as a function of reaction coordinates for the reaction (5) computed in this work. As suggested previously, it can be seen that the Eckart potential is far to be symmetric. Furthermore, the reaction profile is thinner than the square barrier. Since the quantum tunnelling probability of transmission through this barrier depends on the area of the potential energy profile, the Eckart model gives higher probability of transmission than the square barrier (1.4×10^{-7} versus 1.2×10^{-8}).

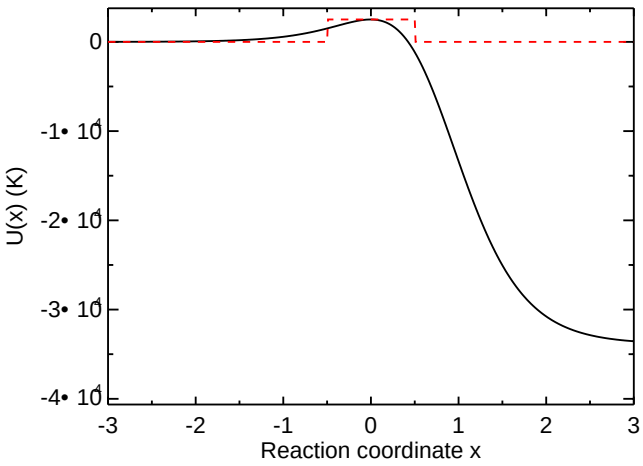

Fig. 2: Potential energy profile as function of the reaction coordinate of the $H_2O_2 + H \rightarrow H_2O + OH$ reaction computed from ab-initio calculations (black solid curve) and adopting a symmetric square barrier of a width of 1 Å (red dashed curve). See Appendix A for more details on calculations.

Table 2 lists the reactions with an activation barrier, as well as the input parameters needed for computing the transmission probabilities. It also compares the transmission probability computed with the Eckart model and with a symmetric square potential barrier of the same activation energy and adopting a width of 1 Å (the value commonly used in most gas-grain astrochemical models). The comparisons between the two approaches show that the assumption of a square barrier width of 1 Å tends to underestimate the reaction probabilities for all the reactions by up to seven orders of magnitude.

The transmission probability of the CO+H reaction computed with the Eckart model is in good agreement with the range of values we deduced in TCK12a. In this latter work, we varied the transmission probability P_r of this reaction and found that a transmission probability higher than 2×10^{-7} was needed to reproduce the solid CH_3OH/CO ratio observed towards high-mass protostars.

2.5. Photodissociation and photodesorption of ices

In addition to Langmuir-Hinshelwood chemical reactions, we also consider the effect of FUV (6 - 13.6 eV) photons on ices, following the results of molecular dynamics (MD) simulations carried out by Andersson et al. (2006) and Andersson & van Dishoeck (2008). They showed that an amorphous ice absorbs UV photons in a 1-2 eV narrow band peaked at $\sim$ 8.5 eV, in good agreement with experimental works by Kobayashi (1983), reaching a maximal absorption probability of 7×10^{-3} per monolayer. We convolve the absorption spectrum with the emission spectrum of the interstellar radiation field (ISRF) deduced by Mathis et al. (1983) and with the emission spectrum of H_2 excited by the secondary electrons produced by the cosmic-rays ionization of H_2 (CRH2RF) computed by Gredel et al. (1987). The absorption probabilities P_{abs} of each monolayer integrated along the 6 - 13.6 eV band are therefore equal to 1.51×10^{-3} for ISRF and 1.03×10^{-3} for CRH2RF. Andersson & van Dishoeck (2008)

Table 2: List of reactions having a barrier, with the forward, backward activation barriers, the imaginary frequency of the transition state, the transmission probabilities computed with the Eckart model and the square barrier method (using a barrier width of 1 Å).

Reactions							Probability type	V_f (K)	V_b (K)	ν_S	$P_{r,Eckart}$	$P_{r,square}$	Reference
OH	+	H_2	→	H_2O	+	H	Eckart	2935	10209	-1293	4.07(-07)	1.49(-13)	1
OH	+	HD	→	H_2O	+	D	Eckart	2855	9396	-1259	3.62(-07)	7.91(-16)	1
OH	+	HD	→	HDO	+	H	Eckart	3051	10508	-970.4	1.00(-09)	2.44(-16)	1
OH	+	D_2	→	HDO	+	D	Eckart	3026	9556	-955.3	8.07(-10)	8.02(-18)	1
OD	+	H_2	→	HDO	+	H	Eckart	2789	10246	-1293	8.74(-07)	2.88(-13)	1
OD	+	HD	→	D_2O	+	H	Eckart	2900	10871	-970.1	2.81(-09)	5.2(-16)	1
OD	+	HD	→	HDO	+	D	Eckart	2703	9736	-1258	7.99(-07)	1.76(-15)	1
OD	+	D_2	→	D_2O	+	D	Eckart	2870	10338	-955.1	2.26(-09)	7.03(-18)	1
H_2O_2	+	H	→	H_2O	+	OH	Eckart	2508	36358	-1054	1.37(-07)	1.18(-08)	2
H_2O_2	+	D	→	HDO	+	OH	Eckart	2355	37118	-843.7	5.54(-09)	8.83(-12)	2
HDO_2	+	H	→	HDO	+	OH	Eckart	2523	36239	-1053	1.23(-07)	1.17(-08)	2
HDO_2	+	H	→	H_2O	+	OD	Eckart	2524	36063	-1053	1.22(-07)	1.17(-08)	2
HDO_2	+	D	→	HDO	+	OD	Eckart	2369	36822	-846.6	5.28(-09)	8.66(-12)	2
HDO_2	+	D	→	D_2O	+	OH	Eckart	2367	37023	-846.1	5.29(-09)	8.66(-12)	2
D_2O_2	+	H	→	HDO	+	OD	Eckart	2540	35938	-1052	1.08(-07)	1.17(-08)	2
D_2O_2	+	D	→	D_2O	+	OD	Eckart	2384	36721	-842.9	4.28(-09)	8.49(-12)	2
CO	+	H	→	HCO			Eckart	1979	8910	-793.6	1.92(-07)	1.83(-08)	3
CO	+	D	→	DCO			Experiments				1.92(-08)	1.83(-09)	4
H_2CO	+	H	→	CH_3O			Experiments				9.60(-08)	9.15(-09)	4
H_2CO	+	D	→	CH_2DO			Experiments				9.60(-09)	9.15(-10)	5
H_2CO	+	D	→	HCO	+	HD	Experiments				9.31(-08)	8.88(-09)	4
H_2CO	+	D	→	HDCO	+	H	Experiments				9.31(-08)	8.88(-09)	4
HDCO	+	H	→	CH_2DO			Experiments				1.11(-07)	1.06(-09)	4
HDCO	+	D	→	CHD_2O			Experiments				1.11(-07)	1.06(-09)	5
HDCO	+	H	→	HCO	+	HD	Experiments				1.54(-07)	1.46(-08)	5
HDCO	+	D	→	DCO	+	HD	Experiments				9.31(-08)	8.87(-09)	5
HDCO	+	D	→	D_2CO	+	H	Experiments				9.31(-08)	8.87(-09)	5
D_2CO	+	H	→	CH_2DO			Experiments				1.27(-07)	1.21(-08)	4
D_2CO	+	D	→	CD_3O			Experiments				1.27(-08)	1.21(-09)	5
D_2CO	+	H	→	DCO	+	HD	Experiments				7.30(-08)	6.95(-09)	4
CH_3OH	+	D	→	CH_2OH	+	HD	Experiments				2.88(-07)	2.75(-08)	4
CH_2DOH	+	D	→	CHDOH	+	HD	Experiments				1.92(-07)	1.83(-08)	4
CHD_2OH	+	D	→	CD_2OH	+	HD	Experiments				1.50(-07)	1.43(-08)	4
CH_3OD	+	D	→	CH_2OD	+	HD	Experiments				2.88(-07)	2.75(-08)	5
CH_2DOD	+	D	→	CHDOD	+	HD	Experiments				1.92(-07)	1.83(-08)	5
CHD_2OD	+	D	→	CD_2OD	+	HD	Experiments				1.50(-07)	1.43(-08)	5

Notes. The probability type refers to the method used for computing the probability. "Experiments" means that the transmission probability is deduced from the CO+H reaction by considering the relative rates experimentally measured by Hidaka et al. (2009) (see TCK12b for more details).

References. 1: Nguyen et al. (2011), 2: This work. 3: Peters et al. (2012), 4: Hidaka et al. (2009), 5: Taquet et al. (2012b).

also showed that the photofragments, OH and H, display different trajectories (desorption, trapping, or mobility on the surface) and they computed the yield of each trajectory as function of the monolayer. Subsequent experimental studies by Yabushita et al. (2006, 2009) and Hama et al. (2009, 2010) have confirmed the different photofragment trajectories revealed by MD simulations. However, our model only considers one chemically reactive layer (the outermost). We deduce the yield of each trajectory by averaging the yields computed by Andersson & van Dishoeck (2008) on each layer. The list of trajectories as well as their averaged yield Y is given in Table 3. The rate of each trajectory can be deduced, via the following equation

$$R_{photo,i}(s^{-1}) = Y_i \times F_{UV} \times \sigma(a_d) \times 5 \times P_{abs} \times 1/N_s \quad (13)$$

where F_{UV} (cm^{-2} s^{-1}) is the photon flux of the 6 - 13.6 eV UV band which is absorbed by the amorphous ice, $\sigma(a_d)$ (cm^2) is the cross section of interstellar grains (= $\pi(a_d/2)^2$ where a_d is the grain diameter), 5 refers to the absorption of the five outermost layers, and N_s is the number of sites on the grain surface. Owing to the lack of quantitative data on the photodesorption of atoms and on the photodissociation of hydrogenated (and deuterated) molecules other than water on ASW ice, we consider the same absorption probability for all atoms and molecules as for water. For atoms, the desorption probability upon absorption is assumed to be unity, whilst we consider the same outcome probabilities for hydrogenated molecules.

Table 3: List of trajectories after H_2O photodissociation with their probability (deduced from Andersson & van Dishoeck 2008, see text).

Outcome	Probability
$H_2O_{ice} \rightarrow H_{gas} + OH_{ice}$	0.5
$H_2O_{ice} \rightarrow H_{ice} + OH_{ice}$	0.2
$H_2O_{ice} \rightarrow H_{ice} + OH_{gas}$	2.2×10^{-3}
$H_2O_{ice} \rightarrow H_{gas} + OH_{gas}$	6.8×10^{-3}
$H_2O_{ice} \rightarrow H_2O_{gas}$	4.0×10^{-3}
$H_2O_{ice} \rightarrow H_2O_{ice}$	0.28

We follow the experimental results by Fayolle et al. (2011) for wavelength-dependent CO photodesorption between 7.5 and 13 eV. The convolution of the CO photodesorption spectrum with the ISRF and CRH2RF fields gives integrated photodesorption yields of 1.2×10^{-2} and 9.4×10^{-3} photon^{-1} molecule $^{-1}$, respectively. Owing to the lack of data on the wavelength-dependent photodesorption of other molecules, we consider the same photodesorption rates for O_2, and N_2.

2.6. Binding energies

Comparisons between the observed absorption 3 μm band of water and laboratory experiments have shown that grain mantles are mainly composed of high-density amorphous solid water (ASW) (Smith et al. 1989; Jenniskens et al. 1995). Therefore, binding energies of adsorbed species relative to ASW must be considered.

It is now accepted that light particles (H, D, H_2, HD, D_2) show a distribution of their binding energies relative to ASW, depending on the ice properties, the adsorption conditions, and the coverage of the accreted particles. Perets et al. (2005) have experimentally highlighted the influence of the ice density on the HD and D_2 binding energies. Molecules adsorbed on low-density amorphous ices (LDI) desorb following three desorption peaks that are at lower temperatures than the single observed desorption peak of molecules evaporating from a high-density amorphous ice (HDI). By depositing D_2 on ASW, Hornekær et al. (2005) showed that D_2 is more efficiently bound to porous surfaces. Furthermore, binding energies follow broad distributions between 300 and 500 K and between 400 and 600 K for non-porous and porous ASW ices, respectively. Amiaud et al. (2006) studied the link between the binding energy distribution of D_2 with its coverage on a porous ASW ice and with ice temperature. More particularly, they showed that the D_2 binding energy decreases with H_2 coverage, from $\sim$ 700 K to $\sim$ 350 K whilst distributions broaden.

The experimental results have been supported by theoretical MD calculations. For example, Hornekær et al. (2005) and Al-Halabi & van Dishoeck (2007) found that the binding energy distributions are essentially a consequence of the variation in the number of water molecules surrounding the adsorbed particle. Thus, the binding energy of H shows a broader distribution peaked at higher values on porous and irregular amorphous water ice than on a structured crystalline ice.

It is believed that deuterated species are more efficiently bound with ices than their main isotopologues because of their higher mass (Tielens 1983). However, the difference in binding energy between H, H_2, and their deuterated counterparts still remains poorly constrained. Experiments by Perets et al. (2005) and Kristensen et al. (2011) have shown that distribution peaks of the H_2, HD, and D_2 binding energies are very close (less than 5 meV $\sim$ 60 K). These differences remain much smaller than the typical full-width-at-half-maximum of binding energy distributions shown by MD simulations ($\sim$ 195 K for a amorphous ice Al-Halabi & van Dishoeck 2007), we, therefore, assume the same binding energy for H, D, H_2, HD, and D_2. We also verify a posteriori that a small difference of 50 K between these binding energies has a very limited influence on the deuteration of water.

To take the binding energy distribution of light adsorbed species on ices into account, we assume the binding energy of H, D, H_2, HD, and D_2 relative to ASW $E_{b,ASW}$ as a free parameter between 400 and 600 K. We consider constant binding energies of heavier species, following several experiments. Table 4 lists the binding energies of selected species. We assume that the deuterated species have the same binding energy as their main isotopologue.

Table 4: List of selected species and binding energies relative to amorphous solid water ice.

Species	E_b (K)
H	400 - 600 [a]
H_2	400 - 600 [a]
C	800 [b]
N	800 [b]
O	800 [b]
CO	1150 [c]
CO_2	2690 [d]
O_2	1000 [c]
O_3	1800 [e]
N_2	1000 [c]
CH_4	1300 [f]
NH_3	1300 [f]
OH	2820 [g]
H_2O	5640 [g]
H_2O_2	5640 [g]
H_2CO	2050 [f]
CH_3OH	5530 [c]

References. [(a)] Hornekær et al. (2005); Al-Halabi & van Dishoeck (2007); [(b)] Tielens & Allamandola (1987); [(c)] Collings et al. (2004); [(d)] Sandford & Allamandola (1990); [(e)]: Cuppen & Herbst (2007); [(f)] Garrod & Herbst (2006); [(g)] Speedy et al. (1996)

H_2 is, by about four orders of magnitude, the most abundant molecule in molecular clouds. Most particles that accrete onto the surface are, therefore, H_2 molecules. At low temperatures, H_2 would become the most abundant icy molecule if binding energies were computed relative to a water ice substrate alone. However, microscopic models by Cuppen & Herbst (2007) and Cuppen et al. (2009) have shown that the total binding energy of a adsorbate relative to a substrate is given by the additive energy contribution of the occupied neighbouring sites. Therefore, an H_2O:H_2 mixture must be considered for computing an effective E_b. Vidali et al. (1991) gave an estimate of the binding energy of H on an H_2 ice, which is about 45 K at 10 K. Following Garrod & Pauly (2011), we compute the effective binding energy of each species i from the fractional coverage of H_2 on the surface, $P(H_2)$

$$E_b(i) = (1 - P(H_2)) \cdot E_{b,\mathrm{wat}}(i) + P(H_2) \cdot E_{b,H_2}(i) \quad (14)$$

where $E_{b,\mathrm{wat}}(i)$ is the binding energy of the species i relative to water ice, the values of selected species are listed in Table 4. To deduce E_{b,H_2} of species other than H, we apply the same scaling factor as for atomic hydrogen ($E_{b,H_2}(H)/E_{b,\mathrm{ASW}}(H)$). The increase in the H_2 abundance in the mantle tends to decrease the effective binding energy $E_b(i)$ of physisorbed species i.

2.7. Physical model

As described in the introduction, water ice is formed at visual extinctions A_V higher than 3 mag (Whittet et al. 1988, 2001), whilst gas phase CO is detected above a visual extinction threshold of 2 mag (Frerking et al. 1982) and PDR models show that hydrogen is already mainly molecular at $A_V < 1$ mag. Water ice is, therefore, thought to be formed when the gas is already molecular.

We consider a two-step model. For each set of input parameters, we first compute the abundances of gas phase species assuming the element abundances shown in Table 1 and considering the gas phase network described in section 2.2. For this, we

assume the steady state values, which are reached after 5×10^6 yr when the density is 10^3 cm^{-3} and after 10^6 yr at 10^4 cm^{-3}. This first step is meant to describe the molecular cloud and the initial pre-collapse phase before the formation of the ice bulk. In practice, we assume that the timescale to reach the chemical equilibrium is shorter than the dynamical timescale for the gas to reach the prestellar core conditions. These gas phase abundances are then considered as the initial abundances for the gas-grain modelling. In the second step, we allow gas and grain surface chemistry to evolve whilst physical conditions (density, temperature, visual extinction) remain constant.

2.8. Multi-parameter approach

Following our previous works (TCK12a, TCK12b), we consider a multi-parameter approach by considering free physical, chemical, and surface input parameters. This approach allows us to study their influence on the formation and the deuteration of key species.

The total density of H nuclei in molecular clouds, where interstellar ices are thought to be formed, show typical variations from 10^3 cm^{-3} at the edge of clouds to 10^6 cm^{-3} in denser prestellar cores. Temperatures of the gas and grains also show variations depending on the location inside the cloud. Here, we consider three fixed temperatures, by assuming that the gas and grain surface temperatures are equal, $T_g = T_d$. We study the influence of the visual extinction on the formation and the deuteration of ices by considering A_V as a free parameter. As previously explained in section 2.2, the ortho/para ratio of H_2 is considered as constant.

In section 2.6 and in TCK12a and TCK12b, we showed the importance of considering distributions of several grain surface parameters (grain diameter a_d, binding energy E_b of light species, diffusion to binding energy ratio E_d/E_b). We therefore consider them as free parameters, the range of values are listed in Table 5.

We keep fixed the following other parameters:
- distance between two sites $d_s = 3.1$ Å, corresponding to a high-density ASW (Jenniskens et al. 1995);
- cosmic-ray ionization rate $\zeta = 3 \times 10^{-17}$ s^{-1};
- interstellar radiation field (ISRF) $F_{ISRF} = 1 \times 10^8$ photons cm^{-2} s^{-1};
- cosmic ray induced radiation field (CRH2RF) $F_{CRH2RF} = 1 \times 10^4$ photons cm^{-2} s^{-1};
- scaling factor in multiples of the local interstellar field $G_0 = 20$, which represents an average value between low interstellar radiation fields seen in molecular clouds, such as B68 ($G_0 = 0.25-1$, Bergin & Snell 2002), and high ISRFs see,n for example, in star-forming molecular clouds in Orion ($G_0 = 10^4$, Giannini et al. 2000).

In the model grid, some of the parameter values are inconsistent with each other and do not necessarily reflect realistic physical models. We use this model grid in order to systematically study the influence of each parameter on the formation and the deuteration of interstellar ices. For this purpose, we compute the mean values and 1-sigma standard deviations of species abundances and deuterations either in the gas phase or grain surfaces, following the method by Wakelam et al. (2010). Table 5 lists all the free parameters and their ranges of values explored in this work.

Table 5: List of the input parameters and the values range explored in this work. Bold values mark the values adopted in the reference models (see text).

Input parameters	Values
Physical conditions	
$n_{H,ini}$	10^3 - 10^4 - 10^5 - 10^6 cm^{-3}
$T_g = T_d$	10 - 15 - 20 K
A_V	0 - 1 - 2 - 3 - 4 - 5 - 6 - 7 - 8 - 9 - 10 mag
ζ	3×10^{-17} s^{-1}
ISRF	1×10^8 photons cm^{-2} s^{-1}
G_0	20
Grain surface parameters	
a_d	0.1 - **0.2** - 0.3 μm
E_b(H)	400 - **500** - 600 K
E_d/E_b	0.5 - **0.65** - 0.8
d_s	3.1 Å
Chemical parameters	
H_2 o/p ratio	3×10^{-6} - 3×10^{-4} - 3×10^{-2} - 3

3. Results

In this section, we present the results in two steps. First, we consider the formation of water and other major ice species, and second, we focus on the deuteration.

Specifically, in section 3.1, we validate our model. For this purpose, i) we compare our predicted gas phase abundances as function of the visual extinction with PDR model predictions; ii) we compare the predicted abundances of gaseous and solid water as function of the visual extinction with published observations; iii) we discuss the multilayer formation of interstellar ices for a set of three reference physical conditions. We emphasize that our approach does not pretend to describe the whole evolution of the cloud. The reference models are meant to quantify the influence of specific physical conditions, which are likely to describe different evolutionary stages, on the ice chemistry.

Second, after validating the model, we focus on the water deuteration. In section 3.2, we emphasize the importance of the CO depletion on the deuterium fractionation of the reference models. Then, in section 3.3, we perform a multiparameter study that allows us to evaluate the influence of each model parameter on the deuterium fractionation of water. Comparing the model predictions with the observations allows us to constrain a range of values for the chemical and physical parameters.

3.1. Validation of the model

3.1.1. Initial gas phase abundances

As described in section 2.7, we adopt a two-step model. The ice formation phase is followed by considering initial abundances that are computed from steady-state calculations of gas phase chemistry. These initial abundances depend on the density and the temperature, but mainly on the visual extinction A_V (hereafter, A_V means the edge-to-centre visual extinction, half of the observed visual extinction), because photolytic processes play a significant role at low visual extinctions. In fact, the abundance of most gas phase species weakly depends on the density and the temperatures (in the range of values considered in this work) but are essentially a function of the visual extinction. Therefore, we compare the gas-phase abundances of key molecules for ice formation (H, D, C, O, CO, O_2) between our model and the Meudon PDR code (Le Petit et al. 2006) for a total density $n_H = 10^4$ cm^{-3}.

Figure 3 shows the depth-dependent chemical abundances of gas phase H, D, O, C, O_2, and CO, for $n_H = 10^4$ cm^{-3} computed by the PDR code in the low visual extinction regime. These abundance profiles are in relative good agreement with the initial abundances computed with our model. The abundances differ by 20% for most abundant species and within one order of magnitude when species display low abundances (C and O_2). This validates the use of the H_2, HD, and CO self-shieldings in our code. The other differences are due to the different chemical networks and physical conditions between the two codes (the PDR and ours). The decrease in UV flux with increasing A_V increases the abundance of molecules such as H_2, HD, and CO, and decreases the abundances of H, D, and then C, and O. D abundance is governed by the high photodissociation of HD at low A_V and by the formation of H_3^+ isotopologues at higher A_V, and shows an abundance minimum at $A_V = 1$ mag.

Molecular oxygen is formed at higher visual extinction, and it reaches its maximal abundance at $A_V > 5$ mag. Our chemical network predicts a high O_2/O abundance ratio ($\sim 1-1.5$). In fact, the O_2 abundance is highly uncertain because it depends on 1) the rate coefficients of some key reactions displaying high uncertainties, and 2) the elemental abundances of carbon and oxygen (see Wakelam et al. 2010; Hincelin et al. 2011). Moreover, observations carried out with the *SWASS*, *Odin*, and *Herschel* space telescopes have revealed that O_2 is not abundant in molecular clouds ($X(O_2) \lesssim 10^{-7}$, see Goldsmith et al. 2011; Liseau et al. 2012). Modelling the formation of ices with high O_2 abundances is not necessarily realistic, and we, therefore, investigate the influence of the gas phase O_2/O abundance ratio on the formation of ices in section 3.1.3.

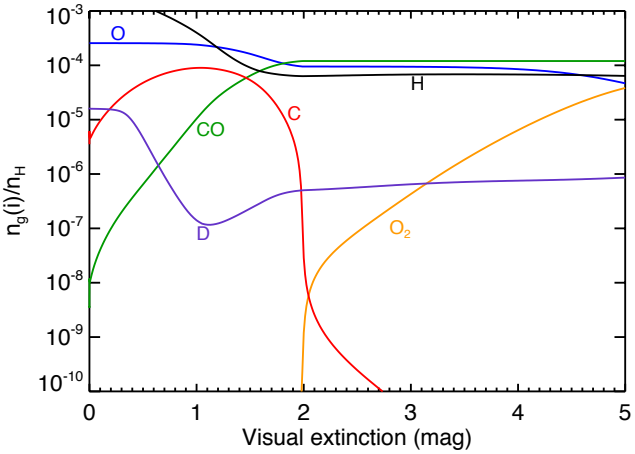

Fig. 3: Initial abundances of C, O, CO, and O_2 as function of the visual extinction computed with the Meudon PDR code at $n_H = 10^4$ cm^{-3}, $G_0 = 20$.

Concluding remarks. As shown in Fig. 3, the chemistry in the gas phase is known to strongly depend on the visual extinction A_V. The steady-state gas phase abundances computed with our model are in good agreement with the results of PDR simulations. The use of a two-step model might overestimate the abundance of gaseous O_2 affecting ice formation. Therefore, the influence of the O_2/O ratio on ice formation needs to be investigated.

3.1.2. Depth-dependent water abundances

Figure 4 shows the final (at 10^7 yr) abundances of water ice and vapour as functions of visual extinction A_V for physical condition representative of molecular clouds (e.g. $n_H = 10^4$ cm^{-3}, $T_g = T_d = 15$ K). The final abundances can be divided into two zones:

i) a photon-dominated layer ($A_V < 2$ mag) where gas phase molecules are photodissociated and ices are photodesorbed. At very low visual extinctions, interstellar ices are efficiently photodesorbed and show a low abundance of $\sim 10^{-7}$ relative to H nuclei corresponding to less than one monolayer. The abundance of water vapour, given by the balance between its formation in gas phase, its photodesorption from interstellar grains, and its photodissociation, reaches steady state values of $10^{-8}-10^{-7}$ (see also Hollenbach et al. 2009).

ii) a darker region ($A_V > 2$ mag) where the decrease in UV flux allows the formation of interstellar ices, mainly composed of water. At $A_V = 2-4$, water ice is mainly formed from the accretion of O atoms via the barrierless reaction (2). Most of the oxygen reservoir not trapped in CO is easily converted into water ice, reaching abundances up to 2×10^{-4}. The increase in gas-phase O_2 initial abundance with A_V slightly decreases the final abundance of water ice. Indeed, water ice is also formed via the accretion of O_2 including the formation of hydrogen peroxide. These formation pathways involve reactions possessing significant activation energies and low transmission probabilities (see Table 2). Finally, water formation also depends on the grain surface parameters E_d/E_b and E_b(H). A highly porous case (high E_d/E_b ratio combined with a high binding energy of H) strongly decreases the diffusion rate of mobile H species, decreasing the final abundance of water ice by one order of magnitude ($\sim 10^{-5}$).

Gas phase abundance of water is mainly governed by the balance between photodesorption and accretion. The decrease in UV flux with increasing A_v decreases water ice photodesorption and therefore the final abundance of water vapour from 10^{-7} at $A_V = 2$ to less than 10^{-9} at $A_V = 5$. We can note that the multilayer nature of grain mantles and the use of a wavelength-dependent absorption of UV photons from ices give similar results to theoretical PDR studies (e.g. Hollenbach et al. 2009).

In spite of the inevitable approximations of our modelling, our predictions are in good agreement with observations of water ice and water vapour, as shown in Fig. 4.

Concluding remarks. For typical conditions representative of a molecular cloud, we are able to reproduce the observed A_V threshold ($A_V \sim 1.5$ mag, $A_{V,obs} \sim 3$ mag) and the high abundance of water ice ($X \sim 10^{-4}$). The low abundance of water vapour observed in molecular clouds is reproduced at higher visual extinctions (4-5 mag).

3.1.3. Reference models

Very likely, the different ice components and their relative deuteration are the result of a long history where the physical conditions evolve. Therefore, a model aiming at reproducing the whole set of observations should take this evolution into account. However, before embarking on such a complicated modelling, it is worth while and even important to make clear what the characteristics (specifically, solid species and deuteration)are at each evolutionary step. To this end, we consider three "reference" models in the following: i) translucent cloud model, forming H_2O and CO_2 ices; ii) dark cloud model, allowing the formation of CO ice; iii) dark core model, showing high depletion of CO. The chemical composition of grain mantles for these refer-

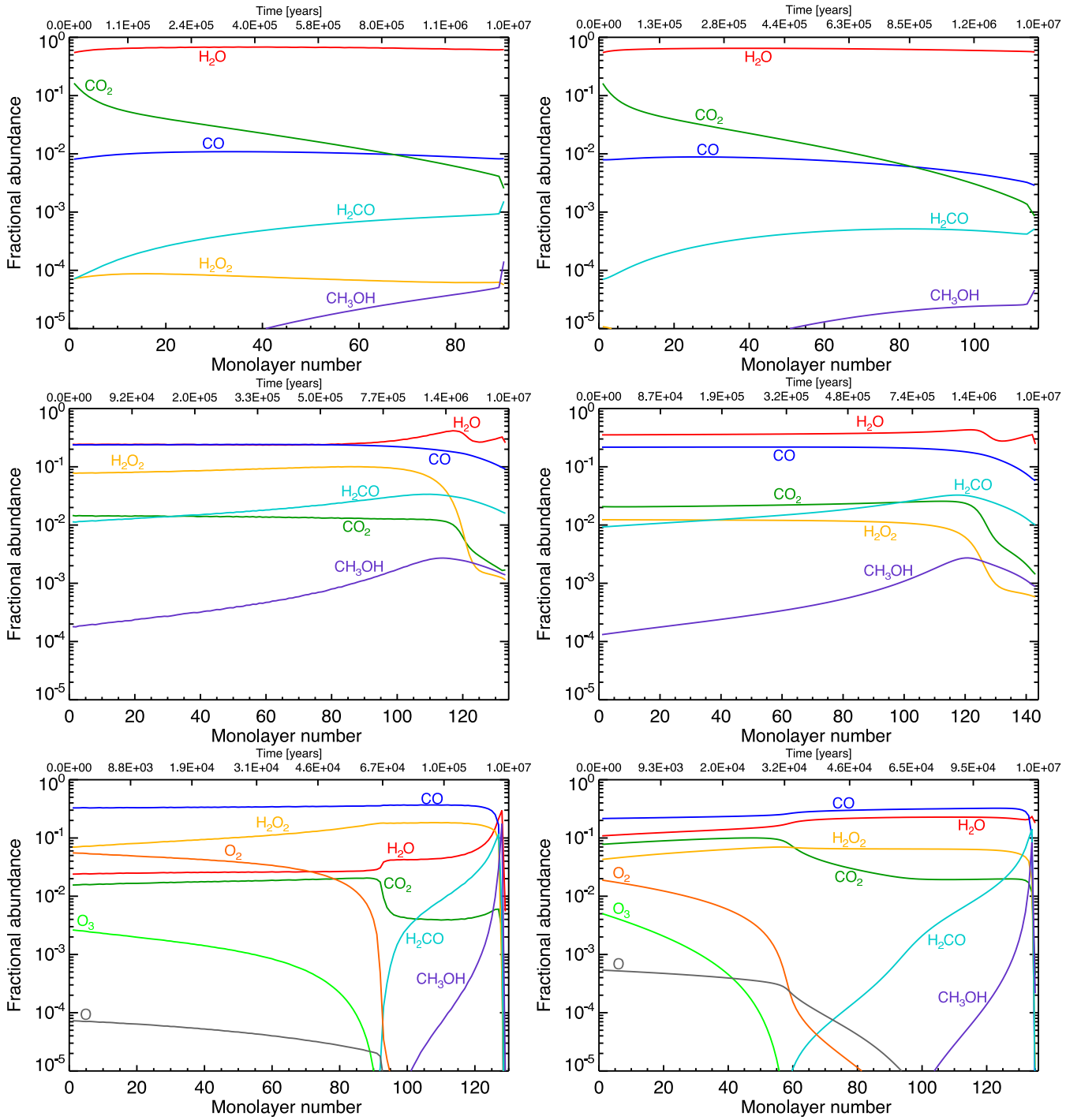

Fig. 5: Fractional ice abundances of main species formed from O, O_2, and CO for three reference models with "normal" gas phase abundances computed with the chemical network presented in section 2.2 (left), and for a gas phase $[O_2]/[O]$ abundance ratio artificially decreased by a factor of 10 (right): top) $n_H = 10^4$ cm^{-3}, $T = 15$ K, $A_V = 2$ mag, middle) $n_H = 1 \times 10^4$ cm^{-3}, $T = 10$ K, $A_V = 4$ mag, bottom) $n_H = 10^5$ cm^{-3}, $T = 10$ K, $A_V = 10$ mag. Values of other parameters are bold values of Table 5.

ence models are shown in Figure 5 for the two sets of runs with different $[O_2]/[O]$ abundance ratios (see section 2.2).

i) *Translucent cloud model* where ices are mainly composed of H_2O and CO_2: $n_H = 10^4$ cm^{-3}, T = 15 K, $A_V = 2$ mag (corresponding to an observed visual extinction of 4 mag). For the conditions considered in this model, grain mantles are mainly composed of water and carbon dioxide. After H_2, the most abundant species that accrete onto grain surfaces are H, O, and CO. For these conditions, the initial O_2/O abundance ratio is low (5×10^{-4}). The decrease in the O_2/O ratio, therefore, does not affect the ice composition significantly. O_2 is involved in the formation of O and CO in the gas phase, and its artificial decrease favours O instead of CO and increases the formation of water ice by 25%, increasing the ice thickness. The relatively high grain temperature (15 K) allows accreted particles to diffuse efficiently and form H_2O and CO_2. At this visual extinction, the UV flux

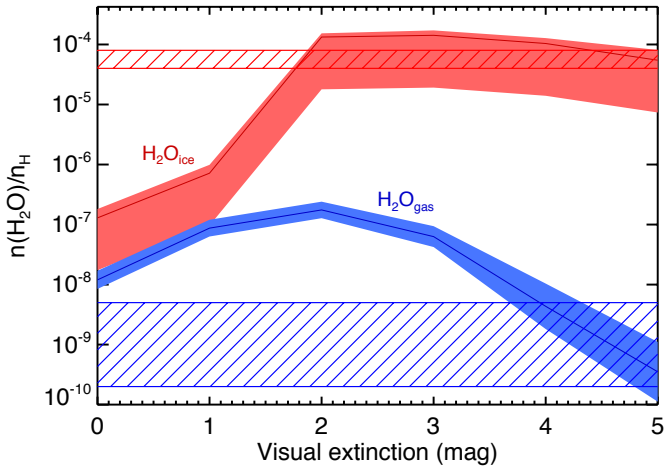

Fig. 4: Final abundances (10^7 yr) of water ice (H_2O_{ice}, red) and water vapour (H_2O_{gas}, blue) as function of the visual extinction A_v for typical molecular cloud conditions ($n_H = 10^4$ cm^{-3}, $T = 15$ K) and including the variation of all other input parameters. Hatched boxes refer to water ice observed by Pontoppidan et al. (2004) towards the Serpens SMM4 regions and water vapour observed by Caselli et al. (2010) towards the L1544 prestellar core (the upper limit represents water abundance in the external part whilst the lower value represents water abundance in the central region).

irradiating grain surfaces is high, and volatile species, such as atoms or light stable molecules (CO), are efficiently photodesorbed.

Water is the main ice component because it is formed from the barrierless reactions (1) and (2) whilst its other reaction routes are negligible (less than 0.1 %). Carbon dioxide is mainly formed from the hydrogenation of the O...CO complex and not by the direct reaction between CO and OH. Indeed, the grain temperature is not high enough to allow a high diffusion of CO and OH, because of their high binding energy. Instead, O atoms that are less attractively bound can meet CO atoms to form the O...CO van der Waals complex. In turn, O...CO readily reacts with H to form a hot HO...CO* complex that forms CO_2 + H. The accretion of CO and O also allow the formation of formaldehyde and methanol, but only in low abundances, lower than 1 % compared to solid water whilst a low fraction of hydrogen peroxide is predicted for a "normal" O_2/O ratio. Indeed, they are formed by reactions involving either heavy atoms or significant activation barriers.

The overall abundance of CO_2 relative to H_2O decreases with time, varying from 30% at the beginning to less than 1% at the end. The decrease in the CO_2 abundance is due to the increase in H abundance once interstellar ices start to form, because of the high photodesorption.

Although H_2O and CO_2 are formed in high abundances, O and CO are not totally depleted on grains. They still show high gas-phase abundances (about 5×10^{-5} relative to H nuclei) at the end of the ice formation. The predicted CO_2 abundance relative to water ice is lower than the observations. However, CO_2 formation is very sensitive to the grain temperature (governing the diffusion of O atoms) and to the hydrogen abundance (governing the reaction rate between O and H atoms). A higher temperature, higher visual extinction, and/or higher density would, therefore, tend to increase the abundance of CO_2 relative to water.

ii) *Dark cloud model* where CO ice starts to form with water, forming a CO:H_2O mixture: $n_H = 1\times10^4$ cm^{-3}, T = 10 K, $A_V = 4$ mag (corresponding to an observed visual extinction of 8 mag), $t = 10^6$ yr. The low temperature limits the diffusion of O atoms and heavier species whilst the higher visual extinction allows CO molecules to stay bound on grain surfaces even if they do not react to form CO_2. Therefore, the main components of grain mantles are H_2O, mainly formed via the reaction (2), and CO.

CO shows an overall abundance relative to water of about 80 %, which is more than two times higher than observed abundance ratios of ices (10-30 %, Whittet et al. 2007; Öberg et al. 2011). This is due to the high O_2/O abundance ratio ($\sim$ 0.5 throughout the calculation) that allows the formation of H_2O_2, via barrierless hydrogenation reactions, instead of water. H_2O_2 is easily trapped within grain mantles before reacting because the reaction destroying hydrogen peroxide has a low transmission probability (see Table 2). The decrease in the O_2/O ratio by one order of magnitude increases the formation of water, giving a CO/H_2O abundance ratio of 30%, whilst the H_2O_2 abundance decreases by one order of magnitude. Hydrogen peroxide has recently been observed by Bergman et al. (2011) towards the ρ Oph A dark cloud, confirming its formation in ices and its subsequent sublimation via non-photolytic processes. The low grain temperature favours the formation of formaldehyde and methanol via CO hydrogenation, compared to the formation of CO_2. Formaldehyde shows an unexpected abundance higher than 8 % compared to water ice. Again, the formation efficiency of formaldehyde and methanol strongly depends on the grain temperature and on the total density. For example, a higher temperature and/or higher density would favour CO_2 formation instead of H_2CO and CH_3OH.

A visual extinction of 4 mag decreases the final gas-phase abundances of O and CO, compared to $A_V = 2$ mag. Indeed, gas-phase CO reaches an abundance of 5×10^{-6} whilst O abundance decreases to 10^{-7} at 10^7 yr. The difference in the two abundances is due to the efficient destruction of O atoms forming solid water, whilst most CO molecules do not react and are still able to photodesorb.

iii) *Dark core model* where most of CO is depleted, allowing the formation of pure CO ice and solid formaldehyde and methanol: $n_H = 10^5$ cm^{-3}, T = 10 K, $A_V = 10$ mag (corresponding to an observed A_V of 20 mag). The low temperature, the high visual extinction, and the high density allow a significant trapping of CO molecules in the inner part of grain mantles whilst the formation efficiency of CO_2 is low owing to the low temperature. H_2CO and CH_3OH are formed via hydrogenation reactions that have high activation barriers. They are, therefore, mainly formed in the outer part of the ice when the CO depletion is high, which allows an efficient hydrogenation (see TCK12a).

At this visual extinction, solid water is less abundant than hydrogen peroxide because the initial gas-phase O_2 abundance is higher than the abundance of atomic oxygen (O_2/O between 1 $\sim$ 3 throughout the calculation). Water formation is mainly formed through the formation of H_2O_2, which involves reactions having high activation barriers. Hydrogen peroxide is most likely trapped in the bulk before forming water owing to the relatively high density. In this case, solid CO reaches an absolute abundance relative to H nuclei of 10^{-4}, water and CO_2 show lower abundances (10^{-5} and 4×10^{-6}), whilst formaldehyde and methanol show an abundance of 2×10^{-6} and 8×10^{-7}, respectively. Decreasing the O_2/O abundance ratio to 0.3 strongly increases the formation efficiency of water and CO_2 instead of hydrogen peroxide. For this case, water is almost as abundant

as CO. Gas-phase abundances of O, O_2, and CO decrease with time and show high depletions (with final abundances lower than 10^{-10}), whereas H abundance remains constant.

Concluding remarks. The chemical composition of ices is very sensitive to the physical conditions and to the initial abundances. Most of the observed ice features are reproduced by the reference models: the water-rich ice seen at low visual extinctions is also composed of abundant CO_2, whilst the abundances of solid CO (and H_2CO and CH_3OH) gradually increase with the visual extinction and the density. The increase in the O_2/O ratio decreases the abundance of water because its formation from O_2 involves reactions that have significant activation barriers (see Table 2). However, since it is likely that O_2 abundance remains low in dark clouds, water formation seems to be efficient in a wide range of physical conditions. Therefore, the study of the water deuteration needs to include the variation of several physical parameters.

3.2. CO depletion and molecular deuteration

As discussed in TCK12b, the deuteration of solid species strongly depends on the values of the CO depletion and the density at the moment of their formation. The initial densities of H and D are roughly constant regardless of the total density. Their abundance relative to H nuclei decreases with increasing $n_{\rm H}$. At low densities, the increase in D abundance is limited by the weak deuterium reservoir, whilst the D/H ratio is able to strongly increase at higher densities. The gas and grain temperatures, as well as the visual extinction, also affect the evolution of the D/H ratio because they influence the desorption rate of H and D. In summary, since all these quantities vary with time, deuteration is not necessarily constant within grain mantles.

The influence of the CO depletion, the density, the temperatures, and the visual extinction on the water deuteration is shown in Figure 6 for the three "reference" models described in the previous section. At the beginning of the gas-grain calculation, CO has already reached its maximal abundance ($\sim 10^{-4}$, see Fig. 3). With time, the CO molecules freeze-out onto grains, decreasing the gas-phase CO abundance and increasing the CO depletion factor. The decrease in the temperatures from 15 to 10 K and the increase in the visual extinction from 2 to 4 mag increase the gas-phase D/H ratio from 0.1 % to 0.4 % at f_D(CO) = 1. The increase in total density from 10^4 to 10^5 cm^{-3} increases the final D/H ratio from 1 % to 10 %. The decrease in the gas-phase O_2/O abundance ratio does not modify the water deuteration for the two low-density cases. However, it slightly decreases the HDO/H_2O ratio for the dense core model by a factor of two because water is more efficiently formed at low CO depletion (see Fig. 5) when the D/H ratio is low.

Concluding remarks. As previously noted, water deuteration is largely influenced by the gas D/H atomic ratio. Consequently, the largest deuteration is obtained where the CO depletion and the gas-phase D/H ratio are high, namely in the latest and less efficient phases of water formation, represented by the reference model iii). Comparison with the observed deuterium fractionation towards IRAS 16293 shows that a part of water ice should have formed during a dark and/or dense phase. In the following section, we investigate the impact of key parameters on water deuteration.

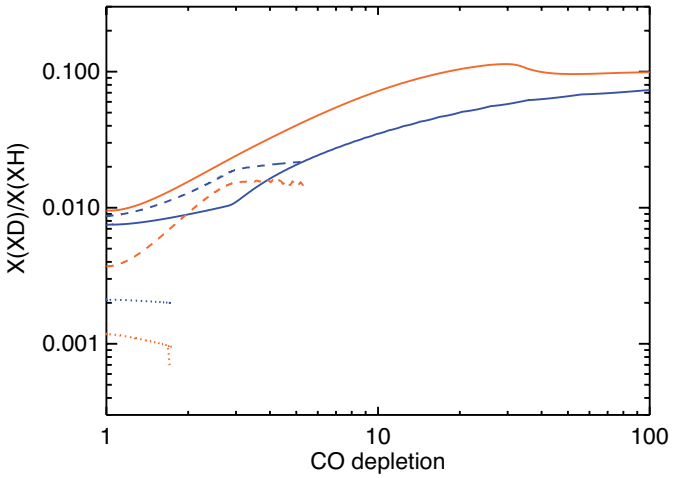

Fig. 6: Solid HDO/H_2O (blue) and gaseous D/H ratio (orange) as function of the CO depletion factor $f_D(\mathrm{CO}) = n_g(\mathrm{CO})/n_{g,ini}(\mathrm{CO})$, which increases with time, for the three reference models: translucent cloud region (dotted), dark cloud region (dashed), dark core region (solid).

3.3. Physical/chemical parameters and water deuteration

In this section, we study the influence on ice deuteration of several physical and chemical parameters which play a key role. Each figure presented in this section shows the influence of one (or two) parameter(s) at a time. For each value of the studied parameters, mean value and standard deviation of absolute abundances and deuterations induced by the variation in other input parameters are computed. Comparisons between the evolution of the mean deuteration induced by the variation in the studied parameter and the standard deviation caused by other parameters allow us to deduce the importance of that parameter on water ice deuteration.

The predicted deuteration levels of water ice are compared with the observed HDO/H_2O and D_2O/H_2O ratios towards the hot corino of IRAS 16293 (Coutens et al. 2012) to constrain the input parameters that reproduce the observations best. For this purpose, we assume that the entire bulk of interstellar ices desorbed in the hot corino and the observed deuteration reflects the deuteration in ices (see Introduction).

3.3.1. Influence of the H_2 o/p ratio

As described in section 2.2, the H_2 opr influences the deuteration of gas-phase species (including atomic D) (Walmsley et al. 2004; Flower et al. 2006; Pagani et al. 2009), thereby affecting the deuteration of solid water. Figure 7 shows the HDO/H_2O and D_2O/H_2O ratios in grain mantles as a function of time for four values of H_2 opr, including the variation in all other parameters, except the visual extinction range, which is limited to 2 - 10 mag (where most of water is believed to form, see Fig. 4). As anticipated, the H_2 opr governs the deuteration of water ice via its influence on the abundance of H_3^+ isotopologues and atomic D, for values higher than about 3×10^{-4}. An increase in H_2 opr between 3×10^{-4} and 3 decreases the HDO/H_2O and D_2O/H_2 ratios by 2.5 orders and 5.5 orders of magnitude, respectively. Furthermore, the ortho/para ratio of H_2 is a key, even the most important, parameter for water deuteration. The decrease in the deuteration due to the increase in the H_2 opr is much greater than

the standard deviation induced by the variation in other parameters.

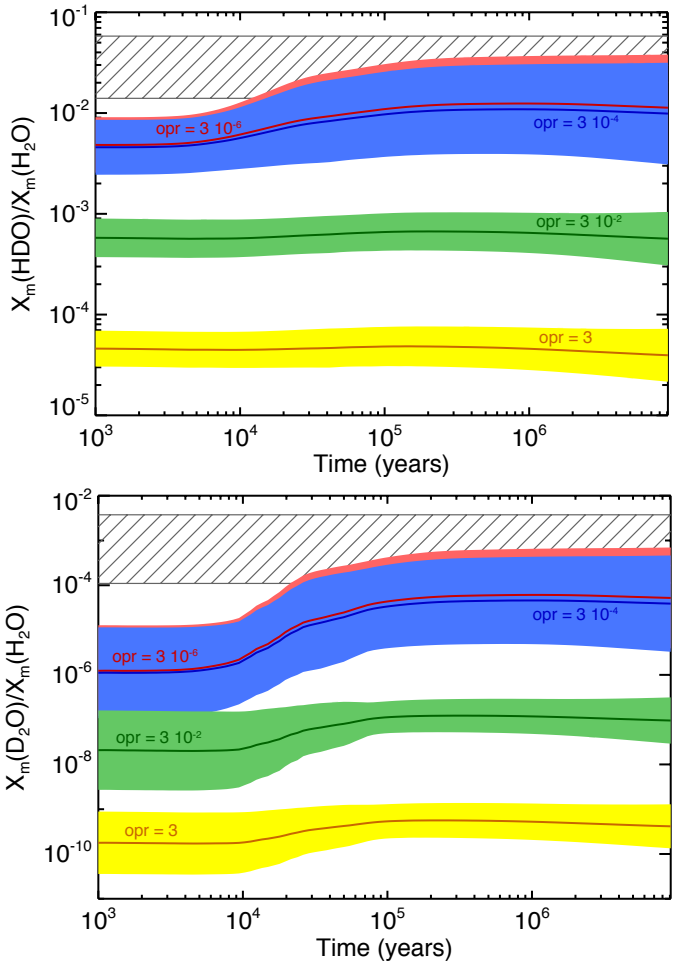

Fig. 7: Deuteration of water ice for four values of H_2 ortho/para ratios: 3×10^{-6} (red), 3×10^{-4} (blue), 3×10^{-2} (green), and 3 (yellow) including the variation in all other input parameters, except the visual extinction range that is limited to 2 - 10 mag. Hatched boxes refer to water deuteration observed by Coutens et al. (2012) towards IRAS 16293.

Comparisons with the observations by Coutens et al. (2012) clearly suggest that a low opr of H_2, lower than 3×10^{-4}, is needed to reproduce the observed deuterium fractionation.

3.3.2. Influence of the total density

As discussed in section 3.2, the gas-phase D/H ratio is a function of the total density $n_{\rm H}$ because high densities allow the gas-phase D/H ratio to increase with the CO depletion. Figure 8 shows the deuteration of HDO and D_2O for the four considered densities, using an H_2 opr of 3×10^{-6}, two temperatures (10 and 20 K), and a high visual extinction (10 mag), including the variation in grain surface parameters.

At low densities ($n_H \leq 10^4$ cm^{-3}), water deuteration is constant and low with time because a significant part of HD is already trapped in atomic D, before the CO depletion. At higher densities ($n_H > 10^5$ cm^{-3}), the efficient increase in the gaseous D/H ratio allows an increase in the deuteration of water up to 10%. In these cases, HDO is mostly located in the outer part of grain mantles, and D_2O is only located in the outermost layers, whilst H_2O is present throughout the mantle bulk. For this reason, the HDO/H_2O is limited and cannot reach the final gas-phase D/H ratio (up to 50 % at $n_H = 10^6$ cm^{-3}).

In summary, the total density plays a key role in the deuteration of water. Indeed, the variation in the total density $n_{\rm H}$ between 10^3 and 10^6 cm^{-3} influences the HDO/H_2O and D_2/H_2O ratios by 2 and 3.5 orders of magnitude, respectively.

The two observed deuteration ratios can be predicted with total densities $n_{\rm H}$ between 10^4 and 10^5 cm^{-3} at 10 K and between 10^5 and 10^6 cm^{-3} at 20 K, regardless of other grain surface parameters. In the following section, we study the case $n_H = 10^4$ cm^{-3} in more detail to investigate the effect of the temperature and the visual extinction on water deuteration.

3.3.3. Influence of the temperature and visual extinction

Temperatures either in the gas-phase and on grain surfaces also influence the deuteration of water. First, an increase in the gas-phase temperature enhances the reactivity of endothermic reactions, which can hydrogenate back H_3^+ isotopologues, decreasing the abundance of gaseous D atoms. Second, an increase in the grain temperature severely increases the desorption rate of volatile species, such as atomic H or D. The abundance of gaseous D is limited by the low deuterium reservoir, whereas the abundance of atomic hydrogen can increase up to two orders of magnitude, decreasing the gaseous D/H ratio. Water is mainly produced via reactions involving atomic H and D, increasing gas and dust temperatures, hence, decreasing the water deuteration on grain surfaces.

Figure 9 shows this effect by presenting the final HDO/H_2O and D_2O/H_2O ratios (at 10^7 yr) with the visual extinction, for the three temperatures, considering an H_2 opr of 3×10^{-6}, a total density of 10^4 cm^{-3}, and including the variation in grain surface parameters. The increase in the (gas and grain) temperatures between 10 and 20 K slightly decreases the water deuteration approximately by a factor of 3 for HDO and of 10 for D_2O at visual extinctions higher than 2 mag. The evolution of deuteration is the same order of magnitude as the standard deviations induced by the variation of other parameters.

The H and CO abundances in the gas-phase increase with decreasing A_V because of the increase in the photodesorption rate, decreasing the gaseous D/H ratio. Visual extinction, therefore, influences water deuteration at low visual extinctions where water starts to form (2mag < A_V < 5 mag). As can be seen in Fig. 9, HDO/H_2O and D_2O/H_2O ratios increase by one and two orders of magnitude respectively, between $A_V = 2$ and 5 mag, .

Comparison with observations shows that observed HDO and D_2O fractionations are reproduced for a low temperature of 10 K and for visual extinctions A_V higher than 4 mag ($A_{V,obs} = 8$ mag), implying that deuterated water needs to be formed in dark regions if $n_H = 10^4$ cm^{-3}.

3.3.4. Influence of grain surface parameters

The grain surface parameters ($a_d, E_d/E_b, E_b$(H)) can also influence the formation of interstellar ices. As discussed in TCK12a, the absolute abundance of the main ice constituents formed on grain surfaces (water, formaldehyde, methanol for instance) decrease with E_d/E_b whilst the grain size does not affect the overall abundance (but only the ice thickness). Moreover, it is also seen that the absolute abundance of water slightly decreases with the binding energy of volatile species.

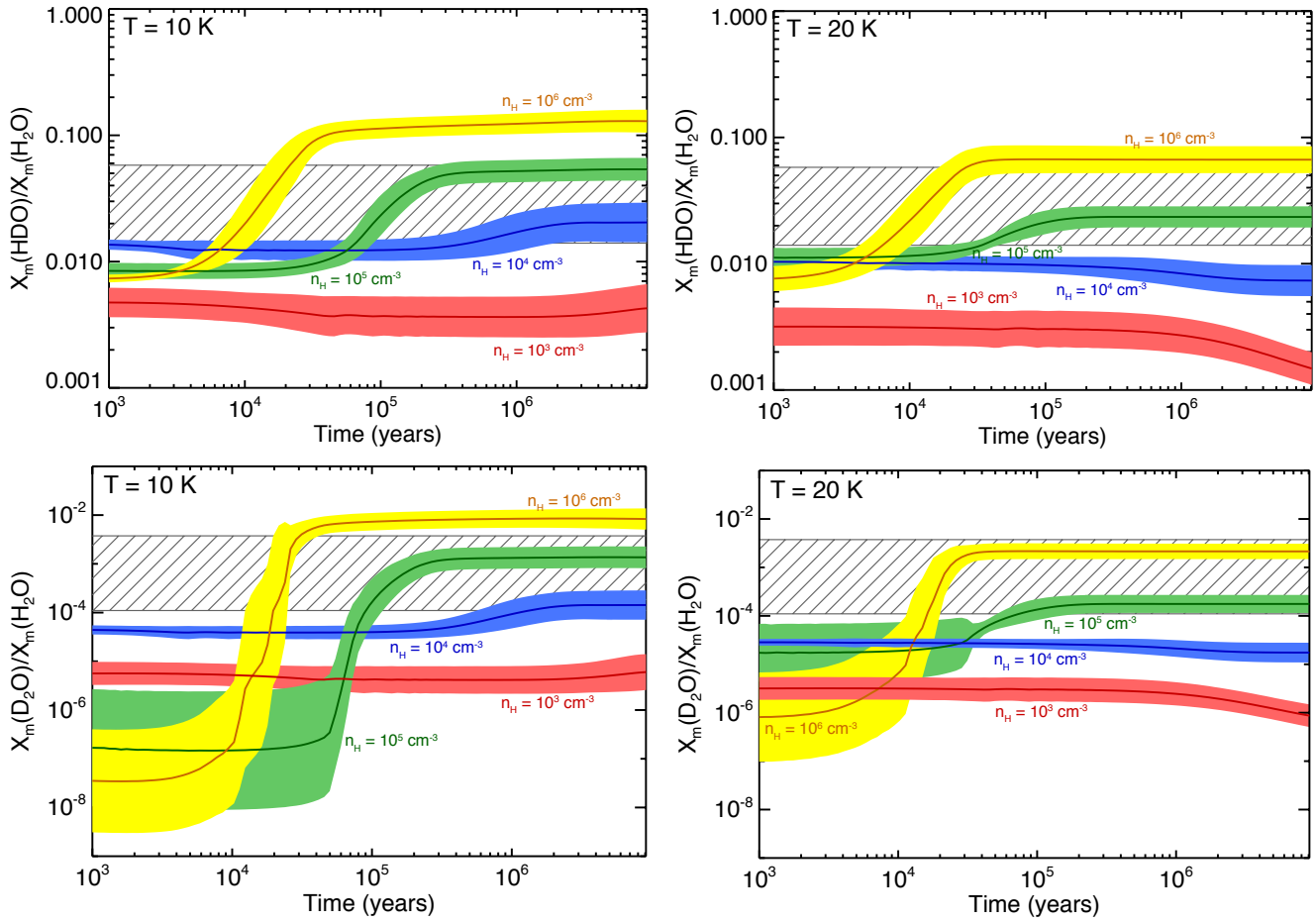

Fig. 8: Deuteration of water ice for four values of total density 10^3 (red), 10^4 (blue), 10^5 (green), 10^6 (yellow) cm^{-3}, and two temperatures: 10 K (left panels), 20 K (right panels), using an H_2 opr of 3×10^{-6}, a visual extinction of 10 mag, including the variation of all other input parameters. Hatched boxes refer to water deuteration observed by Coutens et al. (2012) towards IRAS 16293.

The water deuteration is slightly affected by the variation of the grain surface parameters. As shown in Fig. 9, the standard deviations given by the variation of the grain surface parameters remain lower than the evolution of the water deuteration lead by the variation in the temperature and the visual extinction. The water deuteration slightly decreases with the grain size due to the decrease in the CO depletion efficiency (since the accretion rate is inversely proportional to the grain size), limiting the increase in the deuterium fractionation. On the other hand, the water deuteration slightly increases with E_d/E_b and E_b(H) because the formation efficiency of H_2O decreases with the diffusion energy of volatile species, increasing the overall fractionation.

3.3.5. Concluding remarks

Comparing the average value of the deuterium fractionation with the standard deviation induced by the variation of other parameters allows us to claim that the H_2 opr is the most important parameter for water deuteration, followed by the total density. The visual extinction and the temperature also influence water deuteration but more weakly.

The comparison of our model predictions with observations allows us to constrain some parameters involved in the formation of deuterated water seen towards IRAS 16293. The observations are reproduced for

- a H_2 opr lower than 3×10^{-4};
- a density lower than 10^5 cm^{-3} if $T = 10$ K and $A_V > 4$ mag;
- a higher density n_H between $\sim 5 \times 10^4$ cm^{-3} and 10^6 cm^{-3} if $T = 20$ K.

4. Comparisons with previous models

In this section, we compare our model predictions for the gas-phase deuteration and for water ice deuteration with previous models. The atomic D/H ratio in the gas-phase depends on the deuteration of H_3^+. We compare our predictions from steady state models with those by Flower et al. (2006), specifically their Fig. 5. We obtain the same influence of the H_2 opr on the deuteration of H_3^+, with similar fractionation values.

To our knowledge, the only comprehensive theoretical study focused on the deuterated water formation on grain surfaces was performed by Cazaux et al. (2011), even if other works also included the deuteration of water ice in their astrochemical model (i.e. Tielens 1983; Caselli et al. 2002; Stantcheva & Herbst 2003; Bell et al. 2011). Cazaux et al. (2011) considered a static stage followed by a free-fall collapse phase. However, in their model, the deuterated water is practically formed only during the first static phase. Thus, it is worth comparing their predictions with ours.

The main difference is that they found that the water deuteration is highly temperature-dependent and lower than our predic-

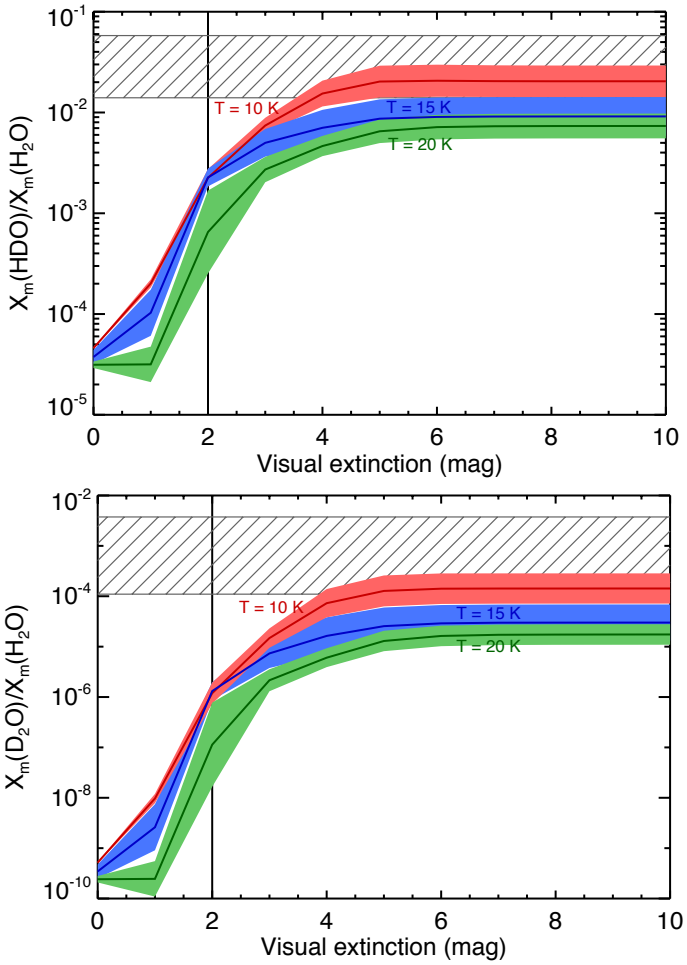

Fig. 9: Final deuteration of water ice (at $t > 10^6$ yr: representative of a typical molecular cloud age) as function of visual extinction for three values of temperatures: 10 (red), 15 (blue), 20 (green) K, using a total density of 10^4 cm^{-3}, an H_2 opr of 3×10^{-6} and including the variation of all other input parameters. The vertical line refers to the A_V threshold of water ice observed by Whittet et al. (1988). Hatched boxes refer to water deuteration observed by Coutens et al. (2012) towards IRAS 16293.

tions at low (< 15 K) temperatures (Fig. 8 of this work versus Fig. 3.c of Cazaux et al. 2011). This is due to a different approach in the reaction probability computation and the use of the endothermic O+H_2 reaction in the chemical network. Cazaux et al. (2011) assumed a competition between the reaction and the diffusion. In their model, if the diffusion timescale of the reactants is larger than the transmission timescale of the reaction, the reaction occurs regardless of its activation barrier. Thus, at low temperatures, the mobility is low and the reaction always occurs. In contrast, in our work, the reaction rate is given by the product of the collision rate of the two reactants and the reaction probability P_r (see Sec. 2.1 and 2.4), giving a much smoother dependence on the temperature. As a consequence, in Cazaux et al. (2011), H_2O is formed, at low temperatures, via reactions involving H_2 because of its large abundance, whilst HDO is formed via reactions involving atomic D. The solid HDO/H_2O ratio, therefore, scales with the gaseous [D]/[H_2] ratio ($\sim 10^{-5}$). In our work, water is always mostly formed via the O+H and OH+H reactions, and the deuteration scales with the [D]/[H] ratio (up to 10^{-1}). At higher temperatures (> 15 K), both models agree since water is formed via the same reactions, namely O+H and OH+H (and their deuterated counterparts). This comparison shows that the chemical route for the water formation is the major actor in the game, whilst other differences in the two models, including the physical evolution treatment, play a minor role in the water deuteration. However, we should point out that the O+H_2 reaction cannot occur at low temperatures given its endothermicity. Therefore, it is unlikely that water deuteration shows a such strong temperature dependence.

5. Discussion

In the previous paragraphs, we have shown that the deuteration of water and other molecules strongly depends on the H_2 opr and the total density, but also on the visual extinction and the temperature where solid molecules are formed. The high deuteration of water (HDO/H_2O > 1 % and D_2O/H_2O > 0.01 %) observed towards the low-mass protostar IRAS 16293 (Coutens et al. 2012) can only be reproduced with an H_2 opr that is lower than 3×10^{-4}, suggesting that most of deuterated water is formed at low H_2 opr. The ortho-para ratio reaches its steady-state value on a timescale proportional to the total density, of about 10^7 yr at $n_H = 10^4$ cm^{-3} (Flower et al. 2006). If the H_2 molecule has an initial opr value of 3 upon its formation on grain surfaces, the high deuteration observed around IRAS 16293 would suggest that water observed in this envelope has been formed in an "old" molecular gas, i.e. a gas old enough to show a low H_2 opr at the moment of the formation of interstellar ices. However, it is possible that the ortho-to-para conversion also occurs on grain surfaces (Le Bourlot 2000) but with an uncertain rate (see Sugimoto & Fukutani 2011; Chehrouri et al. 2011; Hama et al. 2012). The decrease in the H_2 opr could occur, therefore, faster and the molecular cloud age of 10^7 yr deduced from the estimate by Flower et al. (2006) should only be used as an upper limit.

The observed deuterium fractionation of water is only reproduced for dark conditions (high visual extinctions and low temperatures if $n_H = 10^4$ cm^{-3} or higher densities). Therefore, although IR observations of ices show that water ice starts to form at low visual extinctions, the deuterated water observed in IRAS 16293 should instead be formed in darker regions. Consequently, H_2O would be present in the inner part of ice mantles, whilst most of HDO and D_2O molecules should be located in the outer layers. A physical evolution, modelling the accumulation of matter from diffuse molecular clouds to dense cores, would allow us to directly confirm this result. The high observed deuteration of water also confirms that water is mostly formed from reactions involving atomic H and D and not by molecular hydrogen (see Sec. 4).

Observations of water, formaldehyde, and methanol vapours towards low-mass protostars show that these species have different deuterium fractionations. Figure 10 overplots the observed deuteration towards IRAS 16293 with mean theoretical deuteration values reached at $t = 3\times10^5$ yr (i.e., the upper limit of the age of prestellar cores, see Bergin & Tafalla 2007) as function of the density, for two temperatures, a low H_2 opr of 3×10^{-6} and only considering dark regions (A_v = 10 mag). The comparison of our predictions with observations shows that
i) our model reproduces the observed HDO/H_2O and D_2O/H_2O ratios for densities between 1×10^4 and 1×10^5 cm^{-3} at 10 K and between and 2×10^4 and 3×10^5 cm^{-3} at 20 K. Therefore, water deuteration is reproduced within a wide range of physical conditions representative of molecular clouds but not in the too-translucent cloud phase with too low density, too low visual extinctions and too high temperatures.
ii) the observed HDCO/H_2CO can be reproduced at higher

densities ($3 \times 10^5 - 10^6$ cm^{-3}) and lower temperatures ($\sim$ 10 K) as seen in the central regions of prestellar cores. The D_2CO/H_2CO ratio is reproduced at densities higher than 10^6 cm^{-3} (at $\sim 5 \times 10^6$ cm^{-3}, TCK12b).

iii) methanol deuteration (CH_2DOH/CH_3OH and CHD_2OH/CH_3OH ratios) proceeds in the outer parts of grain mantles when the prestellar core condensation reached high densities ($> 5 \times 10^5$ cm^{-3}) and low temperatures (10 K).

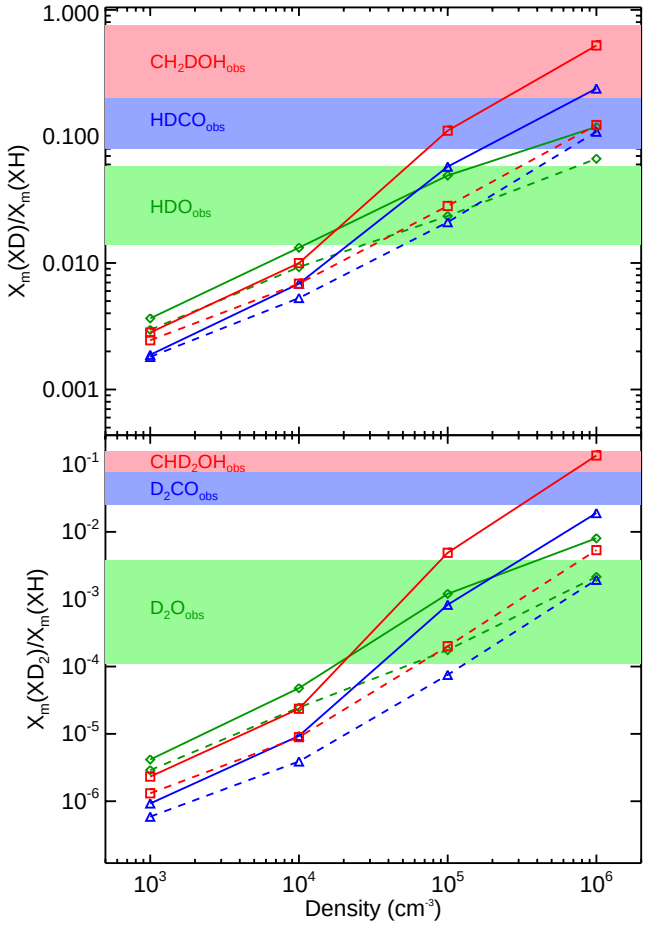

Fig. 10: Averaged deuterations of water (green diamonds), formaldehyde (blue triangles), and methanol (red squares) at 3×10^5 yr (representative of a typical prestellar core age) as function of the total density (abscissa) and temperature (10 K: solid, 20 K: dashed) considering an H_2 opr of 3×10^{-6} and A_V = 10 mag and considering grain surface parameters as free. Solid boxes refer to observations by Coutens et al. (2012) towards IRAS 16293 for water, and by Parise et al. (2006) (and references therein) towards a sample of low-mass protostars for formaldehyde and methanol.

In summary, the difference in the deuterium fractionation of molecules seen in IRAS 16293 can be explained by different periods of formation. Water is mainly formed first in regions showing intermediate densities representative of molecular clouds ($n_H = 10^4 - 10^5$ cm^{-3} where the CO depletion is limited. Formaldehyde and methanol are formed subsequently, at higher CO depletions when the gas is denser and colder. These predictions are in good agreement with infrared observations of interstellar ices presented in the introduction which also show that water ice is formed first, at low visual extinctions, whilst solid methanol forms later on at visual extinctions higher than 15 mag (Whittet et al. 2011).

More generally, the deuterium fractionation of any species, believed to be formed mainly in ices, can be used as a tracer to estimate the physical conditions at the moment of its formation. As shown in Fig. 10, the D/H ratio increases with increasing density and with decreasing temperature. A low deuteration, similar to the deuteration of water, implies that the solid species is mainly formed in regions with relatively low densities, even if its deuterated isotopologues could be formed mainly in a later phase. In contrast, a high deuteration level suggests that the solid species is mostly formed in the dense and cold phase where the deuteration in the gas-phase (and in particular the atomic D/H ratio) is high. Extremely high deuteration, such as methanol deuteration, would also imply the existence of abstraction reactions or other processes enhancing the formation of deuterated isotopologues with respect to the main isotopologue (TCK12b). H/D exchange reactions between solid methanol and water, for example, can also lead to a selective deuteration of functional groups (Ratajczak et al. 2009).

6. Conclusions

We have presented a comprehensive study of the formation and the deuteration of interstellar water ice carried out with our astrochemical model GRAINOBLE. In addition to the multilayer formation of grain mantles presented in a first paper (TCK12a) and the use of abstraction reactions for the deuteration of formaldehyde and methanol (TCK12b), we introduced a better treatment for computing the transmission probabilities of surface reactions based on the Eckart model. We also considered wavelength-dependent UV photodesorption of ices following molecular dynamics (MD) simulations and new experimental works.

The main results of this work are the following:

1) Our model reproduces the abundance of water ice and the visual extinction threshold observed by Whittet et al. (1988), as well as the different ice components seen in different molecular clouds regions.

2) Water deuteration strongly depends on the ortho-to-para ratio of H_2 and the total density, but also, even though more weakly, on the gas and grain temperatures and on the visual extinction.

3) The deuteration of water observed towards the low-mass protostar IRAS 16293 can only be reproduced by considering a H_2 opr lower than 3×10^{-4} and a total density between 8×10^3 and 5×10^5 cm^{-3}. If a low density (10^4 cm^{-3}) is considered, a low temperature (10 K) and a visual extinction higher than 4 mag are necessary. Dark regions (high densities or high visual extinctions) are, therefore, needed to reproduce the observations.

4) Comparison between the observed deuteration of water, formaldehyde, and methanol and our theoretical predictions allowed us to propose the following scenario. Water ice is formed first within relatively wide ranges of physical conditions: H_2O is allowed to start its formation at low densities and low visual extinctions, but HDO and D_2O are instead formed in darker (higher n_H and/or A_V) regions. Formaldehyde and then methanol are mainly formed subsequently, in the dense and cold prestellar cores.

5) Deuterium fractionation can be used to estimate the values of the density and temperature at the moment of formation of solid species because of its sensitivity to the physical conditions. Low deuteration, similar to water deuteration, implies that the species is formed in a wide range of physical conditions, whilst

a high deuteration suggests an efficient formation in the centre of dense and cold prestellar cores.

With this work, we have explored the influence of a wide range of parameters values on the formation of deuterated ices. Now that the influence of the various parameters is clarified, our next step will be a more sophisticated model, based on a realistic physical evolution of a cloud, in a forecoming paper.

Acknowledgements. The authors would like to thank Naoki Watanabe, Yasuhiro Oba, and Tetsuya Hama for fruitful discussions and for their useful comments about the surface reactions occurring in cold conditions, and Guillaume Pineau des Forets for discussions about H_2 photodissociation and gas-phase abundance of deuterium. V. T. would like to thank Alexandre Faure for discussions about the H_2 ortho/para ratio and a careful reading of the manuscript, and Edith Fayolle for providing useful data on photolysis. This work has been supported by l'Agence Nationale pour la Recherche (ANR), France (project FORCOMS, contracts ANR-08-BLAN-022). A.L.S. and C.C. acknowledge funding from the CNES (Centre National dE tudes Spatiales). The computations of the model grid presented in this work were performed at the Service Commun de Calcul Intensif de l'Observatoire de Grenoble (SCCI). Quantum chemical calculations were performed thanks to the HPC resources of CINES under the allocation 2012-088620 made by GENCI (Grand Equipement National de Calcul Intensif). Some kinetic data we used have been downloaded from the online database KIDA (KInetic Database for Astrochemistry, http://kida.obs.u-bordeaux1.fr).

References

Adamo, C. & Barone, V. 1999, J. Chem. Phys., 110, 6158
Aikawa, Y., Kamuro, D., Sakon, I., et al. 2012, A&A, 538, A57
Al-Halabi, A. & van Dishoeck, E. F. 2007, MNRAS, 382, 1648
Amiaud, L., Fillion, J. H., Baouche, S., et al. 2006, The Journal of Chemical Physics, 124, 094702
Andersson, S., Al-Halabi, A., Kroes, G.-J., & van Dishoeck, E. F. 2006, J. Chem. Phys., 124, 064715
Andersson, S., Goumans, T., & Arnaldsson, A. 2011, Chemical Physics Letters, 513, 31
Andersson, S. & van Dishoeck, E. F. 2008, A&A, 491, 907
Andre, P., Ward-Thompson, D., & Barsony, M. 2000, Protostars and Planets IV, 59
Bacmann, A., Caux, E., Hily-Blant, P., et al. 2010, A&A, 521, L42
Bates, D. R. 1986, ApJ, 306, L45
Baulch, D. L., Bowman, C. T., Cobos, C. J., et al. 2005, Journal of Physical and Chemical Reference Data, 34, 757
Baulch, D. L., Cobos, C. J., Cox, R. A., et al. 1992, Journal of Physical and Chemical Reference Data, 21, 411
Bell, T. A., Willacy, K., Phillips, T. G., Allen, M., & Lis, D. C. 2011, ApJ, 731, 48
Bergin, E. A., Melnick, G. J., Stauffer, J. R., et al. 2000, ApJ, 539, L129
Bergin, E. A. & Snell, R. L. 2002, ApJ, 581, L105
Bergin, E. A. & Tafalla, M. 2007, Annual Review of Astronomy & Astrophysics, 45, 339
Bergman, P., Parise, B., Liseau, R., & Larsson, B. 2011, A&A, 527, A39
Boogert, A. C. A., Pontoppidan, K. M., Knez, C., et al. 2008, ApJ, 678, 985
Butner, H. M., Charnley, S. B., Ceccarelli, C., et al. 2007, ApJ, 659, L137
Carr, J. S. & Najita, J. R. 2008, Science, 319, 1504
Caselli, P., Keto, E., Pagani, L., et al. 2010, A&A, 521, L29
Caselli, P., Stantcheva, T., Shalabiea, O., Shematovich, V. I., & Herbst, E. 2002, Planetary and Space Science, 50, 1257
Cazaux, S., Caselli, P., & Spaans, M. 2011, ApJ, 741, L34
Cazaux, S., Cobut, V., Marseille, M., Spaans, M., & Caselli, P. 2010, A&A, 522, A74
Cazaux, S. & Tielens, A. G. G. M. 2004, ApJ, 604, 222
Ceccarelli, C., Castets, A., Caux, E., et al. 2000, Astronomy & Astrophysics, 355, 1129
Ceccarelli, C., Castets, A., Loinard, L., Caux, E., & Tielens, A. G. G. M. 1998, A&A, 338, L43
Ceccarelli, C., Hollenbach, D. J., & Tielens, A. G. G. M. 1996, ApJ, 471, 400
Ceccarelli, C., Loinard, L., Castets, A., et al. 2001, A&A, 372, 998
Charnley, S. B., Tielens, A. G. G. M., & Rodgers, S. D. 1997, ApJ, 482, L203
Chehrouri, M., Fillion, J.-H., Chaabouni, H., et al. 2011, Phys. Chem. Chem. Phys., 13, 2172
Collings, M. P., Anderson, M. A., Chen, R., et al. 2004, Monthly Notices of the Royal Astronomical Society, 354, 1133
Coutens, A., Vastel, C., Caux, E., & Ceccarelli, C. 2012, Astronomy & Astrophysics, 539, A132
Cuppen, H. M. & Herbst, E. 2007, The Astrophysical Journal, 668, 294
Cuppen, H. M., Ioppolo, S., Romanzin, C., & Linnartz, H. 2010a, Physical Chemistry Chemical Physics (Incorporating Faraday Transactions), 12, 12077
Cuppen, H. M., Kristensen, L. E., & Gavardi, E. 2010b, MNRAS, 406, L11
Cuppen, H. M., van Dishoeck, E. F., Herbst, E., & Tielens, A. G. G. M. 2009, Astronomy & Astrophysics, 508, 275
Dalgarno, A., Yan, M., & Liu, W. 1999, ApJS, 125, 237
Dartois, E., Thi, W.-F., Geballe, T. R., et al. 2003, A&A, 399, 1009
Demyk, K., Bottinelli, S., Caux, E., et al. 2010, A&A, 517, A17
Dislaire, V., Hily-Blant, P., Faure, A., et al. 2012, A&A, 537, A20
Dulieu, F., Amiaud, L., Congiu, E., et al. 2010, A&A, 512, A30+
Dunning Jr, T. H. 1989, J. Chem. Phys., 90, 1007
Eckart, C. 1930, Physical Review, 35, 1303
Ellingson, B. A., Theis, D. P., Tishchenko, O., Zheng, J., & Truhlar, D. G. 2007, The Journal of Physical Chemistry A, 111, 13554
Fayolle, E. C., Bertin, M., Romanzin, C., et al. 2011, ApJ, 739, L36
Flower, D. R., Pineau Des Forêts, G., & Walmsley, C. M. 2005, A&A, 436, 933
Flower, D. R., Pineau Des Forêts, G., & Walmsley, C. M. 2006, A&A, 449, 621
Frerking, M. A., Langer, W. D., & Wilson, R. W. 1982, ApJ, 262, 590
Frisch, M. J., Trucks, G. W., Schlegel, H. B., et al. 2009, Gaussian 09 Revision A. 02, ¢
Fuchs, G. W., Cuppen, H. M., Ioppolo, S., et al. 2009, A&A, 505, 629
Garrod, R. T. & Herbst, E. 2006, Astronomy & Astrophysics, 457, 927
Garrod, R. T. & Pauly, T. 2011, ApJ, 735, 15
Garrod, R. T., Wakelam, V., & Herbst, E. 2007, Astronomy & Astrophysics, 467, 1103
Gerakines, P. A., Whittet, D. C. B., Ehrenfreund, P., et al. 1999, ApJ, 522, 357
Giannini, T., Nisini, B., Lorenzetti, D., et al. 2000, A&A, 358, 310
Goldsmith, P. F., Liseau, R., Bell, T. A., et al. 2011, ApJ, 737, 96
Goumans, T. P. M. & Andersson, S. 2010, MNRAS, 406, 2213
Goumans, T. P. M., Uppal, M. A., & Brown, W. A. 2008, MNRAS, 384, 1158
Gredel, R., Lepp, S., & Dalgarno, A. 1987, ApJ, 323, L137
Hama, T., Kuwahata, K., Watanabe, N., et al. 2012, ApJ, 757, 185
Hama, T., Yabushita, A., Yokoyama, M., Kawasaki, M., & Andersson, S. 2009, The Journal of Chemical Physics, 131, 054508
Hama, T., Yokoyama, M., Yabushita, A., et al. 2010, The Journal of Chemical Physics, 132, 164508
Hartogh, P., Lis, D. C., Bockelée-Morvan, D., et al. 2011, Nature, 478, 218
Hasegawa, T. I., Herbst, E., & M., L. C. 1992, The Astrophysical Journal Supplement Series, 82, 167
Hidaka, H., Watanabe, M., Kouchi, A., & Watanabe, N. 2009, ApJ, 702, 291
Hincelin, U., Wakelam, V., Hersant, F., et al. 2011, A&A, 530, A61
Hiraoka, K., Miyagoshi, T., Takayama, T., Yamamoto, K., & Kihara, Y. 1998, ApJ, 498, 710
Hogerheijde, M. R., Bergin, E. A., Brinch, C., et al. 2011, Science, 334, 338
Hollenbach, D., Kaufman, M. J., Bergin, E. A., & Melnick, G. J. 2009, ApJ, 690, 1497
Hornekær, L., Baurichter, A., Petrunin, V. V., et al. 2005, J. Chem. Phys., 122
Hugo, E., Asvany, O., & Schlemmer, S. 2009, Journal of Chemical Physics, 130, 164302
Ioppolo, S., Cuppen, H. M., Romanzin, C., van Dishoeck, E. F., & Linnartz, H. 2010, Physical Chemistry Chemical Physics (Incorporating Faraday Transactions), 12, 12065
Ioppolo, S., van Boheemen, Y., Cuppen, H. M., van Dishoeck, E. F., & Linnartz, H. 2011, MNRAS, 413, 2281
Jenniskens, P., Blake, D. F., Wilson, M. A., & Pohorille, A. 1995, The Astrophysical Journal, 455, 389
Jing, D., He, J., Brucato, J., et al. 2011, ApJ, 741, L9
Johnston, H. S. & Heicklen, J. 1962, The Journal of Physical Chemistry, 66, 532
Jørgensen, J. K. & van Dishoeck, E. F. 2010, ApJ, 725, L172
Kaufman, M. J. & Neufeld, D. A. 1996, ApJ, 456, 611
Kendall, R. A., Dunning Jr, T. H., & Harrison, R. J. 1992, J. Chem. Phys., 96, 6796
Klemm, R. B., Payne, W. A., & Stief, L. J. 1975, in Chemical kinetic data for the upper and lower atmosphere, ed. S. W. B. N. Y. Wiley)
Klotz, A., Harju, J., Ristorcelli, I., et al. 2008, A&A, 488, 559
Kobayashi, K. 1983, The Journal of Physical Chemistry, 87, 4317
Koussa, H., Bahri, M., Jaidane, N., & Ben Lakhdar, Z. 2006, Journal of Molecular Structure: THEOCHEM, 770, 149
Kristensen, L. E., Amiaud, L., Fillion, J.-H., Dulieu, F., & Lemaire, J.-L. 2011, A&A, 527, A44
Kristensen, L. E., van Dishoeck, E. F., Bergin, E. A., et al. 2012, A&A, 542, A8
Kristensen, L. E., Visser, R., van Dishoeck, E. F., et al. 2010, A&A, 521, L30
Kroes, G. J. & Andersson, S. 2005, in IAU Symposium, Vol. 231, Astrochemistry: Recent Successes and Current Challenges, ed. D. C. Lis, G. A. Blake, & E. Herbst, 427–442
Le Bourlot, J. 2000, A&A, 360, 656
Le Petit, F., Nehmé, C., Le Bourlot, J., & Roueff, E. 2006, ApJS, 164, 506

Le Petit, F., Roueff, E., & Le Bourlot, J. 2002, A&A, 390, 369
Lebreton, J., Augereau, J.-C., Thi, W.-F., et al. 2012, A&A, 539, A17
Lefloch, B., Cabrit, S., Codella, C., et al. 2010, A&A, 518, L113
Li, A. & Greenberg, J. M. 1998, A&A, 331, 291
Linsky, J. L. 2003, Space Science Reviews, 106, 49
Liseau, R., Ceccarelli, C., Larsson, B., et al. 1996, A&A, 315, L181
Liseau, R., Goldsmith, P. F., Larsson, B., et al. 2012, A&A, 541, A73
Liu, F.-C., Parise, B., Kristensen, L., et al. 2011, A&A, 527, A19
Loinard, L., Castets, A., Ceccarelli, C., Caux, E., & Tielens, A. G. G. M. 2001, ApJ, 552, L163
Mathis, J. S., Mezger, P. G., & Panagia, N. 1983, A&A, 128, 212
Miyauchi, N., Hidaka, H., Chigai, T., et al. 2008, Chemical Physics Letters, 456, 27
Mokrane, H., Chaabouni, H., Accolla, M., et al. 2009, ApJ, 705, L195
Nagaoka, A., Watanabe, N., & Kouchi, A. 2007, J. Phys. Chem. A, 111, 30163028
Nguyen, T. L., Stanton, J. F., & Barker, J. R. 2011, The Journal of Physical Chemistry A, 115, 5118
Noble, J. A., Dulieu, F., Congiu, E., & Fraser, H. J. 2011, ApJ, 735, 121
Oba, Y., Watanabe, N., Hama, T., et al. 2012, ApJ, 749, 67
Oba, Y., Watanabe, N., Kouchi, A., Hama, T., & Pirronello, V. 2010, ApJ, 712, L174
Oba, Y., Watanabe, N., Kouchi, A., Hama, T., & Pirronello, V. 2011, Physical Chemistry Chemical Physics (Incorporating Faraday Transactions), 13, 15792
Öberg, K. I., Boogert, A. C. A., Pontoppidan, K. M., et al. 2011, ApJ, 740, 109
Owen, T. & Bar-Nun, A. 1995, Icarus, 116, 215
Pagani, L., Vastel, C., Hugo, E., et al. 2009, A&A, 494, 623
Parise, B., Castets, A., Herbst, E., et al. 2004, A&A, 416, 159
Parise, B., Caux, E., Castets, A., et al. 2005, A&A, 431, 547
Parise, B., Ceccarelli, C., Tielens, A. G. G. M., et al. 2006, A&A, 453, 949
Parise, B., Simon, T., Caux, E., et al. 2003, A&A, 410, 897
Perdew, J. P., Burke, K., & Ernzerhof, M. 1996a, Physical Review Letters, 78, 1396
Perdew, J. P., Burke, K., & Ernzerhof, M. 1996b, Physical Review Letters, 77, 3865
Perets, H. B., Biham, O., Manicó, G., et al. 2005, ApJ, 627, 850
Peters, P. S., Duflot, D., Faure, A., et al. 2011, The Journal of Physical Chemistry A, 115, 8983
Peters, P. S., Duflot, D., Monnerville, M., et al. 2012, The Journal of Physical Chemistry A, submitted
Pontoppidan, K. M., Boogert, A. C. A., Fraser, H. J., et al. 2008, ApJ, 678, 1005
Pontoppidan, K. M., van Dishoeck, E. F., & Dartois, E. 2004, A&A, 426, 925
Ratajczak, A., Quirico, E., Faure, A., Schmitt, B., & Ceccarelli, C. 2009, A&A, 496, L21
Raut, U. & Baragiola, R. A. 2011, ApJ, 737, L14
Roberts, H., Herbst, E., & Millar, T. J. 2003, ApJ, 591, L41
Roberts, H., Herbst, E., & Millar, T. J. 2004, A&A, 424, 905
Roberts, H. & Millar, T. J. 2000, A&A, 361, 388
Roberts, H. & Millar, T. J. 2007, A&A, 471, 849
Romanzin, C., Ioppolo, S., Cuppen, H. M., van Dishoeck, E. F., & Linnartz, H. 2011, J. Chem. Phys., 134, 084504
Roser, J. E., Vidali, G., Manicò, G., & Pirronello, V. 2001, ApJ, 555, L61
Ruffle, D. & Herbst, E. 2001, Monthly Notices of the Royal Astronomical Society, 324, 1054
Sandford, S. A. & Allamandola, L. J. 1990, ApJ, 355, 357
Smith, R. G., Sellgren, K., & Tokunaga, A. T. 1989, ApJ, 344, 413
Speedy, R. J., Debenedetti, P. G., Scott Smith, R., Huang, C., & Kay, B. D. 1996, The Journal of Chemical Physics, 105, 240
Stantcheva, T. & Herbst, E. 2003, Monthly Notices of the Royal Astronomical Society, 340, 983
Sugimoto, T. & Fukutani, K. 2011, Nat Phys, 7, 307
Talbi, D., Chandler, G., & Rohl, A. 2006, Chemical Physics, 320, 214
Taquet, V., Ceccarelli, C., & Kahane, C. 2012a, A&A, 538, A42
Taquet, V., Ceccarelli, C., & Kahane, C. 2012b, ApJ, 748, L3
Terada, H., Tokunaga, A. T., Kobayashi, N., et al. 2007, ApJ, 667, 303
Tielens, A. G. G. M. 1983, A&A, 119, 177
Tielens, A. G. G. M. & Allamandola, L. J. 1987, in Interstellar Processes, ed. D. J. Hollenbach & H. A. Thronson, 397–469
Tielens, A. G. G. M. & Hagen, W. 1982, Astronomy & Astrophysics, 114, 245
Troscompt, N., Faure, A., Maret, S., et al. 2009, A&A, 506, 1243
van der Tak, F. F. S., Schilke, P., Müller, H. S. P., et al. 2002, A&A, 388, L53
van Dishoeck, E. F., Blake, G. A., Jansen, D. J., & Groesbeck, T. D. 1995, ApJ, 447, 760
van Dishoeck, E. F., Kristensen, L. E., Benz, A. O., et al. 2011, PASP, 123, 138
Vastel, C., Ceccarelli, C., Caux, E., et al. 2010, A&A, 521, L31
Vastel, C., Phillips, T. G., Ceccarelli, C., & Pearson, J. 2003, ApJ, 593, L97
Vidali, G., Ihm, G., Kim, H., & Cole, M. 1991, Surface Science Reports, 12, 135
Wakelam, V., Herbst, E., Le Bourlot, J., et al. 2010, A&A, 517, A21
Wakelam, V., Herbst, E., Loison, J.-C., et al. 2012, ApJS, 199, 21
Walmsley, C. M., Flower, D. R., & Pineau des Forêts, G. 2004, A&A, 418, 1035
Wang, H., Eyre, J. A., & Dorfman, L. M. 1973, J Chem Phys, 59, 5199
Watanabe, N., Kimura, Y., Kouchi, A., et al. 2010, ApJ, 714, L233
Watanabe, N., Nagaoka, A., Shiraki, T., & Kouchi, A. 2004, ApJ, 616, 638
Whittet, D. C. B., Bode, M. F., Longmore, A. J., et al. 1988, MNRAS, 233, 321
Whittet, D. C. B., Cook, A. M., Herbst, E., Chiar, J. E., & Shenoy, S. S. 2011, ApJ, 742, 28
Whittet, D. C. B. & Duley, W. W. 1991, A&A Rev., 2, 167
Whittet, D. C. B., Gerakines, P. A., Hough, J. H., & Shenoy, S. S. 2001, ApJ, 547, 872
Whittet, D. C. B., Shenoy, S. S., Bergin, E. A., et al. 2007, ApJ, 655, 332
Woon, D. E. 2002, ApJ, 569, 541
Yabushita, A., Hama, T., Yokoyama, M., et al. 2009, ApJ, 699, L80
Yabushita, A., Kanda, D., Kawanaka, N., Kawasaki, M., & Ashfold, M. N. R. 2006, The Journal of Chemical Physics, 125, 133406
Yu, H.-G., Muckerman, J. T., & Sears, T. J. 2001, Chemical Physics Letters, 349, 547

Appendix A: Transmission probability computations

A.1. Eckart model

We compute the transmission probabilities of all the reactions involved in the water-producing and the methanol-producing networks by using the Eckart model (Eckart 1930; Johnston & Heicklen 1962). In this approach, an approximate potential energy surface (PES) is fitted as a function of the zero point energies (ZPEs) of the stationary points. The parameters needed for computing the transmission probability are the zero-point-corrected barrier heights of the forward and reverse reactions V_f and V_r, the frequency of the imaginary mode of the transition state ν_S, and the reduced mass of the reactants μ.

The Eckart potential can be parametrised as

$$U_x = \frac{A\exp\left(\frac{x-x_0}{l}\right)}{1+\exp\left(\frac{x-x_0}{l}\right)} + \frac{B\exp\left(\frac{x-x_0}{l}\right)}{\left(1+\exp\left(\frac{x-x_0}{l}\right)\right)^2} \quad (A.1)$$

where

$$A = V_f - V_r \quad (A.2)$$

$$B = \left(\sqrt{V_f} + \sqrt{V_r}\right)^2 \quad (A.3)$$

$$l = \frac{2\pi}{|\nu_S|}\sqrt{\frac{2}{\mu}}\left(\frac{1}{\sqrt{V_f}} + \frac{1}{\sqrt{V_r}}\right)^{-1}. \quad (A.4)$$

Once one has fitted the potential then the transmission probability, P_r, may be calculated using

$$P_r = \frac{\cosh(\alpha+\beta) - \cosh(\alpha-\beta)}{\cosh(\alpha+\beta) + \cosh(\delta)} \quad (A.5)$$

where

$$\alpha = \frac{4\pi}{|\nu_S|}\left(\frac{1}{\sqrt{V_f}} + \frac{1}{\sqrt{V_r}}\right)^{-1}\sqrt{E} \quad (A.6)$$

$$\beta = \frac{8\pi^2}{h|\nu_S|}\left(\frac{1}{\sqrt{V_f}} + \frac{1}{\sqrt{V_r}}\right)^{-1}\sqrt{E - V_f + V_r} \quad (A.7)$$

$$\delta = 4\pi\sqrt{\frac{V_f V_r 2\pi}{(h|\nu_S|)^2} - \frac{1}{16}}. \quad (A.8)$$

When the reactants are considered as excited by their formation involving an exothermic reaction, E refers to the excess energy of this reaction of formation. Otherwise, E is the thermal energy of the particles.

The Eckart model provides a significant improvement over square barriers but it can underpredict (or overpredict) the transmission probabilities of some reactions at low temperatures compared to more exact methods (see Peters et al. 2011). However, given the number of surface reactions considered in this work, exact quantum chemical computations for all reactions are not feasible.

A.2. CO_2 formation

Based on the experimental work by Oba et al. (2010) who studied the formation of CO_2 from CO and OH, CO_2 is thought to be formed via the pathway

$$CO + OH \rightarrow \text{trans-HOCO} \quad (A.9)$$

$$\text{trans-HOCO} \rightarrow \text{cis-HOCO} \quad (A.10)$$

$$\text{cis-HOCO} \rightarrow CO_2 + H. \quad (A.11)$$

The electronic energy of the intermediate radicals (t-HOCO, c-HOCO) and the products (CO_2 + H) are lower than for the reactants (CO + OH). Reactions involving t-HOCO and c-HOCO possess high activation barriers and/or are endothermic (Yu et al. 2001). Therefore, t-HOCO radicals continue to react only if their excess energy released by the chemical energy of reaction (A.9) is sufficient to overcome the high activation barriers of reactions (A.10) and (A.11). As in Goumans et al. (2008), HOCO radicals can also react with H atoms via barrierless reactions to form three pairs of products: H_2 + CO_2, H_2O + CO, or HCOOH. The lack of more quantitative data leads us to assume a branching ratio of one to three for every product pair.

In fact, the energy released by reaction (A.9) absorbed by HOCO radicals can be transferred to the surface before reacting. However, the transfer rate of the chemical energy to the surface is very uncertain. The absence of formic acid HCOOH and the low abundance of HOCO radicals observed in the experiments of Oba et al. (2010) suggest that CO_2 is readily formed from excited HOCO molecules. Therefore, most HOCO radicals continue to react before relaxing to their stable state. To reproduce these experiments, we assume that 99 % of HOCO radicals are sufficiently excited to form CO_2, whilst 1% of them are stabilized.

Goumans & Andersson (2010) performed gas-phase O-CO potential energy surface calculations, showing that O and CO can form a van der Waals complex, allowing O atoms to stay bound to CO for a long time. Following these results, we consider that O atoms that meet CO molecules (via direct accretion from gas-phase or surface diffusion) form a loosely bound O...CO complex. The H atoms that meet these O..CO complexes react via a barrierless reaction to form an excited HO...CO* complex. If the time for energy transfer to the surface is long enough, the complex can yield OH + CO, or t-HOCO* radical via barrierless reactions. Otherwise, the complex forms the t-HOCO radical through quantum tunneling. We consider that 99% of HO...CO* complexes continue to react without activation barriers.

Appendix B lists all the reactions involved in the formation of CO_2 with their corresponding activation barriers and transmission probabilities.

A.3. Quantum chemical calculations

The OH + H_2 reaction system has been theoretically studied by Nguyen et al. (2011). These authors have computed the forward and reverse reactions, the imaginary frequency of the transition states, and the rate constants of the eight reactions involving H_2, HD, D_2, OH, and OD using the semiclassical transition-state theory (SCTST).

The H_2O_2 + H reaction has been studied by Koussa et al. (2006) and Ellingson et al. (2007). However, data for the reactions involving deuterated isotopologues was not available. Therefore, to obtain the data required for the model, quantum

chemistry calculations have been conducted with the Gaussian 09 (Frisch et al. 2009) program. For these calculations, the PBE0 (Perdew et al. 1996b,a; Adamo & Barone 1999) functional and the aug-cc-pVTZ (Dunning Jr 1989; Kendall et al. 1992) basis set were used because this combination produced results that are in good agreement with the experimentally determined values for the process in gas-phase (Klemm et al. 1975, who measured an activation barrier of 4.6 kcal/mol = 2300 K) .

The CO + H reaction has been theoretically studied by several authors (Woon 2002; Andersson et al. 2011; Peters et al. 2012). We decided to use the work of Peters et al. (2012) because they used the most accurate methodology and obtained a value for the activation energy for the formation of HCO that best agrees the gas-phase experiment (Wang et al. 1973). The transmission probabilities of all the reactions producing deuterated formaldehyde and methanol are computed from this reaction and relative rates measured by Nagaoka et al. (2007) and Hidaka et al. (2009) or deduced by TCK12b.

The formation of carbon dioxide includes two reactions having an activation barrier. Quantum calculations of Talbi et al. (2006); Goumans et al. (2008), and Goumans & Andersson (2010) showed that reaction (11) has an activation barrier of 2500 - 3000 K, leading to a transmission probability of 5×10^{-23} (Goumans & Andersson 2010; Garrod & Pauly 2011). Assuming an activation energy of 2500 K and considering a square barrier, we reproduce this transmission probability with a barrier width of 0.8 Å. The transmission probabilities of the reaction pathways involved in reaction (12), and including HOCO radicals, the van der Waals complex HO...CO, and their deuterated isotopologues, were deduced from the potential energy surface computed by Yu et al. (2001). These authors computed the stationary points of the potential energy surface of this reaction using an extrapolated full coupled cluster/complete basis set (FCC/CBS) method.

Appendix B: List of grain surface reactions

Table B.1: List of grain surface chemical reactions considered in this work along with their activation barriers and transmission probabilities.

Reaction							E_a (K)	P_r
H	+	H	→	(o)H_2			0	0.75
H	+	H	→	(p)H_2			0	0.25
H	+	D	→	HD			0	1
D	+	D	→	(o)D_2			0	0.66
D	+	D	→	(p)D_2			0	0.33
CO	+	H	→	HCO			1763	1.92(-07)
CO	+	D	→	DCO			/	1.92(-08)
HCO	+	H	→	H_2CO			0	1
HCO	+	D	→	HDCO			0	1
DCO	+	H	→	HDCO			0	1
DCO	+	D	→	D_2CO			0	1
H_2CO	+	H	→	CH_3O			/	9.60(-08)
H_2CO	+	D	→	CH_2DO			/	9.60(-09)
H_2CO	+	D	→	HCO	+	HD	/	9.31(-08)
H_2CO	+	D	→	HDCO	+	H	/	9.31(-08)
HDCO	+	H	→	CH_2DO			/	1.11(-07)
HDCO	+	D	→	CHD_2O			/	1.11(-07)
HDCO	+	H	→	HCO	+	HD	/	1.54(-07)
HDCO	+	D	→	DCO	+	HD	/	9.31(-08)
HDCO	+	D	→	D_2CO	+	H	/	9.31(-08)
D_2CO	+	H	→	CHD_2O			/	1.27(-07)
D_2CO	+	D	→	CD_3O			/	1.27(-08)
D_2CO	+	H	→	DCO	+	HD	/	7.30(-08)
CH_3O	+	H	→	CH_3OH			0	1
CH_3O	+	D	→	CH_3OD			0	1
CH_2OH	+	H	→	CH_3OH			0	1
CH_2OH	+	D	→	CH_2DOH			0	1
CH_2OD	+	H	→	CH_3OD			0	1
CH_2OD	+	D	→	CH_2DOD			0	1
CH_2DO	+	H	→	CH_2DOH			0	1
CH_2DO	+	D	→	CH_2DOD			0	1
CHDOH	+	H	→	CH_2DOH			0	1
CHDOH	+	D	→	CHD_2OH			0	1
CHDOD	+	H	→	CH_2DOD			0	1
CHDOD	+	D	→	CHD_2OD			0	1
CHD_2O	+	H	→	CHD_2OH			0	1
CHD_2O	+	D	→	CHD_2OD			0	1
CD_2OH	+	H	→	CHD_2OH			/	1
CD_2OH	+	D	→	CD_3OH			0	1
CD_2OD	+	H	→	CHD_2OD			0	1
CD_2OD	+	D	→	CD_3OD			0	1
CD_3O	+	H	→	CD_3OH			0	1
CD_3O	+	D	→	CD_3OD			0	1
CH_3OH	+	D	→	CH_2OH	+	HD	/	2.88(-07)
CH_2DOH	+	D	→	CHDOH	+	HD	/	1.92(-07)
CHD_2OH	+	D	→	CD_2OH	+	HD	/	1.50(-07)
CH_3OD	+	D	→	CH_2OD	+	HD	/	2.88(-07)
CH_2DOD	+	D	→	CHDOD	+	HD	/	1.92(-07)
CHD_2OD	+	D	→	CD_2OD	+	HD	/	1.50(-07)
O	+	O	→	O_2			0	1
O_2	+	O	→	O_3			0	1
O	+	H	→	OH			0	1
O	+	D	→	OD			0	1
OH	+	H	→	H_2O			0	1
OH	+	D	→	HDO			0	1
OD	+	H	→	HDO			0	1
OD	+	D	→	D_2O			0	1
OH	+	OH	→	H_2O_2			0 (R= 0.8)	1
OD	+	OH	→	HDO_2			0 (R= 0.8)	1
OD	+	OD	→	D_2O_2			0 (R= 0.8)	1

OH	+	OH	→	H_2O	+	O	0 (R=0.2)	1
OD	+	OH	→	HDO	+	O	0 (R=0.2)	1
OD	+	OD	→	D_2O	+	O	0 (R=0.2)	1
OH	+	H_2	→	H_2O	+	H	2935	4.07(-07)
OD	+	H_2	→	HDO	+	H	2855	3.62(-07)
OD	+	HD	→	D_2O	+	H	3051	1.00(-09)
OD	+	HD	→	HDO	+	D	3026	8.07(-10)
OH	+	HD	→	H_2O	+	D	2789	8.74(-07)
OH	+	HD	→	HDO	+	H	2900	2.81(-09)
OH	+	D_2	→	HDO	+	D	2703	7.99(-07)
OD	+	D_2	→	D_2O	+	D	2870	2.26(-09)
O_2	+	H	→	HO_2			0	1
O_2	+	D	→	DO_2			0	1
HO_2	+	H	→	H_2O_2			0	1
HO_2	+	D	→	HDO_2			0	1
DO_2	+	H	→	HDO_2			0	1
DO_2	+	D	→	D_2O_2			0	1
H_2O_2	+	H	→	H_2O	+	OH	2508	1.37(-07)
H_2O_2	+	D	→	HDO	+	OH	2355	5.54(-09)
HDO_2	+	H	→	HDO	+	OH	2523	1.23(-07)
HDO_2	+	H	→	H_2O	+	OD	2524	1.22(-07)
HDO_2	+	D	→	D_2O	+	OH	2369	5.28(-09)
HDO_2	+	D	→	HDO	+	OD	2367	5.29(-09)
D_2O_2	+	H	→	D_2O	+	OH	2540	1.08(-07)
D_2O_2	+	D	→	D_2O	+	OD	2384	4.28(-09)
O_3	+	H	→	O_2	+	OH	0	1
O_3	+	D	→	O_2	+	OD	0	1
N	+	H	→	NH			0	1
N	+	D	→	ND			0	1
NH	+	H	→	NH_2			0	1
NH	+	D	→	NHD			0	1
ND	+	H	→	NHD			0	1
ND	+	D	→	ND_2			0	1
NH_2	+	H	→	NH_3			0	1
NH_2	+	D	→	NH_2D			0	1
NHD	+	H	→	NH_2D			0	1
NHD	+	D	→	NHD_2			0	1
ND_2	+	H	→	NHD_2			0	1
ND_2	+	D	→	ND_3			0	1
C	+	H	→	CH			0	1
C	+	D	→	CD			0	1
CH	+	H	→	CH_2			0	1
CH	+	D	→	CHD			0	1
CD	+	H	→	CHD			0	1
CD	+	D	→	CD_2			0	1
CH_2	+	H	→	CH_3			0	1
CH_2	+	D	→	CH_2D			0	1
CHD	+	H	→	CH_2D			0	1
CHD	+	D	→	CHD_2			0	1
CD_2	+	H	→	CHD_2			0	1
CD_2	+	D	→	CD_3			0	1
CH_3	+	D	→	CH_3D			0	1
CH_2D	+	H	→	CH_3D			0	1
CH_2D	+	D	→	CH_2D_2			0	1
CHD_2	+	H	→	CH_2D_2			0	1
CHD_2	+	D	→	CHD_3			0	1
CD_3	+	H	→	CHD_3			0	1
CD_3	+	D	→	CD_4			0	1
HCO	+	O	→	CO_2	+	H	0	1
DCO	+	O	→	CO_2	+	D	0	1
CO	+	O	→	CO_2			2500	4.80(-23)
CO	+	OH	→	t-HOCO			285	3.50(-03)
CO	+	OD	→	t-DOCO			121	1.63(-01)

CO	+	OH	→	c-HOCO			2128	5.81(-17)
CO	+	OD	→	c-DOCO			1964	9.57(-16)
t-HOCO*	+		→	CO	+	OH	13050	1.63(-10)
t-HOCO*	+		→	c-HOCO			4114	1
t-HOCO	+	H	→	CO_2	+	H_2	0	1
t-HOCO	+	H	→	H_2O	+	CO	0	1
t-HOCO	+	H	→	HCOOH			0	1
t-HOCO	+	D	→	CO_2	+	HD	0	1
t-HOCO	+	D	→	HDO	+	CO	0	1
t-HOCO	+	D	→	HCOOD			0	1
c-HOCO*	+		→	t-HOCO			3272	1
c-HOCO*	+		→	CO_2	+	H	12440	2.63(-01)
c-HOCO	+		→	t-HOCO			3272	1.19(-17)
c-HOCO	+		→	CO_2	+	H	12440	2.94(-21)
c-HOCO	+	H	→	CO_2	+	H_2	0	1
c-HOCO	+	H	→	H_2O	+	CO	0	1
c-HOCO	+	H	→	HCOOH			0	1
c-HOCO	+	D	→	CO_2	+	HD	0	1
c-HOCO	+	D	→	HDO	+	CO	0	1
c-HOCO	+	D	→	HCOOD			0	1
t-DOCO*	+		→	CO	+	OD	13220	9.27(-02)
t-DOCO*	+		→	c-DOCO			4238	1
t-DOCO	+	H	→	CO_2	+	HD	0 (R=0.33)	1
t-DOCO	+	H	→	HDO	+	CO	0 (R=0.33)	1
t-DOCO	+	H	→	DCOOH			0 (R=0.33)	1
t-DOCO	+	D	→	CO_2	+	D_2	0 (R=0.33)	1
t-DOCO	+	D	→	D_2O	+	CO	0 (R=0.33)	1
t-DOCO	+	D	→	DCOOD			0 (R=0.33)	1
c-DOCO*	+		→	t-DOCO			3343	1
c-DOCO*	+		→	CO_2	+	D	13230	6.18(-02)
c-DOCO	+		→	t-DOCO			3343	1.51(-22)
c-DOCO	+	D	→	CO_2	+	D_2	0 (R=0.33)	1
c-DOCO	+	D	→	D_2O	+	CO	0 (R=0.33)	1
c-DOCO	+	D	→	DCOOD			0 (R=0.33)	1
c-DOCO	+	H	→	CO_2	+	HD	0 (R=0.33)	1
c-DOCO	+	H	→	HDO	+	CO	0 (R=0.33)	1
c-DOCO	+	H	→	DCOOH			0 (R=0.33)	1
O	+	CO	→	O...CO			0	1
O...CO	+	H	→	HO...CO			0	1
HO...CO			→	t-HOCO			775	9.46(-09)
HO...CO			→	c-HOCO			2618	8.17(-21)
HO...CO*			→	t-HOCO			775	1
HO...CO*			→	c-HOCO			2618	1
DO...CO			→	t-DOCO			727	2.97(-18)
DO...CO			→	c-DOCO			2769	1.60(-20)
DO...CO*			→	t-DOCO			727	1
DO...CO*			→	c-DOCO			2769	1

Astronomy & Astrophysics manuscript no. sepulcre˙pdb˙fin
December 13, 2012

High angular resolution observations towards OMC-2 FIR 4: Dissecting an intermediate-mass protocluster

A. López-Sepulcre[1], V. Taquet[1], Á. Sánchez-Monge[2], C. Ceccarelli[1], C. Dominik[3,4], M. Kama[3], E. Caux[5,6], F. Fontani[2], A. Fuente[7], P.T.P. Ho[8,9], R. Neri[10], and Y. Shimajiri[11]

[1] UJF-Grenoble 1 / CNRS-INSU, Institut de Planétologie et d'Astrophysique de Grenoble (IPAG) UMR 5274, Grenoble, F-38041, France e-mail: ana.sepulcre@obs.ujf-grenoble.fr
[2] Osservatorio Astrofisico di Arcetri, Largo E. Fermi 5, I-50124 Firenze, Italy
[3] Astronomical Institute Anton Pannekoek, University of Amsterdam, Amsterdam, The Netherlands
[4] Department of Astrophysics/IMAPP, Radboud University Nijmegen, Nijmegen, The Netherlands
[5] Université de Toulouse, UPS-OMP, IRAP, Toulouse, France
[6] CNRS, IRAP, 9 Av. colonel Roche, BP 44346, 31028 Toulouse Cedex 4, France
[7] Observatorio Astronómico Nacional, P.O. Box 112, 28803 Alcalá de Henares, Madrid, Spain
[8] Institute of Astronomy and Astrophysics, Academia Sinica, P.O. Box 23-141, Taipei 106, Taiwan
[9] Harvard-Smithsonian Center for Astrophysics, 60 Garden Street, Cambridge, MA 02138, USA
[10] IRAM, 300 rue de la piscine, F-38406 Saint-Martin d'Hères, France
[11] Nobeyama Radio Observatory, 462-2 Nobeyama, Minamimaki, Minamisaku, Nagano 384-1305, Japan

Received; accepted

ABSTRACT

Context. Intermediate-mass stars are an important ingredient of our Galaxy and key to understand how high- and low-mass stars form in clusters. One of the closest known young intermediate-mass protoclusters is OMC-2 FIR 4, located at a distance of 420 pc, in Orion. This region is one of the few where the complete 500-2000 GHz spectrum has been observed with the heterodyne spectrometer HIFI on board the *Herschel* satellite, and unbiased spectral surveys at 0.8, 1, 2 and 3 mm have been obtained with the JCMT and IRAM 30-m telescopes.

Aims. We aim to disentangle the core multiplicity and to investigate the morphology of this region in order to study the formation of a low- and intermediate-mass protostar cluster, and aid the interpretation of the single-dish line profiles already in our hands.

Methods. We used the IRAM Plateau de Bure Interferometer to image OMC-2 FIR 4 in the 2-mm continuum emission, as well as in DCO^+(2–1), DCN(2–1), $C^{34}S$(3–2), and several CH_3OH lines. In addition, we analysed observations of the NH_3(1,1) and (2,2) inversion transitions made with the Very Large Array of the NRAO. The resulting maps have an angular resolution which allows us to resolve structures of 5″, equivalent to $\sim$ 2000 AU.

Results. Our observations reveal three spatially separated cores of one or several solar masses each, with hints of further unresolved substructure within them. One of these cores displays weak dust continuum emission and a higher abundance of DCO^+ relative to the other two, suggesting a lower temperature and, therefore, an earlier evolutionary state or lower mass protostar. The other two are likely warmer, and one of them also displays radio continuum emission, which may be attributed to a young B3-B4 star that dominates the overall luminosity output of the region ($\sim$ 500 $L_\odot$). This HII region likely forms a cavity surrounded by a shell of molecular gas and dust we detect in our mm maps.

Conclusions. Our interferometric observations evidence the complexity of the intermediate-mass protocluster OMC-2 FIR 4, where multiple cores, chemical differentiation, and an ionised region all coexist within an area of only 10000 AU.

Key words. ISM: individual objects: OMC-2 FIR 4 – ISM: molecules

1. Introduction

Star formation starts in dense fragments within clouds of molecular gas and dust and ends when nuclear hydrogen burning begins at the centre of a newly formed star. During this evolution, the physical processes and different phases involved are not necessarily the same for stars of all masses. Indeed, in the field of star formation there has traditionally been a division between low-mass stars ($M \lesssim 2$ $M_\odot$), intermediate-mass stars (2 $M_\odot < M \lesssim 8$ $M_\odot$), and high-mass stars ($M > 8$ $M_\odot$).

In the past decades, most of the attention has been devoted to the study of low-mass and high-mass star formation, revealing differences between the two which are not only dynamical (Beuther et al. 2007, Zinnecker & Yorke 2007), but also chemical in nature (Bottinelli 2006, Ceccarelli et al. 2007). The formation of intermediate-mass (IM) stars represents the bridge between low-mass and high-mass star formation and can bring important pieces of information to understand how differently the process of star formation works in the two mass extremes. As their high-mass counterparts, IM stars emit a non negligible amount of radiation in the far ultraviolet (FUV), and are thus able to photodissociate and ionise their surroundings. Therefore, the study of IM star formation can aid the current debate on the formation mechanism of high-mass stars (see Zinnecker & Yorke 2007 for a review).

While low-mass stars may form in isolation or in loose stellar aggregates, high-mass stars are always seen to be formed in

⋆ Based on observations carried out with the IRAM Plateau de Bure Interferometer. IRAM is supported by INSU/CNRS (France), MPG (Germany) and IGN (Spain).

densely clustered environments. IM star formation also occurs in clustered mode (e.g. Fuente et al. 2007) and has been found to be the transition between loose low-mass aggregations and tight high-mass clusters (Testi et al. 1999). IM protoclusters represent excellent laboratories to study clustered star formation at almost the full range of stellar masses. Observationally, they can typically be found closer ($d \lesssim 1$ kpc) than high-mass protoclusters, and they are also less complex.

Despite all this, relatively little work has focused on the early stages of IM star formation. Only a few individual sources have been studied in detail (e.g. Fuente at al. 2009, Crimier et al. 2009, 2010, Sánchez-Monge et al. 2010, Palau et al. 2011, van Kempen et al. 2012), and therefore much remains unknown about the formation and first evolutionary stages of these objects.

The present work focuses on the IM protocluster OMC-2 FIR 4, with a luminosity that has been reported to be between 50 $L_\odot$ (Adams et al. 2012) and 1000 $L_\odot$ (Crimier et al. 2009). It is located in the Orion A complex, 2 pc North of the famous Orion Nebula (M42) and the Trapezium OB association, and lies ~420 pc away from the sun (Menten et al. 2007, Hirota et al. 2007).

Due to its relative proximity, multiple studies have been carried out towards this region and the OMC-2/3 filament where it is located. These include continuum observations at several wavelengths (e.g. Chini et al. 1997, Johnstone & Bally 1999, Nielbock et al. 2003), and various molecular line studies (e.g. Tatematsu 1993, Cesaroni & Wilson 1994, Takahashi et al. 2008, Tatematsu et al. 2008, Liu et al. 2011, Li et al. 2012). Most of them, however, are coarse angular-resolution observations, very useful to investigate the overall structure of the whole filament, but not sufficient to resolve the substructure within the OMC-2 FIR 4 region. The only dedicated interferometric observations towards this source are Very Large Array (VLA) maps carried out at 3.6 cm by Reipurth et al. (1999), and a recent study conducted with the Nobeyama Millimeter Array (NMA) at 3 mm by Shimajiri et al. (2008; hereafter S08). The latter reveal several cores and the authors speculate that an external outflow driven by the nearby FIR 3 is responsible for triggering fragmentation in FIR 4, highlighting the complexity of this region.

OMC-2 FIR 4 is also one of the targets of the *Herschel*[1] Guaranteed Time Key Programme Chemical HErschel Surveys of Star forming regions (CHESS[2]; Ceccarelli et al. 2010, Kama et al. 2012), which has conducted unbiased spectral surveys with the HIFI spectrometer (de Graauw et al. 2010) of eight star forming regions, each representative of a particular aspect of the star formation process: evolutionary stage, mass of the forming star, and/or interaction with the surroundings. The HIFI half-power beam width ranges between 11″ at 1900 GHz and 41″ at 500 GHz, thus covering most, if not all, the area of OMC-2 FIR 4. High-angular resolution observations are therefore a crucial tool to help disentangle the information hidden in the HIFI line profiles.

With this in mind, we report in this paper 2-mm continuum and line observations performed with the IRAM Plateau de Bure Interferometer (PdBI) and ammonia maps obtained with the VLA towards OMC-2 FIR 4. We describe these observations in Sect. 2; in Sect. 3 we present the maps and spectra obtained, which we discuss and interpret in Sect. 4. Finally, Sect. 5 summarises the main conclusions of this work.

2. Observations

2.1. Plateau de Bure observations

We observed OMC-2 FIR 4 with the IRAM Plateau de Bure Interferometer (PdBI) in two tracks on 15 October 2010 and 15 April 2011, using the most compact D and C configurations of the array. The data presented in this paper cover a spectral window of 1.8 GHz obtained with the WIDEX correlator, whose channel spacing is 1.95 MHz (~4 km s^{-1}), centred at a frequency of 143.4 GHz. The phase centre of the observations is α(J2000) = 05^{h}35^{m}26.971^s, δ(J2000) = –05°09′56.77″. The systemic velocity of OMC-2 FIR 4 is V_{LSR} = 11.4 km s^{-1}.

The bandpass of the receivers was calibrated by observing 0923+392 in Oct 2010 and NRAO150 in Apr 2011, with a flux density of 3.55 Jy and 2.53 Jy, respectively. Amplitude and phase calibrations were achieved by monitoring 0430+052 and 0528+134, whose flux densities were determined to be 1.32 and 1.67 Jy, respectively, at 143.4 GHz. The uncertainty in the amplitude calibration is estimated to be 30%.

The data were calibrated and analysed with the GILDAS[3] software package developed at IRAM and the Observatoire de Grenoble. We obtained continuum maps from the line free channels and subtracted the continuum from the line emission directly in the (u,v)-domain. The resulting 1σ RMS and beam size for the naturally weighted continuum map are 4.9 mJy beam^{-1} and 4.″87 × 2.″73, respectively (see Table 1).

2.2. Very Large Array ammonia observations

The Very Large Array (VLA[4]) was used to observe the ammonia (J,K) = (1,1) and (2,2) inversion transitions simultaneously (project AC556). Twenty adjacent pointing centres, covering OMC-2 and OMC-3 regions, were carried out on 29 July 2000 and 24 September 2000, with the array in the D (compact) configuration. The FWHM of the primary beam at the frequency of the observations is approximately 2′; the field centres were separated by 1′ to ensure full sampling. Each field was observed for a total on-source integration time of approximately 30 minutes. The absolute flux scale was set by observing the quasar 1328+307 (3C286), for which we adopted a flux of 2.5 Jy. The quasars 0605−085 and 0539−057, with bootstrapped fluxes of 2.4 Jy and 1.0 Jy, respectively, were observed regularly to calibrate the gains and phases. Bandpass calibration was performed by observing the bright quasar 0316+413 (3C84) with a flux density of 14.2 Jy (for July) and 17.5 Jy (for September).

The data reduction followed the VLA standard guidelines for calibration of high-frequency data, using the NRAO package AIPS. The NH_3 (1,1) and NH_3 (2,2) lines were observed simultaneously in the four IF correlator modes of the VLA (with two polarisations for each line), providing 63 channels with a spectral resolution of 0.62 km s^{-1} across a bandwidth of 3.125 MHz, plus an additional continuum channel containing the central 75 per cent of the total bandwidth. The bandwidth was centred at the systemic velocity V_{LSR}=11.4 km s^{-1}.

[1] *Herschel* is a European Space Agency (ESA) space observatory with science instruments provided by European-led principal investigator consortia and with important participation from the National Aeronautics and Space Administration (NASA).

[2] http://www-laog.obs.ujf-grenoble.fr/heberges/chess/

[3] The GILDAS package is available at http://www.iram.fr/IRAMFR/GILDAS

[4] The Very Large Array (VLA) is operated by the National Radio Astronomy Observatory (NRAO), a facility of the National Science Foundation operated under cooperative agreement by Associated Universities, Inc.

Calibrated uv-data were loaded in the software MIRIAD (Sault et al. 1995) to perform the imaging. Continuum emission was subtracted from line-free channels using the task `UVLIN`. We combined and imaged the data from the central part of the mosaic, covering the OMC-2 region, with the task `MOSSDI`. The rms noise in the naturally weighted maps is 5 mJy beam^{-1} per 0.62 km s^{-1} channel. We applied a *uv*-taper function of 60 kλ (3″ in the image plane) to improve the signal-to-noise ratio. The resulting synthesised beam is 6.″2 × 5.″3, with PA=−5°.

3. Results

3.1. Millimetre continuum emission

Figure 1 shows our PdBI naturally and uniformly weighted 2-mm continuum maps (white contours). For comparison, these are overlaid on the 3-mm continuum images obtained by S08 with the Nobeyama Millimeter Array (NMA).

From their uniformly weighted image, S08 identify 11 cores at 3 mm within OMC-2 FIR 4, whose positions according to their Table 4 are marked with black crosses in the figure. The parameters of our continuum observations and those of S08 are listed in Table 1.

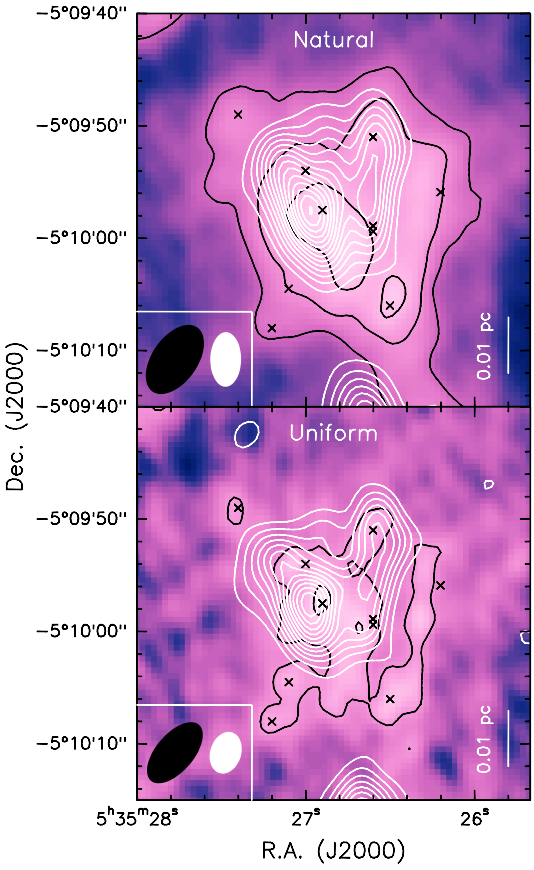

Fig. 1. Interferometric continuum maps of OMC-2 FIR 4 with natural (*top*) and uniform weighting (*bottom*). White contours represent the 2-mm continuum emission obtained with the PdBI, while black contours, as well as the background colour scale, correspond to the 3-mm continuum emission seen with the NMA (S08). Contours for both the PdBI and NMA maps start at 3σ and increase by steps of 3σ. The bottom-left ellipses represent the respective beam sizes. The black crosses mark the NMA 3-mm cores as reported in Table 4 of S08.

The PdBI images allow us to resolve two elongated regions in OMC-2 FIR 4, separated by ∼ 5″, surrounded by more extended emission which covers a total size of about 15″. The uniform map suggests the presence of additional fragmentation which cannot be completely resolved at the angular resolution of the observations. On the other hand, the NMA images display fainter, more complex and more extended emission, which is largely below the 3σ level (first contour) in the case of the uniform map. The shortest baseline attained with the NMA is 2.9 kλ while that of the PdBI is 10 kλ. This results in a higher sensitivity of the NMA to extended structures.

We have several concerns regarding the core identification made by S08. First, it was based on the uniform map, which is very noisy; second, the coordinates given for some of the cores do not coincide with the corresponding emission peak positions in the image; and third, two pairs of cores lie within a beam size of each other. We believe the NMA natural map is more reliable than the uniform one given its higher sensitivity. This already shows a number of clearly separated cores, some of which appear to be followed also by the PdBI contours. In conclusion, even though we prefer to be cautious about the reality of the 11 cores reported in S08, we are convinced that OMC-2 FIR 4 is composed of several cores.

Based on our PdBI maps, we will hereafter refer to the dominant eastern region as *main* core, and to the western one as *west* core. We note that, throughout this paper, we will use the term "core" to denote each of the spatially distinct regions we detect in the OMC-2 FIR 4 molecular clump. These do not necessarily represent the individual physical entities defined by Williams et al. (2000) as cores, but areas we are able to resolve spatially from our observations and which may still contain smaller scale structure within them.

The continuum fluxes, measured inside the 5σ contour of the corresponding maps, are shown in Table 1. We can estimate the mass of the emitting clump by assuming the millimetre continuum dust emission is optically thin. In this case, the mass, $M_{\rm dust}$ is given by

$$M_{\rm dust} = \frac{S_\nu\, d^2}{\kappa_\nu\, B_\nu(T_{\rm d})\, R_{\rm d}} \qquad (1)$$

where S_ν is the flux we meaure inside the 5σ contour at 2 mm, d the distance to OMC-2 FIR 4, $T_{\rm d}$ the dust temperature (adopted to be 50 K from S08), $B_\nu(T_{\rm d})$ is the Planck black body function for a temperature $T_{\rm d}$, and $R_{\rm d}$ is the dust-to-gas ratio, assumed equal to 0.01. $\kappa_\nu = \kappa_0(\frac{\nu}{\nu_0})^\beta$ is the frequency-dependent dust mass opacity coefficient. Chini et al. (1997) derived $\beta = 2$ from the Spectral Energy Distribution fit towards OMC-2 FIR 1 and FIR 2. Since FIR 4 is in the same molecular filament as FIR 1 and FIR 2, we have adopted $\beta = 2$, and $\kappa_0 = 1$ cm^2 g^{-1} at $\nu_0 = 250$ GHz (Ossenkopf & Henning 1994).

The resulting mass, from the naturally-weighted 2-mm continuum map, is 9 ± 3 M$_\odot$. This should be considered as a lower limit to the total mass of OMC-2 FIR 4 (dense cores plus envelope), since a percentage of the total flux is expected to be filtered out by the interferometer. We can estimate the fraction of flux lost with the aid of the work published by Crimier et al. (2009), who modelled the Spectral Energy Distribution (SED) function observed towards OMC-2 FIR 4 at infrared and sub-millimetre wavelengths. The flux they predict at 2 mm is 2 Jy, implying a flux loss of 45% in our PdBI continuum observations.

Crimier et al. (2009) derived a mass of 30 M$_\odot$ for the envelope of OMC-2 FIR 4, i.e. higher than our estimate by a factor 3. While this difference may be partly due to the loss of flux in our

Table 1. Parameters of our continuum observations and those of Shimajiri et al. (2008)

Parameter	This work		Shimajiri et al. (2008)	
Interferometer	PdBI	PdBI	NMA	NMA
Wavelength (mm)	2	2	3	3
Weighting	natural	uniform	natural	uniform
Baseline range (kλ)	10 - 80	10 - 80	2.9 - 115	2.9 - 115
Beam size (arcsec)	4.87×2.73	3.74×2.74	6.96×4.03	6.55×3.34
P.A. of the beam (°)	–0.76	–12.98	–34.59	–40.31
R.M.S. (mJy beam^{-1})	4.9	4.6	1.2	1.4
Measured flux (Jy)^b	1.06 ± 0.32	1.10 ± 0.33	0.09^a	0.06^a

$^{(a)}$ Measured inside the 5σ contour of the naturally-weighted NMA continuum map (Fig. 1)
$^{(b)}$ Assumed a calibration error of 30% in the flux

interferometric maps, we note that a different choice of dust temperature in Eq. 1 can significantly change the obtained mass. For example, adopting $T_{\rm d}$ = 20 K, which is a reasonable dust temperature for the source outer envelope (Lis et al. 1998, Jørgensen et al. 2006, Crimier et al. 2009), yields a mass of 26 $M_\odot$.

3.2. Line emission

The list of detected transitions are presented in Table 2, together with the 1σ RMS values of the corresponding velocity channel maps (see Sects. 3.2.1 and 3.2.2). Out of the nine methanol lines detected, eight are blended due to the poor spectral resolution of the observations. Therefore, the methanol maps shown in this paper correspond to the only isolated transition we observe, i.e. $CH_3OH(3,1,+0 – 2,1,+0)$ at 143.87 GHz, whose upper level energy is 28 K and which will hereafter be referred to as CH_3OH for simplicity.

3.2.1. PdBI molecular line spectra and maps

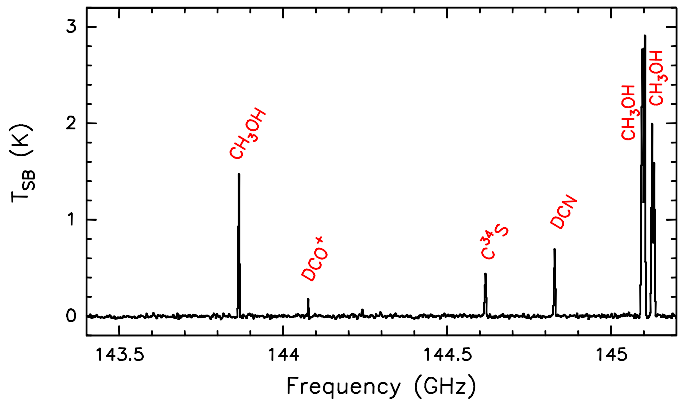

Fig. 2. PdBI spectrum obtained towards the phase centre of OMC-2 FIR 4 with the WIDEX correlator. The species of the detected lines are labelled.

The 1.8-GHz wide spectrum obtained at the peak coordinates of OMC-2 FIR 4 with the WIDEX correlator at PdBI is presented in Fig. 2, where the detected species are labelled. Since we are also in possession of IRAM 30-m single-pointing data towards the same source (López-Sepulcre et al., *in prep.*), we provide in Table 3 an estimate of the velocity-integrated flux loss for each PdBI line. This ranges from 13% for CH_3OH to 73% for $DCO^+(2–1)$, and indicates the presence of an important contribution from extended emission in these tracers which is filtered out by the interferometer.

Table 3. Flux loss for the PdBI molecular lines

Line	Flux loss (%)
CH_3OH	13
$DCO^+(2 – 1)$	73
$C^{34}S(3 – 2)$	60
DCN(2 – 1)	72

Given the low spectral resolution of the WIDEX spectrum (1.95 MHz, i.e. 4 km s^{-1}), it is not possible to analyse the shape of the line profiles. However, this is beyond the scope of the present work, which aims primarily at investigating the spatial distribution of the emission in the different tracers. To this end we provide, for each millimetre molecular tracer, velocity-integrated maps in Fig. 3, and velocity channel maps in Fig. 4. The synthesised beam size of these images is 4.8×2.7 arcsec, and is depicted on the bottom-left corner of each panel in the figures.

If we focus first on the integrated maps (Fig. 3), the morphological complexity of the source becomes evident from a comparison of the emission distribution in the different tracers:

- The CH_3OH emission is dominated by the *main* core (see Sect. 3.1 above), which displays an elongated shape, and shows hints of a secondary component towards the west (the above mentioned *west* core), mimicking the spatial distribution of the 2-mm continuum emission. The morphology of the source does not change when seen in the blended CH_3OH lines around 145 GHz.
- $C^{34}S(3–2)$ displays a more compact emission that traces both the *main* and *west* cores.
- The DCN(2–1) emission peaks at the *main* core, but it expands towards the west and the north, following the elongated morphology of the *west* core as seen in the continuum images.
- $DCO^+(2–1)$ peaks to the South of the *main* and *west* cores, a different region which we name *south* core, not well traced by any other line.

In summary, from the integrated maps we conclude that each molecular line traces the region differently. We differentiate three spatially separated emission components, which we have named *main*, *west*, and *south* cores, lying ∼ 0.01 pc (i.e. 2000 AU) apart from each other. These regions are schematically depicted in the right panel of Fig. 3 by three magenta polygons that have been manually defined to pinpoint similar central areas for each core while keeping approximately their morphological shapes. From these we have extracted the respective continuum and line fluxes for each tracer. The resulting fractional fluxes with respect to the total flux of the entire region are listed in

Table 2. Lines observed with the PdBI and VLA interferometers

Line	ν^a (GHz)	E_{up} (K)	A_{ul} (s^{-1})	1σ RMS^b (mJy beam^{-1})
$CH_3OH(3,1,+0 - 2,1,+0)$	143.865801	28.3	1.07×10^{-5}	3.7
$CH_3OH(3,0,0 - 2,0,0)$	145.093707	27.1	1.23×10^{-5}	—
$CH_3OH(3,-1,0 - 2,-1,0)$	145.097370	19.5	1.10×10^{-5}	—
$CH_3OH(3,0,+0 - 2,0,+0)$	145.103152	13.9	1.23×10^{-5}	—
$CH_3OH(3,2,-0 - 2,2,-0)$	145.124410	51.6	6.89×10^{-6}	—
$CH_3OH(3,2,0 - 2,2,0)$	145.126190	36.2	6.77×10^{-6}	—
$CH_3OH(3,-2,0 - 2,-2,0)$	145.126392	39.8	6.85×10^{-6}	—
$CH_3OH(3,1,0 - 2,1,0)$	145.131855	35.0	1.12×10^{-5}	—
$CH_3OH(3,2,+0 - 2,2,+0)$	145.133460	51.6	6.89×10^{-6}	—
$DCO^+(2-1)^c$	144.077289	10.4	2.12×10^{-4}	3.6
$C^{34}S(3-2)$	144.617101	13.9	5.78×10^{-5}	3.2
$DCN(2-1)^c$	144.828002	10.4	1.27×10^{-4}	3.4
$NH_3(1,1)$	23.69450	23.3	1.68×10^{-7}	5.0
$NH_3(2,2)$	23.72263	64.4	2.24×10^{-7}	4.7

[a] Millimetre line frequencies from the CDMS catalogue: http://www.astro.uni-koeln.de/cdms/
[b] — indicates no map is presented in this paper
[c] Transition with 6 hyperfine components

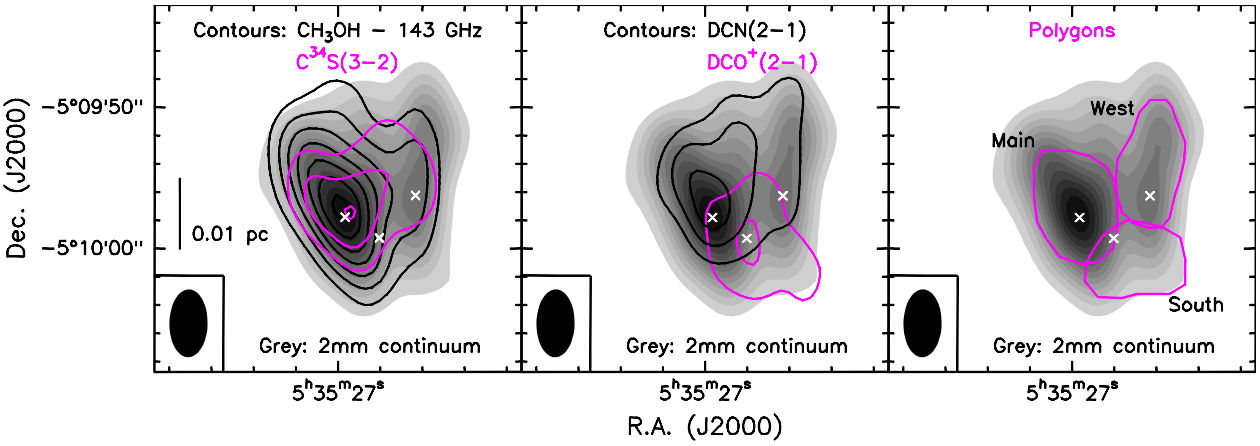

Fig. 3. Velocity-integrated PdBI contour maps obtained towards OMC-2 FIR 4, overlaid on the naturally weighted continuum map (grey scale). The bottom-left ellipse in each panel represents the beam size. *Left*: $CH_3OH(3,1,+0 - 2,1,+0)$ (black) and $C^{34}S(3–2)$ (magenta). *Centre*: DCN(2–1) (black) and $DCO^+(2–1)$ (magenta). All the contours start at 3σ and increase by steps of 3σ. The 1σ RMS values are 0.16, 0.14, 0.17, and 0.08 Jy beam^{-1} km s^{-1}, respectively for the CH_3OH, $C^{34}S(3–2)$, DCN(2–1), and $DCO^+(2–1)$ integrated maps. *Right*: Polygons representing the three differentiated components, *main*, *west*, and *south* (see text), used to extract average spectra. The white crosses mark the positions of the three cores identified in this work (see Table 4).

Table 4. OMC-2 FIR 4 cores: coordinates and fractional fluxes for each tracer

Component	R.A.(J2000)	Dec.(J2000)	CH_3OH	$C^{34}S(3–2)$	DCN(2–1)	$DCO^+(2–1)$	Cont. (natural)
Total^a			13.0	3.7	6.3	1.2	1.1
Main(%)	$05^h35^m26.97^s$	−05°09′57.8″	49	51	61	39	35
West(%)	$05^h35^m26.63^s$	−05°09′56.2″	15	25	30	32	18
South(%)	$05^h35^m26.80^s$	−05°09′59.3″	13	11	12	65	12

[a] Measured within the 5σ and 3σ contour for the continuum and line maps, respectively; flux units in Jy for continuum and Jy km s^{-1} for lines

Table 4. The central coordinates of each core correspond to the emission peaks of the 2-mm continuum image for the *main* and *west* cores, and those of the $DCO^+(2–1)$ map for the *south* one. Notice that, with the exception of $DCO^+(2–1)$, due to the relatively small area of each polygon, the sum of fluxes is smaller than the total flux in the whole region. This table reflects the predominance of the *main* core's flux over that of the other two cores for all the tracers except $DCO^+(2–1)$, for which the *south* core dominates the overall emission.

Using Eq. 1, we have computed the mass, M, of each core for two values of the dust temperature: 20 and 50 K. These are listed in Table 5, together with the corresponding gas column densities derived from the equation:

$$N_{H_2} = \frac{M}{\mu\, m_H\, \Omega\, d^2} \quad (2)$$

where m_H is the mass of the hydrogen atom, $\mu = 2.33$ is the mean molecular mass in units of hydrogen atom masses, and Ω is the solid angle covered by the component.

The channel maps in Fig. 4 reveal more details about the spatial distribution of the molecular line emission. Despite the low spectral resolution of the observations, the emission in all

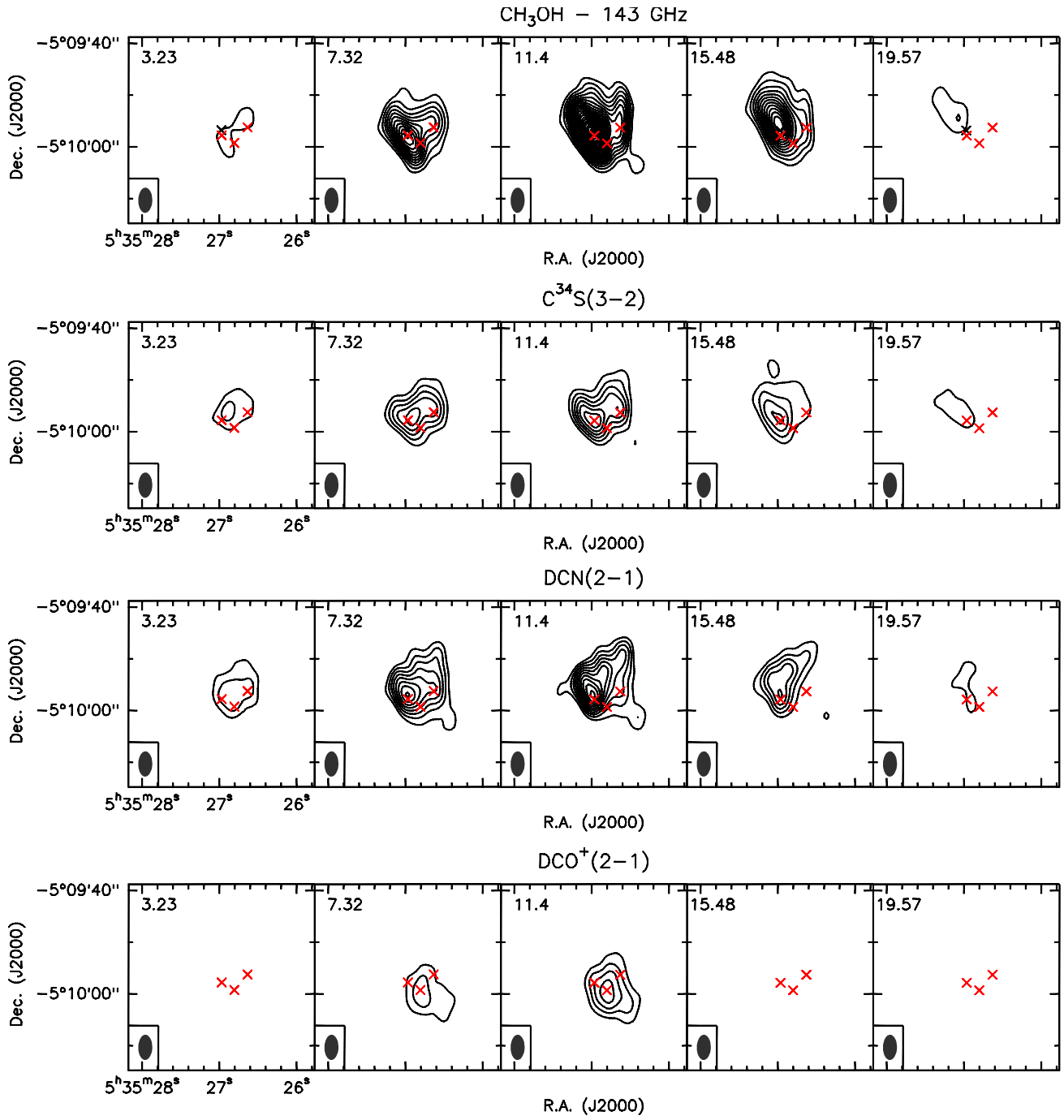

Fig. 4. Channel contour maps of each line detected with PdBI towards OMC-2 FIR 4. Contours start at 5σ and increase by steps of 5σ. The 1σ RMS values are listed in Table 2. The velocity of each channel is marked on the top-left corner of each panel. Black crosses mark the phase centre of the observations, i.e. α(J2000) = 05$^{\rm h}$35$^{\rm m}$26.971$^{\rm s}$, δ(J2000) = –05°09′56.77″, while red crosses mark the positions of the three cores identified in this work (see Table 4). The bottom-left ellipses in each panel represent the beam sizes.

Table 5. OMC-2 FIR 4 cores: masses and column densities[a]

Component	M(20 K) ($M_\odot$)	M(50 K) ($M_\odot$)	N_{H_2}(20 K) (10^{23} cm^{-2})	N_{H_2}(50 K) (10^{23} cm^{-2})
Total	25.7	9.2	19.2	6.9
Main	9.1	3.2	29.0	10.4
West	4.7	1.7	18.7	6.7
South	3.0	1.1	12.4	4.4

[(a)] Derived from the naturally-weighted 2-mm continuum map

the tracers but DCO$^+$(2–1) is detected above 5σ across 5 velocity channels (i.e. covering a width of about 18 km s^{-1}), and therefore some kinematical information can already be extracted from these maps. We note, however, that in the case of DCN(2–1) this velocity spread is partly due to the hyperfine splitting (see Sect. 3.2.3 below). In Fig. 5 we show the average spectra within the *main*, *west*, and *south* cores, defined by the polygons shown in Fig. 3 (right panel). Figure 6 presents the first moment maps for the four molecular tracers observed with the PdBI (colour scale), with overlaying contours of the corresponding velocity-

integrated maps. The spectra, channel maps and velocity maps reflect the following properties :

- The *main* core displays a velocity gradient in the south-west to north-east direction.
- The *west* core as seen by CH_3OH and $C^{34}S(3–2)$ appears slightly blue-shifted with respect to the systemic velocity of the source.
- The $DCO^+(2–1)$ emission is significantly the narrowest in line width and concentrates almost exclusively on the *south* core.
- A secondary, well-separated condensation is distinguished in the CH_3OH and DCN(2–1) maps to the south-west of the *main* core, suggesting the presence of an additional physical source. The DCO^+ emission also extends towards this area.

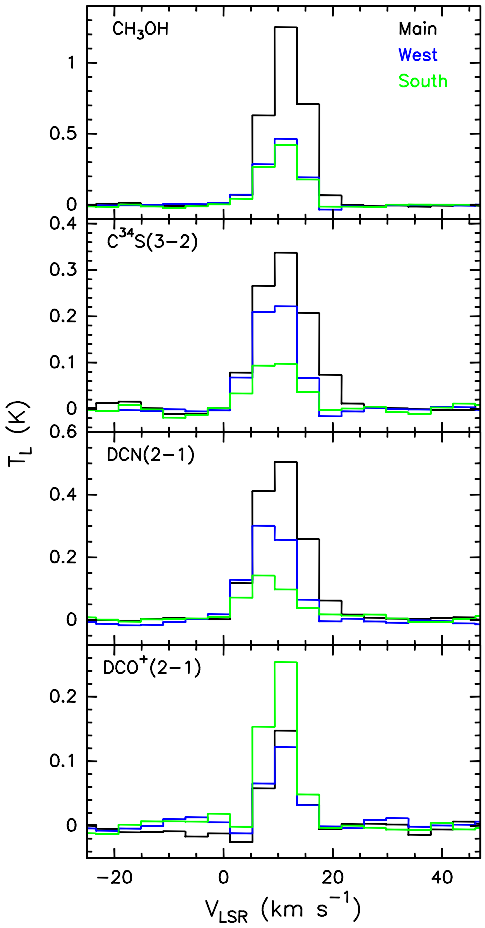

Fig. 5. Spectra in the three main cores identified in OMC-2 FIR 4 (see text) for each line tracer. The vertical scale is the average brightness temperature of the line, T_L, across the area of the corresponding core.

While the channel maps suggest the presence of more cores apart from the three we have identified so far, we cannot confirm it with 100% certainty at this spatial resolution, and even less guess how many more are present. We therefore conclude, as stated above, that there are *at least* three distinct cores within OMC-2 FIR 4, leaving open the possibility of further multiplicity within each of these three regions.

3.2.2. Ammonia emission

The $NH_3(1,1)$ and (2,2) line spectra seen towards the peak $NH_3(1,1)$ emission coordinates are shown in Fig. 7, with the different hyperfine components marked in red. The limited band width of the correlator allows us to cover only one pair of satellites for each transition, apart form the main component. In the case of $NH_3(2,2)$, only the main component is detected.

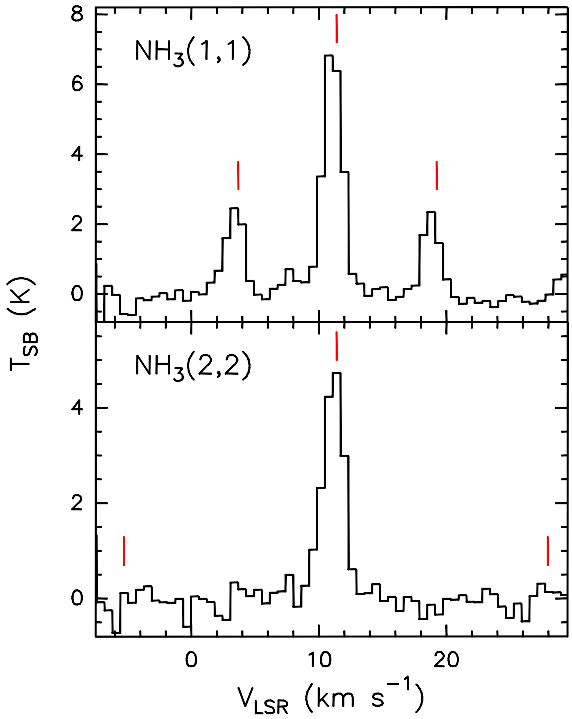

Fig. 7. VLA ammonia spectra obtained towards the peak coordinates of OMC-2 FIR 4, with a channel width of 0.62 km s^{-1}. The different hyperfine components are marked with red vertical lines.

Velocity-integrated ammonia maps are shown in Fig. 8, where the emission corresponds to the main hyperfine component of the $NH_3(1,1)$ and $NH_3(2,2)$ transitions. These are overlaid on the 2-mm continuum PdBI image (grey scale) for comparison. We stress that the presence of extended emission which was filtered out by the VLA results in a relatively high 1σ RMS level in the clean maps. Indeed, Li et al. (2012) recently published these ammonia data merged with single-dish maps obtained with the Green Bank Telescope (GBT), and a comparison with our VLA-only spectra indicates a flux loss of about 40%. Nevertheless, in terms of morphology, the NH_3 emission is well defined around OMC-2 FIR 4 and peaks to the South of the *main* core. The emission appears extended, with a roundish shape, and covers an area which is larger than that of the 2-mm continuum.

For completeness, in Fig. 9 we present the channel maps for the two NH_3 transitions, with the velocity of the channels given on the top-right corner of each panel in km s^{-1}. Unlike the millimetre molecular spectra (Sect. 3.2.1), the NH_3 lines are rather narrow, as can be seen from the velocity range covered by the maps (see also the spectra in Fig. 7 and the $FWHM$ values in Table 8). This may partly be due to the better spectral resolution and lower sensitivity of these observations. Notice indeed that the channel spacing of the VLA observations (~0.6 km s^{-1}) is substantially smaller than that of the WIDEX PdBI spectra.

The channel maps show that the emission is not only extended around the central coordinates of OMC-2 FIR 4, but

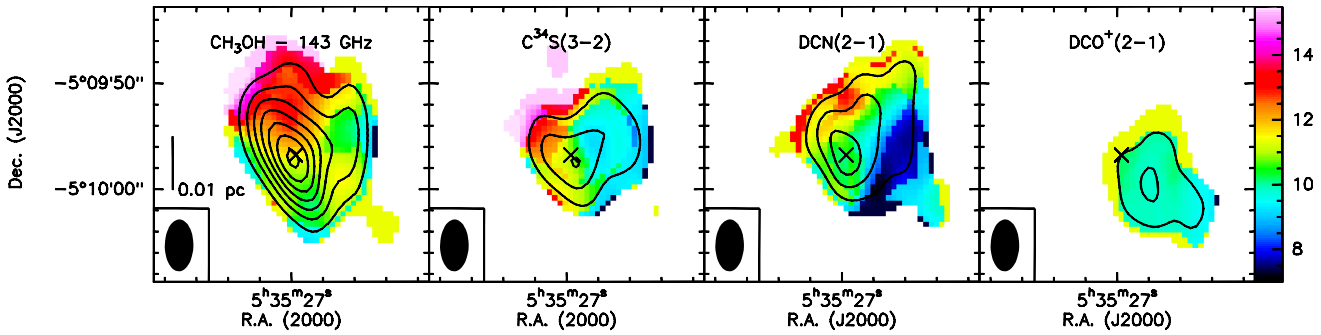

Fig. 6. Velocity maps (colour scale, in km s^{-1}) of each line detected with PdBI towards OMC-2 FIR 4, with overlaying contours of the corresponding velocity-integrated maps. Contour levels are as in Fig. 3. The bottom-left ellipse in each panel represents the beam size. Crosses mark the phase centre of the observations, i.e. α(J2000) = 05$^{\rm h}$35$^{\rm m}$26.971$^{\rm s}$, δ(J2000) = –05°09′56.77″.

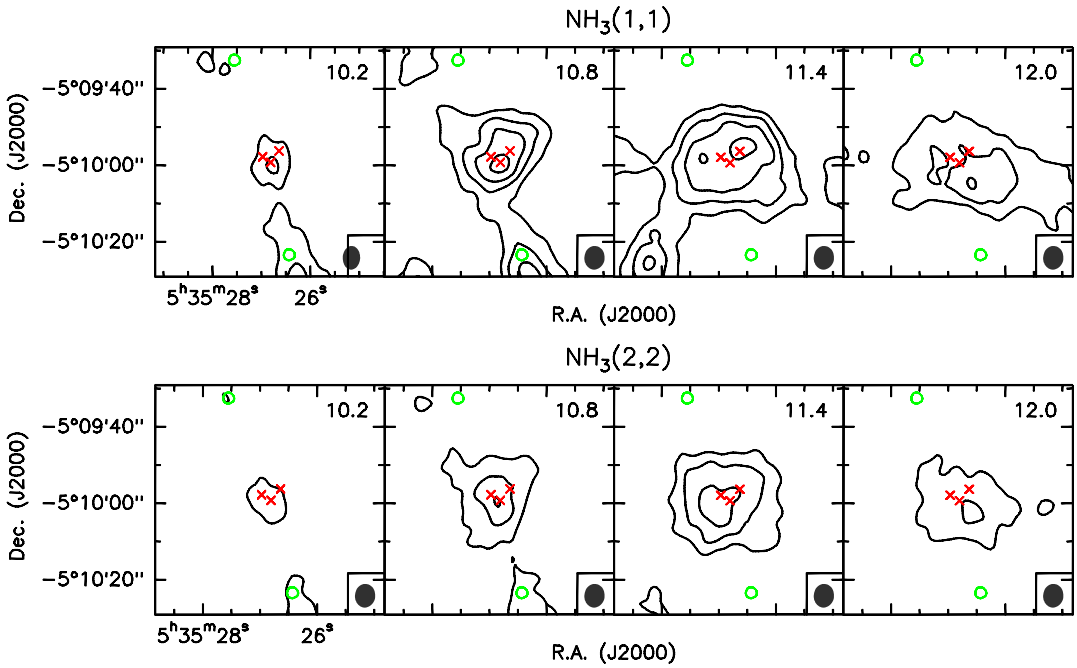

Fig. 9. VLA NH_3(1,1) and NH_3(2,2) channel maps towards OMC-2 FIR 4. Contours start at 5σ and increase by steps of 5σ. The 1σ RMS values are 5.0 and 4.7 mJy beam^{-1} for NH_3(1,1) and NH_3(2,2), respectively. The velocity of each channel is marked on the top-right corner of each panel in units of km s^{-1}. Red crosses mark the positions of the three cores identified in this work (see Table 4). Green circles mark the position of FIR 3 (NE) and FIR 5 (SW) according to the 1.2 mm observations of Chini et al. (1997). The bottom-right ellipses in each panel represent the beam sizes.

it continues towards the north-east and the south-west, where FIR 3 and FIR 5 are located, respectively (green circles). Another source of emission is detected towards the south-east at the systemic velocity of the source (11.4 km s^{-1}), also seen in the single-dish 1.3-mm maps carried out by Chini et al. (1997).

3.2.3. Derivation of physical parameters

Both the DCN(2–1) and DCO$^+$(2–1) lines are split into six hyperfine components. For DCO$^+$(2–1), all of them lie within a velocity range of 0.3 km s^{-1}, while for DCN(2–1) they span 8 km s^{-1}. As a result, at the spectral resolution of our observations, they are all blended and unresolved, and therefore a hyperfine analysis is not possible. We have thus performed a Gaussian fit to each line and adopted a range of $T_{\rm ex}$ between 10 and 100 K to estimate a range of column densities from:

$$N_{\rm mol} = \frac{8\pi\,\nu^3}{c^3}\,\frac{Q}{A_{\rm ul}\,g_{\rm u}}\,\frac{e^{\frac{E_{\rm u}}{kT_{\rm ex}}}}{e^{\frac{h\nu}{kT_{\rm ex}}}-1}\,\frac{\int T_{\rm L}\,dv}{J(T_{\rm ex})-J(T_{\rm bg})} \qquad (3)$$

where ν, c, h, k, $A_{\rm ul}$, $\tau_{\rm peak}$, ΔV, Q, $g_{\rm u}$, $E_{\rm up}$ and $\int T_{\rm L} dv$ are, respectively, the frequency of the transition, the speed of light, Planck constant, Boltzmann constant, the spontaneous emission rate, the optical depth at the line intensity peak, the line $FWHM$, the partition function, the upper state degeneracy, the upper level energy and the velocity-integrated line intensity. This equation assumes optically thin conditions, and $J(T) = \frac{h\nu/k}{e^{h\nu/kT}-1}$, with $T_{\rm bg}$ = 2.7 K. We have applied the same approach for the C^{34}S(3–2) transition.

The results of the Gaussian fits and the derived molecular column densities for each core are shown in Table 6, where it can be seen that we are indeed dealing with optically thin conditions.

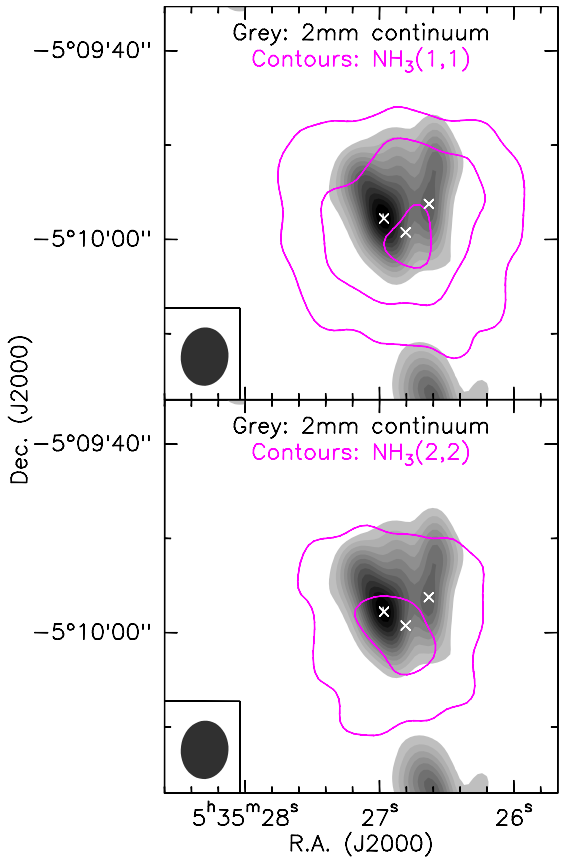

Fig. 8. Velocity-integrated VLA ammonia contour maps obtained towards OMC-2 FIR 4, overlaid on the naturally weighted 2mm-continuum map (grey scale). Contours for all the maps start at 3σ and increase by steps of 3σ. The 1σ RMS values are 20 mJy beam^{-1} km s^{-1}for both NH_3(1,1) and NH_3(2,2). White crosses mark the positions of the three cores identified in this work (see Table 4).

Some of the rows in this Table probably correspond to "artificial" cores, since not all the cores we have identified are well-defined or traced by all the lines, as explained above. We nevertheless present them for comparison and completeness. The abundances of each molecule in the different cores are also listed. They have been obtained from the ratio of $N_{\rm mol}$ to the gas column density, N. For the latter, we have used the values listed in Table 5, adopting both $T_{\rm d}$ = 20 K and $T_{\rm d}$ = 50 K.

As for the methanol lines, we analysed them by means of a Large Velocity Gradient (LVG) code, originally developed by Ceccarelli et al. (2003) and modified to include the methanol collisional coefficients with H_2 by Pottage et al. (2004). We run a large grid of models to cover a wide parameter space: N(CH_3OH) from 10^{13} to 4×10^{15} cm^{-2}, density from 10^4 to 10^9 cm^{-3} and temperature from 10 to 200 K. The observed lines were compared with the LVG model predictions and the best fit solution was found minimising the χ^2 value with respect to the three above parameters, assuming a source size of $15'' \times 15''$, as measured in our maps for the whole OMC-2 FIR 4 clump. We note that for the blended lines the predicted intensities were obtained by adding the intensity by each single line in the velocity interval.

We found that the CH_3OH column density is very well constrained between 0.6 and 1×10^{15} cm^{-2}, roughly consistent with the value of $\sim 2 \times 10^{14}$ cm^{-2} reported by Kama et al. (2010) from the early results of the HIFI data, and the density is between 0.2 and 1×10^7 cm^{-3}. Conversely, the observed lines do not allow to constrain the temperature, except that it is larger than 20 K. The larger the CH_3OH column density the larger the gas temperature. For example, if N(CH_3OH) is 8×10^{14} cm^{-2} then the gas temperature is larger than 50 K; for N(CH_3OH) = 1×10^{15} cm^{-2} the gas temperature is larger than 120 K. More methanol transitions will be necessary to better constrain the temperature, but our analysis already shows that the gas emitting the methanol lines must be relatively dense. The best fit solutions of the LVG modelling are summarised in Table 7.

Table 7. Results from the LVG analysis

N(CH_3OH) (10^{14} cm^{-2})	Density (10^6 cm^{-3})	Temperature (K)
6	> 2	20 - 50
8	> 2	> 50
10	2 - 10	> 120

Finally, we performed a hyperfine line fit to the two ammonia spectra in Fig. 7 using the standard NH_3(1,1) and NH_3(2,2) methods in CLASS. We subsequently derived the corresponding rotational and kinetic temperatures, as well as the NH_3 column density, following the steps summarised in Busquet et al. (2009) and assuming a beam filling factor equal to 1. The results are reported in Table 8, where the peak synthesised beam temperature, $T_{\rm SB}$, the velocity, $V_{\rm LSR}$, and the optical depth, $\tau_{\rm main}$ refer to the main component of the transition. We note that the errors on the temperature and column density estimates are of the order of or greater than the values themselves, mostly due to the large errors on $T_{\rm SB}$ and τ.

4. Discussion

4.1. Multiple cores within OMC-2 FIR 4

Several studies (Jørgensen et al 2006, S08, Crimier et al. 2009, Kama et al. 2010) suggest that OMC-2 FIR 4 contains three main components:

- A large-scale cool envelope about 10000 AU (i.e. 0.05 pc) across.
- An inner hot core, with kinetic temperatures above 100 K and around 400 AU in size.
- A shock region produced by the interaction of an external bipolar outflow driven by the nearby OMC-2 FIR 3, which lies to the north-east of FIR 4.

In addition, S08 report the presence of 11 cores seen at 3-mm inside this region, and speculate that such fragmentation has been externally triggered by the FIR 3 outflow.

The emission of all the maps presented in Sect. 3 covers roughly 10000 AU (0.05 pc) and therefore traces the envelope component of OMC-2 FIR 4. In particular, this component appears to be better traced by the NH_3 maps, which are essentially single-peaked and display the most extended emission, similar in size and morphology to the structures detected in previous single-dish observations (e.g. Chini et al. 1997, Shimajiri et al. 2008). The temperature derived for the ammonia emission, $\sim$ 30 K, is typical of protostellar (in our case protocluster) envelopes (e.g. Olmi et al. 2012).

At the resolution of our PdBI observations, despite being slightly better than that of the NMA observations, we cannot

Table 6. OMC-2 FIR 4 cores: Gaussian fit results, column densities and abundances for each PdBI tracer

Tracer	Comp.	T_L (K)	V_{LSR} (km s^{-1})	$FWHM$ (km s^{-1})	T_{ex}[a] (K)	τ	N_{mol} (10^{12} cm^{-2})	Abu. (20 K)[b] (10^{-12})	Abu. (50 K)[b] (10^{-12})
$C^{34}S$(3–2)	Main	0.37 (0.01)	10.9 (0.1)	11.3 (0.2)	10 - 100	0.055 - 0.004	15.3 - 38.2	5.3 - 13.2	14.7 - 36.7
	West	0.38 (0.01)	9.3 (0.1)	10.5 (0.2)	10 - 100	0.040 - 0.003	8.8 - 22.2	4.7 - 11.9	13.1 - 33.1
	South	0.15 (0.01)	9.3 (0.2)	10.7 (0.6)	10 - 100	0.017 - 0.001	4.0 - 10.3	3.2 - 8.3	9.1 - 23.4
DCN(2–1)	Main	0.55 (0.01)	10.6 (0.1)	10.0 (0.1)	10 - 100	0.085 - 0.006	6.8 - 22.0	2.3 - 7.6	6.5 - 21.2
	West	0.67 (0.01)	9.8 (0.1)	9.8 (0.2)	10 - 100	0.052 - 0.003	3.7 - 12.5	2.0 - 6.7	5.5 - 18.7
	South	0.29 (0.01)	9.0 (0.1)	10.2 (0.4)	10 - 100	0.022 - 0.001	1.8 - 6.0	1.5 - 4.8	4.1 - 13.6
DCO^+(2–1)	Main	0.19 (0.01)	10.8 (0.2)	6.1 (0.3)	10 - 100	0.024 - 0.002	0.6 - 2.3	0.2 - 0.8	0.6 - 2.2
	West	0.20 (0.01)	11.1 (0.2)	6.3 (0.3)	10 - 100	0.020 - 0.001	0.6 - 2.1	0.3 - 1.1	0.9 - 3.1
	South	0.38 (0.01)	10.3 (0.1)	6.3 (0.2)	10 - 100	0.044 - 0.003	1.3 - 4.5	1.0 - 3.6	3.0 - 10.2

[a] Adopted values

[b] Abundance determined using the dust temperature indicated in brackets to derive the total gas column density (see Table 5)

Table 8. Results of the line fitting to the NH_3(1,1) and (2,2) lines and derived physical parameters

Results of the hyperfine line fitting					
Line	T_{SB} (K)	V_{LSR} (km s^{-1})	ΔV (km s^{-1})	τ_{main}	
NH_3(1,1)	7.5 (2.7)	11.1 (0.1)	1.5 (0.1)	0.7 (0.2)	
NH_3(2,2)	4.9 (9.8)	11.2 (0.1)	1.9 (0.1)	0.1 (0.2)	
Physical parameters					
T_{ex} (K)	T_{rot} (K)	T_{kin} (K)	N_{NH_3} (10^{14} cm^{-2})	Abu. (20 K)[a] (10^{-10})	Abu. (50 K)[a] (10^{-10})
18.2	22.7	29.6	2.6	1.4	3.8

[a] Abundance determined using the dust temperature indicated in brackets to derive the total gas column density (see Table 5)

confirm the existence of the 11 cores claimed by S08. Inspection of the different maps presented in this work allows us to clearly separate only three cores, denoted by the identifiers *main*, *west*, and *south* (Sect. 3.2.1). It appears, however, that our 2-mm continuum and some molecular line maps indeed hint at the presence of multiple smaller condensations within the three cores we detect, but these will need to be confirmed by higher angular resolution observations.

At this point, it is worth mentioning that the hot core hypothesis proposed by Crimier et al. (2009) is based on a single source at the centre of the large-scale envelope. S08 and our new observations show that the envelope component breaks down at scales of $\sim$ 2000 AU, much larger than the presumed hot core size (with a radius of 440 AU). Only high-angular resolution imaging of typical hot core tracers (e.g. complex organic molecules) can observationally prove the existence of a hot core.

As shown in Fig. 6, a velocity gradient of about 6 km s^{-1} between the two velocity extremes can be seen along the *main* core in the CH_3OH and $C^{34}S$(3-2) maps, with the north-eastern tip being the most red-shifted. S08 found the same behaviour in their single-dish methanol maps. Additional interferometric observations of CO and SiO lines provided the same authors with morphological and dynamical evidence which led them to suggest that there is an interaction between the north-eastern edge of OMC-2 FIR 4 and the molecular outflow driven by the nearby FIR 3. The red-shifted emission we detect from CH_3OH and $C^{34}S$(3–2) may also be explained by this scenario, i.e., it arises from shocked gas from the interaction between the FIR 3 outflow and the dense gas of FIR 4. It might alternatively be tracing the FIR 3 outflow itself, which cannot be detected much beyond the boundary of the FIR 4 clump due to the limited sensitivity of the PdBI to more extended structures. More observations are necessary to confirm the external outflow interpretation, since with our data alone we are not able to conclude that this is indeed the case. Other possibilities exist that could cause a velocity gradient like the one we detect, such as rotation or internal outflowing/expanding motions.

4.2. Nature of the cores

Our observations allow us to distinguish three separate cores which may or may not present further fragmentation into smaller physical entities:

1. The *main* core, at the nominal coordinates and systemic velocity (11.4 km s^{-1}) of OMC-2 FIR 4. It is the strongest 2-mm continuum and methanol source in the region. Its elongated shape suggests that it harbours two or more individual cores, although this hypothesis can only be confirmed with higher spatial resolution imaging. The red-shifted velocity of its northern portion might indicate an interaction with the red-shifted lobe of the external outflow driven by FIR 3.
2. The *west* core, with a systemic velocity of 9-10 km s^{-1}. It is well traced by $C^{34}S$(3–2) and DCN(2–1), and weaker than the *main* core emission.
3. The *south* core, also with V_{LSR} = 9-10 km s^{-1}, best traced by DCO^+(2–1). It is the faintest methanol, DCN, and 2-mm continuum source, and has no significant emission in $C^{34}S$(3–2). Given its association with DCO^+ and the weakness of its continuum emission, this region is likely colder than the other two, suggesting that it is in an earlier evolutionary stage or has a lower mass protostar (e.g. Jørgensen et al. 2004).

From the results of our LVG analysis on the CH_3OH lines, the whole OMC-2 FIR 4 clump is rather dense ($n > 2 \times 10^6$ cm^{-3}), which suggests that, most likely, the three cores we identify within this region are even denser. We note that the density we derive, i.e. $n \gtrsim 2\times10^6$ cm^{-3} at 15″ (6000 AU), is in good agreement with S08 and with the predictions made by Crimier et al. (2009), both of which report a value of 10^6 cm^{-3}.

4.3. An ionised region in OMC-2 FIR 4

Radio-continuum observations of the OMC2/3 filament were carried out with the VLA by Reipurth et al. (1999) at 3.6 cm. At the position of OMC-2 FIR 4, they detected an elongated source which the authors interpret as a radio jet. When comparing their map with our PdBI map, despite the different angular resolutions (i.e. $\sim$ 4″ for the PdBI maps, 8″ for the VLA maps), we find that the position and shape of the radio source coincides fairly well within the pointing errors of the two maps, with the emission distribution of our 2-mm continuum and methanol PdBI images, which are both elongated in the same direction as the VLA source (see Fig. 10).

While Reipurth et al. (1999) attribute the radio continuum emission to a jet, the interferometric observations performed towards this source so far (e.g. S08, this work) have failed to detect molecular line emission at high velocities indicative of a jet or outflow emanating from this region. This leads us to consider a different possibility, namely that the radio emission arises from a very compact gas cavity ionised by a central young star, i.e. an HII region, which is either surrounded by a shell of dust and molecular gas best traced by the 2-mm continuum and CH_3OH emission, or else harbours two or more unresolved molecular dense cores within it. The HII region scenario is a plausible explanation for the continuum radio emission, since IM protostars can also produce sufficiently intense HII regions to be easily detected at centimetre wavelengths (e.g. Thompson 1984).

Reipurth et al. (1999) measured a flux of 0.64 mJy at 3.6 cm towards OMC-2 FIR 4. In the scenario of an optically thin HII region, and assuming a single zero-age main sequence star is powering it, this implies a B3-B4 spectral type for the central star (using the tables of e.g. Panagia 1973, Thompson 1984, Martins et al. 2005). This translates into a luminosity between 700 and 1000 $L_\odot$ and would indicate that this young star is the most massive source in the protocluster. It is also possible, given the elongated shape of the radio emission, that two (or more) individuals are responsible for the ionisation of their surroundings. Only higher angular resolution and sensitivity images of the continuum emission at different wavelengths will allow us to verify this possibility and find out whether the nature of the centimetre emission is an HII region, as proposed here, or a radio jet.

4.4. A final note on masses and luminosities

According to Mezger et al. (1990) and Crimier et al. (2009), the luminosity of OMC-2 FIR 4 is estimated to be between 400 $L_\odot$ and 1000 $L_\odot$, with an envelope mass of around 30 $M_\odot$. This, coupled with the relatively bright sub-mm emission of the source, has led to classify it as an intermediate-mass Class 0 protostar (Reipurth et al. 1999, Johnstone et al. 2003). Our observations show that OMC-2 FIR 4 is most likely an intermediate-mass protocluster, where indeed an intermediate-mass young star may be dominating the overall luminosity (see Sect. 4.3).

A recent work by Adams et al. (2012) reports new values for the luminosity and mass of OMC-2 FIR 4, based on SOFIA and *Herschel* observations, combined with archival data at IR and (sub-)mm wavelengths. The authors derive a luminosity of only 50 $L_\odot$, an order of magnitude below previous estimates. It is worth trying to explain the source of this huge discrepancy, to avoid confusion in future publications regarding this region. We believe such discrepancy arises from the method used in the flux measurements. Adams et al. (2012) adopt small aperture sizes ranging between 7″ and 13″ at IR and sub-mm wavelengths. In addition, the central coordinates used by the authors are those of the IR emission peak, which is offset by $\sim$ 5″ with respect to the (sub-)mm emission peak. On the other hand, Crimier et al. (2009) and Mezger et al. (1990) take into account a larger area, of 30″ - 50″, which includes the whole envelope of OMC-2 FIR 4. Crimier et al. (2009) use far-IR data from ISO and IRAS, whose coarse angular resolution likely led to overestimated flux measurements.

Table 9. Mass and luminosity estimates for OMC-2 FIR 4[a]

L ($L_\odot$)	M ($M_\odot$)	Size (″)	Ref.
350	34	50	Mezger et al. (1990)
920	30	30	Crimier et al. (2009)
50	10	8	Adams et al. (2012)

[(a)] Values re-scaled to a distance of 420 pc

Table 9 summarises the different values for the luminosity, mass and size of OMC-2 FIR 4 reported in the literature. Based on the discussion above (Sect. 4.3), Adams et al. (2012) very likely underestimated the luminosity of OMC-2 FIR 4, while the value provided by Crimier et al. (2009) is probably an upper limit. Taking into account also that the PdBI and VLA data analysed in the present work may point towards a luminosity of several hundred solar luminosities (see Sect. 4.3), we conclude that the bolometric luminosity of OMC-2 FIR 4 is around 500 $L_\odot$, with an uncertainty of about a factor 2, and that a more detailed investigation is needed in order to establish a more accurate value.

5. Conclusions

We have presented new interferometric observations carried out towards the intermediate-mass protocluster OMC-2 FIR 4, in the Orion A complex. These include PdBI maps of the continuum emission at 143.4 GHz (2 mm) and the $CH_3OH(3,1,+0 - 2,1,+0)$, $C^{34}S(3–2)$, DCN(2–1), and $DCO^+(2–1)$ lines, as well as VLA maps of the $NH_3(1,1)$ and (2,2) inversion transitions. Despite the coarse spectral resolution of the observations (0.6 km s^{-1} for the VLA spectra and 4 km s^{-1} for the PdBI images), we are able to extract important information about the morphology and kinematics of the region. Figure 11 shows a cartoon of the OMC-2 FIR 4/FIR 3 region, summarising all the elements present according to our interpretation of the data presented in this work. Our findings are summarised as follows:

1. Our 2-mm continuum maps reveal one main component and hints of secondary cores or clumps surrounding it. The existence of the 11 cores discovered by S08 cannot be confirmed by our observations, despite our higher angular resolution.
2. Each PdBI line traces the region differently. By comparing their emission, we are able to distinguish three separate cores of one or several solar masses each, which we have named *main*, *west* and *south*. The *main* and *west* ones are warmer. The *south* core displays a stronger line emission in $DCO^+(2-$ $-1)$, suggesting a colder temperature and therefore an earlier evolutionary state or lower mass core. As for the ammonia maps, their emission is more extended and essentially single-peaked, and therefore traces the envelope of the protocluster. An LVG modelling of the CH_3OH lines we observe allows us to conclude that the whole protocluster is very dense, with $n \gtrsim 2 \times 10^6$ cm^{-3}, in agreement with previous theoretical predictions on the structure of the envelope of OMC-2 FIR 4.

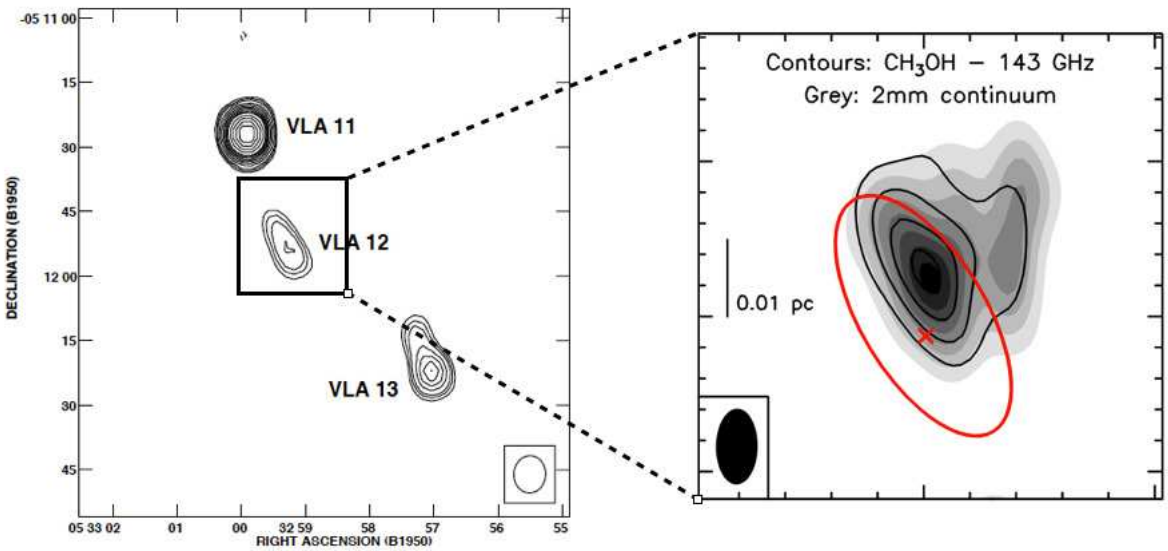

Fig. 10. *Left panel*: VLA map of the 3.6 cm continuum emission in the OMC-2 FIR 4 region and its surroundings (taken from Reipurth et al. 1999). The synthesised beam is shown at the bottom-right corner. The source labelled VLA 12 coincides with the position of OMC-2 FIR 4. *Right panel*: Close-up view showing our PdBI continuum (grey scale) and CH_3OH (black contours) maps. The synthesised beam is shown at the bottom-left corner. The red ellipse schematically represents the 4σ contour of the VLA image (left panel). The red cross marks the position of the cm emission peak.

3. The *main* core as seen by the 2-mm continuum and CH_3OH emission coincides, both in position (within the pointing errors) and in shape, with the radio-continuum emission observed at 3.6 cm with the VLA (Reipurth et al. 1999). In absence of clear interferometric evidence of a molecular outflow driven by FIR 4, we interpret this as an HII region powered either by a B3-B4 type young star, or by two or more lower-mass stellar objects. This region is likely surrounded by a shell of dust and molecular gas (seen by the millimetre continuum and CH_3OH maps). This scenario remains to be verified by higher angular resolution and multi-wavelength observations.
4. There is a considerable discrepancy among luminosity estimates found in the literature for OMC-2 FIR 4 (between 50 and 1000 $L_\odot$). Analysis of the methods used by the different authors who have published such estimates, coupled with the results of our observations, leads us to conclude that the luminosity of OMC-2 FIR 4 is $\sim$ 500 $L_\odot$, with un uncertainty of about a factor 2.

Due to its relative proximity to the Sun, OMC-2 FIR 4 is an ideal laboratory to explore intermediate- and low-mass star formation in the context of a whole protocluster. The evidence of core multiplicity in this region, coupled with the insufficient spatial resolution of our observations to clearly separate them, highlights the need of higher spectral and angular resolution imaging to disentangle the different components and extract more information about the kinematics and the excitation conditions in each of them. This information will be of crucial importance to interpret the *Herschel*-HIFI data obtained towards this source within the CHESS Key Programme.

Acknowledgements. A.L.S. and C.C. acknowledge funding from the CNES (Centre National d'Études Spatiales) and from the Agence Nationale pour la Recherche (ANR), France (project FORCOMS, contracts ANR-08-BLAN-022). M.K. gratefully acknowledges funding from an NWO grant, NOVA, Leids Kerkhoven-Bosscha Fonds and the COST Action on Astrochemistry. C.D. acknowledges funding from Leids Kerkhoven-Bosscha Fonds.

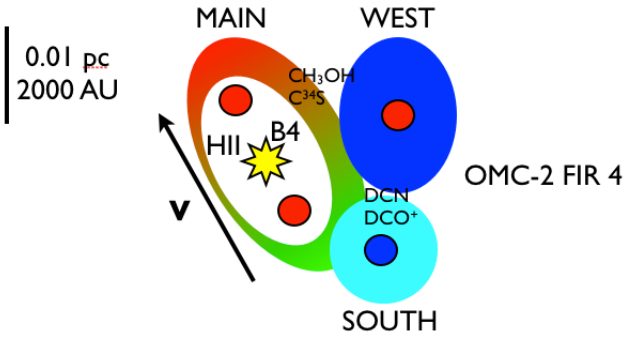

Fig. 11. Schematic cartoon of OMC-2 FIR 4 and the nearby OMC-2 FIR 3, summarising all the physical elements in the region that we propose according to the data presented in this work (see Sect. 4). The white ellipse inside the *main* core depicts the ionised region powered by a B4 young star. The colours of the *main*, *west*, and *south* cores represent their systemic velocities with respect to the nominal value for OMC-2 FIR 4 (V_{LSR} = 11.4 km s^{-1}), represented in green. The small red and blue circles within the three cores represent the possibility of each core of harbouring smaller unresolved molecular condensations, with the colour blue denoting a colder temperature than red.

References

Adams, J.D., Herter, T.L., Osorio, M. et al. 2012, ApJ, 749, L24
Beuther, H., Churchwell, E. B., McKee, C. F., Tan, J. C. 2007, in *Protostars and Planets V*, ed. B. Reipurth, D. Jewitt, K. Keil, 165-180
Bottinelli, S. 2006, PhD thesis, University of Hawaii at Manoa
Busquet, G., Palau, A., Estalella, R. et al. 2009, A&A, 506, 1183
Ceccarelli, C., Bacmann, A., Boogert, A. et al. 2010, A&A, 521, L22
Ceccarelli, C., Caselli, P., Herbst, E., Tielens, A. G. G. M., Caux, E. 2007, in *Protostars and Planets V*, ed. B. Reipurth, D. Jewitt, K. Keil, 47-62
Ceccarelli, C., Maret, S., Tielens, A. G. G. M., Castets, A., Caux, E. 2003, A&A, 410, 587
Cesaroni, R.; Wilson, T. L. 1994, A&A, 281, 209
Chini, R., Reipurth, B., Ward-Thompson, D. et al. 1997, ApJ, 474, L135
Crapsi, A., Caselli, P., Walmsley, C.M., et al. 2005, ApJ, 619, 379
Crimier. N., Ceccarelli, C., Lefloch, B., Faure, A. 2009, A&A, 506, 1229
Crimier, N., Ceccarelli, C., Alonso-Albi, T. et al. 2010, A&A, 516, 102

Fuente, A., Castro-Carrizo, A., Alonso-Albi, T. et al. 2009, A&A, 507, 1475
Fuente, A., Ceccarelli, C., Neri, R. et al. 2007, A&A, 468, 37
de Graauw, Th., Helmich, F.P., Phillips, T.G. et al. 2010, A&A, 518, L6
Hildebrand, R.H. 1983, QJRAS, 24, 267
Hirota, T., Bushimata, T., Choi, Y.K. et al. 2007, PASJ, 59, 897
Johnstone, D. & Bally, J. 1999, ApJ, 510, L49
Johnstone, D., Boonman, A.M.S., van Dishoeck, E.F. 2003, A&A, 412, 157
Jørgensen, J. K., Johnstone, D., van Dishoeck, E. F., Doty, S. D. 2006, A&A, 449, 609
Jørgensen, J. K., Schöier, F.L., van Dishoeck, E. F. 2004, A&A, 416, 603
Kama, M., Dominik, C., Maret, S. et al. 2010, A&A, 521, 39
Kama, M., López-Sepulcre, A., Dominik, C. et al. 2012, *submitted* to A&A
Li, D., Kauffmann, J., Zhang, Q., Chen, W. 2012, arXiv1207.1178L
Lis, D. C., Serabyn, E., Keene, J. 1998, ApJ, 509, 299
Liu, Q., Yang, J., Sun, Y., Xu, Y. 2011, RAA, 11, 67
Martins, F., Schaerer, D., Hillier, D.J. 2005, A&A, 436, 1049
Menten, K. M. Reid, M. J. Forbrich, J. Brunthaler, A. 2007, A&A, 474, 515
Mezger, P.G., Wink, J.E., Zylka, R. 1990, A&A, 228, 95
Nielbock, M., Chini, R., Müller, S. A. H. 2003, A&A, 408, 245
Olmi, L. Angles-Alcazar, D., Elia, D. et al. 2012, arXiv:1209.4465
Ossenkopf, V. & Henning, T. 1994, A&A, 291, 943
Palau, A., Fuente, A., Girart, J.M. et al. 2011, ApJ, 743, 32
Panagia, N. 1973, AJ, 78, 929
Pottage, J.T., Flower, D.R., Davis, S.L. 2004, MNRAS, 352, 39
Reipurth, B., Rodríguez, L.F., Chini, R. 1999, ApJ, 118, 983
Sánchez-Monge, Á., Palau, A., Estalella, R. et al. 2010, ApJL, 721, 107
Shimajiri, Y., Takahashi, S., Takakuwa, S., Saito, M., Kawabe, R. 2008, ApJ, 683, 255
Shu, F.H., Adams, F.C., Lizano, S. 1987, Ann. Rev. A&A, 25, 23
Takahashi, S., Saito, M., Ohashi, N. 2008, ApJ, 688, 344
Tatematsu, K., Kandori, R., Umemoto, T., Sekimoto, Y. 2008, PASJ, 60, 407
Tatematsu, K., Umemoto, T., Kameya, O. 1993, ApJ, 404, 643
Testi, L., Palla, F., Natta, A. 1999, A&A, 342, 515
Thompson, R.I. 1984, ApJ, 283, 165
van Kempen, T.A., Longmore, S.N., Johnstone, D., Pillai, T. 2012, ApJ, 751, 137
Williams, J. P., Blitz, L., McKee, C. F. 2000 in *Protostars and Plantes IV*, p. 97, Univ. Arizona Press, Tucson
Zinnecker, H. & Yorke, H.W. 2007, Ann. Rev. A&A, 45, 481

Grain surface chemistry in star-forming regions

The first stages of star formation are accompanied by an evolution of the chemistry, starting from simple molecules in cold dark clouds to the detection of complex organic molecules around Class 0 protostars. Although mostly composed of gas, these clouds also contain small amounts of microscopic dust. The contribution of this dust is nevertheless important because it acts as a catalyst for the formation of key molecules seen in cold interstellar ices, such as water or methanol. These ices are believed to be the first step towards the rich chemistry seen in the warm envelope of protostars. During my thesis, I focused on this first step and I did so by taking a twofold approach.

i) Modelling. I have developed an astrochemical model coupling the chemistry in the gas phase and on the grain surfaces. This model follows the multilayer formation of interstellar ices and allows us to investigate the influence of key physical, chemical, and surface parameters, such as the grain porosity, on the chemical composition of ices via a multiparameter approach. The model has been applied to predict the chemical differentiation and the deuteration of interstellar ices. To this end, I have built up a chemical network taking into account the most recent experimental and theoretical works. I applied then the model to various cases. For example, I showed that ices are heterogeneous and their composition are sensitive to the physical conditions as well as several grain surface parameters. The high deuteration of formaldehyde, and methanol observed around low-mass protostars has been predicted by a dense ($n_H \sim 5 \times 10^6$ cm^{-3}) and fast ($\sim$ 5000 years) phase while the lower deuteration of water is predicted for typical molecular cloud conditions. The deuterium fractionation is very sensitive and can be used as a tracer of the physical conditions.

ii) Observations. I have been involved in observational projects whose goals are related to the grain surface chemical problems. I obtained the following three results. We showed an evolution of the selective deuteration with the protostar type, the [CH_2DOH]/[CH_3OD] abundance ratio decreasing with the protostar mass. Interferometric mapping of deuterated water towards low-mass protostars has allowed us to constrain a relatively high deuteration level of water in new sources. Finally, we detected several complex organic molecules in a cold prestellar core for the first time, challenging the current scenario of complex organic molecules in warm conditions.

Keywords: Astrochemistry, ISM: clouds, ISM: molecules, Molecular processes, Stars: formation

Chimie à la surface des grains dans les régions de formation stellaire

Les premières étapes de la formation stellaire sont accompagnées d'une évolution de la chimie, à partir de molécules simples dans les nuages froids et sombres vers la détection de molécules organiques complexes autour des étoiles de Classe 0. Bien que principalement composés de gaz, ces nuages contiennent également une petite quantité de poussière microscopique. La contribution de cette poussière est toutefois importante car elle agit comme un catalyseur pour la formation de molécules clés observées dans les glaces froides interstellaires, telles que l'eau ou le méthanol. Ces glaces seraient la première étape d'une chimie riche observée dans les enveloppes tièdes des protoétoiles. Durant cette thèse, je me suis concentré sur la première étape en utilisant une double approche.

i) Modélisation. J'ai développé un modèle astrochimique couplant la chimie en phase gazeuse et à la surface des grains. Ce modèle suit la formation multicouche des glaces interstellaires et, grace à une approche multiparamètre, nous permet également d'étudier l'influence de paramètres physiques, chimiques, et de surface, tels que la porosité des grains, sur la composition chimique des glaces. Le modèle a ensuite été utilisé pour prédire la différenciation chimique et la deutération des glaces interstellaires. Ainsi, j'ai construit un réseau chimique en prenant en compte les travaux expérimentaux et théoriques les plus récents. J'ai ensuite appliqué ce modèle à différents cas. J'ai par exemple montré que les glaces sont très hétérogènes et que leurs compositions sont très sensibles aux conditions physiques ainsi qu'à différents paramètres de surface. La deutération élevée du formaldehyde et du méthanol a été prédite pour une phase dense ($n_H \sim 5 \times 10^6$ cm^{-3}) et rapide ($\sim$ 5000 ans) tandis que la deutération plus faible de l'eau est prédite pour des conditions typiques de nuages moléculaires. La deutération est très sensible et peut donc etre utilisée comme un traceur des conditions physiques.

ii) Observations. J'ai été impliqué dans différents projets observationnels dont les buts étaient reliés aux problèmes de la chimie à la surface des grains. J'ai obtenu les trois résultats suivants. Nous avons montré une évolution de la deutération sélective du méthanol avec le type de la protoétoile, le rapport d'abondance [CH_2DOH]/[CH_3OD] diminuant avec la masse de la protoétoile. Une cartographie interféromètrique de l'eau deutérée vers deux protoétoiles de faible masse nous a permis de contraindre un degré relativement élevé de deutération de l'eau dans de nouvelles sources. Finalement, nous avons détecté pour la première fois plusieurs molécules organiques complexes dans un coeur prestellaire, remettant en question le scénario actuel de formation des molécules organiques complexes dans des conditions tièdes.

Mots-clés: Astrochimie, MIS: nuages, MIS: molécules, Processus moléculaires, Etoiles: formation

Vianney Taquet